

Additional CASE STUDIES

VADOSE ZONE

SCIENCE AND
TECHNOLOGY
SOLUTIONS

EDITED BY

Brian B. Looney, Ph.D.

AND

Ronald W. Falta, Ph.D.



Battelle Press

Columbus • Richland

ELECTROMAGNETIC IMAGING OF CHEMICAL AND MIXED WASTE LANDFILLS

David J. Borns

Geophysics Department
Sandia National Laboratories
Albuquerque, NM 87185-0750

We have demonstrated the use of electromagnetic imaging for waste site characterization and monitoring in arid alluvial environments. The approach is based on the radio imaging method. This continuous waveform technique measures the amplitude and phase relative to the transmitter waveform (15 MHz) as the signal propagates from borehole-to-borehole or borehole-to-surface. At one site, we used a pulsed ABEM system (radar >20MHz) for imaging in the same borehole configuration as the continuous wave system for a comparison between methods. One demonstration utilized test boreholes at the Chemical Waste Landfill, Sandia National Laboratories, Albuquerque, NM. Another demonstration was performed under a complex of burial pits named RB-11 on the Kirtland Airforce Base (KAFB), Albuquerque, NM.

At the Chemical Waste Landfill, we have obtained tomographic data from four vertical boreholes (30 m deep and 6 to 15 m separation) that straddle a chromic acid pit. Analysis of the tomographic data delineates the boundaries between alluvial facies (e.g., zones of granitic and limestone cobbles; and variations in the soil density and grain-size). Such variations may control contaminant migration at the site. The surveys also detect portions of the contaminant plumes beneath the pit.

Another survey configuration at the Chemical Waste Landfill and the RB-11 site used slant boreholes for borehole-to-borehole and borehole-to-surface surveys through a series of disposal trenches. Regions of varying conductivity in the resulting images delineate pits and contaminant plumes. An advantage of the borehole-to-surface approach is that a waste site can be characterized using only one slant or directional borehole.

ADAPTIVE SAMPLING APPROACH TO ENVIRONMENTAL SITE CHARACTERIZATION

Grace Bujewski, Sandia National Laboratories

A technology demonstration that optimizes sampling strategies and real-time data collection was carried out in August 1994 at the Kirtland Air Force Base (KAFB) RB-11 Radioactive Burial Site, Albuquerque, New Mexico. The project, funded by the Strategic Environmental Research and Development Program (SERDP), involved the application of a geostatistics-based adaptive sampling methodology and software with on-site field screening of soils for radiation, organic compounds, and metals. The software, known as Plume™, was developed at Argonne National Laboratory as part of the DOE/OTD-funded Mixed Waste Landfill Integrated Demonstration (MWLID). During the field demonstration, a SunSPARC workstation containing the geostatistical program was successfully linked via the Internet with an identical workstation at Argonne.

The objective of the investigation was to compare an innovative adaptive sampling approach that stressed real-time decision-making with a conventional Resource Conservation and Recovery Act (RCRA)-driven site characterization carried out by the Air Force. The latter investigation used a standard drilling and sampling plan as mandated by the Environmental Protection Agency (EPA). To make the comparison realistic, the same contractors and sampling equipment (Geoprobe® soil samplers) were used. In both investigations, soil samples were collected at several depths at numerous locations adjacent to burial trenches. These trenches contained low-level radioactive waste and animal carcasses; and some trenches might also have contained mixed waste. Neither study revealed the presence of contaminants appreciably above risk-based action levels, indicating that minimal to no migration away from the trenches had occurred. The combination of adaptive sampling with field screening achieved a level of confidence similar to the RCRA investigation regarding potential migration of contaminants at the site. By comparison, according to the adaptive sampling program, drilling was conducted at 28 locations (vs. 36 for the conventional investigation), 81 samples were collected (vs. 163), and 15 samples (vs. 163) were sent off-site for laboratory analysis for confirmation. In addition, the field work took 3 ½ days compared to 13 days for the RCRA investigation. These figures translate into large cost savings, because 22 percent fewer boreholes were drilled, 50 percent fewer samples were collected, and 91 percent fewer samples were analyzed off-site. Of these costs, the most significant savings involved laboratory analyses, which typically cost over \$1000 per sample. Additional costs associated with the increased level of field screening and the use of the adaptive sampling software were relatively minor compared to the savings achieved.

The UFA Method for Characterization of Vadose Zone Behavior

James L. Conca and Judith Wright, UFA Ventures, Inc., 2000 Logston Blvd, Richland,
Washington 99352 james@ufaventures.com <http://www.ufaventures.com/>

A newly-developed Unsaturated/Saturated Flow Apparatus, the UFA, decreases the time required to obtain direct measurements of most transport parameters for any porous media, even in unsaturated or relatively impermeable materials. These properties include hydraulic conductivity (K) or intrinsic permeability (k_a), diffusion coefficient (D), matric potential (ψ), electrical conductivity (G), vapor diffusivity (D_v), distribution coefficient (K_d), retardation factor (R_p), dispersivity (α) and thermal conductivity (κ). All are strong, non-linear functions of the volumetric water content (θ). The UFA achieves steady-state in hours, uniformly at any water content in any porous media, by using an adjustable, body force together with precision fluid flow. Detailed, complete and economic characterization of subsurface and engineered systems is provided by using the UFA in combination with other methods such as electrical conductivity, gas permeametry, or thermal probes. This case study describes the UFA Method and comparisons to traditional methods.

The UFA Method

The UFA instrument consists of an ultracentrifuge with a constant, ultralow flow pump that provides fluid to the sample surface through a rotating seal assembly and microdispersal system (Figure 3.3.3.2-1). The ultracentrifuge can reach accelerations of up to 20,000 g (soils are generally run only up to 1,000 g (3,000 rpm), an effective hydrostatic pressure of only 2.5 bars), temperatures can be adjusted from -20° to 150°C, and constant flow rates can be reduced to 0.001 ml/h. Effluent

from the sample is collected in a transparent, volumetrically-calibrated chamber at the bottom of the sample assembly. Using a strobe light, an observer can view the chamber while the sample is being centrifuged. Materials can be run in the UFA as recomposited samples or as samples that have been subcored directly into the UFA sample chamber. Cores of whole rock, ceramic, grout, and other solids are cast in an appropriate epoxy sleeve for use in the UFA.

There are specific advantages to using an acceleration as a fluid driving force (Nimmo *et al.*, 1987; Conca and Wright, 1992). It is a body force similar to gravity and, so, acts simultaneously over the entire system and independently of other driving forces, e.g., gravity or matric potential. Although the centrifugal force is usually thought of as an inertial effect in the non-rotating frame, it is a real force in the sample's rotating frame of reference. Centrifugation has been used to investigate moisture potential relationships in soils and rocks for over 60 years (Russell and Richards, 1938). However, the use of centrifugation to measure steady-state hydraulic conductivity on various porous media has only recently been demonstrated, for soils by Nimmo and co-workers (Nimmo *et al.*, 1987; Nimmo *et al.*, 1994) and for sediments and rocks by Conca and co-workers (Conca and Wright, 1990 and 1992; Wright *et al.*, 1994). The UFA Method is effective because it allows the operator to control the variables of flux and driving force in Darcy's Law. Darcy's Law states that the fluid flux equals the hydraulic conductivity times the fluid driving force. Under an acceleration in which water is driven by both the matric potential gradient and the centrifugal force per unit volume, Darcy's Law is given by (Nimmo *et al.*, 1987)

$$q = -K(\psi) [d\psi/dr - \rho\omega^2 r] \quad (1)$$

where q is the flux density into the sample, K is the hydraulic conductivity, ψ is the matric potential, $d\psi/dr$ is the matric potential gradient, $\rho\omega^2 r$ is the centrifugal force per unit volume, r is the radius from the axis of rotation, ρ is the fluid density, and ω is the rotation speed in radians per second.

Hydraulic conductivity can be presented as a function of either the matric potential or the volumetric water content. If sufficient flux density exists, the matric potential is much less than the acceleration, $d\psi/dr \ll \rho\omega^2 r$. Therefore, Darcy's Law may be approximated by $q = -K(\psi) [-\rho\omega^2 r]$ under these conditions. Rearranging the equation and expressing hydraulic conductivity as a function of volumetric water content, θ , Darcy's Law becomes

$$K(\theta) = q/\rho\omega^2 r \quad (2)$$

As an example, a homogeneous silt accelerated to 2500 rpm with a flow rate of 0.01 ml/h achieved hydraulic steady state in 10 hours at a target volumetric water content of 16.4% and an unsaturated hydraulic conductivity of 4×10^{-10} cm/s. The water content distribution in the sample was homogeneous to within $\pm 1\%$. Appropriate values of rotation speed and flow rate into the sample can be chosen to obtain desired values of flux density, water content, and hydraulic conductivity within the sample. Previous studies have verified the linear dependence of hydraulic conductivity on flux and the second order dependence on rotation speed. This method provides hydraulic conductivity to within $\pm 8\%$ at a volumetric water content known to within $\pm 2\%$ (Nimmo and Akstin, 1988). The high accuracy comes from the tight control on flow rate ($\pm 1\%$ non-pulsating) and rotation speed (± 5 rpm) and the ability to measure weight to ± 0.001 g.

$K(\theta)$ relationships that are known with any reliability have several applications beyond the immediate knowledge of hydraulic conductivity. $K(\theta)$ relationships can be compared with field moisture contents to yield information on subsurface flux or infiltration (see Chapter 4). Comparisons between samples can be made to investigate transport behavior of various fluids and contaminants for modelling purposes. $K(\theta)$ relationships can be used to investigate pore connectivity and grain packing issues or fracture versus matrix characteristics in rock or concrete.

An example of this is shown in Figures 3.3.3.2-2 and 3.3.3.2-3. The absolute position of a $K(\theta)$

curve along the x-axis is determined by the mean pore size, whereas the shape of the curve is determined by the pore-size distribution or variance about the mean. Figure 3.3.3.2-2a shows three examples of typical 3-day UFA runs. These soils were subcored directly into the UFA sample holder to preserve as much of the internal structure as possible. Sample 1 is a sand, sample 2 is a silt, and sample 3 is a silt loam with almost no sand. Figure 3.3.3.2-2b shows the grain size distribution of these samples. As is usual in a UFA run for soils or sediments, the samples were slowly vacuumed-saturated and the saturated hydraulic conductivity (K_s) measured using a traditional constant-head or falling-head set-up depending upon the K_s . The samples were then put into the UFA at low speed and high flow rate (300 rpm and 50 ml/hr for the sand; 1000 rpm and 5 ml/hr for the silt loam) for the first unsaturated point. Steady-state was reached in less than 1 hour for the sand and in less than 2 hours for the silt loam because of the relatively high flow rates. The samples were weighed for water content and then the speed and flow rate adjusted to set the next unsaturated point. This was repeated until the final point. The samples are then oven-dried to determine the dry weight which is then used to determine all of the subsequent water contents. As the samples desaturated and the flow rate was decreased, steady-state was reached in slightly longer times, up to twelve hours for the final points. The number of points measured using the UFA, the beginning flow rates and rotation speeds depend upon the saturated hydraulic conductivity of the sample, e.g., rock cores versus soils versus concrete will all have different ranges of operation. For these three samples, the runs were stopped at about 8×10^{-9} cm/s. The routine operation of the UFA is from 10^{-4} cm/s to 10^{-11} cm/s. Figure 3.3.3.2-2 illustrates the control of grain size on the gross hydraulic behavior, i.e., the finer the sample, the more the $K(\theta)$ curve is displaced towards the higher water contents. However, it is the pore size distribution that determines the hydraulic properties of the sample not the grain size, although the grain size distribution is the most important factor in the pore size distribution. Samples

with similar grain size distributions usually have similar hydraulic properties (Arya and Paris, 1981) and this has been observed in many cases (Wright et al., 1994). However, occasionally samples with similar grain size distributions are packed or arranged differently such that the pore size distribution or mean pore size is different, and the $K(\theta)$ curve should reflect that difference. Figure 3.3.3.2-3 shows the $K(\theta)$ curves and the grain size distributions for two samples with very similar grain size distributions and bulk density. Both have $K(\theta)$ curves that are similar in shape but are displaced, indicating a similar variance about a different mean pore size.

Figures 3.3.3.2-2 and 3.3.3.2-3 illustrate an important advantage of using the UFA to directly determine $K(\theta)$ relationships. UFA-generated $K(\theta)$ curves exhibit the kinks and other structures that reflect subtle pore-size distribution and sorting effects as well as pore connectivity changes associated with desaturation, structures which are not reflected in $\psi(\theta)$ relationships.

John Nimmo and co-workers at the US Geological Survey in Menlo Park developed a steady-state centrifuge method (SSCM) in the early 1980's for investigating problems in soil physics (Nimmo *et al.*, 1987) such as determining solutions to the Richards equation. Although both the UFA and the SSCM use an acceleration as the fluid driving force, they are different instruments that developed independently. The internal instrumentation is also different for each system. The SSCM is a pressure-controlled method that arose out of soil physics applications and the UFA is a flux-controlled method that arose out of geologic applications, e.g., contaminant transport in geologic sediments and whole rock cores. In the SSCM, a 5 cm-diameter, 4 cm-long soil core is bounded on the top and bottom by changeable porous ceramic plates of fixed saturated hydraulic conductivity and potential characteristics. A reservoir of water sits atop the sample above the upper porous plate and leaks into the sample as it is spinning. Use of overflow points determine reservoir depth, and control of the flux is achieved in the region about the saturated conductivity of each of the

commercially available ceramic plates. The bottom of the sample is a free water surface and the distribution and magnitude of the matric potential within the sample is extremely well-known. Nimmo also can measure electrical conductivity in the SSCM apparatus while the sample is rotating (Nimmo, 1990).

The UFA, on the other hand, is a flux-controlled system and is open at either end. The pressures at the top and bottom of the sample are not fixed at any particular value. The matric potential at all points throughout the sample is allowed to attain whatever magnitude is in equilibrium with the choice of flux and rotation speed. Because the driving force is an acceleration, the bottom of the sample does not need to saturate in order for water to leave the sample, or the saturated layer is ultrathin, removing the effect in traditional soil columns that $\psi = 0$ for a significant amount of sample at the bottom of the sample. Although the acceleration can be used to calculate an equivalent pressure for comparison with the matric potential, the acceleration is not a pressure, but is a body force acting at all points simultaneously within the system, whereas the matric potential is a surface force acting as a function of distance and is slow to respond to changes in water content especially at low water contents. In the UFA, redistribution of water and attainment of hydraulic steady-state occurs rapidly, within hours, in response to the imposed acceleration and flux. The water content within the sample also attains the steady-state value at every point, and $d\psi/dr \rightarrow 0$ throughout the sample. If the sample is homogeneous, then the water content will be uniform throughout the sample and is easily measured (Nimmo *et al.*, 1987; Conca and Wright, 1992). In the hundreds of relatively homogeneous samples measured thus far at all speeds and fluxes, water content has been uniform to within $\pm 1\%$. This indicates that the system is very close to $d\psi/dr = 0$ and that any buildup of water at the sample bottom is negligible. If the sample is heterogeneous, such as a silt lens in a coarse sand or a fractured tuff rock core, then each component reaches its own steady-state water

content, but $d\psi/dr$ still approaches zero throughout the sample.

It should be noted that the use of the UFA to achieve hydraulic steady-state with a flux is completely different than the use of centrifuges to measure the matric potential, or water retention, as is traditionally done for the petroleum industry by not having flow into the sample while it is spinning. Without a flux into the sample, there is no steady-state and there will be a non-uniform water distribution from top to bottom. There is a fundamental difference in these two applications. The traditional method of using a centrifuge to determine fluid retention, or matric potential, in a sample makes the assumption that a pressure and an acceleration are equivalent in their effect. This is only true at equilibrium when the sample is no longer draining, i.e., the sample drains at a particular speed until the matric potential gradient is equivalent and opposite to the centrifugal force at each point. The speed is then raised to a new value and the sample drains again until the matric potential gradient is again equivalent and opposite to the centrifugal force. To calculate this tension or pressure difference, Hassler and Brunner (1945), and many others since, use some form of the following expression

$$\Delta P = \rho \omega^2 / 2g (r_1^2 - r_2^2) \quad (3)$$

where ΔP is the equivalent pressure difference (cm of H_2O), g is the acceleration due to gravity (981 cm/s^2), r_1 is radial distance to the sample top (cm), r_2 is radial distance to the sample bottom (cm), ω is the rotation speed (radians/s), and ρ is the fluid density (g/cm^3). This tension can be thought of as similar to a negative hydrostatic pressure. For the geometries used in the UFA, some routine equivalent pressures are given in Table 1 (in bars).

But the situation changes when there is a flux into the sample while it is rotating and the system reaches steady-state instead of equilibrium. With a flux, the difference in pressure along the sample approaches zero and the only significant Darcy driving force is the centrifugal force, which in the

rotating frame of reference of the sample is a true force. The centrifugal force is a body force which acts instantaneously and simultaneously throughout the sample. The pressure, or tension, is a surface force which depends upon distance and local properties. The entire system responds rapidly to an imposed acceleration, but slowly to a negative pressure gradient, especially at low water contents when the hydraulic conductivity is so low. For discussion purposes only, one might think of the acceleration as a "fast force" while the tension is a "slow force." In the presence of a constant flux and acceleration, the system is never allowed to reach equilibrium. The ΔP expression of equation (3) does not apply in the calculation of the hydraulic conductivity, because the system is not at equilibrium but is at steady-state, and there is no difference in the matric potential over any significant volume of the sample.

TABLE 1. UFA Equivalent Pressures

Rotation Speed (rpm)	Pressure (bar)
300	.04
600	.20
800	.30
1000	.47
1200	.68
1500	1.1
1800	1.5
2100	2.1
2500	3.0
3000	4.2
3500	5.8
4000	7.6

5000	12
6000	17
7000	23
8000	30
9000	38
10000	47

Several variations of the UFA have been developed to accommodate the different aspects of multiphase/multicomponent systems encountered in mixed waste environments. Three rotor sizes and three rotating seal designs (face, mechanical and ferromagnetic) accommodate applications such as non-aqueous phase liquids, tank waste sludge, and multiphase flow. The prototype face seal is ideal for routine aqueous systems, while the ferromagnetic liquid-metal rotating seal allows temperature-abating sealing against vapor loss during operation with volatile organic compounds. The mechanical seal allows minimal internal contamination during adsorption/retardation flow experiments using heavy metals, lanthanides and actinides. Excellent agreement among the different designs of the UFA have been demonstrated for splits of the same samples, and excellent agreement between the UFA and other techniques has also been demonstrated (Wright *et al.*, 1994, Lindenmeier *et al.*, 1995). Various sample holders of different materials, e.g., teflon, titanium, stainless steel, copolymers, and nylon, address many chemical compatibility requirements and can accommodate sample sizes between 20 cm³ and 200 cm³.

The van Genuchten/Mualem Method

As discussed in Khaleel *et al.* (1995) and van Genuchten *et al.* (1991), several theoretical models can be used to estimate unsaturated hydraulic conductivity (Toledo *et al.*, 1990; Mualem, 1976; Jackson, 1972; Millington and Quirk, 1961; Kunze *et al.*, 1968; Marshall, 1958; Burdine, 1953;

Childs and Collins-George, 1950). Most comparison studies with the UFA were carried out with the van Genuchten/Mualem approach (van Genuchten, 1980; Mualem, 1976; Hopmans *et al.*, 1988; Carsel and Parrish, 1988; Jensen and Mantoglou, 1992; Hills *et al.*, 1989). Van Genuchten (1980) derived the following empirical relationship to describe moisture retention data

$$\theta = \theta_r + \frac{(\theta_s - \theta_r)}{[1 + |\alpha\psi|^n]^m} \quad (4)$$

where θ is the volumetric water content, θ_s is the saturated water content, θ_r is the residual water content, α is a curve-fitting parameter (equivalent to the reciprocal of the air-entry value), ψ is the matric potential or pressure head, n is another curve-fitting parameter, and $m = (1 - 1/n)$. The Mualem (1976) model is used to predict the hydraulic conductivity, K , from retention data

$$K(S_e) = K_s S_e^l \left[\frac{f(S_e)}{f(1)} \right]^2 \quad (5)$$

where

$$S_e = (\theta - \theta_r) / (\theta_s - \theta_r) \quad (7)$$

S_e is the effective degree of saturation (also called the reduced water content, $0 \leq S_e \leq 1$), K_s is the saturated hydraulic conductivity, and l is a pore-connectivity parameter. Mualem (1976) estimated that the optimum pore-connectivity parameter for many ordinary soils was about 0.5. However, this connectivity can vary from -5 to +20, and may account for the discrepancies in predicting unsaturated behavior in non-ideal soils and fractured media such as rock and concrete. Using the Mualem (1976) model, van Genuchten (1980) derived a closed-form analytic solution to equation (5) to predict the relative hydraulic conductivity (K_r) at specified moisture contents,

$$K_r = S_e^1 \{1 - [1 - S_e^{1/m}]^m\}^2 \quad (8)$$

$$K(\theta) = K_s K_r \quad (9)$$

With the match point for the hydraulic conductivity at some arbitrary moisture content, θ_0 , and associated hydraulic conductivity, K_0 , equation (7) in the Mualem (1976) model, is redefined as

$$K(S_e) = K S_{e0} \left[\frac{f(S_e)}{f(S_{e0})} \right]^2 \quad (10)$$

where S_{e0} is given by

$$S_{e0} = S_{e0}(\theta_0) = (\theta_0 - \theta_r) / (\theta_s - \theta_r) \quad (11)$$

For the restricted case in which $m = 1 - 1/n$, equation (10) becomes (Luckner *et al.*, 1989)

$$K(S_e) = K(S_{e0}) \left[\frac{(S_e)}{(S_{e0})} \right]^1 \left[\frac{1 - (1 - S_e^{1/m})^m}{1 - (1 - S_{e0}^{1/m})^m} \right]^2 \quad (12)$$

In the following comparisons, laboratory water retention data were analyzed using the RETC and RETC-GMI programs (van Genuchten *et al.*, 1991), computer programs that use a nonlinear, least squares curve-fitting procedure to match the measured moisture retention data to equation (4). In estimating the unsaturated hydraulic conductivity function from water retention data, several parameter estimation procedures can be used. A predictive method, equation (8), uses the measured moisture retention data and saturated conductivity, K_s , as a match point. A scaled-predictive method, equation (12), uses moisture retention data and a measured unsaturated conductivity as a match point. For most predictive methods the pore connectivity parameter, ι , is typically fixed at 0.5 and θ_r , θ_s , α , and n are fitted to the moisture retention data with $m = 1 - 1/n$. Estimation techniques have routinely been used to obtain the unsaturated hydraulic conductivity versus moisture content

relationships for soils in the moderate to high moisture regime (Yates *et al.*, 1992; Stephens and Rehfeldt, 1985). Comparison of these techniques with the UFA explores their application to lower moisture contents.

Comparison of Unsaturated Hydraulic Conductivity Determined Using the UFA

Method, van Genuchten/Mualem Methods, and Other Methods

Comparisons between centrifuge methods, soil columns, van Genuchten/Mualem estimations and lysimeter measurements on the same materials have shown general agreement (Nimmo *et al.*, 1994; Wright *et al.*, 1994; Lindenmeier *et al.*, 1995; Khaleel *et al.*, 1995; Conca and Wright, 1998). Figures 3.3.3.2-4 and 3.3.3.2-5 illustrate some comparisons for soil and rock. Several more are given in Conca and Wright (1998). Most water retention data was obtained using traditional methods, e.g., Tempe cells, pressure plates, hanging water columns, and psychrometry.

Figure 3.3.3.2-4 shows a comparison between UFA results and a van Genuchten/Mualem estimation for a sand from the Hanford Site in Washington State (courtesy of Peter Wierenga's group at the University of Arizona). The RETC fit to the retention data was very good. The deviations between the RETC-predicted unsaturated hydraulic conductivity and the UFA direct measurements come at the lowest water contents, because of the differences in the residual water contents between the two methods. The saturated conductivities were almost identical.

Figure 3.3.3.2-5 shows results from two separate UFA runs on rock cores of non-welded volcanic tuff compared to a van Genuchten/Mualem estimation using water retention data from splits of the same core (courtesy of Daniel B. Stephens and Associates). It is noteworthy that both the van Genuchten estimation and the UFA work so well for a material that is not a soil. However, being a non-welded tuff, this rock core is friable and little more than a slightly cemented soil or sediment. In this instance, the lower end of the curves fit the best because of the close fits of the residual water

contents. The only significant difference is among the values of the saturated hydraulic conductivities, which were determined separately using constant head methods (Klute and Dirksen 1986). This has been the general finding of comparisons between direct measurements and estimation methods, such as van Genuchten/Campbell/Brooks-Corey/Mualem, etc. Estimation methods are very sensitive to the choices of residual water content and match point (Stephens and Rehfeldt-1985), but agree very well with direct measurements when the residual water contents and match points are similar (Wright *et al.* 1994; Khaleel *et al.* 1995).

References

- Arya, L. M., and J. F. Paris, A physicoempirical model to predict the soil moisture characteristic from particle-size distribution and bulk density data, *Soil Science Society of America Journal*, 45, 1023-1030, 1981.
- Burdine, N. T., Relative permeability calculations from pore-size distribution data, *Trans. Am. Inst. Min. Metall. Pet. Eng.*, 198, 71-77, 1953.
- Carsel, R. F., and R. S. Parrish, Developing joint probability distributions of soil water retention characteristics, *Water Resources Research*, 24, 755-769, 1988.
- Childs, E. C., and N. Collis-George, The permeability of porous materials, *Proc. R. Soc. London, Ser. A*, 201, 392-405, 1950.
- Conca, J. L., and J. V. Wright, Diffusion Coefficients in Gravel Under Unsaturated Conditions, *Water Resources Research*, 26, 1055-1066, 1990.
- Conca, J. L., and J. V. Wright, Diffusion and Flow in Gravel, Soil, and Whole Rock, *Applied Hydrogeology*, 1, 5-24, 1992.
- Conca, J. L. and J. V. Wright, The UFA Method for Rapid, Direct Measurements of Unsaturated Soil Transport Properties, *Australian J. of Soil Research*, 36, 291-315, 1998.

Hassler, G. L., and E. Brunner, Measurement of Capillary Pressures in Small Core Samples, *Trans. Am. Inst. Min. Metall. Eng.*, 160, 114-123, 1945.

Hills, R. G., D. B. Hudson, I. Porro, and P. J. Wierenga, Modeling one-dimensional infiltration into very dry soils, 2, Estimation of soil-water parameters and model predictions, *Water Resources Research*, 25, 1271-1282, 1989.

Hopmans, J. W., H. Schukking, and P. J. J. F. Torfs, Two-dimensional steady state unsaturated water flow in heterogeneous soils with autocorrelated soil hydraulic properties, *Water Resources Research*, 24, 2005-2018, 1989.

Jackson, R.D., On the calculation of hydraulic conductivity, *Soil Science Society of America Journal*, 36, 380-382, 1972.

Jensen, K. H., and A. Mantoglou, Applications of stochastic unsaturated flow theory, numerical simulations, and comparisons to field observations, *Water Resources Research*, 28, 269-284, 1992.

Khaleel, R., J. F. Relyea, and J. L. Conca, Estimation of van Genuchten-Mualem Relationships to Estimate Unsaturated Hydraulic Conductivity at Low Water Contents, *Water Resources Research*, 31, 2659-2668, 1995.

Klute, A., and C. Dirksen, Hydraulic Conductivity and Diffusivity: Laboratory Methods, In *Methods of Soil Analysis, Part 1, Physical and Mineralogical Methods*, Second Edition, ed. A. Klute, pp. 687-734, American Society of Agronomy, Inc., and Soil Science Society of America, Inc., Madison, Wisconsin, 1986.

Kunze, R. J., G. Uehara, and K. Graham, Factors important in the calculation of hydraulic conductivity, *Soil Science Society of America Journal*, 32, 760-765, 1968.

Lindenmeier, C. W., R. J. Serne, J. L. Conca, A. T. Owen, and M. I. Wood, *Solid Waste Leach Characteristic and Contaminant-Sediment Interactions, Volume 2: Contaminant Transport Under*

Unsaturated Conditions, Technical Report PNL-10722, Pacific Northwest Laboratory, Richland, WA, 60 p., 1995.

Luckner, L., M. T. van Genuchten, and D. R. Nielsen, A Consistent Set of Parametric Models for the Two-Phase Flow of Immiscible Fluids in the Subsurface, *Water Resources Research* 25, 2187-2193, 1989.

Marshall, T. J., A relation between permeability and size distribution of pores, *Journal of Soil Science*, 9, 1-8, 1958.

Millington, R. J., and J. P. Quirk, Permeability of porous solids, *Trans. Faraday Society*, 57, 1200-1207, 1961.

Mualem, Y., A new model for predicting the hydraulic conductivity of unsaturated porous media, *Water Resources Research*, 12, 513-522, 1976.

Nimmo, J. R., Experimental Testing of Unsaturated Flow Theory at Low Water Contents in a Centrifugal Field, *Water Resources Research*, 26, 1951-1960, 1990.

Nimmo, J. R., and K. C. Akstin, Hydraulic Conductivity of a Sandy Soil at Low Water Content After Compaction By Various Methods, *Soil Science Society of America Journal*, 52, 303-310, 1988.

Nimmo, J. R., J. Rubin, and D. P. Hammermeister, Unsaturated Flow in a Centrifugal Field: Measurement of Hydraulic Conductivity and Testing of Darcy's Law, *Water Resources Research*, 23, 124-134, 1987.

Nimmo, J. R., D. A. Stonestrom, and K. C. Akstin, The Feasibility of Recharge Rate Determination Using the Steady-State Centrifuge Method, *Soil Science Society of America Journal*. 58, 49-56, 1994.

Russell, M. B., and L. A. Richards, The Determination of Soil Moisture Energy Relations by Centrifugation, *Soil Science Society of America Proceedings*, 3, 65-69, 1938.

Stephens, D. B., and K. R. Rehfeldt, Evaluation of Closed-Form Analytical Models to Calculate Conductivity in a Fine Sand, *Soil Science Society of America Journal*, 49, 12-19, 1985.

Toledo, P.G., R. A. Novy, H. T. Davis, and L. E. Scriven, Hydraulic conductivity of porous media at low water content, *Soil Science Society of America Journal*, 54, 673-679, 1990.

van Genuchten, M. T., A closed-form solution for predicting the conductivity of unsaturated soils, *Soil Science Society of America Journal*, 44, 892-898, 1980.

van Genuchten, M. T., Leij, F. J., and Yates, S. R., The RETC Code for Quantifying the Hydraulic Functions of Unsaturated Soils, *Rep. EPA/ 600/2-91/095*, U. S. Environ. Prot. Agency, Washington, D. C., 1991.

Wright, J. V., J. L. Conca, and X. Chen, *Hydrostratigraphy and Recharge Distributions from Direct Measurements of Hydraulic Conductivity Using the UFA™ Method*, PNL Technical Report PNL-9424, Pacific Northwest Laboratory, Richland, WA, 1994.

Yates, S. R., M. T. van Genuchten, A. W. Warrick, and F. J. Leij, Analysis of measured, predicted, and estimated hydraulic conductivity using the RETC computer program, *Soil Science Society of America Journal*, 56, 347-354, 1992.

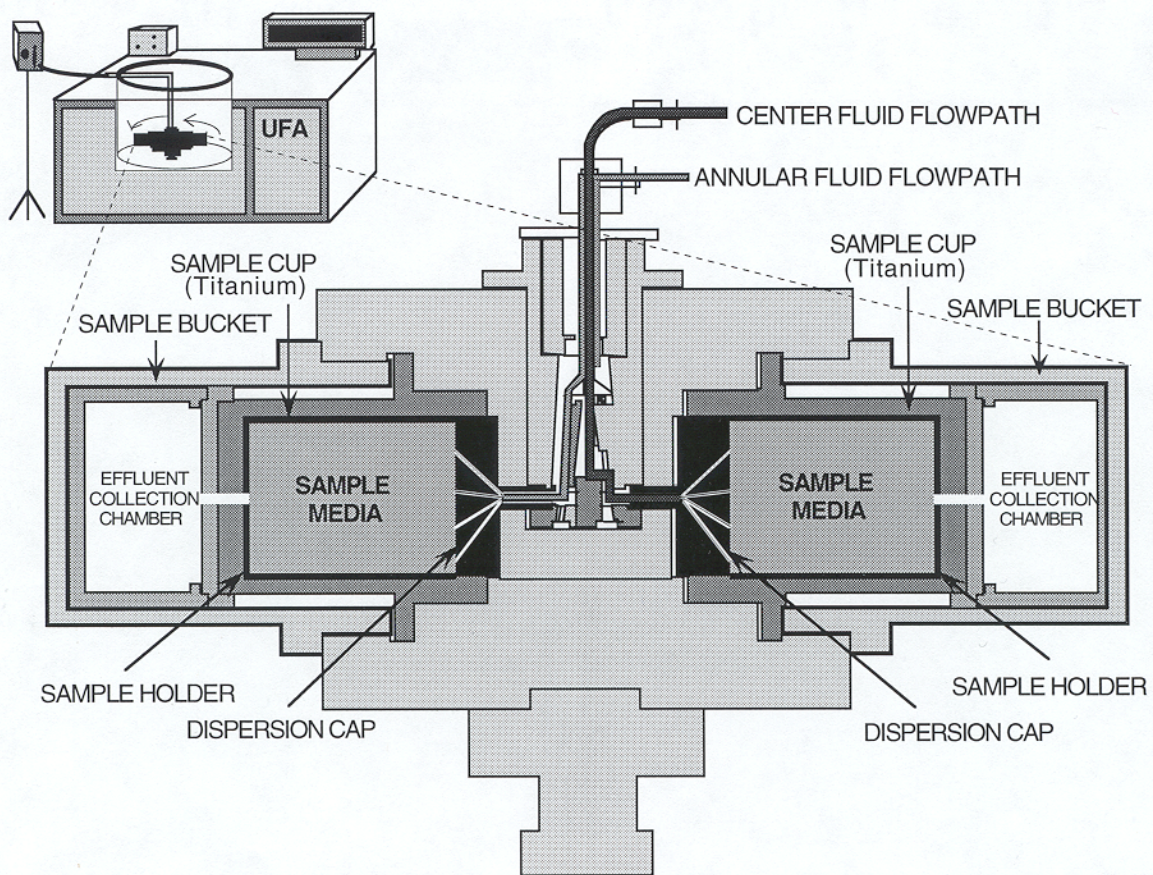


Figure 3.3.3.2-1. UFA Rotor with Seal Assembly

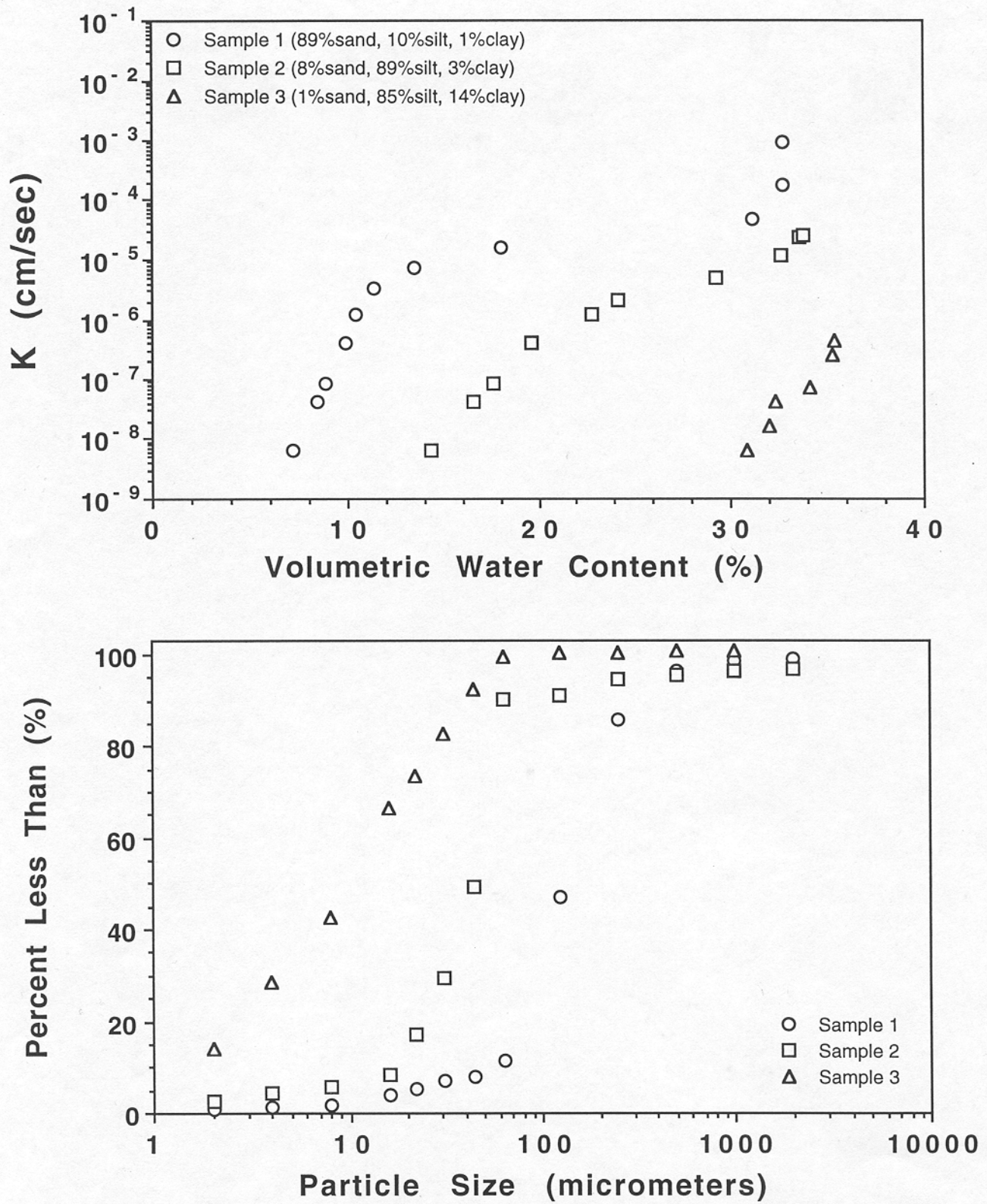


Fig. 3.3.3.2-2.a) Hydraulic conductivity as a function of water content and b) grain size distribution in a sand, a silt and a silt loam.

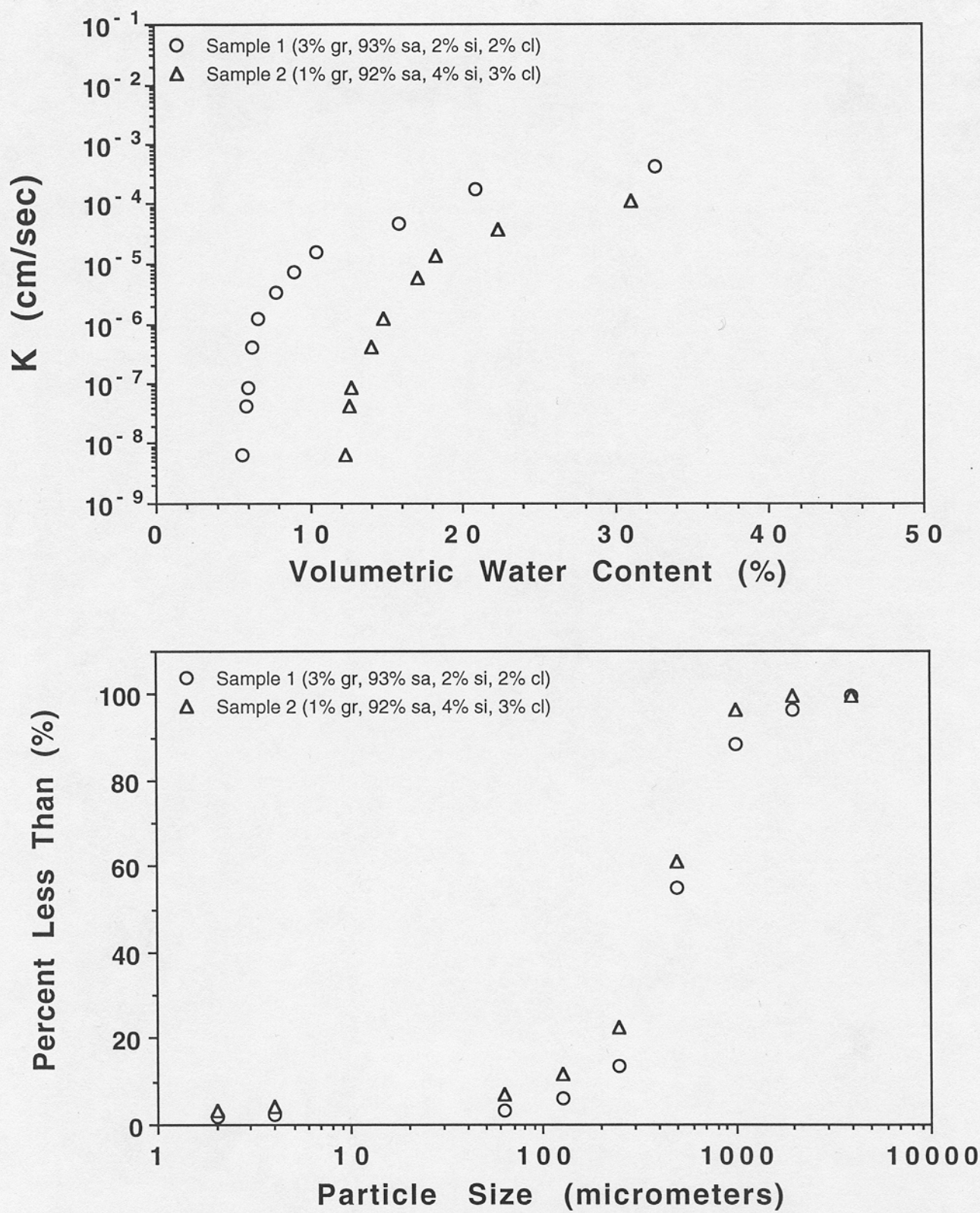


Fig. 3.3.3.2-3.a) Hydraulic conductivity as a function of water content and b) grain size distribution in two sands with the same grain size distribution.

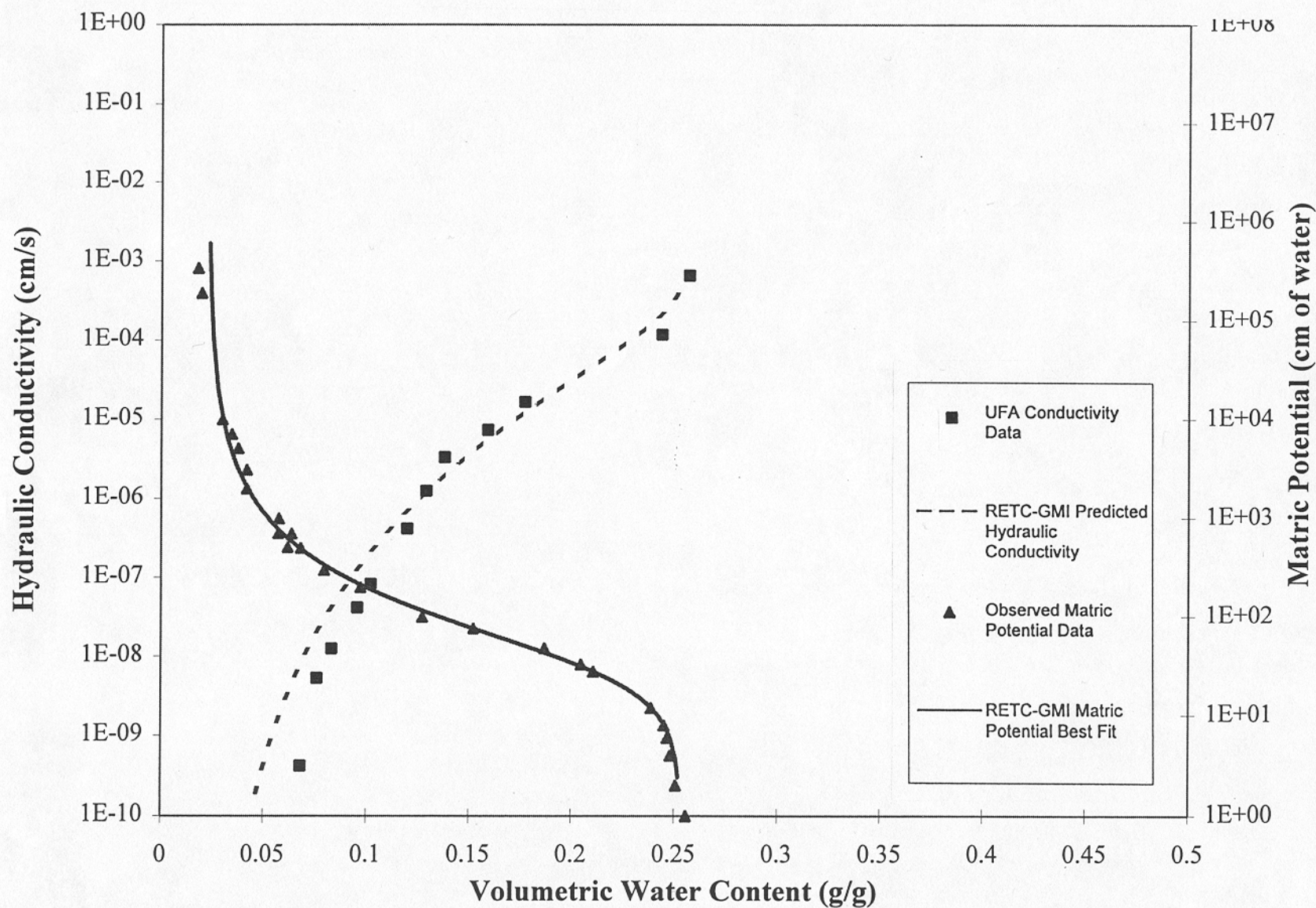


Fig. 3.3.3.2-4. Comparison of direct UFA measurements to prediction of hydraulic conductivity from matric potential data using van Genuchten/Mualem (RETC) for a sandy soil (courtesy of Peter Wierenga's group at the University of Arizona).

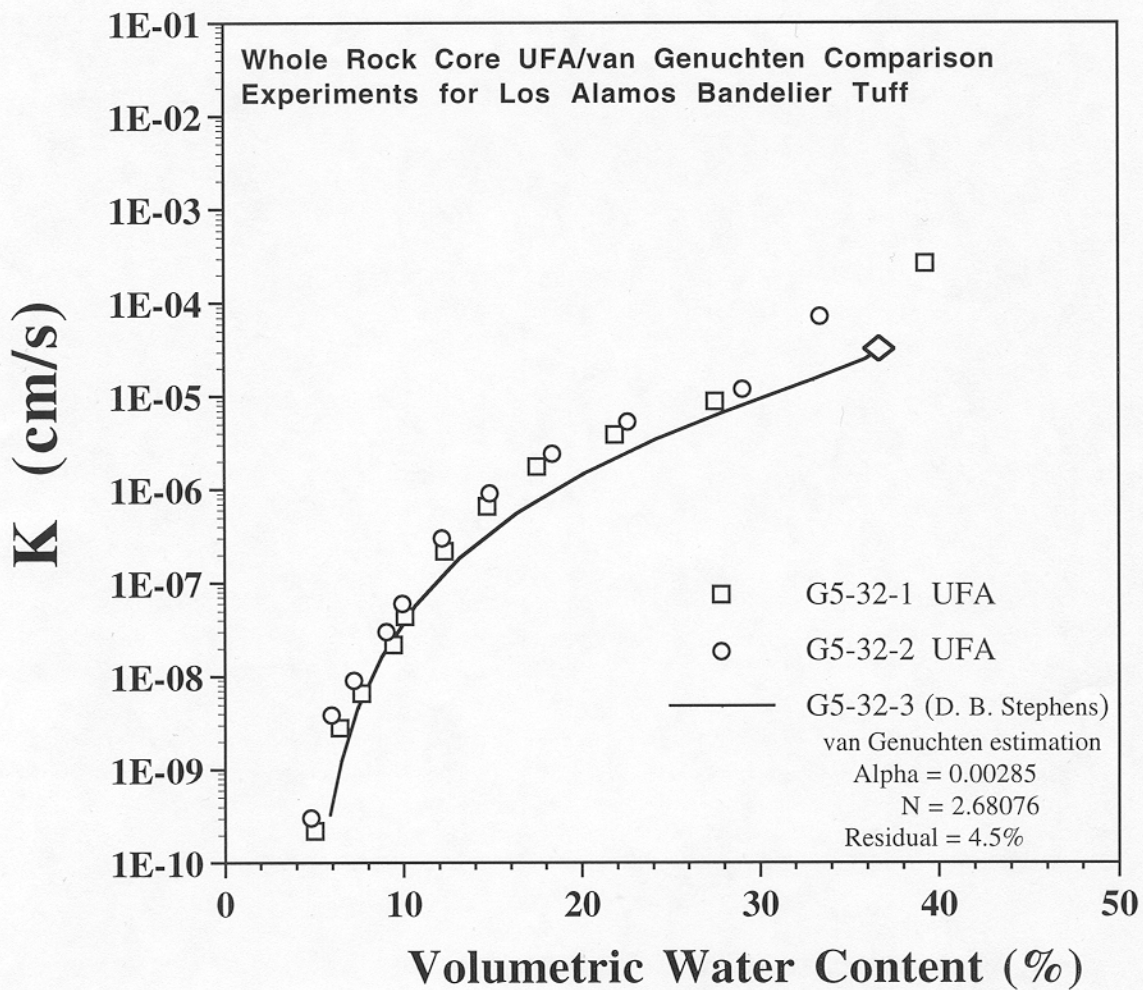


Figure 3.3.3.2-5. Hydraulic Conductivity Results Using UFA and van Genuchten/Mualem on splits of the same rock core.

MONITORING REMEDIATION ACTIVITIES USING THE MULTISCAN SYSTEM

Sandi Dunn, Science & Engineering Associates

Cecelia Williams, Sandia National Laboratories

MULTISCAN™ – CASE STUDY #1: LOS ALAMOS NATIONAL LABORATORY VAPOR EXTRACTION SYSTEM

INTRODUCTION

In 1993, Los Alamos National Laboratory (LANL) initiated a study to determine the feasibility of expanding an existing radioactive waste site. Of primary concern was adequate characterization of the site and assurance that there was no liquid or sorbed waste in the expansion area. Soil gas analysis in the area showed the presence of chlorinated hydrocarbons, but whether the product was sorbed or free vapor phase was unknown. The site in question was large (several hundred feet) and the underlying geology was layered, with several of the layers being highly fractured. Additionally, the site was located on a mesa approximately 600 ft wide in the area of question. The effect of air influx via the mesa walls on the contaminant plume was unknown. LANL, with help from Science and Engineering Associates (SEA) and ERM, undertook an aggressive program to ascertain the viability of expanding the radioactive waste site. The program included characterization of the site, and the designing and testing of a remediation system for the existing contaminant plume.

SETTING

Extensive characterization of the site was conducted in 1994. Eight drill holes were bored in the area to depths ranging to 340 ft. Five distinct geologic layers were encountered, all of which were part of the Bandelier Tuff. The layers ranged in thickness from 10 to over 150 ft, and several of the layers were highly fractured. *In situ* air flow measurements were conducted. Straddle packer measurements provided discreet permeability data, while open borehole anemometry measurements determined air production as a function of depth, showing how the different geologic layers contributed to total flow from the wells. Thermocouple psychrometers

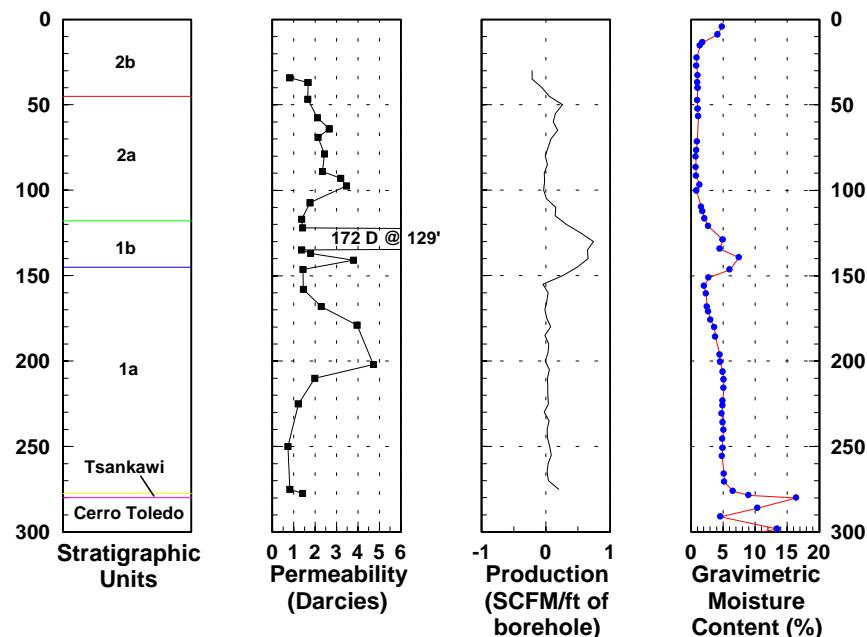


Figure 1: Sample of characterization data collected at the site

measured the matrix potential of the medium with depth. Figure 1 shows some of the data collected in one of the monitoring wells. Numerous chlorinated hydrocarbons, including trichloroethane (TCA), trichloroethylene (TCE), and tetrachloroethylene (PCE), were detected in the quarterly samples from monitoring wells in the area. Contaminant concentrations were highest in the first 100 ft bgs, but were found at all depths measured (up to 250 ft bgs).

REMEDATION

Using the characterization data, a Pilot Vapor Extraction Test (PVET) was designed. The PVET was performed within the plume at least 150 ft away from the nearest waste burial point, and thus did not significantly impact the source area. The extraction system was run for 34 days. A MultiScan™ system was used to monitor the PVET. The vapor monitoring points were embedded in monitoring boreholes using the SEAMIST™ instrumentation system, and were located 20 to 180 ft from the extraction well. The monitoring system used a palmtop computer to control analog/digital hardware, a 16-port sampling manifold, and a photoacoustic gas analyzer. The analyzer measured TCA, TCE, Freon, CCl₄, CO₂, and water vapor. The system also measured pressures at all of the monitoring ports, as well as barometric pressure and temperature. Figure 2 shows a plan view of the PVET, including locations of the extraction and monitoring wells.

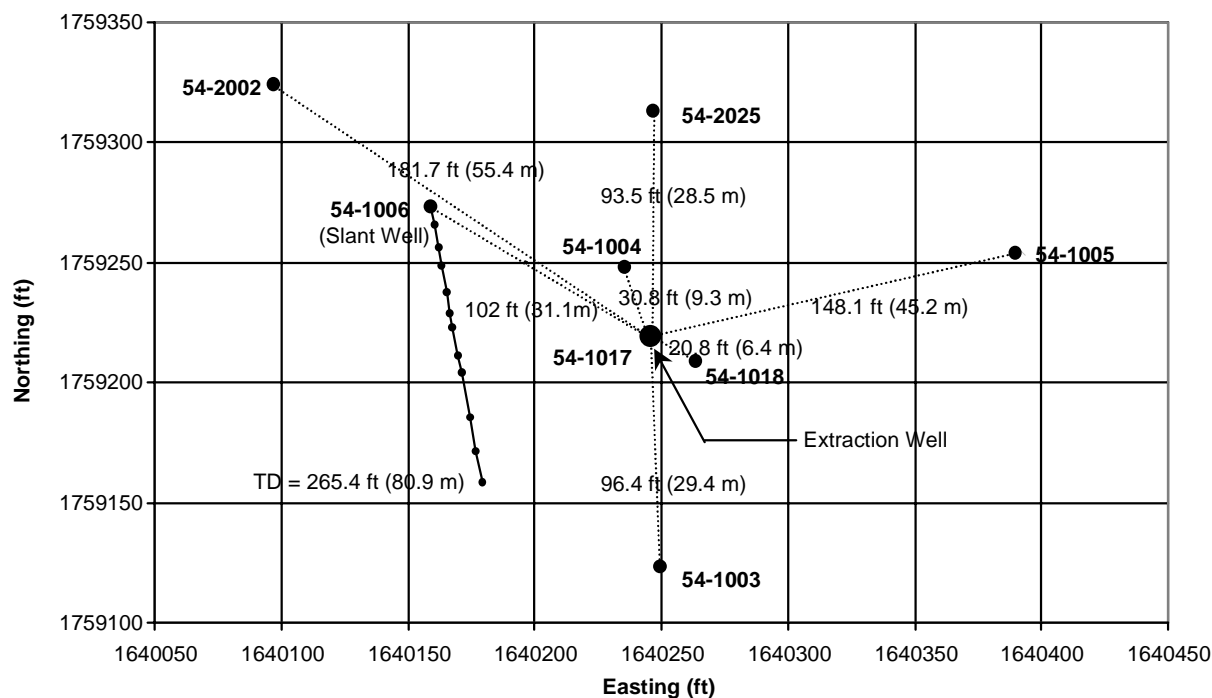


Figure 2: Plan view of the PVET showing extraction and monitoring well locations and depths

RESULTS

At 4-hour intervals for the duration of the test, data were collected that included information on the background, the extraction, and the monitoring of the plume rebound. Figure 3 shows a data record obtained during the test from the monitoring well closest to the extraction well. The graph indicates measured concentrations of TCA over time for four different sampling elevations. The plot clearly denotes where the TCA vapor plume was affected by the extraction

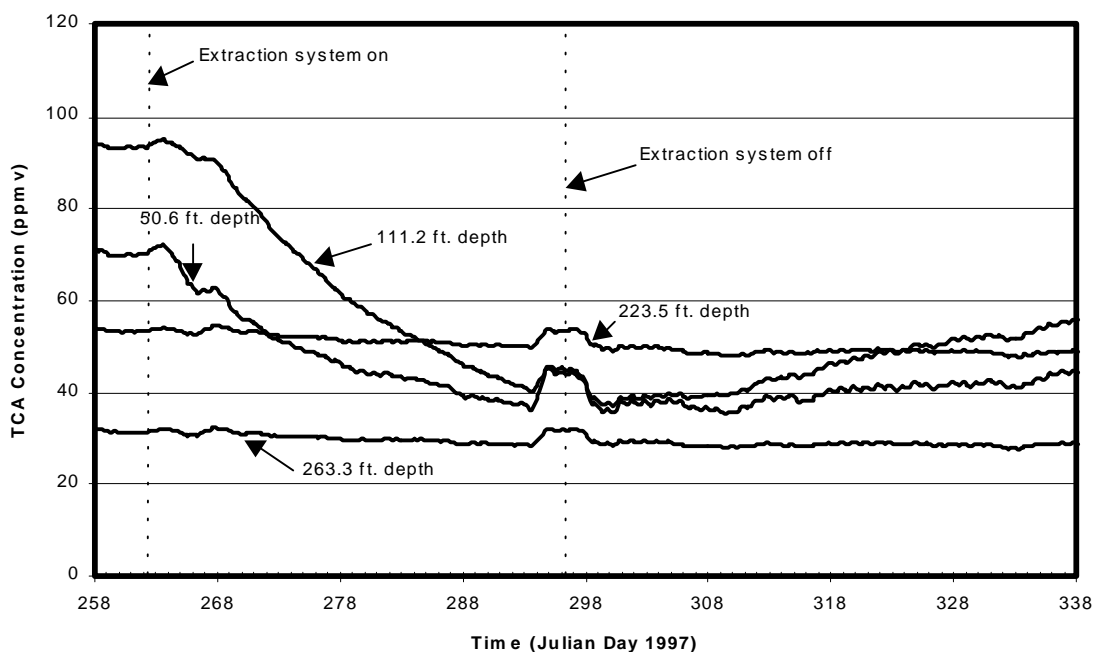


Figure 3: Data record taken with the MultiScanTM monitoring system of TCA concentration with time. Data were collected in monitoring well 54-1018, the well closest to the extraction well.

well, as well as the vapor recovery after the extraction system was turned off. Figure 4 shows several contours or plots of subsurface pressure histories that were collected with the system and demonstrate the influence of barometric pressure changes. Using the measured data, it was shown that the extraction system used in the test was capable of extracting all monitored volatile organic compounds (VOCs) within a radius of influence of 120 to 140 ft and to the depth of the bottom of the extraction well (150 ft). By extrapolating the data, clean-up time was estimated to be 4 months.

CONCLUSION

Data obtained with the scanning system were instrumental in understanding the test results, and predicting future results in the area. Measured concentration histories of specific contaminants provided data to determine:

- the extraction rate of the compounds with time,
- the radial extent and depth of the impacted volume by the extraction process, and
- an estimate for the total time required to remediate the site.

The data also showed that the vapor recovery after the extraction was turned off did not show classic rebound due to sorbed contaminants in the soil. Rather, the recovery was due to diffusion.

Measured concentration histories of CO₂ helped the researchers to determine that there was a significant matrix air recharge from the atmosphere during extraction. Measured pressure histories helped confirm the presence of fractured regions within the medium and demonstrated a clear response between the soil gas pressure and barometric pressure changes.

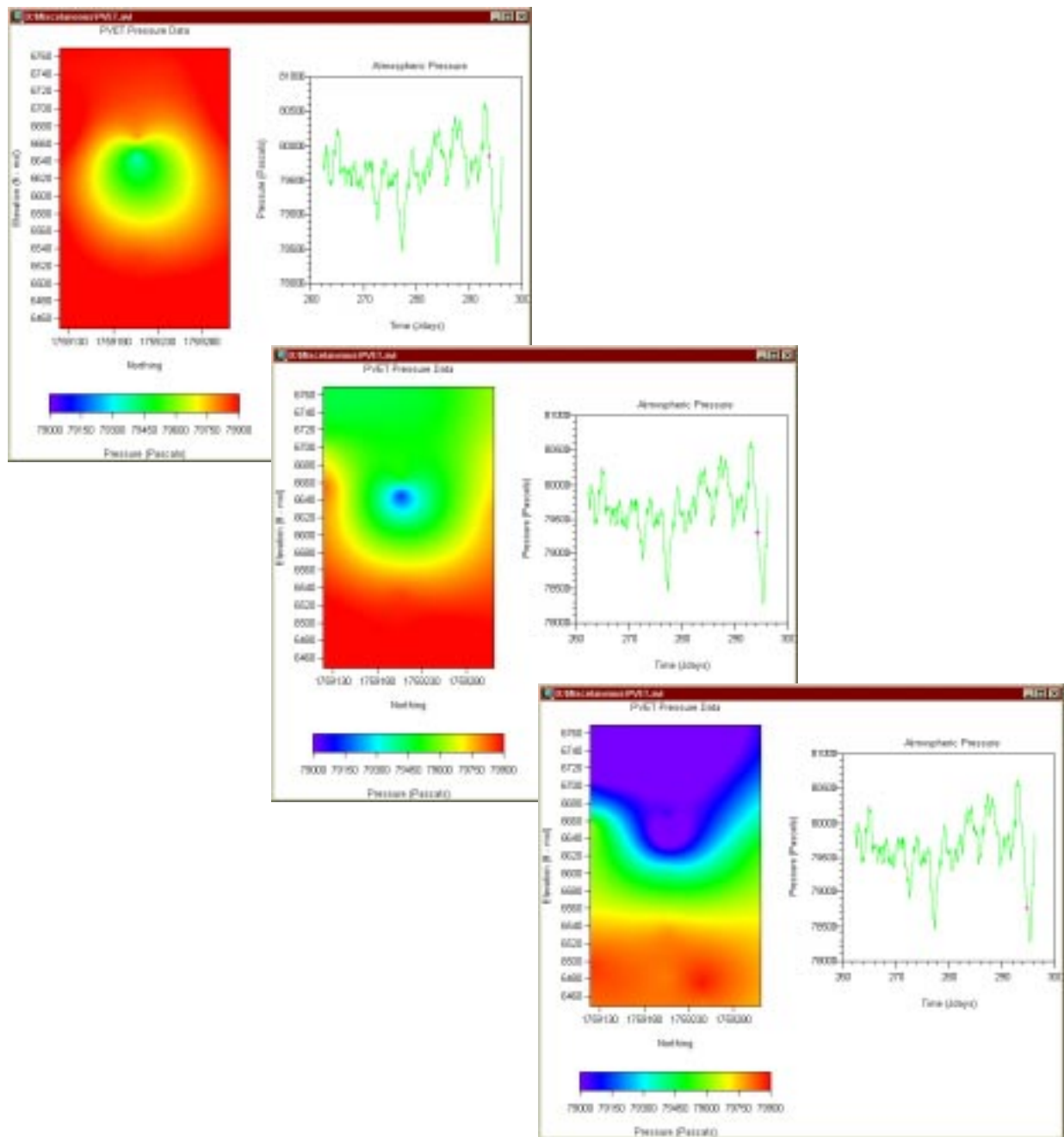


Figure 4: Contours/plots of several subsurface pressure histories collected with the system

MULTISCAN™ – CASE STUDY #2: SUBSURFACE BARRIER VERIFICATION

INTRODUCTION

In situ barrier emplacement techniques for the containment of high-risk contaminants in the vadose zone are currently being developed by the Department of Energy (DOE). These barriers are primarily intended for use in the high-risk sites where few viable alternatives exist to stop the movement of contaminants in the near term. Assessing the integrity of the barrier once it is emplaced, as well as during its anticipated life, is a very difficult but necessary requirement. While surface-based geophysical techniques such as cross borehole electromagnetic surveys, ground penetrating radar, and electrical resistance tomography can detect the presence of emplaced barrier materials, their resolution is typically inadequate for leak detection purposes. Nuclear borehole logging is capable of greater resolution, but because of its limited penetration, would require an excessive number of boreholes, rendering it impractical for barrier assessment. Hydraulic testing in the vadose zone is not likely, because the introduction of water to the contained volume would mobilize contaminants otherwise in an immobile state. Only gaseous tracer testing of barrier installation shows the promise of resolving large and small flaws in barrier walls. Therefore, it is an attractive approach for conservative verification of barrier integrity.

Science and Engineering Associates, Inc. (SEA), in conjunction with the DOE, has developed a tracer-based monitoring/verification system¹. This system, called SEAttrace™, is able to locate and size leaks with a high degree of accuracy in subsurface barriers that are in an unsaturated medium. It combines the MultiScan™ monitoring system with gaseous tracer injection and real time data analysis to evaluate barrier integrity.

APPROACH

A schematic of the SEAttrace™ system is shown in Figure 1. Multiple sample points are located outside the barrier, and one or more injection and sample ports are inside the barrier. These ports are connected to a stand-alone data acquisition and analysis system. A tracer gas (sulfur hexafluoride) is injected into the barrier. If the barrier is breached, the tracer will diffuse into the surrounding medium and the exterior sample ports will measure the amount of tracer in the soil gas with time. These concentration histories can then be input (along with the known sample locations and the ranges for the medium properties and the source

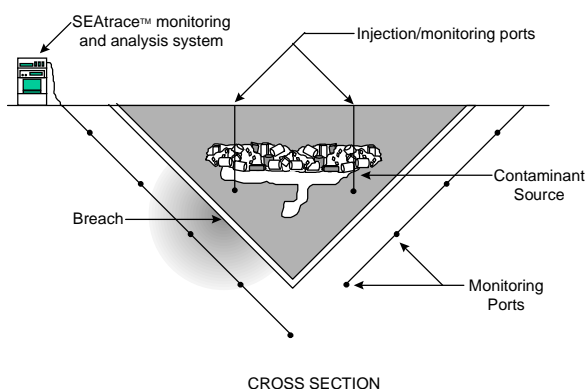


Figure 1: Schematic of the SEAttrace™ system

¹ Initial development of the SEAttrace™ system was funded and supported by the Environmental Restoration Division of Sandia National Laboratory. Later funding was provided by the DOE/Federal Energy Technology Center.

concentration) into a global optimization code. The code iterates to find a best fit solution given all the input parameters.

In addition to measuring the tracer gas, the MultiScan™ monitoring system can measure up to four other compounds or contaminants. Thus, the system can be used not only to verify the integrity of the barrier after it has been emplaced, but can also be used to quantify the performance of the barrier over time.

DEMONSTRATIONS

The SEAttrace™ system has been used to evaluate two barriers constructed by the DOE, a colloidal silica permeation-grouted barrier at Brookhaven National Laboratory and a thinwall jet-grouted barrier at the Dover Air Force Base. The setting and characteristics of the two demonstration sites were very dissimilar. The colloidal silica barrier was a V-shaped trough formed of three vertical and one slant walls, forming a contained volume. The barrier began roughly 3 feet below the surface of the ground. Each wall was constructed of overlapping columns (primary and secondary injections) formed by stacking “bulbs” of the viscous liquid on top of each other. The area between the grout columns was filled by tertiary injections. The completed wall was approximately 3 ft thick. The barrier was located in a homogeneous, sandy medium. The barriers at Dover were formed by creating individual panels using a jet-grouting technique. Panels were vertical, roughly 12 ft wide and 8 in. thick, and were keyed into a clay aquitard. The barriers were box shaped. The barriers were located in a heterogeneous media with clay and sand layers.

SEAttrace™ is also currently being demonstrated on a slurry wall at the Naval Air Station in Brunswick, ME.

RESULTS

The SEAttrace™ system was able to detect flaws in each of the barriers tested. Results from the system proved to be faster and to have greater spatial resolution than other barrier technologies tested. At the Dover jet-grouted barrier, two engineered leaks were included in the study, and SEAttrace™ was able to locate these leaks very accurately (within 0.3 m of their actual location). Results of the system for the non-engineered leaks were corroborated by a combination of the construction records of the barrier, independent tracer tests, or geophysical verification methods. Figures 2 and 3 show samples of the results for the two demonstrations.

CONCLUSIONS

The MultiScan™ system is an integral part of SEAttrace™. The scanning system collects concentration histories of the tracer gas at multiple (up to 64) monitoring ports at a user-defined interval, typically eight to 24 hours, for the duration of the test. The measured tracer concentrations are used with the inversion code to determine the size and location of breaches. The unit can also measure concentrations for up to four other compounds or contaminants. During the initial verification test, these other measurements can be used to determine problems with the system (for example, CO₂ concentrations are monitored to check for damage to the

sample tubing). After the initial verification is completed, the other measurements can be used to quantify the performance of the barrier over time.

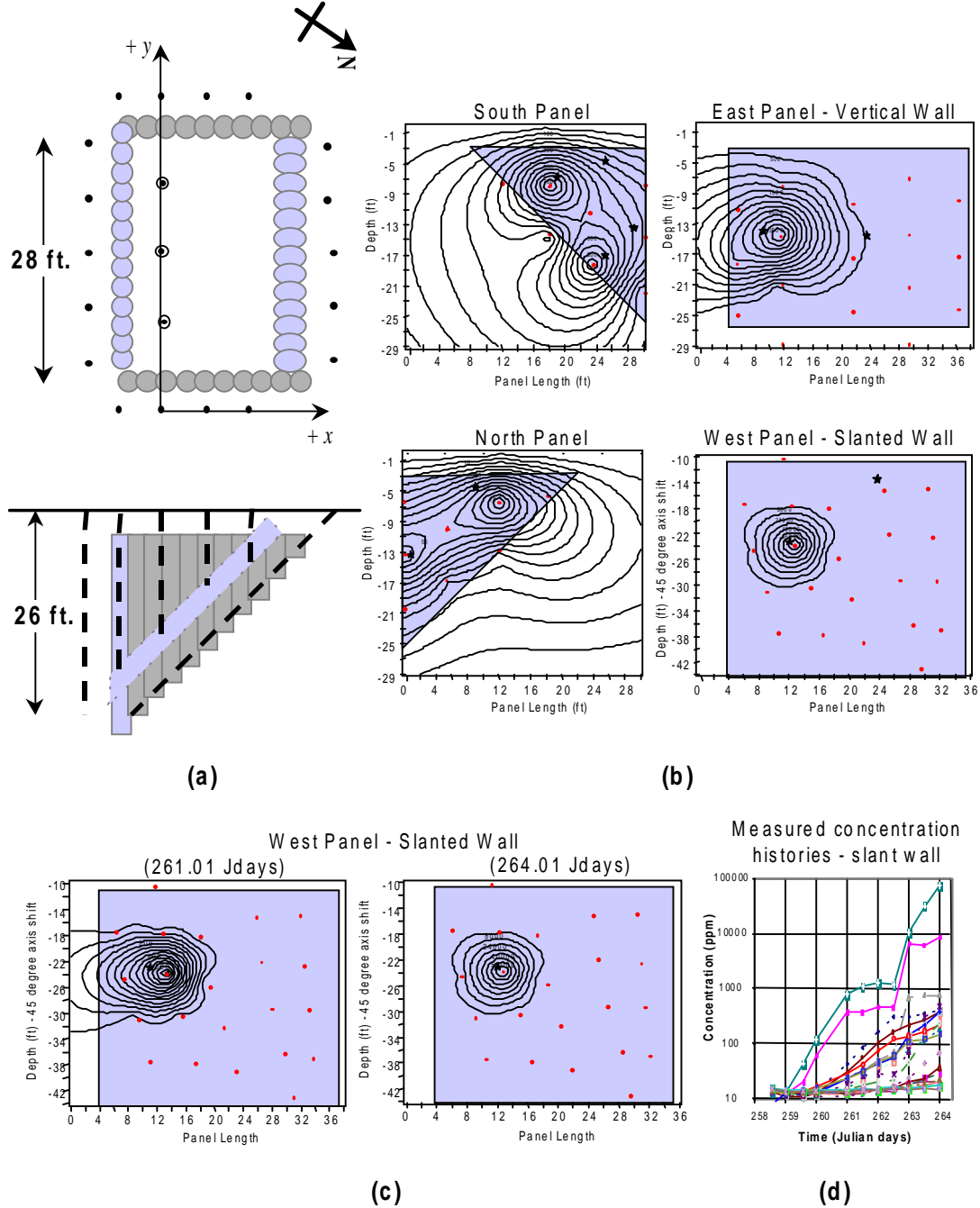


Figure 2: Viscous Liquid Barrier at Brookhaven National Laboratory. (a) Plan and side view of the barrier, showing monitoring well locations. (b) Contour plots from data collected one week after injections (Julian day 264.01). Shaded area depicts the barrier panels. Dots show monitoring port locations, stars depict SEATRACE™ calculated leak locations. (c) Contour plots of the slant wall for two different times, Julian day 261.01 and 264.01 (d) Measured concentration histories for ports near the slant wall.

MULTISCAN™ – CASE STUDY #3: MONITORING OF A PASSIVE VADOSE ZONE REMEDIATION SYSTEM AT INEEL

INTRODUCTION

The majority of the planned remediation sites within the DOE Complex are contaminated with volatile organic compounds (VOCs). In many instances, the contamination does not pose an immediate threat, but will ultimately require remediation of some type.

A low cost, simple solution has been developed by SEA as an *in situ* containment and extraction methodology for sites where the contamination resides at shallow depths in the vadose zone. Known as BERT™ (Barometrically Enhanced Remediation Technology) the approach capitalizes on wind effects and the vertical soil gas movement resulting from natural barometric pressure oscillations. Harnessing this mechanism, BERT™ ensures a net vertical upward soil gas flux in the contaminated soil. The design requires no boreholes or site power, resulting in a low-cost, low-maintenance remediation system.

Naturally occurring variations in barometric pressure can either be diurnal (corresponding to daily heating and cooling of the atmosphere) or of a longer time period (several days), depending on the passage of weather fronts. As the barometric pressure rises, a gradient is imposed on the soil gas that drives fresh air into the soil. As the barometric pressure drops, the gas vents upward from the near-surface soil into the atmosphere. Displacement of soil gas can be controlled using surface features that impede the downward movement of vapor in the plume area, but allow upward movement (Figure 1). BERT™ ratchets the soil gas flow upward by allowing normal upward flow during barometric lows while restricting downward air flow during high-pressure cycles.

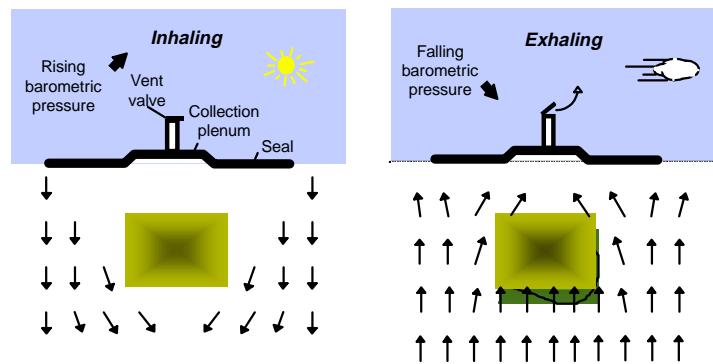


Figure 1: BERT™ barometric remediation system operation

APPLICATION

From the fall of 1996 to the spring of 1999, the system was tested at a contaminated landfill site of the Idaho National Engineering and Environmental Laboratory (INEEL). To evaluate the system's performance, a MultiScan™ system monitored subsurface and atmospheric pressures, wind speed, vent speed, and soil gas oxygen and carbon dioxide levels. MultiScan™ was able to monitor the system performance under very adverse conditions (such as below-freezing weather). To accommodate the extreme temperature variations, the monitoring system incorporated an environmental enclosure that moderated the internal temperature of the instrument case and prevented overheating during the summer months. Known as a Cool Cell (manufactured by Zomeworks, Albuquerque, NM) the system uses a large water mass and passive thermosyphon cooling to maintain the internal diurnal temperature variations to less than 4 °C.

The monitoring system quantified the very small soil gas pressure gradients resulting from the barometric pressure oscillations. Figure 2 shows a sequence of *in situ* soil gas pressure correlated with barometric pressure. There is a distinct change in contours when the barometric pressure begins to rise, indicating the desired effect of the surface seal. Results from the MultiScan™ system have confirmed that the system responds to barometric pressure changes as desired. These results have also been used to determine ways to boost the remediation system's performance.

RESULTS

The MultiScan™ system monitored critical parameters during the barometric pumping system test. Dynamic effects of barometric pressure changes upon soil gas pressures were clearly delineated (Figure 2). The system installation was impacting the soil gas pressures as desired, inducing net upward gas flow in the near-surface soils. Other critical parameters measured by the system included wind speed and vent system outflow. These data, combined with the barometric pressure, indicated the enhancement posed by winds on the system flow performance (see Figure 3). As winds pass over the top of the vent system pipe, a vacuum is

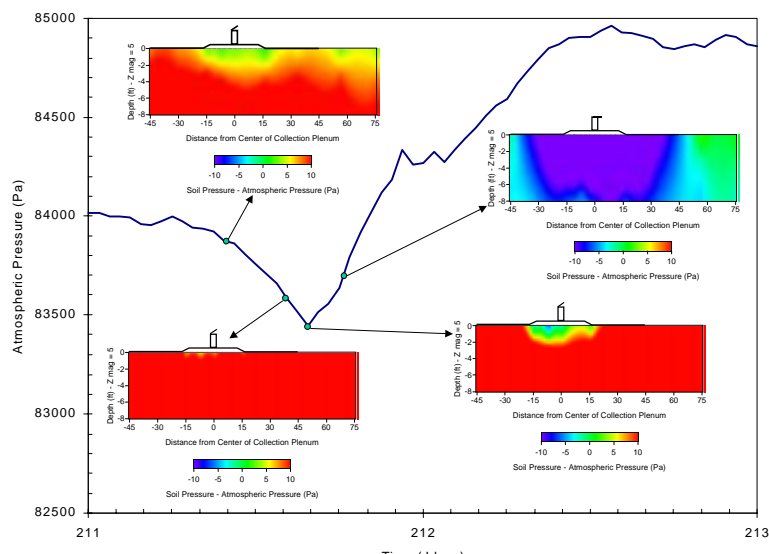


Figure 2: Barometric pressure-induced soil gas pressure gradients resulting from the BERT™ system operation

induced by the Bernoulli effect, which boosts the outward flow from the vent system. This effect was shown to dominate the process, and resulted in a design change to capitalize on the process. Subsequent testing showed that the improved design resulted in a four-fold increase in system vent flow.

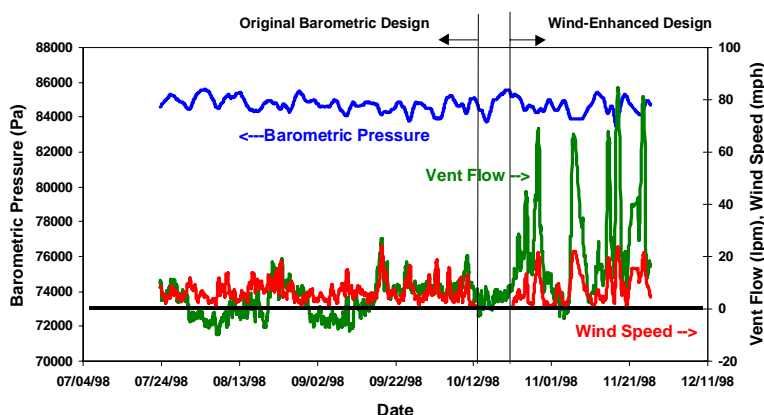


Figure 3: Combined effects of wind and barometric pressure changes on vent system outflow

CONCLUSION

The ability of the monitoring system to delineate the effects of wind and barometric pressure changes on the vent

system performance lead to design optimization of the BERT™ installation at the INEEL demonstration. Critical data obtained by the system included:

- Barometric pressure changes and the resulting soil gas pressure gradients,
- Wind speed enhancements on the system outflow,
- Temperature distributions in the soil beneath the surface installation, and
- Soil gas oxygen and carbon dioxide content distribution.

The ability to automatically record this data with high time resolution, and with relatively high spacial resolution (with 32 vapor ports available for pressure and soil gas analysis), resulted in effective assessment and redesigning of the system to boost overall performance.



Figure 4: BERT™ system installation at the Idaho National Engineering and Environmental Laboratory Radioactive Waste Management Complex (RWMC) facility

Sandia is a multiprogram laboratory operated by Sandia Corporation, a Lockheed Martin Company, for the United States Department of Energy under contract DE-AC04-94AL85000.

Hybrid Directional Boring and Horizontal Logging

Brian Dwyer

Directional access is needed for site characterization and evaluation of appropriate remediation technologies. Before directional drilling was applied to environmental sites, there was no way to create an angled hole that could provide access under a landfill or contaminated zone. Hybrid directional boring machinery capable of exerting hydraulic thrust forces greater than 80,000 pounds are used to push directional boring heads into the earth. Directional control is obtained by proper positioning of the face of the boring head. Slow rotation of the boring head will cut and compact the soil. Pushing a non-rotating boring head will cause a direction change. This machinery is capable of initiating a borehole at ground or shallow pit level, steering down to the desired horizontal depth, continuing at that depth (boring a horizontal hole) and then steering back to the surface. Casing and/or screen material can be installed in the borehole by attachment to the drill rod being retrieved from the exit point through the borehole to the entrance point.

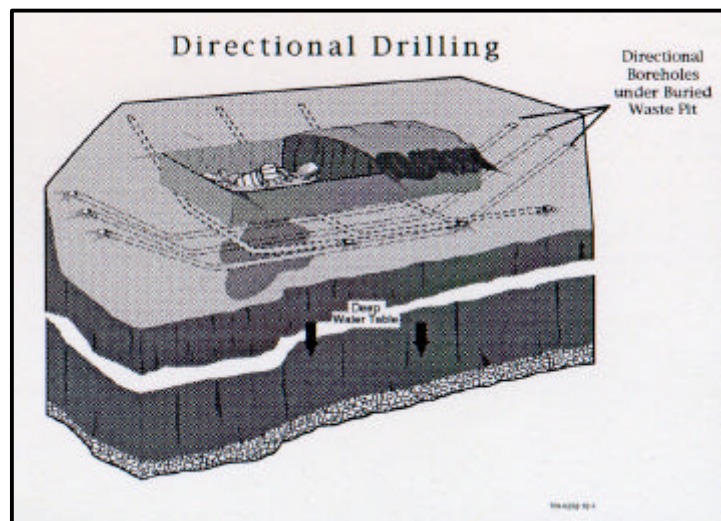
Start-up cost is estimated at \$200,000, which is approximately 10 times less than oil & gas or river-crossing drilling equipment. The goal for operation and maintenance costs is to drill for around \$25-75 per foot. Oil and gas industry drilling is about \$300-350 per foot, river-crossing industry is about \$75-150 per foot, and utilities industry drilling is about \$10-15 per foot.

In this drilling technology, minimal fluid (water) is added to the site, and since cuttings are compacted in the borehole, very little material is returned to the surface as secondary waste. This provides quality access beneath landfills, buildings and buried tanks. Depth will be limited to approximately 80 feet. Maximum horizontal reach is estimated at 1000 feet, compared to several thousand feet for oil and gas rigs. On-board position sensing is less sophisticated than the larger, more powerful rigs. Use may ultimately be limited to compactable soils although hardrock air drilling or downhole pneumatic hammers may eventually be options.

Currently, technical challenges include: adequate steering control in a variety of geologic materials, adequate position sensing in environment of high heating (from friction of drill head and the soil) and mechanical stress, proper boring head design for penetration of various geologic materials, and extension of depth capability while keeping technology affordable. A new generation of hybrid machinery has been field tested and is commercially available. Refinement of the directional drilling system continues by industrial suppliers.

For further information, please contact:

Brian Dwyer
Sandia National Laboratories
505/845-9894



Vadose Zone Monitoring – In-Situ Soil Moisture Monitoring

By: Stephen F. Dwyer, Sandia National Laboratories, PO Box 5800, MS 0719,
Albuquerque, NM 87185

Soil Moisture Measurements – Highest Accuracy (Automated):

Time Domain Reflectometry (TDR):

The process of sending pulses through a cable and observing the reflected waveform is called time-domain reflectometry (TDR). The type of material surrounding the conductors influences a waveform traveling down a coaxial cable or waveguide. If the dielectric constant of the material or medium surrounding the conductors is high, the electronic signal propagates slower. Because the dielectric constant of water is much higher than most materials, a signal within a wet or moist medium propagates slower than in the same medium when dry. Ionic conductivity affects the amplitude of the signal but not the propagation time. Thus, moisture content can be determined by measuring the propagation over a fixed length probe embedded in the soil medium being measured.

TDR equipment generally consists of a cable tester (e.g., Tektronix model 1502b) or a specially designed commercial TDR unit, multiplexor units (assuming multiple probes are used), probes and associated coaxial cable. A generic calibration equation developed by Topp et al. (1980) can be used. However, the probes should be calibrated for their specific application (e.g., soil texture and density, and cable length) to yield accurate soil moisture measurements (Lopez, Dwyer 1997). This calibration can be very time consuming.

A major advantage to the use of TDR for soil moisture content measurement is the ability to fully automate the system. Once automated, operator errors caused by inconsistencies between readings can be eliminated. Additionally, once installed the system can have a long life span. Accuracy in many soil types is very good. A TDR system's accuracy in general is about the same as that for neutron probes (Schofield et. al., 1994). TDR however, is quite expensive to use. Besides the greater expense, a major disadvantage of TDR is the fact that accuracy decreases with increased cable length between the probe and the cable tester; generally a maximum range of about 60 m is recommended. Soils with a high water content lengthen the propagation time of the electrical pulse and this phenomenon is reflected as an apparent increase in the travel distance. Soils with a high water content and a high electrical conductivity rapidly attenuate the electrical pulse. If the attenuation is great enough there will be no return signal and the probe cannot be used. However, probes can be coated to help reduce the errors created by this problem.

Recent developments by Campbell Scientific have attempted to minimize the cable length problem and reduce the costs of the TDR system. The latest development is called a CS615 Water Content Reflectometer. This probe does not require a cable tester or TDR unit but rather connects directly to a data logger. Calibration similar to the traditional TDR system is required for best results. The CS615 Water Content Reflectometer

consists of two stainless steel rods connected to a printed circuit board. A five-conductor cable is connected to the circuit board to supply power, activate the probe and monitor pulse output. The circuit board is potted in an epoxy block.

Another significant problem with TDR not often discussed is with the associated electronics. The data loggers and particularly the cable testers break down in temperature extremes. Extreme cold and extreme heat have shut our systems down on a number of occasions. Nearby lightning strikes have shut the systems down as well. The cable testers have quit working several times requiring repairs be made by the manufacturer. These repairs are very expensive and time consuming. Consequently, if the TDR system is to be used for lengthy periods, it is recommended that backup cable testers be available for substitution when one goes bad. This increases the costs further.

Soil Moisture Measurements – Highest Accuracy (Manual Readings):

Neutron Probe:

The neutron probe, when calibrated, can yield very good indirect measurement of soil water content. The probe is inserted into a cased access borehole where readings are taken at various depths. The casing material is generally aluminum or PVC piping. The principle is based upon the neutron thermalization process, wherein a radioactive source emits high-energy neutrons into the soil. These neutrons are then reduced to a lower energy state upon colliding with hydrogen atoms associated with soil water (Gardner 1987). Higher molecular weight elements such as oxygen also slow the neutrons, but far fewer collisions are required with hydrogen to slow the reaction to thermal energy levels. The source of the high-energy neutrons in most commercially available neutron probes is a radioactive americium and beryllium mix. The americium emits an alpha particle that bombards the beryllium atoms, which in turn, emit a neutron. The fast neutrons are emitted approximately radially and form a sphere around the source within which the neutrons are attenuated. The size of this spherical influence varies inversely with the moisture content. The sphere is about 70 cm for dry soils while about 16 cm for saturated soils; sphere diameter is unaffected by the strength of the radioactive source (Gardner 1987). The number of electrical pulses counted by the probe detector is proportional to the number of slow neutrons encountered. If hydrogen is the only variable affecting the density of slow or thermal neutrons, then a calibration curve can be developed to correlate count rate with soil water content. While the probe's manufacturer usually supplies calibration curves, calibration for each application is recommended. Calibration involves taking multiple readings in a given soil against a range of gravimetrically determined water contents. Soil heterogeneity and organic matter can have adverse affects on accuracy of neutron probe readings. Irregularities in the borehole casing or contact with the soil around the perimeter of the borehole can also produce error in water content values obtained. A major disadvantage to the use of a neutron probe is the fact that a radioactive source is present, thereby posing a potential hazard for the operator as well as imposing difficulty in its use and maintenance (i.e. regulatory constraints).

Frequency Domain Reflectometry:

Frequency domain reflectometry (FDR) methods of soil water content measurements are also known as radio frequency (RF) capacitance techniques. Those techniques actually measure soil capacitance. A pair of electrodes is inserted into the soil and the soil then acts as the dielectric medium completing a capacitance circuit comprising part of a feedback loop of a high frequency transistor oscillator. As high frequency radio waves (about 150 MHz) are pulsed through the capacitance circuitry, a natural resonant frequency dependent upon the soil capacitance is established. The soil capacitance is related to the dielectric constant by the geometry of the electric field established around the electrodes. There are currently two commercially available instruments using this technique: the Troxler Sentry 200-AP probe and the Aquaterr probe.

The Troxler probe uses an access tube (cased borehole) similar to the neutron probe for measuring volumetric soil water content at various depths. The probe is inserted into the access tube and the natural resonant frequency or the probe measures frequency shift between the emitted and received frequency. The access tube must consist of 2-inch diameter Schedule 40 PVC pipe. This size and wall thickness of pipe ensures tight fit of the probe inside the access tube, thereby minimizing annular air gaps that greatly affect the travel of the electronic signal into the soil; installation of the access tube requires special attention to ensure complete soil contact with the casing within the augured hole. Annular air gaps or soil cracks around the outside of the tube produce erroneously low readings.

The manufacturer's calibration of the probe is for sand and yields generally high volumetric soil water percentages on other soil textures. Calibration of the probe for soils other than sands is therefore required. Bulk density differences in soil profiles also require additional calibration. With proper calibration and use, the FDR's accuracy for measuring soil water content is adequate. With the exception of the concerns associated with the presence of a radioactive source presence, FDR limitations are similar to those associated with the neutron probe. The accuracy of FDR is generally not as good as neutron probes because the area of influence for moisture measurements is smaller (radius around the tube is smaller).

Soil Moisture Measurements – Lower Accuracy:

Tensiometers:

A tensiometer measures the matric potential of a given soil for suction values between 0 and 1 bar (Morrison 1983). With careful calibration, the measured matric potential can be converted to estimate soil moisture content through the use of an acceptable soil-moisture characteristic curve. The device commonly consists of a porous ceramic cup attached to the bottom of a rigid plastic tube (plastic is the preferred material for the tube because of its non-corrosive nature and lower heat conduction properties). The tube is sealed at the top with a removable cap allowing the tensiometer to be filled with water and accumulated air to be purged. A Bourdon gauge or manometer is installed through the upper portion of the water-filled tube, which measures the pressure of the water in the tensiometer. When the tensiometer is inserted into the soil, the soil absorbs water from

the tensiometer and as this occurs the water tension in the tensiometer increases until the tensiometer fluid pressure is in equilibrium with soil water outside the cup. Tensiometers are generally not effective in very dry soils and are best suited for coarse, sandy soils. They are less effective in clayey soils where a significant change in suction corresponds to a minor change in volumetric water content. Tensiometers are not recommended where a high level of accuracy is warranted.

Psychrometer:

A psychrometer measures the relative humidity within a soil system by measuring the difference between a dry bulb (non-evaporating) temperature and a wet bulb (evaporating) temperature. Soil psychrometers are usually restricted to suction between 0.9 to 72 bars (Morrison 1983). This range is generally greater than the tensiometer's range and, consequently, psychrometers are better suited for vadose zone monitoring in dry climates where tensiometers are generally ineffective. The majority of psychrometers used in the field utilize the Spanner design. This design is composed of a thermocouple, a reference electrode, a heat sink, a porous ceramic bulb or wire mesh screen, and a recorder. A variety of automatic and semiautomatic recorders are available for psychrometer measurement. Calibration curves are developed by immersing the unit in a series of sodium or potassium chloride solutions of known concentration {generally 0.1, 0.3, 0.5, 0.8, and 1.0 molar (Morrison 1983)}. The calibration curves are used to compute the in-situ soil-water potential from the measured field output voltage. Some of the problems encountered with psychrometers are that their calibration can change over time due to corrosion (Daniel et. al., 1981) and/or microbial growth on the thermocouple wires (Merrill and Rawlins, 1972). Psychrometers are not recommended where a high level of accuracy is warranted.

Electrical Resistance Blocks:

Electrical resistance blocks consist of electrodes embedded in a gypsum, nylon, or fiberglass porous material. The electrode has leads connected to a Wheatstone bridge to measure resistance. . When the sensor is placed in firm contact with the soil, water flows into or out of the sensor due to the gradient established between the potential in the sensor and the soil until equilibrium is established. As the water content of the resistance block decreases, the electrical conductivity of the block decreases. These resistance blocks are calibrated in site-specific soil against a range of known soil-water contents. Resistance blocks have been used in the agricultural arena for many years because they are relatively inexpensive and easy to use. However, they do have several drawbacks including a limited life span (approximately two years), significant hysteresis during calibration and field use, and sensitivity to salt concentrations, temperature effects, and proper soil contact. Additionally limited operational ranges reduce marginal accuracy. Electrical resistance blocks are not recommended where a high level of accuracy is warranted.

Moisture Measurements:

Lysimeters:

Soil lysimeters are used for collecting deep drainage or percolation data and estimating recharge. The most commonly used lysimeter in covered systems is a simple variation of the soil lysimeter called a pan lysimeter. The pan lysimeter is an impervious pan installed beneath or within the soil in the plot of interest. Water collected in the pan drains to a collection system where it is subsequently quantified. There are numerous designs of lysimeters, however, they are typically less than 2-m in depth (Stephens 1996) and their plan dimensions are proportioned according to the desired accuracy and shape of the plot being monitored. Generally, the larger the lysimeter, the greater the accuracy. The rate of soil water collected per unit area monitored is extrapolated and used to estimate the percolation rate of the entire cover system. It is important to note that only an estimate can be gained with this method. Quality of construction of the lysimeter is directly proportional to its accuracy. However, a certain amount of uncertainty always exists with lysimeter measurements. The principal advantage of soil lysimeters is that they provide direct and precise measures of soil-water flux.

References:

1. Stephens, Daniel B. 1996. *Vadose Zone Hydrology*. CRC Press, Boca Raton, FL. p.53, 203-260.
2. Morrison, Robert D. 1983. *Ground Water Monitoring Technology*. Timco Mfg., Inc., Prairie du Sac, Wisconsin. p. 2-31.
3. Merrill, S.D., and Rawlins, S.L. 1972. Field Measurement of Soil Water Potential with Thermocouple Psychrometers. *Soil Science*, 113, p. 102.
4. Daniel, D., Hamilton, J. , and Olson, R. 1981. Suitability of Thermocouple Psychrometers for Studying Moisture Movement in Unsaturated Soils, *in* Permeability and Groundwater Contaminant Transport, ASTM STP 746. Zimmie, T.F., and Riggs, C.O., Eds., ASTM, Philadelphia, PA.
5. Gardner, W.R. 1987. Water Content: An Overview. *in* International Conference on Measurement of Soil and Plant Water Status. Volume 1, Soils, Utah State University, Logan, Utah. p. 7.
6. Schofield, Tracy G., Gary J. Langhorst, George Trujillo, Kenneth Bostick, Wayne Hansen. 1994. Comparison of Neutron Probe and Time Domain Reflectometry Techniques of Soil Moisture Analysis. Los Alamos National Laboratory document LA-UR-94-981.
7. Lopez, Jesus, Stephen F. Dwyer. 1997. TDR Calibration for the Alternative Landfill cover Demonstration (ALCD). Sandia National Laboratories document SAND97-2317 - UC-2040.
8. Topp, G.C., Davis, J.L., and Annan, A.P. 1980. Electromagnetic Determination of Soil Water Content Measurement: Measurement in Coaxial Transmission Lines. *Water Resources Res.*, 16. p. 579.

UNSATURATED HYDRAULIC PARAMETERS DETERMINED FROM DIRECT AND INDIRECT METHODS

Lorraine E. Flint, U.S. Geological Survey, Placer Hall, 6000 J Street, Sacramento, CA 95819

David B. Hudson, U.S. Geological Survey, 1180 Town Center Dr., Las Vegas, NV 89136

Alan L. Flint, U.S. Geological Survey, Placer Hall, 6000 J Street, Sacramento, CA 95819

INTRODUCTION

Hydrologic conditions (initial and boundary conditions) and hydraulic parameters are required for numerical flow models of the unsaturated zone at Yucca Mountain, Nevada. At this potential high-level radioactive waste repository site, unsaturated conditions are numerically simulated to estimate the potential transport of radionuclides to the accessible environment under current and possible future climatic conditions. Extreme vertical variability of the lithostratigraphic features throughout the unsaturated zone (Buesch and others, 1996) contributes to the necessity of various levels of detail in constructing numerical models and parameter sets. Figure 1 illustrates properties of the major units. The Tiva Canyon and Topopah Spring Tuffs are fractured, welded flow deposits with low matrix permeability and low porosity which lie above and below the Paintbrush Tuff nonwelded and bedded units (PTn) which have relatively high matrix permeability and relatively high porosity (Flint, 1998). The nonwelded zone is variably saturated with a large range of physical and hydraulic properties and may modulate the penetration of episodic pulses of water due to capillary or permeability effects. The saturation profile shown in figure 1 indicates the potential for the presence of a capillary barrier which reduces the downward penetration of water. At approximately 33 meters below the surface small pores overlie large pores at the contact between the nonwelded base of the Tiva Canyon Tuff (the unit just below the moderately welded Tiva Canyon Tuff) and the underlying bedded tuff. Saturations exceeding 95 percent are common in this lithostratigraphic position at Yucca Mountain (Flint, 1998), but whether this condition promotes lateral diversion, which may reduce the proportion of downward percolation that reaches the repository horizon or whether it promotes the convergence of flow into preferential paths, has not been confirmed by field evidence.

The development of parameter sets based on physical rock properties data to produce saturation profiles such as that shown in figure 1 requires the separation of rocks into units or layers with similar properties. The numerical representation of the transition at the base of the Tiva Canyon Tuff influences whether or not physical properties theoretically will induce lateral diversion. Bulk rock properties of porosity, bulk density and particle density, and saturated hydraulic conductivity are easily measured on nonwelded rock samples, and are somewhat more difficult to measure on welded rock samples. Unsaturated flow properties are much more difficult to measure. Moisture retention measurements typically are used with curve fitting parameter estimations and capillary models (Mualem, 1976) to estimate unsaturated hydraulic conductivity (van Genuchten, 1980). There are two issues regarding these measurements: whether the estimated parameters can accurately determine the unsaturated hydraulic conductivity, and whether the estimated parameters can represent individual model layers without creating numerical artifacts due to the selection of discrete layers to represent a natural system with gradual transitions, and the assignment of properties which have spatial variability.

One approach to these issues uses steady state measurements of unsaturated hydraulic conductivity. Such measurements are made using a centrifuge and specialized rotor (UFA, Unsaturated Flow Apparatus, UFA Ventures Inc., Richland, WA.) [The use of trade, product, industry, or firm names is for descriptive purposes only and does not imply endorsement by the U.S. Government.] (Conca and Wright, 1998). Another method for measuring moisture retention uses a chilled-mirror psychrometer in a water activity meter (Model CX2, Decagon Devices, Pullman, WA.) that provides data collected under vapor phase equilibrium conditions (Gee and others, 1992). The methods used and conditions under which the moisture retention data is collected appear to have a bearing on the application of the data that is discussed in the results section.

In order to test the sensitivity of flux simulations to the parameters used in a numerical model, a two-dimensional numerical flow model representing a simplified version of the layered tuff sequence at the base of the Tiva Canyon Tuff was developed. The modeled system was tilted to correspond with existing structural relations at Yucca Mountain to provide a lateral vector with a gravity component to evaluate the influence of the parameter sets formulated from the various methods, on saturation and flux direction, based on different upper boundary fluxes. The model represents two layers of the moderately welded tuffs of the Tiva Canyon Tuff that overlie nonwelded tuff.

MEASUREMENTS AND METHODOLOGY

Data Set

Samples of five rock types were used that represented a vertical sequence of moderately to nonwelded tuff at the base of the Tiva Canyon Tuff. Porosity, bulk density and particle density were measured on each sample using Archimedes=principle of volume displacement, as well as saturated hydraulic conductivity using a steady-state, Hassler-type permeameter (ASTM, 1985). The chilled-mirror psychrometer (CX2) and the centrifuge were used to measure moisture retention data for each sample, and parameter estimation was used to fit curves and estimate unsaturated hydraulic conductivity (van Genuchten, 1980). Direct measurements of unsaturated hydraulic conductivity for each sample were made using the centrifuge with its specialized rotor.

The CX2 is an instrument that measures the water activity, or relative humidity of the atmosphere, in a chamber with which a sample has come into equilibrium. Equilibrium is based on the stabilization of repeated measurements that usually occurs from 2 to 15 minutes from the inception of the test. Water potential is calculated from the relative humidity and temperature of the sample using the Kelvin equation in which water potential equals a conversion factor (C) times temperature (in degrees Kelvin) times the natural logarithm of the relative humidity. The core sample is approximately 0.5 cm high and 2-3 cm in diameter. The water content is established and the water potential is determined. As water evaporates the sample equilibrates at a new water content for 3-5 days, and the measurement is repeated until a series of points is collected. The measurement has a resolution of 1.3 bars and a range of 0 to -2300 bars. The centrifuge moisture retention measurement establishes a water potential under steady flow conditions in a centrifugal

field, and the sample drains to the corresponding water content, which is measured gravimetrically. Steady state and equilibrium conditions are assessed by mass balance measurements of inputs and outputs and repeated measurements of water content with time. The core sample is 2.5 to 4.0 cm in diameter and 5.0 to 7.0 cm in height. The resolution of the water potential imposed is virtually infinite due to the accuracy of the centrifuge settings and control system and the range of water potential measured is from 0 to approximately -50 bars. The unsaturated hydraulic conductivity measurement is steady state and has a range limited to at least 1×10^{-12} m/s, which limits its use in low permeability materials if very low water contents are to be represented. Steady state unsaturated hydraulic conductivity data are measured by applying known constant fluxes to freely draining cores rotating at constant velocities in a centrifuge. The hydraulic gradient in the core is defined by the rotational velocity and the distance from the core to the rotation axis, and the flux is defined by the application rate and the area of the core. At sufficiently high speeds and flux density the centrifugal forces greatly dominate the matric potential forces and the hydraulic gradient can be calculated directly from the rotational velocity and distance from the axis. (For more detailed descriptions and discussion of assumptions see Conca and Wright, 1998). At steady state, the water content converges to a time invariant value giving the unsaturated hydraulic conductivity defined by the applied flux and gradient. Various (K , θ) data points between 10^{-7} and 10^{-12} m/s are measured by changing the applied flux or the rotation speed (for a more complete description see Conca and Wright, 1998).

There are two major issues related to the estimation of hydraulic parameters to estimate unsaturated hydraulic conductivity. The first issue is the resolution of hydrologic measurements near full saturation which includes the problem of fully saturating a sample. Measurements of water potential near saturation are particularly difficult in rock samples. Near saturation, numerical flow models are very sensitive to the parameters in the hydraulic conductivity and moisture retention relations due to the behavior of the water diffusivity. The air entry value, that water potential at which the largest pores in a sample begin to drain, has a large influence on the calculation of water contents determined from numerical flow models. For example, unsaturated hydraulic conductivity near saturation is not always accurately represented by equations used to estimate conductivity from moisture retention data (Corey, A.T., written communication, October 1997). Therefore, the choice of parameter estimation techniques can have a large impact on the accurate translation of static characteristics such as moisture retention.

The second issue related to estimation of hydraulic parameters is the definition and use of the residual saturation, S_r . Common definitions claim that S_r is the water content at which the gradient, $d\theta/d\psi$ becomes zero, or the water content where liquid flow stops due to discontinuous columns of water, and vapor flow predominates. Despite these definitions S_r is often used as a dry-end fitted parameter in the parameter estimation schemes for hydraulic properties, because of the uncertainty of its determination and the large influence its magnitude imposes on the resultant parameters. According to Rossi and Nimmo (1994), and a correction for dry-end water content proposed by Ross and others (1991), a reasonable approach to defining S_r is that water content equals 0 at a finite value of water potential. They state a value of -10,000 bars reasonably represents a typical case of oven drying at 105°-110° C at 50 percent relative humidity. Based on a review of selected literature (Jackson, 1964; Rose, 1963; Bush and Jenkins, 1970), it was determined that S_r could be represented by the amount of water left in the pores after equilibrating

in an environment of approximately -700 bars water potential, or about 65 percent relative humidity at 60° C. The volumetric water content at this potential is not very different from that existing at a water potential of -10,000 bars. It defines a residual water content as that water left in the smallest pores and in mineral structures such as clay minerals or zeolites, such that anything wetter could be drained under advective conditions. This definition of residual water content is similar empirically to the first one previously specified, which is where the ratio of water content to water potential becomes zero. The volumetric water content present in the sample at -700 bars (RH drying), determined relative to zero water content at standard 105° C oven drying is found to be correlated to saturated hydraulic conductivity, degree of mineral alteration and pore size distribution (Flint, 1998). For this analysis, it is assumed that this water content represents S_r and a comparison of curve fits of S_r using both data sets to the empirically determined S_r was made. Note in figure 1 the difference in porosity calculated using the two drying methods which represent the residual water content, and the large amount of water held in the rocks within and just below the moderately welded Tiva Canyon Tuff. The high S_r indicates a large degree of alteration, in this case montmorillonite, that corresponds to a probable capillary barrier due to the contrast in pore sizes between the altered and underlying layers. The residual water content based on simple measurements of porosity is a relative measure of the degree of alteration, thus helping to define the appropriate representation of model layers to correctly model field conditions.

Data sets of moisture retention and unsaturated hydraulic conductivity are shown for three samples in figure 2. Figures 2(a), 2(c), and 2(e) include moisture retention determined using the CX2 and the centrifuge, and the curve fit models using the method of van Genuchten (1980). The corresponding figures 2(b), 2(d) and 2(f) show the measured unsaturated hydraulic conductivity data plus the models from the moisture retention curve fit parameters using the Mualem/van Genuchten equations (van Genuchten, 1980). The fit of the moisture retention curves replicate the measured data points well. The estimated conductivity from the centrifuge retention data fits the measured conductivity data very well, while the CX2 model results do not correspond well with measured conductivity data throughout the range of saturation for all three samples. The two issues discussed above are readily indicated by these figures. Figure 2(a) shows the disparity generated by using S_r measured with a vapor phase equilibrium method, and set as fixed in the curve fit routine; whereas a much higher estimate of S_r was obtained for curve-fit centrifuge data. This indicates that the method chosen to measure S_r with the intent to provide a value at which advective flow stops is in error, as advective flow appears to have stopped at a higher saturation in each of these samples, or at least within the limits of the ability to detect it with the existing methodology. There is the possibility that the drier points of both the centrifuge data sets did not fully equilibrate or drain during measurement, and this would reduce the estimated value of S_r . The disparity in the dry-end data between the measured and modeled values results in errors when estimating conductivity in this region. In this case, however, only one sample out of three had a discrepancy of more than one order of magnitude with the exception of the data collected on samples that were almost completely dry.

The complete parameter data set for all 5 samples is listed in Table 1, including the values for porosity determined from the standard oven drying method, saturated hydraulic conductivity, and the three van Genuchten curve fit parameters used to estimate unsaturated hydraulic properties

(van Genuchten, 1980). $1/\alpha$ approximates the pressure required to drain the largest pores of a rock layer that overlies another layer with larger pores. Unsaturated hydraulic conductivity, $K_{rel}(\gamma)$, can be estimated from moisture-retention fit parameters using the model of van Genuchten/Mualem (van Genuchten, 1980).

Table 1. Parameters used in numerical models from data collected using two methods.

Layer ID		Porosity	K_s (m/s)	Methods	$1/\alpha$ (m)	n	m
Moderately welded	CMW	0.335	1.4E-8	CX2	17.1	1.18	0.15
				Centrifuge	38.6	1.73	0.42
	MWA	0.270	1.7E-9	CX2	100.0	1.32	0.24
				Centrifuge	45.5	1.33	0.25
Nonwelded	PV2	0.397	1.6E-6	CX2	2.8	1.27	0.21
				Centrifuge	2.8	1.89	0.47
	BT4	0.510	1.6E-6	CX2	3.8	1.20	0.17
				Centrifuge	1.3	1.43	0.30
	TPY	0.450	5.2E-5	CX2	14.5	1.96	0.49
				Centrifuge	0.9	1.82	0.45

The code used for numerical simulations is TOUGH2 (Pruess, 1987), an integrated, finite-difference method that accommodates heterogeneous media and calculates coupled flow and transport of air, water and heat. In this study, a 2-dimensional grid with 1 meter x 2 meter rectangular grid blocks, 40 meters high by 80 meters wide was used. There were 5 horizontal layers, each 8 grid blocks high. In order to evaluate the effects of the contrasting model parameters on lateral diversion, the entire model block was tilted by 6.5 degrees. Lower boundary conditions were set by estimates of in situ water potential maintained as a constant head of -0.5 bars with infinite storage. The lateral boundaries were specified as no flow zones and the upper boundary was set at selected constant fluxes.

RESULTS

Parameters

Based on comparisons of measurements on 5 samples, there is a range of porosity from 0.27 to 0.51, and a range of saturated hydraulic conductivity from 5.2E-5 m/s to 1.7E-9 m/s. The curve fit parameters showed varying degrees of contrast between the two methods used to collect the data for the different samples. The biggest difference was for the nonwelded TPY with more than an order of magnitude difference in $1/\alpha$ between the CX2 method at 14.5 m and the centrifuge method at 0.9 m. The n values for this sample differed by less than 8 percent. In contrast, the n values differed by about 40 percent for the PV2 sample, but the values indicated by $1/\alpha$ were identical. Capillary barrier theory indicates that small pores overlying large pores will contribute to the capillary barrier effect whereby water will be held in the overlying pores until enough

pressure head of water is accumulated to overcome the air entry pressure of the pores. If the boundary is sloping then the degree of slope and the saturated hydraulic conductivity will determine when water will flow into the underlying pores (Ross, 1990). The larger the saturated hydraulic conductivity, the greater the formation of pressure head at the contact, thus reaching the air entry potential and flowing into the underlying pores and therefore reducing lateral diversion. A numerical model calculates the unsaturated hydraulic conductivity according to degree of saturation for a given layer, and a useful evaluation of the effects of the parameter differences is based on saturation profiles and flux profiles.

Saturation Profiles

In order to avoid effects of the down-gradient lateral boundary, hydraulic conditions from vertical profiles that were located in the center of the grid were examined. Under no-flow upper boundary conditions, both parameter sets came to equilibrated saturations (figures 3a, b). For both models the no-flow conditions resulted in the lowest saturations for all layers, as expected. For the model using the CX2 parameters, 5 mm/year and 20 mm/year upper boundary conditions applied for 300 years increased the saturation in the upper 4 layers of the model. The top two layers were nearly saturated, with the biggest contrast between the second and third layers, probably due to the large difference between the $1/\alpha$ values, as well as the large increase in porosity. This model was unable to transmit the 60 mm/year upper boundary condition that was used in the model with the centrifuge parameters, and in which the upper two layers were completely saturated (Fig. 3b). In this model the third and fourth layers drained to lower saturations.

Horizontal Flux Estimates

In order to estimate the relative amounts of lateral diversion produced by the contrasting layers in each model, the horizontal flux that was calculated was scaled by dividing it by the upper boundary flux applied for each model (Fig. 4a, b). These are all very small numbers in mm/year, but the relative differences will increase when models are run for thousands of years. From the CX2 method the second layer which is the lowest in permeability has the highest horizontal flux, due to the contrast in α parameters between layers 2 and 3. The higher the vertical flux, the less horizontal flux there was, because the saturation would increase, thus increasing the unsaturated hydraulic conductivity. These conditions are magnified in the model using the centrifuge parameters for the first two layers, with the highest lateral fluxes for the lowest upper boundary flux. This is reversed in the third and fourth layers because the saturations are so low for the lower upper flux conditions (Fig. 3b) that the unsaturated hydraulic conductivity was extremely low and very little water could be conducted laterally. For the CX2 parameters, the air entry ($\sim 1/\alpha$) is higher in the underlying fourth layer, whereas for the centrifuge parameters, the air entry is lower in the underlying fourth layer. As shown in figure 4b this promotes lateral diversion.

CONCLUSIONS

In general there were substantial differences between parameters developed using two different measurement approaches for collecting moisture retention data. The unsaturated hydraulic

conductivity measured directly using the centrifuge was estimated very well using the moisture retention data collected by the advective method with the centrifuge. Most of the differences between moisture retention data sets were primarily due to the lack of resolution near saturation when using the vapor phase equilibrium method employed by the CX2 chilled-mirror psychrometer, and the advective method using the centrifuge resulting in less water drained at low water contents thus maintaining a high residual water content. If it is chosen to use this point as a dry-end fitted parameter the resultant moisture retention parameters will be quite different. For field conditions, where saturations are typically higher than 20-30 percent in the subsurface but may approach dryness at the surface, a dual approach may be useful where both sets of curves are integrated into the final parameter set.

The numerical flow simulations of layered media estimated differences in saturation and lateral fluxes between the two parameter sets usually because of contrasts in properties between layers. Methods that use fully advective conditions may represent unsaturated conditions at this arid site, while vapor phase equilibrium methods may represent surface soils and rocks where vapor transport is a dominant feature. Based on the simplified geometry and properties used in the simulations done in this study, and the resulting differences in fluxes between layers, site specific simulations are required that represent detailed properties and boundary conditions to evaluate which parameter sets can correctly simulate existing conditions at the particular site of interest.

REFERENCES

- American Society for Testing and Materials, 1985, Standard Test Method for Permeability of Rocks by Flowing Air, Designation: D4525-85, Annual Book of ASTM Standards, ASTM Committee on Standards, Philadelphia, PA, Nov. 1985.
- Buesch, D.C., R.W. Spengler, T.W. Moyer, and J.K. Geslin (1996), Proposed stratigraphic nomenclature and macroscopic identification of lithostratigraphic units of the paintbrush Group exposed at Yucca Mountain, Nevada, *U.S. Geological Survey Open-File Report* 94-469, 47 p.
- Bush, D.C., and R.E. Jenkins (1970), Proper hydration of clays for rock property determinations, *Journal of Petroleum Technology*, 22(7):800-804.
- Conca, J. L. and J.V. Wright (1998), The UFA method for rapid, direct measurements of unsaturated soil transport properties, *Australian J. of Soil Res.*, 36:291-315.
- Conca, J. L. and J.V. Wright (1990), Diffusion coefficients in gravel under unsaturated conditions, *Water Resour. Res.*, 26:1055-1066.
- Flint, L.E. (1998), Characterization of hydrogeologic units using matrix properties at Yucca Mountain, Nevada, *U.S. Geological Survey Water Resour. Investigations Rep.* 97-4342, Denver, Colo., 64 p.
- Gee, G.W., M.D. Campbell, G.S. Campbell, and J.H. Campbell (1992), Rapid measurement of low soil water potentials using a water activity meter, *Soil Sci. Soc. Amer. J.*, 56: 1068-1070.
- Jackson, R.D. (1964), Water vapor diffusion in relatively dry soil-- III. Steady-state experiments, *Soil Sci. Soc. Amer. Proc.*, 28:467-470.

- Mualem, Y. (1976), A new model for predicting the hydraulic conductivity of unsaturated porous media, *Water Resour. Res.*, 12:513-522.
- Pruess, K. (1987), *TOUGH User's Guide*, Lawrence Berkeley Laboratory LBL20700, University of California, Berkeley, Calif., 101 pp.
- Rose, D.A. (1963), Water movement in porous materials, Part 2--The separation of the components of water movement, *British J. App. Phys.*, 14: 491-496.
- Ross, Benjamin (1990), The diversion capacity of capillary barriers, *Water Resour. Res.* 26(10):2625-2629.
- Ross, P.J., J. Williams, and K.L. Bristow (1991), Equation for extending water-retention curves to dryness, *Soil Sci. Soc. Amer. J.*, 55:923-927.
- Rossi, C. and J.R. Nimmo (1994), Modeling of soil water retention from saturation to oven dryness, *Water Resour. Res.*, 30(3):701-708.
- van Genuchten, M.Th. (1980), A closed-form equation for predicting the hydraulic conductivity of unsaturated soils, *Soil Sci. Soc. Amer. J.*, 44:892-898.

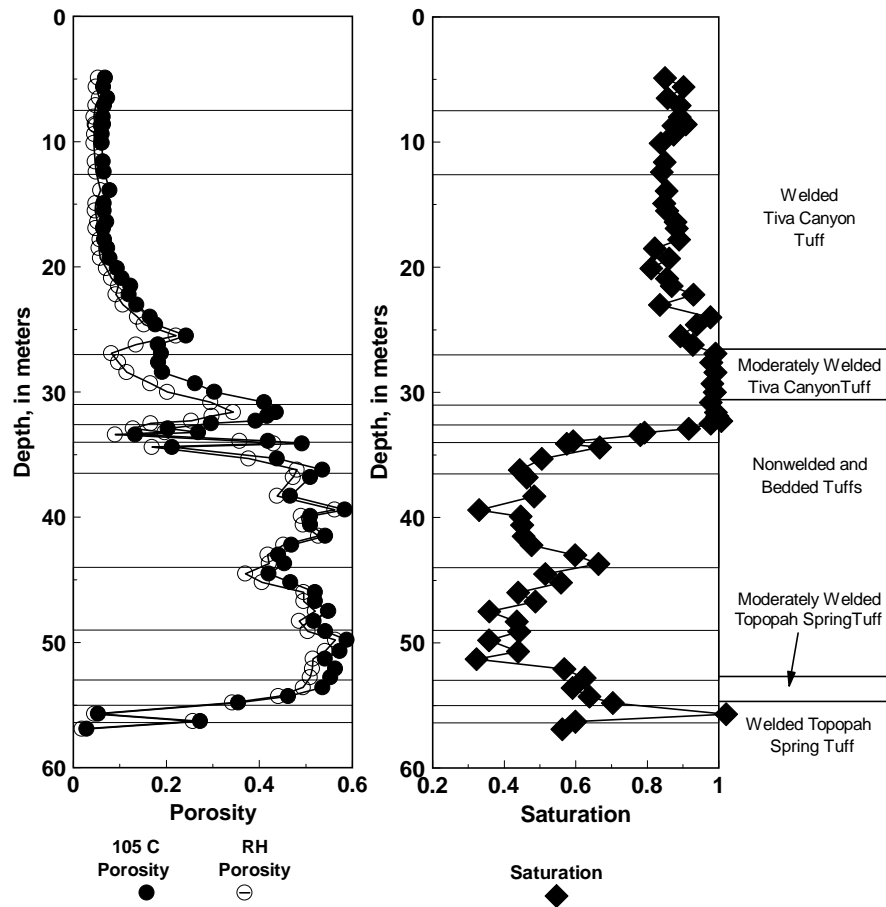


Figure 1. Porosity calculated from samples dried in 65% relative humidity and 60 C oven and standard oven drying, and saturation, for a transition from welded to nonwelded tuffs. Horizontal lines indicating lithostratigraphic zones are included within the major tuffs listed.

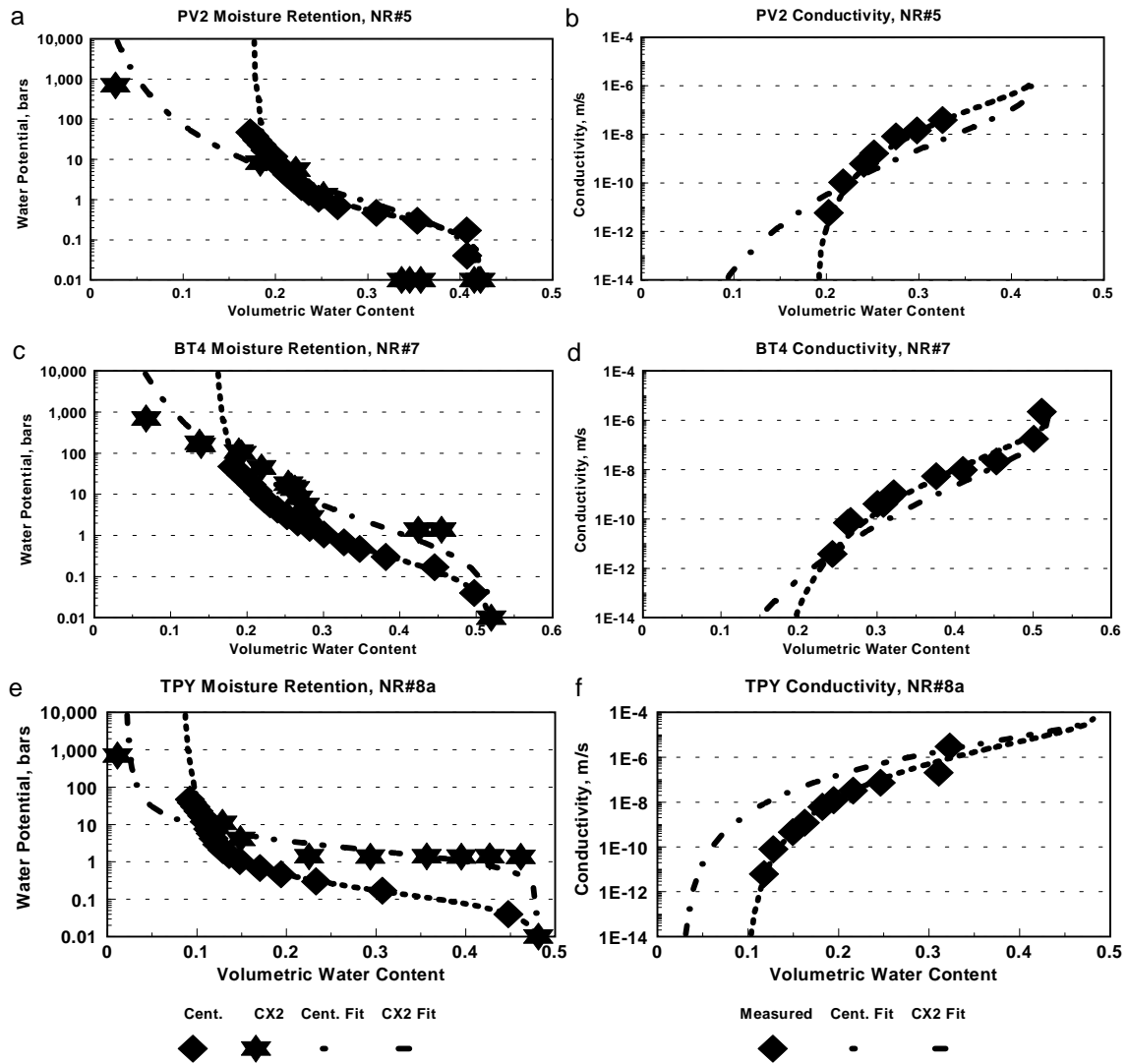


Figure 2. Moisture retention data sets and curve fit models, and measured and predicted unsaturated hydraulic conductivities for 3 samples of nonwelded tuff.

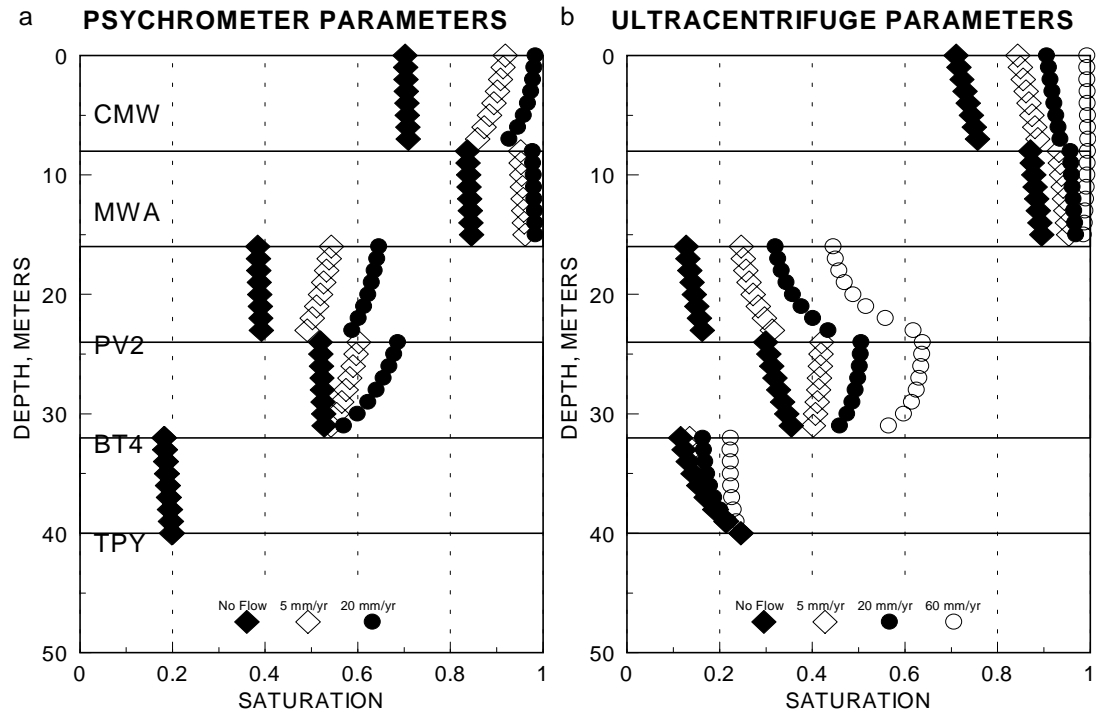


Figure 3. Saturation profiles for different upper boundary conditions for numerical model using parameter sets from two methods.

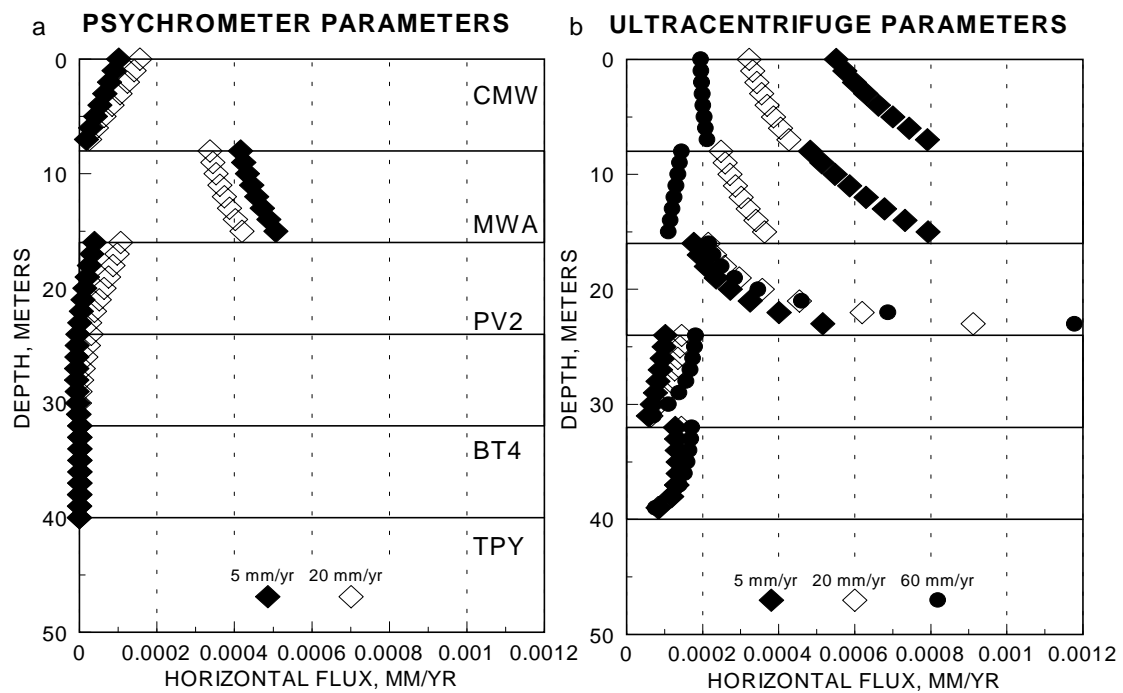


Figure 4. Profiles of horizontal flux scaled by applied boundary flux, generated with two hydraulic parameter sets.

Hydrogeological Characterization Using High Resolution Geophysical Data

Susan Hubbard and Ernie Majer; Lawrence Berkeley National Laboratory
Yoram Rubin, Dept. of Civil & Environmental Engineering, U. C. Berkeley

INTRODUCTION

Much of the problem and initial cost of subsurface remediation comes from field site characterization. Three-dimensional information about the heterogeneous subsurface is needed in order to identify the key controls on the flow and contaminant transport processes. It is widely recognized that natural heterogeneity and the large spatial variability of permeability predominantly control the flow field and hence the transport. Moreover, natural heterogeneity exhibits variability over a wide range of scales and hence is difficult to characterize due to scarcity of data and the costliness and intrusiveness of conventional field sampling techniques such as drilling. With poor site characterization, remediation schemes are unnecessarily expensive, because costly over-design and characterization at a detailed scale may be required to compensate for uncertainty.

To mitigate these problems, we investigate the use of tomographic radar and seismic data for investigating properties that influence flow and transport. Geophysical data complement direct characterization data by providing a denser grid of subsurface measurements than is obtainable from core point measurements or from volume-averaged pump test measurements alone. Geophysical data can be collected in a non-invasive manner and can be used to reduce the number of direct measurements needed to fully characterize a site. The geophysical techniques used within the following studies include radar and seismic methods, both of which are commercially available.

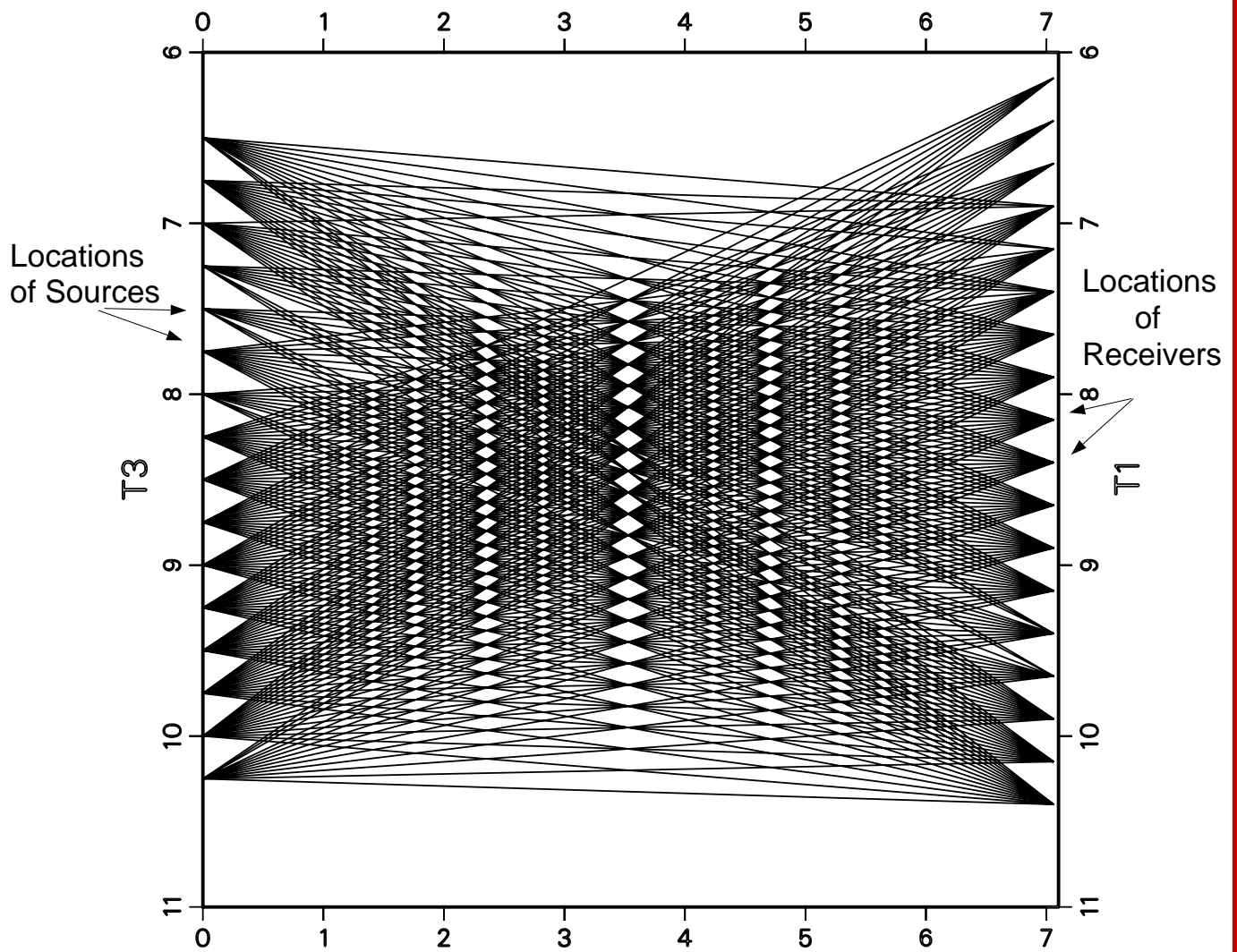
Ground penetrating radar (GPR) methods use electromagnetic energy at frequencies of 10-1000 MHz to probe the subsurface. At these frequencies, the separation of opposite electric charges within a material that has been subjected to an external electric field dominates over the electrical conductive properties. These capacitive properties are described by the dielectric constant, which can be estimated using radar data. Performance is optimal in moderately- to coarse-textured sediments, and can be poor in electrically conductive environments such as those dominated by the presence of clays. High-resolution seismic methods employ high frequency pulses of acoustic energy (~50-10000 Hz) which are produced at a point and propagate out as a series of wavefronts. The passage of the wavefront creates a motion that can be detected by sensitive geophones. From the time of flight of this energy, or from the seismic travel time data, information about the interwell seismic velocity can be obtained. Analysis of seismic amplitudes yields information about interwell seismic attenuation.

Tomographic acquisition methods transmit direct energy, electromagnetic in the case of radar and acoustic in the seismic case, from a transmitter in one borehole to a receiver in another borehole over several transmitting/receiving locations. The energy from the sources to the receivers is envisioned as traveling along raypaths through the interwell area. This transmitted energy is processed to obtain estimates of acoustic or electromagnetic wave velocity or attenuation; this procedure is known as tomographic inversion. Crosshole tomographic data can produce high-resolution images of physical/hydrological properties at a single point in time and are also well suited for dynamic process monitoring where data are collected at the same location as a function of time. Observing the data as "time difference" cross sections (data set collected at an earlier time subtracted from data set collected at a later time) enhances the image of subtle

geophysical attribute changes due to, for example, steam flooding, hydraulic fracturing and the spread of contaminant plumes.

Although the use of geophysical techniques for hydrological investigations has increased in the past five years, there have been relatively few investigations that have focused on quantitatively coupling geophysics and hydrogeology. In the case studies presented here, the geophysical attributes are used to detect moisture content, fracture, and NAPL distribution and to estimate hydrogeological parameters including permeability, porosity, and lithofacies.

OYSTER BAY T3-T1

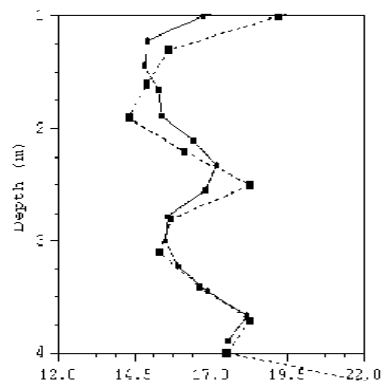


Example of Tomographic Data Acquisition Geometry



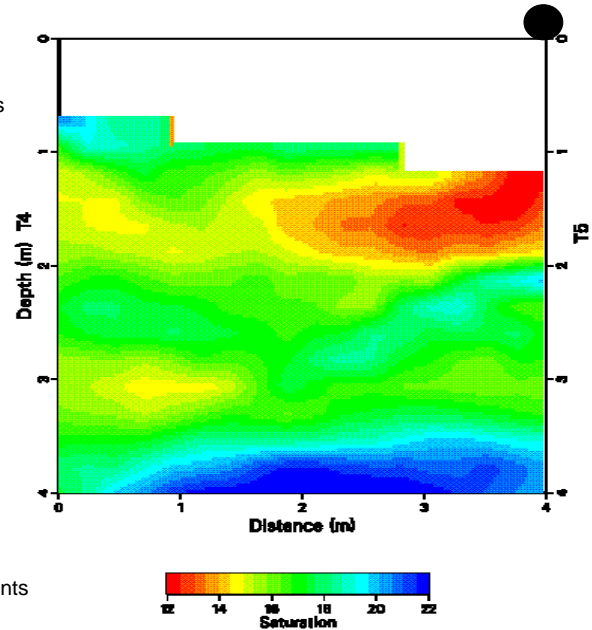
CASE STUDY 1: Saturation Estimation using Tomographic Radar Data

Comparison of Geophysical
Estimates and Neutron Measurements
at well T4



—●— Radar Estimates
- - ■ - - Neutron Probe Measurements

Saturation Estimates
T4-T5



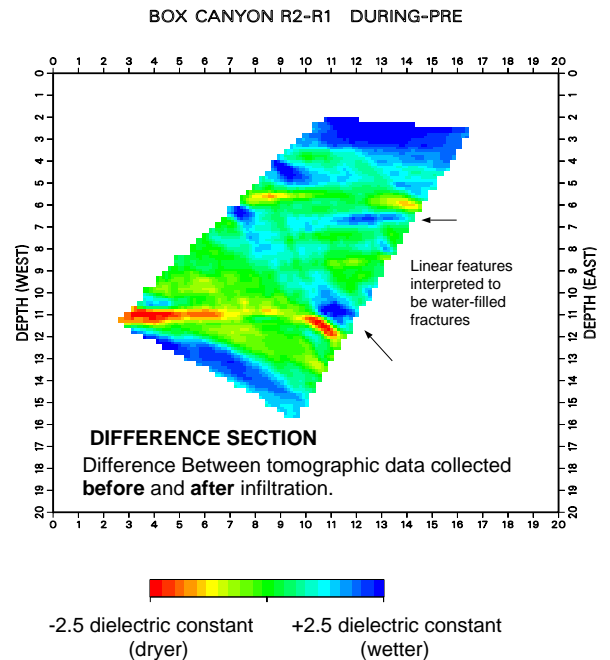
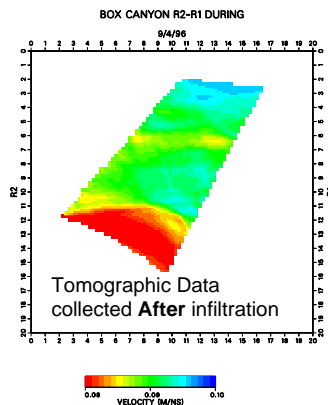
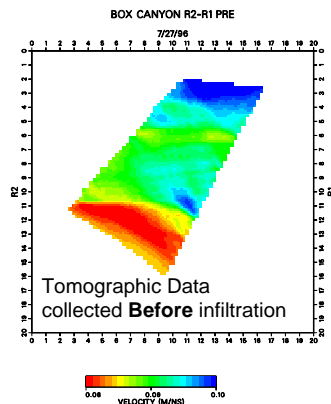
Tomographic radar data were collected at the D.O.E. Bacterial Transport Site in Oyster, Virginia, where the near subsurface consists of unconsolidated gravelly sand. Here we focus on radar data collected in the vadose zone to estimate saturation. The tomographic data were initially processed to obtain electromagnetic wave velocities. Assuming wave-like behavior, these velocities (V) were transferred into dielectric constant estimates (k) using: $k = \sqrt{c/V}$, where c is the plane-wave propagation velocity of electromagnetic waves in free space. The dielectric constants obtained from this conversion were used to predict water content using the well-known empirical Topp's relation. The water content estimates were converted to saturation estimates using a constant porosity value obtained from local core data. Saturation estimates obtained from one tomographic profile collected between wellbores T4 and T5 are shown above on the right. To validate our estimates, we compared them with neutron probe saturation measurements collected in co-located boreholes. Shown on the left above are neutron probe saturation measurements collected in well T4 compared with saturation estimates obtained at that wellbore from tomographic data. The agreement between predicted and observed is excellent, and suggests that **tomographic radar data are useful for providing multi-dimensional saturation information.**

Reference: Hubbard, S.S., et al., *Estimation of Permeable Pathways and Water Content using Tomographic Radar data*, *The Leading Edge of Exploration*, 1623-1628, 1997. Contact: Susan Hubbard (shubbard@lbl.gov).

CASE STUDY 2: Delineation of Permeable Pathways using Time-Lapse Tomographic Radar



Site Locator Map for the Box Canyon Study Area



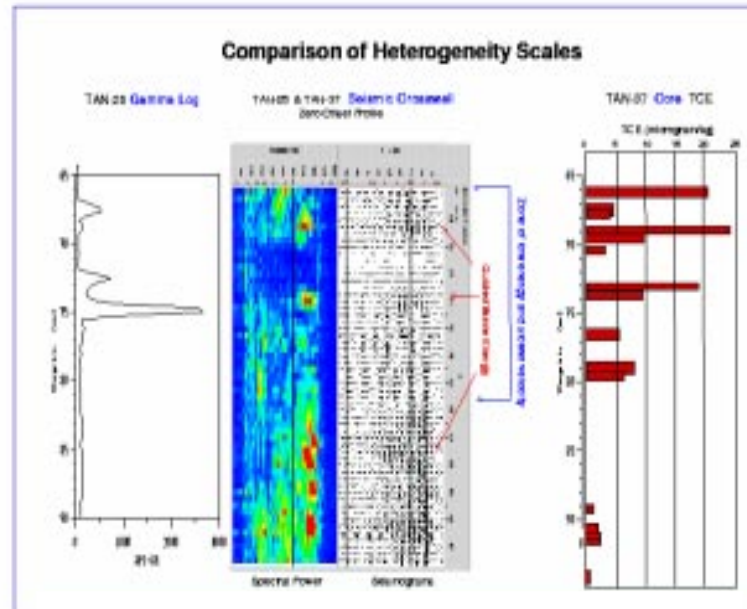
Radar data were collected at the Box Canyon Site in Idaho to identify fast flow paths within the Snake River Plain Quaternary fractured and vesicular basalt flows and interlayered "rubble zones", which form during basalt cooling. The Box Canyon Site is a study site that serves as an analogue for the contaminated subsurface at the nearby Idaho National Engineering Laboratory. Radar tomographic profiles were collected in a time-lapse fashion during an infiltration test. Radar data (processed as described in Case Study 1) collected prior to and during infiltration are shown on the left. As the subsurface geology remains constant during the infiltration test, the differences between the "before" and "during" tomograms are attributed to variations in saturation due to water infiltration. The "difference" section is shown on the right; the increase in dielectric constant near the surface and along permeable pathways (fractures, rubble zones) is interpreted to be due to an increase in saturation associated with the infiltration test. This interpretation was validated using core and borehole televiewer information. This study suggests **that time-lapse radar tomographic data collected during an infiltration test are useful for illuminating preferential flow paths.**

Reference: S.S. Hubbard et al., *Estimation of Permeable Pathways and Water Content using Tomographic Radar Data*, *The Leading Edge of Exploration*, 1623-1628, 1997. Contacts: John Peterson (barstow@ccs.lbl.gov) and Boris Faybisenko (bfayb@lbl.gov).



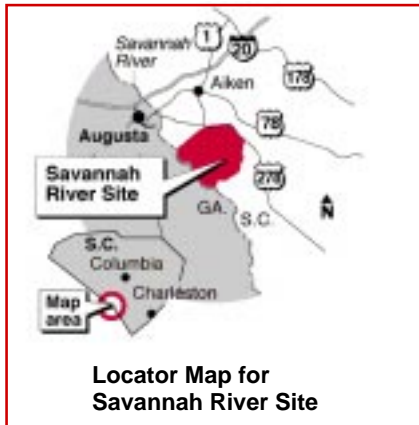
Site Locator Map for the INEEL
TAN Area

CASE STUDY 3: Identification of Contamination-filled Fractures using Crosshole Seismic Amplitude Information



Seismic crosshole data were collected at the INEEL Test Area North (TAN) site to delineate horizontal fracture zones which serve as radionuclide and TCE pathways. These zones were interpreted using both seismic velocity and amplitude information collected using a zero-offset acquisition mode. In this acquisition mode, energy can travel as guided waves, and resolution is on the order of the geophone spacing. The seismic section and corresponding spectral power of the amplitudes shown above indicate that there are zones of variable seismic attenuation. On the left side of the seismic information is the co-located gamma log, which indicates the presence of radionuclides (and by inference, TCE). On the right side of the seismic plots are core measurements of TCE. Comparison of the seismic amplitude and core/log information indicates that high spectral power, or similarly, low seismic attenuation, are correlable with increased contaminate concentrations; these zones of low attenuation are likely fractured zones that are continuous between wells. **Seismic crosswell data at the TAN site have provided a cost-effective method for delineating the volume and distribution of highly contaminated fracture zones.**

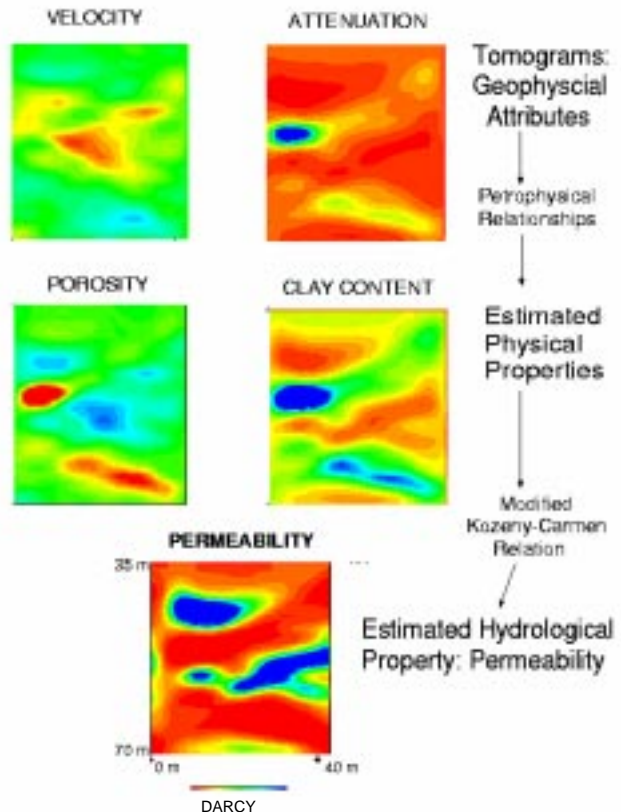
Reference: <http://www-esd.lbl.gov/SG/tan.html>. Contact: Tom Daley (tmdaley@lbl.gov).



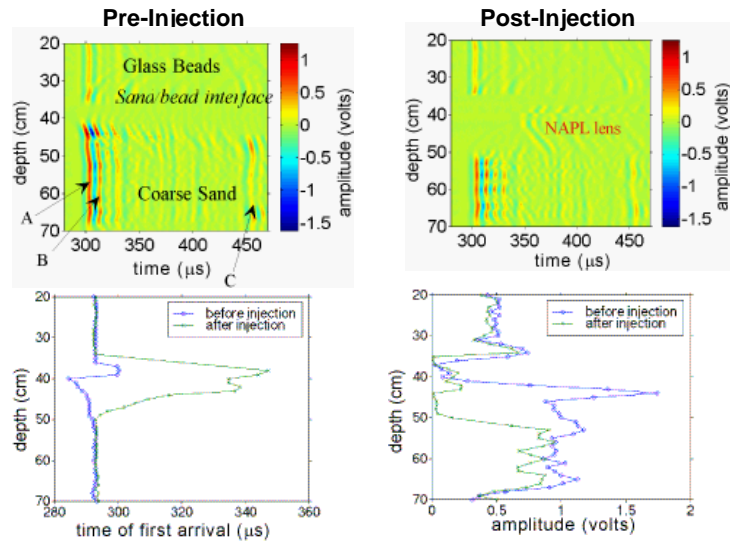
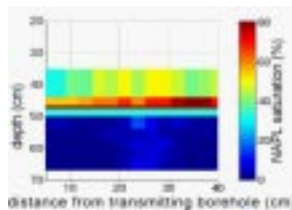
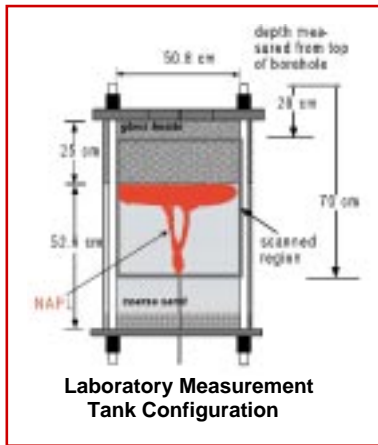
CASE STUDY 4: Hydrogeologic Parameter Estimation using Seismic Velocity and Attenuation Tomography at Savannah River Site H-Tank Area

Seismic velocity and attenuation tomographic data were collected at the Savannah River Site to detect variations in hydrogeological properties including porosity, clay content, and permeability. Published empirical petrophysical relationships were used to relate seismic velocity to porosity and clay content as well as seismic attenuation to porosity and clay content. Using these petrophysical relationships together with the seismic velocity and attenuation fields obtained from the tomography data, two-dimensional fields of porosity and clay content were estimated and are shown on the right. These clay and porosity fields were then used in a modified Koseny-Carman to produce the estimated permeability field; these estimates were confirmed by subsequent core analysis. **This example shows how joint seismic velocity and attenuation data can be used to estimate hydrogeological properties.**

Reference: Majer, E. et al., Final Report: Evaluation of the Applicability of High Resolution Crosshole Seismic Imaging Beneath the H-Tank Area for Geomechanical Properties. Contact: Ernie Majer (ELMajer@lbl.gov).



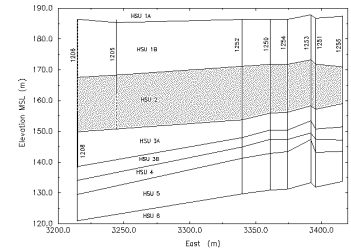
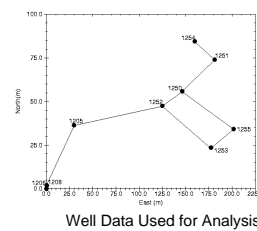
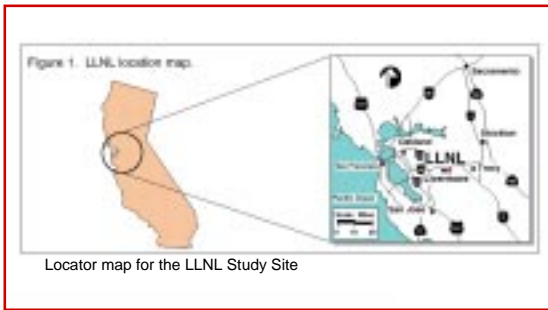
CASE STUDY 5: NAPL detection using Seismic Tomographic Data



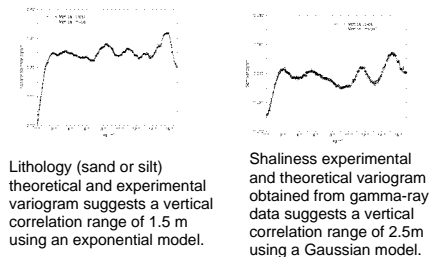
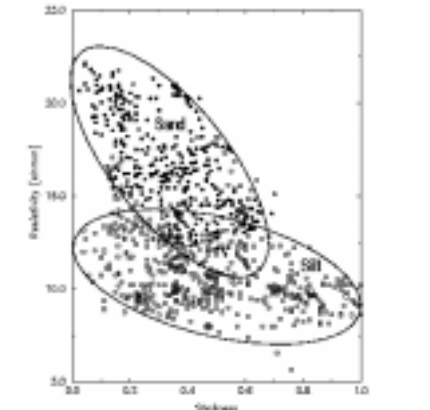
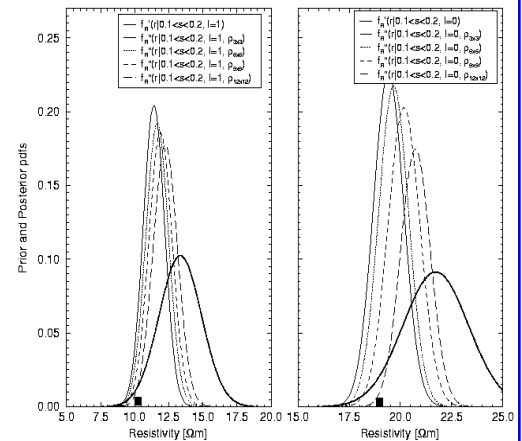
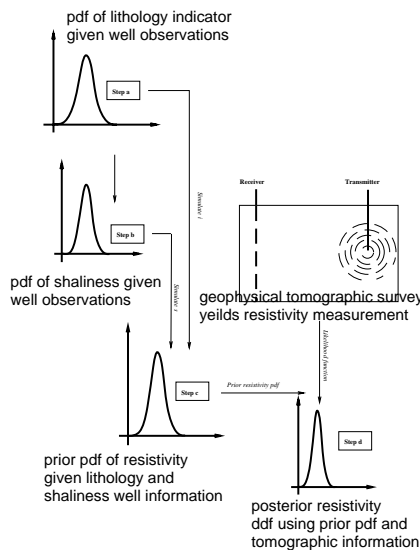
Laboratory seismic transmission at 90kHz was measured in water-saturated sand pack before and after the introduction of a non-aqueous phase organic liquid (NAPL), n-dodecane. The bottom of the tank was packed with coarse quartz sand and a 25-cm thick layer of fine glass beads was placed over the sand to form a capillary barrier to the upward flowing NAPL and to promote the formation of a NAPL lens within the coarse sand. NAPL was introduced into the bottom of the sample and then channeled upward due to buoyancy forces associated with the contrast in fluid density. The NAPL caused significant changes in seismic travel time and amplitude of the P-wave arrivals as shown by the "pre" and "post" figures above. Using this data, we estimated a saturation of 40-80% within the lens using a mixing model and the presence of residual saturation within the coarse-grained layer; excavation of the tank confirmed these estimates. **The results suggest that NAPL saturations within heterogeneous media are detectable with seismic travel time and amplitude data, and that amplitudes are potentially more sensitive than travel time but require more complex interpretation.**

Reference: Geller et al., *Acoustic detection of immiscible liquids in unconsolidated sand*, GRL, Vol. 27(3), April 1999, 417-420. Contacts: Mike Kowalsky (mikek@friction.lbl.gov) and Jil Geller (jtgeller@lbl.gov).

CASE STUDY 6: Mapping of Lithology and Electrical Resistivity at the LLNL Superfund Site using Electromagnetic Tomography Data



A Flow Chart for obtaining a posterior resistivity pdf at a generic point x .



A stochastic Bayesian approach for combining well logs and geophysical surveys to estimate lithology and resistivity was developed using data from the LLNL Superfund Site. The rationale for this approach is that resistivity and shaliness information, obtained from well logs, can be used for lithology identification. Once a type of lithology is determined, further mapping of hydrogeological properties can be pursued. Using LLNL data, electrical resistivity measurements were obtained from induction logs, and shaliness values were obtained from co-located gamma ray logs. A cross-plot of resistivity and shaliness shown above indicates that there are two dominant lithologies within the studied hydrostratigraphic unit (HSU 2) at the LLNL site (sand and silt). The first step in the approach (as schematically illustrated by the flow chart above) was to stochastically generate lithology images using indicator statistics and spatial statistical information obtained from variogram analysis as shown above; these images were made conditional to the wellbore data. Similarly, images of shaliness were generated. Using the simulated lithology and shaliness value at each point in the study domain, a prior pdf (f') of resistivity was defined. These prior estimates were then updated in a Bayesian sense into posterior pdfs (f'') using tomographic electromagnetic resistivity data. The information offered by tomographic data varies as a function of the acquisition parameters and geometry of the geophysical survey, or as a function of the resolution. A comparison of prior pdfs and posterior pdfs is shown above for different tomographic resolutions. This plot shows that as the resolution increases the estimate improves, and that even low-resolution resistivity surveys offer substantial improvement over those estimates obtained from wellbore data alone. The resistivity images can be converted to porosity and conductivity using site-specific relationships or well-known models such as Archie's equation. **This stochastic Bayesian approach allows for conditioning on what is clearly a set of complex and non-linear petrophysical models and results in an improved hydrogeological site characterization even when using low-resolution resistivity survey data.**

Reference: Ezzedine, S. et al., Bayesian method for Hydrogeological Site Characterization using Borehole and Geophysical Survey Data: Theory and Applications to the LLNL Superfund Site, Accepted for publication in Water Resources Research, April, 1999. Contact: Yoram Rubin (rubin@ce.berkeley.edu).

SEAMIST™ (a. k. a. FLUTe™ Systems)

Carl Keller, Flexible Liner Underground Tech.
Cecelia V. Williams, Sandia National Laboratories

SEAMIST™ has been developed, demonstrated, and deployed as an innovative tool for the access to the subsurface for characterization and monitoring on contaminants in both vertical and horizontal boreholes. The technique it was invented by Carl Keller at Science and Engineering Associates (1989). It is simple in concept and relatively inexpensive to use; yet, it provides quality samples of subsurface environment. The Department of Energy Environmental Management, Office of Science and Technology supported its development and deployment through the Mixed Waste Landfill Integrated Demonstration and Sandia National Laboratories. SEAMIST received an R&D/100 award in 1994.

SEAMIST is an innovative technology that can function both as a borehole casing and as a support platform for sampling devices and instrumentation. SEAMIST consists of the borehole liner of a tubular, impermeable membrane, a tether that gathers the bottom of the membrane and extends up the center of the hole to a reel, in a canister, at the surface. SEAMIST employs an everting/inverting, flexible liner to seal and support an open borehole while carrying instruments into place isolating them one from another (Figure 1). The everting liner is driven into the hole by air pressure (imagine the reverse of peeling the liner from the hole, inside out). As the liner propagates into the hole, it carries a variety of “instruments” into place and seals the hole between the instrument locations.

The impermeable membrane is emplaced downhole at speeds of approximately 20 to 50 feet/minute using the apparatus shown in Figure 2. Positive pressure is supplied to maintain the integrity of the borehole once the liner is emplaced. A filler material such as sand, or grout may be used instead of air for long-term installations. Because the hole filling material is located inside the liner, there is no contamination of the geologic medium with hole-filling material. If the system is later removed from the subsurface, the membrane is wound onto the reel and into the canister by inversion. Thus, there is no cross contamination of absorbent pads or sensors as the membrane is removed. Liners can be made of a wide variety of impermeable materials, including plastic tubular films and laminates. Liner materials are selected on the basis of cost, durability, fabrication ease, impermeability, and chemical compatibility.

SEAMIST liners have been used in horizontal, vertical, enlarged, constricted, and curved holes. SEAMIST can be used in open and cased boreholes. The liners have been demonstrated both above and below the water table. They can line the borehole temporarily or permanently, preventing the borehole collapse, limiting movement of air into the subsurface, and preventing fluid flow into and within the borehole. It acts as a downhole support platform for sampling devices and instrumentation. Sampling can be accomplished using sampling ports with attached tubes running back to the surface, while larger instruments that can “see”

through the membrane can be carried into the hole on the tether (e.g. gamma logs, neutron logs, resistance logs, TV cameras, etc.). The sample collection instruments that have been emplaced downhole include:

- Absorbers pressed against the hole wall for wicking of liquid samples,
- Absorbent material can completely cover the SEAMIST liner from top to bottom of the borehole. A continuous map of the subsurface at that location can then be obtained.
- Gas sampling ports and tubing for vapor collection in discrete intervals of the hole,
- Electrical contacts for resistance measurements.

Many of the problems with conventional vadose zone monitoring techniques are eliminated or minimized by the SEAMIST design. The problems reduced include: borehole instability, single point sampling with screened wells, the inability to retrieve and repair instrumentation buried in backfill, and cross contamination of samples due to inadequate backfill seals. These advantages are achieved with a portable, lightweight, and robust emplacement system, which is fast as well as relatively inexpensive. The main limitation of the technology is that the borehole must remain open after drilling long enough to allow deployment of the membrane (typically less than 30 minutes). If regions of swelling clays are encountered in the lithology, the membrane pressurized with air may not prevent closure of the borehole, unless the liner is sand filled. The seal of the interface between the membrane and the borehole wall may not be as absolute as in a grouted hole, but appears to be adequate for most applications.

The basic everting liner method has evolved to a large family of techniques of use in vadose zone measurements. A newer application of the device uses two liners. A sealing liner to support and seal a hole, and a second instrumented liner which is deployed in parallel in the same hole to measure anywhere and anytime without violating the seal or support of the hole. (the Duet™ technique).

The LAHD™ application is a “Liner Augmentation of Horizontal Drilling” which uses a propagating liner to support a horizontal hole while it is being reamed by a horizontal drill rig. The result is an exceptionally clean, sealed hole with little mud invasion, no mud cake, and complete support against hole collapse. The liner is also used to case and/or instrument the horizontal hole while fully supported.

The latest technique is to use the liner to install a color reactive ribbon, which turns bright red in the presence of DNAPLs. The everting liner has been deployed in cone penetrometer holes and through cone penetrometer rods to emplace the reactive ribbon with dramatic color changes at DNAPL layers. The multilevel sampling in the vadose zone has been extended to ground water sampling with a downhole pump for each port.

Trademarks: SEAMIST, Robert Alpert Companies
 FLUTe, DUET, LAHD, Flexible Liner Underground Tech.

Contacts

Carl Keller
Flexible Liner Underground Tech.
6 easy Street
Santa Fe, NM 87505
(505) 983-3199 phone
(505) 983-3476 fax
CKmist@Aol.com

Cecelia V. Williams
Sandia National Laboratories
P.O. Box 5800, MS-0706
Albuquerque, NM 87185-0706
(505) 844-5722 phone
(505) 844-0240 fax
cvwilli@sandia.gov

Summary of SEAMIST Field Applications

APPLICATION	DESCRIPTION	CLIENT	SITE	PERIOD OF USE	CONTACT
Tritium plume monitoring	Two systems installed at Lawrence Livermore National Laboratory, CA are continuing to track the movement and concentrations of a tritiated water plume (both vapor and liquid water sampling to 40 ft).	Lawrence Livermore National Laboratory	Lawrence Livermore National Laboratory	May 1991 - Present	Barbara Mallon Lawrence Livermore National Laboratory
Carbon tetrachloride monitoring	Two emplacement systems with disposable membrane liners are in use at Hanford, WA. in a carbon tetrachloride plume monitoring program. The membranes pack off the cased borehole while sample tubing to the bottom draws the vapor sample.	Westinghouse	Hanford	Fall 1992- Present	Virginia Rohay WHC
Fracture flow mapping and rate measurement	SEAMIST membranes coated with liquid indicating and wicking layers mapped and measured brine flows (grams per day) underground at Waste Isolation Pilot Project, NM.	Sandia National Laboratory	WIPP	January 1992	Lee Jenson Sandia National Laboratory
Tritium and VOC sampling	SEAMIST system transported vapor sampling tubes and absorbent collectors 230 ft horizontally beneath an old radwaste landfill at Los Alamos.	Los Alamos National Laboratory	Los Alamos National Laboratory	April 1992	Steve McLin Los Alamos National Laboratory
Sandia National Laboratory - integrated demonstrations	<ul style="list-style-type: none"> • Demonstrated capability to transport logging tools and cameras in horizontal boreholes up to 230 ft long, 1.75 to 4 in. diam. • Performed gas sampling and permeability measurements in two 11.5 in., 110 ft deep boreholes immediately after auguring in the Chemical Waste Landfill. • Installed three 110 ft borehole liners to support holes during logging. 	Sandia National Laboratory	Sandia National Laboratory	Spring through Fall 1992	John Stormont Sandia National Laboratory

APPLICATION	DESCRIPTION	CLIENT	SITE	PERIOD OF USE	CONTACT
Vapor sampling/permeability measurements	Three membranes were instrumented and installed at the Savannah River Site in July 1992 for soil vapor, vapor pressure, and permeability measurements in the remediation demonstration project. Maximum depth is 130 ft with ten sampling elevations per membrane.	Westinghouse	Savannah River Site	July 1992 (Continuing for up to 2 years)	Carol Eddy Westinghouse Savannah River Company
Neutron logging tool transport	SEAMIST membrane was used to tow a neutron moisture logging tool in horizontal boreholes underneath waste landfill in Los Alamos. Typically, four holes (200-250 ft long) were logged in one day, with data taken every 2 ft.	Los Alamos National Laboratory	Los Alamos National Laboratory	August 1992	Steve McLin Los Alamos National Laboratory
Vapor sampling	Vapor sampling SEAMIST system with nine sampling points was installed to 90 ft deep for long-term monitoring.	Daniel B. Stephens & Associates, Inc.	Tucson	Sept. 1992	Jeff Forbes (DBS&A)

Summary of SEAMIST Field Applications, continued

Summary of SEAMIST™ Field Applications					
Borehole liners	SEAMIST liners installed after holes drilled to support/seal holes while long-term monitoring system is designed (8.5 ft diameter, 100 ft deep).	Lawrence Livermore National Laboratory	Lawrence Livermore National Laboratory	Sept. 1992	Joe Lovenitti Weiss & Associates
High pressure borehole liners	Two Kevlar reinforced SEAMIST membranes were installed to a maximum depth of 155 ft, then filled with water inside cased wells to prevent collapse of the PVC casing during steam injection remediation experiments.	Lawrence Livermore National Laboratory	Lawrence Livermore National Laboratory	Oct. 1992	Robin Newmark Lawrence Livermore National Laboratory
Borehole liner	One SEAMIST liner was installed after hole drilled to support/seal hole while long-term monitoring system is designed (8.5 diam, 90 ft deep).	Argonne/Dept. of Agriculture	Utica, Nebraska	Oct. 1992	John Walker Argonne National Laboratory
Sandia National Laboratory - integrated demonstration	Installed gas sampling tubing to 393 ft in a horizontal borehole of 4 in. diam.	Sandia National Laboratory	Sandia National Laboratory Albuquerque	Fall 1993-Fall 1994	Cecelia Williams
Monitor fuel oil plume position	Monitor the position of the plume via closely spaced soil vapor sampling ports in a vertical hole.	Hart Crowser, Seattle, Washington	Swedish Hospital	May 1993 to present	Chad Armour
Characterize the site and map contamination	Install SEAMIST in numerous boreholes to sample pore vapor for VOC's and to emplace other monitoring instruments	Los Alamos National Laboratory	Mixed waste landfill site, Los Alamos, NM	Fall 1993 to present	Don Krier
Monitoring under new mixed waste landfill	The SEAMIST system is a critical part of the landfill monitoring design being developed for a mixed waste disposal facility.	Los Alamos National Laboratory	Mixed waste landfill site, Los Alamos, NM	Prototype testing in 1994	Robert Crowley
Stabilization of contamination in ducting	SEAMIST is being used to apply strip coat to the interior of ducting to immobilize hazardous dust (e.g., U&Pu)	Los Alamos National Laboratory	Old plutonium facility	Spring 1994 to present	Dan Stout
Monitoring of soil vapor extraction	Nine vertical SEAMIST systems with 10 vapor sampling ports to 80 ft used for pressure, permeability, and concentration monitoring.	Kleinfelder	Sacramento Army Depot, California	March 1994 to present	Randy Wheeler

Mapping of contamination at radioactive waste site	Installation, in a 4.5 in. diam. mole hole, of an absorbent covering on SEAMIST	Oak Ridge National Laboratory	Oak Ridge WAG6	August 1994 to present	
Monitoring of a radioactive waste landfill	Use of SEAMIST in tunnels built in trenches below low level radioactive waste landfill to monitor for leachate migration.	Los Alamos National Laboratory	TA-54, Pit 39	Sept. 1994 to present	Bill Purtyman
Sampling at discrete levels below the water table	Installation of SEAMIST with water and vapor sampling ports. The water table is at 40 ft below the surface.	Weiss Associates	March AFB, Riverside, CA	Being Installed	Joe Lovenitti
Permeability measurements	Use of SEAMIST in 60 ft deep hole for measurement of permeability and changes during thermal enhanced vapor extraction.	Sandia National Laboratory	TA-3, Chemical Waste Landfill	July 1994 to present	Jim Phelan
Tritium plume measurement	Installation of absorbers on SEAMIST membrane to 300 ft for wicking of water in vadose zone.	Los Alamos National Laboratory	TA-33	August 1994 to present	Jake Turin
Vapor Sampling	Multilevel water sampling to 80 ft below SLW.	Geraghty & Miller	Saegertown, PA	Sept. 1997	Dennis Balcer Arcadis Geraghty & Miller
Vapor Pressure	Pore pressure monitoring to 800 ft	USGS & DOE	Nevada Test Site, NV	1995-present	Gary Patterson, USGS
Monitoring	Landfill monitoring in horizontal holes	Los Alamos National Laboratory	Los Alamos, NM	Apr. 1998-present	Dennis Newell, LANL
Vapor Sampling	Installation in Sonic Casing to 300 ft.	OHM Corp.	Asuza, CA	Oct. 1997-present	Bob Cox, OHM Remediation Services
Liquid sampling	Ground Water Sampling (6 ports in 3" hole)	Duke Eng./INEEL/EPA	Milford, NH	Nov. 1998-present	John Londergan, Duke Engineering
Vapor Sampling and Absorber installations	Duet™ double liners	TRW/DOE Lawrence Livermore National Laboratory	Yucca Mt., NV	Sept. 1997-Present	Laura Deloach, LLNL
Vapor sampling	Gas sampling in CPT holes	Westinghouse /DOE	Savannah River Site, SC	Sept. 1997	Joe Rossabi, Westinghouse Savannah River Company
DNAPL Location	Installation of color reactive ribbon	Westinghouse /DOE	Savannah River Site, SC	Aug. 1998	Brian Rhia, Westinghouse Savannah River Company
Liquid Monitoring	Absorbers for fracture flow	USGS/DOE	Yucca Mt., NV	1998	Gary Patterson, USGS

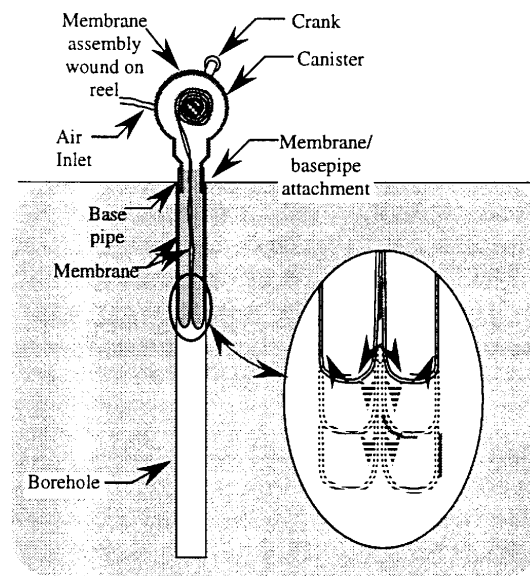
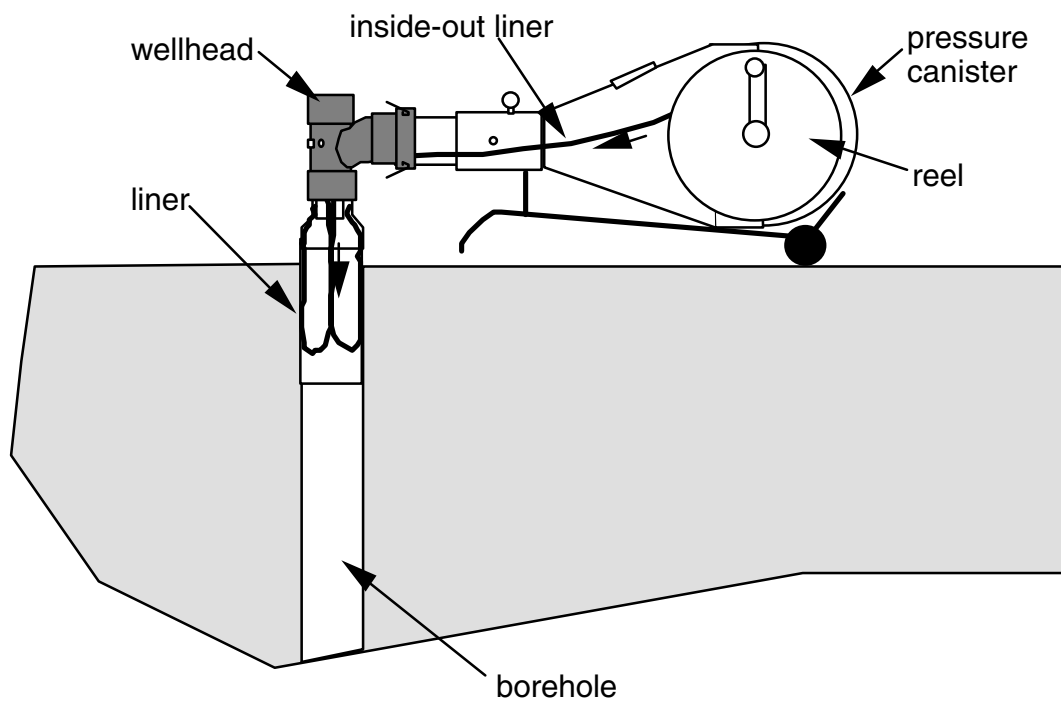


Figure 1. Components of a SEAMIST System

Figure 2.

Typical Liner Installation Geometry



Sandia is a multiprogram laboratory operated by Sandia Corporation, a Lockheed Martin Company, for the United States Department of Energy under contract DE-AC04-94AL85000.

THE USE OF DQO'S IN DESIGNING VADOSE ZONE MONITORING SYSTEMS

By

Kevin D. Leary

Department of Energy—Nevada Operations Office-Waste Management Division

Data Quality Objectives

There is a significant need to methodically develop innovative technologies and concurrently incorporate Data Quality Objectives (DQO's) in designing long-term, post-closure, vadose zone monitoring systems. Systematic use of the DQO process will assist in identifying technology development needs for long-term vadose zone monitoring challenges such as those faced by the Department of Energy at their low-level radioactive landfills. The DQO process is basically a roadmap of focused questions and processes leading one to the type, quantity, and quality of data necessary to fulfill specific project objectives. For example, a site closure monitoring program should be the by-product of site characterization and performance assessment data, performance assessment and modeling validation, remediation confirmation sampling (if applicable), regulator/stakeholder buy-in, uncertainty reduction and the resultant projected risk generated from either a contaminated ("dirty closure") or remediated site ("clean closure"). The majority of waste disposal sites are located in the vadose zone and therefore require innovative unsaturated zone instrumentation and monitoring technologies.

The use of the DQO process will assist:

- ❑ Determining the type and extent of regulatory constraints
- ❑ Selecting monitoring instrumentation, frequency, duration, type and extent of monitoring
- ❑ Selecting the types and applications of vadose zone models
- ❑ Establishing levels of acceptable uncertainty related to risk and the critical exposure pathways and resultant receptors
- ❑ Identifying data limitations
- ❑ Enhancing regulator and stakeholder acceptance of the monitoring system installed

It is critical that the right people be present during the DQO process including scientists, statisticians, people with historic knowledge, and regulators.

Establishing a monitoring program should be an iterative process and should change as monitoring data is generated. Therefore, the site monitoring design should be flexible in nature with the monitoring data used to evaluate the overall performance of your project.

The following is a summary of the DQO process as it applies to incorporating or developing and designing long-term vadose zone monitoring systems.

1. State the problem

- a) Develop clear and concise problem statement. Keep it focused, simple, reasonable, and flexible.
- b) Develop a site conceptual model
- c) Define the overall vadose zone monitoring project—e.g.
 - ❑ What are the overall objectives of your monitoring system? What types of monitoring are being considered (e.g., compliance or verification)? Are the objectives to monitor overall system performance or is it strictly to monitor for pollutant migration, or to establish baseline/background database ?
 - ❑ Evaluate the exposure scenarios. Is there a technology available that will adequately address each exposure pathway?
 - ❑ What is the duration of monitoring required to fulfill internal as well as regulatory requirements?
 - ❑ What are the contaminants of concern and what are their physical, chemical, and biological behaviors?
 - ❑ What are the future land-uses of the area? Will they impact monitoring? Will the future land uses impact the overall site risk? What type of monitoring system(s) is appropriate for the specified site? Will the system selected be able to demonstrate no long-term releases to the accessible environment?
 - ❑ Will the proposed monitoring system meet regulatory requirements?

2. Identify the decision

- a) What will the data be used for? (e.g., regulatory compliance, uncertainty reduction, validation of conceptual and/or analytical model, performance assessment validation, closure maintenance, alleviation of stakeholder concerns, or a demonstration that no contaminant transport and resultant exposure routes exists, etc.)
- b) Perform a preliminary risk assessment. How can monitoring data be used to reduce risk in a cost-efficient, timely manner? Can additional, supportive monitoring data be used to reduce overall total life-cycle costs of the project? (e.g., the use of monitoring to avoid or reduce clean-up—the feasibility of a “dirty” closure). Can closure design be “over-engineered” to reduce site risk and reduce overall site monitoring systems thereby reducing overall total life-cycle costs of the project?
- c) Bench-scale and pilot testing— What type, duration, cost and overall impact will bench-scale and pilot testing have on monitoring implementation?
- d) If a new vadose zone technology is used, how will the regulators and other stakeholders accept it? How can the project manager enhance stakeholder acceptability? Will the project manager be willing to “step out of the box” and try new technologies? What other risks are involved in installing new vadose zone technologies?
- e) How much and what can be done to assist in reducing the failure of the monitoring devices over a long period of time? What type of modifications may be needed to promote longevity of instrument operability, say 250 years? If the instrument fails during the required period of monitoring, can the instrument be repaired or replaced? Identify monitoring contingencies to mitigate the threat of instrumentation failure.
- f) What type and how much vadose zone monitoring can be accomplished within the project budget and project schedule?

- g) How and what internal trigger levels will be established for a regulator-approved vadose zone monitoring program? For example, under the federal Resource Conservation Recovery Act (RCRA), the groundwater is the regulatory point of compliance. Some regulators may be reluctant to permit a groundwater waiver in lieu of a vadose zone monitoring system, especially since they generally have no regulatory authority over the vadose zone. Will the regulator be inclined to move the point-of-compliance from the groundwater to the vadose zone? One would have to design a fairly rigorous, methodical, graded-approach vadose zone monitoring system if the site were granted a groundwater monitoring waiver by the regulator.

Graded Approach to Vadose Zone Monitoring: When applying vadose zone monitoring via the graded approach, the DQO process should be utilized to establish the following types of trigger levels:

- ❑ What soil moisture content (at a specified depth determined using DQO's) will be used as an internal trigger level?
- ❑ Movement of water below the internal trigger point depth does not necessarily mean that the contaminant moved with the water. Water movement should just be used as an indicator that the potential for downward contaminant transport exists. If the internal soil moisture level is exceeded, at what concentration should the constituent(s) of concern activate the next trigger level? Should it be the lowest analytical detection limit? In the case of vapor or gaseous transport, concentration trigger levels for specified constituents should be the first established trigger levels and should be established above the contaminant or any other likely exposure pathway.
- ❑ If the internal contaminant trigger level is exceeded, should a more rigorous sampling program be implemented? What will be the overall significance of this contaminant release? If the impact is significant and you approach regulatory sensitivity, what type of corrective or remedial actions can be effectively employed to mitigate or terminate contaminant transport?
- ❑ If there is no effective corrective or remedial action available to mitigate or terminate contaminant transport, what type of technologies are available to remediate the vadose zone?
- ❑ If there is no effective technology for remediating the vadose zone, what type of groundwater wells should be installed? Monitoring? Collector wells for a pump and treat system? Should horizontal collector wells (i.e., Raney collector wells) be installed? Should wells be installed for in-situ biodegradation? The DQO process should now be applied to establishing a groundwater monitoring (or remediation) network (e.g., how many wells, well location, screen depth location, well construction and completion, etc.).

Note: Identify and prioritize specific action/decision items based on each decision (e.g., the use of “if..then” statements)

Identify Data Needs

- a) Identify the data needs, associated costs and time required for each decision listed in step #2 above.
- b) List physical, chemical, and biological data by media (soil, soil water, etc.) and general analyte group
- c) What data will you collect and what will you do with the data? What type of data recording, transmission, and compatible data storage base will be used and how will it be integrated with the overall monitoring scheme? What other groups may have a need to acquire your data and what types of databases do they use that are compatible with your proposed system?
- d) Separate data into two categories: (1)-required data to support the long-term decisions of the monitoring program; (2)-desired data needs
- e) Identify and analyze all data sources that will assist in designing a vadose zone monitoring system (e.g., historical VS proposed). Is there a possibility of using existing on-site natural analogs as a vadose zone monitoring system such as the process of bioaccumulation by plants and animals, natural, in-situ bacteria, etc.?
- f) Identify analytical needs that are compatible with the type of vadose zone instrumentation installed.
- g) Is the chemical composition of the monitoring device compatible with the constituent evaluated (e.g., with PVC and organic solvents there will likely be problems)? Will the analytical methods and types of monitoring methods used meet or exceed the required regulatory detection limits, precision, and accuracy? If the monitoring equipment introduces sample results error, can the data be adjusted to reflect actual site conditions (e.g., sampling lysimeter)? In the case of environmental clean-up, is the precision and accuracy of the monitoring instrument capable of verifying established compliance clean-up standards?
- h) How often should the data be collected? Note that the frequency of data collection may influence the type of monitoring device selected. What will be the impacts of collecting unnecessary data be on project costs, schedule, stakeholder and scientific credibility, data base management, etc.?
- i) The length of the cable or other instrument limitations such as the need for remote access via a computer communication link may also influence the type of monitoring devices selected. Is this a potential problem?
- j) Does the unsaturated gradient need to be monitored or is the vertical moisture distribution sufficient? If the matric potential needs to be monitored, how reliable are the instruments (e.g., thermocouple psychrometers)?

3. Define Study Area(s)

- a) Define the vertical and horizontal spatial extent of your monitoring area—if necessary breakout into monitoring sub-units
- b) Define the temporal extent of your monitoring needs. How long should monitoring be conducted?
- c) Define data collection constraints (e.g., access, weather, budget, schedule, personnel limitations, technology constraints, etc..)
- d) Identify optimum time(s) for sampling

4. **Develop Decision Rules**

- a) Develop strategy to obtain quality and quantity of monitoring data (e.g., an outline of a vadose zone sampling and analysis plan; and a QA/QC plan) required to meet or exceed confidence levels established during the decision ruling. Incorporate the previous steps, especially step #2, into the development of the final decisions.
- b) The “if..then” statements derived in step #2 should now be developed for each primary decision. For example: If the tritium levels in the soil exceed the Maximum Contaminant level (MCL) equivalency of 20,000 picocuries/liter established for groundwater, then we should examine who or what may be threatened and evaluate the risk to human health. If there is a threat, what steps can we take to mitigate the problem?
- c) The “if...then” statements can also be used to develop best management practices or remedial actions to mitigate or terminate off-site contaminant transport and therefore reduce subsequent exposure pathways and overall site risk.

5. **Specify Acceptable Limits of Uncertainty**

- a) How much uncertainty are you willing to accept based upon the spatial and temporal distribution and instrument limitations of the vadose zone monitoring system? How much risk is there in equipment failure during the required monitoring period?
- b) What is the quality and quantity of data needed to support your verification or compliance vadose zone monitoring system?

6. **Optimize Study Design for Data Acquisition**

- a) Evaluate the results of the previous 6 steps and develop the most resource-efficient methodology that meets or exceeds all of the DQO's.
- b) For example, the DQO's could be summarized in a matrix table taking into account the following factors:
 - ❑ Specific monitoring objectives
 - ❑ Designated monitoring equipment and analytical data acceptance criteria (e.g., precision, accuracy, completeness, and QA/QC criteria)
 - ❑ Prioritize data applications
 - ❑ Use of historical field and analytical data
 - ❑ Site characteristics that will impact/influence monitoring system design
 - ❑ Statistical validity and number of samples required
 - ❑ Various levels of monitoring effort and associated costs and schedules
 - ❑ Contaminants of concern: types, sources and rationale for selection
 - ❑ Preliminary site risks using existing site characteristics data
 - ❑ Target level of clean-up and regulatory level of clean-up
 - ❑ Required field and laboratory instrument detection limits.
 - ❑ The use of on-site laboratories and field screening techniques to supplement field vadose zone monitoring devices. If field screening is used, what types of chemicals may interfere with the analysis? Are they present at the site?
 - ❑ Critical sampling locations

The primary intent of steps #6 and #7 is to establish a sampling program that is acceptable to both the regulators and other interested parties. Sample size is primarily dependent upon the acceptable limits of uncertainty. The DQO process should evaluate the consequences of a contaminated site if the sampling size is too small and the probability of error is great. However, using classical statistics to develop the “appropriate” number of samples can result in an extremely expensive monitoring program. It is generally best to restrict statistical approaches to readily approachable media (e.g., surface soils during characterization and verification sampling). Monitoring locations need to be spatially, temporally, physically and chemically representative of the media.

The establishment and number of monitoring locations is dependent upon a variety of factors including:

- ❑ Site complexity
- ❑ Spatial and temporal detail of the contaminant required to meet the sampling objectives
- ❑ The acceptable level of uncertainty established during the DQO process

For example, in detection monitoring, the detection of a contaminant and the establishment of a baseline for vadose zone water quality are the primary objectives. In contrast, assessment monitoring is much more detailed and involves the nature, extent, and dynamics of the contaminated pore water. Sampling objectives generally dictate the following:

- ❑ The number, type and location of monitoring devices
- ❑ Parameters to be measured
- ❑ Number of samples and/or readings
- ❑ The reliability of the pore water quality data
- ❑ Monitoring and sampling procedures
- ❑ Analytical methods, detection limits, and precision to meet these objectives

Supportive data gathered during the site characterization phase (e.g., soil borings, geophysical surveys, soil gas surveys, topography, site vegetation, climate, etc.) will assist the experienced scientist in the placement and number of monitoring devices. The validity of these “point” measurements from individual monitoring instruments depends upon the extent to which these “points” are representative of the contaminant spatial distribution. The number and location of vadose zone monitoring devices installed at a site is a continual process that evolves throughout the field site characterization process. The installation or abandonment of monitoring devices at one stage is dependent upon the trends and anomalies revealed in the previous stage.

A vadose zone monitoring program should be an evolutionary process that should improve as the available database expands. The number of monitoring devices may expand or contract as the needs of the program evolve. Because there is so much variability from site to site, there is no set number of monitoring devices recommended for each soil, geologic and/or hydrogeologic investigation.

Properly locating vadose zone monitoring instruments involves evaluating numerous factors including:

- ❑ Surface-water features (e.g., ponds, streams, irrigation, etc.)
- ❑ Groundwater discharge/recharge boundaries and groundwater barriers
- ❑ Relative risk and exposure pathways
- ❑ Soil type and/or geologic distribution
- ❑ Vegetative distribution that indicate certain characteristics about the subsurface
- ❑ Representative selection of background, upgradient sampling locations
- ❑ Geologic features (e.g., faults, topography, contact zones, bedding planes, etc.)
- ❑ Instrument limitations
- ❑ Contaminant characteristics (e.g., source location, density, mobility, volatility, etc.)
- ❑ Property boundaries
- ❑ Legal issues (e.g., regulatory requirements, potential litigation from adjacent property owners, etc.)

Vadose Zone Monitoring Site Design

The spatial and vertical location of vadose zone monitoring devices to ensure that the unsaturated zone is being characterized and monitored sufficiently and accurately is one of the most important components of any vadose zone monitoring program. The vertical and horizontal emplacement should not only consider the scientific supportive data, but should also consider the various routes of exposure. For example, a contrasting soil textural boundary (i.e., a capillary barrier) may function as a horizontal drain for a contaminant, say radon gas. Assume that this soil horizon is located at about the same depth as most basements in an urban area. This soil horizon may not appear to have any significance during the initial planning stages of a monitoring program. However, when evaluating a combination of exposure route, relative risk of exposure, the physical and chemical nature of the contaminant and the resultant contaminant pathway, this soil horizon would be an ideal location for establishing a vadose zone monitoring network for radon.

Therefore, final monitoring locations should only be determined after thoroughly examining all information gathered during office and field site characterization phases including:

- ❑ Soil surveys
- ❑ Aerial photographs
- ❑ Topographic and geologic maps
- ❑ Well logs
- ❑ Geologic cross-sections
- ❑ Facility characterization
- ❑ Contaminant source
- ❑ Contaminant characteristics
- ❑ Models
- ❑ Conducting an on-site inspection/evaluation of the site including drilling/auguring exploratory borings, and performing other subsurface tests if warranted (e.g., surface and borehole geophysics)

The above activities are conducted to evaluate various contaminant properties and subsurface soil and geologic conditions. All of these factors can be used in formulating a conceptual model and all have a major influence on the location, number, and type of vadose zone monitoring devices installed. Furthermore, this type of analysis will assist the project manager in determining the need for vadose zone instrumentation technology development. However, the objective of the study, project schedule and budget, and the size of the area will have the primary influence on the number and placement of the monitoring devices. The more complex the site geology/hydrogeology, characteristics and quantity of the contaminant, and the larger the area being evaluated, the greater the number of monitoring locations that will be required.

It is preferable from a cost and schedule standpoint that all boreholes be converted to permanent monitoring locations. Therefore, it is critical that as much information be gathered and an accurate conceptual model be formulated prior to initializing any drilling program.

A positive sample from a monitoring location may prove the existence of vadose zone contamination (provided the monitoring device was “aseptically” installed), however, the absence of contamination in a vadose zone sample does not prove the absence of contamination in the unsaturated zone. The heterogeneity of the subsurface environment and the various properties of the contaminant make the location and number of sampling points extremely difficult. Because of this common scenario of site-specific heterogeneity, it is impossible to prescribe a specific number, type, and specific location of monitoring devices for all sites.

Information sources necessary for determining the number and location of monitoring stations are described above. However, professional experience and common sense are two other primary factors that should be used in determining the number and location of monitoring devices. The monitoring system should be sufficient to detect contamination that is moving off-site, detecting trends in vadose zone pore water quality, and accurately establish background vadose zone pore water quality.

It must be remembered that many contaminants flow in a “finger-like” fashion following the path of least resistance. Therefore, this must be kept in mind when establishing vadose zone monitoring locations. Again, it is critical that all site characterization data be evaluated prior to selecting monitoring locations.

For example, landfills are often located in gullies and ravines. If the monitoring system is installed after the landfill has been established, a quick look at old aerial photographs may reveal an old buried stream channel that would be a likely pathway of contaminant transport. A monitoring system could then be sited downgradient of the landfill installed in the buried creek channel—perhaps in a contrasting soil textural horizon that may promote lateral off-site contaminant transport. However, if this feature is not discovered during site characterization, the downgradient monitoring devices, unless by chance

installed in the buried creek channel, would completely miss any off-site contaminant transport.

All rationale and assumptions used in determining the number, location, and type of vadose monitoring instruments must be well documented. Once the horizontal locations are determined for each instrument, the actual vertical location of the device is the next critical factor in collecting a representative, in-situ sample.

An analysis of over-designing your closure structure or adhering to conservative clean-up standards versus the total life-cycle costs of long-term monitoring should be conducted (where feasible). Depending on the site, number, and type of vadose zone monitoring stations, at times it may be far more cost effective to over-design your closure structure or adhere to conservative clean-up standards than to conduct long-term monitoring. This may be especially true at several DOE low-level radioactive disposal sites where monitoring may be required up to 250 years.

CLOSED-FORM EXPRESSIONS FOR WATER RETENTION AND CONDUCTIVITY DATA

Feike J. Leij, Walter B. Russell, and Scott M. Lesch^a

*U.S. Salinity Laboratory, U.S. Department of Agriculture, Agricultural Research Service,
Riverside, CA 92507-4617*

Adapted from Ground Water 35(5):848-858, 1997

Closed-form expressions for quantifying the unsaturated soil hydraulic properties are widely used to model subsurface flow and transport and to investigate indirect methods for estimating these properties. There are few comprehensive investigations of the suitability of different functions to describe relationships between soil water pressure head (h), effective water saturation (S_e), and the unsaturated hydraulic conductivity (K). We attempted to fit fourteen retention and eleven conductivity functions to 903 sets of water retention and hydraulic conductivity data measured on soil and rock samples or horizons reported in the unsaturated hydraulic database UNSODA. Some of the best mean values for r^2 and MSE for fitting $S_e(h)$ data were obtained with the retention functions reported by van Genuchten (1980), Globus (1987), and Hutson and Cass (1987). A function reported by Gardner (1958) could describe $K(h)$ data quite well whereas functions reported by Brooks and Corey (1964) and van Genuchten (1980), which are respectively based on the conductivity models by Burdine and Mualem, yielded a relatively good description of $K(S_e)$ data.

Introduction

Closed-form expressions have been employed to describe the unsaturated hydraulic properties for many reasons (van Genuchten and Leij, 1992; Marion et al., 1994). They are attractive to model the $S_e(h)$ and $K(h)$ or $K(S_e)$ relationships in numerical models; the nontabular data will simplify input to computer models (although at the expense of computational efficiency) and allow the estimation of hydraulic properties using inverse procedures. Analytical expressions facilitate rapid comparison of hydraulic properties of different porous media. They are used to estimate hydraulic properties for media containing different types of fluids, they are convenient for scaling approaches or for use with Geographic Information Systems, and they may be used to estimate hydraulic properties in the dry range. Closed-form expressions play an important role in *indirectly* quantifying unsaturated hydraulic data using soil properties that are already available or can easily be determined. Parameters in the analytical expressions for $S_e(h)$, $K(h)$, and $K(S_e)$ can be estimated empirically with regression equations that correlate textural and other data with unsaturated soil hydraulic data. Inasmuch the measurement of the hydraulic conductivity is considerably more difficult and less accurate than that of the water retention curve, a number of physico-empirical approaches have been proposed to estimate $K(h)$ or $K(S_e)$ from a closed-form expression for $S_e(h)$ data.

Because of the aforementioned utility and convenience, analytical expressions have become quite popular for describing hydraulic properties. Many functions have been proposed for this purpose. Regardless of their application, it is imperative that these functions accurately describe the unsaturated soil hydraulic data. Only a limited number of independent studies have been published that evaluate the suitability of several popular empirical and semi-empirical functions (Alexander and Skaggs, 1986; van Genuchten and Nielsen, 1985). In the following a relatively comprehensive study is carried out to evaluate a variety of functional expressions for $S_e(h)$ and $K(h)$ or $K(S_e)$ to describe the hydraulic data. The data and other relevant information are contained in the international UNsaturated SOil hydraulic DAtabase (Leij et al., 1996), which is described as case study 107.

Closed-Form Expressions

Closed-form expressions were selected after a review of the literature and a preliminary screening of retention and conductivity functions. Only models were selected for which we believed that the parameter estimation would converge for a majority of data sets. Furthermore, we have attempted to assemble different types of mathematical formulations, including expressions based on power functions, polynomials, and exponential and error functions. Additional functions for the hydraulic curves, especially the water retention, can be found in the literature (cf. Globus, 1987; Mualem, 1986; Vereecken, 1992).

Retention Functions

The fourteen retention models used for this study are listed in Table 1. Note that $S_e = (\theta - \theta_r) / (\theta_s - \theta_r)$ is an effective, dimensionless reduced water content, and θ is the water content expressed as volume of water per volume of porous medium. The subscripts r and s denote the residual and saturated water contents, respectively. The retention functions may also contain up to three empirical shape factors α , β , and γ . The model by Brooks and Corey (1964), which is given by function 11, has been successfully used to describe retention data for relatively homogeneous and isotropic samples, which have a narrow pore-size distribution, with a typical value for β of 2 (lower for structured soils and higher for sands). Parameter values can be readily obtained from a plot of the $S_e(h)$ curve on double logarithmic paper. Function 11 may not describe the data well near saturation and a discontinuity occurs at $h=1/\alpha$. The same problem plagues the function by Campbell (1974). Several functions have been suggested to improve the description near saturation.

Function 12 is a variation of the function presented by Laliberte (1969), it is intended to provide a smooth description of the data near saturation with a continuous derivative. We investigated function 12 without imposing any conditions on α , β , and γ . Retention function 13 of Vauclin et al.

(1979) has been used by El-Kadi (1985); its form is similar to the expression proposed by Brutsaert (1966) except that a log-transformed pressure head is being used. Note that $S_e=1$ for $0 \leq h < 1$. Function 14 of van Genuchten (1980) has been widely used for describing retention data. This function allows for a smooth transition zone near $h=1/\alpha$ in contrast with function 11 (see also conductivity function 31). A similar function, with $\gamma=1$, has been used by Ahuja and Swartzendruber (1972) and Varallyay and Mironenko (1979). To facilitate the use of function 14 in hydraulic conductivity models, the value of γ is sometimes restricted. Function 15 involves the restriction $\gamma=1-1/\beta$, which is used in conjunction with the conductivity model by Mualem (1976).

The previously mentioned function by Campbell (1974) was modified by Clapp and Hornberger (1978) by describing h as a function of $S=\theta/\theta_s$ with a parabolic equation close to saturation ($S_i < S \leq 1$) in addition to the power function of Campbell for $S \leq S_i$. Continuity in h and dh/dS was imposed at S_i , which was arbitrarily set equal to 0.92. Hutson and Cass (1987) employed this concept by using a parabolic equation that did not lead to additional unknown parameters while allowing for a flexible S_i . Function 16 gives their two-part expression for the water retention and the definition for S_i .

Russo (1988) derived retention function 17 for use with conductivity function 32 of Gardner (1958), shown in Table 2, using the constraint that the retention function satisfies the capillary model for predicting conductivity by Mualem (1976). Zhang and van Genuchten (1994) proposed function 18, which is the ratio of a first- and second-order polynomial, to describe retention data for porous media with a bimodal pore-size distribution. Retention curves of media with a multi-modal pore-size distribution have also been described by summing functions of the same form, such as function 14 (cf. Othmer et al., 1991; Durner, 1994) or of a different form (Ross and Smettem, 1993). Retention function 19, which was reported in the monograph by Globus (1987), is similar to function 18 except that there is no independent variable in the numerator. Farrell and Larson (1972) arbitrarily assumed a linear relationship between h and $\exp(\theta_s - \theta)$; function 20 is obtained by changing the dependency.

Several recent publications present retention equations that were modified to improve the

description of water retention for dry conditions (Ross et al., 1991; Rossi and Nimmo, 1994; Fayer and Simmons, 1995). Function 21 serves as an example of these expressions. This function consists of a power function for the wet range similar to function 16, and the Brooks-Corey function 11 with a logarithmic correction term according to Ross et al. (1991) for the dry range. The saturation and its derivative are continuous at the junction point $h=\beta$.

Kosugi (1994) derived retention function 22 by assuming a modified three-parameter lognormal expression for the pore-size probability density function. The maximum pore size of the medium determines the pressure $1/\alpha$ below which the water content is constant ($S_e=1$). At the inflection point, $h=\beta$, the value for S_e is equal to $\frac{1}{2} \operatorname{erfc}(-\gamma/\sqrt{2})$ where erfc denotes the complementary error function.

Finally, Bumb et al. (1992) evaluated expressions 23 and 24 for fitting water retention data. Both contain exponential functions and were identified as the Boltzmann and Fermi distribution, respectively. The Boltzmann distribution is convenient for deriving expressions of the hydraulic conductivity because it can be easily inverted to the $h(S_e)$ form and integrated. However, it does not provide a smooth description of the water content for low pressures like the Fermi distribution.

Conductivity Functions

Many general models for the hydraulic conductivity conceptualize flow in the microscopic pore space and use Darcy's law to estimate the (macroscopic) hydraulic conductivity. Explicit functions for the hydraulic conductivity can be defined from these models by specifying a water retention curve, which is expressed in functional form as $h(S_e)$, to estimate the pore-size distribution. Two of the more popular models were proposed by Burdine (1953):

$$K(S_e) = K_s S_e^\delta \frac{g(S_e)}{g(1)} \quad \text{where} \quad g(S_e) = \int_0^{S_e} \frac{d\xi}{[h(\xi)]^2} \quad (1)$$

and Mualem (1976)

$$K(S_e) = K_s S_e^\delta \left[\frac{f(S_e)}{f(1)} \right]^2 \quad \text{where} \quad f(S_e) = \int_0^{S_e} \frac{d\xi}{h(\xi)} \quad (2)$$

with ξ as a dummy integration variable. Our description of conductivity data typically involves the use of two additional parameters. The fourth empirical constant δ , which is frequently set to 2 for the Burdine model and 0.5 for the Mualem model, and the saturated conductivity, K_s , although this may involve a substantial error (Schaap and Leij, 1999). Finally, it should be noted that these types of conductivity models are not applicable for flow in very dry media.

Table 2 contains the functions that were used to describe the relative conductivity, K/K_s . These expressions are either completely empirical or based on a pore-size distribution model. A distinction is made between conductivity functions based on the pressure head, i.e., $K(h)$, and those based on the water content, i.e., $K(S_e)$.

Gardner (1958) derived analytical solutions for steady one-dimensional unsaturated flow assuming two simplified expressions for $K(h)$. Function 31 is a generalization of the function by Gardner, who assumed $\gamma=1$, to obtain an expression similar to retention function 14. Gardner (1958) reported that function 31 ($\gamma=1$) seems to fit conductivity data quite well. The analytical solution of unsaturated flow problems may be facilitated if function 32 is used. Gardner (1958) pointed out that this function does not provide a good description of K over a wide range of h . Function 33 is obtained by first evaluating the Burdine model (1) for the Brooks and Corey retention function 11 and then expressing the conductivity in terms of h instead of S_e with the help of function 11.

Function 34 is based on the conductivity model of Mualem (1976) given by (2) for a retention function that may be selected from twelve expressions in Table 1. Application of the chain rule allows a change in integration variable that obviates the need for an explicit inversion from the $S_e(h)$ to the $h(S_e)$ form. We may write (cf. Russo, 1988; Fayer and Simmons, 1995):

$$f(S_e) = \int_0^{S_e} \frac{dS_e}{h} = \int_\infty^h \frac{1}{h} \frac{dS_e}{dh} dh \equiv f(h) \quad (3)$$

Integration according to either equation (2) or (3) can sometimes be done analytically and otherwise

has to be carried out numerically. The analytical expression may contain the complete Beta or exponential integral functions, which also have to be evaluated numerically (Leij et al, 1997)

The next group of conductivity functions uses S_e as the independent variable. Function 41, which was presented by Brooks and Corey (1964), is readily obtained by substituting function 11 into equation (1). Van Genuchten (1980) derived function 42 by simplifying function 14 to 15 ($\gamma=1-1/\beta$) and by subsequently evaluating Mualem's conductivity model. It should be noted that the corresponding $K(h)$ function in Table 3 follows from inserting function 15 for S_e into 42. Conductivity function 43 of van Genuchten and Nielsen (1985) was derived according to Mualem's model from the less restrictive retention function 14. We have used the notation of these authors for the incomplete beta function, $I_\gamma(p,q)$. Van Genuchten et al. (1991) list a number of disadvantages in using the saturated hydraulic conductivity as a matching point for the hydraulic conductivity. It may be desirable to use a water content below saturation as a reference value. Conductivity function 44 uses a water content $S_e=\delta$ for this purpose. Function 44 gives the ratio of the conductivities according to function 42 at an arbitrary S_e . A similar approach can be taken for other conductivity models than 42. Furthermore $K(S_e=\delta)$ is ideally fixed to represent a reliable observation point.

The following two functions are slight modifications of the original expressions to improve the parameter optimization while using uniform initial estimates. Function 45 is obtained by modifying the expression reported, among others, by Warrick (1995) and attributed to Fujita (1952). Function 46 follows from changing the equation used by Setiawan and Nakano (1993). Finally, an expression similar to function 47 was used by Libardi et al. (1980).

Parameter Optimization

We adapted the program RETC of van Genuchten et al. (1991) to estimate the parameters of all the combinations of retention and conductivity functions. The parameter values were determined by minimizing the objective function according to

$$O(\mathbf{b}) = \sum_{i=1}^N [\theta_i - \hat{\theta}_i(\mathbf{b})]^2 + \sum_{i=1}^M \{W[\log K_i - \log \hat{K}_i(\mathbf{b})]\}^2 \quad (4)$$

where θ_i and $\hat{\theta}_i$ are the observed and fitted water contents, respectively; where K_i and \hat{K}_i are the observed and fitted values for the hydraulic conductivity data; N is the number of retention data, M is the number of conductivity data, and the trial parameter vector, $\mathbf{b} = (\theta_r, \theta_s, \alpha, \beta, \gamma, \delta, K_s)^T$, contains the unknown model parameters to be fitted. The weight W is internally determined according to

$$W = M \sum_{i=1}^N \theta_i / N \sum_{i=1}^M \log K_i \quad (5)$$

This weight is intended to minimize bias in the optimization procedure toward the data type with the greater numerical values by normalizing the conductivity data with respect to the retention data. The optimization was done according to the Levenberg-Marquardt method (Marquardt, 1963).

The goodness of fit for the individual retention and conductivity data sets was assessed with the correlation coefficient (r^2)

$$r^2 = 1 - \frac{\sum_{i=1}^N (\theta_i - \hat{\theta}_i)^2 + \sum_{i=1}^M (\log K_i - \log \hat{K}_i)^2}{\sum_{i=1}^N (\theta_i - \bar{\theta})^2 + \sum_{i=1}^M (\log K_i - \log \bar{K})^2} \quad \bar{\theta} = \frac{1}{N} \sum_{i=1}^N \theta_i, \quad \log \bar{K} = \frac{1}{M} \sum_{i=1}^M \log K_i \quad (6)$$

and the mean squared error (MSE) is given by

$$MSE = \frac{\sum_{i=1}^N (\theta_i - \hat{\theta}_i)^2 + \sum_{i=1}^M (\log K_i - \log \hat{K}_i)^2}{M + N - p} \quad (7)$$

where p is the number of fitting parameters. We have arbitrarily limited the maximum number of fitting parameters to seven but such a limitation is not necessary. The variation in statistical and model parameters, x , is quantified with the standard error of the mean:

$$SE = \sqrt{\frac{\sum_{i=1}^n (x_i - \mu_x)^2}{(n-1)n}} \quad (8)$$

where μ_x is the arithmetic mean and n is the number of data sets. In addition to these mathematical

criteria, one should also check whether the fitting parameters provide a physically realistic description of the hydraulic data.

Fitting parameters for the combinations of the 14 retention with the 11 conductivity functions are listed in Table 4 of Leij et al. (1997). Combinations will be denoted by a four-digit number; the first two digits of the combination number refer to the retention function and the last two to the conductivity function. Each of the 54 combinations of $S_e(h)$ - $K(h)$ functions was fitted to 346 data sets. No results are reported for combinations 1734 and 2034 because of a lack of data sets that could be successfully optimized. Similarly, we tried to fit all 98 combinations of $S_e(h)$ - $K(S_e)$ functions to 557 data sets. Initial estimates for the optimization procedure are according to the results of Carsel and Parrish (1988), these are not necessarily the best for all mathematical expressions. Values for θ_r , θ_s , and δ were constrained as discussed by Leij et al. (1997).

Results

Table 3 contains the number of data sets (n) that could be optimized for each combination of retention and conductivity functions and the corresponding median values for r^2 and MSE. The retention functions are identified in the first column and the numbers for the conductivity function are given in the top row. Also included is the arithmetic mean (μ) of n , r^2 , and MSE for individual retention functions, obtained as an average of the results for a particular $S_e(h)$ function for all $K(h)$ and $K(S_e)$ functions, as shown in the last column of Table 3. Conversely, μ_n , μ_{r^2} , and μ_{MSE} values for individual conductivity functions were obtained by averaging over results for all $S_e(h)$ functions.

The information in Table 3 was used to rank the performance of the hydraulic functions with respect to n , r^2 , and MSE. Figure 1 shows the ranking for the $S_e(h)$ functions. On average, function 17 described the most data sets (417) and received a rank of 1; it was followed by functions 14 (412), 16 (410) and 11 (409). The last column of Table 3 shows that function 22 only fitted an average of 109 functions; of course, the number of fitted data sets may be increased by modifying the optimization

algorithm or initial estimates. We were able to improve the results for combination 2234 by changing the initial estimate for γ . The rankings for the $K(S_e)$ and $K(h)$ functions are given in Figures 2 and 3, respectively. The most data sets could be described with functions 34 and 47, respectively.

The rankings for r^2 and MSE are closely related. Function 15 has the highest r^2 (.910) and lowest MSE (.947) for fitting $S_e(h)$ data with function 14 having the next best r^2 and function 16 the next best MSE. Both functions 15 and 16 use only four parameters (Table 1). The MSE for function 16 (1.07) is considerable greater than for function 15 but it is obtained for a somewhat larger data set (410) than for function 15 (375). Figure 2 illustrates that the fitting of $K(h)$ data is best done with function 31 in view of its high rankings for r^2 and MSE. The relatively poor performance of function 32 was already alluded to by Gardner (1958), this expression may still be useful for conductivities close to saturation. Functions 33 and 34 appear to provide a reasonable description of the data. In view of the additional effort associated in using model 34, we did not further pursue its use or the development of conductivity functions based on other models than Mualem's equation (2). According to Fig. 3, functions 41 and 43 appear to provide the best description of $K(S_e)$ data. The reader may study Table 3 to make additional inferences regarding the suitability of particular functions or combinations of conductivity and retention functions.

A more detailed comparison was subsequently made for the results of the most promising functions to a uniform data set. First we determined six $S_e(h)$, two $K(h)$, and four $K(S_e)$ functions with the best combined ranking for r^2 and MSE. Secondly, retention functions 11, 13, 14, 15, 16, and 19 were combined with conductivity functions 31, 33, 41, 42, 43, and 46 to select combinations that tended to have the best combined ranking for n , r^2 , and MSE in Table 3. We used the seven combinations 1431, 1433, 1531, 1533, 1631, 1633, and 1931 for $S_e(h)$ - $K(h)$ data and eight combinations 1441, 1442, 1443, 1541, 1543, 1641, 1642, and 1643 for $S_e(h)$ - $K(S_e)$ data. It should be noted that combinations 1342 and 1542 could describe relatively few data sets and they were omitted despite their favorable combined ranking relative to some of the selected combinations. Thirdly, 306

$S_e(h)$ - $K(h)$ data sets were identified that could be described by each of the above seven combinations and, similarly, 401 $S_e(h)$ - $K(S_e)$ data sets were found for which a parameter set could be optimized for all eight combinations of $S_e(h)$ and $K(S_e)$ functions.

Table 4 shows the extended results for the $S_e(h)$ - $K(h)$ data. All combinations appear to describe the hydraulic data reasonably well with similar values for r^2 and MSE. Combinations 1931 and 1431 have the lowest median and mean value for MSE, respectively. Now that a comparison for the same data sets is being made, retention functions 15 and 16 appear somewhat less attractive than depicted in Fig. 1. It is apparent that 31 is the preferred $K(h)$ function. It is less clear what function is best used to describe corresponding retention data. Based on the mean values for r^2 and MSE, the order of preference may be functions 14, 15 or 19, and 16. Table 4 also shows the similar median values for either θ_r or θ_s , which reflect the constraints that were imposed on these parameters during the optimization. A considerable difference exists between the median and mean for α and, especially, for K_s ; the SE is relatively large. This suggests a skewed probability density function of these parameters. Clearly, K_s is not an attractive fitting parameter and it would be better to use a value for the conductivity at a higher suction or omit K_s as a fitting parameter altogether. The remaining parameters, particularly β and γ , appear to have a more favorable SE. Note that γ does not occur in combinations 1533 and 1633.

Values for r^2 , MSE, and parameters for fitting $S_e(h)$ - $K(S_e)$ data with eight combinations are given in Table 5. A comparison of Tables 4 and 5 reveals that the data are not as well described as the $S_e(h)$ - $K(h)$ data. The considerable number of outlying results causes a discrepancy between the median and arithmetic mean. Examination of the mean for r^2 and MSE indicates that function 43 tends to give the poorest results among the three $K(S_e)$ functions. Notice that a better performance was obtained for function 43 than 42 using the variably-sized data set (Table 3). If we compare the means of r^2 and MSE for combinations 1441, 1541, and 1641 it appears that retention functions 15 and 16 perform slightly better than 14. The results reported in Table 4 also indicate that these three functions are

attractive for describing retention data. The behavior of the functional parameters in Table 5 tends to be similar to that in Table 4. However the parameter δ , which is now exclusively a power of the saturation except for combination 1643, exhibits a greater standard error. The importance of this parameter in the model of Mualem (1976) has been investigated by a number of authors (Schuh and Cline, 1990; Yates et al., 1992). Yates et al. (1992) concluded that this parameter may fluctuate considerably while an independent means of predicting its value will not necessarily lead to a better prediction of the hydraulic conductivity. Hence we are not as concerned about the effect of δ on the accuracy of the optimization compared to K_s .

Conclusions

We attempted to fit the fourteen retention and eleven conductivity functions that are shown in Tables 1 and 2 to 346 $S_e(h)$ - $K(h)$ and 557 $S_e(h)$ - $K(S_e)$ data sets of the unsaturated hydraulic database UNSODA. Table 3 presents the number of data sets that could be described with each of the 152 combinations of retention and conductivity functions as well as the corresponding median values for r^2 and MSE. Subsequently, we screened the results for desirable combinations of retention and conductivity functions (this amounted to the omission of a few attractive combinations such as 1334 and 2234). Seven combinations of $S_e(h)$ and $K(h)$ functions with favorable optimization results were fitted to 306 data sets (cf. Table 4). The best mean values for r^2 and MSE were obtained with retention functions 14 and 15 (van Genuchten, 1980), 19 (Globus, 1987), and 16 (Hutson and Cass, 1987). Function 31 of Gardner (1958) was the most attractive for describing $K(h)$ data. Eight combinations were used for fitting 401 $S_e(h)$ - $K(S_e)$ data sets (cf. Table 5). Retention functions 14, 15, and 16 performed reasonably well, although function 14 has a slightly higher MSE than the other two functions when used with conductivity function 41. Examination of the mean for r^2 and MSE indicates that functions 41 (Brooks and Corey, 1964) and 42 (van Genuchten, 1980) can fit $K(S_e)$ data with comparable accuracy. In view of the relatively poor performance of the $K(S_e)$ functions, the use and

development of alternative $K(S_e)$ functions seems appropriate.

References

- Ahuja, L. R. and D. Swartzendruber. 1972. An improved form of the soil-water diffusivity function. Soil Sci. Soc. Am. Proc. v. 36, pp. 9-14.
- Alexander, L. and R. W. Skaggs. 1986. Predicting unsaturated hydraulic conductivity from the soil water characteristic. Trans. ASAE v. 29, pp. 176-184.
- Brooks, R. H. and A. T. Corey. 1964. Hydraulic properties of porous media. Hydrology Paper. Colorado State Univ., Fort Collins, CO. No. 3.
- Brutsaert, W. 1966. Probability for pore-size distributions. Soil Sci. v. 101, pp. 400-404.
- Bumb, A. C., C. L. Murphy, and L. G. Everett. 1992. A comparison of three functional forms for representing soil moisture characteristics. Ground Water. v. 3, pp. 177-185.
- Burdine, N. T. 1953. Relative permeability calculations from pore-size distribution data. Petrol. Trans., Am. Inst. Min. Eng. v. 198, pp. 71-77.
- Campbell, G. S. 1974. A simple method for determining unsaturated conductivity from moisture retention data. Soil Sci. v. 117, pp. 311-314.
- Carsel, R. F. and R. S. Parrish. 1988. Developing joint probability distributions of soil water retention characteristics. Water Resour. Res. v. 24, pp. 755-769.
- Clapp, R. B. and G. M. Hornberger. 1978. Empirical equations for some soil hydraulic properties.
- Durner, W. 1994. Hydraulic conductivity estimation for soils with heterogeneous pore structure. Water Resour. Res. v. 30, pp. 211-223.
- El-Kadi, A. I. 1985. On estimating the hydraulic properties of soil, Part I. Comparison between forms to estimate the soil-water characteristic function. Adv. Water Resour. v. 8, pp. 136-147.
- Farrell, D.W., and W.E. Larson. 1972. Modeling the pore structure of porous media. Water Resour. Res. v. 3, pp. 699-706.
- Fayer, M. J., and C. S. Simmons. 1995. Modified soil water retention functions for all matric suctions. Water Resour. Res. v. 31, pp. 1233-1238.

- Fujita, H. 1952. The exact pattern of concentration-dependent diffusion on a semi-infinite medium. II. Text. Res. J. v. 22, pp. 823-827.
- Gardner, W. R. 1958. Some steady-state solutions of the unsaturated moisture flow equation with application to evaporation from a water table. Soil Sci. v. 85, pp. 228-232.
- Globus, A. M. 1987. Soil hydrophysical description of agroecological mathematical models (in Russian). Gidrometeoizdat, St. Petersburg, Russia.
- Hutson, J. L. and A. Cass. 1987. A retentivity function for use in soil-water simulation models. J. Soil Sci. v. 38, pp. 105-113.
- Kosugi, K. 1994. Three-parameter lognormal distribution model for soil water retention. Water Resour. Res. v. 30, pp. 891-901.
- Laliberte, G. E. 1969. A mathematical function for describing capillary pressure-desaturation data. Bull. Int. Ass. Sci. Hydrol. v. 14, pp. 131-149.
- Leij, F. J., W. J. Alves, and M. Th. van Genuchten. 1996. The UNSODA Unsaturated Soil Hydraulic Database. EPA, Ada, OK.
- Leij, F. J., W. B. Russell, and S. M. Lesch. 1997. Closed-form expressions for water retention and conductivity data. Ground Water v. 35, pp. 848-858.
- Libardi, P. L., K. Reichardt, D. R. Nielsen, and J. W. Biggar. 1980. Simple field methods for estimating soil hydraulic conductivity. Soil Sci. Soc. Am. J. v. 44, pp. 3-7.
- Marion, J.M., D. Or, D.E. Rolston, M.L. Kavas, and J.W. Biggar. 1994. Evaluation of methods for determining soil-water retentivity and unsaturated hydraulic conductivity. Soil Sci. v. 158, pp. 1-13.
- Marquardt, D. W. 1963. An algorithm for least-squares estimation of nonlinear parameters. J. Soc. Ind. Appl. Math. v. 11, pp. 431-441.
- Mualem, Y. 1976. A new model for predicting the hydraulic conductivity of unsaturated porous media. Water Resour. Res. v. 12, pp. 513-522.

- Mualem, Y. 1986. Hydraulic conductivity of unsaturated soil: Prediction and formulas. In: A. Klute (ed.) *Methods of Soil Analysis. Part 1.* ASA and SSSA, Madison, WI. *Agronomy Monogr.* v. 9. pp. 799-823.
- Othmer, H. B., B. Diekkrüger, and M. Kutilek. 1991. Bimodal porosity and unsaturated hydraulic conductivity. *Soil Sci.* v. 152, pp. 139-150.
- Ross, P. J., and K. J. Smettem. 1993. Describing soil hydraulic properties with sums of simple functions. *Soil Sci. Soc. Am. J.* v. 57, pp. 26-29.
- Ross, P. J., J. Williams, and K. L. Bristow. 1991. Equation for extending water-retention curves to dryness. *Soil Sci. Soc. Am. J.* v. 55, pp. 923-927.
- Rossi, C., and J. R. Nimmo. 1994. Modeling of soil water retention from saturation to oven dryness. *Water Resour. Res.* v. 30, pp. 701-708.
- Russo, D. 1988. Determining soil hydraulic properties by parameter estimation: On the selection of a model for the hydraulic properties. *Water Resour. Res.* v. 24, pp. 453-459.
- Schaap, M. G., and F. J. Leij. 1999. Improved prediction of unsaturated hydraulic conductivity with the Mualem-van Genuchten model. *Soil Sci. Soc. Am. J.* (submitted).
- Schuh, W. M. and R. L. Cline. 1990. Effect of soil properties on unsaturated hydraulic conductivity pore-interaction factors. *Soil Sci. Soc. Am. J.* v. 54, pp. 1509-1519.
- Setiawan, B. I., and M. Nakano. 1993. On the determination of unsaturated hydraulic conductivity from soil moisture profiles and from water retention curves. *Soil Sci.* v. 156, pp. 389-395.
- van Genuchten, M. Th. 1980. A closed-form equation for predicting the hydraulic conductivity of unsaturated soils. *Soil Sci. Soc. Am. J.* v. 44, pp. 892-898.
- van Genuchten, M. Th. and F. J. Leij. 1992. On estimating the hydraulic properties of unsaturated soils. In: *Proceedings International Workshop on Indirect Methods for Estimating the Hydraulic Properties of Unsaturated Soils.* Univ. of California, Riverside, CA. pp. 1-14.
- van Genuchten, M. Th., F. J. Leij, and S. R. Yates. 1991. The RETC code for quantifying the

- hydraulic functions of unsaturated soils. EPA/600/2-91/065.
- van Genuchten, M. Th. and D. R. Nielsen. 1985. On describing and predicting the hydraulic conductivity of unsaturated soils. *Annales Geophysicae* v. 3, pp. 615-628.
- Varallyay, G. and E. V. Mironenko. 1979. Soil-water relationships in saline and alkali conditions. In: V. A. Kovda and I. Szabolcs (ed.) *Modelling of salinization and alkalization. Agrokemia es Talajtan* v. 28 (Suppl.), pp. 33-82.
- Vauclin, M., R. Haverkamp, and G. Vachaud. 1979. *Résolution numérique d'une équation de diffusion non linéaire*. Presses Univ. de Grenoble. 183 pp.
- Vereecken, H. 1992. Derivation and validation of pedotransfer functions for soil hydraulic properties. In: *Proceedings International Workshop on Indirect Methods for Estimating the Hydraulic Properties of Unsaturated Soils*. Univ. of California, Riverside, CA. pp. 473-488.
- Warrick, A. W. 1995. Correspondence of hydraulic functions for unsaturated soils. *Soil Sci. Soc. Am. J.* v. 59, pp. 292-299.
- Yates, S. R., M. Th. van Genuchten, A. W. Warrick, and F. J. Leij. 1992. Analysis of measured, predicted, and estimated hydraulic conductivity using the RETC computer program. *Soil Sci. Soc. Am. J.* v. 56, pp. 347-354.
- Zhang, R., and M. Th. van Genuchten. 1994. New models for unsaturated soil hydraulic properties. *Soil Sci.* v. 158, pp. 77-85.

Table 1. Expressions for Water Retention, $S_e(h)$

Model	Expression	Reference
11	$\begin{cases} 1 & \alpha h \leq 1 \\ (\alpha h)^{-\beta} & \alpha h > 1 \end{cases}$	Brooks and Corey (1964)
12	$\frac{1}{2} \operatorname{erfc}[\gamma - \frac{\beta}{1+\alpha h}]$	Laliberte (1969)
13	$\alpha / [\alpha + (\ln h)^\beta] \quad (h \geq 1)$	Vauclin et al. (1979)
14	$[1 + (\alpha h)^\beta]^{-\gamma}$	van Genuchten (1980)
15	$[1 + (\alpha h)^\beta]^{(1-\beta)/\beta}$	van Genuchten (1980)
16	$\begin{cases} 1 - (\alpha h)^2 S_i^{2/\beta} (1 - S_i) & h \leq h_i \\ (\alpha h)^{-\beta} & h > h_i \end{cases}$ where $h_i = 1/\alpha S_i^{1/\beta}$ and $S_i = 2/(2 + \beta)$	Hutson and Cass (1987)
17	$[(1 + \frac{1}{2} \alpha h) \exp(-\frac{1}{2} \alpha h)]^{1/(1+\beta)}$	Russo (1988)
18	$\frac{(1 + \gamma \alpha h)}{[1 + \alpha h + \beta (\alpha h)^2]}$	Zhang and van Genuchten (1994)
19	$\frac{1 + (\alpha \beta)^\gamma}{1 + [\alpha(h + \beta)]^\gamma}$	Globus (1987)
20	$1 - \beta \ln(\alpha h)$	Farrell and Larson (1972)
21	$\begin{aligned} & 1 - b(\alpha h)^2 \quad 0 < h < \beta \\ & (\alpha h)^{-\gamma} - (\alpha h_d)^{-\gamma} + a \ln(h_d/h) \quad h > \beta \\ & a = \frac{2 - (2 + \gamma)(\alpha \beta)^\gamma + 2(\alpha h_d)^{-\gamma}}{1 + 2 \ln(h_d/\beta)} \\ & b = [\frac{\gamma}{(\alpha \beta)^\gamma} + a] / [2(\alpha \beta)^2] \end{aligned}$	Rossi and Nimmo (1994)
22	$\begin{cases} \frac{1}{2} \operatorname{erfc}(\frac{\ln[(1-\alpha h)/(1-\alpha \beta)] - \gamma^2}{\gamma \sqrt{2}}) & \alpha h > 1 \\ 1 & \alpha h \leq 1 \end{cases}$	Kosugi (1994)
23	$\exp[\beta(1 - \alpha h)]$	Bumb et al. (1992)
24	$\{1 + \exp[\beta(\alpha h - 1)]\}^{-1}$	Bumb et al. (1992)

Table 2. Expressions for Relative Hydraulic Conductivity, K/K_s

Function	Expression	Reference
<u>h based</u>		
31	$[1 + (\alpha h)^\delta]^{-\gamma}$	Gardner (1958)
32	$\exp(-\delta h)$	Gardner (1958)
33	$\begin{cases} 1 & \alpha h < 1 \\ (\alpha h)^{-2-3\delta} & \alpha h > 1 \end{cases}$	Brooks and Corey (1964)
34 ^a	$S_e^\delta \left[\frac{\int_0^{S_e} \frac{d\xi}{h(\xi)}}{\int_0^1 \frac{d\xi}{h(\xi)}} \right]^2$	Mualem (1976)
<u>S_e based</u>		
41	$S_e^{3+2/\delta}$	Brooks and Corey (1964)
42	$S_e^\delta [1 - (1 - S_e^{1/\gamma})^\gamma]^2$	van Genuchten (1980)
43	$S_e^\delta [I_\zeta(p, q)]^2$ ($p = \gamma + 1/\beta$; $q = 1 - 1/\beta$; $\zeta = S_e^{1/\gamma}$)	van Genuchten and Nielsen (1985)
44	$\left(\frac{S_e}{\delta} \right)^{0.5} \left(\frac{1 - (1 - S_e^{1/\gamma})^\gamma}{1 - (1 - \delta^{1/\gamma})^\gamma} \right)^2$	van Genuchten et al. (1991)
45	$\frac{(1 - \gamma) S_e^\delta}{1 - S_e}$	Fujita (1952)
46	$\exp(-\gamma S_e^\delta)$	Setiawan and Nakano (1993)
47	$\exp[-\gamma (S_e - \delta)]$	Libardi et al. (1980)

^a cf. Leij et al. (1997)

Table 3. Number of Fitted Data Sets (n) and Median Value for r^2 and MSE^a

S_e		$K(h)$				$K(S_e)$							μ
		31	32	33	34	41	42	43	44	45	46	47	
11	n	320	314	320	318	454	466	466	422	455	483	484	409
	r^2	.956	.858	.946	.945	.887	.888	.891	.901	.875	.883	.852	.898
	MSE	.673	1.85	.648	.784	1.05	1.15	1.13	.923	1.25	1.17	1.67	1.12
12	n	217	213	209	299	366	461	458	360	450	461	464	360
	r^2	.958	.870	.953	.947	.911	.854	.861	.868	.846	.863	.830	.887
	MSE	.704	2.05	.765	.865	1.01	1.85	1.87	1.66	2.01	1.70	2.19	1.52
13	n	276	200	65	321	343	345	375	302	357	307	456	304
	r^2	.893	.864	.821	.887	.899	.912	.891	.891	.892	.909	.847	.882
	MSE	1.23	2.06	2.31	1.39	1.04	.921	1.07	1.18	1.23	.969	1.71	1.37
14	n	321	316	321	321	466	486	483	385	465	486	487	412
	r^2	.967	.861	.963	.912	.905	.901	.892	.906	.879	.890	.864	.904
	MSE	.524	1.93	.559	1.17	1.10	.955	1.07	.840	1.25	1.20	1.63	1.11
15	n	320	222	320	320	431	379	482	358	410	465	422	375
	r^2	.964	.867	.958	.945	.907	.906	.898	.915	.891	.890	.871	.910
	MSE	.566	1.35	.537	.632	.893	.807	1.05	.776	1.16	1.05	1.60	.947
16	n	320	315	321	321	466	483	473	374	468	487	487	410
	r^2	.961	.858	.951	.944	.894	.894	.899	.906	.882	.885	.860	.903
	MSE	.606	1.81	.583	.649	.996	1.04	1.11	.940	1.22	1.16	1.68	1.07
17	n	305	313	308	-	452	475	468	419	460	482	485	417
	r^2	.880	.803	.874	-	.869	.861	.866	.865	.846	.853	.823	.854
	MSE	1.47	2.31	1.46	-	1.33	1.44	1.36	1.33	1.48	1.40	2.14	1.57
18	n	318	310	316	177	437	486	475	463	471	486	487	402
	r^2	.958	.856	.956	.852	.904	.884	.875	.888	.859	.860	.739	.875
	MSE	.587	2.06	.635	1.67	1.05	1.22	1.37	1.14	1.37	1.34	2.91	1.40
19	n	308	274	301	303	358	131	397	115	162	160	162	243
	r^2	.967	.848	.958	.947	.862	.914	.865	.923	.890	.875	.719	.888
	MSE	.520	2.08	.565	.827	1.38	.858	1.27	.753	1.03	1.31	2.36	1.18
20	n	259	314	132	-	453	484	469	443	450	338	464	381
	r^2	.925	.838	.566	-	.886	.888	.888	.887	.872	.820	.815	.839
	MSE	1.03	1.92	4.95	-	1.18	1.25	1.31	1.31	1.33	1.88	2.22	1.84
21	n	246	257	259	226	369	486	469	386	460	485	487	375
	r^2	.968	.869	.966	.936	.911	.829	.844	.866	.816	.822	.796	.875
	MSE	.457	1.95	.553	.938	.846	1.85	1.84	1.54	2.07	1.99	2.45	1.50
22	n	66	58	60	320	145	83	68	106	88	88	115	109
	r^2	.908	.819	.886	.932	.865	.472	.908	-2.82	.376	.701	.090	.376
	MSE	.970	2.19	1.12	.915	1.61	4.59	.699	41.9	9.13	4.03	9.16	6.94
23	n	318	315	319	240	456	484	426	459	469	479	485	405
	r^2	.886	.807	.882	.777	.867	.871	.879	.874	.849	.841	.792	.848
	MSE	1.38	2.30	1.36	2.44	1.23	1.33	1.24	1.29	1.38	1.54	2.58	1.64
24	n	244	287	236	305	442	447	431	391	438	441	476	376
	r^2	.947	.842	.927	.748	.895	.899	.905	.904	.864	.879	.839	.877
	MSE	.886	2.21	1.14	2.63	1.15	1.02	1.06	1.04	1.46	1.28	2.01	1.45
μ_n		274	265	249	289	403	407	424	356	400	403	426	
μ_{r^2}		.938	.847	.901	.898	.890	.855	.883	.627	.831	.855	.767	
μ_{MSE}		.828	2.01	1.23	1.25	1.13	1.45	1.25	4.05	1.96	1.57	2.59	

^aMSE $\times 10^2$

Table 4. Median (med), Mean, and Standard Error (SE) of r^2 , MSE^a, and the Parameters of Seven Combinations Fitted to 306 S_e(h)-K(h) Data Sets

S _e (h)-K(h)		1431	1433	1531	1533	1631	1633	1931
r^2	med	.965	.963	.962	.957	.958	.951	.966
	mean	.923	.911	.920	.905	.913	.897	.916
	SE	.0067	.0080	.0070	.0079	.0073	.0083	.0076
MSE	med	.530	.561	.566	.537	.618	.589	.520
	mean	1.31	1.71	1.49	1.49	1.53	1.53	1.47
	SE	.178	.333	.222	.236	.219	.223	.209
θ_r	med	.033	.057	.057	.057	.057	.057	.000
	mean	.028	.036	.051	.047	.053	.052	.009
	SE	.0016	.0015	.0001	.0012	.0007	.0009	.0012
θ_s	med	.465	.470	.460	.463	.461	.467	.461
	mean	.506	.506	.502	.504	.504	.506	.504
	SE	.0071	.0067	.0065	.0065	.0064	.0065	.0069
α	med	.059	.067	.067	.082	.097	.120	.111
	mean	.644	.289	.715	.487	.960	.492	12.5
	SE	.224	.117	.338	.156	.497	.144	5.52
β	med	1.08	1.09	1.21	1.19	.196	.185	11.1
	mean	1.98	1.83	1.53	1.46	.516	.440	104.2
	SE	.183	.154	.051	.046	.047	.037	32.1
γ	med	.207	.193	.653	-	.677	-	.257
	mean	.297	.279	1.11	-	1.07	-	33.6
	SE	.016	.015	.078	-	.073	-	7.24
δ	med	2.72	.155	4.30	.135	3.90	.113	2.64
	mean	3.95	.432	6.17	.418	5.79	.392	3.44
	SE	.294	.057	.348	.058	.400	.070	.149
K _s	med	18.9	14.7	18.3	18.0	28.6	26.0	33.6
	mean	7041	5008	4028	4168	7784	7872	14648
	SE	3925	2806	1308	1307	3528	3523	4150

^aMSE $\times 10^2$

Table 5. Median (med), Mean, and Standard Error (SE) of r^2 , MSE^a, and the Parameters of Eight Combinations Fitted to 401 S_e(h)-K(S_e) Data Sets

S _e (h)-K(S _e)		1441	1442	1443	1541	1543	1641	1642	1643
r^2	med	.910	.913	.904	.909	.912	.907	.913	.913
	mean	.846	.847	.770	.844	.745	.844	.846	.782
	SE	.0090	.0090	.0675	.0091	.0756	.0090	.0090	.0673
MSE	med	.858	.847	.898	.868	.849	.808	.856	.853
	mean	3.23	3.19	4.06	2.73	4.85	2.78	3.12	4.33
	SE	.400	.444	1.01	.290	1.35	.300	.432	1.15
θ_r	med	.057	.034	.057	.057	.057	.057	.057	.057
	mean	.042	.029	.038	.045	.047	.046	.038	.041
	SE	.0012	.0014	.0013	.0011	.0010	.0010	.0013	.0012
θ_s	med	.410	.410	.410	.410	.410	.410	.410	.410
	mean	.451	.449	.447	.451	.447	.453	.448	.452
	SE	.0035	.0035	.0034	.0036	.0034	.0034	.0035	.0036
α	med	.033	.055	.050	.072	.061	.114	.101	.102
1/cm	mean	8.76	15.5	.689	3.88	3.34	4.62	4.16	5.35
	SE	7.42	10.8	.280	2.09	1.70	2.47	2.13	3.30
β	med	1.14	1.36	1.48	1.31	1.33	.264	.247	1.99
	mean	1.96	2.63	2.57	1.66	1.68	.604	.554	4.18
	SE	.183	.154	.051	.046	.047	.037	32.1	.283
γ	med	.339	.196	.201	-	.149	-	.129	.116
	mean	.673	.256	.447	-	.440	-	.150	.601
	SE	.049	.011	.084	-	.119	-	.004	.146
δ	med	.363	0.00	0.00	.370	0.00	.375	-3.60	.249
	mean	.997	-.72	1.50	2.60	-1.33	7.88	-5.44	.530
	SE	.203	.536	.247	1.55	.251	5.66	.525	.035
K _s	med	69.6	673	416	68.9	520	69.1	1406	304
cm/d	mean	12757	32321	27275	9905	27363	9006	58491	14189
	SE	3235	4584	5282	2731	4837	2449	6651	3495

^aMSE $\times 10^2$

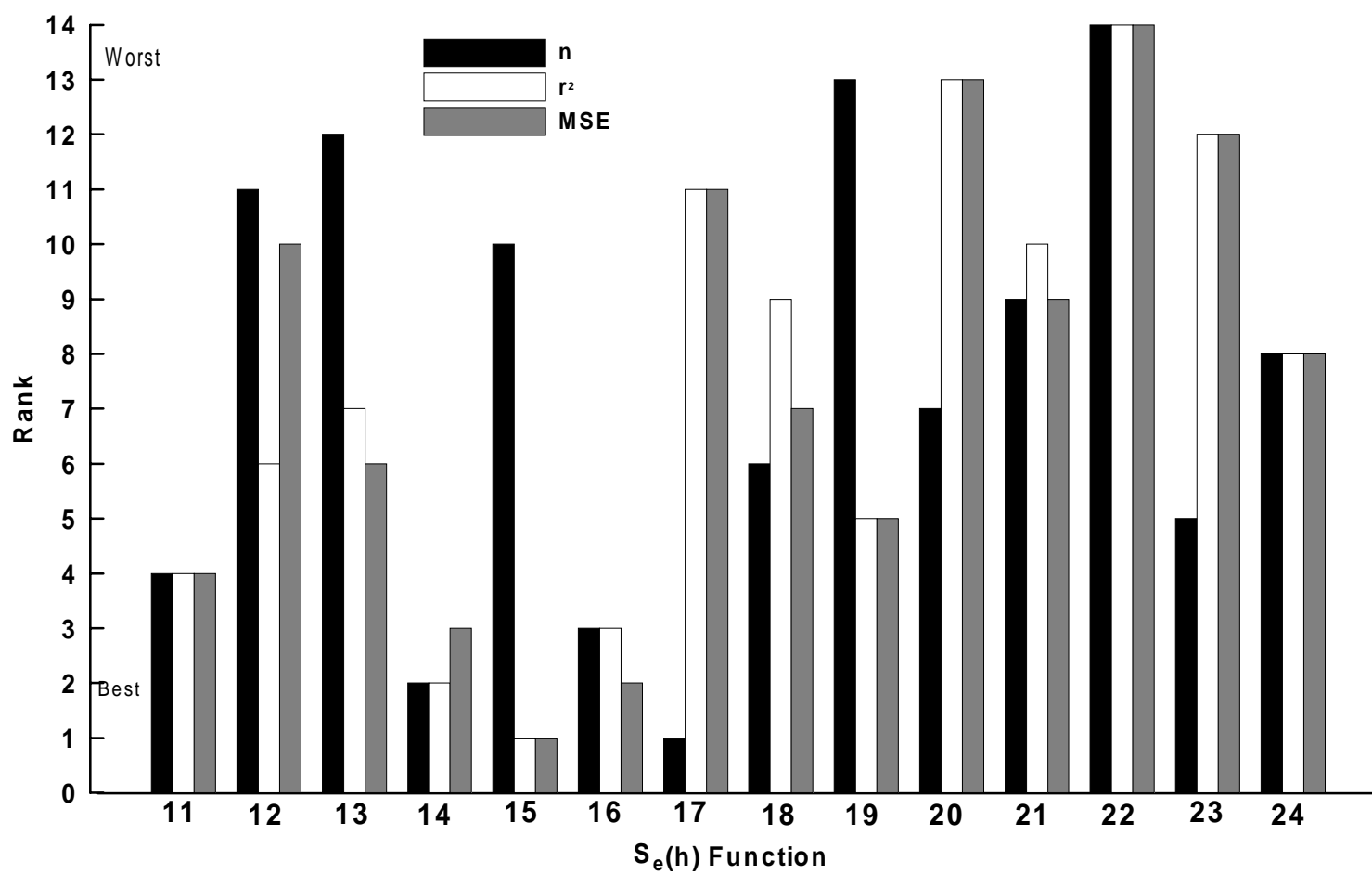


Fig. 1. Relative ranking of $S_e(h)$ functions.

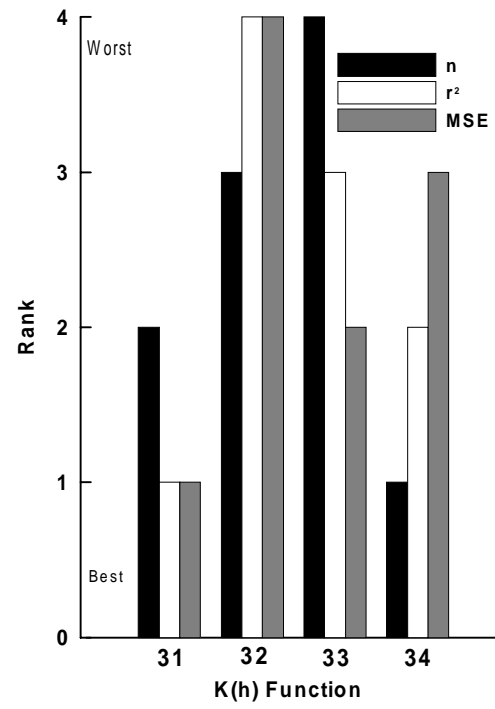


Fig. 2. Relative ranking of K(h) functions.

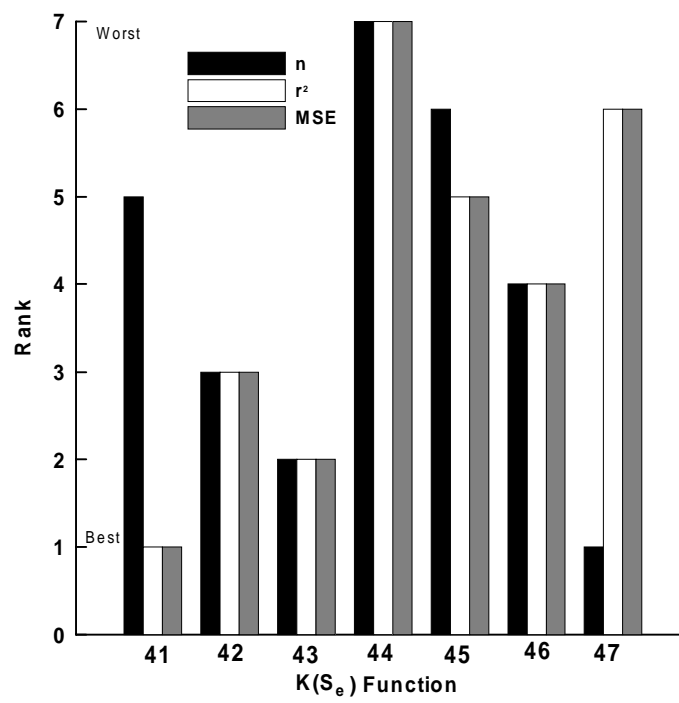


Fig. 3. Relative ranking of $K(S_e)$ functions.

Cone Permeameter™

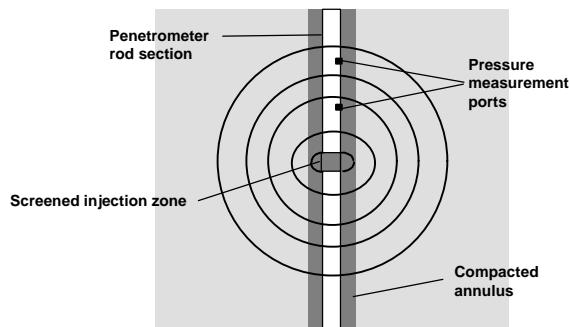
IN-SITU PERMEABILITY MEASUREMENTS WITH DIRECT PUSH TECHNIQUES

Bill Lowry and Sandi Dunn, Science & Engineering Associates

INTRODUCTION

Soil permeability, which defines the magnitude of fluid flow (gas or liquid) under imposed pressure gradients, is one of the most important hydrologic parameters to measure when predicting fluid or contaminant movement in the subsurface, designing environmental remediation systems, or simply characterizing a geologic site. Soil permeability can vary by several orders of magnitude in a given geologic or hydrogeologic setting.

Baseline technologies used in obtaining soil permeability include both borehole and cone penetrometer methods. The most common borehole technique is the measurement of total flow from the borehole under vapor extraction or pump test drawdown conditions. This method has the disadvantage in that there is no vertical resolution of the permeability distribution. Another borehole method is to use straddle packers to isolate a section of the borehole and then measure the flow rate and pressure drop from the isolated region under extraction conditions. The equipment is bulky and ideally requires an open borehole. Both methods require expensive drilled boreholes. Cone penetrometers have been used to measure permeability in saturated media by measuring pore pressure with standard geophysical tools. This approach requires understanding of soil properties and is limited to saturated soils of very low permeability.



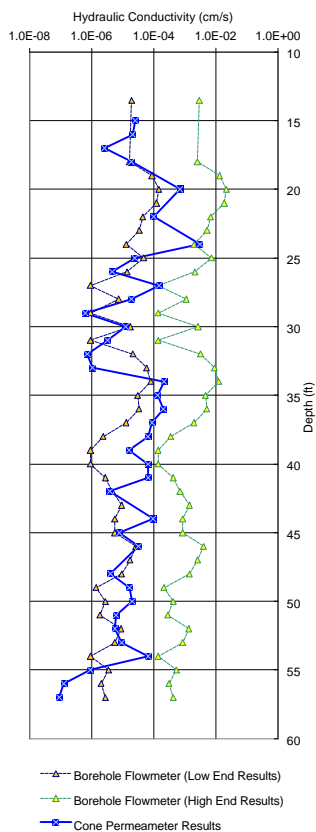
APPROACH

Science & Engineering Associates has developed a tool to measure in-situ permeability that overcomes the disadvantages of the baseline techniques. The Cone Permeameter™ incorporates multiple pressure measurements along the axis of a cone penetrometer rod with a well-defined injection zone and measured flow rate. The permeability value is obtained by applying a one-dimensional,

spherical, steady-state Darcy flow model to the measured injection rate and pressure profile. A fundamental premise of the measurement is that, as the distance from the injection point is increased, the resulting pressure distribution will become spherical (near to the injection point the pressure field is distorted by a combination of the cylindrical injection zone and the compacted soil near the rod surface). A second benefit of the measurement geometry is that, as the radial distance from the source increases, the isobars intersect the cone rod in an almost perpendicular fashion, minimizing any azimuthal gradient that exists across the compacted annulus. By sensing the pressure

Benefits of the Cone Permeameter™ method

- Small volumes of injected fluid due to small region of influence
- Rapid measurements (3-5 minutes per station)
- Minimizes impact of compacted soil due to penetrometer emplacement
- Integrated with CPT geophysical measurements
- All the benefits of cone penetrometer emplacements:
 - Minimal secondary waste
 - Rapid mobilization and setup
 - Low unit measurement cost
 - Mature technology



gradient along the rod at a distance from the injection point, this method essentially ignores the near field effects.

DEMONSTRATIONS

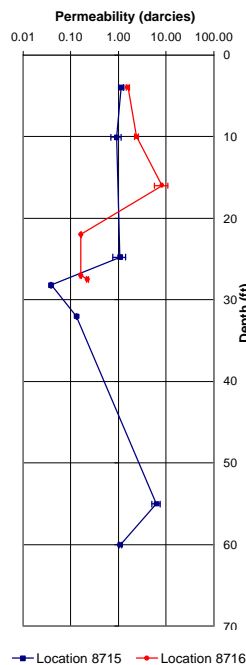
The first demonstration of the Cone Permeameter™ measurement system was conducted at the Savannah River Site D Area Coal Pile Runoff Basin. The Cone Permeameter™ was integrated with a standard CPT cone tip and deployed by Applied Research Associates using a 30-ton truck loaded to 26 tons. CPT data (pore pressure, sleeve stress, tip stress) was obtained simultaneously with the permeameter measurements. The permeameter measurements typically required pushing the rod to the desired depth, starting water injection, and observing flow and pressure histories until a relatively steady condition was attained. This required from 3 to 10 minutes per measurement station.

A comparison of the Cone Permeameter™ data and baseline data (using a borehole flowmeter survey) is shown in the figure. Results were in good agreement, with the Cone Permeameter™ data generally falling between the high and low conductivity values. Comparison of the permeameter data with geologic log data showed the permeability values were consistent with soil types, showing higher values in the sands and lower values in the silts and clays.

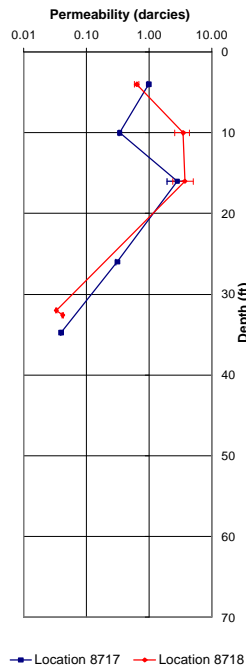
The second demonstration of the system was conducted at the Hanford Site. The Cone Permeameter™ was deployed at the 200 East Area of the site to conduct in-situ air permeability measurements. This demonstration was a joint effort with Applied Research Associates and was funded by Lockheed Martin Hanford Company. Four pushes were performed and a total of 33 permeability measurements were achieved. The average measurement time was 8 to 10 minutes. Resulting permeabilities

ranged 0.03 to 8.2 Darcies with an average uncertainty of 12%. Data showed the ability of the Cone Permeameter™ to measure a consistent permeability profile when pushes were very close to one another. For the purpose of comparing the Cone Permeameter™ results to laboratory

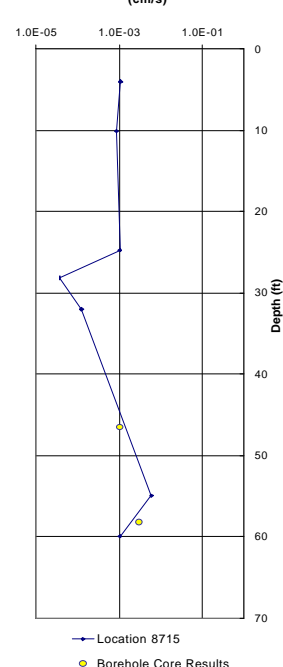
Permeability Profile of the 200 East Area, Locations 8715 and 8716



Permeability Profile of the 200 East Area, Locations 8717 and 8718



Equivalent Hydraulic Conductivity (cm/s)



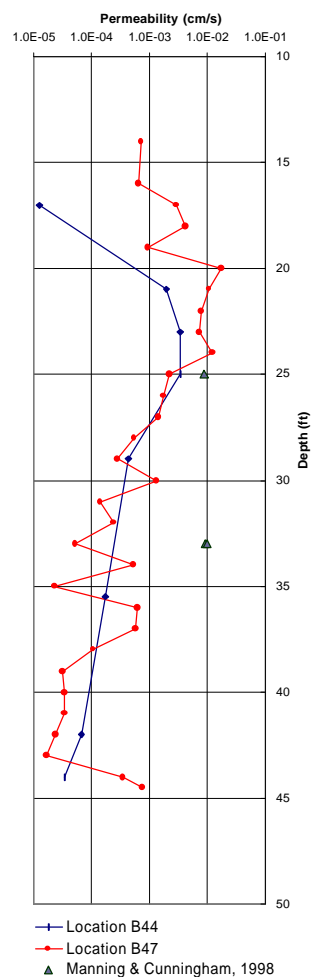
hydraulic conductivity measurements of borehole core samples, the air permeability profiles were converted to an equivalent saturated hydraulic conductivity. The resulting comparison was favorable, comparing within an order of magnitude.

A third demonstration was conducted at the Cape Canaveral Air Station launch complex 34. This site was selected by the Interagency DNAPL Consortium (IDC) as a location to conduct demonstrations of innovative DNAPL remediation and monitoring technologies because high levels of TCE were discovered in the groundwater. SEA was contacted to be part of the pre-characterization team, with the task of performing saturated hydraulic conductivity measurements in a specific area. The DOE SCAPS truck deployed the system.

The site was located on a surficial aquifer that is defined as fine-grained sediments with varying amounts of shell fragments, which lie above a confining unit located 45 feet bgs. The water table is located between 6 and 10 feet bgs. Successful measurements were obtained in two pushes and a total of 44 measurements were taken. Resulting saturated hydraulic conductivities ranged from 1.28×10^{-5} to 1.78×10^{-2} cm/s. Two separate pushes located within 20 ft. of each other showed very consistent distributions (see figure).

CONCLUSIONS

Field applications of the Cone Permeameter™ have demonstrated the ability of the system to provide in-situ air permeability and saturated hydraulic conductivity data critical to vadose zone and saturated zone projects (data obtained with limited or no success by existing in-situ techniques). Measurements are achieved rapidly and at a low overall cost compared to existing techniques. The Cone Permeameter™ is a valuable new addition to the cone penetrometer toolbox.



INSTRUMENTED MEMBRANE TECHNOLOGY: CURRENT USES AT LAWRENCE LIVERMORE NATIONAL LABORATORY (LLNL)

Stan Martins, LLNL

Introduction:

Instrumented Membrane Technology (IMT) uses a flexible, removable, plastic-coated membrane-tube to deploy various types of instruments and at least two different kinds of sampling systems in uncased boreholes. The IMT membrane-tube is “blown” down the borehole from a spool within a pressurized canister by compressed air. Once in place, the membrane-tube is held against the sides of the borehole by filling the tube with compressed air, sand, water or with a foam packer.

Sorbent-pads affixed to the outside of these membrane-tubes are used to collect and retrieve soil pore-water samples for laboratory analysis. Measuring the electronic resistance across two electrodes mounted on these pads can be used to make estimates of soil moisture tension.

Small diameter tubes installed on these membranes are used to collect soil-vapor or liquid-water from known depths in the borehole and to transport these materials to the surface where they can be sampled. These tubes can also be connected to pressure transducers that log soil-pressures when these tubes are not needed for sampling.

A wide variety of electronic and mechanical sensors can be incorporated into the IMT systems when they are manufactured. An example of this approach would be the soil moisture tension measurements made with the sorbant-pads, described above. The disadvantage of this approach is it 1) increases the cost of the IMT device and 2) makes the replacement or relocation of these devices difficult.

A more flexible and economic approach to the deployment of these kinds of sensors is the Beavertail Strap. These straps are foam-filled membrane-tubes that look like a beavertail in cross section (tapering from a thicker center to minimal thickenings on either side). When the Beavertail Strap is constructed, wires and/or tubes are run from the end that is to be attached to the surface, through the center of the Beaver-tail strap to the desired position in the borehole. Prior to deployment, sensors are attached to these wires and/or at each level. When deployed, the strap is attached at the surface and hung down the annulus of the borehole. Once the strap is in place, the IMT membrane-tube is deployed in the same borehole and is used to press the Beavertail Strap and its instruments against the soil. The IMT devices used with Beavertail Straps may be fitted with their own set of sampling and/or measurement instruments.

Applications:

IMT systems are currently being used at five different sites in thirteen different boreholes at LLNL. One of these sites was constructed as a vadose zone observatory in pristine soil.

Two of the other sites are contaminated with tritium, while three of the five sites contain VOCs.

The Sites

Building 292

The vadose zone under the Building 292 area at LLNL was contaminated by tritium from a leaking underground tank some time between 1986 and 1989. Two IMT systems were installed near this tank during May of 1992 in two uncased four-inch boreholes that were drilled to a depth of about 40 feet. At the time these systems were installed, there was as much as 1×10^8 pCi of tritium per liter of condensed soil moisture. A soil-gas sampling IMT system was deployed in one these boreholes while a sorbant-pad IMT system was deployed in the other.

Once the soil-gas system was in place, it was filled with sand to keep the vapor ports sealed against the soil. Because this resulted in a semi-permanent installation, the membrane was never removed during the course of the study. Periodically, soil-gas samples were taken from these ports and analyzed for tritium. On one occasion, soil-gas samples were analyzed by mass-spectrometry to get the ratio of carbon dioxide to oxygen. It was thought that an increase in this ratio would indicate soil-microbial activity.

Because the IMT membrane-tube must be removed from the borehole to recover the sorbant-pads, this installation was pressurized by compressed air while the membrane was in place. Eight levels of thermistors were subsequently added to the sorbant-pad system so that soil temperatures could be monitored. This was accomplished by hanging two strings of four thermistors each in the annulus of the borehole prior to deploying the IMT sorbant-pad or blank-membrane system. When sorbant pads were not deployed in this borehole, a blank-membrane was deployed to keep the borehole open. On several occasions when the blank-membrane was in place, a neutron-logging tool was passed through the annulus of the IMT membrane-tube, which allowed us to estimate changes in soil-moisture content.

Building 5475

Soils under the Building 5475 area contain both tritium and VOCs. VOCs were introduced into these soils during the Second World War as a result of aircraft engine maintenance in the area. Later on, tritiated-water evaporation ponds were constructed in the area. These ponds eventually formed leaks and tritium escaped into these soils by infiltration.

Four IMT systems were eventually deployed in the Building 5475 area in three different eight-inch boreholes that were drilled as deep as 110 feet. A sorbant-pad system was used in the first borehole for about eight months. During this time sorbant-pads were deployed and retrieved several times. These pads provided data on both the tritium and the VOC content of these soils, as well as seasonal soil moisture variations. Attempts to use a neutron-logging tool in this borehole resulted in ambiguous data.

After the last of the sorbent-pads were retrieved, a soil-gas system equipped with thermocouples was deployed in this borehole. Soil-vapor samples were collected from the soil-gas ports and analyzed for both VOCs and tritium. Soil temperatures have been logged from this borehole since December of 1993.

The two new IMT systems were deployed towards the end of 1996. These units were equipped with gas-port sampling systems and Beavertail Straps. The Beavertail Straps were instrumented each with eight levels of thermistors to measure soil temperature and gypsum blocks to measure soil moisture. Tritium and VOCs were sampled periodically from the gas-ports in each system. At all other times, soil-gas pressures were logged automatically with pressure transducers connected to each of these ports. These soil-pressure measurements were used to characterize soil-pressure gradients produced by soil-gas extraction and re-injection during a vapor-extraction feasibility test. When vapor extraction was not underway, these pressure data were logged to evaluate natural diurnal changes caused by changes in barometric pressure. Five-minute averages of these data were logged each hour since 1996 (Berg et al., 1998).

Building 518

Soils in the Building 518 area contain VOCs as a result of unplanned releases from an adjacent solvent storage yard. This resulted in high concentrations of these compounds in the vadose zone. Two IMT systems were installed in the area in late 1995 to characterize this area and to monitor the effects of soil-vapor extraction planned to commence later on that year.

Both IMT systems were equipped with soil-gas ports and Beavertail Straps. Both Beavertail straps were equipped with thermistors to measure soil temperature and with gypsum blocks to measure soil-moisture tension.

Soil-pressure measurements made at the IMT soil-gas ports, and adjacent grouted wells provide information on the pressure fields generated by the vapor-extraction system as well as diurnal soil-pressure changes caused by daily fluctuations of barometric pressure. A continuous record of all of these parameters has been kept since October of 1995 (Berg et al., 1994).

Building 875

Soils in the Building 875 area contain VOCs that had been undergoing remediation for a number of years by soil-vapor extraction. Two IMT systems were installed in the area in late 1996 to characterize this area and to monitor the effects of remediation efforts.

Both IMT systems were equipped with soil-gas ports and Beavertail Straps. Both Beavertail straps were equipped with thermistors to measure soil temperature and with gypsum blocks to measure soil-moisture tension. In addition, one of the IMT systems was equipped with a second IMT membrane equipped with sorbent-pads. This double membrane system is called a “Duet” system by the manufacturer, FLUTE of Santa Fe, NM. The advantage of this system is that it allows uninterrupted measurements to be

made from the soil-gas port systems and Beavertail-Strap systems and the ability to deploy and retrieve soil-moisture samples with the sorbant-pads.

Vadose Zone Observatory

The vadose zone observatory was constructed in 1997 over uncontaminated soils and was designed to study the fate of substances injected into soils as gas or in the aqueous phase. Four IMT systems were installed around a central injection well. Three IMT systems fitted with gas-ports were deployed during the first year of these studies. A Beavertail Strap with thermistors and gypsum was deployed along with one of these membranes. During the second year, a sorbant-pad system was installed in the fourth borehole along with a Beavertail Strap equipped with tensiometers. The soil-gas membrane from one of the three original boreholes was replaced with a second sorbant-pad system. The pads on both of the sorbant-pad membranes were equipped with electrodes in order to make soil-moisture tension estimates.

Soil pressure measurements were made from each of the gas-port membranes and from three other wells that were completed with grout. Surface barometric pressures were measured at this site so that changes in soil pressures could be related to diurnal changes in barometric pressures. Vapor samples were also taken from each of these sample ports (Carrigan et al., 1999; Carrigan et al., 1998).

Measurements

Tritium vapor sampling: Tritium in the form of water vapor was sampled from IMT gas-port systems by pumping soil-gas from each port through a cold trap. Water vapor from the gas-stream out of each port was condensed and frozen in individual vials. When vapor collection was complete, the samples were thawed into liquid water and were analyzed for tritium in a scintillation counter (Martins, 1992a).

Tritium pore-water sampling: Tritium from soil pore-water is sampled with IMT sorbant-pad systems. Dry pads are deployed in these boreholes and left in place for at least 24 hours so that the pads can soak up soil-pore water, and come to equilibrium with the soil around it. The pads that have been exposed to the soils in this way are carefully removed from the membrane and placed in sealed containers. Prior to analysis, the wet pads are weighed. After all liquid is extracted from the pads by lyophilization, the pads are re-weighed so that their moisture content can be determined. Liquid water recovered from the pads by lyophilization is analyzed for tritium in a scintillation counter (Mallon et al., 1992).

VOC vapor sampling: VOCs were sampled from IMT gas-port systems in several ways. With all methods, the void-volume of the sample lines between the gas-port and soil were purged by pumping at least 3 line-volumes of soil-gas before sampling. The most straightforward approach uses a PID Organic Vapor Analyzer (OVA) to make direct measurements of total VOC concentration. Soil-gas is pumped from the gas-port to the OVA. The OVA then analyses the gas stream and displays concentration as ppmv.

Other methods involve collecting the soil VOCs into some type of container followed by laboratory analysis. We have used at least three different methods. They are sorbant-cartridge (such as Tenax), Tedlar Bags and Summa Canisters.

VOC pore-water sampling: Soil pore-water is sampled with pads from the IMT sorbant-pad systems. Dry pads are deployed in these boreholes and left in place for at least 24 hours so that the pads could soak up soil-pore water, and come to equilibrium with the soil around it. The pads that have been exposed to the soils in this way are carefully removed from the membrane and placed in soil-VOAs. Prior to analysis, the VOAs containing the wet pads were weighed. After the VOC fraction of the pore-water was removed by a purge-and-trap system, the VOCs containing the extracted pads were dried and re-weighed so that the moisture content of the pads could be determined. When the volume of pore-water on the pads and the total mass of VOCs extracted from the pads are known the concentration of VOCs in pore-water can be expressed as ppm (Martins, 1992b).

Soil-gas pressure measurements: Because the overall rate of change of soil-gas pressures is fairly slow, and there are usually a large number of soil gas-ports to monitor for pressure, a system was developed to multiplex up to eight different ports through a single pressure transducer. This arrangement allowed us to observe each port once or twice each hour and to reduce the cost and size of the system by limiting the number of sensors and data loggers used.

Each of the gas-ports on an IMT system can be switched to the same pressure transducer with solenoid valves that are controlled by a data logger. The data logger acquires and averages the soil pressure data from each port over a period of time (usually five minutes) and then logs the pressure data along with the gas-port ID and a time/date stamp. Because pressures measured from several gas-ports are made by the same pressure transducer, these values can be compared one to another without regard to differences caused by individual pressure transducer calibration.

Soil temperature measurements: A thermistor is an electronic device that changes its resistance in a predictable way with temperature. When placed in soils and connected to a suitable data logger, thermistors can be used to measure and log soil temperature data. We have spent some effort acquiring these kinds of data from the vadose zone because annual cooling of our soils causes liquid water to flow through the soil column due to reflux-condensation. This can effect the migration of contaminants in these soils as much as, or more than, water infiltration from seasonal rains.

Soil moisture measurements: Soil moisture measurements are made in several ways. One of the first devices we used for these measurements was the agricultural gypsum block. These blocks are actually cylinders of gypsum with two concentric stainless steel cylinders embedded within. When placed in soil, the moisture content of the gypsum will eventually come to equilibrium with that of the soil. Wires connected to each of the cylinders are attached to a data logger where the electronic resistance between the cylinders is measured and logged. Water entering the gypsum block causes the resistance of the block to drop. Conversely, dry blocks have a higher resistance. A standard formula

is used to convert the resistance measurements to soil-suction expressed as bar of soil moisture tension.

We are currently experimenting with sorbant-pad electrical resistance measurements. The theory here is the same as used with the gypsum blocks. Wet pads have low resistance and dry pads have high resistance. While no data are currently available that relate these measurements to soil-moisture tension, we believe that these data can indicate an infiltration front passing the sorbant-pad. With a little additional work, it may be possible to develop the same kind of mathematical relationship between sorbant-pad resistance and soil-moisture tension that is used with gypsum blocks.

We currently have plans to deploy remote-controlled tensiometers with a Beavertail Strap at one of our installations. Tensiometers measure soil-suction directly through a pressure transducer and have the added advantage of allowing the investigator to sample soil-pore moisture as liquid water. If the pressure transducer is connected to a data logger, soil moisture tension may be logged more-or-less continuously.

REFERENCES

- Berg, L.L.; Dresen, M.D.; Folsom, E.N.; Bainer, R.W.; Gelinas, R.J.; Nichols, E.M.; Bishop, D.J.; Ziagos, J.P.; Hassan, S.E.; Hoffman, J.D.; Kita, L.S.; Kulshrestha, A.; Macdonald, J.K.; Martins, S.A.; Nitao, J.J.; Noyes, C.M.; Ridley, M.N.; Sorensen, E.A.; Underwood, D.H. (1994), *Remedial Design Report No. 6 for the Building 518 Treatment Facilities*, Lawrence Livermore National Laboratory, Livermore, Calif. (UCRL-AR-115997).
- Berg, L.L.; Dresen, M.D.; Bainer, R.W.; Folsom, E.N.; Lamarre, A.L.; Blake, R.G.; Hassan, S.E.; Hoffman, J.D.; Kita, L.S.; Maley, M.P.; Martins, S.A.; McKereghan, P.F.; McNab, W.W.; Metzger, G.A.; Ruiz, R.; Shukla, S.N. (1998), *Remedial Design Report No. 4 for the Trailer 5475 Treatment Facilities*, Lawrence Livermore National Laboratory, Livermore, Calif. (UCRL-AR-126014).
- Carrigan, C.R.; Hudson, G.B.; Martins, S.A.; Ramirez, A.L.; Daily, W.D.; Buettner, H.M. (1998), "Vadose Zone Observatory: Dynamical Characterization of Liquid- and Gas-Phase Contaminant Transport in a Heterogeneous Soil Regime", Lawrence Livermore National Laboratory, Livermore, Calif. (UCRL-JC-131755-ABS). Presented at *American Geophysical Union 1998 Fall Meeting, San Francisco, CA, December 6-10, 1998*.
- Carrigan, C.R.; Hudson, G.B.; Martins, S.A.; Ramirez, A.L.; Daily, W.D.; Buettner, H.M.; Nitao, J.J.; Ralston, D.; Ekwurzel, B.; Moran, J.E.; McCarthy, J.F. (1999), "Lessons About Transport and Monitoring at the Vadose Zone Observatory at LLNL", Lawrence Livermore National Laboratory, Livermore, Calif. (UCRL-JC-133288-ABS). Presented at *American Geophysical Union 1999 Spring Meeting, Boston, MA, May 31-June 4, 1999*.

Mallon, B.; Martins, S.A.; Lowry, W.; Cremer, C. (1992), *SEAMIST(TM) Soil Sampling for Tritiated Water: First Years' Results*, Lawrence Livermore National Laboratory, Livermore, Calif. (UCRL-JR-109015).

Martins, S.A. (1992), *A Method For Collecting Soil Vapor from the Vadose Zone with an Instrumented Membrane System*, Lawrence Livermore National Laboratory, Livermore, Calif. (UCRL-ID-109765 1992).

Martins, S.A., McQueen, G.L., Martinelli, R.E., Jovanovich, M.C. (1992), *Factors Affecting Trichloroethylene (TCE) Recovery from SEAMIST Pads*, Lawrence Livermore National Laboratory, Livermore, Calif. (UCRL-JR-110604ABS).

This work was performed under the auspices of the U.S. Department of Energy by University of California Lawrence Livermore National Laboratory under contract No. W-7405-Eng-48. (UCRL-JC-137680)

Lawrence Livermore National Laboratory (LLNL) Flux Chamber Modifications

Stan Martins, LLNL

Three flux chambers were constructed at LLNL using the basic EPA design as described by Kinbush (1985). These chambers were modified to provide more reliable data with lower detection limits and quicker sample rates.

- (In the EPA design, air within the chamber is stirred by the sweep air, which is emitted from a ring of perforated tubing affixed to the side of the chamber just under the dome. This method requires sweep air rates of about 5 L/min to achieve gas equilibrium in about 60 minutes.

The LLNL chambers are fitted with a variable speed fan suspended from the dome to circulate air inside the chamber (Figures 1 and 2). Because this fan mixes the chamber air far better than the sweep air by itself, sweep-air flow rates can be reduced to 3 L/min and samples can be taken at about 35 minutes after the sweep air is started. This cuts sample times by about 25 minutes.

Because sweep air rates in LLNL chambers are lower than with the EPA design, soil emission concentrations in the LLNL chambers will always be greater than in EPA style chambers. A higher vapor concentration results in lower detection limits.

- (In the EPA design, a hand held thermocouple is used to measure chamber temperature. Because there is no solar shading for this instrument, chamber temperature measurements are almost always higher than the actual air temperature in the chamber.

Temperatures in LLNL chambers are measured with thermistors that are permanently mounted in the chamber inside an aspirated solar shield. Because air is pulled past the sensor by the internal fan, air temperature measurements are more representative of the internal chamber temperature.

- (In the EPA design, sweep air is forced into the chamber at 5 L/min. Because there is no provision made to equalize the internal chamber pressure to ambient air pressure, the chamber can become pressurized. This can cause a reduction in apparent surface flux rate.

Air is removed from the LLNL chambers at the same rate at which it is added. This results in a pressure drop of zero between the inside of the chamber and the outside air. Because the pressure drop is zero, more representative flux rates are achieved.

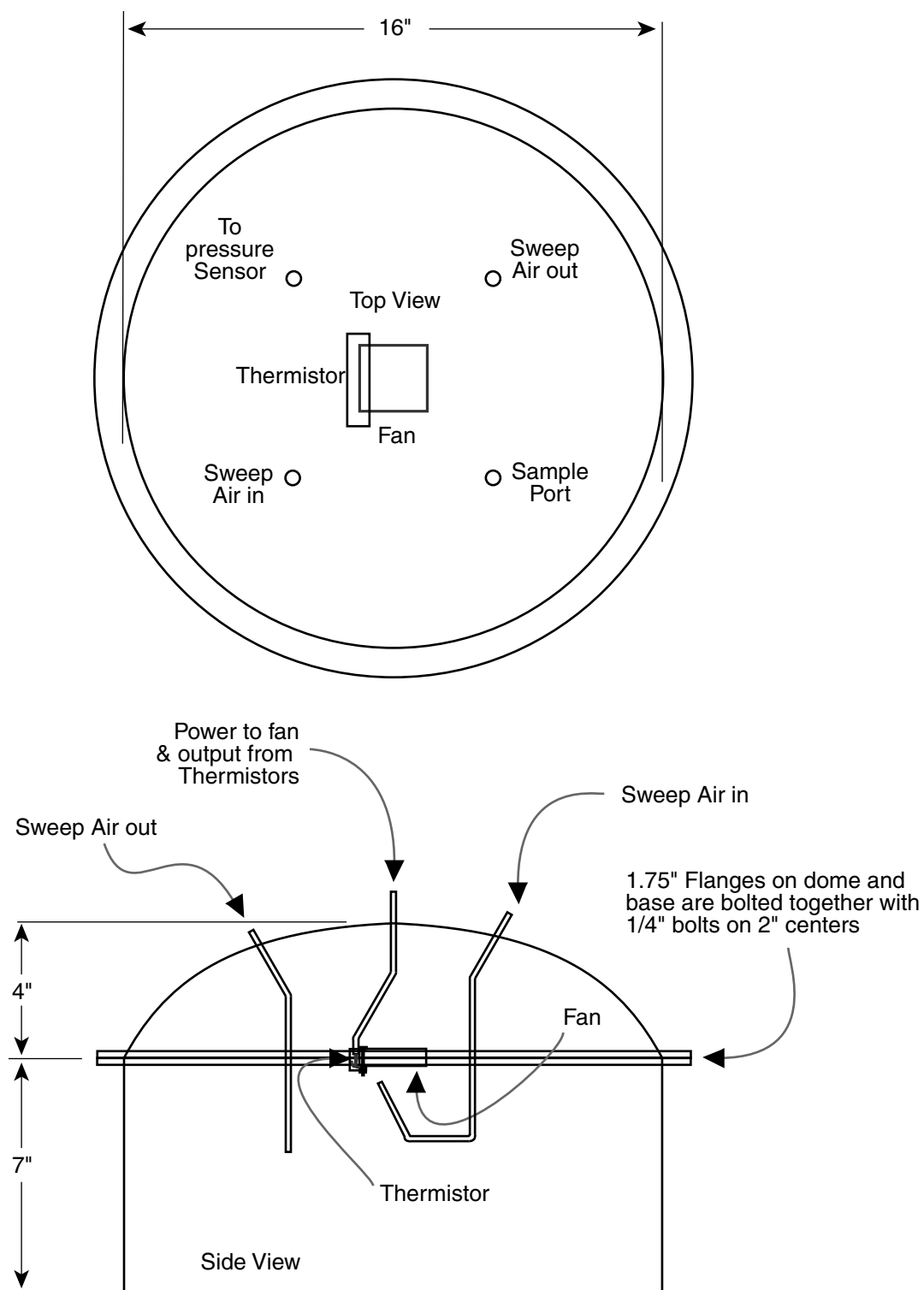


Figure 1: Soil surface flux chamber schematic.

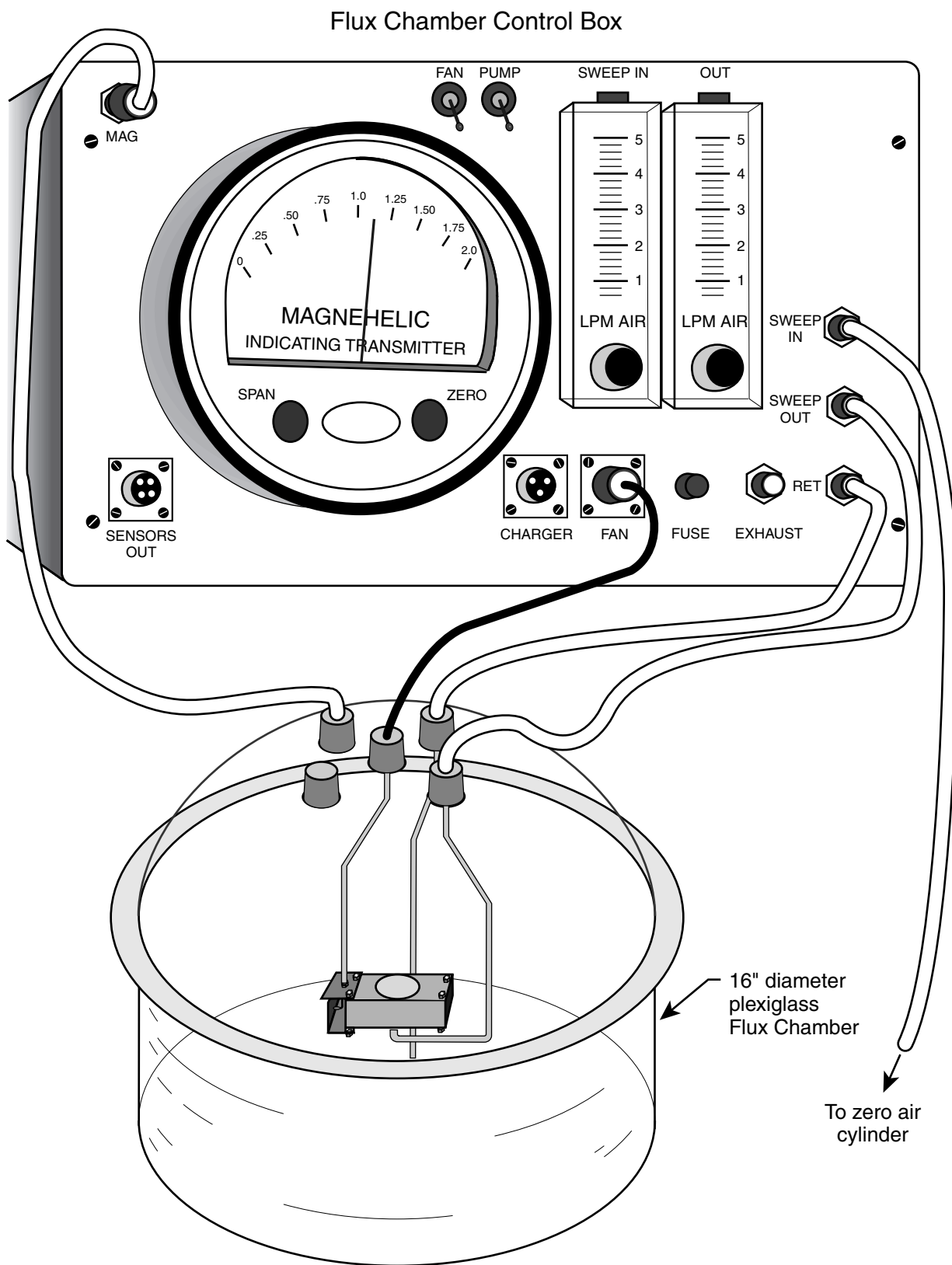


Figure 2: Soil surface flux chamber connections.

Flux Chamber Physical Characteristics

	Volume	Height	Diameter	Area
Chamber	L	m	m	m ²
1	26.4	0.178	0.394	0.1219
2	27.3	0.178	0.394	0.1219
3	26.9	0.178	0.394	0.1219

Flux Chamber Temperature Calibration

Unit	Internal Thermistor	Omega Thermocouple	Mercury Thermometer
1	22.0	22.0	22.0
	33.7	33.5	33.6
	35.6	35.6	35.6
2	22.8	22.9	22.9
	30.5	30.4	30.5
	33.4	33.4	33.4
3	21.0	21.2	21.1
	32.3	32.2	32.2
	35.7	35.6	35.2

REFERENCES

Kinbush, M. (1985), *Measurement of Gaseous Emissions Rates from Land Surfaces Using an Emission Isolation Flux Chamber: User's Guide*, EPA User's Guide, Contract No. 68-02-03389-WA18.

This work was performed under the auspices of the U.S. Department of Energy by University of California Lawrence Livermore National Laboratory under contract No. W-7405-Eng-48. (UCRL-JC-137682)

SOIL SURFACE FLUX MEASUREMENT: USES AT LAWRENCE LIVERMORE NATIONAL LABORATORY (LLNL)

Stan Martins, LLNL

Introduction:

An emission isolation flux chamber is an enclosure of known volume. The chamber has an open end with a known area that is placed on the soil surface to quantify fugitive soil emissions. The chamber contains several penetrations that are used to introduce “sweep air”, to allow chamber-air to exit, and to deploy temperature and pressure sensors.

Soil surface flux (SSF) is the rate of exchange of one or more gases between soils and the atmosphere. An emission isolation flux chamber is used to measure this rate by placing the chamber on a soil surface and passing very pure sweep-air at a known rate through the chamber. Gases that diffuse from the soil surface enter the flux chamber and mix with the sweep air. Once the gases in the chamber are at equilibrium with gases emitted from the soil, the concentration of each target gas in the chamber is measured. If the target gas is a VOC, the flux rate is calculated as $\mu\text{g}/\text{m}^2/\text{min}$ of this substance. If the target gas is tritium or radon, the flux rate is calculated as $\text{pCi}/\text{m}^2/\text{min}$.

Applications:

SSF measurements have been made at many different LLNL Main Site and Site 300 locations, as well other non-LLNL locations. We have measured the flux rates of VOCs, tritium, and noble gases. Flux measurements have been used to monitor the progress of remediation, to identify new areas of contamination, to monitor the progress of an infiltration study, to identify the source of soil contaminants, and to study barometric pumping.

The Sites

Building 518

Soils in the Building 518 area contain VOCs as a result of unplanned releases from an adjacent solvent storage yard. These releases resulted in high concentration VOCs in the vadose zone. SSF measurements were made monthly at five different sites between 9/92 and 7/93. Each site was located over zones of known VOC soil-vapor concentration (from about 20 ppmv to about 1800 ppmv) as determined by a soil vapor survey of gas samples taken at depths of five feet. The correlation between SSF measurements of VOCs and the results of the soil vapor survey were good, with an average $R^2 = 0.984319$ (Std = 0.0148) between 10/92 and 5/93.

In June of 1993, a vapor extraction feasibility test was performed over a period of three days (Berg et al., 1994). During this test, soil gas was extracted from the site where the VOC concentration was highest. Extractions were performed with vacuums as high as 18" Hg and flow rates as high as 100 standard cubic feet per minute (SCFM) for periods up to 10 hours each day. Surface flux measurements made during this time showed that VOC emissions from the soil surface dropped over the course of each day. The SSF rates partially recovered over night when the pumping ceased. SSF measurements made at all five sites during this test demonstrated a reduced correlation (when compared to earlier results) between SSF results and soil vapor survey results, with $R^2 = 0.638229$.

By July 20, 1993 the correlation between the soil vapor survey results and SSF measurements was $R^2 = 0.945688$. Because the correlation between soil vapor survey results and SSF did not return to their former levels, it is likely that the three days of vapor extraction during the test permanently changed the VOC concentration in the vadose zone around the extraction borehole. Subsequent calculations made with the analytical data from this test indicate that about 10 Kg of VOCs were removed from the soil.

In October of 1995, a vapor extraction treatment facility went on line at this site, with an extraction rate of about 15 SCFM and a vacuum of 5" Hg. By July of 1996 an additional 51 Kg of VOCs had been removed from these soils. At the end of this time, SSF emissions had been reduced by 95% over soils with the highest initial vapor concentrations and were undetectable over soil with the lowest concentrations.

Seasonal variations in SSF rates were noted during these studies, with the highest rates observed in September and the lowest rates observed in January or February. This seems to be correlated with the amount of water saturation of the soil. Our rainy season is usually between October and April, with little or no rain between June and September.

Health Risk Assessment

Because high concentrations of VOCs are found in soils at four different locations at LLNL Site 300 and at one site at the Stanford Linear Accelerator in Palo Alto, it was determined that health risk assessments should be made at each of these sites. SSF measurements made at each site were used with a box model to develop these health risk assessments. The results of using this model with SSF generated data indicated that no active remediation was required at any of these sites. One might conclude that remediation was required if only VOC analytical data from soil cores were used to model the health effects of soil off gassing. The reason for this discrepancy is that no matter how many soil cores are sampled, these data can never be very representative of the whole area. SSF results actually represent the amount of off-gassing at the surface, and does not depend on a model to arrive at these estimates (Carlsen et al., 1996; Carlsen et al., 1995).

Hanford Passive Remediation Investigation

A large plume of Carbon Tetrachloride (CCl_4) resulted from releases in soils under a Hanford, WA plutonium facility many years ago. CCl_4 soil vapor concentrations at the

periphery of this plume are high enough to be of concern, but too low to make active remediation economical. As part of a feasibility study to determine the efficacy of passive remediation, two flux chambers were set up over this plume, and continuous SSF measurements were made for a period of three days. Analysis of these data shows that diurnal changes in the SSF rate of CCl_4 were proportional to changes in barometric pressure. As a result of these and other measurements, attempts to install a pilot-scale passive remediation system were made.

Vadose Zone Observatory: The vadose zone observatory was constructed in 1997 over uncontaminated soils and was designed to study the fate of substances injected into soils as gas or with water. As part of these studies, a cocktail of several noble gases was injected into a well that was screened at 15 to 16 feet. SSF measurements were made three different times after the initial injection from 0 to 30 feet away from the injection point. Analysis of the SSF samples by mass spectrometer revealed that portions of the noble gas cocktail were escaping from the soil at distances as great as 20 feet (Ralson et al., 1999; Carrigan et al., 1999; Carrigan et al., 1998).

Building 511

Recently, VOCs have been detected in ground water under the Building 511 area. A general survey of this area with SSF measurements has identified a possible source of this plume. Plans have been made to make a more detailed survey of the area, so that remediation by soil-vapor extraction may start when an extraction skid is available.

Building 292

The vadose zone under the Building 292 area at LLNL was contaminated by tritium from a leaking underground tank some time between 1986 and 1989. Soil over the release site has been covered with asphalt, but there is bare soil within 10 feet of the tank.

Several SSF measurements were made at this site, some over bare soil and others over asphalt. Because tritium at this site is in the form THO, most of the tritium is found in soil gas as water vapor. The sweep air for these measurements was circulated through the chamber by a pump. Air pumped from the chamber was passed through a cold trap where most of the water vapor was condensed and frozen as water ice. This air was then re-introduced into the chamber. After the chamber was purged for 35 minutes through a cold trap, the air stream was switched to a new cold trap where the SSF sample was collected. At the end of the sampling period, the sample was thawed, its volume measured, and tritium content measured by scintillation counter. The flux rate was then calculated as $\text{pCi/m}^2/\text{min}$.

The results of this study were interesting because water condensed from three SSF vapor samples taken between 12/92 and 3/93 contained less tritium than water condensed from vapor in ambient air during each SSF sample period. This suggests that the atmospheric release of tritium from some other source was greater than that released from the soil above the tank leak.

Advances in Mass Spectrometry make this analytical technique an attractive alternative to the use of a scintillation counter to detect tritium. The major advantages of using the newer technique are that sample time could be reduced to minutes from hours and that detection limits could be improved.

Building 5475

Soils under the Building 5475 area contain both tritium and VOCs. VOCs were introduced into these soils during the Second World War as a result of aircraft engine maintenance in the area. Later on, tritiated-water evaporation ponds were constructed in the area. These ponds eventually formed leaks and tritium escaped into these soils by infiltration.

SSF measurement at six different sites revealed the presence of PCE in concentrations of 0.02 to 0.4 $\mu\text{g}/\text{m}^2/\text{min.}$ on at least one occasion, while TCE was present at only one of these sites.

The tritium concentration in these samples was so low that no tritium was detected in SSF samples taken in this area. Use of a Mass Spectrometer instead of scintillation counting may have dropped the detection limit to the point where a flux rate could have been made (Berg et al., 1998).

REFERENCES

- Berg, L.L.; Dresen, M.D.; Folsom, E.N.; Bainer, R.W.; Gelinas, R.J.; Nichols, E.M.; Bishop, D.J.; Ziagos, J.P.; Hassan, S.E.; Hoffman, J.D.; Kita, L.S.; Kulshrestha, A.; Macdonald, J.K.; Martins, S.A.; Nitao, J.J.; Noyes, C.M.; Ridley, M.N.; Sorensen, E.A.; Underwood, D.H. (1994), *Remedial Design Report No. 6 for the Building 518 Treatment Facilities*, Lawrence Livermore National Laboratory, Livermore, Calif. (UCRL-AR-115997).
- Berg, L.L.; Dresen, M.D.; Bainer, R.W.; Folsom, E.N.; Lamarre, A.L.; Blake, R.G.; Hassan, S.E.; Hoffman, J.D.; Kita, L.S.; Maley, M.P.; Martins, S.A.; McKereghan, P.F.; McNab, W.W.; Metzger, G.A.; Ruiz, R.; Shukla, S.N. (1998), *Remedial Design Report No. 4 for the Trailer 5475 Treatment Facilities*, Lawrence Livermore National Laboratory, Livermore, Calif. (UCRL-AR-126014).
- Carlsen, T.; Martins, S.A.; Caviness, G.; McNeel, P. (1995), "Emission Isolation Flux Chambers and Risk Assessments: The Use of Empirical Data and Appropriate Models to Eliminate Insignificant Exposure Pathways", Lawrence Livermore National Laboratory, Livermore, Calif. (UCRL-JC-120621-ABS). Presented at *Environmental Restoration Conference '95, Denver, CO, August 13-18, 1995*.
- Carlsen, T.; Martins, S.A.; McNeel, P. (1996), "Emission Isolation Flux Chambers and Risk Assessments: Applications for Cost-Effective Risk Assessment and Risk Management", Lawrence Livermore National Laboratory, Livermore, Calif. (UCRL-

JC-122294-EXT-ABS). Presented at *Annual Technical Information Exchange Conference, 8th, Santa Fe, NM, April 18-20, 1996.*

Carrigan, C.R.; Hudson, G.B.; Martins, S.A.; Ramirez, A.L.; Daily, W.D.; Buettner, H.M. (1998), "Vadose Zone Observatory: Dynamical Characterization of Liquid-and Gas-Phase Contaminant Transport in a Heterogeneous Soil Regime", Lawrence Livermore National Laboratory, Livermore, Calif. (UCRL-JC-131755-ABS). Presented at *American Geophysical Union 1998 Fall Meeting, San Francisco, CA, December 6-10, 1998.*

Carrigan, C.R.; Hudson, G.B.; Martins, S.A.; Ramirez, A.L.; Daily, W.D.; Buettner, H.M.; Nitao, J.J.; Ralston, D.; Ekwurzel, B.; Moran, J.E.; McCarthy, J.F. (1999), "Lessons About Transport and Monitoring at the Vadose Zone Observatory at LLNL", Lawrence Livermore National Laboratory, Livermore, Calif. (UCRL-JC-133288-ABS). Presented at *American Geophysical Union 1999 Spring Meeting, Boston, MA, May 31-June 4, 1999.*

Ralston, D.K.; Carrigan, C.R.; Hudson, G.B.; Martins, S.A.; Nitao, J.J. (1999), "Implications of Modeling for Gas-Phase Transport at the LLNL Vadose Zone Observatory", Lawrence Livermore National Laboratory, Livermore, Calif. (UCRL-JC-133289-ABS). Presented at *American Geophysical Union 1999 Spring Meeting, Boston, MA, May 31-June 4, 1999.*

This work was performed under the auspices of the U.S. Department of Energy by University of California Lawrence Livermore National Laboratory under contract No. W-7405-Eng-48. (UCRL-JC-137681)

Scaling of Soil Hydraulic Properties Near Saturation - Two Case Studies

B.P. Mohanty and P.J. Shouse

U.S. Salinity Laboratory, USDA-ARS, Riverside, California

Introduction

Functions which relate the unsaturated soil hydraulic conductivity, K , and the soil water pressure head, h , are most important for understanding and predicting water flow and chemical transport in the vadose zone. The $K(h)$ function near saturation is especially critical for describing preferential flow through soil macropores and other structural voids. Among others, Warrick et al. [1977], and Jarvis and Messing [1995] suggested that further research should be carried out with respect to both experimental technology and scaling concepts for an optimum coevolution of techniques addressing soil heterogeneity. More recently, *in situ* measurements of the near-saturated hydraulic conductivity $K(h)$ using disc (both ponded and tension) infiltrometers has opened new avenues to assess spatial variability of hydraulic properties of field soils. Here we will present two case studies from two different geographic locations having different soil types and climatic conditions. The objective of our study was to develop appropriate scaling approaches for describing near-saturated $K(h)$ data for different soil types, field positions, and pore size (unimodal and bimodal) distributions.

Iowa Study

Infiltration measurements were made along two parallel transects running orthogonal to crop rows in a field at the Agronomy and Agricultural Engineering Research Center near Boone in central Iowa. The soil type in this field is predominantly silt loam belonging to the Clarion-Nicollet-Webster soil association. The soils were developed from calcareous glacial till (Des Moines lobe, Wisconsin age) with surface texture ranging from loam to sandy loam. All measurements were limited to a plot under no-tillage management of continuous row-corn production for 8 years prior to the experiment. Ponded [Prieksat et al., 1992] and tension infiltrometers [Ankeny, 1992] were used to measure infiltration rates. The infiltrometers were run in sequence at the same positions at 0-, 30-, 60-, and 150-mm water tensions, at regular time intervals for 25 min, with automatic recording of the infiltration volume using pressure transducers and data loggers. The infiltration measurements at the 296 sites were completed in less than one week, thus minimizing temporal variability in the data. Tension infiltrometer readings were taken at 160 corn row sites and 136 interrow sites (including trafficked and nontrafficked locations).

Scaling Analysis: Miller and Miller [1956] introduced the concept of geometric similitude and similar media scaling in soil physics. This approach relies on the definition of a characteristic length scale that is related to the particle sizes and pore dimensions in particular geometric arrangements. Tillotson and Nielsen [1984] gave a review of different scaling methods including dimensional analysis, inspectional analysis, and functional normalization. Hopmans [1987] and Vogel et al. [1991] compared different methods for scaling soil hydraulic properties. In most studies scaling characterizes the spatial variability of soil properties, thus facilitating the application of numerical or other solution procedures for modeling variably-saturated flow in highly heterogeneous subsurface systems.

In this study we scaled the near-saturated $K(h)$ data collected for different soil types and field positions using the relative hydraulic conductivity ($K_{rel}(h) = K(h)/K_{sat}$) against h as proposed by Jury et al. [1987]. The relative hydraulic conductivity was used to remove gravity dominated macropore flow near saturation caused by soil structural features that have little or no influence on water flow under unsaturated conditions. However, our scaling approach should be distinguished from Jury et al. [1987] that we did not use any further scaling beyond K_{rel} . In other words, K_{sat} is viewed as a (physical) scale factor for the hydraulic conductivity based on similar media concept. Hence, we suggest that for the near-saturated K , the similar media concept is not necessarily limited to geometrical similarity as in Miller and Miller [1956] but more of a combination of dynamic, kinematic, and geometric similarity represented by K_{sat} . In contrast, Jury et al. [1987] used an additional empirical factor to scale K , thus causing their approach to resemble a functional normalization scheme [Tillotson and Nielsen, 1984]. A unimodal Gardner-type function was found to describe our relative hydraulic conductivity data sets, i.e.,

$$\frac{K(h)}{K_{sat}} = K_{rel}(h) = \frac{1}{[1 + (\frac{h}{h_c})^n]} \quad (1)$$

The scaling procedure involved the following steps. First, $K(h)_x$ data were scaled to $K_{rel}(h)_x$ in a 0 to 1 scale using field measured $K_{sat, x}$. Subsequently, one arbitrary $[(K_{rel}(h), h)]$ data set was chosen as the reference and equation (1) was fitted by nonlinear regression, giving $h_c = 2.41$ cm, and $n=1.29$. Next, paired $[K_{rel}(h), h]_{i=1...N, x=1...X}$ data points were subsequently scaled to the reference curve using the functional normalization of h [Tillotson and Nielsen, 1984]. The (empirical) h scale factor, α_x , for a certain infiltration sequence at site x consisting of N data points (i.e., tension steps) was found by minimizing the sum-of-squared differences (SS) between the reference relative hydraulic conductivity curve and the scaled data points. Once α_x for a spatial location (x) was known, scaled $h_{i,x}^*$ ($= \alpha_x h_{i,x}$) were calculated for all tension steps ($i = 1...N$). This scaling procedure is neither strictly similar media scaling based on geometric similitude as in Miller and Miller [1956], nor functional normalization based on empiricism. It is somewhat a hybrid of similar media scaling and functional normalization. Further details of the procedure can be found in Shouse and Mohanty [1998].

Results and Discussion: A sample result of raw versus scaled K - h data for the pooled data set is presented in Figure 1. Results for individual treatments and soil types can be found in Shouse and Mohanty [1998]. Visual examination of the raw and scaled data shows that scaling coalesced the $K(h)$ data very well and matched the reference Gardner model, except for a few outliers. Note that only one set of model parameters was used for all different soil types and field positions. These findings signify the important advantage of scaling in describing the apparent field-scale variability of the hydraulic conductivity. The significance of this finding is that effective dynamic, kinematic, and geometrical similarities remained intact in the soil pore system across the field, even after human-induced disturbance (e.g., row cropping, wheel traffic). These characteristics of the soils at our field site (in terms of their particle, pore, and aggregate arrangements) can be used to advantage in field-scale hydrologic and/or flow-transport modeling efforts by reducing the number of soil

hydraulic parameters for describing field-scale heterogeneity as demonstrated by Hopmans et al. [1988], and Rockhold et al. [1996].

New Mexico Study

In a second study, we investigated the usefulness of our hybrid similar media-functional normalization scaling approach to describe the spatial variability of the hydraulic conductivity ($K(h)$) functions of a macroporous soil in Las Nutrias, New Mexico. Surface horizons contained visible root channels, worm holes, and cracks, thereby composing a complex network of preferential flow paths. Surface infiltration measurements using disc infiltrometers at 0-, 3-, 5-, 7-, 10-, 13-, 15-, 17-, 20-, 25-, 30-, 60-, and 150-mm soil water tensions followed by laboratory measurements up to 1700 mm tension on soil cores (extracted from the same exact locations) were made at nine sites representing different soil series and textures across the field. The different pore domains of the macroporous soil at the field site exhibited significant differences in their hydraulic properties. At all measurement locations, soil hydraulic conductivities between 0 and 30 mm soil water tension were found to be several orders of magnitude higher than the hydraulic conductivity at 30 mm tension, thus, indicating an approximate matching point between the gravity-dominated macropore flow region and the capillarity-dominated matrix flow region (Figure 2a). An arbitrarily selected (K, h) data set was used to define the reference model for the bimodal piecewise-continuous formulation [Mohanty et al., 1997], i.e.,

$$K(h) = K^* \frac{(1 - (\alpha/h)^n)^{n-1} [1 + (\alpha/h)^n]^m}{[1 + (\alpha/h)^n]^{m/2}} \quad h \leq -30 \text{ mm} \quad (2)$$

$$K(h) = K^* + K^* [\exp^{(h+30)\delta} - 1] \quad -30 \text{ mm} < h \leq 0 \quad (3)$$

$$K(h) = K^* + K^* [\exp^{(30)\delta} - 1] \quad h > 0 \quad (4)$$

where $K^* = 0.0555 \text{ mm/s}$; $\alpha = 0.0015 \text{ mm}^{-1}$; $n = 1.80$; $m = 0.444$; $\delta = 0.098 \text{ mm}^{-1}$. As in our Iowa study, $K_{\text{sat},x}$ at any position x in the field was used to scale $K(h)_x$ for the entire tension range (0-1700 mm). This was repeated for all measurement locations. Before conducting any scaling for h , we examined the scaled K for inherent characteristics associated with the bimodal-type hydraulic conductivity functions. The translation of the raw K data to relative or scaled K data showed two important features: (1) K between 0 and 30 mm soil water tension (gravity-dominated flow region) showed better coalescing behavior as compared to K below 30 mm soil water tension (capillary-dominated flow region), and (2) $K_{\text{sat},x}$ was a suitable and effective physical scale factor for K near saturation, consistent with observations by Shouse and Mohanty [1998]. In the individual flow regions (gravity-dominated flow ($h > -30 \text{ mm}$) and capillary-dominated flow ($h < -30 \text{ mm}$)), paired $[K_{\text{rel}}(h), h]_{i=1 \dots N, x=1 \dots X}$ data points were subsequently scaled to the reference curve using functional normalization of h [Tillotson and Nielsen, 1984]. Figure 2b shows the scaled K - h curves for the biporous soil system; the hybrid scaling approach appears quite adequate in representing the hydraulic conductivity variability of the gravity-dominated flow region ($h > -30 \text{ mm}$) across the study area. However, as in Jury et al. [1987], in the capillary-dominated flow region ($h < -30 \text{ mm}$), further scaling of K is necessary. In other words, gravity-dominated flow and the related hydraulic

conductivity ($K(h)$) functions of the macropore region are better scalable than capillary-dominated flow properties of the mesopore and micropore regions. A possible reason for this behavior is that gravity-dominated flow in the larger pores is mostly influenced by the pore diameter which remains more uniform as compared to tortuous mesopores and micropores with variable neck and body sizes along the pore length, thus causing different water particles to move significantly different distances in time. Further details of this work can be found elsewhere [Mohanty, 1999].

References

- Ankeny, M.D., Methods and theory for unconfined infiltrometer measurements. *In* Advances in Measurement of Soil Physical Properties, Spec. Publ. 30, G.C. Topp and W.D. Reynolds, and R.E. Green (eds.) *Soil Sci. Soc. Am.*, Madison, WI, pp. 123-141, 1992.
- Hopmans, J.W., A comparison of various methods to scale soil hydraulic properties, *J. of Hydrol.*, 93, 241-256, 1987.
- Hopmans, J.W., H. Schukking, and P.J.J.F. Torfs, Two-dimensional steady state unsaturated water flow in heterogeneous soils with autocorrelated soil hydraulic properties, *Water Resour. Res.*, 24, 2005-2017, 1988.
- Jarvis, N.J. and I. Messing, Near saturated hydraulic conductivity in soils of contrasting texture measured by tension infiltrometers, *Soil Sci. Soc. Am. J.*, 59, 27-34, 1995.
- Jury, W.A., D. Russo, and G. Sposito, The spatial variability of water and solute transport properties in unsaturated soil. II. Scaling models of water transport, *Hilgardia*, 55, 33-56, 1987.
- Miller, E.E. and R.D. Miller, Physical theory for capillary flow phenomena, *J. Appl. Phys.*, 27, 324-332, 1956.
- Mohanty, B.P. Scaling hydraulic properties of a macroporous soil, *Water Resour. Res.*, 35, 1927-1931, 1999.
- Mohanty, B.P., R.S. Bowman, J.M.H. Hendrickx, and M.Th. van Genuchten, New piecewise-continuous hydraulic functions for modeling preferential flow in an intermittent-flood-irrigated field, *Water Resour. Res.*, 33, 2049-2063, 1997.
- Prieksat, M.A., M.D. Ankeny, and T.C. Kaspar, Design for an automated, self-regulating, single-ring infiltrometer, *Soil Sci. Soc. Am. J.*, 56, 1409-1411, 1992.
- Rockhold, M.L., R.E. Rossi, and R.G. Hills, Application of similar media scaling and conditional simulation for modeling water flow and tritium transport at the Las Cruces trench site, *Water Resour. Res.*, 32, 595-609, 1996.
- Shouse, P.J. and B.P. Mohanty, Scaling of near-saturated hydraulic conductivity measured using disc infiltrometers, *Water Resour. Res.*, 34, 1195-1205, 1998.
- Tillotson, P.M. and D.R. Nielsen, Scale factors in soil science, *Soil Sci. Soc. Am. J.*, 48, 953-959, 1984.
- Vogel, T., M. Cislerova, and J.W. Hopmans, Porous media with linearly variable hydraulic properties, *Water Resour. Res.*, 27, 2735-2741, 1991.
- Warrick, A.W., G.J. Mullen, and D.R. Nielsen, Scaling field-measured soil hydraulic properties using a similar media concept, *Water Resour. Res.*, 13, 355-362, 1977.

Figure 1: Raw (a) versus scaled (b) hydraulic conductivity ($K(h)$) in the Iowa study. (after Shouse and Mohanty, 1998).

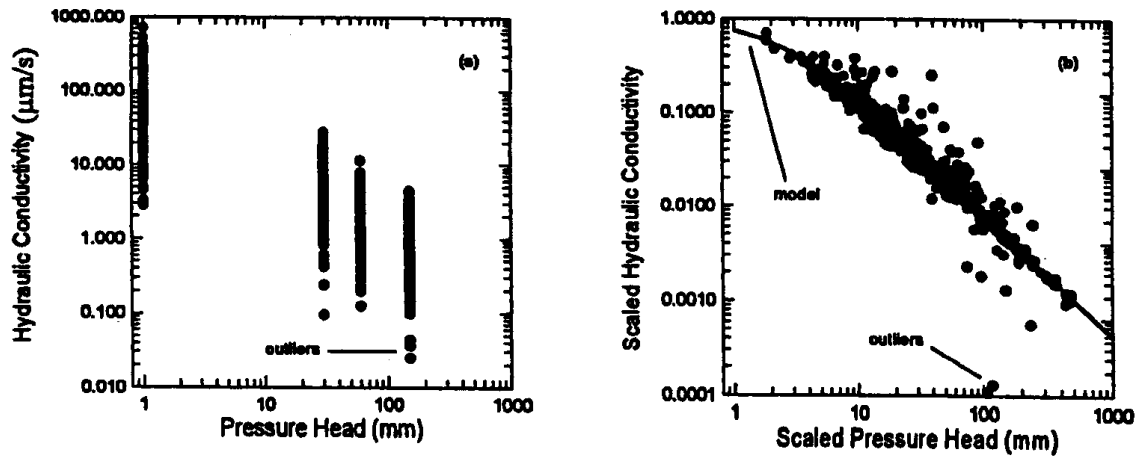
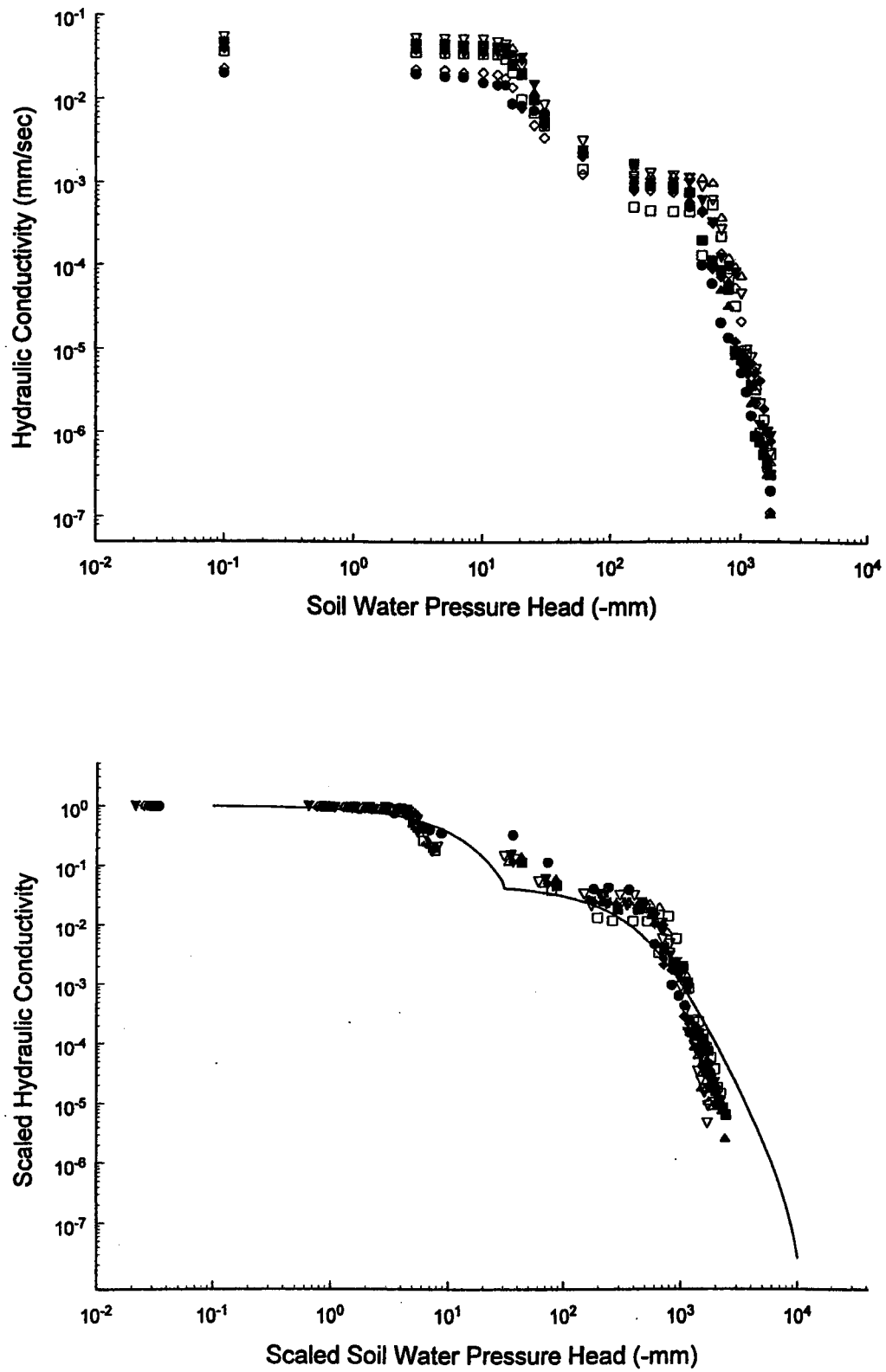


Figure 2: Raw (a) versus scaled (b) hydraulic conductivity ($K(h)$) in the New Mexico study. (after Mohanty, 1999).



EMBEDDED SIDEWALL SENSORS

L. C. Murdoch

Assistant Professor, Clemson University and President, FRx Inc., Cincinnati, OH

Maximizing the quality and quantity of data from each borehole is central to efficient environmental programs. Innovative access methods, such as embedded sidewall sensors, are effective tools for this objective. As briefly listed below, several recent projects have effectively used such methods to meet their data collection needs.

Embedded sidewall sensors (22 water samplers and 19 resistivity electrodes) were installed in a single borehole to measure hydraulic head gradients and to monitor the vertical migration of ionic tracers at a site near Flakkebjerg, Denmark. At a Superfund site in Connecticut, time domain reflectometry (TDR) wave guides were installed to a depth of 12 m in glacial till and used to measure moisture content (Figure 1). Other recent applications include measurement of Eh at the Portsmouth Gaseous Diffusion Plant where horizontal reactive barriers were created to intercept organic contaminants moving downward through the vadose zone. The reactive barriers were filled with potassium permanganate, a strong oxidant, and two dozen Eh electrodes were installed in a borehole to measure the changing redox field associated with migration of the oxidant during remediation (Figure 2).

The sidewall technique currently can place as many as 60 sensors in a single boring, and offers the potential for markedly increasing the spatial resolution with which processes in the vadose zone can be monitored. The method can also be used for embedding sensors in

the sidewalls of horizontal and directional boreholes. This application could provide a platform for placing sensors beneath sensitive structures, such as the tanks containing high-level nuclear and organic wastes at Hanford.

REFERENCES

Murdoch, L.C., W.W. Slack, W. Harrar, R.L. Siegrist (1999), Embedded sidewall samplers and sensors to monitor subsurface conditions, *Ground Water* (in press).

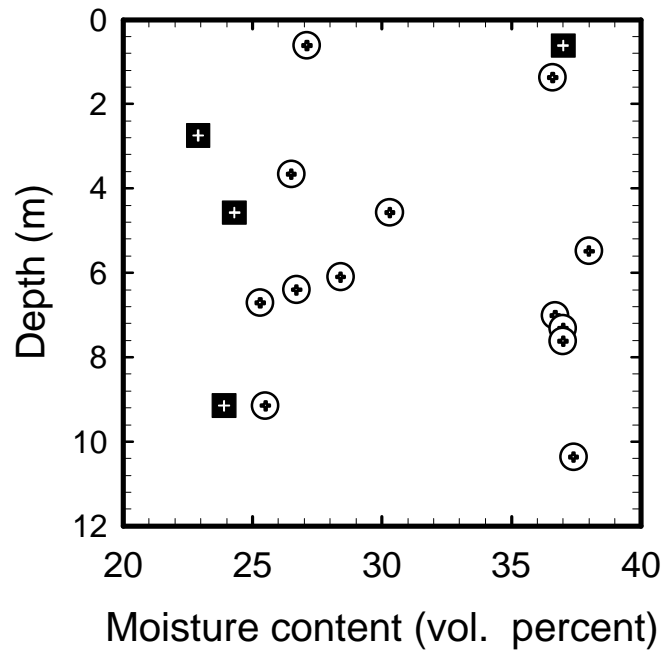


Figure 1. Moisture content in a silty clay till as a function of depth, measured using TDR waveguides embedded into the sidewall of a borehole (circles) and in the lab (squares) as a function of depth (Murdoch et. al., 1999).

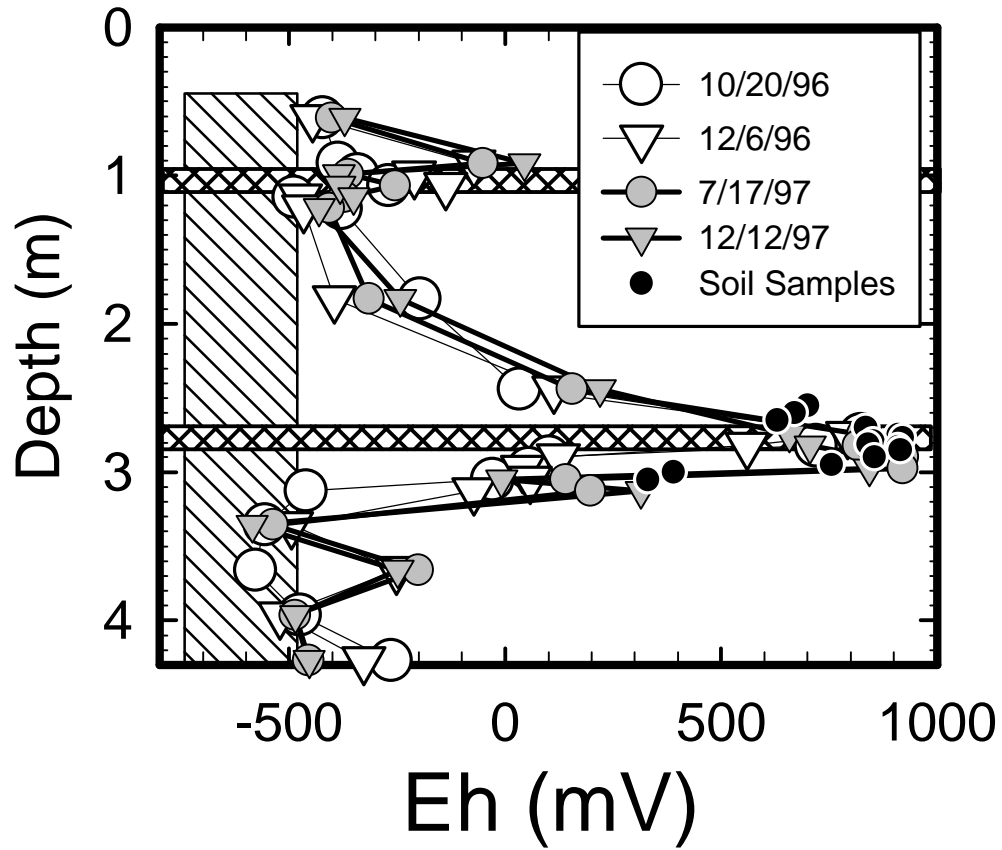


Figure 2. Redox potential as a function of depth and time, measured using electrodes embedded into the sidewall of a borehole. The horizontal bars are hydraulic fractures filled with highly oxidizing potassium permanganate (Murdoch et. al., 1999).

INVESTIGATION OF FAST MIGRATION IN THE VADOSE ZONE FOR ASSESSMENT OF GROUNDWATER CONTAMINATION BY CHERNOBYL RADIONUCLIDES

V.M. Shestopalov, V.N. Bublias, D.E. Kukharenko, Radioecological Center, NAS of Ukraine

INTRODUCTION

This report describes the investigation of enhanced migration of liquid and gas in soils of flatland areas. The Chernobyl exclusion zone was chosen as the area of study, because it contained all of the elements necessary for this type of research: a complicated tectonic situation and geological composition (sedimentary rocks of different composition and genesis); plain relief; sandy substrate of different genesis in covering rock, which serves as a good migration medium; spotted soil and vegetation cover; radioactive contamination as a migration tracer; and a high degree of development of closed, depressed, round, and linear morphosculptures with anomalous properties (Figure 1).

Despite the fact that the total area of the Chernobyl exclusion zone with anomalous geomorphological properties does not exceed 10 percent, it controls more than 50 percent of redistribution of liquid and solid runoff due to large water catchment areas and higher infiltration rates. Moreover, the sediments of more than 90 percent of anomalous zones have permanent excessive moisture and more acid reaction of porous solutions. Under these conditions, the coefficient of redistribution of radionuclides in both rock and biological components exceeds its background values by several times, especially for ^{90}Sr .

Attempts during the first post-accident years to predict the dynamics of radionuclides in the geological environment have shown that the questions concerning dynamic characteristics in various lithogenetic differences are the most problematic. Studies of covering deposits in natural conditions within the weak zones show that infiltration rises sharply, by 1 to 1.5 order(s) of magnitude. Moreover, these characteristics also require attention because the areas adjacent to the Chernobyl Nuclear Power Plant (NPP) are characterized by high tectonic splitting and a low surface runoff coefficient.

The study of the evolution and character of morphosculptures with anomalous properties of energy and mass exchange is similar to the study of most natural objects, including:

- First-stage studies of different facets of external outlook and features of occurrence
- Second-stage studies describing morphology, genesis, and material composition by specialists
- Present-state studies investigating development regularities, and development rate and direction of different components for use in various industries and to make forecast assessments (Bublias, 1993 ; Shestopalov et al., 1995; Shestopalov et al., 1996; Shestopalov et al., 1997).

During recent years, works have been published on methodological character, in which the anomalous zones were studied using different highly mobile tracers, such as special dyes (M. Ghodrati, and W.A. Jury, 1990), isotopes, and pesticides. There are works in which the fast migration zones (in different soils) are regarded as pathways of groundwater contamination. Reports from the Boston conference of May 1998, which was devoted especially to fast migration zones, address these issues.

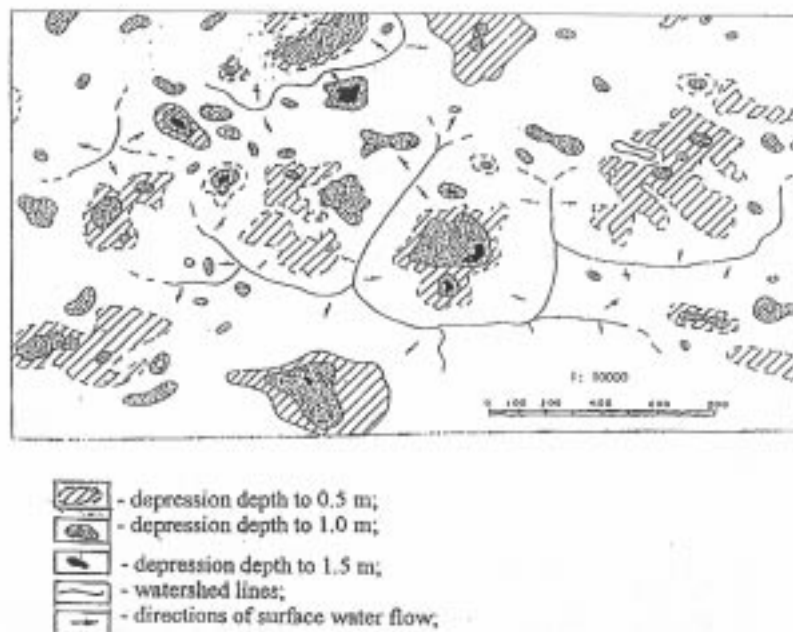


Figure 1. Scheme of the occurrence of depression morphosculptures for a typical site of the Chernobyl exclusion zone, depicting depth of depressions, watershed lines, and directions of surface runoff.

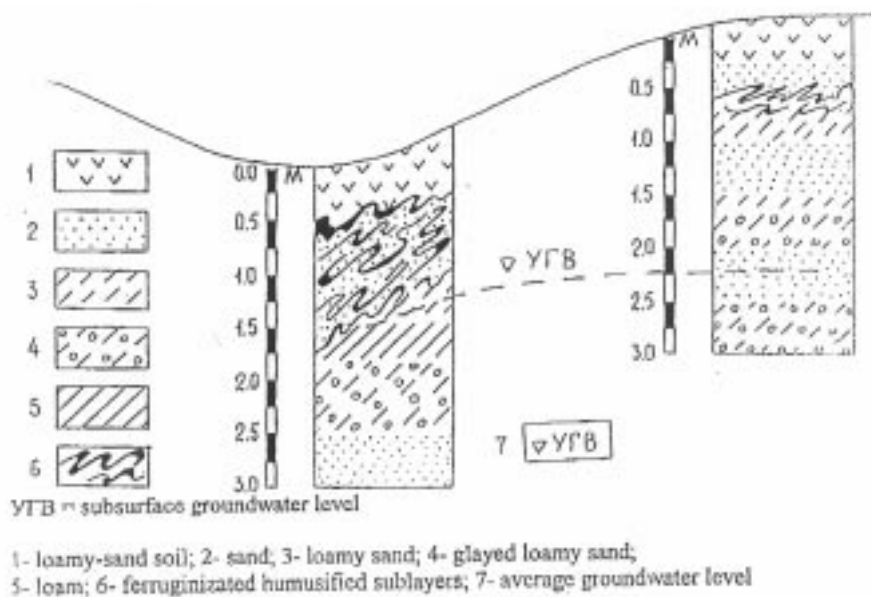


Figure 2. Geological sections of anomalous and background zones of the Stary Shepelichi Observation Plot

An analysis of existing publications on fast migration zones shows that depressed morphosculptures with anomalous migration properties have been the subject of very few studies; therefore, ours is a pioneer work.

The authors of this report conducted a five-year study of fast migration zones and their influence on groundwater contaminated with radionuclides within the Chernobyl exclusion zone (Shestopalov et al., 1995; Shestopalov et al., 1996; Shestopalov et al., 1997). During this period, results were obtained on the methodology of research of anomalous morphosculptures, their genesis, features of occurrence, morphology, regularities of development, and the parameters for their dynamic component.

These issues will be studied in relation to fast migration pathways in the unsaturated zone.

RESEARCH METHODOLOGY AND RESULTS

During research of morphosculptures with anomalous properties in regions of Polesye, a series of methodologies was developed during investigation of stepper dishes (Bublias, 1993). These new methodological procedures, which were tested at areas contaminated with radionuclides from Chernobyl fallouts, were as follows:

- Morphometric
- Morphogenetic
- Geophysical
- Hydrophysical

- Methods for studying migration characteristics of radionuclides

Morphometric and Morphogenetic Characteristics of Observation Plots and Morphosculptures with Anomalous Properties

This paper is based principally on field experimental and laboratory data obtained at the Stary Shepelichi observation plot, where research has been conducted with varying intensity since 1987. For comparison of genetic and dynamic characteristics, and typification of morphosculptures, data obtained at three additional sites, Buryakovka, Novoshepelichi, and Benevka, were also incorporated. Work at these sites was performed primarily in 1998.

The sites for detailed research (observation plots) were chosen with regard to peculiarities of their geological structure, hydrogeology, relief type, composition, and properties of rocks, vegetation cover, structure, and genesis of anomalous morphosculptures. They represent the main types of landscapes of the territory – Chistogalovka water-glacial ridge, first floodplain terrace, and the floodplain.

Each observation plot represents a separate genetic type of anomalous morphosculpture. Within the closed linear form, originating from the ancient water course, the rounded depression morphosculpture is developed. Based upon its metrical parameters, it may be classified as a middle dimension type. Its depth is 2.2 m (higher border), and 2.1 m (lower border) with the diameter along its shorter axis measuring 120 m. The bottom of the depression is flat and elongated in the direction of the linear form.

At the Buryakovka observation plot, there is a round depression of the large-dimension type (110 m in diameter (longer axis) and 3.12 m in depth (higher border) (Figure 1). The bottom of the depression is inflexed in its central part. The slope angles are 4.6 degrees and 3.2 degrees for steep and low-grade slopes respectively.

A combined anomalous morphosculpture was developed at the Sary Shepelichi observation plot. The round-form depression morphosculpture, the origin of which is related to an ancient water course, exists within the borders of a closed linear structure. Its metrical characteristics classify it as an average dimension type. Its depth is 2.2 m at the higher border and 2.1 m at the lower border, and the diameter along its shorter axis measures 120 m. The bottom of the depression is flat and elongated in the direction of the linear structure.

The Novoshepelichi observation plot represents a rounded depression with an ancient water course as the base of its formation. It is obvious that after its burial under eolian sands, deflation and suffosion processes took part in its formation: deflation contributed to composition features of external relief elements; suffosion to morphology of genetic horizons. The depth of this form is 1.02 m at the steeper slope, and 0.86 m at the easier slope; the diameter is 104 m at the shorter axis and 122 m at the longer axis. In area, this structure corresponds to large depression types, but in depth, to shallow depression formations. The bottom of the depression is rounded and slightly inflexed in the northwestern part, which characterizes the displacement of the anomalous zone towards the Pripyat river located 1 km away.

The depression of the Benevka observation plot is referenced as a typical deflation-suffosion genetic type, having the average depth of 2.2 m and diameter of 120 m. Its bottom is rounded and slightly inflexed.

A series of genetic and lithodynamical conclusions were made based on morphometric analysis of the depressions within the region under study. The oval form with its longer axis oriented to the northwest, a steeper slope, and a hill adjacent to the depression in the northwestern part prove its deflation origin. The inflexed bottom shows the highly active anomalous zone in the central part, and bossed one – adjacent to the slope. Depressions with a flat bottom usually have a combined complex structure of active migration pathways, low angle borders (which prove the regression of morphosculpture), and steep borders (which prove its progressive development). For assessment of the surface runoff of the territory, the water catchment area of these depressions is calculated taking into account their slope angles.

The rocks of depression structures are characterized by substantially different features than the rocks of background sites. In deposits of depression central zones, higher clay content is observed, as well as hydromorphy, formation of geochemical barriers, higher humidity, and the existence of zones with a higher rate of moisture transport.

Analysis of the morphology of the background sections reveals zonal development features. By contrast, analysis of depression forms result in zonal development features (Figure 2).

Results of Geophysical Researches

The structural elements of a depression and its zone with anomalous migrational properties were previously studied by field instrumental methods. The results of the study revealed anomalous occurrences in pore gases of radon-222, toron-219, CO₂, and specific reactions of different rocks on ultra-short radio-wave impulses.

Research was conducted along predetermined profiles according to the principle of full involvement of basic structural morphological elements of depressions – along longer and shorter axes, additional profiles, and in places of sharp variations of nanorelief.

The results of the studies showed that the greatest number of anomalous zones occurred in depression structures (Figure 3). After mathematically processing the observation data and interpolating it over the area using leveling data, it was determined that the anomalous fields fit the profile of morphological elements of a depression. The anomalous fields of the central part (the bottom), the slope, and the subbackground zones of a depression are clearly seen. These fields differ in the intensity of definite characteristics. At the Stary Shepelichi plot, the highest characteristics are observed in the central zone, their values decreasing towards the background bed (Figure 3). At the Buryakovka site, anomalous zones adjacent to the slope, and slope zones, are more active.

The georadar method produced the best results in these studies, revealing the structure and composition of the anomalous zones. Georadar surveying was performed at the Stary Shepelichi and Buryakovka plots.

An antenna with a working frequency of 300 MHz was used to create a series of parallel profiles. At the Stary Shepelichi research plot, profiles were done on 25 areas, each 120 m long, with a distance of 2 m to 5 m between the profile piquets.

The field research results were interpreted to obtain information about the characteristic features of the structure in the upper 5 to 7 m of the geological section under study. It is necessary to note that original materials are of a qualitative nature and depict primarily the structural peculiarities of the section, but not the numerical characteristics of structural elements.

In the georadar section of Figure 3, the layers with weak radio wave penetration are clearly visible as having a lighter hue. In most cases, these layers have a mechanical composition, a small amount of organic material, and lower humidity. Characteristics of the darker layers include higher humidity and density, and heavier mechanical composition.

Moreover, the character of the occurrence of layers shows their degree of scattering and homogeneity. In the central part of the section, there is a prominent zone with vertically split and deformed layers. This zone is reflected also on the plots of emanation profiling and in the structure of the geological section.

Smaller zones with a disturbed texture of layers are also present at the morphosculpture slopes.

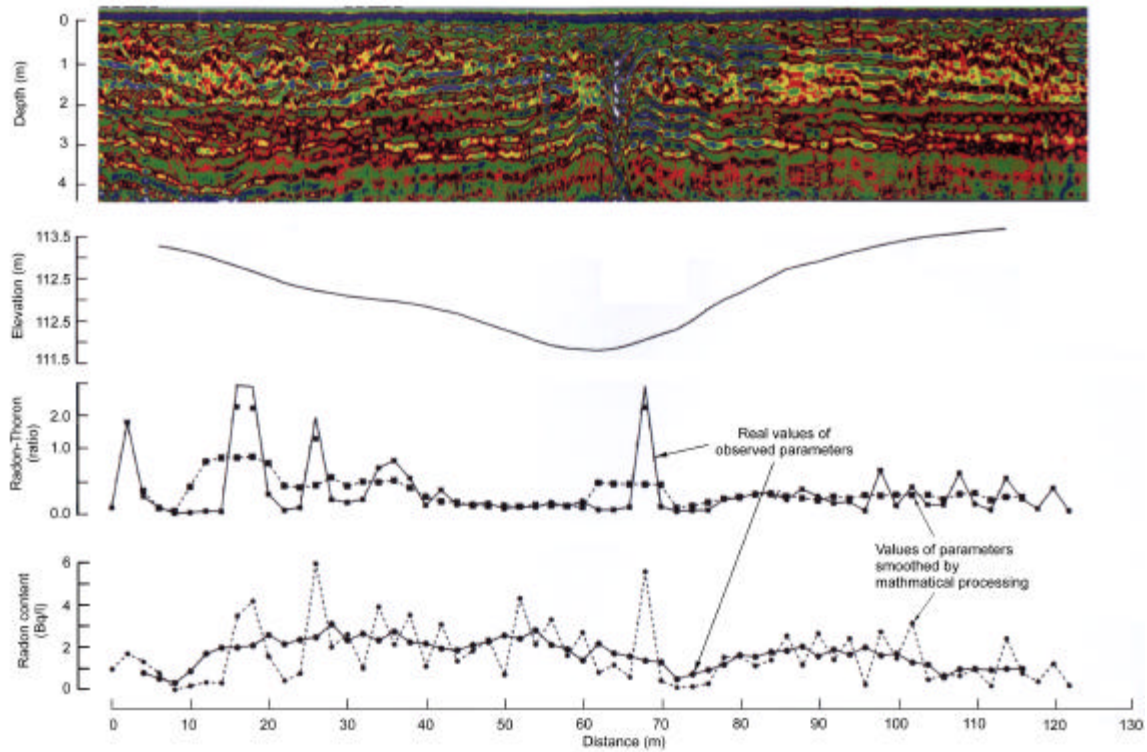


Figure 3. Results of complex geophysical researches (georadar profile, relief, radon content, radon-toron ratio). Profile f, observation plot “Stary Shepelich”.

Studying the Dynamics of Groundwater Levels

Data for groundwater levels from six boreholes at observation plots show that the character of variations in the groundwater level is different in anomalous zones as compared to the background area. In the anomalous zone of the Stary Shepelichi site, the formation of depression cones is clearly observed, especially in periods of intensive dewatering of the unsaturated zone (absence of moisture recharge in rock from atmospheric deposits). A maximal depression of 15 cm was registered in a cone (Figure 4).

Based upon the facts that total water catchment area of all combined (linear-closed) morphosculpture is about 3 hectares; the central anomalous zone is estimated to receive about 1000 mm of water per year for infiltration; the groundwater level cupola is not formed; and the groundwater level gradient of the upper aquifer over the area (with discharge to Sachan river) does not exceed 0.001, it can be concluded that the vertical downward flow of groundwater in this anomalous zone dominates the horizontal flow.

A different picture emerges in the anomalous zone of the closed-type rounded morphosculpture of the Benevka site. Its water catchment area does not exceed 1 hectare, and the amount of water for infiltration varies from 700 to 750 mm per year. However, during the seasonal cycle, the height of the groundwater level cupola varies; the maximum height of the cupola observed on October 15, 1998, was 80 cm (Figure 5).

Analysis of research data for groundwater level dynamics within the depression morphosculpture of the Benevka site indicates that the horizontal groundwater flow in this structure is more intensive than the vertical flow, and that anomalous zones of this type play an important role in groundwater contamination, mainly (for the first) from the

surface aquifer. This differs from the Stary Shepelichi site, where it was observed that the surface water and upper aquifer groundwater actively interact with deeper aquifers.

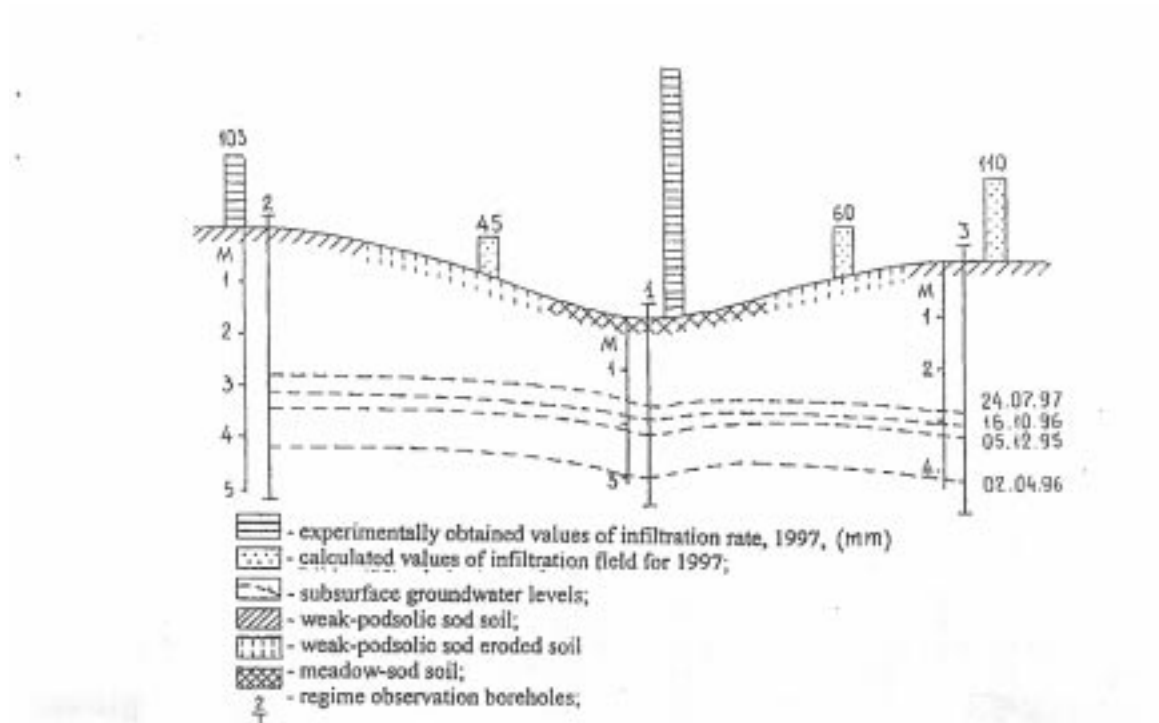


Figure 4. Scheme of infiltration recharge and variation of groundwater levels in upper aquifer at observation plot [Stary Shepelichi]

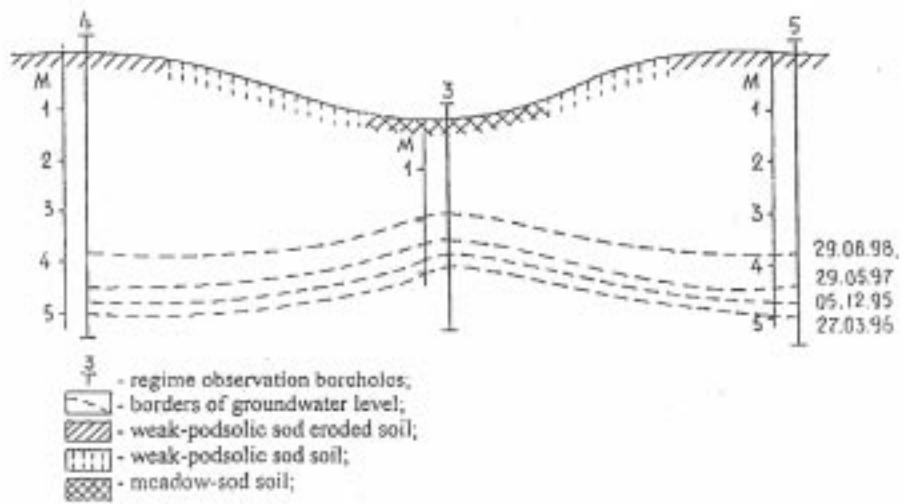


Figure 5: Scheme of variation of groundwater level for upper aquifer at observation plot [Benevka]

Hydrophysical Study of Moisture Exchange

The principle of this method is based upon measuring the suction pressure in unsaturated rocks, using a tensiometer with a ceramic working device, and determining the hydrophysical parameters of rocks; that is, moisture transport coefficient as a factor of suction pressure (K_sP), and volume of moved water (determined in monoliths under laboratory conditions) as dependent on suction pressure. Based on this, the moisture content of rocks at different depths in the aeration zone, the moisture flow velocity, and the volume of infiltration water for a definite period of time are calculated.

The moisture flow velocity is determined using the difference of water heads of suction pressure for pore moisture at different depths of the aeration zone as registered by ceramic gauges.

The rates of infiltration recharge of the groundwater on different elements of anomalous morphosculture were obtained by experimental-estimated and estimated methods.

The first variant performed for two sites only, which stand in the central (anomalous) and the background parts of more steep depression side, based on estimated data of the suction pressure difference during a warm period of 1997 and parameters of water transport (moisture transport coefficient and volume of moved water as dependent on suction pressure) determined experimentally in monoliths in laboratory conditions.

The infiltration recharge rate on hillslopes of depression and background part of its more flat slope side was calculated based upon data of annual precipitation, evaporation intensity, surface flow, and velocity of soil drench.

Figure 4 shows that most humidity misses the central part of a depression; that is, the hillside area has the least humidity.

Characteristics of Dynamics of Radionuclides

An analysis of radioactive contamination along the vertical profile within the anomalous zone of the Stary Shepeliichi site (Figure 5) during 9 years of study (1987-1999) reveals a series of regularities of radionuclides redistribution. They are related by time factor, rock characteristics, and weather conditions. Using characteristics of radionuclide dynamics, the geological section can be subdivided into the following: humus layer (0-0.2 m), full aeration layer (0.2-1.3 m), partial aeration layer (1.3-1.6 m), capillary fringe (1.6-2.0 m), and the aquifer (below 2 m).

Within the humus layer, the clear tendency was toward a deepening of the bulk of radionuclides, and in 1997 its boundary reached 0.3 m. The character of radionuclides dynamics in this layer is relatively stable.

In ground-forming rock (the full aeration layer composed of thin- and middle-grained sands with strong paleocriogene deformation), the dynamics of radionuclides are of discrete character, related primarily to the moisture content and flow rate, and, in the spring, with thixotropy of rock after melting. More radionuclides in this layer were recorded in a wet spring period and in autumn after rainfalls (April 1987, September 1988, September 1994).

In layers of partial aeration composed of heavy, clayey loamy sands, the higher content of radionuclides was observed only after intensive rainfalls (in September 1994).

The higher content of radionuclides in capillary fringe and water-bearing aquifers is also related to atmospheric precipitations.

In the background area with a lower quantity of infiltrational moisture, the rate and amount of moving radionuclides was also lower (Figure 6).

From the statements above, we conclude that the dynamics of radionuclides are closely correlated with the geological structure and infiltration rate of definite areas.

CONCLUSIONS

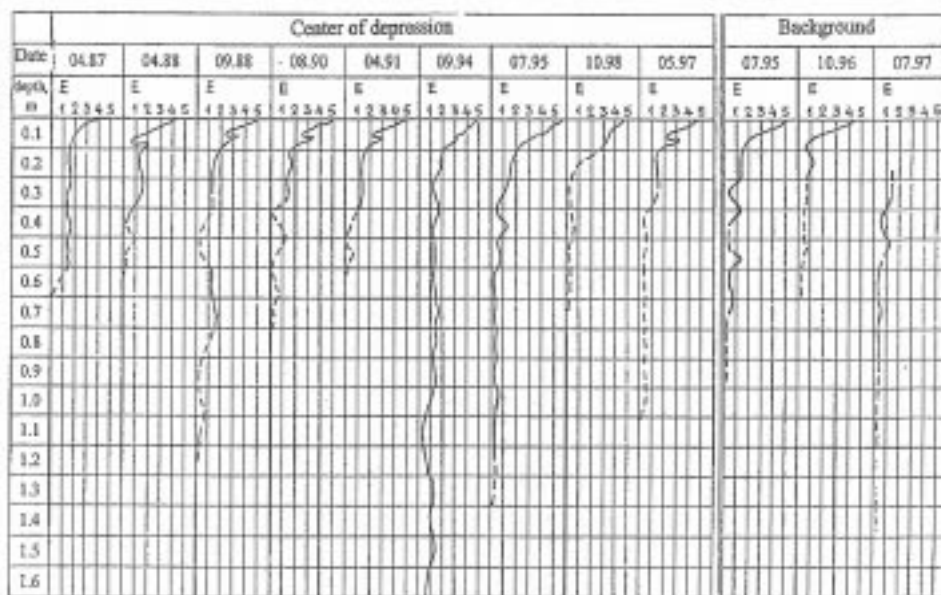
The following results were obtained during works implementation:

1. The genetic variability of types for anomalous morphosculptures at different landscape types is determined: at Chistogalovka ridge, depressions are developed of glacial origin; on the first floodplain terrace, of oxbow-suffosion, and on high floodplain, of oxbow-deflational origin.
2. Rocks of depression structures have substantially different features than rocks of background area sites. In deposits of central zones, higher clay content, excessive humidity, hydromorphosis, formation of geochemical barriers, and zones with higher intensity of moisture transport are observed.
3. Geophysical research into emanation profiling shows the plane structure of anomalous zones and their relative activity; radar surveying shows their internal structure with clear separation of anomalous structure of depression forms.
4. Using groundwater regime data, two types of water exchange are determined within boundaries of anomalous zones: 1) high-active with depression cone and prevalence

of vertical water exchange in the aquifer system; 2) low-active with spreading cupola and prevalent lateral water exchange in the upper part of subsurface aquifer

5. Data on suction pressure show that moisture transport in depressions is significantly higher than at the background area.
6. Analysis of radioactive contamination of rocks over vertical profiles shows its more intensive dynamics within central (anomalous) zones of depressions. Within the layer of partial aeration composed of heavy clayey loamy sands, the raised content of radionuclides is observed only after intensive rainfalls. In general, the character of movement of radioactive elements is closely correlated with geological structure of definite locations and the infiltration rate.

This work is being continued under the subject study.



E - decimal logarithm of radionuclide concentration in the rock;

Figure 6: Features of the Dynamics for ^{137}Cs in Aeration Zone within Depression and Background Sections at Observation Plot [Stary Shepelichi] (Bq/kg)

ACKNOWLEDGEMENTS

The research described in this publication was made possible in part by Award No. UGI-369 of the Government of Ukraine and U.S. Civilian Research & Development Foundation for the Independent States of the Former Soviet Union (CRDF). Any opinions, findings, and conclusions or recommendations expressed in this material are those of the authors and do not necessarily reflect those of the Government of Ukraine or the U.S. Civilian Research & Development Foundation.

REFERENCES

1. Bublias, V.N. Particularities of the development of depression morphostructures in the middle part of the basin of the Dnieper River, Summary of the Ph.D. Dissertation, 23 p., Kiev, 1993. (Title translated from Russian.)
2. Shestopalov, V.M., V.N. Bublias, V.V. Goudzenko, I.P. Onyshchenko, I.P. Borodavko, and A.S. Bohuslavsky (1995), Research into vertical radionuclide migration at the R&D Center of radioenvironmental studies on field test sites, National Academy of Sciences of Ukraine, 5th International Conference on radioactive waste management and environment remediation. ICEM 95. V.2. Management of Low-Level Waste and Remediation of Contaminated Sites and Facilities, Berlin, 3-7 September, 1347-1351.
3. Shestopalov, V.M., V.N. Bublias, V.V. Gudzenko, et al., Investigation of the process of fast vertical migration of radionuclides in geologic media, Chernobyl-94, Conference Materials, V.1, pp. 110-119, Chernobyl, 1996. (Title translated from Russian.)
4. Shestopalov, V.M., A.S. Bohuslavsky, V.N. Bublias, V.V. Gudzenko, I.P. Onishchenko, Yu.F. Rudenko, Investigation of migration of Chernobyl's radionuclides in groundwater used for water supply of the city of Kiev, Chemistry and Water Technology, Kiev, V. 18, No. 2, pp. 120-127, 1996. (Title translated from Russian.)
5. Shestopalov, V.M., I.P. Onishchenko, V.V. Gudzenko, Yu.F. Rudneko, A.S. Boguslavsky, V.N. Bublias (1996), Effects of the Chernobyl Accident on radioactive contamination of water utilized for water supply, EC-IAEA-WHO International Conference "One Decade after Chernobyl: Summing up the Consequences of the Accident", Book of Extended Synopses, Vienna, 8-12 April, 474-475.

6. Shestopalov, V.M., V.V. Gudzenko, Yu.F.Rudenko, V.N. Bublias, A.S. Boguslavsky (1997), Assessment and forecast of groundwater and rock contamination within the Kyiv industrial agglomeration influenced by Chernobyl fallout, Proc. of the XXVIII AN Congress on Groundwater in the Urban Environment, Nottingham, UK, 21-27 September, Volume 1, Problems, Processes and Management, 171-174, aa Balkema, Rotterdam, Brookfield.
7. Omoti, U., and A. Wild (1979), Use of fluorescent dyes to mark the pathways of solute movement through soils under leaching conditions, 2, Field experiments, *Soil Sci.* 128, 98-103.
8. Simpson, T., and R.L. Cunningham (1982), The occurrence of flow channels in soils, *J. Environ. Qual.* 11, 29-30.
9. M. Ghodrati and W.A. Juri (1990), A Field Study Using to Characterize Preferential Flow of Water, *Soil Sci Soc. Am J.* 54, 1558-1563.

*Idaho National Engineering and
Environmental Laboratory*



The Advanced Tensiometer



INEEL
IDAHO NATIONAL ENGINEERING & ENVIRONMENTAL LABORATORY



LOCKHEED MARTIN



Table of Contents

Introduction.....	4
Advanced Tensiometer for Shallow or Deep Soil Water Potential Measurements	5
Water Potential to Depths of 30 Meters in Fractured Basalt and Sedimentary Interbeds	15
Portable Tensiometer Use in Deep Bore Holes	28

Introduction

This document contains three papers on advanced and portable tensiometers. The first paper describes the construction and use of the advanced tensiometer and compares it to existing conventional tensiometers. The second paper presents data from two sites (0-30 m depth) instrumented with advanced tensiometers in sediment and basalt and suggests that deep vadose zones will generally be within the tensiometric (0-1000 cm) range. The third paper describes the construction and uses of the portable tensiometer, a portable version of the advanced tensiometer.

Dr. James Sisson and Joel Hubbell are recipients of the 1997 Research and Development 100 Award for the Advanced Tensiometer.

James “Buck” Sisson is an Advisory Scientist in the Integrated Earth Sciences department. He has worked on research relating to soil physics for over 20 years. He taught Soil physics at Kansas State University for 7 years and was a senior Soil Physicist at Rockwell Hanford Operations for 5 years. He has been granted 3 patents and has five patents pending for vadose zone instrumentation. Six technologies that he and Mr. Hubbell invented have been licensed to In Situ, Inc. of Laramie, WY.

Joel Hubbell is an Advisory Scientist in the Integrated Earth Sciences Department of the Applied Engineering and Development Laboratory of Lockheed Martin Idaho Technology Company. He has over 13 years experience at the Idaho National Engineering and Environmental Laboratory working on vadose (unsaturated) zone and ground water projects.

He has designed and developed an array of vadose and groundwater monitoring instruments. He has been granted 4 patents and has five patents pending relating to vadose zone/ground water monitoring and sampling technologies. He has submitted nearly 20 invention disclosures in the past 9 years, and authored over 20 internal and external documents.

Joel M. Hubbell and Buck Sisson can be contacted at the Idaho National Engineering and Environmental Laboratory, P.O. Box 1625, MS 2107, Idaho Falls, Idaho 83415 jmh@inel.gov and jys@inel.gov.





*Advanced Tensiometer for Shallow
or Deep Soil Water
Potential Measurements*



Advanced Tensiometer for Shallow or Deep Soil Water Potential Measurements

J. M. Hubbell

J. B. Sisson

*Idaho National Engineering and Environmental Laboratory
Idaho Falls, Idaho USA*

ABSTRACT

Tensiometers are required for measuring soil water potential at depths exceeding several meters to quantify the direction and rate of soil water movement. This paper describes a permanently installed tensiometer (advanced tensiometer) to measure soil water potentials at any depth below land surface. The advanced tensiometer was designed with a removable pressure transducer to allow for field calibration and servicing. The advanced tensiometer has two parts, a permanently installed outer tensiometer assembly and a removable transducer assembly. The permanently installed portion has a porous cup, an adapter containing a reservoir of water, and an outer guide pipe that extends to land surface. The removable electronic pressure transducer assembly has a stopper on the bottom, a connector to attach the stopper to a pressure transducer and an inner guide tube to raise and lower the assembly. The transducer assembly is lowered into the outer tensiometer assembly until the stopper connects and seals into the permanently installed adapter. This configuration of the advanced tensiometer allows it to be installed at any depth. Advanced tensiometers were operated at depths of 2 to 4.8 meters for periods exceeding 3 months with no maintenance. The nearly constant temperature condition in boreholes provided for stable, long-term water potential values and reduced field maintenance.

INTRODUCTION

Tensiometers are used to obtain measurements of soil water potential between 0 and about -1000 cm (Gardner et al. 1922; Richards 1931; Cassel and Klute 1986). Tensiometers work in the soil water potential range with the highest unsaturated hydraulic conductivities and thus the greatest potential for rapid water movement. Multiple tensiometers in a profile are used to calculate hydraulic gradients to determine the direction of water movement and to estimate water flux using unsaturated hydraulic conductivity (Morrison 1983). The movement of water in the unsaturated zone is important for engineering investigations (Wilson et al. 1995), hazardous-waste site monitoring (Healy et al. 1984; Everett et al. 1984), recharge studies (Sophocleous and Perry 1985), and irrigation management practices (Cassel and Bauer 1976; Hagan et al. 1967). Numerous configurations of tensiometers have been built

since their conception (Gardner et al. 1922; Richards 1931; Morrison 1983; Cassel and Klute 1986; EPA 1993; Hubbell and Sisson 1996). Tensiometers are comprised of three components: a porous cup or plate, a pressure sensor, and a reservoir filled with water connecting the porous cup to the pressure sensor.

Conventional tensiometers are equipped with the pressure sensor mounted above land surface limiting installations to a few meters below land surface. The length of the water column adds to the vacuum in conventional tensiometers, thereby reducing the effective range by the length of the water column. Tensiometers have been constructed with a pressure transducer buried at or near the sensing tip to circumvent this depth limitation and allow automated data collection (Klute and Peters 1962; Strebel et al. 1973; Williams 1978; Trotter 1984; Nyhan and Drennon 1990). However,

this technique does not provide easy access for field calibration, replacement or maintenance of the transducer. An air filled tensiometer was proposed to eliminate the depth limitations by Faybishenko (1986) by partially filling a lysimeter (tensiometer) with fluid and recording soil water potential using the fill tubes at land surface. These instruments have a delayed response to water potential changes and require two pressure measurements to obtain soil water potential measurements. Tokunaga (1992) and Tokunaga and Salve (1994) presented test results from air filled tensiometers. Hubbell and Sisson (1996) presented a technique to obtain soil water potential measurements using a portable tensiometer. This instrument can be installed at nearly any depth and operated for extended time periods without field maintenance. The portable tensiometer has a slower response time than a conventional tensiometer due to the small contact area between the porous cup and the sediment and it must be removed to land surface to service or calibrate.

Conventional tensiometers exhibit significant diurnal measurement fluctuations from temperature changes in the transducer-tensiometer system (Watson and Jackson 1967) and the gases trapped in the tensiometer (Cassel and Klute 1986). As a result, the instruments have to be serviced regularly to remove air that can accumulate in the tensiometer and influence tensiometer measurements.

Tensiometers need to meet several requirements before they are used for monitoring landfills. They must: (a) operate from near land surface to depths exceeding 30 m, (b) be designed so that sensors can be checked for proper operation in the field, (c) allow calibration of the sensor, (d) permit replacement of the sensor if required, and (e) have reduced maintenance or servicing needs (monthly or preferably quarterly).

A new design for permanently installed tensiometers is presented. This design allows soil moisture potential measurements at any depth, reduces measurement errors from diurnal temperature effects, uses a replaceable transducer, allows in-place sensor calibration and verification, and reduces field maintenance requirements. This tensiometer has been named

the advanced tensiometer. Advanced tensiometers were constructed and evaluated under field conditions. This paper presents construction details, installation procedures, and results of field trials.

MATERIALS AND METHODS

Figure 1 presents a cut-away of an advanced tensiometer. The pressure transducer assembly has a single hole rubber stopper or gasket on the bottom, a connector that attaches the stopper to the pressure transducer, and an inner guide pipe (1/2 in. schedule 40 PVC) that extends to land surface (Figure 1a). The connector allows pressure to be transmitted from the end of the stopper to the diaphragm of the transducer. The stopper size is chosen to firmly connect with the gasket throat of the adapter (Figure 1b). Electrical leads and an air line from the pressure transducer (gauge pressure) are contained within the inner guide and connect to a data logger (Figure 1c).

The permanently installed porous cup assembly consists of a porous cup bonded to a plastic adapter and PVC pipe that extends to land surface (Figure 1b). The adapter is machined to provide a seat to the pressure sensor (gasket throat), fitting between the porous ceramic on bottom and an outer guide pipe on top. The adapter is attached to commercially available tubing (outer guide pipe) which extends to land surface (1 in. class 200 PVC). A surface cap is placed on top of the outer guide pipe at land surface. The advanced tensiometer is formed by sliding the stopper, transducer, and inner tubing (Figure 1a) inside the outer guide tubing (Figure 1b) until the stopper/gasket seals to the adapter (Figure 1c).

Advanced tensiometers can be installed in any uncased borehole (>3.6 cm diameter). The porous cup, adapter and outer guide pipe are assembled at land surface and lowered to the specified monitoring depth. The outer guide pipe should be kept straight in the borehole so the stopper can make a good connection with the adapter. The borehole can be backfilled with a permeable material adjacent to the porous cup and with low permeability materials (bentonite or grout) between the monitored

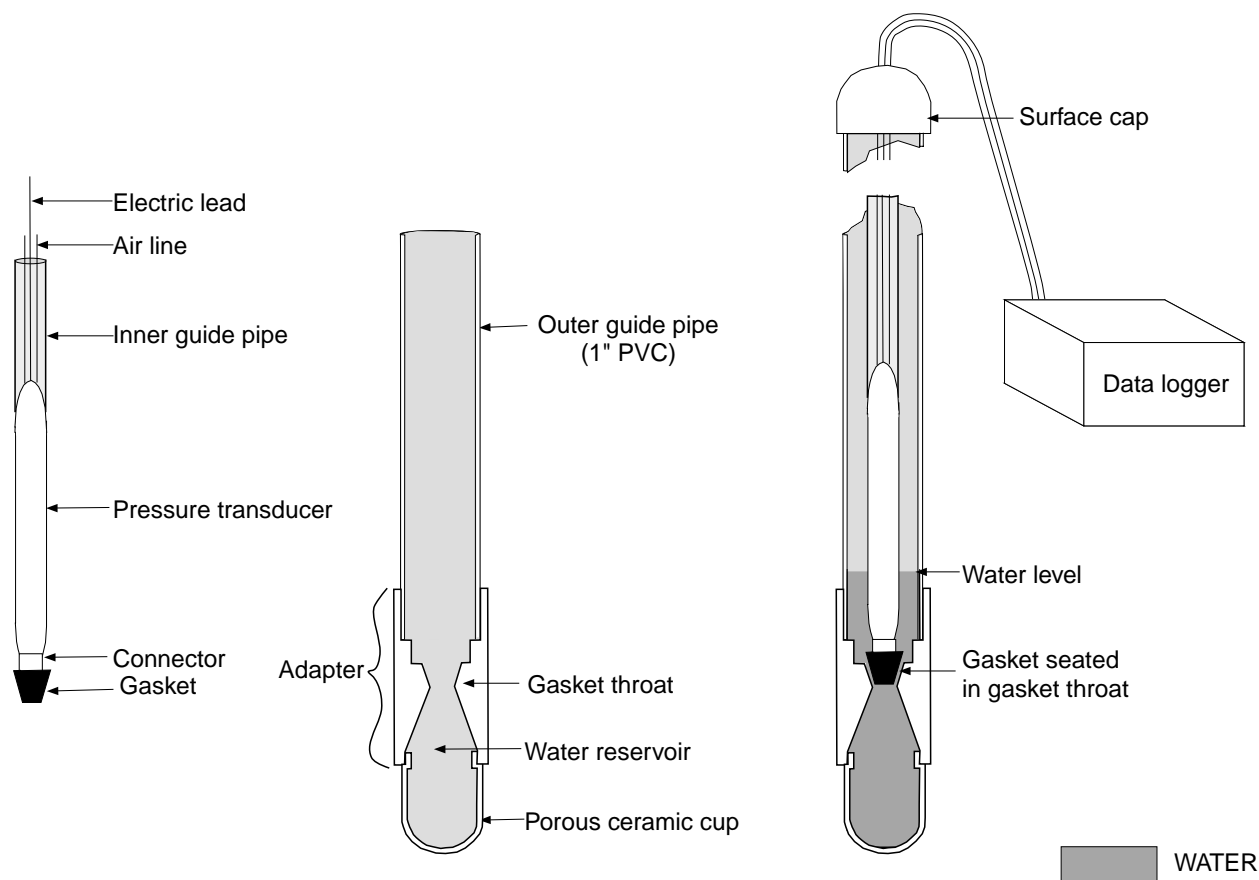


Fig. 1. Configuration of an advanced tensiometer.

intervals. Backfill techniques are presented by Morrison (1983) and Cassel and Klute (1986).

The advanced tensiometer is activated by filling the water reservoir with water and seating the stopper/transducer into the gasket throat. About 100 ml water is poured between the inner guide pipe and outer tensiometer assembly and the inner guide pipe assembly is raised a few cm to fill the cup and adapter (Figure 1c). The weight of the inner guide pipe and transducer presses the stopper into the adapter while the water moving from the reservoir into the surrounding unsaturated sediments applies a force that also holds the stopper in place.

The advanced tensiometer is serviced (deaired) by raising the inner guide pipe allowing the water reservoir to refill from water located above the stopper. Servicing should be performed before readings are affected by air entrapment in the water reservoir. The inner guide pipe and stopper only need to be pulled

up a few cm. Water is added to the tensiometer periodically to maintain a small volume of water above the stopper. Excess water that is not required to fill the sealed bottom chamber adjacent to the porous cup is retained above the stopper and used to fill the chamber at a later time. The tensiometer readings equilibrate in a few hours following servicing.

Calibration procedures were developed for pressure transducers used in the advanced tensiometer. The advanced tensiometers can be deaired or the transducers replaced in a few minutes from land surface. The transducer's calibration (y-intercept and slope) can be tested without having to remove it from the borehole. The y-intercept is determined by pulling the transducer upward out of the water, and then sensing the value with the data logger, while the air line is open to the atmosphere. The slope is determined following the y-intercept calculation by sealing the air line at the data logger, applying

a known pressure on the air line and recording the pressure from the transducer. The pressure applied on the air line corresponds to the measurement recorded on the data logger.

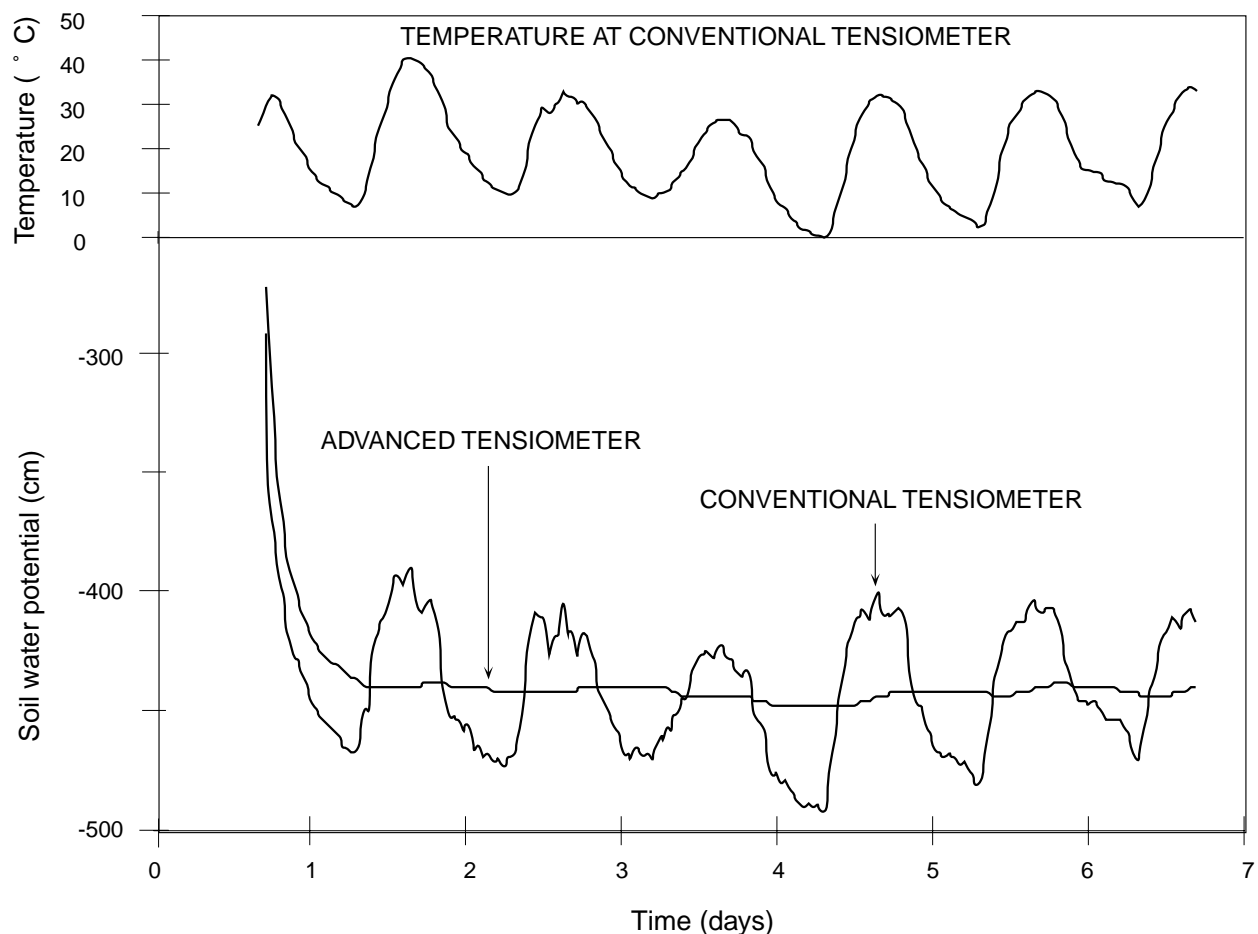
Data from field tests comparing a conventional tensiometer (Soilmoisture Equipment Corp., Santa Barbara CA), and an advanced tensiometer are presented. A single 1.3 m deep by 10 cm diameter borehole was hand augered in Paul silty clay loam. The porous cups of the two instruments were set adjacent to each other and the borehole backfilled with native materials that was tamped into place. Pressure measurements were obtained on 30 min increments with temperature compensated ± 15 psi transducers (Electronic Engineering Innovations, Las Cruces NM) using a data logger (Tumult Gadara, Brookline NH). The transducer on the

conventional tensiometer was covered with a 1.2 cm thick plastic insulation and reflective foil. Temperature was recorded at the conventional tensiometer using a model 107b temperature probe and a 21X data logger (Campbell Scientific, Inc., Logan, UT).

Water usage with time was determined by placing a conventional and advanced tensiometer in a fallow field in Bannock loam at 6-inch depth with the porous cups a few cm apart. The instruments were filled with water and allowed to run for a week. The instruments were disassembled and the volume of water required to refill the tensiometers recorded.

Long term reliability of the advanced tensiometers is shown by operating four instruments at depths of 1.3 to 4 m in sediment for over 90 days without maintenance. A 15 cm borehole was augered in Pancheri loam and four

Fig. 2. Water potential from advanced and conventional tensiometers over a 6 day period.



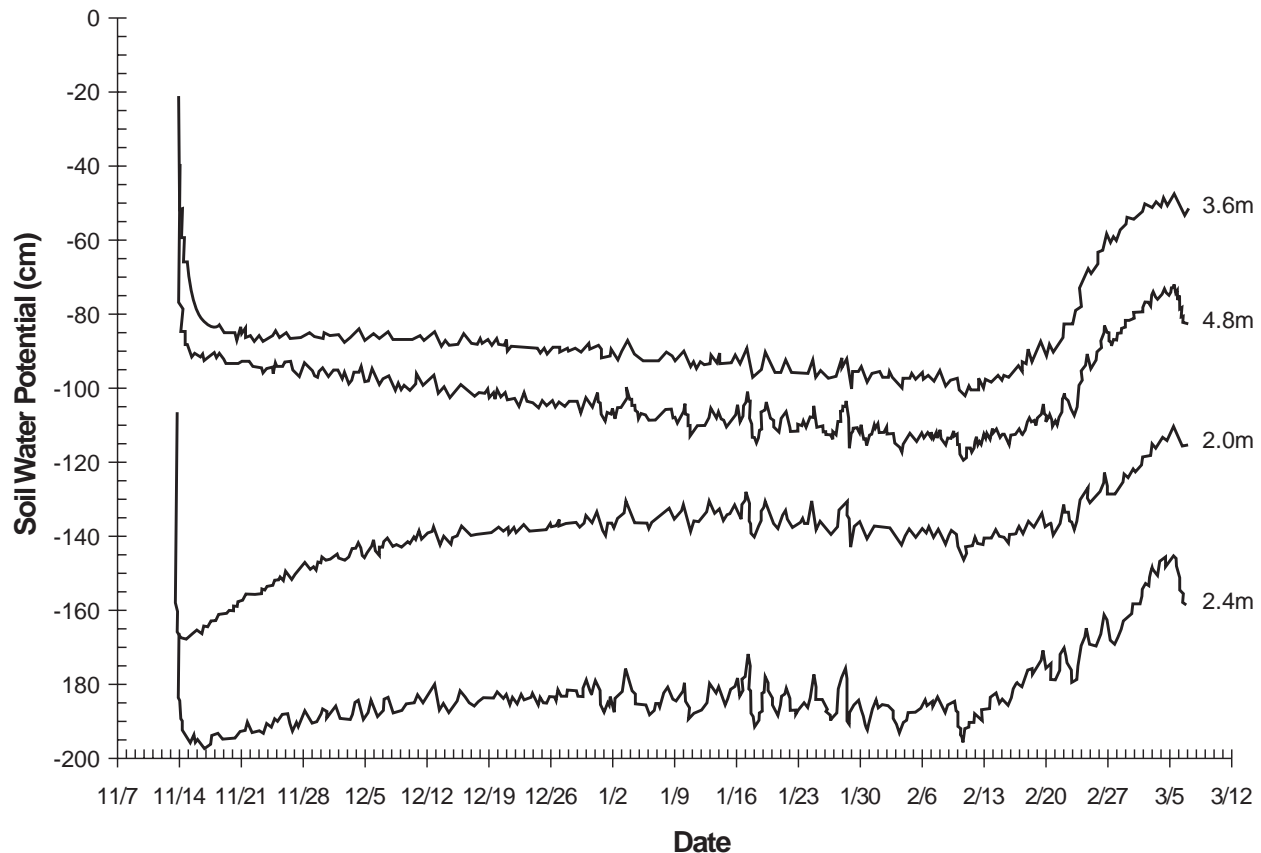


Fig. 3. Water potential measurements from advanced tensiometers over 90 days at 2, 2.4, 3.6 and 4.8 m depths.

advanced tensiometers installed using native backfill with 10 cm layers of bentonite separating the monitored intervals. Water potentials were obtained on 1 hour increments.

RESULTS AND DISCUSSION

Figure 2 presents six days of soil water potential data from a conventional and advanced tensiometer at 1.3 m depth along with temperature data at the conventional tensiometer. The advanced tensiometer readings stabilized to about -440 cm water potential in a day while the conventional tensiometer varied from -400 to -490 cm water potential. The large oscillations in readings of the conventional tensiometer are primarily due to temperature fluctuations from the transducer, expanding air in the headspace above the water column, and materials in the tensiometer. It is

difficult to determine the actual soil water potential with the conventional tensiometer without averaging measurements. These diurnal fluctuations can also make it difficult to see subtle short term water potential changes. If manual measurements were obtained in the field at the same time each day using conventional tensiometers, trends in the data likely would be missed. Soil water potential data obtained from the advanced tensiometer on days 4-6 varied only 8 cm (439 to 447 cm) while the conventional tensiometer varied more than 90 cm. In this test, the diurnal fluctuations of soil water potential were reduced an order of magnitude by placing the water reservoir and pressure transducer below land surface. These data show that the advanced tensiometer has more stable measurements than the conventional tensiometer.

The advanced tensiometer can operate for extended time periods without servicing (deairing) compared to conventional tensiometers. Air in the tensiometer tends to degrade the readings, dampens the response to soil water potential changes, and may cause failure of the tensiometer if sufficient air enters. Conventional tensiometers accumulate air when water moves in and out by temperature induced pressure changes (Cassel and Klute 1986). Apparently not all of the water drawn out returns to the tensiometer. A test of water withdrawn from a conventional and advanced tensiometer indicated the conventional tensiometer filled with air at a rate four times that of the advanced tensiometer. The conventional tensiometer required 25 ml of water while the advanced tensiometer only required 6.5 ml to refill the tensiometers following the 7-day test. This suggests that the advanced tensiometer will operate without maintenance for longer periods of time than conventional tensiometers.

Lowering of the water level within the advanced and conventional tensiometers will affect the soil water potential measurements. The water reservoir on the conventional tensiometers is long and narrow (9 mm diameter) whereas the advanced tensiometer has a short large-diameter water reservoir. A loss of 50 ml in a conventional tensiometer lowers the measured head by 30 cm. The advanced tensiometer should only lose about 13 ml which corresponds to a water level change of 2-3 cm head.

A long term test was carried out using four advanced tensiometers placed at depths of 2, 2.4, 3.6, and 4.8 m. Tension values were recorded over a 90-day period (Figure 3). No water was added to these instruments during this test. In general, the soil water potential is relatively constant from November to February at all four depths. The instrument at 2 m shows an increase in soil water potential, with a period of stability, suggestive of wetting. The tensiometer at 2.4 m shows a similar but muted trend. Tensiometers at 3.6 and 4.8 m show an overall decrease in soil water potential of about 15 cm over the time period. These instruments operated over the entire winter without adding

chemicals to prevent freezing. The instruments initially took 1 to several days to equilibrate with the surrounding sediments. The measurements show some variation over time that is related to changes in barometric pressure. The effects of barometric fluctuations on ground water are well-documented (Jacob 1940; Freeze and Cherry 1979; Rasmussen and Crawford 1997). In ground water, the barometric pressure changes are dependent upon the barometric efficiency of the well and can cause fluctuations in water level about 6 cm per day and up to 36 cm per year (Turk 1975; Hare and Morse 1997). Techniques to remove barometric effects by models and convolution algorithms are presented by Weeks 1979; Rojstaczer 1988a and b; and Rasmussen and Crawford 1997.

CONCLUSIONS

A permanently installed advanced tensiometer for measurement of soil water potential was presented and evaluated. The advanced tensiometer has a porous cup, water reservoir and outer guide tube that are permanently installed, with a pressure transducer and inner guide pipe that can be removed from the instrument. The instrument can be installed to nearly any depth from 0.15 m to greater than 30 m. The transducer can be calibrated in place without removing the transducer to land surface or it can be removed and replaced if it is inoperative. The tensiometer can be deaired and refilled with water from land surface in a few seconds. Placing the transducer at the bottom of the borehole increased the length of time between purging events to remove entrapped gases and reduced the diurnal measurement fluctuations seen in tensiometers with the pressure transducer at land surface. Continuous soil water potential measurements were obtained for a period of over 90 days without adding water to the tensiometer. The length of the hanging water column is nearly the same for all the advanced tensiometers allowing the data to be treated as matric potential by subtracting this length. This simplifies the analysis of the data since a file of these lengths does not have to be maintained. The advanced tensiometer can also operate during periods where the surface

temperature is below 0°C if the porous cup and transducer is below the frost depth. This reduces field maintenance on the tensiometers and permits monitoring throughout the year to capture episodic events such as snow melt. Thus, the advanced tensiometer can be used to measure soil water potential for long-term monitoring at shallow and deep depths with little instrument maintenance.

ACKNOWLEDGMENTS

Work was supported by the Laboratory Directed Research and Development program

and EM-50 of the U.S. Department of Energy, Assistant Secretary of Environmental Management, under DOE Idaho Operations Office Contract DE-AC07-94ID13223 at the Idaho National Engineering Laboratory. Thanks to Indrek Porro, Debbie McElroy and Swen Magnuson who reviewed this document. Mention of a trademark or a propriety product is for the benefit of the reader and does not constitute an endorsement for the product by the Department of Energy to the exclusion of other products that may also be suitable.

REFERENCES

- Cassel, D.K., A. Bauer. 1976. Irrigation schedules for sugarbeets on medium and coarse textured soils in the Northern Great Plains. *Agron. J.* 70:100-104.
- Cassel, D.K. and A. Klute. 1986. Water Potential: Tensiometry in Methods of Soil Analysis, Part One. Physical and Mineralogical Methods. A. Klute. (ed.), Agronomy Monograph #9, second edition, American Society of Agronomy, Inc. Madison, WI. 563-596.
- EPA (U.S. Environmental Protection Agency). 1993. Subsurface Characterization and Monitoring Techniques, A Desk Reference Guide, Volume II: The Vadose Zone, Field Screening and Analytical Methods. Appendices C and D. EPA/625/R-93/003b.
- Everett, L.G., L.G. Wilson, and E.W. Hoylman. 1984. Vadose Zone Monitoring for Hazardous Waste Sites, Pollution Technology Review No. 112. Noyes Data Corporation. Park Ridge. New Jersey.
- Faybishenko, B.A. 1986. Water-salt regime of soils under irrigation (in Russian). Agropromizdat, Moscow.
- Freeze, R.A. and J.A. Cherry. 1979. Groundwater. Prentice-Hall, Englewood Cliffs, NJ. 229-234.
- Gardner, W., O.W. Israelsen, N.E. Edlesfsen, and D. Klide. 1922. The capillary potential function and its relation to irrigation practices. (Abstract) *Phys. Rev.* 20:196.
- Hagan, R.M., H.R. Haise, and T.W. Edminster. 1967. Irrigation of Agricultural Lands. *Agronomy* 11.
- Hare, P.W. and R.E. Morse. 1997. Water-level fluctuations due to barometric pressure changes in a isolated portion of an unconfined aquifer. *Ground Water*. 35:667-671.
- Healy, R.W., C.A. Peters, M.P. DeVries, P.C. Mills and D.L. Moffett. 1984. Study of the unsaturated zone at a low-level radioactive-waste disposal site near Sheffield, Ill., in Proceedings, National Water Well Association Conference on Characterization and Monitoring of the Vadose Zone. Las Vegas, NV. 820-831.
- Hubbell, J.M. and J.B. Sisson. 1996. Portable tensiometer use in deep boreholes. *Soil Science*. 161:376-381.
- Jacob, C.E. 1940. On the flow of water in an elastic artesian aquifer. *Transactions American Geophysical Union*. 21:574-568.
- Klute, A. and D.B. Peters. 1962. A recording tensiometer with a short response time. *Soil Soc. Sci. Am. Proc.* 26:87-88.
- Morrison, R.D. 1983. Ground Water Monitoring Technology; Procedures, Equipment and Applications. Timco MFG., Inc., Prairie Du Sac, WI. 2-7.
- Nyhan, J.W. and B.J. Drennon. 1990. Tensiometer data acquisition system for hydrologic studies requiring high temporal resolution, *Soil Sci. Soc. Am. J.*, 54:293-296.

REFERENCES

- Peck, A.J. 1960. The water table as affected by atmospheric pressure. *Journal of Geophysical Research*. 65:2383-2388.
- Rasmussen, T.C. and L.A. Crawford. 1997. Identifying and removing barometric pressure effects in confined and unconfined aquifers. *Ground Water*. 35:502-511.
- Rojstaczer, S. 1988a. Determination of fluid flow properties from the response of water level in wells to atmospheric loading. *Water Resources Research*. 24:1927-198.
- Rojstaczer, S. 1988b. Intermediate period response of water level in wells to crustal strain: sensitivity and noise level. *Journal of Geophysical Research*. 94:13,619-13,634..
- Richards, L.A. 1931. Capillary conduction of liquids in porous mediums, *Physics*. 1:318-333.
- Sophocleous, M. and C.A. Perry. 1985. Experimental studies in natural groundwater recharge dynamics: Analysis of observed recharge events. *Journal of Hydrology*. 81:297-332.
- Strebel, O., M. Renger, and W. Giesel. 1973. Soil-suction measurements for evaluation of vertical water flow at greater depths with a pressure transducer tensiometer. *Journal of Hydrology*. 18:367-370.
- Todd, D.K. 1959, *Ground Water Hydrology*. John Wiley and Sons. New York.
- Tokunaga, T.K. 1992. The pressure response for the soil water sampler and possibilities for simultaneous soil solution sampling and tensiometry. *Soil Sci*. 154:171-183.
- Tokunaga, T.K. and R. Salve. 1994. Gauge sensitivity optimization in air-pocket tensiometry: Implications for deep vadose zone monitoring. *Soil Science*. 168:389-397.
- Trotter, C.M. 1984. Errors in reading tensiometer vacuum with pressure transducers. *Soil Sci*. 138:314-316.
- Turk, L.J. 1975. Diurnal fluctuations of water tables induced by atmospheric pressure changes. *Journal of Hydrology*. 26,1/2:1-16.
- Watson, K.K., and R.D. Jackson. 1967. Temperature effects in a tensiometer-pressure transducer system. *Soil Sci. Soc. Am. Proc*. 31:156-160.
- Weeks, E.P. 1979. Barometric fluctuations in wells tapping deep unconfined aquifers. *Water Resources Research*. 15:1167-1176.
- Williams, T. 1978. An automatic scanning and recording tensiometer system. *J. Hydrology*. 39:175-183.
- Wilson L.G., L.G. Everett and S.J. Cullen. 1995. *Handbook of Vadose Zone Characterization and Monitoring*. Lewis Publishers. Ann Arbor.



*Water Potential to Depths of
30 Meters in Fractured Basalt and
Sedimentary Interbeds*



Water Potential to Depths of 30 Meters in Fractured Basalt and Sedimentary Interbeds

J. B. Sisson
J. M. Hubbell

Idaho National Engineering and Environmental Laboratory
Idaho Falls, Idaho USA

ABSTRACT

Water potential data are important for estimating moisture flow through the unsaturated zone at waste disposal sites. This paper discusses the results of a study conducted to determine whether tensiometers could be used to monitor moisture conditions at depths of concern at disposal sites. Tensiometers were installed at two sites at depths ranging from 3 to 30 m in porous rock and sedimentary interbeds. These measurements were made with tensiometers modified by placing the pressure sensor in close proximity to the porous ceramic cup. At one site the water potential ranged from -250 to -70 cm and appeared relatively constant over the 7-month monitoring period. At the second site the water potentials ranged from -250 to +100 cm, and data indicated two infiltration events occurred over the 16-month monitoring period. The results of the study indicate that water potential at depths of concern at waste disposal sites can be monitored by using the modified tensiometers.

INTRODUCTION

Infiltration and drainage at waste disposal sites control contaminant migration to underlying aquifers. Water potential measurements can be used to identify infiltration and drainage conditions below a waste site, and gradients in the total water potential indicate the direction of moisture movement. Changes over time in the water potential indicate seasonal infiltration and drainage. Because tensiometers directly measure the soil water potential, they provide soil water potential measurements that are more precise than other techniques [Everett *et al.*, 1984]. However, tensiometers must meet several criteria to be useful for monitoring at waste disposal sites: (1) the ability to operate at depths below the level of buried waste, (2) the capability of providing continuous, easily interpreted output that can be evaluated in real time, (3) the ability to operate for several months without maintenance, and (4) the capability to allow calibration in the field. A tensiometer that meets these criteria is the Advanced Tensiometer [Hubbell and Sisson, 1998]. An additional requirement for using

tensiometers at the Idaho National Engineering and Environmental Laboratory (INEEL) is the ability to monitor water potential in porous rock.

PRELIMINARY ANALYSIS

At depths below a waste site, the water potentials will be similar to those found for a soil column that is undergoing gravity drainage. When profiles are undergoing gravity drainage (e.g., unit gradient), the flux is approximately equal to the hydraulic conductivity, K . A frequently used hydraulic conductivity water potential relationship $K(h)$ is given by van Genuchten [1980]

$$K(h) = K_s \frac{\{1 - (\alpha |h|)^{n-1} [1 + (\alpha |h|)^n]^{-m}\}^2}{[1 + (\alpha |h|)^n]^{-m/2}}$$

where h is the water potential, K_s is the saturated hydraulic conductivity, α and n are curve fitting parameters, and $m = 1 - 1/n$. Parameters for selected soils and basalt are presented in Table 1.

TABLE 1. Properties of selected soils and materials.

Material	θ_s	θ_r	K_s	α	n
Hygiene sandstone	0.25	0.153	108	0.0079	10.4
Touchet silt loam G.E.3	0.469	0.19	303	0.005	7.09
Silt loam G.E.3 ^a	0.396	0.131	4.96	0.00423	2.06
Guelph loam drying ^a	0.52	0.218	31.6	0.0115	2.03
Beit Netofa clay	0.446	0	0.082	0.00152	1.17
W02 silt (Material 1)	0.5	0.06	21.6	0.01	1.6
W02 sand (Material 5)	0.44	0.038	578.4	0.04	2.55
W02 sandy silt (Material 8)	0.51	0.12	45.6	0.025	1.59
W02 silt (Material 12)	0.50	0.14	14.4	0.0036	1.58
W02 sandy silt (Material 15)	0.51	0.12	24	0.009	1.59
W02 basalt (Material 16)	0.23	0.015	24	0.0384	1.474

Sources: *van Genuchten* [1980]; *Martian and Magnuson* [1994].

Table 2 was constructed assuming a unit gradient and solving for the water potential at the assumed fluxes (i.e., hydraulic conductivities). The fluxes chosen were 11 cm/year (the currently accepted value for the annual infiltration rate below portions of a waste disposal site at the INEEL), 3.15 cm/year (i.e., 1.0E-7cm/second—a value commonly

recommended for clay liner construction), and an arbitrary value of 1 cm/year. The water potentials given in Table 2 are in tensiometer range with the notable exception of W02 silt (Material 12). Thus, most soils should be in the tensiometric range at waste sites in which there is downward water movement.

TABLE 2. Water potentials (cm) at the given flux, assuming a unit gradient.

Material	Flux		
	11 cm/year	3.15 cm/year	1 cm/year
Hygiene sandstone ^a	172	181	190
Touchet silt loam G.E.3 ^a	334	360	385
Silt loam G.E.3 ^a	488	667	869
Guelph loam drying ^a	283	381	494
Beit Netofa Clay ^a	2	69	252
W02 silt (Material 1) ^b	349	517	728
W02 sand (Material 5) ^b	112	139	170
W02 sandy silt (Material 8) ^b	176	260	366
W02 silt (Material 12) ^b	856	1284	1820
W02 sandy silt (Material 15) ^b	402	597	841
W02 basalt (Material 16) ^b	96	149	216

a. *van Genuchten* [1980]

b. *Martian and Magnuson* [1994]

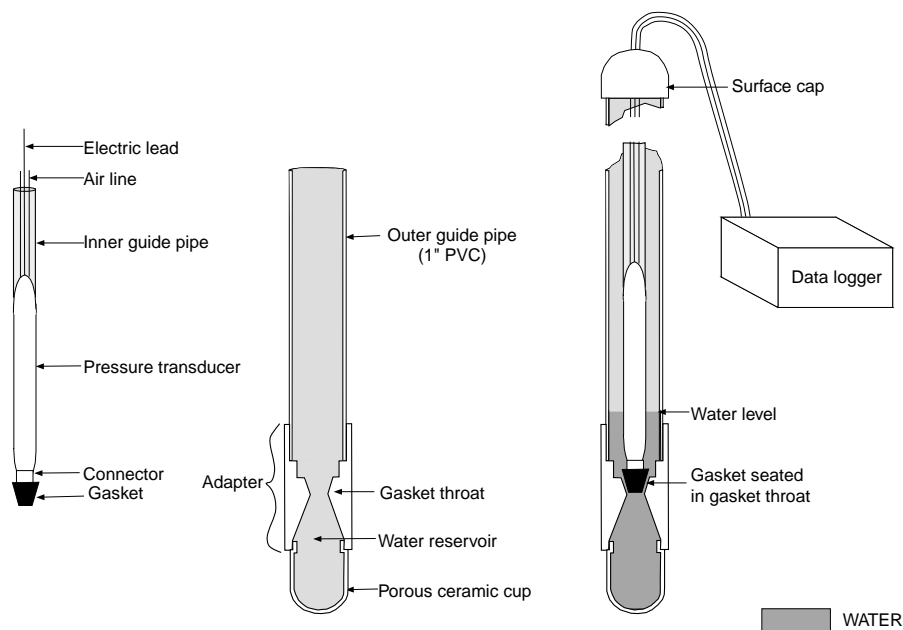


Fig. 1. Internal design of the Advanced Tensiometer (Hubbell and Sisson, 1998).

METHODS AND MATERIALS

Figure 1 presents the modified tensiometer (i.e., Advanced Tensiometer) showing its component parts: a permanently installed casing (1b) and a removable transducer assembly (1a). The permanently installed casing is equipped with a porous ceramic cup on the bottom, an adapter containing a reservoir of water, and casing that extends to land surface. The removable electronic pressure transducer assembly consists of a rubber gasket and pressure transducer attached to an inner guide tube for installing the transducer assembly from land surface. The transducer assembly is lowered into the casing until the gasket seats into the permanently installed adapter. The Advanced Tensiometer is activated by filling the porous cup/adapter with water, sliding the pressure transducer assembly (1a) inside the casing (1b) until the stopper/gasket seats in the adapter (1c). Additional details on construction and installation of Advanced Tensiometers are presented by Hubbell and Sisson [1998].

Two wells were instrumented with Advanced Tensiometers at depths of 3 to 30 m, and data were collected for 7 and 16 months in

southeastern Idaho (Figure 2). Well 76-5 is located in the southern portion of the INEEL. Well IRC-3 is located in Idaho Falls, about 70 km east of Well 76-5. Both sites are located on the Snake River Plain, which is composed of Quaternary volcanics (olivine basalt) overlain by loess and stream channel deposits [Hackett and Smith, 1992]. The INEEL and Idaho Falls are located on the Eastern Snake River Plain (ESRP), which is a large flat valley surrounded by mountains that rise to about 3,300 m. The ESRP is generally classified as arid to semiarid with an annual precipitation of 200 to 300 mm. The 76-5 site receives about 250 mm of precipitation annually, and the IRC-3 site receives 300 mm annually [Clawson *et al.*, 1989]. The average snowfall is about 700 mm with maximum average accumulations of about 100 mm in January and February. The average summer temperature is 28°C and the average winter temperature is -0.6°C.

Well 76-5 was air rotary (core) drilled and sampled with a 14.9-cm-diameter bit to a depth of 73 m. The bottom of the well was sealed to a depth of 32 m. Figure 3 presents the stratigraphy of Well 76-5. The well has loam

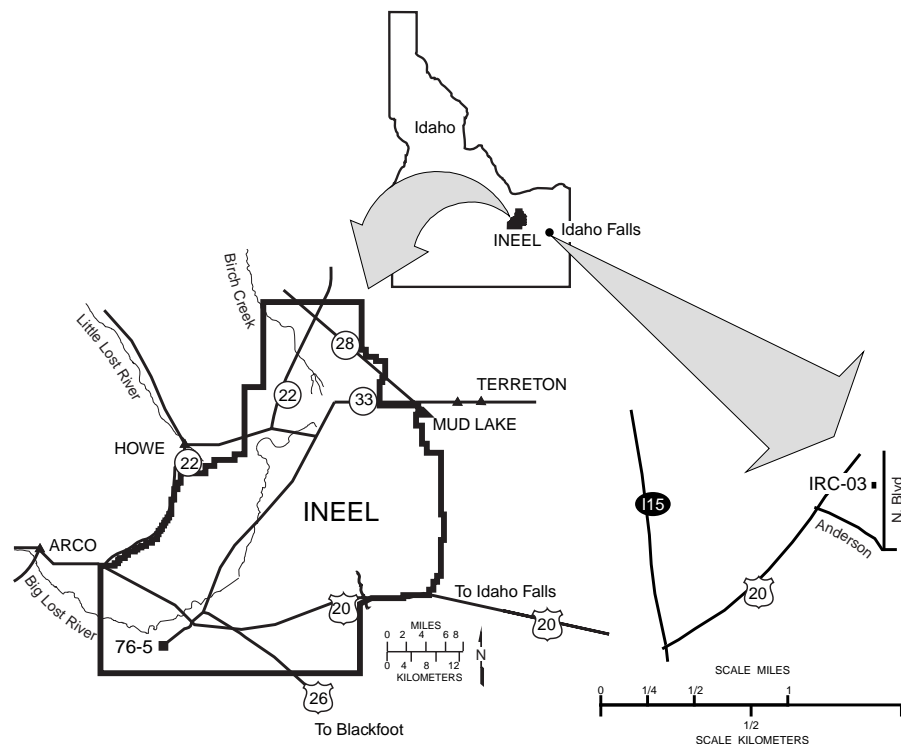


Fig. 2. Location of wells 76-5 and IRC-03

backfill and undisturbed loam from land surface to basalt at about 4 m. Basalt is located from about 4 to 9.4 m and from about 10.4 to about 31 m. Sedimentary interbeds composed of loam materials are located between the basalts. The basalt has a relatively high porosity of about $0.22 \text{ m}^3 \text{ m}^{-3}$, a permeability of about $1\text{E-}6 \text{ cm/second}$, and a low water retention capacity of about 1 to $5 \text{ m}^3 \text{ m}^{-3}$ at 100 cm of tension [Bishop, 1991]. The loam has a porosity of about $0.45 \text{ m}^3 \text{ m}^{-3}$, a saturated hydraulic conductivity of about $1\text{E-}5 \text{ cm/second}$, and a water retention capacity of about $0.40 \text{ m}^3 \text{ m}^{-3}$ at 100 cm [McElroy and Hubbell, 1990].

Drillers, video, geologic, and geophysical logs were examined and evaluated to determine the optimum depths for locating tensiometers adjacent to the rubble zones, sedimentary interbeds, sediment infilled fractures, and basalt that appeared moist. Well 76-5 was backfilled and instrumented with Advanced Tensiometers in June 1996. The well was backfilled with a layer of silt loam 0.3 to 1 m thick placed adjacent to the porous cups on the tensiometers and granular bentonite layers (about 0.3 m) placed between the monitoring depths. Course

sand Number 6-8) was used to fill the remaining portions of the well between the tensiometer monitoring depths [Cassel and Klute, 1986].

The lithology of the instrumented depths is presented in Figure 3. The uppermost tensiometer was placed adjacent to the first sediment-filled fracture in basalt below the surficial sediment. The second tensiometer was placed adjacent to a sedimentary interbed at about the 9-m depth. The next three tensiometers were installed adjacent to sediment infilled fractures within basalt. A tensiometer was located adjacent to moist unfractured basalt a few meters above a sedimentary interbed and the lowermost tensiometer was placed adjacent to a sedimentary interbed comprised of clayey silt at about the 31-m depth. Several pressure transducers in the tensiometers failed over the test period, and the data from those tensiometers were omitted.

Well IRC 3 was drilled to a depth of 15.2 m in September 1995 using the air rotary drilling technique with a 14.9-cm-diameter bit. The well is located in the same general geologic formation as Well 76-5 (in Snake River Plain basalt). The site is characterized by loam and

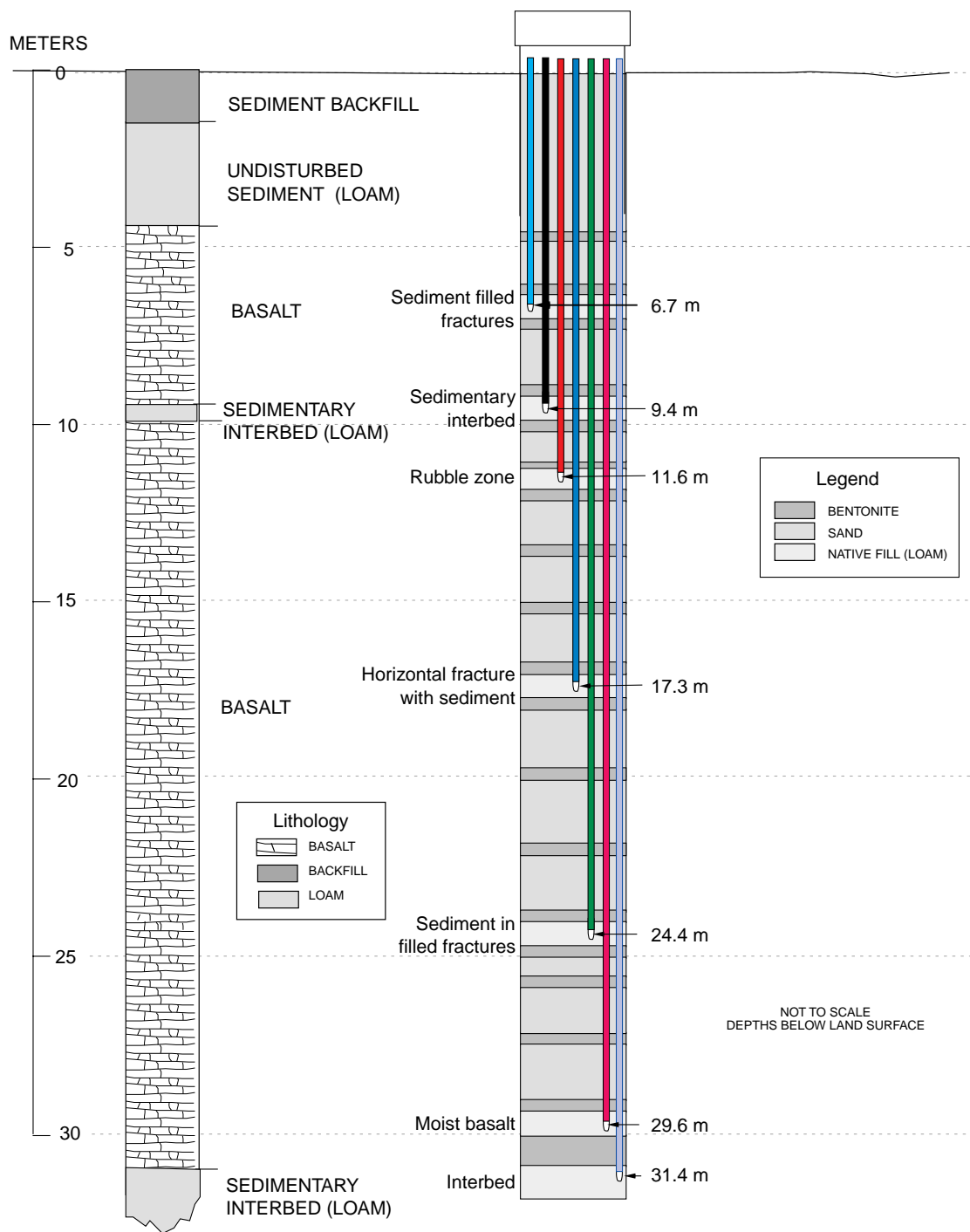


Fig. 3. Geologic log and completion diagram for 76-5.

alluvial sediment extending from land surface to a depth of 2.7 m and basalt from 2.7 to 15.5 m (Figure 4). Sedimentary interbeds were not present at this site.

Tensiometers were located at the sediment-basalt contact, adjacent to nonfractured basalt, fractured basalt, and “moist” or “wet” nonfractured basalt based on examination of

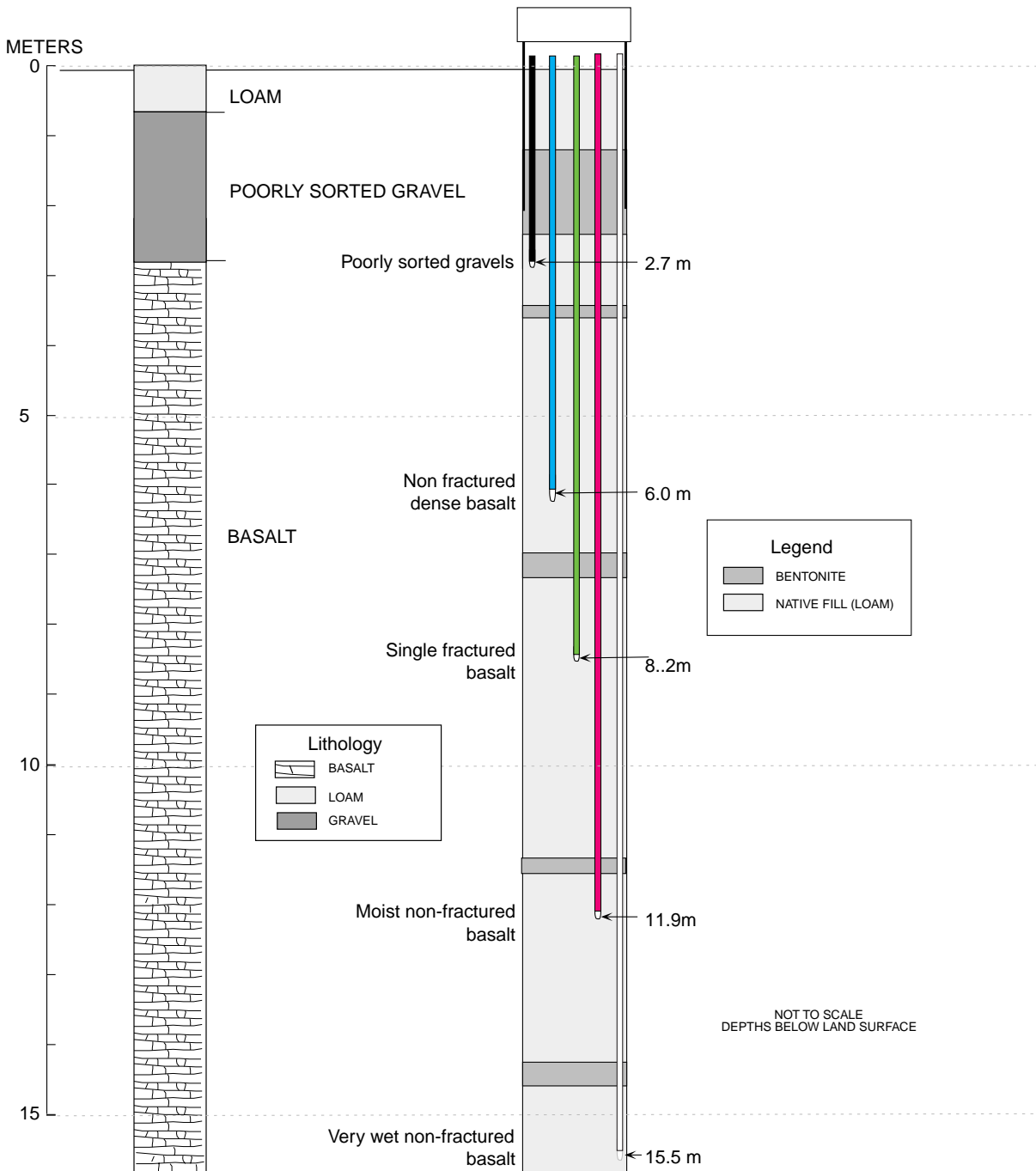


Fig. 4. Geologic log and completion diagram for Well IRC-03

drillers, video, caliper, gamma, and neutron logs. During the installation of the tensiometers, the well was backfilled using the technique outlined in *Cassel and Klute* [1986]. The construction of

the well varied from Well 76-5 in that loam was used to backfill most of the borehole with a single layer of bentonite 0.3 to 0.6 m thick placed between the monitored intervals

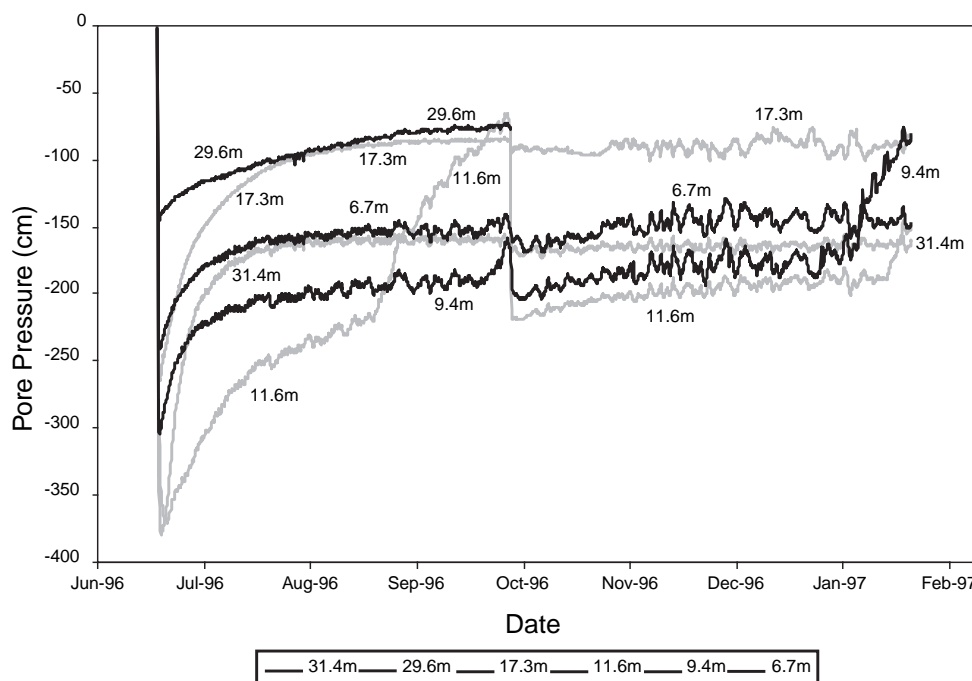


Fig. 5. Soil water potential data from Well 76-5.

(Figure 4). The shallowest tensiometer is placed adjacent to a sandy gravel at the sediment-basalt interface, and the other four tensiometers are located adjacent to dense or fractured basalt.

RESULTS AND DISCUSSION

Figure 5 presents water potential data from Well 76-5 for the period from July 1996 through February 1997. Water potentials initially were in the range of -375 to -150 cm and increased over several months to a range of -220 to -70 cm. Low initial water potential measurements in July and August 1996 are representative of the sediment (loam) used to backfill around the tensiometers. Sediment used for backfill had water potentials at about -300 to -400 cm of pressure before placement in the boreholes. The tensiometers equilibrated with the backfill in a few hours to days while the backfill took several weeks at the 17.3-m depth and more than 2 months at the 9.4-m depth to equilibrate with the water potential in the surrounding basalt. This equilibration time is related to the time for moisture to move from the basalt into the drier sediment backfill. The tensiometer

measurements show a rapid increase in pressure that levels off as the pressure approaches an equilibrium range. The tensiometer measurements do not approach a single value but vary over a range of about ± 20 cm. These fluctuations were found to be correlated to changes in barometric pressure.

Water potential appeared to be unaffected by daily or yearly infiltration events at these depths. The total variation in water potential was less than 50 cm in all the tensiometers over the 7-month period. The gradients in total water potential were found to be near unity, which indicates that water was moving downward. The highest water potentials were located in the basalt while the sedimentary interbeds generally had lower potentials. The trend of higher water potential in basalt was assumed to be related to the basalt having a lower unsaturated hydraulic conductivity than the interbeds, and thereby retained more water. The trend corresponds with modeling results obtained by *Martian and Magnuson* [1994] using the UNSAT-H code [*Fayer and Jones*, 1990].

The apparent increase in the water potential in the 11.6-m tensiometer from September to

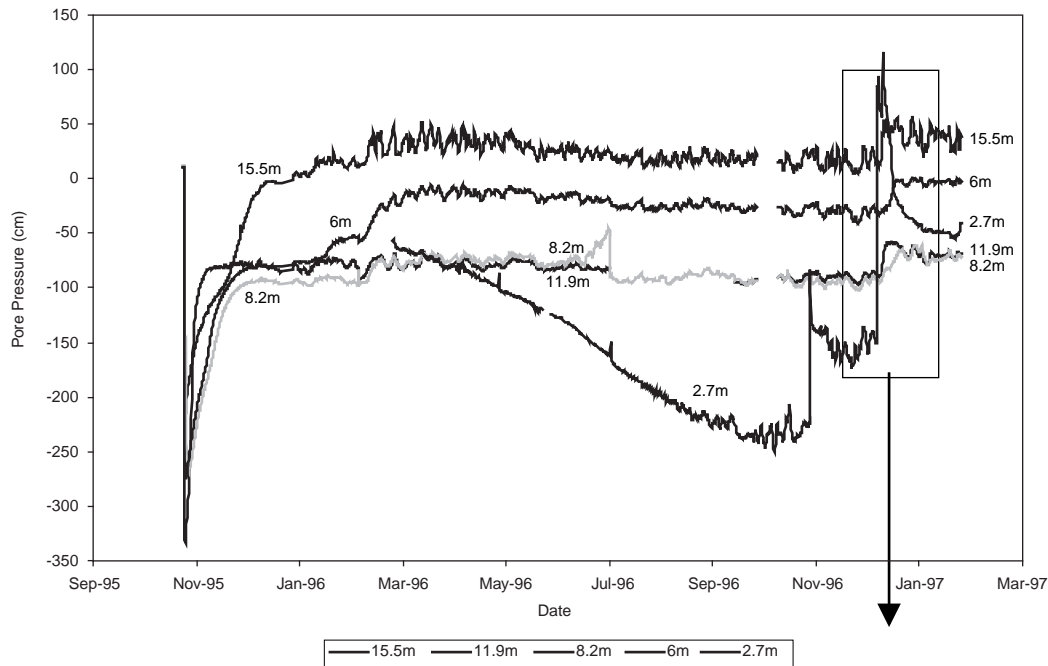


Fig. 6. Soil water potential from Well IRC-03.

mid-October reflects air entering the tensiometer and lowering of water in the instrument and is not an increase in the actual water potential. Similar trends were recorded at the 9.4- and 11.6-m depths in January 1997. The tensiometers were filled with water at the beginning of the test in June 1996, in mid-October, and at the end of the test in February 1997. This data indicated that the tensiometers operated for more than 3 months without filling with water, following initial equilibration.

Several pressure transducer measurements shifted slightly toward lower water potential (about 10 cm) after being refilled with water in October. The decrease in the water potential is assumed to be caused by changes in the hanging water column in the tensiometer. Filling the tensiometer with water maximizes the hanging water column, which decreases the apparent water potential.

In Figure 7, data from Well IRC-3 are presented for 16 months, from November 1995 to March 1997. Tensiometer measurements within basalt showed an initial period when the sediment used for backfill came into equilibrium with the surrounding basalt similar to the

measurements for Well 76-5. Water potentials equilibrated to the range of +120 to -220 cm in all of the tensiometers. The tensiometers at 6- to 15-m depths indicated nearly constant values over the period of measurement. The 2.7-m tensiometer indicated a drying trend of -50 to -220 cm from March to December 1996 then several wetting events from late December 1996 to March 1997.

Water potential data indicated several wetting events over the 16 months of measurements. The most pronounced occurred from a snow melt event in late December 1996 (Figure 7). The wetting front passed from the depth of 2.7 m to 15.5 m in a few days. All of the tensiometers responded to this infiltration event; however, the sequence of first arrival indicated preferential flow paths within the basalt. Following the formation of perched water at 2.7 m at the basalt-sediment interface, the water potential responded first at the 11.9- and 15.5-m depths and then a few days later at the 6-m and finally the 8.2-m depth. The greatest change in water potential caused by infiltration was observed at 15.5 and 11.9 m, adjacent to moist to wet nonfractured basalt and in dense nonfractured basalt at 6 m. The least

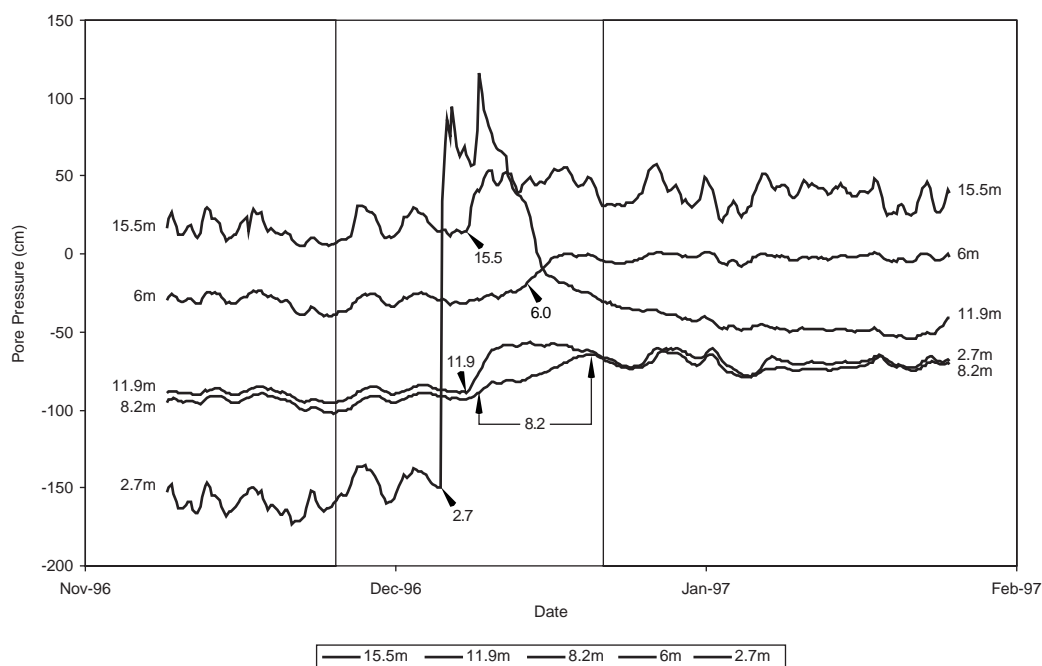


Fig. 7. Detail of infiltration event in Well IRC-03

distinct response was recorded from the tensiometer adjacent to a single fracture at 8.2 m. These data show infiltration occurring rapidly through the basalt. The velocity of the water pressure pulse ranged from 1 m/day to 3 m/day through the basalt.

Several wetting episodes occurred during January and March 1996 after snow-melt and precipitation events. The January event indicated an increase in water potential of about 15 cm at the 6- and 15.5-m depths that was followed by a 20-cm increase in March 1996. Following the wetting episodes, the tensiometer measurements showed decreases in water potential until the wetting event in December 1996. These data indicated the water potentials changed quickly to infiltration events and more slowly to drainage. This would happen when wetting resulted from infiltration through preferential flow paths followed by drainage through the basalt matrix.

CONCLUSIONS

A comparison of water potential data from Wells 76-5 and IRC-3 indicated that all

measurements are within the tensiometric range of +120 to -220 cm. Within basalt, Well 76-5 has lower water potentials from -70 to -220 cm while Well IRC-3 is in the range of +120 to -80 cm. Comparing similar depths, Well IRC-3 had water potentials of about 100 cm higher than Well 76-5. The higher water potentials may be caused by more infiltration having taken place at Well IRC-3 or by differences in hydraulic properties at the two sites.

Water potential trends over time varied between these wells. Tensiometers in Well 76-5 indicated nearly constant water potentials over the 7-month monitoring period, while Well IRC-3 had several increases in water potential over the 16-month monitoring period. Well IRC-3 showed a wetting front that moved to 15 m in a few days while Well 76-5 showed no evidence of formation of a wetting front during the same time period. The time for the water potentials within the loam backfill to equilibrate with the surrounding basalt was from several weeks to more than 2 months at both wells.

The relatively uniform water potentials obtained with depth indicated the hydraulic

gradient to be downward and near unity at both wells. Thus water movement was downward at a rate near the hydraulic conductivity.

Tensiometers in one well showed episodic moisture movement to depths of 15.5 m in a few days after snow melt events. Water potential measurements were affected by barometric pressure fluctuations, and equilibration time was found to depend on the backfill material used in installation and hydraulic conductivity of the porous material being monitored. Results indicated the Advanced Tensiometers can be used successfully

to monitor moisture conditions in porous rock and sediments at waste disposal sites.

ACKNOWLEDGMENTS.

This project was supported by the Laboratory Directed Research and Development (LDRD) program and EM-50 of the U.S. Department of Energy, Assistant Secretary of Environmental Management, under the Department of Energy Idaho Operations Office Contract DE-AC07-94ID13223 at the Idaho National Engineering and Environmental Laboratory.

REFERENCES

- Bishop, C. W. 1991. Hydraulic properties of vesicular basalt. 115 pp. M.S. thesis. Department of Hydrology and Water Resources, University of Arizona. Tucson, AZ.
- Cassel, D. K., and A. Klute. 1986. Water potential: Tensiometry. p. 563–596. In A. Klute. (ed.) *Methods of Soil Analysis*. Part 1. 2nd ed. Agronomy Monograph. 9. ASA and SSSA, Madison, WI.
- Clawson K. L., G. E. Start and N. R. Ricks. 1989. Climatology of the Idaho National Engineering Laboratory. 155 pp. 2nd ed. DOE/ID-12118, U.S. Department of Commerce, National Oceanic and Atmospheric Administration, Environmental Research laboratories Air Resources Laboratory, Field Research Division, U.S. Department of Energy Idaho Operation Office, Idaho Falls, ID.
- Everett L. G., L. G. Wilson, and E. W. Hoylman. 1984. Vadose zone monitoring for hazardous waste sites. 360 pp. Noyes Data Corporation, Park Ridge, NJ.
- Fayer, M. J., and T. L. Jones. 1990. UNSAT-H version 2.0: Unsaturated soil water and heat flow model. 83 pp. PNL-6779, Pacific Northwest Laboratory, Richland, WA.
- Hackett, W. R., and R. P. Smith. 1992. Quaternary volcanism, tectonics, and sedimentation in the Idaho National Engineering Laboratory area. p. 2-19. In J.R. Wilson. (ed.) *Field Guide to Geologic Excursions in Utah and Adjacent Area of Nevada, Idaho, and Wyoming*. Geological Society of America, Rocky Mountain Section.
- Hubbell, J. M., and J. B. Sisson. 1998. Advanced tensiometer for shallow or deep soil water potential measurements. in press. *Soil Science*.
- McElroy, D. L., and J. M. Hubbell. 1990. Hydrologic and physical properties of sediments at the Radioactive Waste Management Complex. 62 pp. EGG-BG-9147, EG&G Idaho, Inc., Idaho Falls, ID.
- Martian, P., and S. O. Magnuson. 1994. A simulation study of infiltration into surficial sediments at the Subsurface Disposal Area, Idaho National Engineering Laboratory. EGG-WM-11250, EG&G Idaho, Inc., Idaho Falls, ID.
- van Genuchten, M. Th. 1980. A closed-form equation for predicting the hydraulic conductivity of unsaturated soils. *Soil Sc. Soc. Am. J.* 44:892-898.



Portable Tensiometer Use in Deep Bore Holes



Portable Tensiometer Use in Deep Boreholes

J. M. Hubbell
J. B. Sisson¹

*Idaho National Engineering and Environmental Laboratory
Idaho Falls, Idaho USA*

ABSTRACT

Quantifying the direction and rate of soil water movement beneath landfill disposal areas requires tensiometers capable of monitoring soil water potentials from one to several hundred meters below land surface. This paper describes a new way to use tensiometers to measure soil water potentials at nearly any depth. Two portable tensiometers were constructed and tested in the field. One portable tensiometer was sealed with a septum stopper, lowered to the bottom of a borehole, allowed to equilibrate, and retrieved to land surface. The soil water potentials were then determined through the septum stopper using a pressure transducer equipped with a hypodermic needle. A second portable tensiometer was constructed with an electronic pressure transducer with leads brought to land surface to allow continuous monitoring of soil water potentials without removing the tensiometer from the borehole for extended time periods. The portable tensiometers are retrieved to land surface periodically to refill with deaired water. Both portable tensiometers were operated in the field for periods exceeding 2 months with little maintenance at depths of 4-6 meters. The response time of the portable tensiometers ranged from a few hours to several days and was limited by the contact between the porous cup and the soil. The slow response time was not found to be a serious problem in deep boreholes. The nearly constant temperature conditions found in deep boreholes were found to contribute to stable, long-term tension values and to reducing maintenance normally required by standard tensiometers.

INTRODUCTION

Tensiometry is an established technique for obtaining accurate measurements of soil water potential between 0 and -1000 cm (Richards, 1928, Cassel and Klute, 1986). Multiple tensiometers in a profile can be used to determine hydraulic gradients to estimate the direction of water movement. The hydraulic gradients are used with the unsaturated hydraulic conductivity to estimate water flux. Tensiometers work in the water potential range associated with the highest unsaturated hydraulic conductivities and thus the greatest potential for water movement. The movement of water in the unsaturated zone is important for irrigation

management practices (Cassel and Bauer 1976; Hagan et al. 1967), recharge studies (Sophocleous and Perry 1985), hazardous-waste site monitoring (Healy et al. 1984; Everett et al. 1984), and engineering studies (Wilson et al. 1995).

Standard tensiometers are generally installed within a few meters of land surface because the length of the water column connecting the porous cup to the pressure transducer adds to the vacuum in the tensiometer. Tensiometers may be constructed with the pressure transducer buried at or near the sensing tip to circumvent this depth limitation and allow automated data collection (Klute and Peters 1962; Williams 1978; Trotter 1984; Nyhan and Drennon 1990). However, this technique does not allow periodic calibration of the transducer or refilling of the instrument unless there is physical access to the pressure sensor (i.e. caisson). An air filled

¹ *Idaho National Engineering Laboratory, Lockheed Martin Idaho Technologies, P.O. Box 1625, MS 2107, Idaho Falls, Idaho 83415, jmh@inel.gov and sys@inel.gov.*

tensiometer was proposed to eliminate the depth limitations by Fabishenko (1986) by partially filling a lysimeter (tensiometer) with fluid and recording soil water potential using the fill tubes at land surface. Tokunaga (1992) and Tokunaga and Salve (1994) present results from tests of the air filled tensiometer, to optimize the fractional air filled length, absolute matric head, vapor pressure and the depth of the tensiometer porous cup in deep vadose zones. This technique works for permanently installed tensiometers (lysimeters) but is not installed on a temporary basis.

Another problem with standard tensiometers is that they frequently exhibit significant diurnal fluctuations in measurements primarily due to temperature changes of the material in the tensiometer (Cassel and Klute 1986) or the transducer-tensiometer system (Watson and Jackson 1967). These diurnal fluctuations are in part related to the limitation of shallow installation depth.

A new technique has been employed for tensiometers to obtain soil moisture potential measurements at nearly any depth. We call the tensiometer used with this technique a portable tensiometer. The portable tensiometer is lowered to the bottom of a borehole so the porous cup is in contact with sediment. Following a suitable equilibration time, the tensiometer is withdrawn to land surface to read the sensor or data is relayed to land surface by way of a pressure transducer/data logger.

Two portable tensiometers were constructed and evaluated in the laboratory and under field conditions. This paper presents construction details and installation procedures for the portable tensiometers and results of laboratory and field tests.

TENSIOMETER CONSTRUCTION AND INSTALLATION

Numerous configurations of tensiometers have been built since their conception (Gardner et al. 1922; Richards 1931; Morrison 1983; Cassel and Klute 1986; EPA 1993). While the construction of tensiometers can vary, all tensiometers consist of three basic components: a porous cup or plate, a pressure sensor, and a

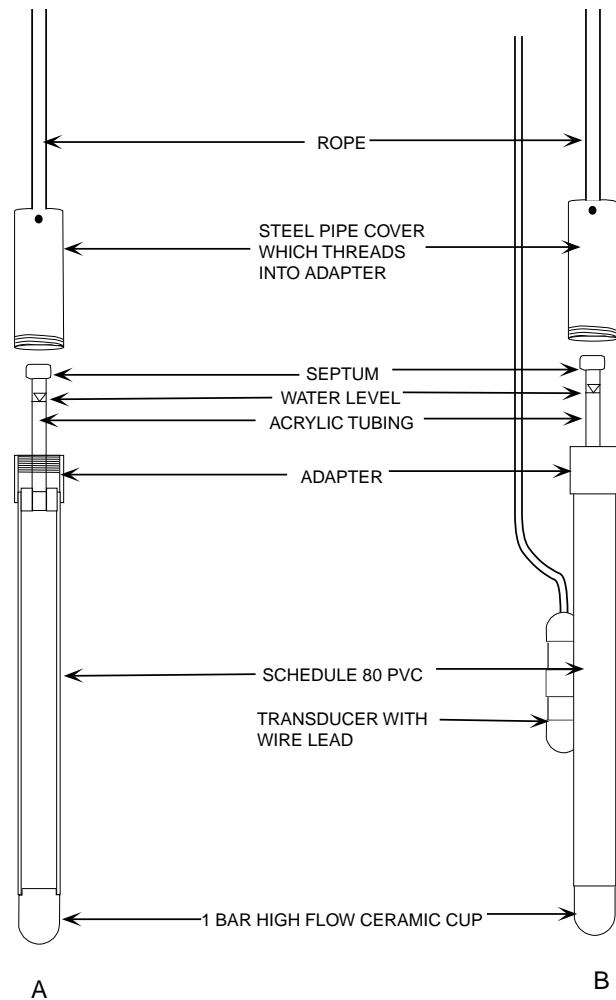


Fig. 1. Configuration of the portable tensiometers.

chamber filled with water that connects the porous cup to the pressure sensor.

Figure 1a shows a cut-away of a portable tensiometer designed to obtain single measurements from the bottom of a borehole. The tensiometer is approximately 30 cm long. The portable tensiometer was sealed with a septum to reduce costs and the complexity of the instrument. Costs were considered important since operating the instruments at drill sites was found to increase the chance of breakage from rough handling. The tensiometer has a one-bar high- flow porous cup on the bottom, a chamber that contains water and a septum that seals the instrument. Acrylic tubing (3/8 inch) is used to visually determine the water level in the instrument. A length of steel

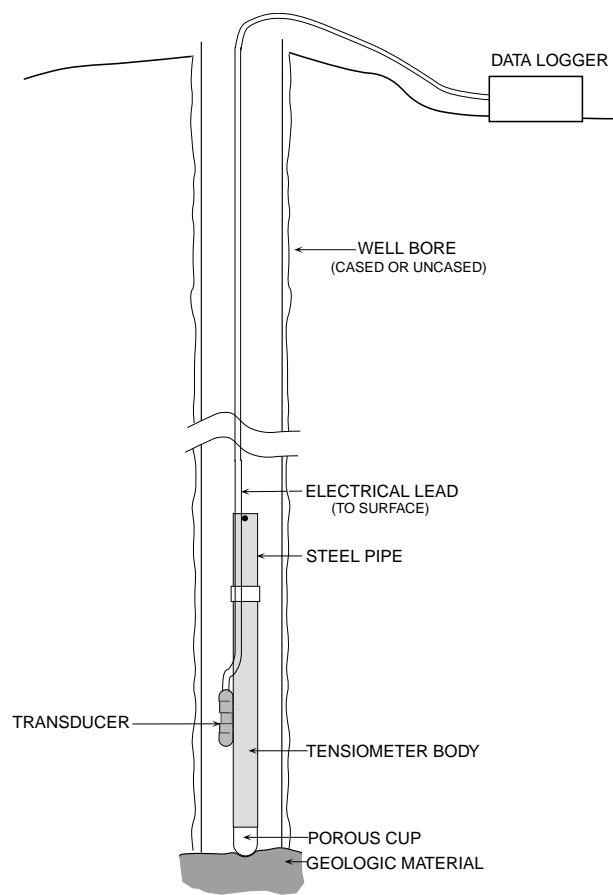


Fig. 2. Schematic showing field use of a portable tensiometer.

pipe (0.5 to 1.5 kg) threads into the top of the tensiometer to provide additional weight. Rope is connected to the steel pipe to install and retrieve the tensiometer. The portable tensiometer is retrieved to land surface and the septum penetrated with a hypodermic needle with a transducer attached to obtain a single measurement of the soil moisture tension in the sediment at the bottom of the borehole. The tensiometer in Figure 1b is equipped with a pressure transducer to obtain continuous soil water potential measurements over time.

A tensiometer was sealed with a septum and read using a syringe needle connected to a direct reading pressure transducer (Tensimeter™, Soil Measurement Systems, Tuscon, AZ). A Bourdon gauge was also used in place of the

septum to obtain direct measurements. This instrument allowed single measurements to be collected following retrieval of the instrument to land surface. A second tensiometer was equipped with a pressure transducer, connected to a data logger at land surface, used to obtain soil water potential data for the 233-day test period and to obtain tensiometer response time data following installation.

The portable tensiometers were transported to the field in a short piece of PVC tubing with a cap holding a sponge against the ceramic cup. The porous cup was protected against breakage by the PVC tubing and kept moist by the wet sponge.

Once at the field site, the steel pipe was attached to the tensiometer and the entire assembly was lowered to the bottom of the borehole and allowed to equilibrate with the soil surface (Figure 2).

Conventional wisdom regarding tensiometer operation requires a through hydraulic contact with the soil in which it is emplaced. Standing a tensiometer on a soil surface limits the contact area between the porous cup and soils and could significantly impact the response time of the tensiometer. The response time provided by standing a tensiometer on a soil surface was evaluated in a laboratory study using a short soil column filled with Pancheri loam, fitted with a hanging water column, and instrumented with a conventionally installed tensiometer. After the hanging water column was set to a given tension, the portable tensiometer was placed on the soil surface and the water potential was monitored with an electronic transducer (Electronic Engineering Innovations, Las Cruces, NM) and data logger (Tumut Gadara, Columbus, OH). Moisture proof plastic film was placed over the hanging water column and portable tensiometer to reduce evaporation. Water potentials were obtained in 10-minute time increments from the portable tensiometer at the soil water potentials of 10, 55, 180, and 240 cm of water.

RESULTS AND DISCUSSION

The results of the laboratory response time test are shown in Figure 3. These results show that the limited contact provided by simply

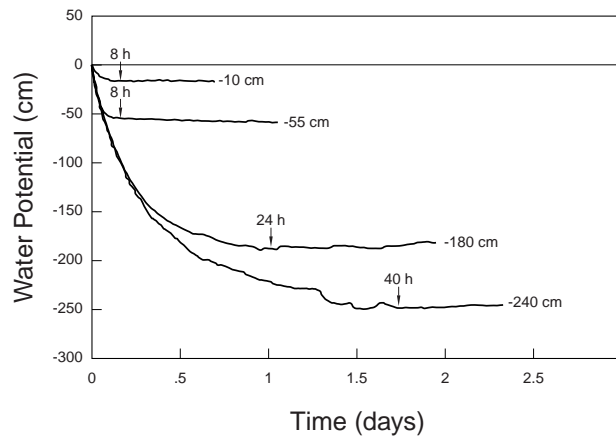


Fig. 3. Measurements from a portable tensiometer at water potentials of 10, 55, 180, and 240 cm versus time.

placing the tip of a tensiometer on the soil surface can require 36 to 48 hours for the water potential to reach the final value of 240 cm. At higher water potentials, the response time is less than 24 hours. While a more than 24-hour response time could be critical under conditions of rapidly changing water potentials it was considered acceptable for installations several meters below land surface where water potentials are believed to change slowly.

The response time of the portable tensiometer is a function of the texture of the sediment, in situ water potential, hydraulic properties of the sediment, hydraulic properties of the porous cup, the area of contact, volume of air in the tensiometer, and the hydraulic connection to the sediment. The first three factors cannot be modified but the latter four can be controlled within limits to decrease the time for equilibrated measurements. A larger cup size with a high conductivity will facilitate readings and increasing the weight of the tensiometer will press the porous cup with greater force to the sediment, increasing the hydraulic connection and decreasing the response time. Decreasing the volume of air in the portable tensiometer will reduce the volume of water required to move between the tensiometer and the sediment. If measurements are required over a limited time period a pressure transducer and recorder should be used to insure the pressure in the tensiometer has equilibrated with the in situ water potential.

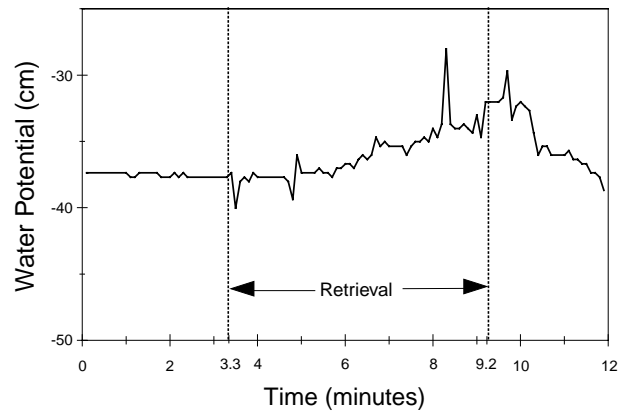


Fig. 4. Water potential measurements while retrieving the portable tensiometer to land surface.

The portable tensiometer designed to obtain single measurements during drilling operations requires retrieval to land surface, where the water potential is determined. The water potential indicated by a tensiometer was expected to change as the instrument was retrieved to land surface. The change in water potential during retrieval was evaluated using a tensiometer equipped with an electronic pressure transducer. The tensiometer was placed in a borehole, allowed to come into equilibration with the soil water for several days, and retrieved slowly to land surface while recording tension values (Figure 4). These data show that pulling the tensiometer away from the soil surface and retrieving to near land surface did not significantly change the water potential during retrieval (± 5 cm), provided the porous cup was not exposed to strong evaporative conditions such as direct sunlight or wind. The sharp transient spikes in the data are caused by acceleration effects from moving the transducer while recording a measurement. Tests at water potentials of -300 and -600 cm produced variations of 1-3 cm during tensiometer retrieval to land surface. Thus, a low-cost tensiometer can be used during lulls in drilling activities to obtain reconnaissance type data and aid in designing final well completion.

The portable tensiometer needs to have long term stability to identify trends in water movement patterns in addition to a quick response time and reproducible results. A long

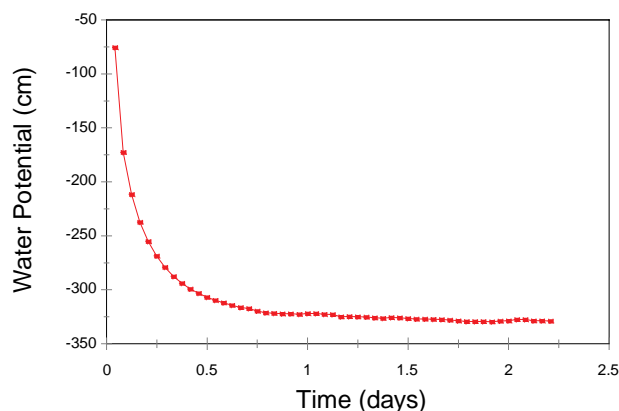


Fig. 5. Borehole tensiometer response time results.

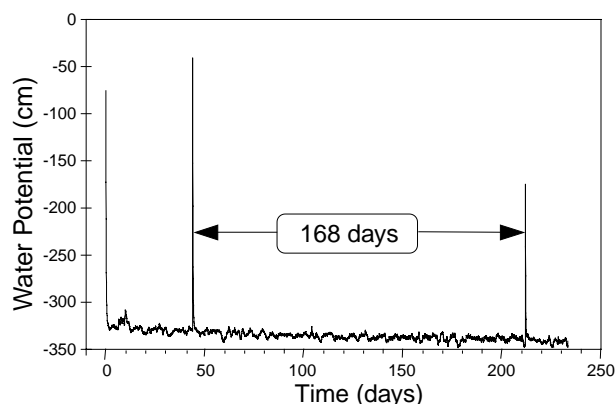


Fig. 6. Borehole tensiometer results during a 233-day test with a 168-day period without purging.

term test was carried out in which a tensiometer equipped with an electronic pressure transducer was placed at the bottom of a 6-m borehole, and the tension values were recorded over a 233-day time period. The results of this test are shown in Figures 5 and 6. Figure 5 shows that due to the limited contact between the porous cup and loam at the bottom of the borehole, approximately 24 hours was required for the tension values to reach equilibrium with the soil water tension. Figure 6 shows the data obtained over the 233-day long-term evaluation test. The sharp rises in soil water potential that occurred on 0, 44, and 212 days into the test correspond to times at which the tensiometer was refilled. Each refilling required between 10 and 20 mL of water. The downward trend in water potential indicated on Figure 6 was fitted with a linear regression line over the 168-day period between refilling, and it indicated that the water potential was declining at a rate of 0.051 ± 0.001 cm/day. Day zero of the long term test was February 21, 1995 and the last date for which data are shown is October 12, 1995. The observed downward trend could be due to either evapotranspiration or deep drainage losses or both. The small fluctuations in water potential about the long-term trend indicate that a noise level of approximately ± 10 cm of water corresponds to barometric fluctuations and temperature effects on the data logger.

Considering the tension values were obtained at a field site with surface temperature

variations between -7 to over 90°F during winter as well as summer, at depths well beyond the range of conventional tensiometers, and the tension values are in the high tension range where conventional tensiometers tend to behave erratically, the results were considered encouraging.

The portable tensiometer can be used for both reconnaissance measurements or for long-term monitoring in wells open at the bottom at depths previously not possible. The portable tensiometer can be used during drilling of boreholes to obtain measurements at specific depths to allow planning for placement of instrumentation. Portable tensiometers can be used as a survey instrument to measure soil water potential at the bottom of boreholes at any depth. The low cost of the portable tensiometer allows many instruments to be placed in multiple boreholes. The portable tensiometer with a pressure transducer/data logger allows continuous measurements for extended times. Soil water potential changes over extended periods of time such as the passing of a wetting front or the formation of perched water can be monitored at depth.

CONCLUSIONS

A retrievable tensiometer for use in reconnaissance surveys of subsurface soil water conditions was evaluated. Operating the tensiometer by lowering it to the bottom of a borehole required a 24-hour response time at

low tensions due to the restricted contact between soil and the porous cup. The response time increased with decreasing soil water potential. The portable tensiometer can be retrieved to land surface from deep boreholes without significantly affecting the pressure in the instrument.

It was found that placing the entire tensiometer at the bottom of the borehole increased the length of time between purging events to remove entrapped gases and reduced the diurnal fluctuations seen in tensiometer values obtained where the pressure transducer was maintained at land surface. Nearly continuous tension values were obtained for a period of 233 days at a depth of 6 m. Thus, tension readings at depths applicable to managing landfills are now attainable. The portable tensiometer can be used to obtain single measurements or collect continuous

measurements over long time periods with little maintenance of the instrument.

ACKNOWLEDGMENTS

Work was supported by the U.S. Department of Energy, Assistant Secretary of Environmental Management, under DOE Idaho Operations Office Contract DE-AC07-94ID13223 at the Idaho National Engineering Laboratory. Thanks to F. J. Wobber, DOE Subsurface Science, Program Manager, Office of Health and Environmental Research. Thanks to Indrek Porro, Debbie McElroy and Swen Magnuson who reviewed this document. Mention of a trademark or a propriety product is for the benefit of the reader and does not constitute an endorsement for the product by the Department of Energy to the exclusion of other products that may also be suitable.

REFERENCES

- Cassel, D.K., A. Bauer. 1976. Irrigation schedules for sugarbeets on medium and coarse textured soils in the Northern Great Plains. *Agron. J.* 70:100-104.
- Cassel, D.K. and A. Klute. 1986. Water Potential: Tensiometry *in* Methods of Soil Analysis, Part One. Physical and Mineralogical Methods. A. Klute. (ed.), Agronomy Monograph #9, second edition, American Society of Agronomy, Inc. Madison, WI. 563-596.
- EPA (U.S. Environmental Protection Agency), 1993, Subsurface Characterization and Monitoring Techniques, A Desk Reference Guide, Volume II: The Vadose Zone, Field Screening and Analytical Methods, Appendices C and D. EPA/625/R-93/003b.
- Everett, L.G., L.G. Wilson, and E.W. Hoylamm. 1984. Vadose Zone Monitoring for Hazardous Waste Sites, Pollution Technology Review No. 112. Noyes Data Corporation. Park Ridge. New Jersey.
- Faybishenko, B.A. 1986. Water-salt regime of soils under irrigation (in Russian). *Agroproizgat*, Moscow.
- Gardner, W., O.W. Israelsen, N.E. Edlesfsen, and D. Klide. 1922. The capillary potential function and its relation to irrigation practices. (Abstract) *Phys. Rev.* 20:196.
- Hagan, R.M., H.R. Haise, and T.W. Edminster. 1967. Irrigation of Agricultural Lands. *Agronomy* 11.
- Healy, R.W., C.A. Peters, M.P. DeVries, P.C. Mills and D.L. Moffett. 1983. Study of the unsaturated zone at a low-level radioactive-waste disposal site near Sheffield, Ill., *in* Proceedings, National Water Well Association Conference on Characterization and Monitoring of the Vadose Zone. Los Vegas, NV. 820-831.
- Klute, A. and D.B. Peters. 1962. A recording tensiometer with a short response time. *Soil Soc. Sci. Am. Proc.* 26:87-88.
- Morrison, R.D. 1983. Ground Water Monitoring Technology; Procedures, Equipment and Applications. Timco MFG., Inc., Prairie Du Sac, WI. 2-7.
- Nyhan, J.W. and B.J. Drennon. 1990. Tensiometer data acquisition system for hydrologic studies requiring high temporal resolution, *Soil Sci. Soc. Am. J.*, 54:293-296.
- Richards, L.A. 1931. Capillary conduction of liquids in porous mediums, *Physics*, 1:318-333.
- Sophocleous, M. and C.A. Perry. 1985. Experimental studies in natural groundwater recharge dynamics: Analysis of observed recharge events. *Journal of Hydrology*. 81:297-332.
- Tokunaga, T.K. 1992. The pressure response for the soil water sampler and possibilities for simultaneous soil solution sampling and tensiometry. *Soil Sci.* 154:171-183.
- Tokunaga T.K. and R. Slave. 1994. Gauge sensitivity optimization in air-pocket tensiometry: Implications for deep vadose zone monitoring. *Soil Science*. 168:389-397.
- Trotter, C.M. 1984. Errors in reading tensiometer vacuum with pressure transducers. *Soil Sci.* 138:314-316.
- Watson, K.K., and R.D. Jackson. 1967. Temperature effects in a tensiometer-pressure transducer system. *Soil Sci. Soc. Am. Proc.* 31:156-160.
- Williams, T. 1978. An automatic scanning and recording tensiometer system. *J. Hydrology*. 39:175-183.
- Wilson L.G., L.G. Everett and S.J. Cullen. 1995. Handbook of Vadose Zone Characterization and Monitoring. Lewis Publishers. Ann Arbor.

ENVIRONMENTAL MEASUREMENT-WHILE-DRILLING (EMWD) SYSTEM

FOR REAL-TIME SCREENING OF CONTAMINANTS

Cecelia V. Williams, Sandia National Laboratories

Information on environmental conditions and drill bit location and temperature during drilling is required in many environmental restoration operations. An inexpensive data collection system for identifying and tracking contaminant concentrations and monitoring drill bit conditions is needed for many waste site operations.

The Environmental Measurement-While-Drilling (EMWD) system represents an innovative blending of new and existing technology to obtain real-time data during drilling. The objective of this project was to distinguish contaminated from non-contaminated areas in real time while drilling at hazardous waste sites.

Preliminary field tests of the EMWD system were successfully completed at the radioactive calibration facility in Grants, New Mexico, at Sandia National Laboratory (SNL), and at the Charles Machine Works, Inc. (CMW) directional boring test site. The EMWD Gamma Ray Spectrometer (EMWD-GRS) system was field demonstrated at Westinghouse Savannah River Site F-Area Retention Basin in April 1996. The "Hot Site" demonstration continuously monitored for gamma activity in real time while drilling two boreholes. The purpose of the demonstration was to evaluate the radionuclide concentration data collected in real-time while drilling using the GRS-EMWD tool against the radionuclide concentration data obtained from the off-site soil samples. Two boreholes were drilled through the F-Area Retention Basin to intersect previous soil sample locations and adjacent to another soil sample

location. We detected and quantified gamma radiation emitting contamination at the sites previously known. In addition we identified two new gamma radiation “hot spots.” Contaminant levels of Cs-137 recorded by EMWD-GRS during drilling (Figure 1) agree with contaminant levels previously determined through quantitative laboratory analysis of soil samples. In addition, previously unidentified gamma radiation “hot spots” were identified. The pull back of the drill rod was extremely successful in that no radiation-contaminated equipment or waste was produced.

The EMWD-GRS with orientation sensor package was tested in a cold site demonstration. No problems were encountered recording the orientation sensor data along with the gamma spectrometer data. Sandia, Lockheed Martin Hanford Corporation/Tank Waste Remediation System, and A & L Underground have successfully demonstrated horizontal directional drilling and the EMWD tool at Hanford. The demonstration at Hanford included drilling one directional borehole at the Tank Leak Simulation Site in the 200 East Area, Hanford, WA, and one directional borehole at the drilling test facility.

The borehole drilled at the Tank Leak Simulation Site was approximately 250 ft and was developed under a tank that was 50 ft in diameter and set approximately 5 ft into the ground. The purpose of this test was to demonstrate directional drilling and the tracking capability of the EMWD system while under a tank. The borehole was drilled using a rotary jet at an angle of 12.5 degrees, and reached a depth of about 25 ft. The bore was continued horizontally at this depth for approximately 100 ft. Therefore, the drill bit was well past the far perimeter of the mock tank. The EMWD tracking system and the Tensor survey conducted by A & L Underground indicated depths of 26.5 ft and 24.9 ft. (Figure 2). The SNL EMWD tracking system agreed with the Tensor tracking system’s indicated depths to within ± 2 ft (Table 1). A & L Underground also used a TruTracker system that indicated a depth of 23.8 ft. The drill bit position was known within a

sphere having a radius of ± 5 ft and a known direction relative to the prescribed baseline at all times. The EMWD-GRS was also operational, and background gamma was recorded.

The second borehole was drilled at the drilling test facility using a mud motor to penetrate approximately 20 vertical ft of boulders/cobbles and the remainder of the hole was drilled with a rotary jet. The purpose of this test was to demonstrate the capability of drilling to a depth of about 70, the depth required to go under a Hanford tank. The borehole was drilled at an angle of 16 degrees until it reached an approximate depth of 70 ft, after which it was drilled horizontally for roughly 60 ft. Again, the SNL and A & L tracking systems agreed on bit location. We deviated from the drill plan and went outside the sphere having a radius of ± 5 ft. Rather than to pull back and kick out of the current hole, it was decided to redirect to stay within the sphere. This decision was made due to the lack of time and funding. We attempted to take a sample from this borehole using a small sampler, but were unsuccessful. The sampler was not designed to be used in the cobble/boulder environment at Hanford. We feel that the use of a coring tool would probably be successful. The EMWD-GRS was also operational, and background gamma was recorded.

The EMWD system has many applications, including site characterization for contaminant detection and delineation. Therefore, the system can also guide sampling activities and borehole emplacement options (for example, a drill operator can back out of contaminated soils and redirect a drilling operation around the contamination). Other potential users of EMWD include utility emplacement and petroleum industries.

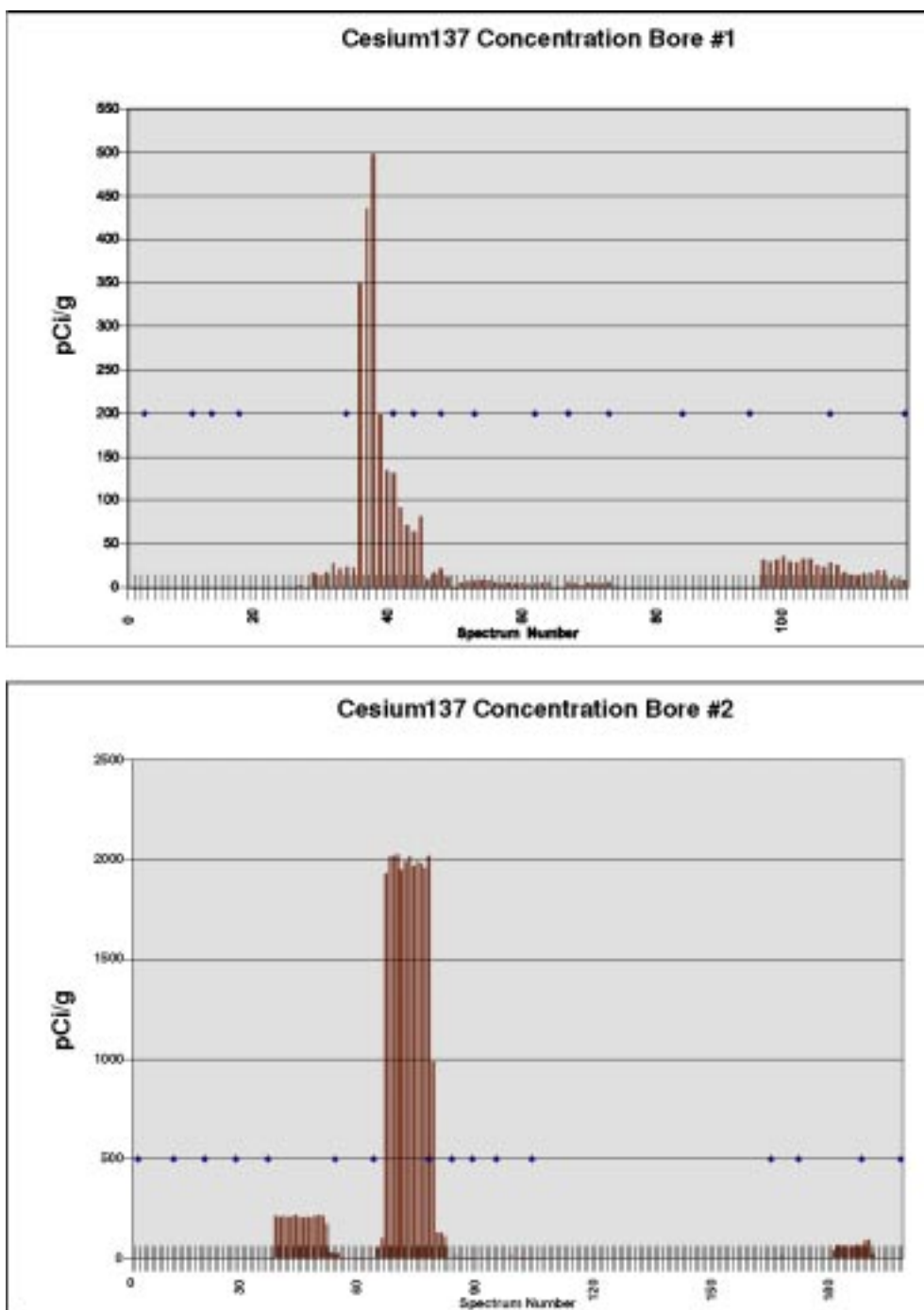


Figure 1. EMWD Gamma spectrometry data from Westinghouse Savannah River Site F-Area Retention Basin demonstration. Note that blue diamonds indicate the end of a drill rod

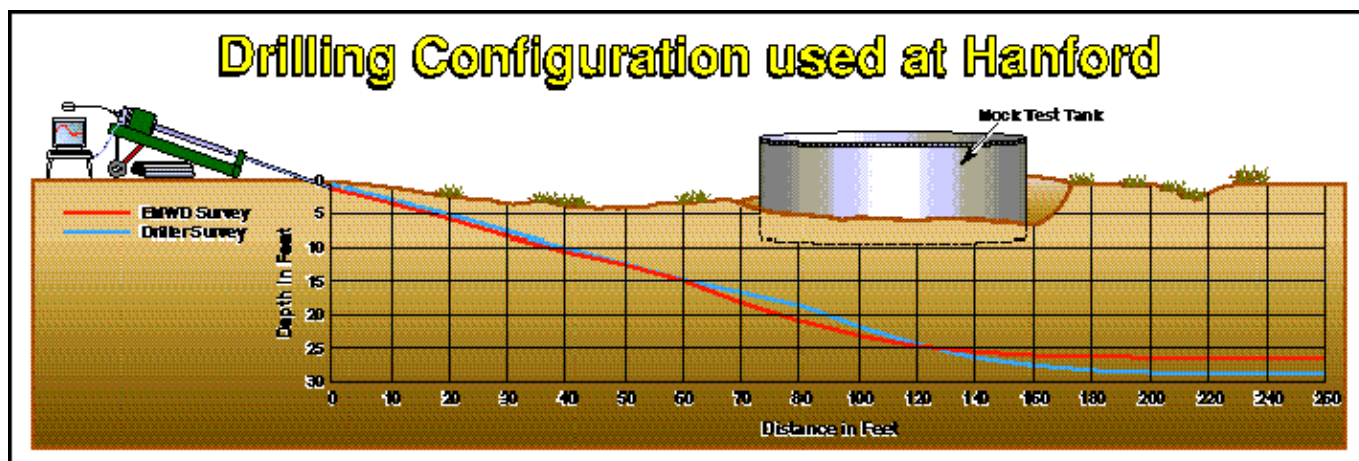


Figure 2. Comparison of depth data from the EMWD tool and drillers survey.

TABLE 1. Comparison of depth data from the EMWD tool and drillers survey.

Drill Path Distance (ft)	DEPTH (ft)		
	EMWD Survey	Driller Survey	Absolute Difference
0	-1.0		
10	-3.1		
20	-5.3	-4.7	0.6
30	-7.7		
40	-9.8	-9.3	0.6
50	-11.6		
60	-13.8	-13.7	0.1
70	-16.9		
80	-19.5	-17.3	2.2
100	-21.6	-20.3	1.3
120	-23.1	-22.8	0.3
140	-23.9	-24.7	0.8
160	-24.4	-25.8	1.4
180	-24.6	-26.5	1.9
200	-24.7	-26.8	2.1
220	-24.9	-26.8	1.9
240	-24.9	-26.9	2.0
260	-24.9	-26.9	2.0

CONCLUSION

There are time, cost, and safety advantages to using the field screening approach of the EMWD system:

(1) data on the nature of contamination will be available in minutes, as opposed to weeks or months from an off-site laboratory; (2) field screening while drilling can reduce the number of costly drilling operations; (3) substantial cost savings will result by minimizing the number of samples required for off-site confirmatory analyses; (4) worker safety will be enhanced as a result of minimizing waste generation and by quickly alerting field personnel to potentially hazardous conditions; and (5) contamination can be mapped with no site disturbance.

This project has developed a prototype system that costs less than \$20,000, not including research and development cost. Operations and maintenance costs are likely to be low, while recurring costs will be limited to the replacement of an inexpensive spool of coaxial wire for each drilling operation.

Sandia is a multiprogram laboratory operated by Sandia Corporation, a Lockheed Martin Company, for the United States Department of Energy under contract DE-AC04-94AL85000.

SMALL SCALE FIELD TESTS OF WATER FLOW IN A FRACTURED ROCK VADOSE ZONE

Thomas R. Wood¹, Robert K. Podgorney¹ and
Boris Faybishenko²

¹Geosciences Department
Idaho National Engineering and Environmental Laboratory
Idaho Falls, ID

²Earth Sciences Division
Lawrence Berkeley National Laboratory
Berkeley, CA

1.1 INTRODUCTION

1.1.1 Significance and Practical Application

Significant efforts have been devoted to the development of alternative models for water flow and chemical transport in heterogeneous media using simple approximations, for example, a transfer function approach (Chesnut, 1994; Jury and Roth, 1990) and percolation theory (Sahimi, 1993). Basic laws governing flow and transport were initially developed from theoretical studies (Witherspoon et al., 1980). However, for most fractured rocks, and particularly for a complex system of fractured basalt, the results of field and laboratory investigations are more important than simple approximations. Few field experiments have been carried out in fractured rock vadose zones. Often for these complex systems, simplified conceptual models are assumed for estimating water flow and chemical transport (National Research Council, 1996). Our work at the Hell's Half Acre research site suggests that at the meter scale alternative models for water flow should be employed. Furthermore, the importance of the placement and type of monitoring devices has a significant influence on the development of a site conceptual model.

The objective of the field investigations at the Hell's Half Acre research site was to collect data for assessing the physics of flow in fractures and determine if the movement of water through fractured basalt exhibits chaotic behavior. There were two types of measurements selected to characterize the physics of flow; 1) recording of temporal and spatial evolution of drip events and flow at the exit from fractures, and 2) measuring water pressure in the rock matrix and fracture using tensiometers at different depths and distances along the flow path.

1.1.2 Background

Understanding the physics of flow and transport in fractured rock vadose zones is critical for long-term operation of waste sites and for predicting the migration of organic, inorganic and radioactive contaminants. Several Department of Energy (DOE) waste disposal sites that are situated in geologic provinces with fractured rock, including the Idaho National Engineering and Environmental Laboratory (INEEL) and Nevada Test Site, have discovered low levels of plutonium and other contaminants in ground water. These low level "hits" were not expected or predicted using conventional flow and transport theory for contaminant migration through the vadose zone. For the past several years, the INEEL and Lawrence Berkley National Laboratory (LBNL) have gained important experience from joint investigations of flow and transport through the fractured basalt vadose zone at Hell's Half Acre and Box Canyon Sites in Idaho (Long et al., 1995; Faybishenko, et al. 1998; Podgorney et al., 1998, 1999).

Our investigations were conducted in fractured basalt of the Eastern Snake River Plain of southeastern Idaho near the INEEL. Contaminants of concern, such as VOCs (TCE, Carbon

Tetrachloride, etc.) and radionuclides (Cs, Sr, U, Pu, etc.), were buried in soils overlying the basalt vadose zone or were injected directly into basalt using wells or pits. The prevailing thought at the time of burial was that contaminants would not migrate downward through the thick vadose zone to the underlying Snake River Plain aquifer. However, contaminants have been found in perched water zones, interbed sediments, and the aquifer. Currently, several INEEL sites are being remediated and instrumented for long-term monitoring. It has become apparent that monitoring technologies and site characterization methods, developed for porous media, are not sufficient for predicting water flow and transport in fractured basalt vadose zones.

1.2 GEOLOGIC SETTING

1.2.1 Geology of the Snake River Plain

The Snake River Plain is primarily composed of fractured Quaternary basalts, inter-layered with sedimentary deposits (Knutson et al., 1993). Multiple basalt flows (Figure 1) within a flow unit were formed by closely related eruption. Individual basalt flows are typically highly fractured, with a thickness that range from less than 1 m to more than 30 m, and an areal extent of up to several thousand square meters. Fracturing was caused by thermal contraction as the flow cooled and formed polygonal, often hexagonal, columns (Korvin, 1992). The upper portion of the flow is usually densely fractured, even rubblelized, due to exposure to the atmosphere that produced an increased cooling rate. The lower half of the flow contains fewer fractures because of a slower cooling rate. Therefore, fracture density decreases toward the center of the flow. When the basalt columns were exposed to weathering over geologic time, their upper surfaces weathered to

breccia and were often covered with sediments, which now separates flow units (Welhan and Reed, 1997). Sedimentary interbeds may have a significant lateral extent (often exceeding that of the individual basalt flows) and their thickness range from a few centimeters to as much as 15 m. Geophysical logging suggests that the total thickness of the basalt in the Snake River Plain may exceed three kilometers. In the region near INEEL, the depth to the water table of the regional aquifer ranges from 60 to 200 m.

1.2.2 The Research Site Used for this Study

The research site we discuss in this paper is located within the Hells Half Acre (HHA) Lava Field in southeastern Idaho. The HHA site is designed to evaluate flow at the meter scale. The site consists of an overhanging basalt block on the edge of a collapsed lava tube. The basalt at the site is moderately vesicular to dense with a single fracture exposed on the surface of the block. The fracture bifurcates in the lower part of the block, resulting in two fracture traces on the underside. A horizontal fracture, which intersects the vertical fracture, is exposed on the face of the block, approximately 25-cm from the underside. The physical layout of the site allowed access to the top, front, and underside faces of the basalt block, thus allowing for detailed instrumentation and data collection of both infiltration and outflow rates from the fracture. The access to the underside also allowed for collection of time intervals between drips falling from discrete locations along the fracture, which were then used for a chaotic data analysis.

1.3 TEST DESIGN AND METHODS

1.3.1 Field Design

The Hell's Half Acre research site was instrumented to collect extensive data sets to describe both the temporal and spatial variations of the following parameters: water head in the infiltration pond, water and rock temperature, tensiometric pressure, barometric pressure, infiltration rates, outflow rates as water drip intervals and discharge on the underside of the outcrop. A 40 by 80-cm infiltration pond was built on the upper surface of the basalt block, surrounding the surface expression of the fracture (Figure 2). The design of this test allowed us to investigate the flow processes for elemental and small-scale components. The water dripping rates, or time intervals between drip events, can be used to characterize the flow from individual points of a flow path (elemental components). The area below the fracture is covered with a grid of 20 by 30-cm pans, which are used to collect the water drops from the fracture. Each pan collected one or more drops, combining several elemental components or drip locations, thus, averaging the outflow rate from the area above it. The water is routed from the pans to bottles attached to load cells to measure the outflow. The outflow rate determined from the pans integrates flow from several drip points, providing a measure of flow at a small-scale.

During infiltration experiments, the upper boundary condition was a constant water level in the surface pond. The infiltration tests were run for 1 to 18 days. The drainage periods between infiltration tests were up to several weeks to allow for sufficient drying of the fracture and rock matrix. Successive tests started when the water pressure in the rock was approximately -100 mBars. We can assume that under this pressure the fractures were empty, and the matrix was partially desaturated.

1.3.2 Innovations

Instrument development efforts for the project required designing several measurement and sensor systems, including:

- Sensors to time-stamp individual drip events
- Measurement system of water flowing from various points of the fracture
- Surveying system to map the fracturing and topography of the underside of the outcrop

Design and testing of the drip sensing and collection measurement systems took place prior to and during the early part of the field testing. Final refinements took place after field trials. The surveying system evolved over the course of the field activities and was completed near the end of the field season. The patent process is ongoing for the drip sensing system and the surveying system.

1.4 RESULTS AND DISCUSSION

1.4.1 Test Results and Conceptual Model of Flow on a Small Scale

In order to provide a general understanding of the flow processes, we begin with the analysis of data obtained using the infiltration and volumetric outflow rates. Typical plots of the time

variations in the volumetric infiltration rate and outflow rates at five locations along the fracture on the underside of the outcrop are shown in Figures 3a and 3b. We subdivided the time of the experiment into two periods as shown in these figures.

Period 1. Immediately following the beginning of flooding, the infiltration rate increases due to the quick saturation of fractures and initially high water imbibition into the dry basalt. As water imbibes into the porous matrix, air is presumably pushed out into the surrounding fractures. In fractures, air becomes entrapped in the low aperture zones, thus blocking some flow pathways. This leads to the overall decrease in the hydraulic conductivity of rocks and, consequently, to the decrease in both the infiltration and outflow rates to minimum values at the time from 50 to 100 hours (Figure 3a, b.) Figure 3b shows that the outflow rates become nearly the same at all observation locations. At this time, the water pressure measured at the same depth in both the fracture and matrix is practically the same (Figure 3c, tensiometers 2, 4, and 5), which indicates no flow between the fracture and matrix. Note that tensiometer 9, which is located outside the footprint of the infiltration gallery, also showed the decrease in the water pressure.

Subsequently, the flow rate increases, presumably as entrapped air dissolves into moving water and is removed in both free and dissolved phases. An identical flow behavior was observed in soils in the presence of entrapped air (Faybishenko, 1995). Comparison of Figures 3a and 3b shows that during Period 1 the trend and magnitude of the volumetric outflow rates are different from those of the infiltration rate. The simultaneous increase in the flow rates and tensiometric pressure (Figure 3c) supports the hypothesis of increasing rock saturation. The flow rates increased until the saturation reached a critical value, and most likely some flow paths were

opened, at which time the flow rate increased drastically. This is shown in Figure 3a as a boundary between Periods 1 and 2.

Period 2. During Period 2, the pattern of the infiltration rate is similar to that of the volumetric outflow rates for locations 2, 3, and 5. This indicates a direct hydraulic connection between the surface pond and these locations. The trend of the outflow rates for locations 8 and 12 is different because they are situated outside of the footprint of the pond. The magnitude of the increase in the flow rate at different locations along the fracture is quite varied and is accompanied by significant high frequency flow rate fluctuations.

In general, it can be seen that small variations in the minimum values of the flow rate (between the time from 50 to 100 hours during Period 1) may lead to a wide range of flow rates thereafter. This shows that flow is quite unstable in time and space. The cumulative outflow through fractures was about 60 % of the total inflow, indicating that the remainder was presumably imbibed into the matrix, trapped in dead-end fractures, or lost to evaporation.

Figure 3c shows that despite an increase in flow during Period 2, the general increasing trend of tensiometric pressure decreased slightly compared to the trend in Period 1. This indicates that the matrix continued to imbibe water with time and did not reach total saturation even after eighteen days of flooding. It is important to note that tensiometers are not able to reflect rapid high frequency fluctuations, which were observed for inflow and outflow rates. Under field conditions tensiometers may not detect a positive water pressure, which is likely to develop in fractures under ponded conditions. This occurs because the porous tip of the tensiometer averages the

pressure over the volume of the tensiometer (Finsterle and Faybishenko, 1997), which includes both fracture and the adjacent unsaturated rock matrix. In summary, the tensiometry (Figure 3c), combined with the inflow and outflow data (Figures 3a and 3b), show: (1) two periods of heavy flow through the fracture, (2) continuous imbibition of water into the rock matrix independent of flow through the fracture, and (3) flow through the system never achieved steady state during the period of the test.

1.4.2 Elemental Scale Evaluation

An analysis of the results of water dripping from Drip Point 6 is shown in Figure 4. A random-looking time variation of water drip intervals is shown in Figure 4a. The analysis of these data showed that the optimum time delay $\tau = 3$, and the dimension needed to unfold the attractor is 5. Figure 4b shows a two-dimensional attractor that has a definite structure. The spread of the points on the attractor reveals the presence of a combination of both chaotic and random components for the frequency of water dripping from a fracture.

The small-scale investigations discussed here involve a volume of rock within a single basalt flow with one or a few fractures over an areal extent of approximately $0.5\text{-}1\text{ m}^2$. Figure 5 illustrates a conceptual model of water flow through a block of fractured basalt that occurs as dripping phenomena from many locations along the fracture. These locations are stable with time, however, flow from each point varies overtime. The intervals of water dripping from a single location can be described using a chaotic model with a random component. At the same time, the volumetric outflow rates combined from several dripping locations exhibit spatial and

temporal instability with primary low frequency fluctuations and secondary high frequency fluctuations. The fracture-matrix water interaction and entrapped air (Persoff and Pruess, 1995) are presumably the main factors affecting the spatial and temporal flow instability, which were also identified in several of these studies (Glass et al., 1991; Lenormand and Zarcone, 1989; Nicholl et al., 1993, 1994).

Our analysis of data from other, larger scale sites and HHA suggests that small variation in initial conditions and properties of the fracture network, particularly, fracture intersections, lead to significant divergence of flow paths within the basalt flow. In other words, two nearby particle trajectories that are initiated from slightly different initial locations may not stay close to each other with time. They may diverge and follow entirely different paths, which directly leads to limitations in predictability of flow behavior. We plan to perform tracer tests during the FY-99 field season to further explore transport phenomena at the small scale. The HHA site will allow for direct measurement of the flow path variability.

1.5 CONCLUSIONS

An important feature of flow in the basalt vadose zone is that the hydraulic system includes both unsaturated and saturated rocks. During flooding at the surface, the saturated zones have a limited and local extent within flow channels in the fractures and vesicular zones. Single probes, which cross the saturated fractures, also intersect the matrix, and, therefore, the probes measure an averaged water pressure in the fracture-matrix system. However, it is difficult to separate the contribution of the fracture from that of the matrix (Finsterle and Faybishenko, 1997). Using

available monitoring techniques under field conditions, we cannot perfect our knowledge of initial conditions; we can only measure approximate values of different parameters (pressure, moisture content, temperature, and concentrations) or determine the ranges of these parameters.

Fluid flow in fractured basalt of the vadose zone can be considered a nonlinear dynamic process, in which the behavior, both temporally and spatially, may be chaotic (Sposito and Weeks, 1997). The chaotic nature of the flow is due to the nonlinear flow processes and because there are strong spatial and temporal variations in moisture content, hydraulic conductivity, and fracture connectedness. As a result, in fractured basalt, which is a nonlinear system, small variations in flow parameters or boundary conditions may lead to significant variations in predicted results. The chaotic nature of the system implies that its phase-space volume changes with time, leading to the formation of strange attractors characterizing the range in which the flow parameters are expected to change. The dynamics of such systems are sensitive to the initial conditions. The response of such systems may include a stochastic component that it is not necessarily a dominant factor on the system behavior. If the stochastic component is not dominant, then a stochastic analysis will not provide useful information.

We find that under field conditions with a limited number of single-probe measurements, one can detect neither the spatial nor temporal chaotic variations of the flow parameters, and therefore, one must use conventional (i.e. non-chaotic) stochastic or deterministic methods to describe flow and transport processes. However, this approach is not always appropriate. For instance, if the stochastic component is not a dominant factor, then a stochastic analysis will provide incorrect answers, and should be replaced by a chaotic analysis. If the stochastic

component is significant (or if the phase-space dimension is so large that the dynamics look stochastic), then a stochastic analysis is the most appropriate tool to use. At this point in time we do not possess the ability to determine the proper analysis using data collected by standard methods. In conclusion, where elemental and small-scale components are involved, the flow data can be analyzed using methods of nonlinear dynamics. Where intermediate and large-scale components are involved, a combination of deterministic and stochastic methods of flow analysis can be used.

1.6 REFERENCES

- Chesnut, D.A. (1994), *Dispersivity in heterogeneous permeable media*, Fifth Annual International High-Level Radioactive Waste Management Conference, May, Las Vegas, NV, American Nuclear Society, La Grange Park, IL, 4, 1822-1841.
- Faybishenko, B.A., C. Doughty, M. Steiger, J.C.S. Long, T. Wood, J. Jacobsen, J. Lore, and P. Zawislanski (1998), Conceptual Model of the Geometry and Physics of Water Flow in a Fractured Basalt Vadose Zone: Box Canyon Site, Idaho, in review *Water Resources Research*.
- Faybishenko, B.A. (1995), Hydraulic behavior of quasi-saturated soils in the presence of entrapped air: laboratory experiments, *Water Resources Research*, 31(10), 2421-2435.
- Finsterle, S., and B. Faybishenko (1997), *What does a tensiometer measure in fractured rock?* in Characterization and Measurement of the Hydraulics Properties of Unsaturated Media, International Symposium, 22-24 October, Riverside, California.
- Glass, R.J., T.S. Steenhuis, and J.Y. Parlange (1991), Immiscible displacement in porous media: Stability analysis of three-dimensional, axisymmetric disturbances with application to gravity-driven wetting front instability, *Water Resources Research*, 27(8), 1947-1956.
- Jury, W.A. and K. Roth (1990), *Transfer Functions and Solute Movement through Soil: Theory and Applications*, Birkhäuser Verlag, Basel, Switzerland.
- Korvin G. (1992), *Fractal Models in the Earth Sciences*, Elsevier, Amsterdam
- Knutson, C.F., D.O. Cox, K.J. Dooley, and J.B. Sisson (1993), *Characterization of low-permeability media using outcrop measurements*, in 68th Annual Technical Conference

- and Exhibition of the Society of Petroleum Engineers, October 3-6, 1993, Houston, TX, *SPE Paper 26487*.
- Lenormand, R. and C. Zarcone (1989), Capillary fingering: percolation and fractal dimension, *Transport in Porous Media*, 4, 599-612.
- Long, J.C.S., C. Doughty, B. Faybishenko, A. Aydin, B. Freifeld, K. Grossenbacher, P. Holland, J. Horsman, J. Jacobsen, T. Johnson, K. -H. Lee, J. Lore, K. Nihei, J. Peterson, Jr., R. Salve, J. Sisson, B. Thapa, D. Vasco, K. Williams, T. Wood, and P. Zawislanski (1995), *Analog site for fractured rock characterization, annual report FY 1995*, Lawrence Berkeley National Laboratory Report LBNL-38095.
- National Research Council (1996), *Rock Fractures and Fluid Flow*, National Academy Press, Washington, DC.
- Nicholl, M.J., R.J. Glass, and H.A. Nguyen (1993), *Wetting front instability in an initially wet unsaturated fracture*, Fourth High Level Radioactive Waste Management International Conference, Las Vegas, Nevada.
- Nicholl, M.J., R.J. Glass, and S.W. Wheatcraft (1994), Gravity-driven infiltration instability in initially dry nonhorizontal fractures, *Water Resources Research*, 30(9), 2533-2546.
- Persoff, P. and K. Pruess (1995), Two-Phase Flow Visualization and Relative Permeability Measurement in Natural Rough-Walled Rock Fractures, *Water Resour. Res.*, 31(5), 1175-1186.
- Podgorney, R., T.R. Wood, and T. M. Stoops (1997), *Outcrop infiltration experiments, Data Summary Report—1997 Field Season*, Idaho National Engineering and Environmental Laboratory Internal Report.
- Podgorney, R. K. and T.R. Wood (1999), *Observations of water movement in variably saturated fractured basalt and possible implications on advective contaminant transport*, Dynamics of Fluids in Fractured Rocks: Concepts and Recent Advances, 10-12 February, Berkeley, California.
- Sahimi, M. (1993), Flow, dispersion, and displacement processes in porous media and fractured rocks: From continuum models to fractals, percolation, cellular automata and simulated annealing, *Reviews of Modern Physics*, 65(4), 1393-1534.
- Sposito, G., and S.W. Weeks (1997), *Dynamical systems theory and fluid flow in subsurface zones*, 1997 Fall AGU Meeting, San Francisco, California.
- Welhan, J.A., and M.F. Reed (1997), Geostatistical analysis of regional hydraulic conductivity variations in the Snake River Plain aquifer, eastern Idaho, *GSA Bulletin*, 109(7), 855-868.
- Witherspoon, P.A., J.S.W. Wang, K. Iwai, and J.E. Gale (1980), Validity of cubic law for fluid flow in a deformable rock fracture, *Water Resour. Res.*, 16(6), 10106-1024.

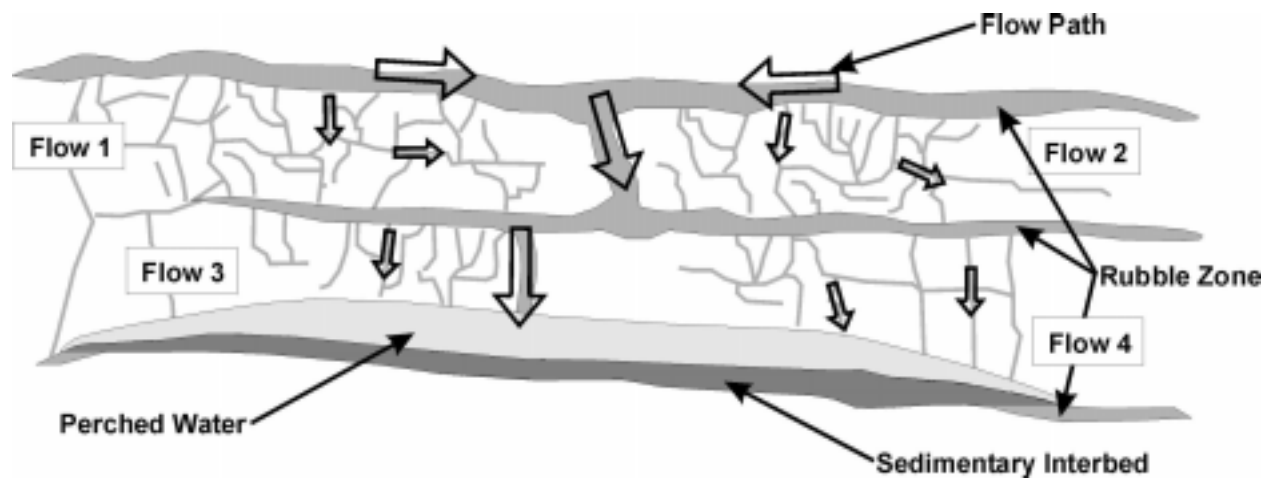


Figure 1. Schematic illustration of water flow and contaminant transport in fractured basalt, including flow through rubble zones between basalt flows and through an intra-basalt flow fracture pattern. Note that perched water zones are formed above the sedimentary layer. Figure modified after Faybishenko et al. (1999).

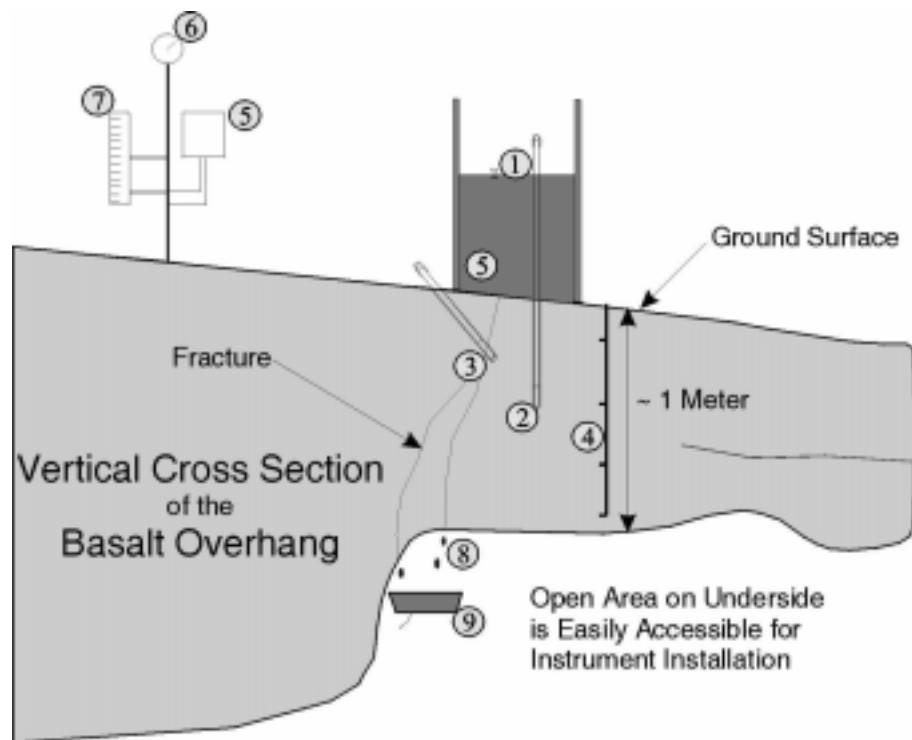


Figure 2. Design of a small-scale infiltration test at the Hell's Acre site in Idaho and the types of measurements conducted: 1-Water level and infiltration rate in the water gallery, 2-Basalt-matrix water pressure using tensiometers, 3-Fracture-matrix water pressure using tensiometers, 4-Temperature of rocks, 5-Ambient air and water temperature, 6-Barometric pressure, 7-Precipitation, 8-Outflow drip intervals, and 9-Outflow volumetric flow rate in 20x30 cm pans.

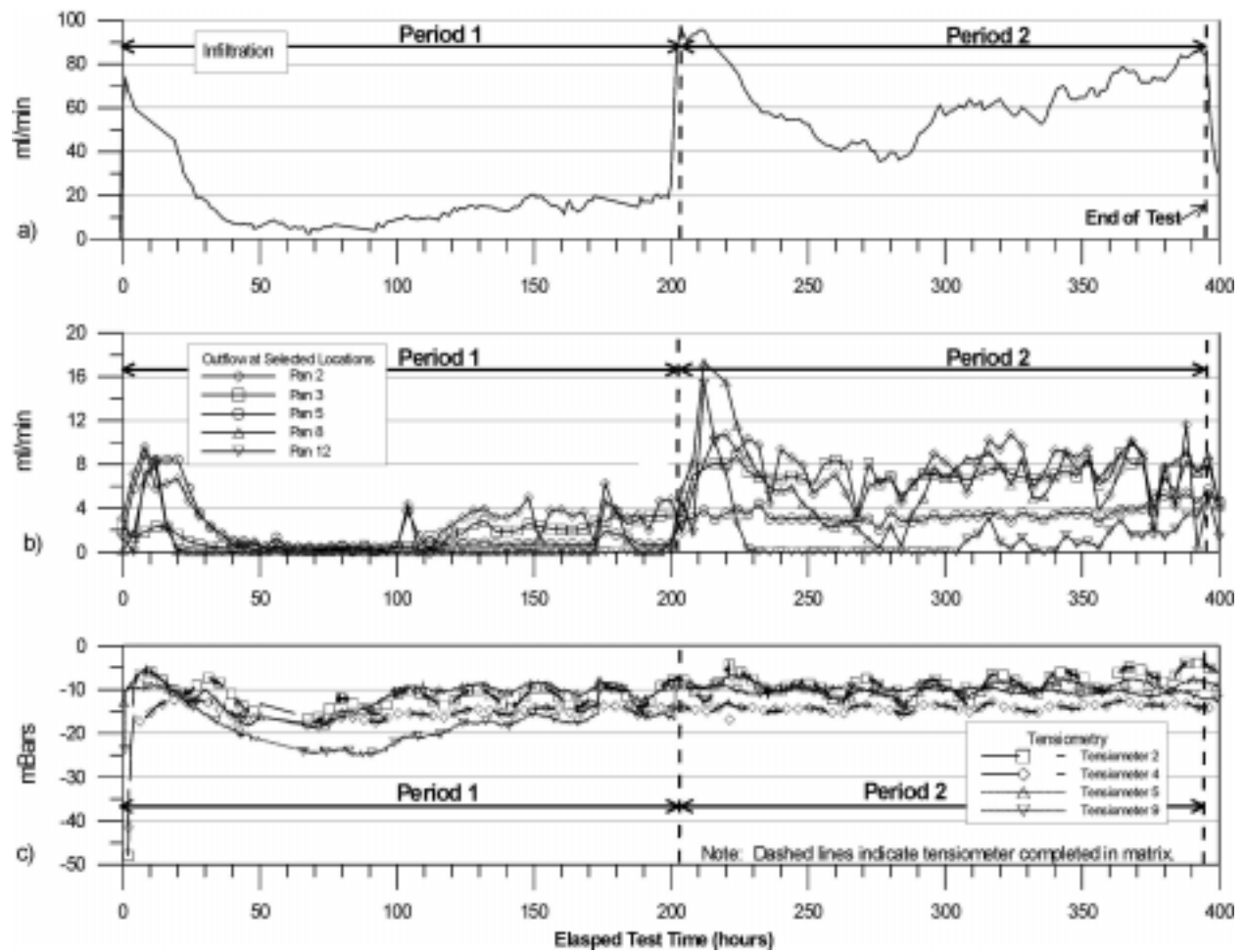


Figure 3. Results of a small-scale infiltration test: (a) Infiltration rate, (b) Outflow rates in several pans, and (c) Tensiometric pressure.

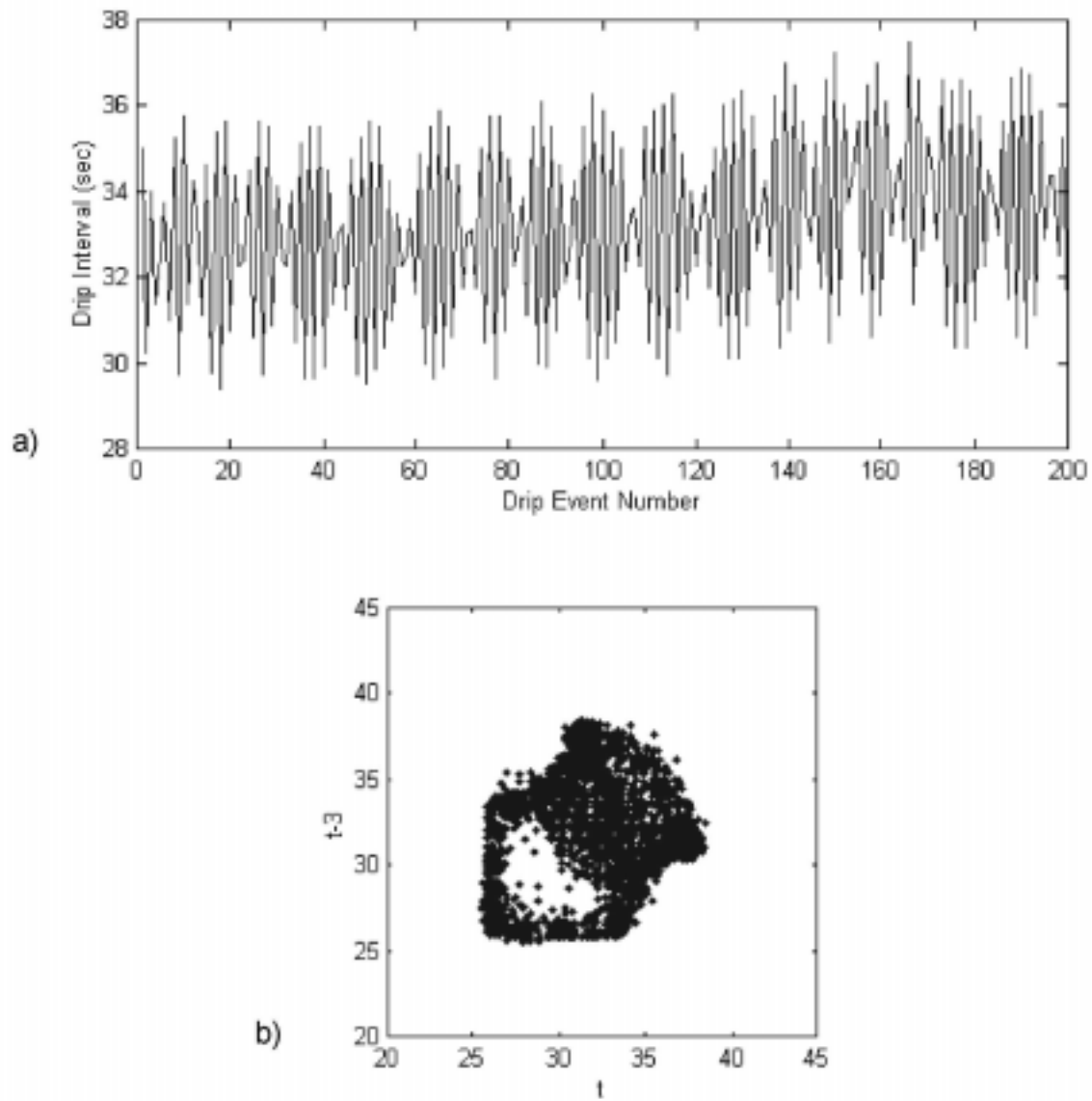


Figure 4. Variations of time-intervals of water dripping: (a) time-series data (only first 200 points are shown), (b) a 2D attractor using $\tau=3$, which was plotted using 2,000 points.

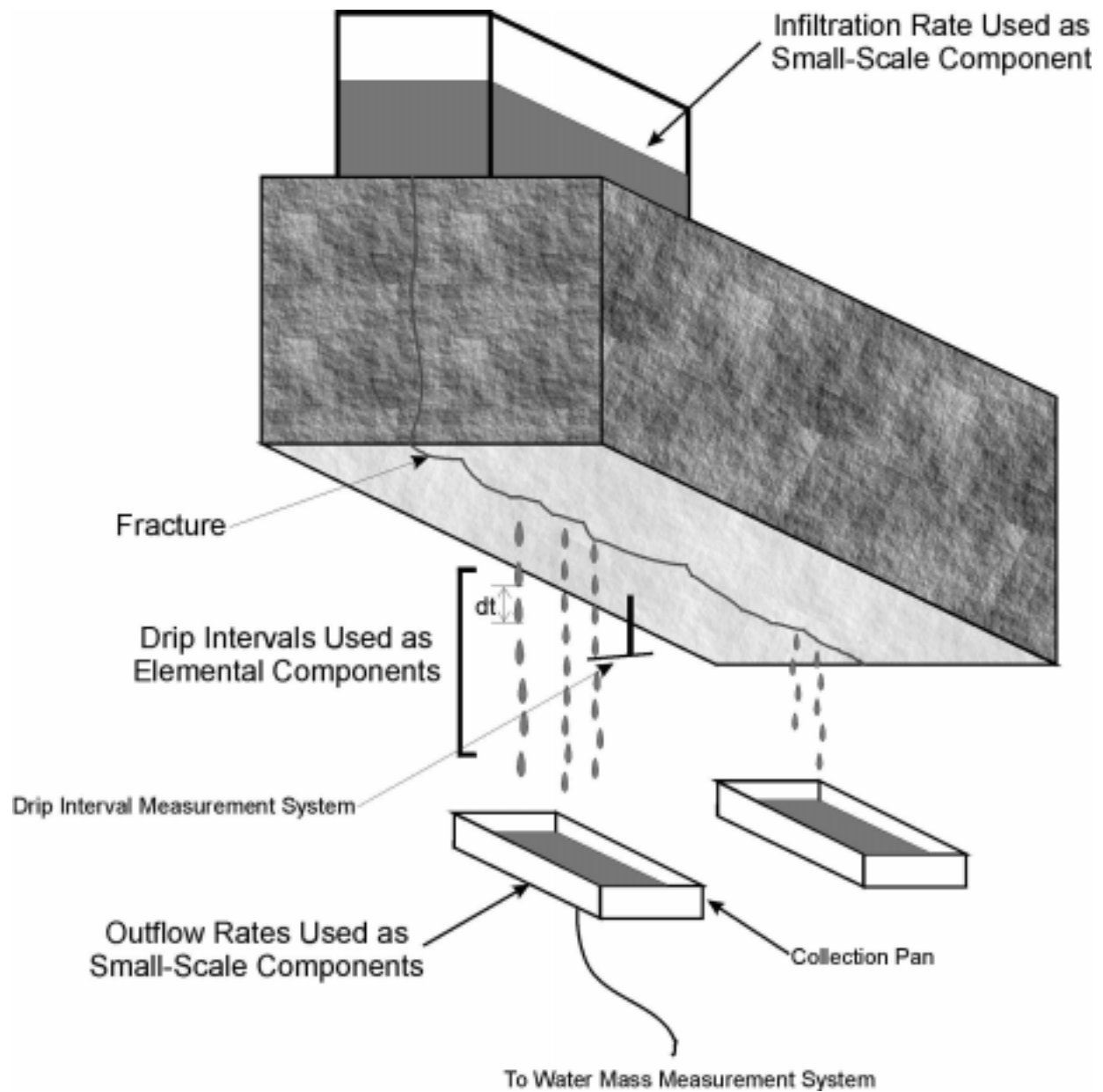


Figure 5. A conceptual model of a field infiltration test showing water dripping, which can be considered as an elemental component, and a collection of water into pans that can be considered as a small-scale component.

Electromagnetic Radiography

Dr. Aka G. Finci, Mission Research Corporation

Liquid contaminants trapped in the pore spaces of the soil in the vadose zone can be directly imaged with Electromagnetic Radiography (EMR)(tm) 1. This new technology is an outgrowth of numerous field observations made with customized, high-performance ground-penetrating radar equipment. Much like minerals that fluoresce in various colors when irradiated with ultraviolet light, it has been discovered that brief impulses of electromagnetic radiation can induce specific responses from chemicals in the ground. These responses result from the excitation of discrete energy bands at the molecular level. The chemical signatures, which are in the megahertz (MHz) region of the radio frequency (RF) spectrum, are different for each chemical. Research is going forward on the radio frequency characterization, or "fingerprinting," of chlorinated solvents and other common contaminants to permit future in-situ identification of these chemicals.

The detection threshold of EMR(tm) equipment is currently in the parts-per-billion ($\mu\text{g/kg}$) range. Direct images showing the lateral and vertical extent of low-level liquid-phase contaminants in the vadose zone not only show the presence of these contaminants, but also reveal stratification, concentration gradients, vertical phase fronts, retardation and other "structural" aspects of the contamination. Dense, non-aqueous phase liquids (DNAPLs) can be distinguished from light, non-aqueous phase liquids (LNAPLs), and the dissolved phase can be distinguished from the liquid phase. The technology is still in the early stages of development, but it is sufficiently mature to be routinely used for field survey work to locate and map contamination in the vadose zone as well as locating and mapping dissolved phase contaminants in the water table.

At present, it is necessary to rely on conventional borings and soil samples for identification of the contaminant(s) observed with EMR(tm). Although EMR(tm) technology has not yet progressed to the point where it can quantitatively measure concentration levels, it is currently possible to provide rough, order-of-magnitude estimates of the concentration levels. EMR(tm) can also pinpoint the optimum locations for obtaining representative soil samples to provide quantitative measurements of contamination levels. The EMR(tm) equipment functions much like ground-penetrating radar, the principal difference being the electronic signal processing that is used to detect the molecular responses of the chemical contaminants.

Starting in 1979 with the Picillo Property, "Pig Farm" in Coventry, Rhode Island, a Superfund site that held some 18,000 buried drums of chemicals, we have performed hundreds of hazardous waste surveys using both GPR and its successor, **Electromagnetic Radiography (EMR)™**. These surveys have entailed thousands of man-hours of hands-on field experience as well as laboratory time spent in processing and interpreting the geophysical data. We believe

that the Picillo Property survey, which was sponsored by U.S. EPA Cincinnati/MITRE Corporation, marked the first time that GPR was ever used on a hazardous waste site.

There have been many “landmark” surveys where we achieved some sort of landmark result or technical breakthrough. One such survey was performed in 1993 for the US Air Force at Newark AFB, Ohio (O’Brien & Gere Engineers, AF contractor). Here, we were able to detect low level contamination beneath a reinforced concrete floor inside a steel building. (To the best of our knowledge, no other GPR contractor can accomplish this feat). Using a custom designed, high performance GPR system (the predecessor to EMR™) we were able to locate a vertical migration column of CFC 113 (Freon 113) beneath the reinforced concrete floor of a clean room in Building 5. Slant drilling (by O’Brien & Gere) outside the wall of the building showed the concentration level of the column to be **31 ppm**. At the other end of the room, dissolved phase CFC 113 could be seen layered in two distinct strata in the shallow water table beneath the concrete floor. Slant drilling showed the upper stratum to be **2.7 ppm** CFC 113. The lower stratum was **1.3 ppm**. The USAF personnel assigned to this project indicated that they would be communicating these outstanding GPR results to AFCEE.

Another, more recent landmark case was a project in Princeton, Illinois. It was known by the contractor (ERM-North Central) that TCE was on the property, but the distribution was not known. We performed a survey (*DSI, Final Report-GPR Survey, Princeton, Illinois*) with the results shown in **Figure 1**. A few weeks before the Princeton survey, we teamed with the Remote Sensing Institute of Boston University working for the Ministry of Water Resources in the Sultanate of Oman searching for water in the desert. We were paying particular attention to naturally occurring infiltration zones because their location and presence implies the existence of an underlying aquifer. Infiltration zones have a more “grainy” appearance than the surrounding

soils because of the loss of fine grain material. Because the fines must have gone somewhere (matter doesn't just disappear), there must be a means of transporting the fines away from the infiltration zone. An underlying aquifer can act as a horizontal conveyor belt to transport the fines away from the infiltration zone, leaving the soils less dense and more permeable at this location.

One of the most important discoveries to come out of our work with EMR™ is the ability to locate infiltration zones. When rainwater infiltrates the ground, it does not do so in a uniform manner. There are preferential locations, or infiltration zones, where surface water more easily percolates into the ground. These locations are often topological lows. They are characterized by a loss of fine grain material (fines) and are less dense and more permeable than the surrounding soil. **Figure 2** shows such a zone located in Oman. The loss of fines implies the existence of an underlying aquifer that acts as a horizontal conveyor belt to carry away the fines. Otherwise, the fines would have no place to go, and would “pile up” and decrease, rather than increase, the permeability.

When DNAPLs are held above a confining layer, they are laterally transported in response to the hydrology of the site. When the DNAPL encounters an infiltration zone, the zone acts as a natural “sump,” or collection point, to vertically transport the DNAPL down to the underlying aquifer. The EMR™ technology is uniquely suited to finding these locations, which are often the controlling features on the site. Needless to say, an infiltration column containing DNAPL contaminants is the ideal location to put a recovery well and will also result in the highest yields. Even on an existing site where "pump and treat" methods are being used, there can be a dramatic improvement in yield and recovery simply by placing wells in these infiltration zones.

Figure 2 shows infiltration zones in the desert of Oman. There was also a *graben* at this location, (*DSI, Final Report-GPR Survey, Sultanate of Oman*). The "tick marks" along the top of the chart are increments of 5 feet of travel.

After many years of observing and reporting the locations of “sinkers” (vertical migration columns of DNAPLs), we made the important connection: *Sinkers tend to occur within infiltration zones*. And EMR™ is a unique tool for finding these features, which we believe, can be the controlling features on a site. We regard this discovery as a fundamental breakthrough in hazardous waste assessment. DNAPLs move laterally in response to the hydrology of the site, until they encounter an infiltration zone. Then, they migrate down to the underlying aquifer! The infiltration zones are naturally occurring sinks, or sumps, where DNAPLs collect. More insidiously, they will continue to act as a source to feed the DNAPL into aquifer for many years to come, thus thwarting the "pump and treat" efforts in downstream wells.

Figure 3 shows a vertical migration column of TCE at Princeton, Illinois, where we first realized the importance of infiltration zones on the migration characteristics of DNAPLs and nature of the connection pathways that these features provide by communicating with underlying aquifer. Smaller “patches” of TCE on the map (Figure 1) are also individual infiltration zones.

Now that we appreciate the importance of infiltration zones, we can look back at earlier projects to gain a greater understanding of what we have seen. One such effort was a project we performed in 1993 for a Fortune 500 company at a manufacturing facility in Shreveport, Louisiana, (*DSI, Final Report-GPR Survey, Shreveport, Louisiana*). This was also a TCE site. The owner’s contractor had spent nearly 10 years and millions of dollars trying to clean up the site with pump and treat methods. Over the life of the project, only a few hundred gallons of product had been recovered. (We estimate that the cost was more than \$10,000 per gallon!).

Our mission was to profile the confining layer and to look for a suspected ancient river channel. We found that the so-called confining “layer” did not exist, but instead consisted of a graded zone where the clays became progressively tighter (less permeable) over a vertical span of several feet. There were no significant, discrete “layers” in the clay. Under high magnification, there were numerous, small bedding layers in the deposited clays (this is in the Mississippi Delta), but no single layer could be defined as the “confining layer.” Moreover, the bedding deposits were horizontally discontinuous, and could not be “traced” for any significant distance across the site. This result flew directly in the face of the models that had been carefully constructed by the site contractor. The models showed well-behaved stratigraphy in the vertical profiles between boreholes. The EMR™ showed variations in vertical permeability in the relatively uniform clays, allowing us to identify a zone where some degree of confinement or retardation was taking place, but there was no single, specific boundary to define the depth profile of the “confining layer” as such.

Faced with a dispute with the contractor, whose professional reputation was on the line, we recommended to the owner that the project should be put on hold until our claims could be verified by drilling.

Figure 4 shows two localized, vertical migration columns of TCE that we now know to be infiltration zones. We proposed placing a boring at this location, despite the fact that there was a recovery well less than 20 feet away. Upon drilling at this location, the owner’s (new) contractor encountered vapor levels indicating concentration levels in the thousands of ppm. There is now a recovery well at that location. Whereas the neighboring well was producing less than a half a gallon of product per day, the yields in the new well are now running much higher

than the old well. We attribute the difference to the horizontal tightness of the clay, where the permeability of the infiltration zone is much higher than that of the surrounding clay.

There are subtle clues to be observed in Figure 4. The apparent lack of product (dark reflectors) in the upper clay indicates that the product spread laterally across the semi-confining zone until it ran down the infiltration zones. In other words, this was not a surface spill, or else there would be a lot more product trapped in the pore spaces of the upper clays above the infiltration zones. We can also see evidence of vertical retardation taking place within the vertical column, thereby producing the more dark "banding" starting at a depth of about 24 feet down the migration columns. This banding provides direct evidence of the decrease in permeability (confinement) that is taking place at these depths. The bottom line is that we have identified pathways where the product is getting into the underlying aquifer.

We did find the ancient (Pleistocene) river channel at a depth of about 38 feet. It appeared to be acting as a conduit to transport contamination off site. The original site contractor was planning to drill a "confirmation" boring several hundred feet off site to confirm that the contamination had not moved that far off site. We proposed relocating the boring to coincide with the extended alignment of the river channel (we did not have any EMR™ data for this off-site location other than our projection for the direction of flow). There was significant dissolved phase TCE in the groundwater at the new location. Drilling confirmed the existence of this ancient river channel.

We have *hundreds* of other case histories showing how the EMR™ results are vastly superior to conventional methods and contribute much better understanding of site conditions — including existing sites where conditions are presumably well known — than any other method of site evaluation.

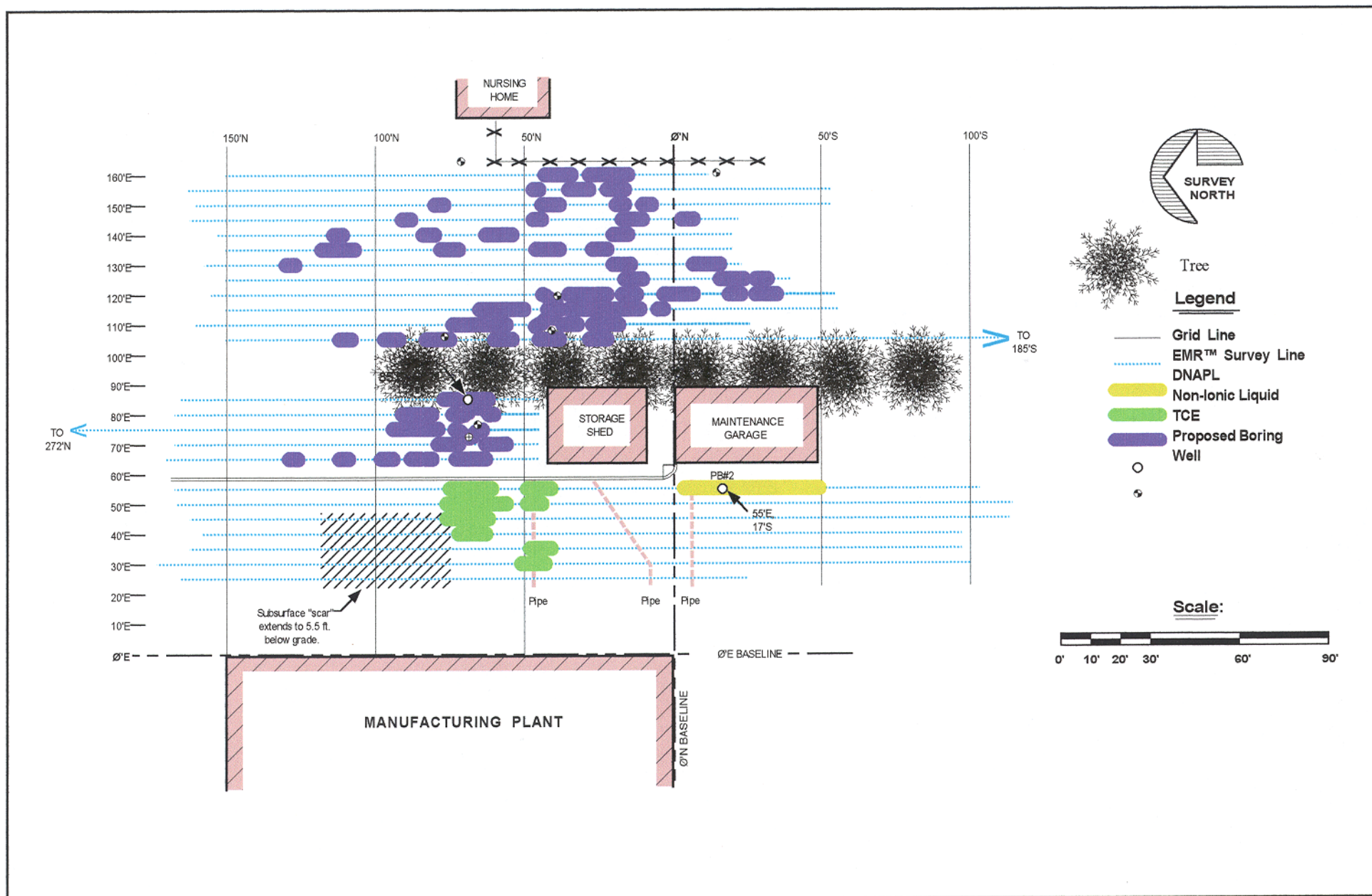


Figure 1. EMR™ Site Map Showing the Distribution of TCE / Princeton.

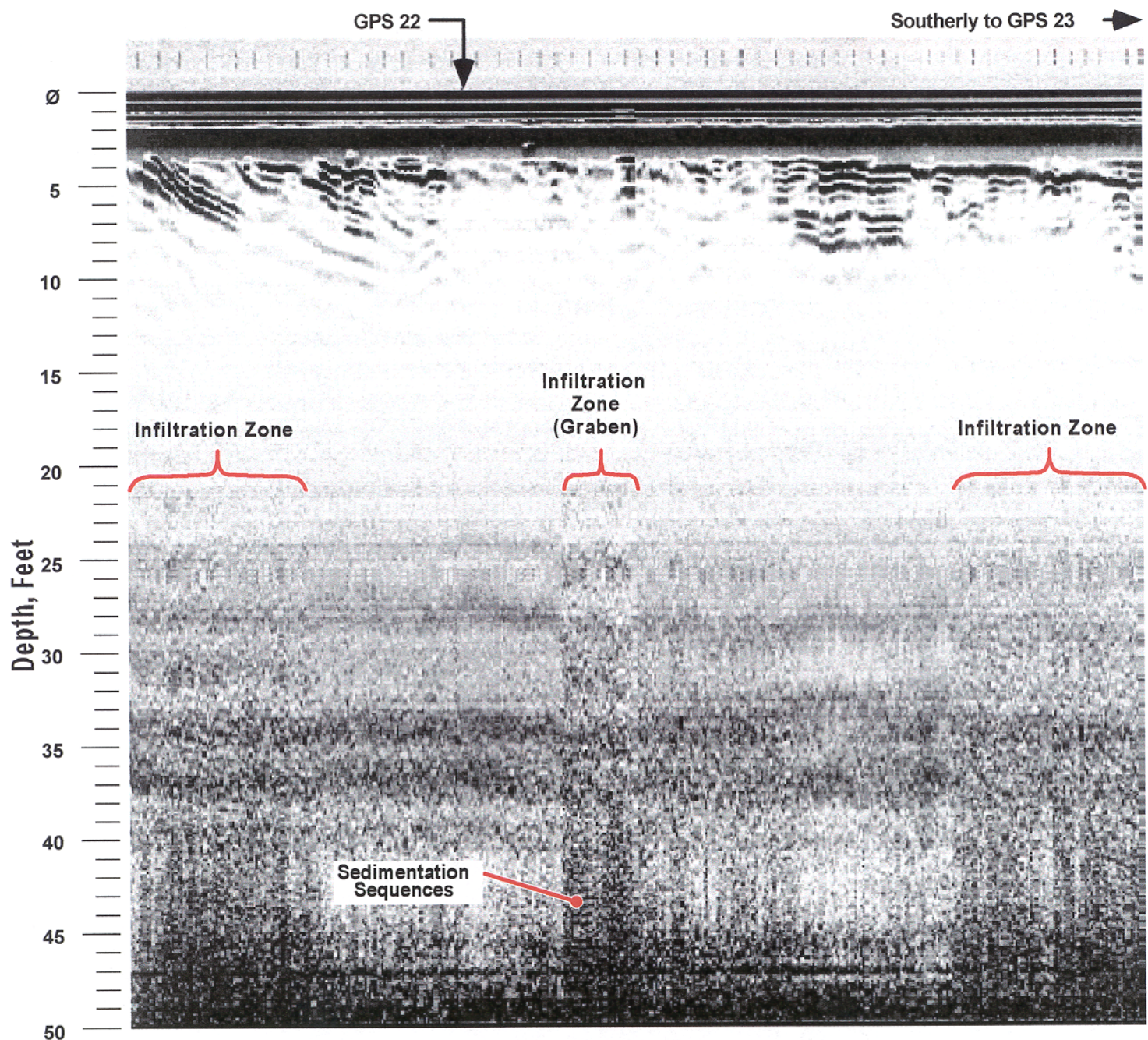


Figure 2. EMRTM Profile of Natural Infiltration Zones, Sultanate of Oman.

EMR™ PROFILE OF INFILTRATION ZONE WITH TCE.

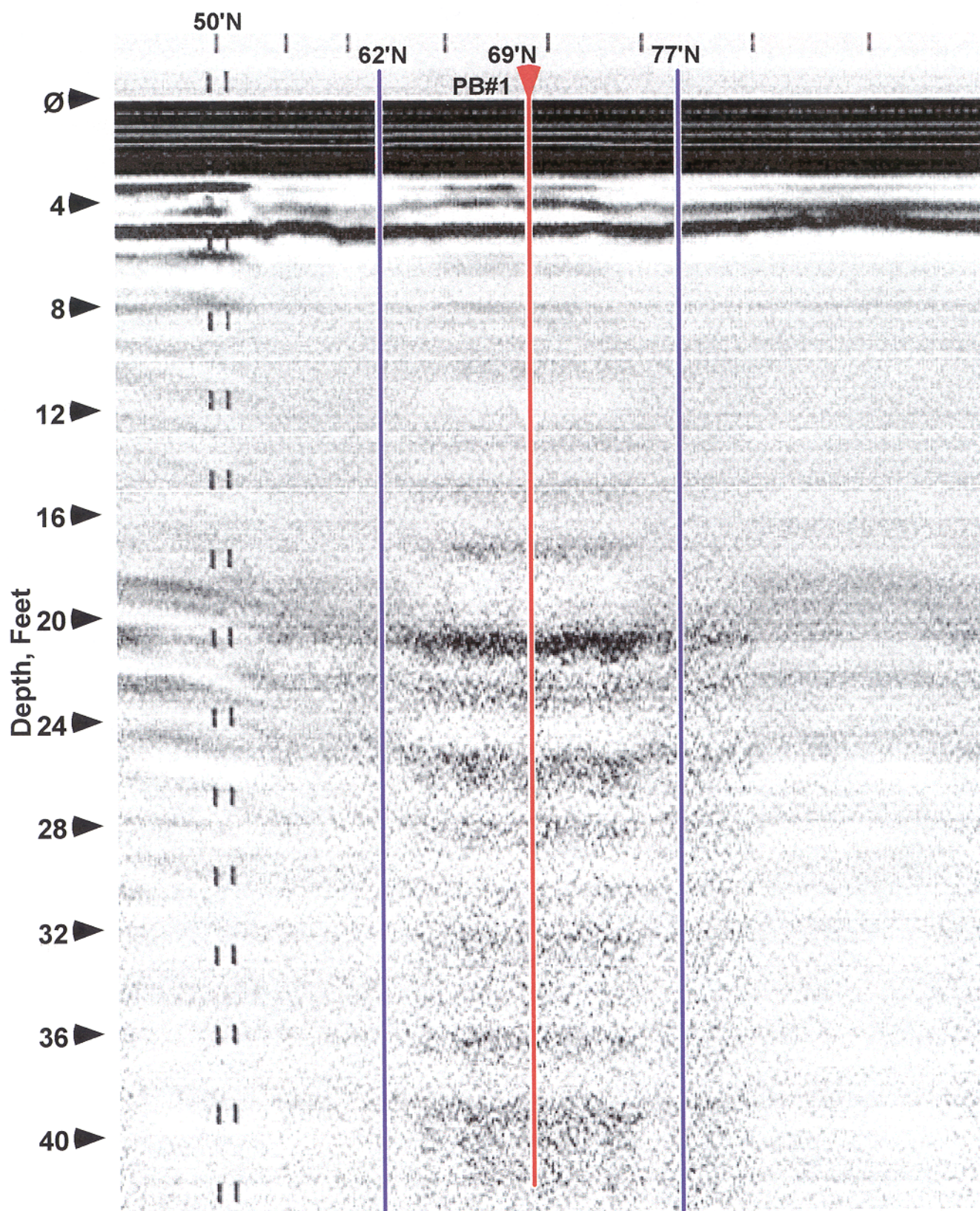


Figure 3. Vertical Migration of TCE in Infiltration Zone, Princeton, IL.

EMR™ SURVEY LINE 10'E

Proposed Boring 194'N

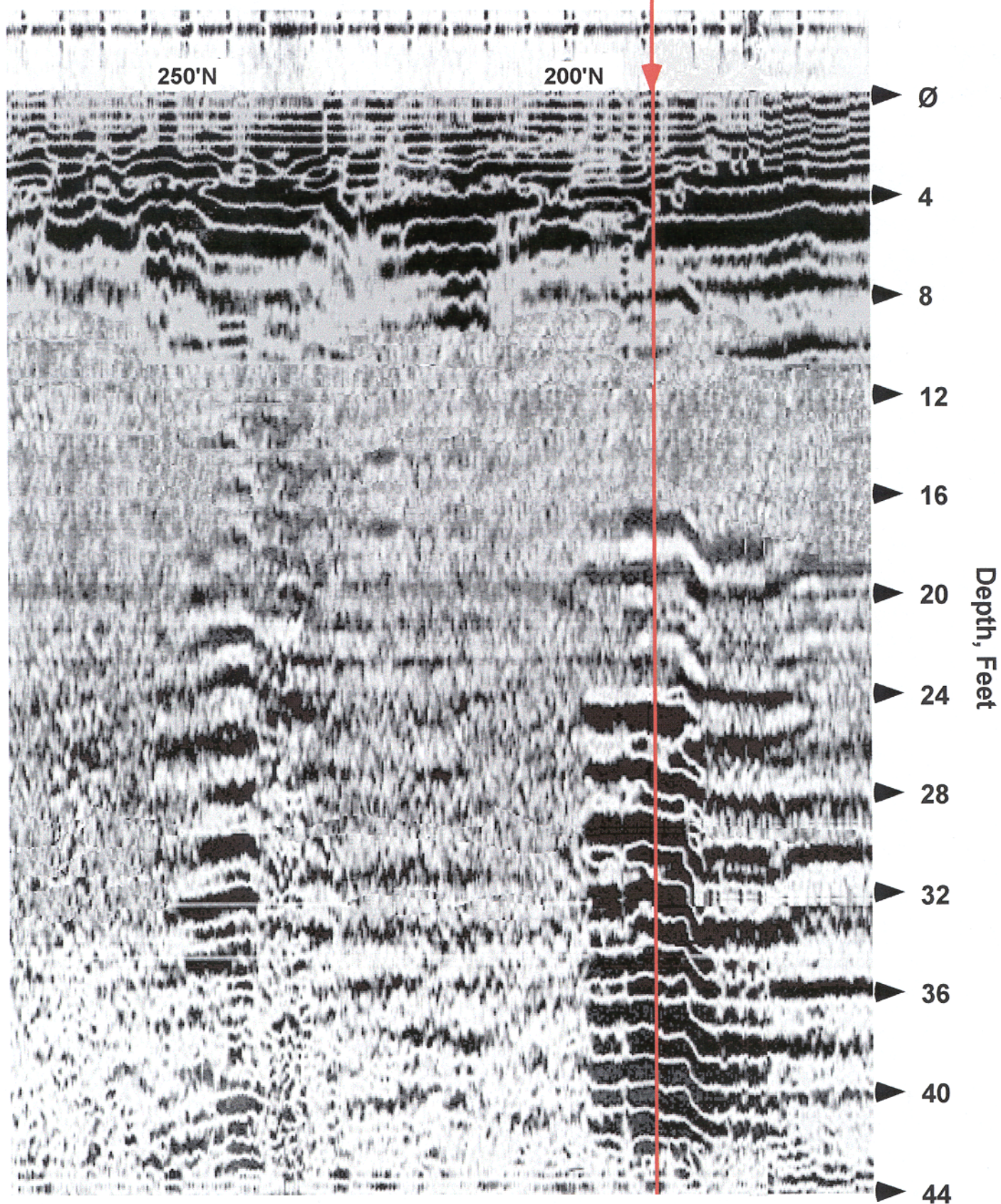


Figure 4. Vertical Migration of TCE in Infiltration Zone, Shreveport, LA.

CALIBRATION AND TESTING OF PREDICTIVE MODELS OF GAS-PHASE TRANSPORT IN THE VADOSE ZONE: AN EXAMPLE FROM THE NEVADA TEST SITE

Charles R. Carrigan
Lawrence Livermore National Laboratory

INTRODUCTION

The development of a numerical model with meaningful diagnostic or predictive capabilities necessarily involves a calibration and testing phase. The failure to properly calibrate or test a numerical model may result in simulations that are both quantitatively incorrect and fail to include important physical processes. An example of calibration and testing of vadose zone models that happened to be extraordinarily effective involved the modeling of trace gas transport in the unsaturated, fractured tuff of Rainier Mesa at the Nevada Test Site [Carrigan *et al.*, 1996]. The intent of this was to develop an improved understanding of gas emanations from natural faults and fractures driven by weather-induced barometric lows following an underground nuclear explosion. This work would also produce a modeling capability that was used with some confidence to predict the detectability of radionuclide-gas emanations during inspections of clandestine underground nuclear test sites.

THE FIELD EXPERIMENT

A simulated 400-m-deep, 1-kiloton nuclear explosion was produced by the detonation of over a million kilograms of chemical explosives in a mined cavity (Fig. 1). This thickness of overburden is more than adequate to contain such an explosion. While a somewhat shallower detonation might have produced a collapse crater or extensive fractures connecting the cavity with the surface, this explosion produced no visible structural changes including fissuring at the surface. Such an event is an extreme challenge to those on-site, forensic techniques that are intended to provide a legal basis for declaring the violation of a nuclear treaty.

Before the detonation, gas bottles containing ^3He (helium-3) and SF_6 (sulfur hexafluoride) were placed in the cavity with the explosives. Following detonation and release of the tracers, gas chromatography was used to detect the heavy SF_6 gas (mole. wt. 146) in air samples which have a low background level of less than 3 parts-per-trillion-by-volume (pptv) at the test site. Similarly, the low atmospheric background level (7.34 pptv) of ^3He (at. wt. 3) permits a very low threshold for detection using mass spectrometry.

Nearly 200 gas samples were obtained over approximately 500 days during which a wide variety of barometric events were recorded by a weather station on Rainier Mesa (elev. 2286 m). Most of the sampling occurred in the fall and spring, when large barometric depressions occur. Typically, several stations were sampled during an atmospheric low. At some stations, stainless-steel tubes with porous end caps were driven into the ground to depths between 1.5 and 5 m along fractures and faults. At other stations, which were set out more or less radially from the point on the surface directly above the cavity or surface ground zero, plastic sheeting covered

tubes laid on the ground for extracting rising soil gases that became trapped beneath the sheeting.

Sulfur hexafluoride was first detected at concentrations of 340 parts-per-trillion-by-volume (pptv) in fractures along a fault approximately 0.5 km or 1.3 overburden thicknesses from surface ground zero 50 days after the detonation (Fig. 2b). After its arrival, SF₆ was found to be well above background a number of times in later sample suites as indicated by the "detect" symbols on the timeline. Helium-3 was initially detected at levels exceeding two standard deviations (1 pptv in excess of the 7.34 pptv atmospheric level for ³He) 325 days following the first detection of SF₆ and 375 days after the detonation (Fig. 2d). The first detected arrivals of ³He and SF₆ occurred at the same sampling location, which is not on the nearest fault to surface ground zero.

MODELING

These arrivals cannot be explained by gaseous diffusion alone; numerical simulations show that tens to hundreds of years are required to produce detectable concentrations of SF₆ at the surface. Analytical and numerical models of gas transport in a fractured porous medium subject to barometric surface pressure variations indicate that the speed of transport along fractures over a vertical scale of hundreds of meters is orders of magnitude greater than the diffusion rate. We used such a transport model that assumed vertical, millimeter width fractures traversing the uniform porous matrix of the overburden into a region of uniform tracer concentration around the detonation point. In the model, flow along the fractures is driven by barometric pressure variations obtained from the Rainier Mesa weather station records (Fig. 2a).

Parameter Sensitivity Studies

Hydrologic parameters used in the models, such as gas-phase porosity (0.10), permeability (10^{-15} m²), fracture separation (6.4 m) and tortuosity (0.1), are thought to be appropriate in a bulk sense for the fractured tuffs of Rainier Mesa and nearby Yucca Mountain with its well-studied hydrologic system. An integrated finite difference, multi-phase, flow and transport computer program called NUFT [Nitao, 1995] performs the gas transport simulations on a 2100 element, 6.4 m wide by 400 m deep biased grid using the hydrologic parameters as input. In the simulations, the initial concentration distribution of SF₆ and ³He occupies a region in the fractured porous medium extending upward to 200 m beneath the surface of the mesa. This fracture model is consistent with models used in detonation containment studies. Parameter sensitivity studies show that large changes in model parameters such as fracture width (0.001 - 0.004 m, 0.00125 m used), fracture separation (3.3 - 12.8 m, 6.4 m used), and initial halo concentration of SF₆ (3.0×10^{-7} to 2.2×10^{-5} , 2.2×10^{-5} used) all resulted in changes to the arrival time of 13 days or less for SF₆. Given the uncertainties inherent in these parameter values, it was admittedly fortunate that the rate of gas transport did not have a stronger dependence on them. If this had not been the case, as sometimes happens, a bounding-envelope approach would probably have been used. That is, reasonable ranges of parameters would have been used to bound the time of gas transport to the surface from the source region. The

width of the envelope of arrival times is determined by the maximum variation in these times resulting from simulations using all possible combinations of the parameters.

Model Calibration

The same fracture-matrix model and surface-barometric-pressure history is used to simulate the SF₆ and ³He surface-concentration histories illustrated in Fig. 2c and e; only the binary gas diffusivities and initial concentrations are different in keeping with the different gases and amounts initially used. It is reasonable to use the same model since the first arrivals of both gases were detected at the same surface location and, therefore, both gases probably moved along the same fracture. The width of the fracture, which transported the gas, was thought to be the most poorly controlled parameter in this experiment. The fracture width was adjusted to a value (0.00125 m) necessary to yield an ³He concentration similar to what was observed in the field at its apparent arrival time. The arrival of the helium tracer was used to calibrate the model since its arrival concentration was thought to be generally better determined than that of the less diffusive SF₆ gas.

Model Testing

With all the parameters thus fixed, the model was then used to calculate the concentration of SF₆ at arrival as well as its arrival time (point where concentration exceeds detection-threshold values) assuming the initial concentration and binary diffusivity appropriate for this tracer. The calculated arrival time for SF₆ (Fig. 2c) was, in fact, found to be in excellent agreement with the apparent (observed) arrival, and the calculated concentration of SF₆ at arrival (Fig. 2c) is well within an order of magnitude of the observed value. It is important to recognize that this type of model testing would not have been possible if two different gas tracers had not been released during the underground explosion. This suggests the fundamental importance of designing experiments to produce observations that allow calibration and testing of the associated diagnostic models.

Model Prediction

Given the excellent agreement between the gas-transport model and the observations, it was used to predict the arrival of detectable concentrations of trace radionuclide products assuming the hypothetical occurrence of a 1-kiloton fission detonation under precisely the same circumstances as the actual chemical explosion. Again, the design of the field experiment was useful for enhancing the confidence that might be placed in the prediction of the numerical model. The most important distinguishing property of the two tracers used in the field experiment, the binary gas diffusivity, is significantly different for both tracers and also bounds the values appropriate to the hypothetical radionuclides that are of interest. Thus, the prediction is an interpolation of the results of the tested model rather than an extrapolation of them. This suggests a higher level of confidence in the prediction since the model has been tested over the range of parameters that are input to obtain the arrival times for the hypothetical trace radionuclides. Had an

underground nuclear explosion released rare radionuclide gases, the model predicted that they would have been detectable using present laboratory capabilities.

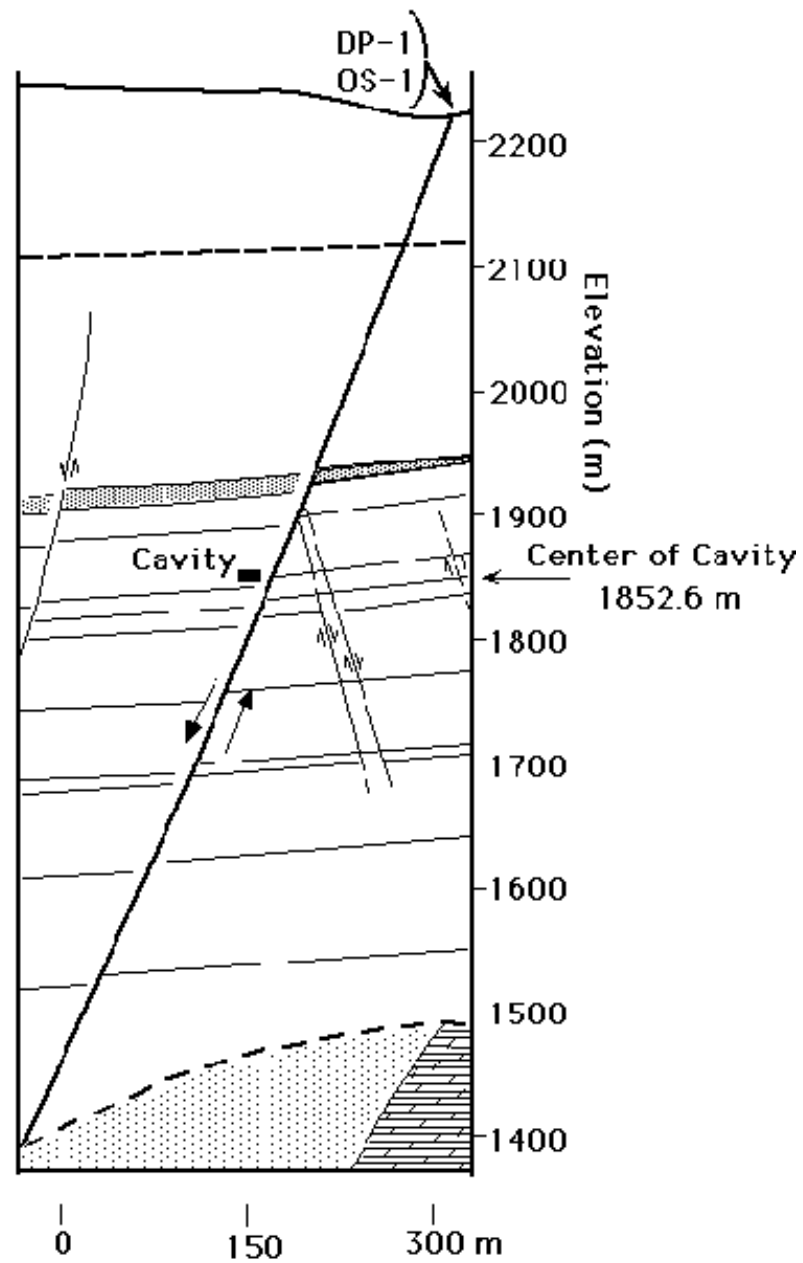
CONCLUSION

From this work, it was learned that carrying out a field experiment that is consciously designed to support the modeling effort is critical to success. In this case, multiple tracers released in the vadose zone were required to allow proper calibration and testing of the numerical model. Further, the value of the model as a means of predicting the arrival of radionuclides was enhanced by using tracers that bracketed the transport behavior of the radionuclides. The results of this integrated modeling and field effort influenced changes to the on-site inspection protocol of the proposed Comprehensive Test-Ban Treaty and a recognition of the important role of trace-radionuclide gas sampling and analysis for detecting clandestine underground nuclear explosions.

REFERENCES

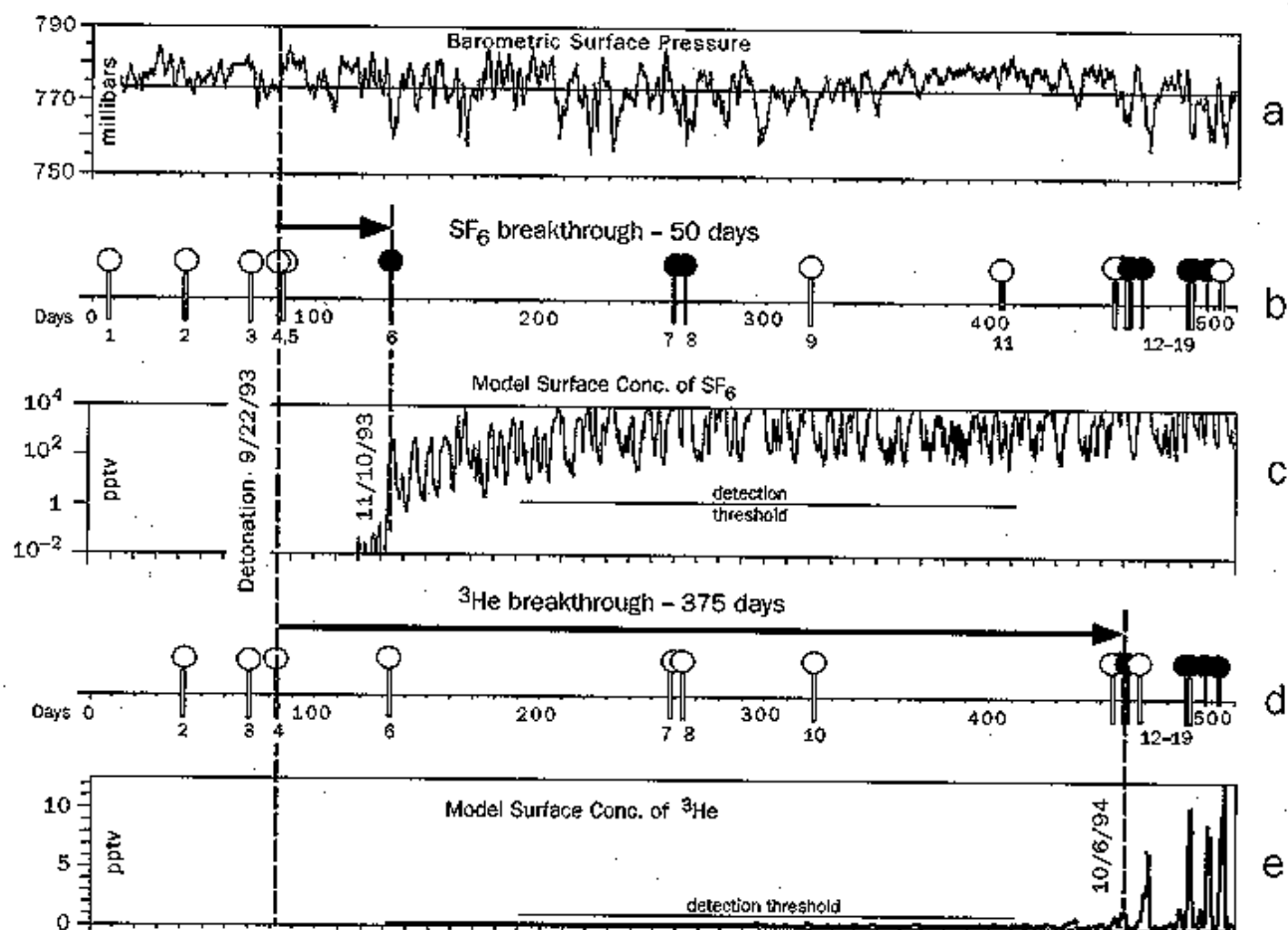
- Carrigan, C.R., R.A. Heinle, G.B. Hudson, J.J. Nitao and J.J. Zucca (1996), Trace gas emissions on geological faults as indicators of underground nuclear testing, *Nature*, 382, 528-531.
- Nitao, J. J. (1995), Reference manual for the NUFT flow and transport code, version 1.0, Lawrence Livermore National Laboratory Report (UCRL-ID-113520), Livermore, CA.

Figure 1



Cross section of field experiment showing detonation cavity 400 m beneath the surface of Rainer Mesa. Cavity is near fault that eventually allowed gas to be transported to surface. However, first arrivals of tracer gases were not on this fault.

Figure 2



Barometric surface pressure history covering a period of more than 500 days is illustrated in Fig. 2a. Figures 2c and e show the predicted histories of the numerical model for the sulfur hexafluoride and helium concentrations at the surface. Figures 2b and d show the apparent arrivals of these two gases as determined by gas sampling at numerous stations located on faults and fractures on Rainier Mesa.

Recharge and Infiltration Distribution at the Nevada Test Site and the Hanford Site

James L. Conca^{A,B}, Daniel G. Levitt^C, Paula R. Heller^B, T. Joseph Mockler^B, and Michael J. Sully^D

^AWashington State University Tri-Cities and ^BUFA Ventures, Inc., 2000 Logston Blvd, Richland, Washington 99352. james@ufaventures.com <http://www.ufaventures.com/>

^CBechtel Nevada, M/S NLV-081, P.O. Box 98521, Las Vegas, NV 89193

^DHSI Geotrans, P.O. Box 93838, Las Vegas, NV 89193-3838

Measurement of Infiltration in Sediments from the Nevada Test Site

The UFA Method was used to measure water retention and unsaturated hydraulic conductivity relations for 156 sediment core samples from boreholes drilled in and around nuclear chimneys by Bechtel Nevada Company. These cores were collected from the Area 3 Radioactive Waste Management Site (RWMS), located in Yucca Flat on the Nevada Test Site (NTS) in Nye County, Nevada. The purpose of this characterization effort was to provide physical and hydraulic properties and other hydrologic information required to develop a conceptual hydrogeologic model and complete flow and transport modeling in the Area 3 Performance Assessment and Composite Analysis [Bechtel Nevada, 1998].

The topography of the region is distinguished by north-south trending mountain ranges separated by alluvial valleys. The geology of Yucca Flat in the vicinity of the RWMS is characterized by thick sections of sedimentary rocks overlain by volcanic rocks and deposits of alluvium consisting of postvolcanic sands and gravels [US DOE, 1996]. At the Area 3 RWMS, alluvium is 305 m (1,000 ft) thick and the depth to groundwater is 488 m (1,600 ft). Precipitation at this site averages 159 mm/yr (6.3 in/yr) and monthly average temperatures range from 2 °C (36 °F) in January to 25 °C (77 °F) in July.

The craters within the Area 3 RWMS were formed by testing of nuclear devices in the early 1960's. These tests were conducted hundreds of meters below the ground surface in shafts bored vertically into the

alluvium. Upon detonation of the nuclear device, pressures and temperatures increased forming a cavity in the alluvium. When the gas pressure dissipated to a point at which it could no longer support the overburden, the roof of the cavity collapsed and the void region propagated upward to the surface forming a saucer-like subsidence crater on the surface (U.S. Congress, 1989). The region through which the void propagates is referred to as the collapse zone or nuclear chimney. At the time of formation, seven craters within the Area 3 RWMS ranged from 122 to 178 m (400 to 580 ft) in diameter and from 14 to 32 m (46 to 105 ft) in depth.

Five of the seven craters have been used for the disposal of low-level bulk radioactive waste. The locations of the characterization boreholes with respect to the waste cells are shown in Figure 1. The maximum distance between any two boreholes was 500 m. These boreholes were drilled using only air as a drilling fluid to minimize disturbance of the core samples. Core samples were recovered at approximately 3-m (10-ft) intervals over the sampling range and geologic descriptions were recorded. Core segments from the boreholes were used for measurement of the field moisture status; laboratory analyses for physical and hydraulic characteristics; and measurement for chloride, tritium, and stable isotope concentrations. Data reports contain detailed characterization information from these projects [Bechtel Nevada, 1998].

The thick vadose zones found in the alluvial valleys of the NTS possess characteristics favorable for the isolation of radioactive waste [Winograd, 1981]. Among other considerations, the great depth to the water table and the arid climate in these regions combine to inhibit the transport of radionuclides to the groundwater below the waste. An important consideration in the use of craters for waste disposal is whether the ability of the climate and geologic formation to isolate the waste from the water table is compromised by the presence of the collapse zone below the crater. The advantages of climate and geologic setting could be negated by several processes and occurrences. First, it has been assumed, by analogy with tests conducted in competent formations, that the detonation of the device and the subsequent collapse of the alluvium below the crater have altered the alluvium to make the collapse zone more

permeable. Second, it has been postulated that the saucer-shaped crater on the surface resulting from the collapse acts to focus runoff into the crater, leading to higher water contents in the collapse zone and eventual recharge to the groundwater table [Tyler et al., 1992].

Because of the presence of low-level waste in certain craters, these craters could not be accessed directly from the surface, and angle drilling was employed to reach the collapse zone at depth without disturbing the waste. Three angled boreholes (30 to 45 degrees) provided samples from the intermediate depths in collapse zones below U-3bl and U-3at (boreholes U-3at-D1, U-3at-D2, and U-3bl-D2). These samples ranged in depth from 30 to 148 (98 to 486 ft). Because of the uncertainty in defining collapse zone boundaries, it was assumed that samples from the angle boreholes above 30 m (98 ft) were undisturbed and that samples from below this depth were either from the collapse zone or influenced by the presence of the crater. The disadvantage of the angle drilling was that the collapse zone from the crater floor to a depth of 30 to 50 m (98 to 164 ft) was not sampled. To correct this deficiency, characteristics of the collapse zone of an open crater were obtained from analyses of samples from two boreholes drilled vertically from the bottom of the U-3bh crater (boreholes U-3bh-C1 and U-3bh-C2). These boreholes provided samples representative of the region immediately below the crater floor which was bypassed by the angled boreholes.

For many risk and performance assessments contaminant release rates and carrier fluid travel times must be determined. For the vadose zone, the most important factor for travel time is the recharge rate. Recharge is the water that accumulates in the near-surface and moves downward through the vadose zone to the groundwater table. Arid regions, such as the Nevada Test Site and the Hanford Site, are characterized by low precipitation and high evapotranspiration, and often have deep vadose zones. In vadose zones with small net annual downward movement of water, it is possible to trap infiltrating water in the near-surface and immobilize the water in the vadose zone [Milly, 1996]. However, a thick vadose zone and an arid climate do not ensure that no recharge will occur. The water flux at any point in the subsurface depends

upon climatically-controlled annual precipitation rates, type of surface cover, and any lateral flow that may occur from perched saturated zones or from artificial infiltration. For a normally undisturbed surface at these sites, the background flux is negligible, less than 10^{-9} cm/s [Gee et al., 1992]. However, it is useful to determine the subsurface flux at specific positions to track local variations or disturbances in the infiltration rate, especially from anthropogenic influences, i.e., liquid waste disposal, or from focusing by topographic features such as subsidence craters.

If detailed, long-term vadose zone monitoring is not possible, two methods can be used to determine subsurface flux or recharge. Both require many samples for precision and accuracy. One method is geochemical or isotopic, using ^{36}Cl and/or ^3H as tracers for age dating the infiltrating water, and makes various chemical and hydrologic assumptions [Scanlon, 1992]. The other is the hydraulic method, which uses the *in situ* volumetric water content (field moisture content) of the sample and the unsaturated hydraulic conductivity relationship, $K(\theta)$. The hydraulic method assumes that both $K(\theta)$ and the *in situ* volumetric water content are accurate, that the boundary effects between layers are volumetrically unimportant, and works best in arid or semi-arid regions with low background recharge [Nimmo et al., 1994]. Because it is necessary to obtain accurate $K(\theta)$ rapidly on many samples, the UFA Method is ideal for determining recharge using the hydraulic method.

Under normal conditions, hydraulic steady state is usually achieved in the vadose zone within a few meters of the surface, i.e., the recharge is everywhere the same, each material has reached its steady-state volumetric water content for that water flux, and the recharge is equal to the hydraulic conductivity of the materials at that water content. This condition is sometimes referred to as unit gradient conditions.

Additional changes to transient recharge can occur from 1) changing the surface cover through defoliation, emplacement of gravel covers, or surface barriers, 2) disposal of liquid wastes in cribs directly above the area, or 3) lateral input of liquid from migrating plumes, often along boundaries between sedimentary units where differences in permeability cause local saturation. Because the borehole samples in these studies

were collected in as undisturbed condition as possible, the *in situ* volumetric water content and the actual hydraulic conductivity behavior can be measured and used together to determine what the infiltration rate into that sample was prior to sampling.

Figure 2 is a plot of hydraulic conductivity curves for two samples from borehole U-3bh-C1 and can be used to illustrate the hydraulic method of subsurface flux determination. The field moisture content of each sample, measured after the sample was removed from the borehole, is marked on the horizontal axis. A line is drawn from the field moisture content of the sample to the hydraulic conductivity curve. A second line is then drawn from the point intersected on the curve to the vertical axis. This point on the vertical axis indicates the subsurface flux, or infiltration rate, at the time of sampling. This can be compared to the background flux to determine any local variations or disturbances. The sample from 51.5 ft, with an *in situ* water content of 11.3%, had a flux that is less than 10^{-10} cm/s. Because tens to hundreds of years are required to achieve hydraulic steady state when fluxes are 10^{-9} cm/s or less, it can be assumed that this sample has not undergone artificially high flux from recent activities at the Nevada Test Site, e.g., changes in basin infiltration rates. Therefore, this flux is probably close to the background recharge rate in this region.

For the next lower sample in the borehole, at 61.5 ft, with an *in situ* water content of 16.3%, the flux is anomalously high, 1.4×10^{-5} cm/s. This does not provide any specific information about the timing and/or magnitude of the subsurface flux, e.g., the sample could be experiencing a flux of 1.4×10^{-5} cm/s and never have been subjected to any greater flux, or the sample could have experienced a flux of 2×10^{-2} cm/s ten years ago that saturated the sample and since that time has drained to this water content. Depending upon local effects and vapor flow, this flux may never reach the water table.

Subsurface flux determinations were made for each of the 156 samples from the nuclear chimneys. The samples were collected with minimal disturbance and inspection and cross-checking indicated no significant water loss. Therefore, the water contents in these samples represent as closely as possible the

water contents of the units at depth. Because of radioactivity and safety issues, continuous sampling was not possible for all boreholes and only borehole U-3at-D1 was continuous down to 150 m. The subsurface flux determination results are given in Figures 3 through 7 which show both the water content as a function of depth and the subsurface flux determination as a function of depth. No obvious correlation is seen from the water contents alone, but the flux graphs show zones of higher flux against a background of vanishingly low infiltration rates of less than 10^{-10} cm/s. The hydraulic conductivities of all these units are fairly high, greater than 10^{-4} cm/s. There appear to be no aquitards that would allow perched water zones to form. Therefore, these samples probably reflect infiltration events that are redistributing at very slow rates. When both the $K(\theta)$ relationships and the field moisture contents are known then bounds can be made on the rates of vertical fluxes because water cannot advectively redistribute faster than the hydraulic conductivity at that water content. The two boreholes drilled directly beneath the craters both show relatively high fluxes in the upper 40 m reflecting recent increased infiltration (Figures 6 and 7). Evidence of these infiltration events are not seen in samples outside of the craters [Bechtel Nevada, 1998]. Deeper infiltration from borehole U-3at-D1 reflects older infiltration events (Figure 12). Between these two suites of events, the flux is below 10^{-10} cm/s, i.e., no measurable subsurface flux. From advective transport, it takes well over 100 years to reach steady-state at 10^{-10} cm/s suggesting that these deeper infiltration events predate the detonations.

Comparing the properties of samples obtained outside the affected zones with samples obtained from beneath the craters, there is no discernable affect of the detonation on the hydraulic properties of these sediments. The similarity of the distributions for physical and hydraulic properties demonstrates that the physical and hydraulic properties of the collapse zones to a depth of 148 m (486 ft) have not been noticeably altered by the nuclear tests. These results indicate that the collapse zone will not be a preferential pathway due to enhanced permeability.

However, the crater appears to have enhanced infiltration by focusing runoff, which has led to

development of a zone of water content higher than background below the floor of the craters. The depth of this zone varies, depending on past precipitation events and the size of the catchment area for the particular crater. For crater U-3bh, this zone extends from the bottom of the crater to a depth from the land surface of approximately 80 m (263 ft). The depth of the wetting front movement in any individual infiltration event varies with the magnitude of the precipitation event and the magnitude and frequency of past infiltration events. Stable isotope and tritium concentration profiles suggest that there is a highly transient zone of thickness varying from 10 to 20 m (33 to 66 ft) which has experienced a relatively high frequency of infiltration events. The extent of this zone is indicated by a region of alternating depletion and enrichment of stable isotopes with depth and the depths of the tritium concentration peaks [Bechtel Nevada, 1998]. The area approximately 40 m (131 ft) below this zone is characterized by higher water content which is slowly redistributing. Within this zone, the water flux is downward, but currently quite small. Stable isotope concentrations from characterization of crater U-3bh show effects of evaporation extending to as deep as 45 m (148 ft). This pattern is due not only to enrichment resulting from evaporation, but also to the downward movement of enriched pore water caused by intermittent infiltration events. At present, the vadose zone below 80 m (263 ft) from the land surface shows no evidence of current subsurface flux due to the presence of the crater.

Hydrostratigraphic and Recharge Mapping At the Hanford Site

Subsurface mapping involves knowing the spatial distribution of some physical or chemical property of the system, either the porous medium itself or some chemical phase of interest. In the study area, measurements of hydraulic conductivity, subsurface flux, porewater chemistry and gas permeability using the UFA Method have allowed detailed mapping of the hydrostratigraphy, subsurface flux or recharge, porewater chemistry and vapor diffusivity. This case history presents the hydrostratigraphic map and the subsurface flux or recharge map for this area.

The Plutonium Finishing Plant in the 200-West Area at the Hanford Site in Washington State (Figure 8) is

the site of a mixed-waste contaminant plume. The area is a semi-arid shrub steppe with a deep vadose zone made up of various aridisols, paleosols and sediments. The plume contains carbon tetrachloride (CCl_4) as the primary VOC, plutonium (Pu) and americium (Am) as the primary radionuclides, water, aqueous sodium nitrate solutions, and other organics (lard oil, tributylphosphate, and chloroform). An estimated $13,200 \text{ m}^3$ (13.2 million liters; 3.5 million gallons) of liquid waste was discharged to three unlined cribs (similar to septic tank drain fields) between 1955 and 1973 [Last and Rohay, 1993]. CCl_4 concentrations in the groundwater have been recorded as high as 8.1 ppm (mg/L), or 1600 times the maximum concentration limit allowed by the United States Environmental Protection Agency. Vapor concentrations for CCl_4 in pore atmospheres in the vadose zone averages about 1,000 ppm (mg/L) by volume, but has been recorded as high as 38,000 ppm (mg/L) near Z-9 Trench [Last and Rohay, 1993]. These vapor concentrations indicate the presence of liquid CCl_4 . However, no liquid CCl_4 has yet been found, although some CCl_4 is dissolved in water [CCl_4 solubility in water is 805 ppm (mg/L)] and in the other organic phases. Vapor extraction methods have removed over 72,000 kg of CCl_4 from the vadose zone at this site, the CCl_4 having been collected using granular activated charcoal (GAC) in containers that could be regenerated through incineration or steam stripping.

The water table at this site is the top of an unconfined aquifer approximately 73 m (240 ft) below the surface in conglomerates of the middle Ringold Formation. Groundwater velocities vary greatly but have been estimated as high as 47 m/d (153 ft/d; Last and Rohay, 1993). The overlying vadose zone consists of unconsolidated clastic sediments of poorly sorted glacio-fluvial gravel, sand, and silt (designated as the Hanford formation). Beneath it lie semi-continuous layers of loess, paleosols, and low-permeability paleoplaya lake deposits that have developed extensive calcium carbonate cementation, or caliche (previously grouped as Early Palouse and Plio-Pleistocene units). These vadose zone sediments have a variety of water contents and a wide range of field hydrologic properties with respect to water and organic liquids.

The UFA Method was used to characterize the transport behavior of over sixty samples from boreholes drilled in and around these disposal facilities. The boreholes are shown as labelled filled circles in Figure 8. Figure 9 gives the results from one of the boreholes, 299-W18-96, directly beneath Z-18 Crib. Each curve has from eight to twelve independent, steady-state unsaturated hydraulic conductivity measurements. The entire curve was obtained in three to four days. In addition, grain-size distributions and mineralogical analyses were obtained for each sample from each borehole [Wright et al., 1994]. The total time required to obtain the seven hundred steady-state hydraulic conductivity measurements was only six months using a single UFA.

Well logs and other field and geophysical information are generally used to map the subsurface at a site, including the Hanford Site, with respect to lithology and sediment type. Hydraulic behavior for the mapped sedimentary units are then inferred from lithology and a few hydraulic conductivity measurements. Figure 10 shows a hydrostratigraphic map of the subsurface at this site based upon the lithology and sediment type, a typical layer-cake cross-section. Figure 10 is a projection onto a NE-SW trending vertical plane across the site. Perspective is given by the apparent width of each borehole. Shown are the borehole sample positions and boundaries between different sediment units and subunits. The inset shows the generalized regions of hydraulic behavior *roughly* correlated with gravel and sands, silty-sand, sandy-silt, and fine silts and clays moving from left to right in the inset, and describes the general hydraulic behavior of the units of the same color shown in Figure 10.

However, different samples which appear to be similar in appearance, grain-size distribution and other characteristics can have very different transport behaviors. The hydraulic conductivity data provided by the UFA Method allow the subsurface to be mapped with respect to the hydrologic properties of the sediments which are more relevant than lithologic information to predictive modelling, conceptual test plans and actual transport behavior. Figure 11 shows the hydrostratigraphic map based upon UFA data and uses the same generalized regions of hydraulic behavior (inset) as Figure 10. Each sample was assigned the shading

of the region in which its unsaturated hydraulic conductivity falls. This map provides direct information of subsurface transport behavior independent of lithology or soil type, and shows greater detail within each unit. This level of detail allows easier development of defensible restoration strategies or reliable predictions of contaminant transport.

There are some important points to note. General characteristics of the hydrostratigraphy and the lithostratigraphy are correlative, e.g., the Hanford formation is gravelly sand with some silty sand. At about 16.8 m (55 ft) below the surface, there apparently is a relatively fine layer that may have hydrologic significance across the area, but the Hanford Fine subunit is not much different in hydraulic behavior throughout the lower portion than the Hanford Coarse subunit. The Early Palouse unit exhibited the greatest hydrostratigraphic heterogeneity, yet in hand specimen appeared extremely homogeneous. Traditionally, this unit would never be assigned anything but a single hydraulic behavior, yet its actual measured hydraulic behavior is very heterogeneous. In 299-W15-216, this unit also has 4.7 m (15.5 ft). of perched water over the sample at 33.3 m (109.2 ft). Based upon the few samples obtained from below the Plio-Pleistocene unit, the Upper Ringold is similar in hydraulic behavior to the Hanford formation, although it is more cemented.

Hydraulic recharge determinations were made for each sample as discussed above (Figure 2) and then used to assemble a subsurface flux or recharge distribution map for the subsurface beneath the Z-cribs showing which samples have had artificially high recharges, presumably from the disposal cribs and ponds. Figure 12 is the resultant recharge or subsurface flux distribution map projected onto the same NE-SW trending vertical plane as in Figures 10 and 11. It can be seen from Figure 12 that most borehole samples investigated, thus far, have natural recharges expected at the Hanford Site, i.e., recharges less than 10^{-9} cm/s. Recharge through the Hanford formation is essentially vertical and channelized as evidenced by the lack of increased recharge into borehole samples from the Hanford formation adjacent to the cribs. Vertical, channelized flow in the Hanford formation has been observed throughout the site.

The only Hanford formation samples showing increased recharge are those directly below the cribs and one sample in borehole 299-W18-223. It can be concluded that no extensive lateral sheet flow is occurring in this area. Of course, narrow lateral fingering can occur that would not necessarily intersect these nine boreholes, and evidence of this has been seen at other sites in the 200 Areas although not below Z-Plant (Last and Rohay 1993).

On the other hand, lateral dispersion of the plume and increased recharge is definitely occurring within the Palouse/Plio-Pleistocene units and along or near their boundaries as indicated in Figure 12 by the samples that have relatively high recharges. These results also suggest that the plume is heterogeneously distributed. A possible plume geometry is shown in Figure 13 that is consistent with these observations, with the hydrostratigraphy shown in Figure 11, and with other site-specific observations [Last and Rohay, 1993].

Detailed hydraulic data of subsurface samples can be used for a variety of problems, such as determining the maximum age of a transient perched water body. In borehole 299-W15-216, 4.7 m (15.5 ft) of perched water was encountered sitting on the unit beginning at 33.1 m (108.5 ft) that included the sample at 33.3 m (109.2 ft). The recharge for the perched water is believed to be coming from Z-21 pond [Last and Rohay, 1993]. However, the sample at 35.6 m (116.8 ft), only 2.3 m (7.5 ft) below the 33.3 m (109.2 ft) sample, was very dry, suggesting that the perched water is relatively recent. With a hydraulic head of 4.6 m (15 ft), and a saturated hydraulic conductivity of 10^{-6} cm/s [that of the 33.3 m (109.2 ft) sample], it would take approximately 8 years for a water front to go the 2.5 m (8.3 ft) from the bottom of the perched water to the sample at 35.6 m (116.8 ft). This is consistent with observations from other studies that this particular perched water is young, less than 5 years, and is from disposal of water into 216-Z-21 Pond, not older disposal into Z-9 Trench [Last and Rohay, 1993].

References

- Bechtel Nevada, *Hydrogeologic Characterization of the Unsaturated Zone at the Area 3 Radioactive Waste Management Site*, BNC Technical Report DOE/NV/11718-210, Bechtel Nevada Company, Las Vegas, NV, 1998.
- Gee, G. W., Fayer, M. J., Rockhold, M. L., and Campbell, M. D. (1992). Variations in Recharge at the Hanford Site. *Northwest Science*. **66**, 237-50.
- Last, G. V., and Rohay, V. (1993). Refined Conceptual Model for the Volatile Organic Compound-Arid Integrated Demonstration and 200-West Area Carbon Tetrachloride Expedited Response Action. *PNL Technical Report PNL-8597*. (Pacific Northwest Laboratory, Richland, WA.)
- Milly, P. C. D., Effects of thermal vapor diffusion on seasonal dynamics of water in the unsaturated zone, *Water Resources Research*, *30*, 509-518, 1996.
- Nimmo, J. R., D. A. Stonestrom, and K. C. Akstin, The Feasibility of Recharge Rate Determination Using the Steady-State Centrifuge Method, *Soil Science Society of America Journal*, *58*, 49-56, 1994.
- Scanlon, B. R., Evaluation of liquid and vapor water flow in desert soils based on chlorine 36 and tritium tracers and nonisothermal flow simulation, *Water Resources Research*, *28*, 285, 1992.
- Tyler, S. W., W. A. McKay, and T. M. Mihevc, Assessment of Soil Moisture Movement in Nuclear Subsidence Craters, *J. Hydrology*, *139*, 159-181, 1992.
- U.S. Department of Energy, *The Environmental Impact Statement for the Nevada Test Site and Off-Site Locations in the State of Nevada*. DOE/EIS 0243, Las Vegas, Nevada, 1996.
- Winograd, I. J., Radioactive Waste Disposal in Thick Unsaturated Zones, *Science*, *212*, 1457-1467, 1981.
- Wright, J. V., J. L. Conca, and X. Chen, *Hydrostratigraphy and Recharge Distributions from Direct Measurements of Hydraulic Conductivity Using the UFA Method*, PNL Technical Report PNL-9424, Pacific Northwest Laboratory, Richland, WA, 1994.

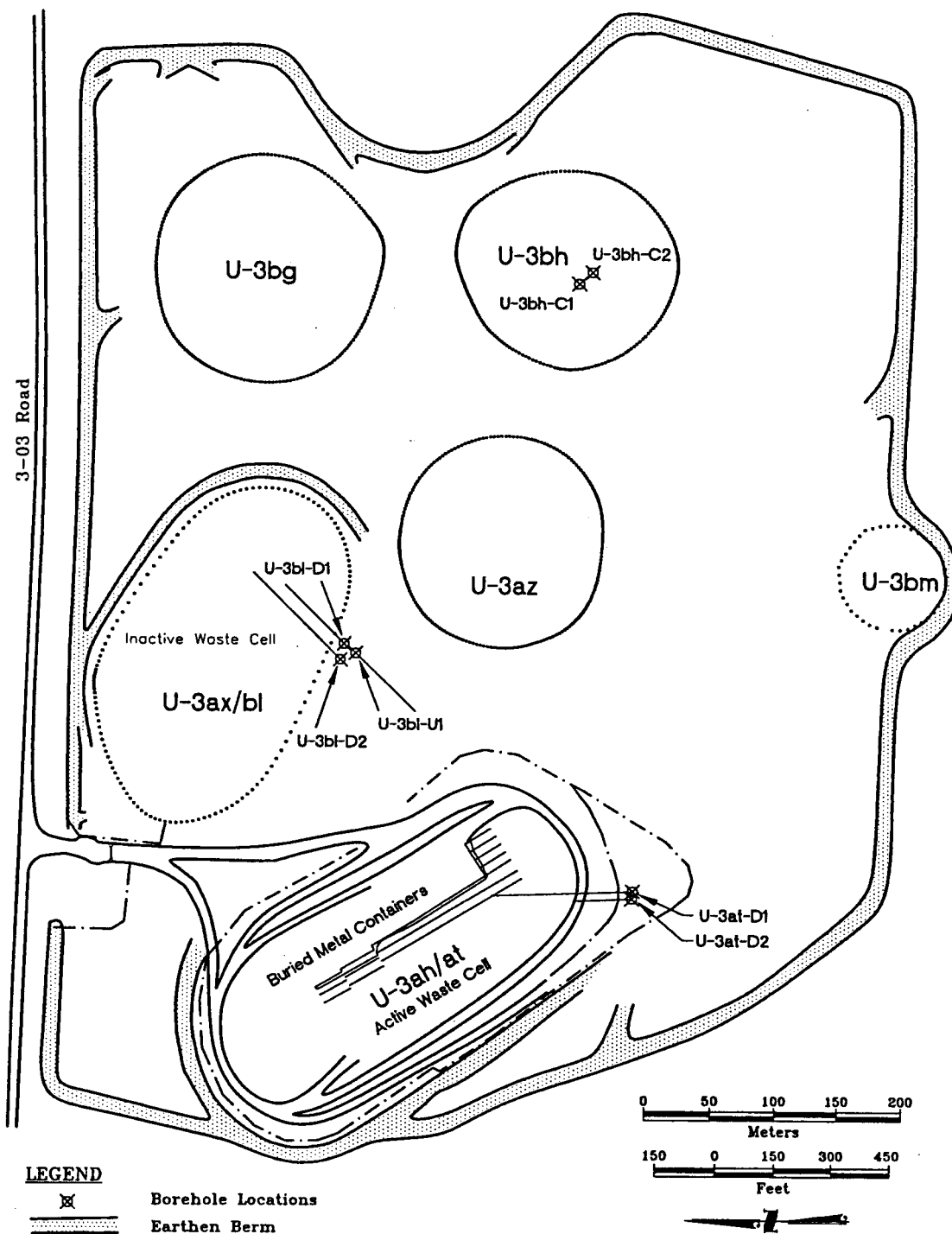


Fig. 1. Location map of the boreholes in and around the five subsidence craters in the Area 3 Radioactive Waste Management Site located in Yucca Flat on the Nevada Test Site in Nye County, Nevada.

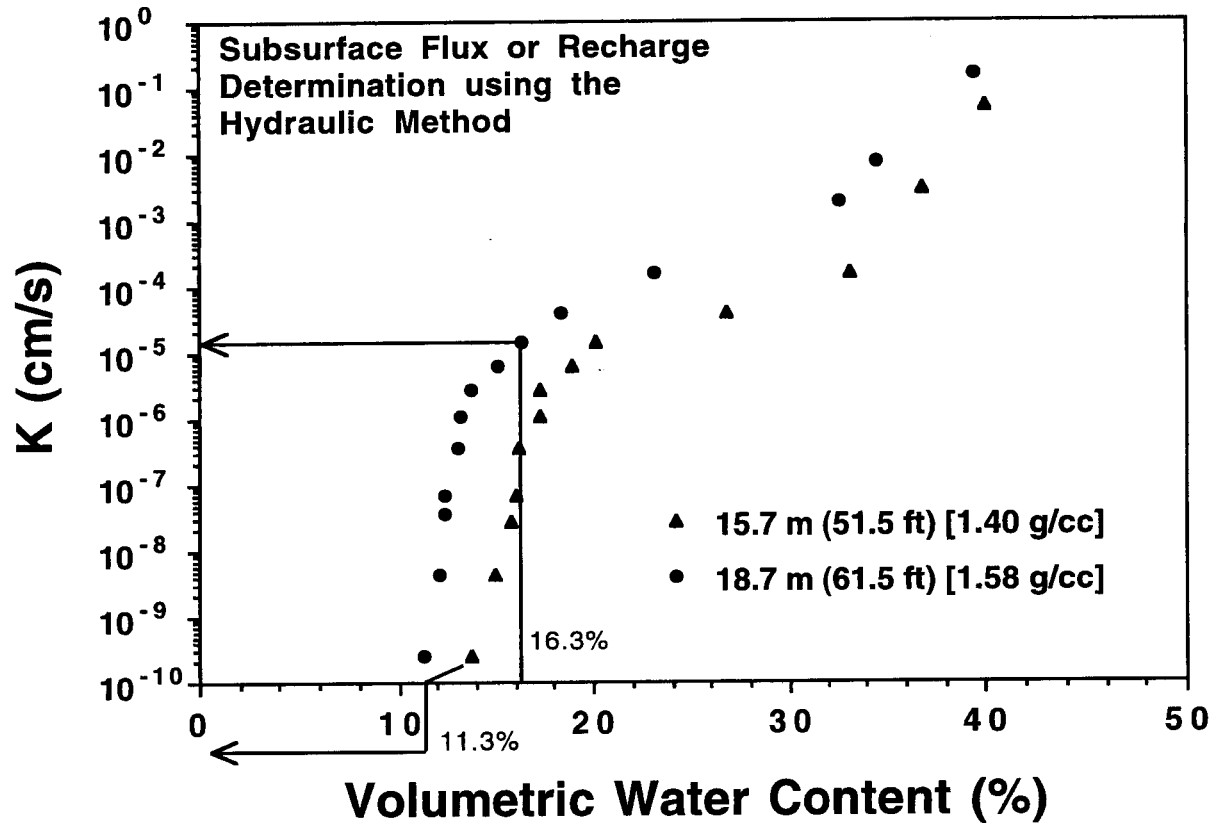


Fig. 2. The hydraulic method of subsurface flux determination using hydraulic conductivity curves and field moisture contents for two samples from borehole U-3bh-C1.

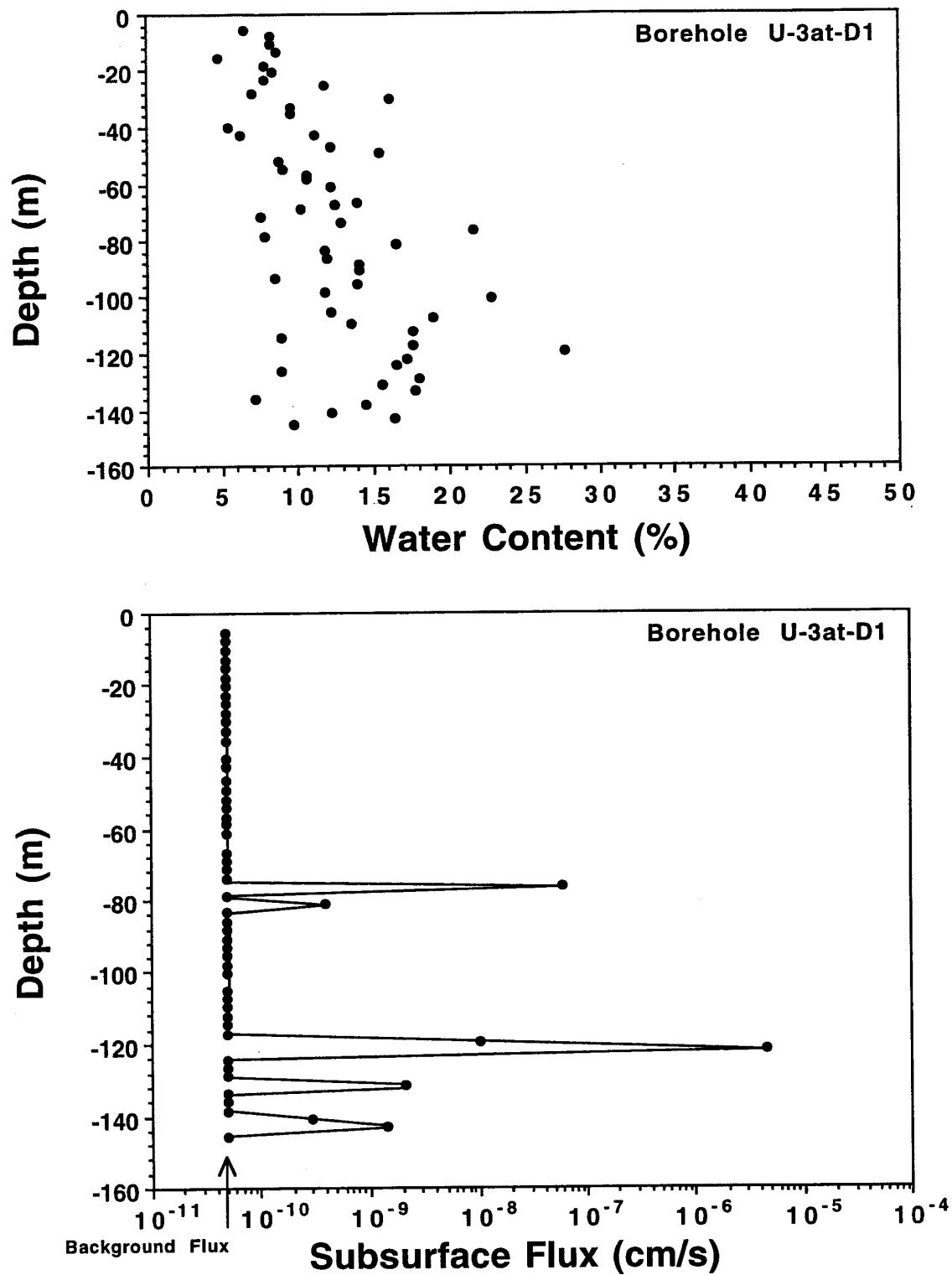


Fig. 3. The water content as a function of depth and the subsurface flux determination as a function of depth in borehole U-3at-D1.

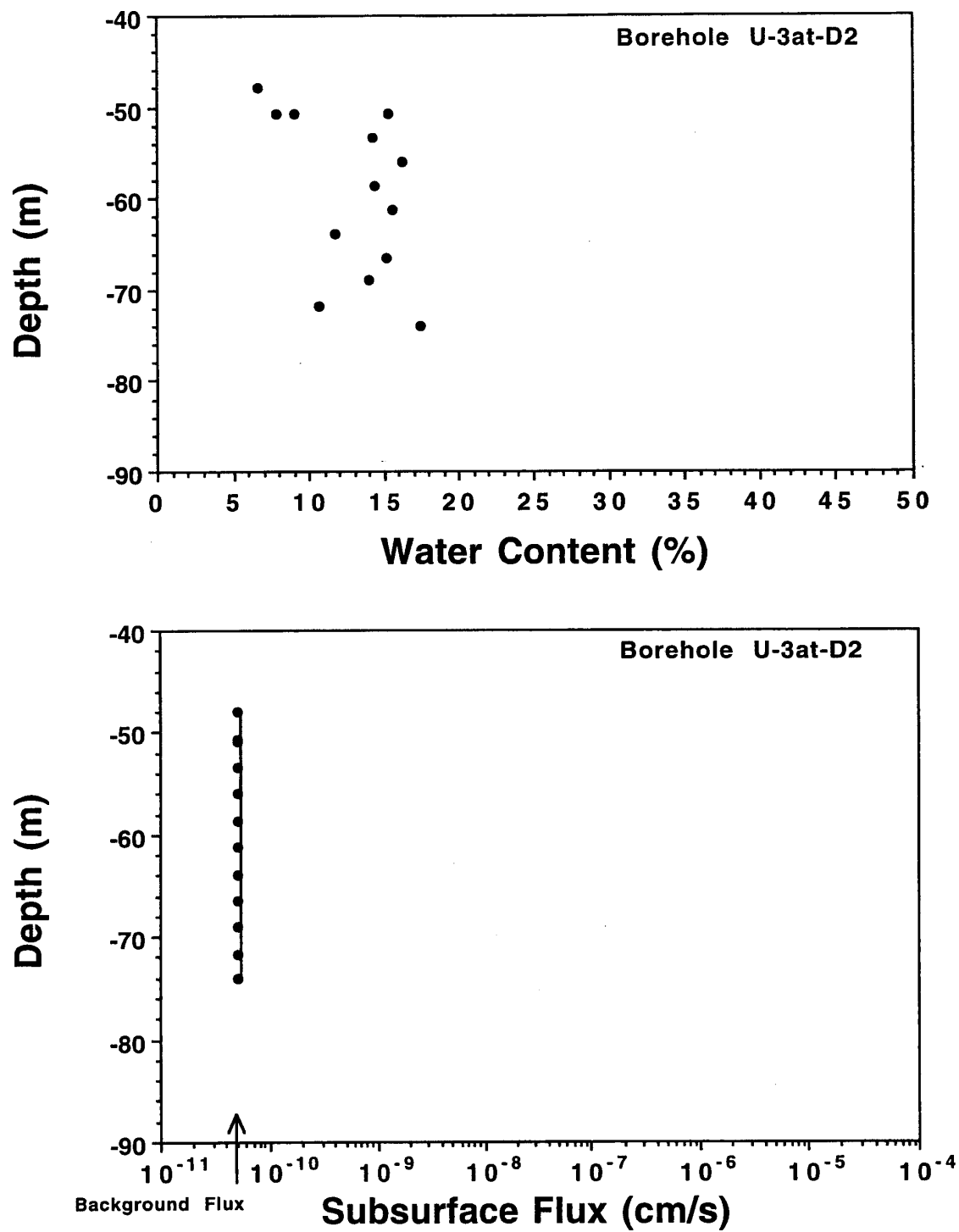


Fig. 4. The water content as a function of depth and the subsurface flux determination as a function of depth in borehole U-3at-D2.

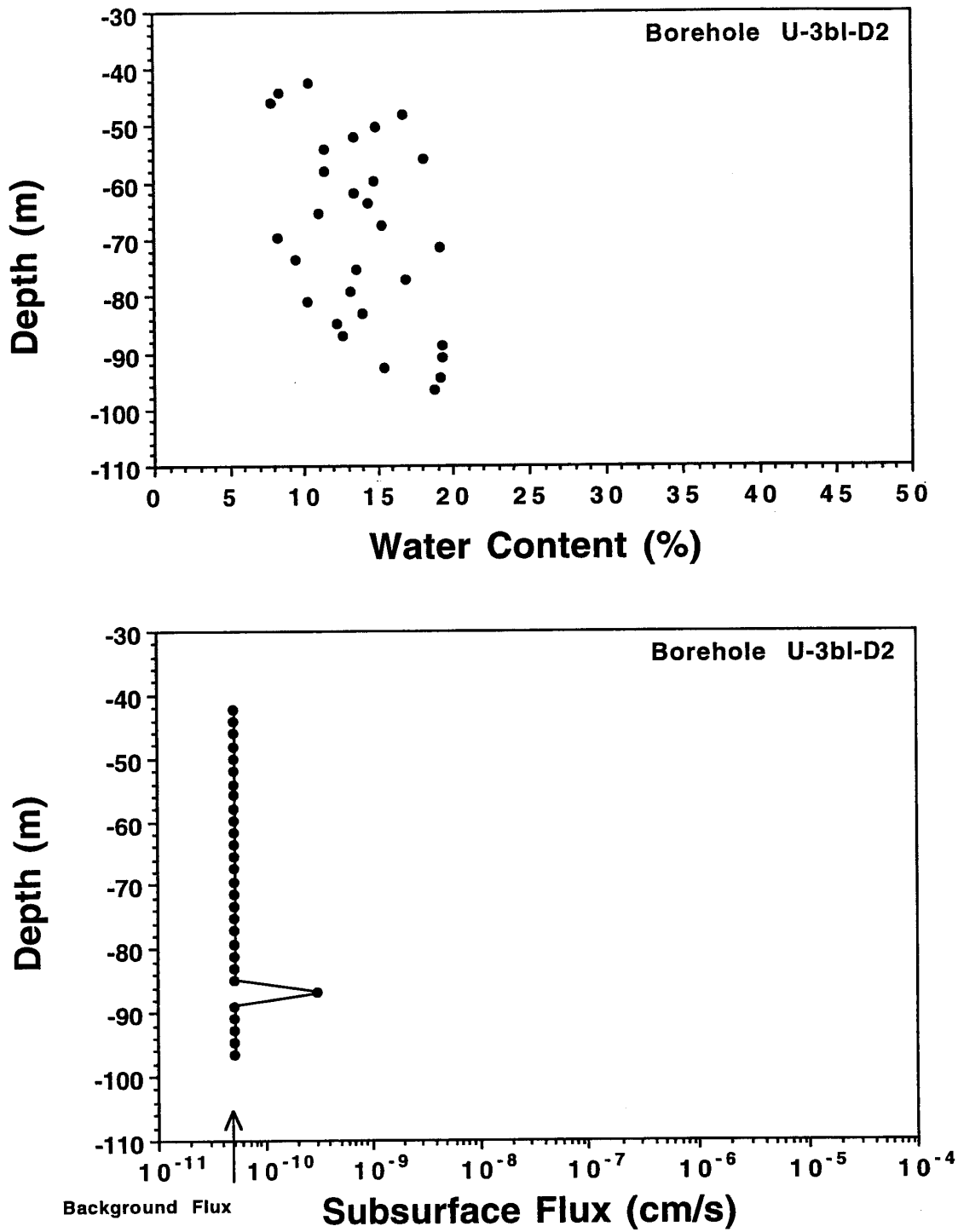


Fig. 5. The water content as a function of depth and the subsurface flux determination as a function of depth in borehole U-3bl-D2.

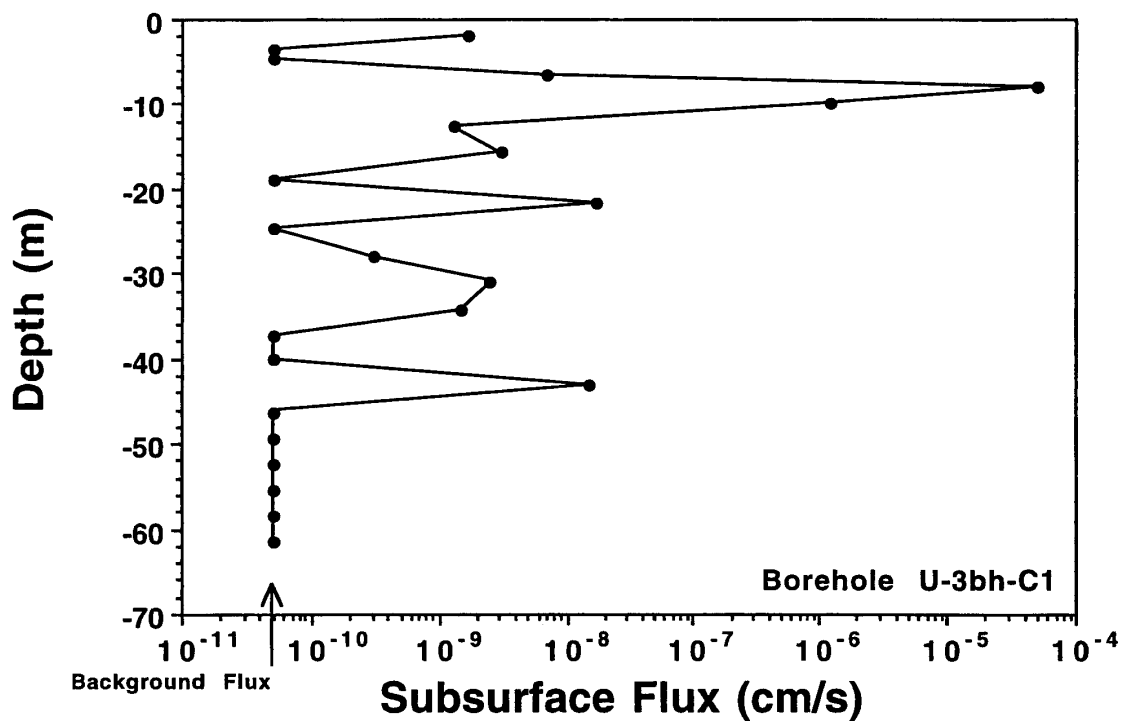
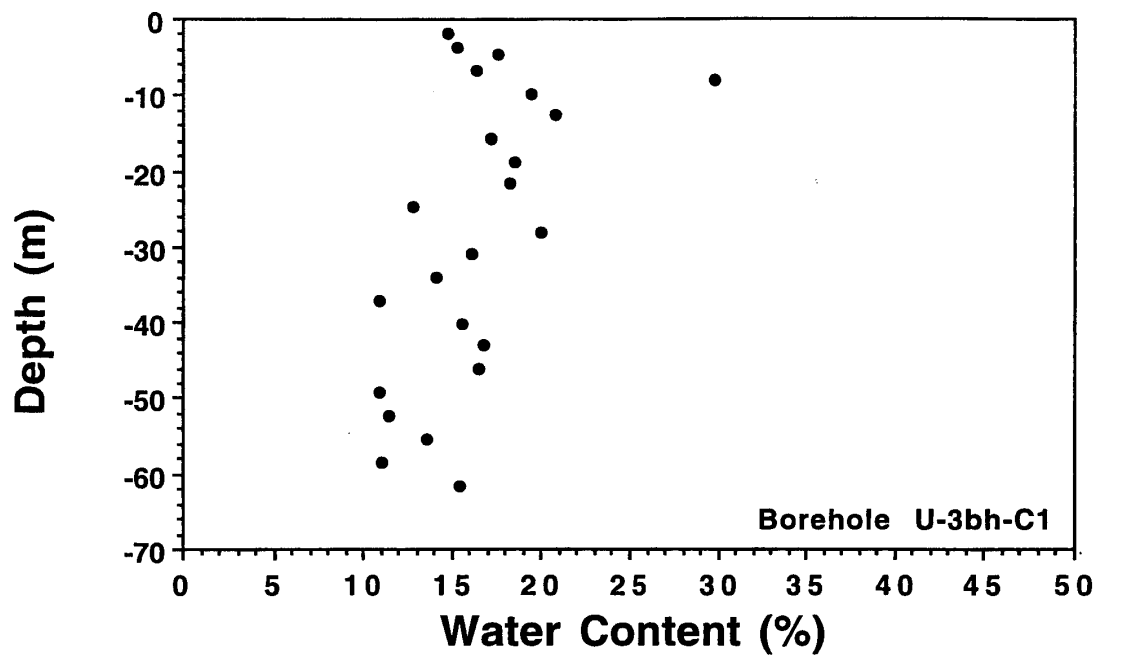


Fig. 6. The water content as a function of depth and the subsurface flux determination as a function of depth in borehole U-3bh-C1.

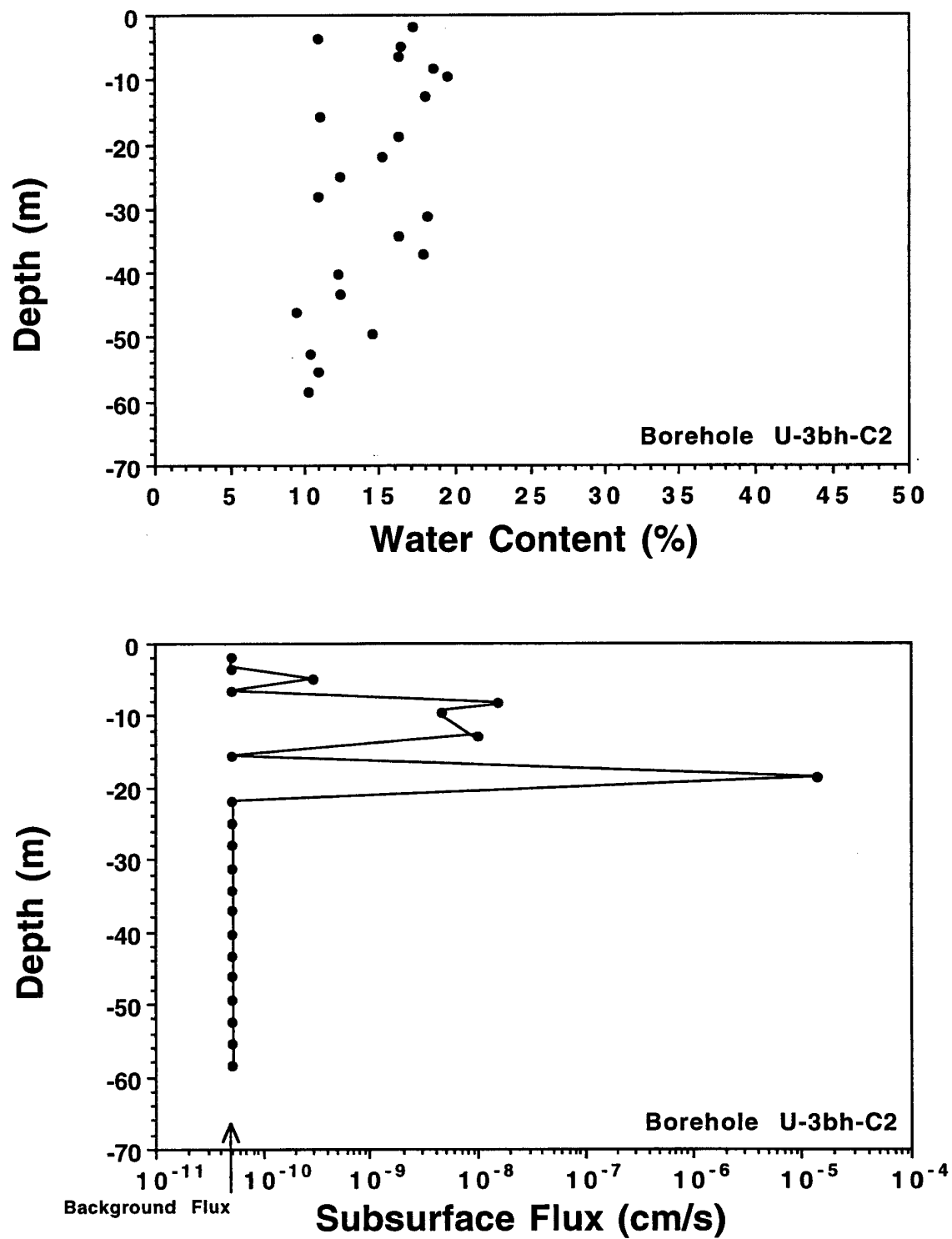


Fig. 7. The water content as a function of depth and the subsurface flux determination as a function of depth in borehole U-3bh-C2.

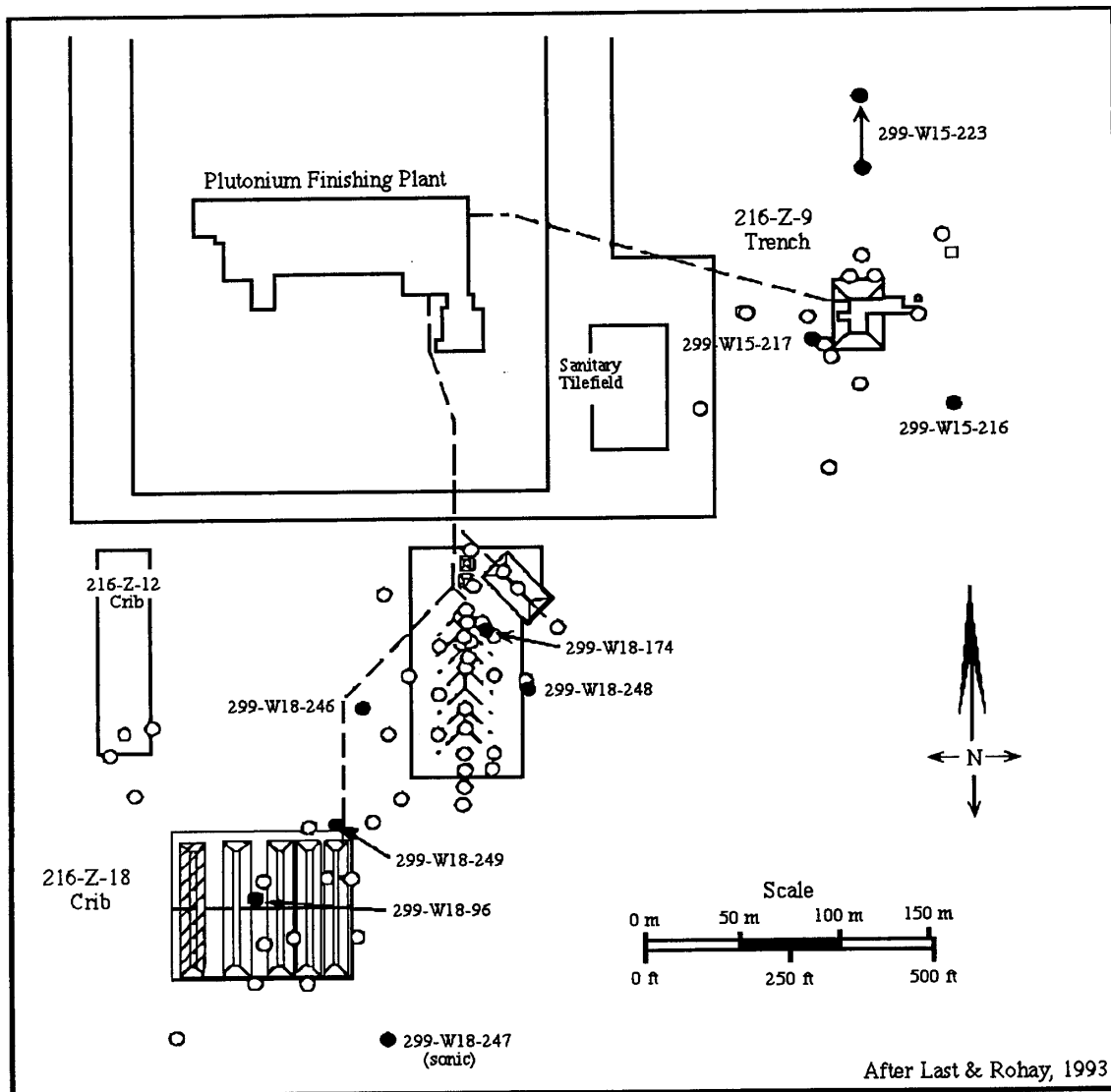


Fig. 8. The VOC-Arid ID Site in the 200 West Area at the Hanford Site. Numbered boreholes shown are the same as in subsequent cross-sections.

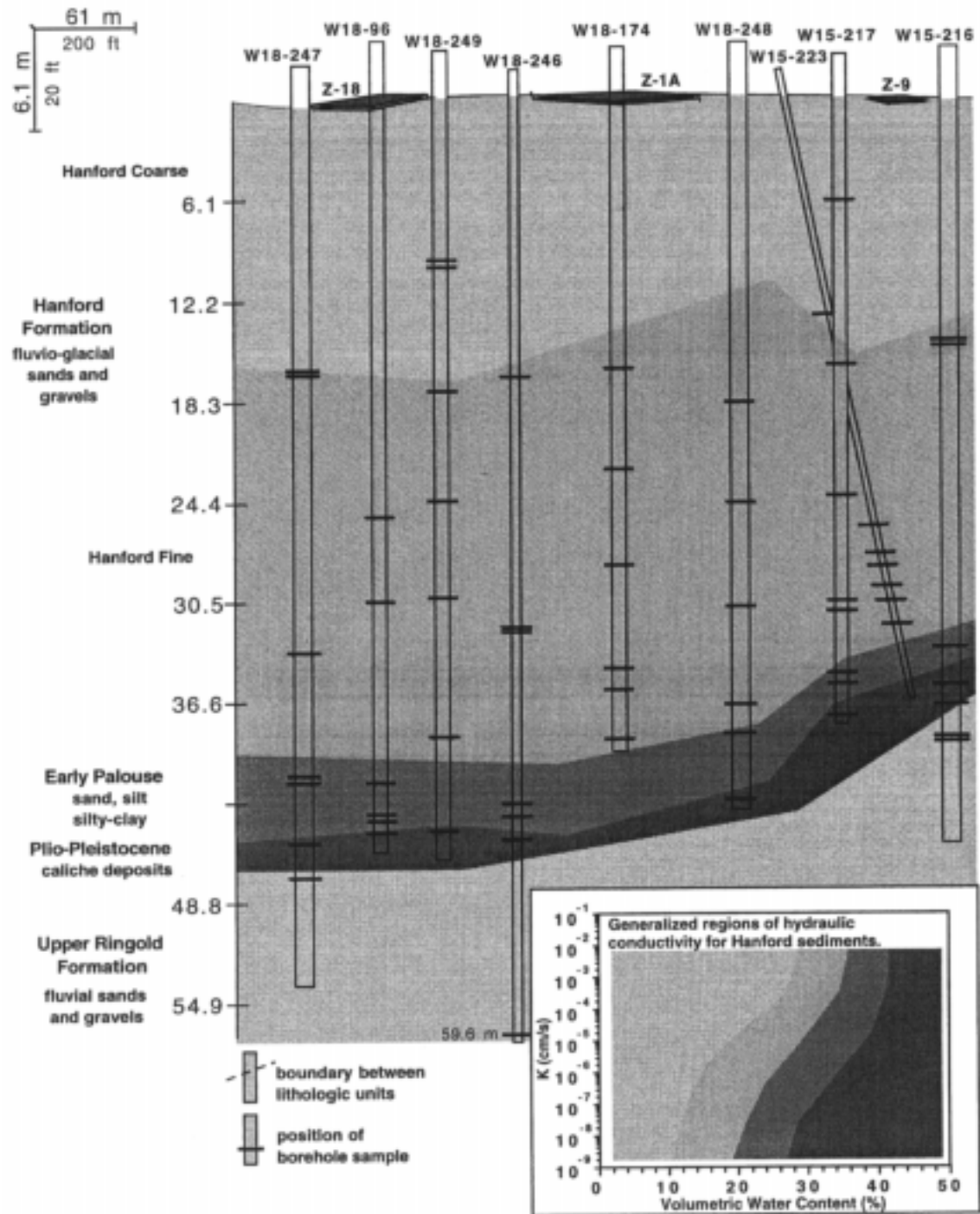


Fig. 9. Hydrostratigraphic Map of Subsurface Below Z-Plant Inferred from Lithology and Sediment Type Looking NW from 241-U.

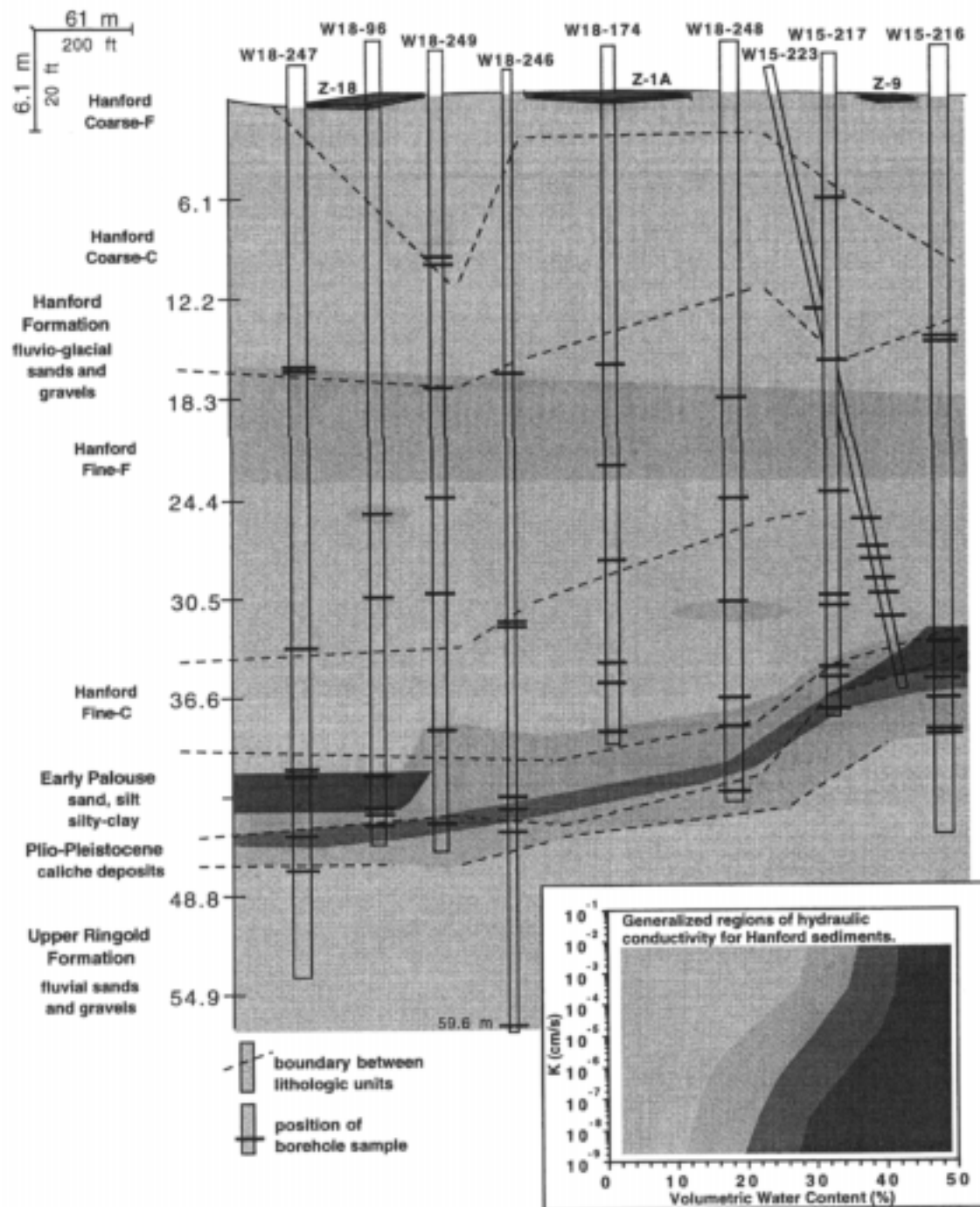


Fig. 10. Hydrostratigraphic Map of Subsurface Below Z-Plant Determined from Actual Hydraulic Behavior Measured in the UFA.

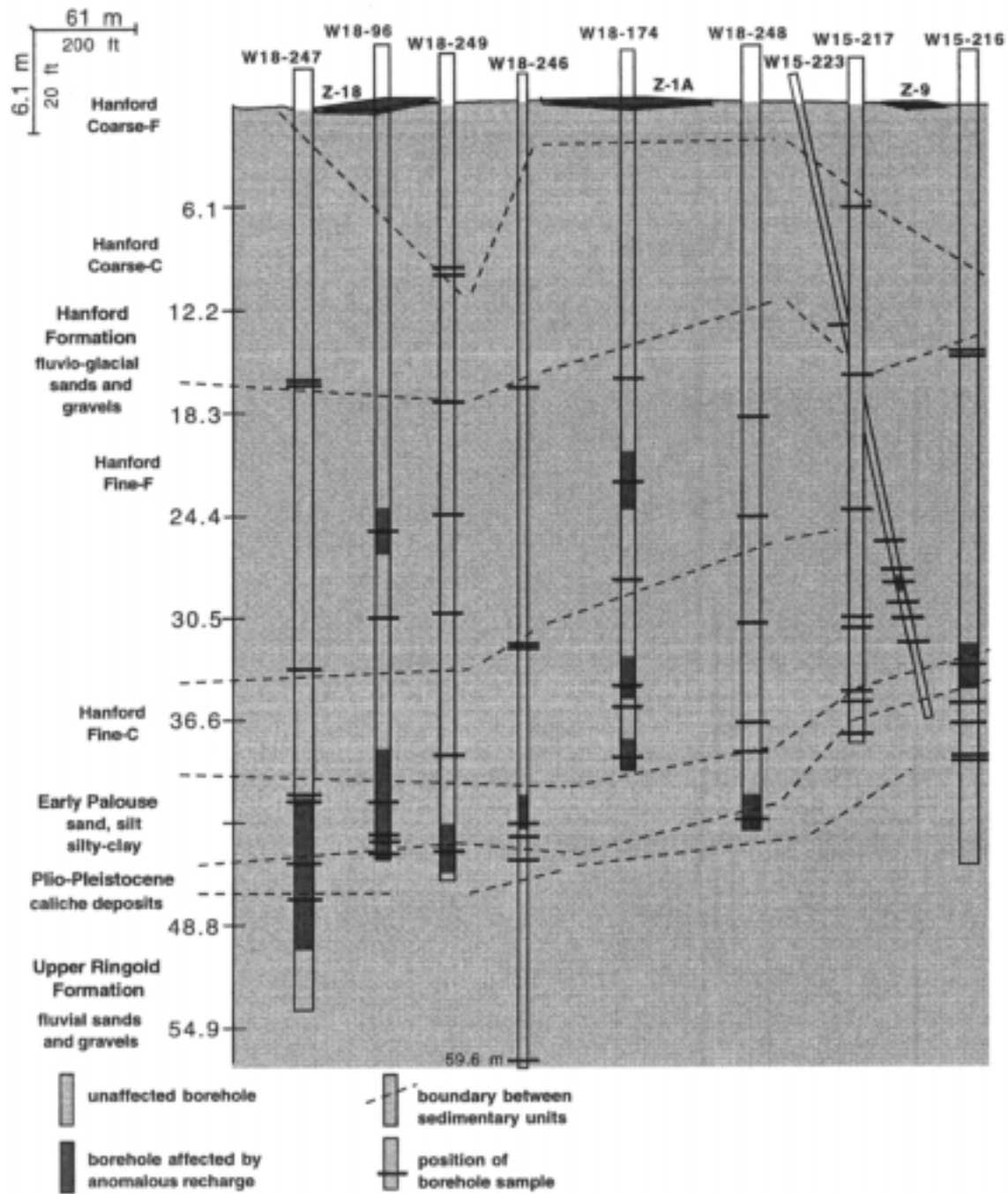


Fig. 11. Distribution of Borehole Samples Below Z-Plant Affected by Anomalously High Flux or Recharge.

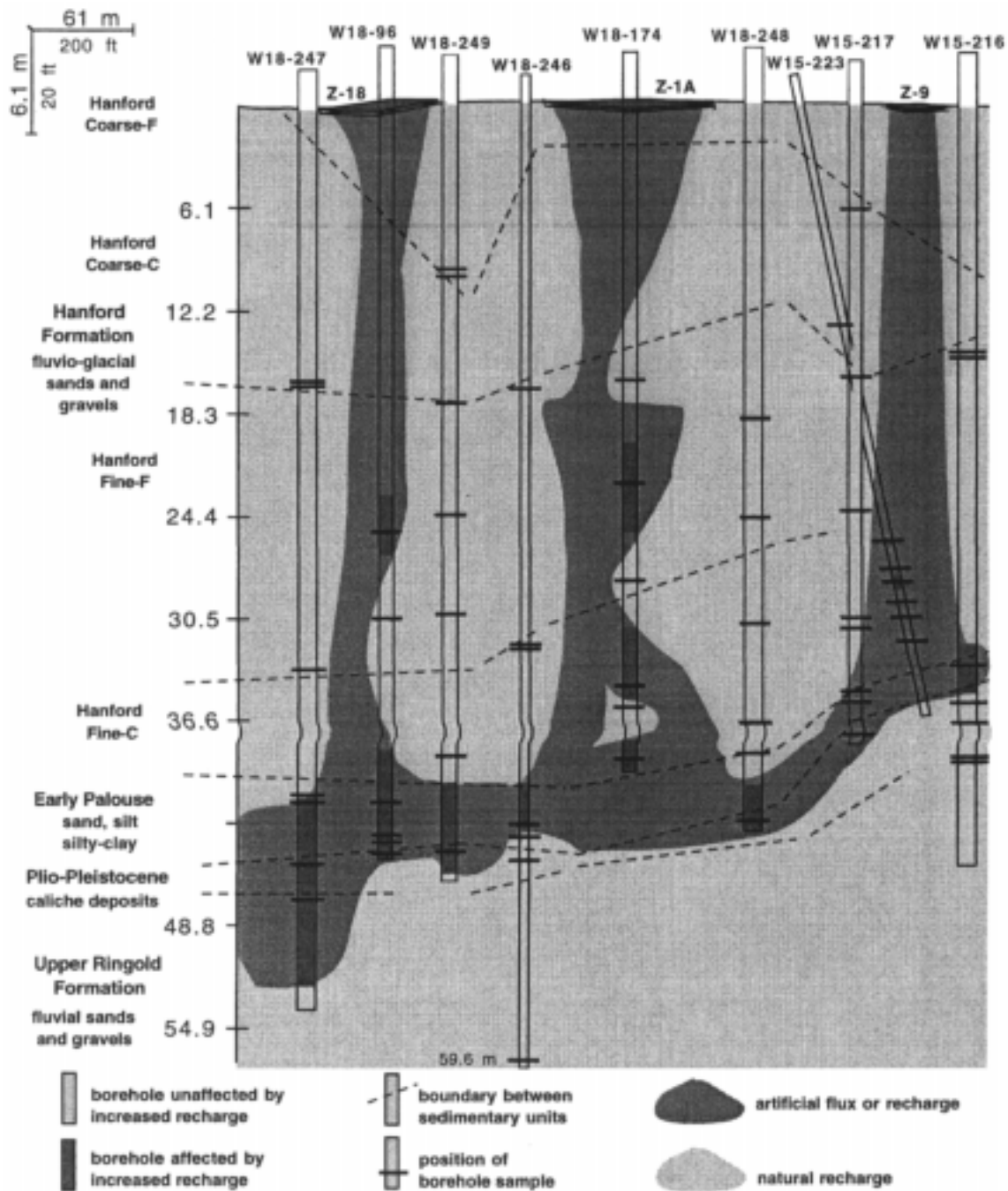


Fig. 12. Recharge or Subsurface Flux Distribution Map Below Z-Plant Showing Possible Plume Geometry.

Modeling of Water Flow and Tracer Breakthrough Curves in Fractured Basalt (Lessons Learned and Future Investigations)

C. Doughty and B. Faybishenko
Lawrence Berkeley National Laboratory

Introduction. The fractured basalt of the Snake River Plain in Idaho is highly heterogeneous, with a fracture pattern that is strongly structured. This makes the connectivity of the conductive fractures of key importance in determining flow and transport patterns. Hence the medium is not well suited to a stochastic representation as a correlated random field, as is conventionally done using geostatistics, because such representations, while maintaining information on spatial correlations, do not preserve information about connectivity (Doughty, 1998). While recognizing the 3D nature of flow in fractured basalt, we used a relatively simple 2D numerical model with a deterministic representation of the observed fracture pattern to simulate water flow and conservative tracer migration in the subsurface during a ponded infiltration test at the Box Canyon site in Idaho (Faybishenko et al., 1998).

Model Design. We used the numerical simulator TOUGH2 (Pruess, 1987, 1991) and created a vertical cross-section model of 20 by 20-m extent, using a regular rectangular grid with a 0.5-m discretization, as shown in Figure 1. The domain properties were assigned using a deterministic approach designed to approximately duplicate the fracture pattern and types of rocks observed at the Box Canyon cliff face and in boreholes. Grid blocks representing vertical fractures were assigned high vertical permeability to allow preferential flow through the fracture, low horizontal permeability to limit fracture/matrix flow, and small porosity to account for the small aperture of the fracture. For grid blocks representing horizontal fractures, the assignment of horizontal and vertical permeability was reversed. Other hydrogeologic components present include a shallow soil layer overlying the basalt, lenses of vesicular basalt, blocks of massive basalt, and an underlying sub-horizontal rubble zone, all of which were assigned isotropic permeabilities. Processes modeled include two-phase (water and air) flow and transport of a conservative liquid tracer. The pond is treated as a constant pressure, constant concentration boundary.

Infiltration Rate and Preferential Flow. During the infiltration test, the measured infiltration rate from the pond steadily decreased with time, probably due to fracture clogging and microbial growth. Despite the fact that the model does not explicitly include a temporal decrease in the hydraulic conductivity of any layer, it does show a temporal decrease in the infiltration rate. Sensitivity studies show that the infiltration rate from the pond is sensitive to the intrinsic permeability of the highest permeability column-bounding fractures, which are shown as primary vertical fractures in Figure 1, and the water retention and unsaturated hydraulic conductivity functions, in addition to the permeability of the soil layer immediately underlying the infiltration pond. It appears that the decreasing fracture density with depth results in an overall decrease in rock permeability with depth, which also contributes to the decrease in the infiltration rate.

The model predicts an irregular pattern of flow through the subsurface during the ponded infiltration test, with a significant increase in the moisture content in and around the zones of the highest permeability in vertical fractures (Figure 2). The geometry of the fracture pattern leads to a funneling effect. Therefore, flow is localized in only a few

locations as fracturing becomes sparse. Modeling of moisture content changes is consistent with field observations and shows that vertical preferential flow occurs primarily along the column-bounding fractures, followed by imbibition into smaller fractures and the surrounding rock matrix. Layers and lenses of vesicular basalt, a central sub-horizontal fracture zone, and the underlying rubble zone provide conduits for lateral flow of both water and air.

The Role of Entrapped Air. Modeling results suggest that airflow and entrapped air significantly affect infiltration, creating a more non-uniform moisture distribution in the subsurface and decreasing the infiltration rate by about 30%. Examination of gas-phase flow paths shows that while much of the air is purged from the subsurface region below the pond via lateral flow through the central fracture zone and rubble zone, some does become entrapped and subsequently flows upward into the pond through the column-bounding fractures.

Tracer Breakthrough Curves. Figure 3 shows a wide range of behaviors among the tracer breakthrough curves (BTCs) for the locations identified in Figure 1. For example, curves 1 and 4 show sharp peaks, suggesting strongly preferential flow with little fracture/matrix interaction. Curves 2, 3, 5, and 7 show long tails, indicating significant matrix diffusion. Curves 4, 5, 6, and 7 show double humps, suggesting the convergence of multiple flow paths. The BTC at a given location depends on the entire flow path from the pond to that location, and may also be affected by the geometry of flow below the monitoring point.

Conclusions. 2D Numerical modeling using TOUGH2 was conducted using a relatively simple model designed to represent deterministically the main geometrical and geological features of the fractured basalt at the Box Canyon site in Idaho, and in particular to duplicate the connectivity of the main conductive features. This modeling approach is a useful tool to obtain a general understanding of the effects of geometry, types of rocks, and entrapped air, which cannot be monitored in detail in the field or laboratory, on water and air velocity fields, the infiltration rate, and tracer breakthrough curves.

Unresolved Problems to be Investigated. There are problems associated with representing infiltration through a 3D fracture network with a 2D model. In a 2D model, an infiltrating plume cannot spread laterally enough, and, in general, water becomes trapped more easily because the connectivity of the model is too low. Additionally, higher resolution of the fractures would allow a better treatment of fracture intersections, including relaxing the present assumption of full mixing. Incorporating heterogeneity within fractures would enable us to represent channeling of flow in fractures. Higher resolution at fracture/matrix interfaces would enable an improved representation of transient fracture/matrix interaction processes. Based on a comparison with field observations, it would be desirable to include in the model the effect of a time-variable hydraulic conductivity of the near-surface zone and fractures. All of these issues can be addressed within the scope of the present approach using TOUGH2. As we incorporate additional features that are quite uncertain, such as the aperture distribution within a fracture, it may prove beneficial to develop a hybrid deterministic/stochastic approach, in which less-understood features are treated stochastically within the deterministic representation of the fracture geometry.

References

Doughty, C., Mathematical Modeling of a Poned Infiltration Test in Unsaturated Fractured Basalt at Box Canyon, Idaho, Rep. LBNL-40630, Lawrence Berkeley National Laboratory, Berkeley, CA, 1998.

Faybishenko, B., R. Salve, P. Zawislanski, C. Doughty, K.H. Lee, P. Cook, B. Freifeld, J. Jacobsen, J.B. Sisson, J. Hubbell, and K. Dooley, Poned infiltration test at the Box Canyon site: Data report and preliminary analysis, Rep. LBNL-40183, Lawrence Berkeley National Laboratory, Berkeley, CA, 1998.

Pruess, K., TOUGH user's guide, Rep. LBL-20700, Lawrence Berkeley Laboratory, Berkeley, CA, 1987.

Pruess, K., TOUGH2 - A general-purpose numerical simulator for multiphase fluid and heat flow, Rep. LBL-29400, Lawrence Berkeley Laboratory, Berkeley, CA, 1991.

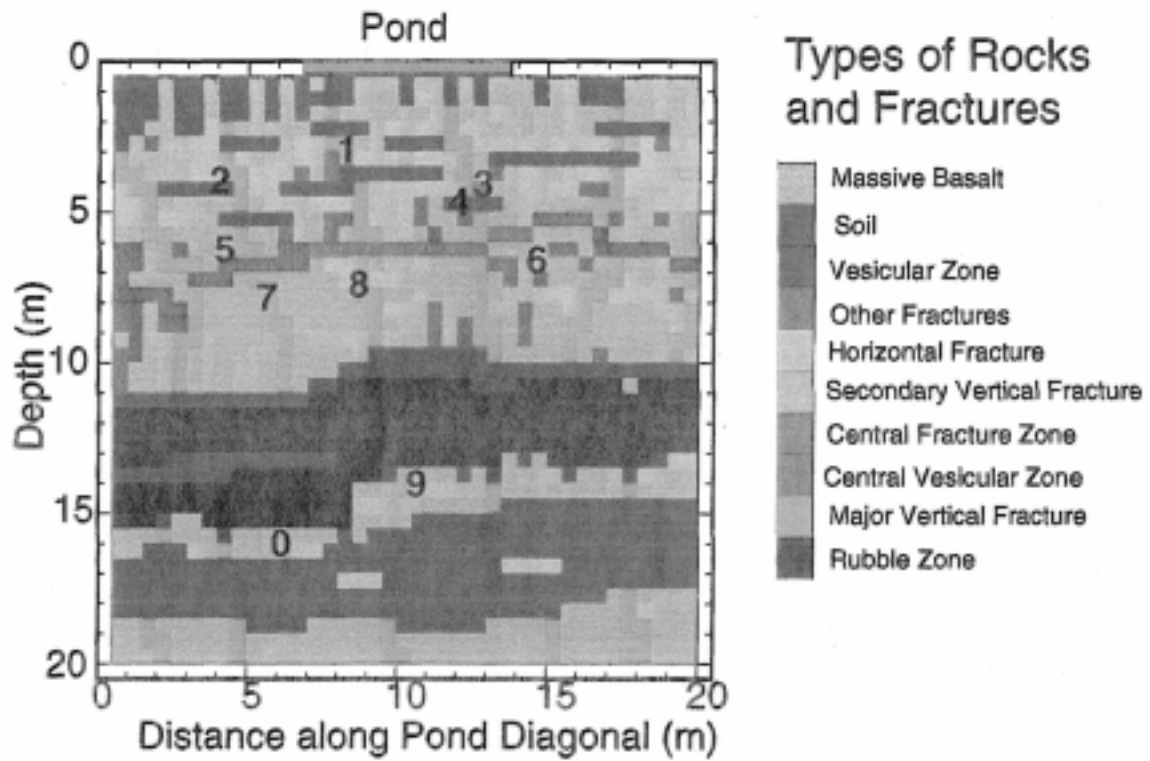


Figure 1. The geometry and types of rocks used for the 2D modeling of the Box Canyon infiltration test. Location numbers correspond to the BTC labels shown on Figure 3.

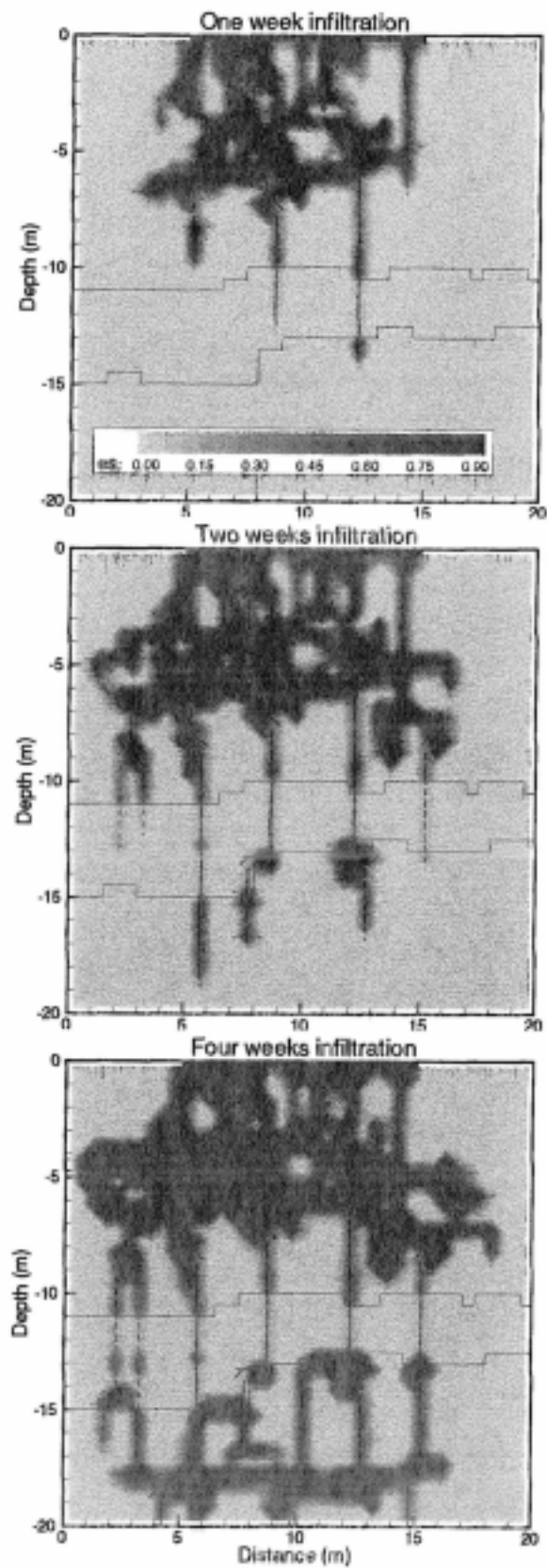


Figure 2. Simulated change in liquid saturation from the initial state and liquid flow field at a series of times during the infiltration test.

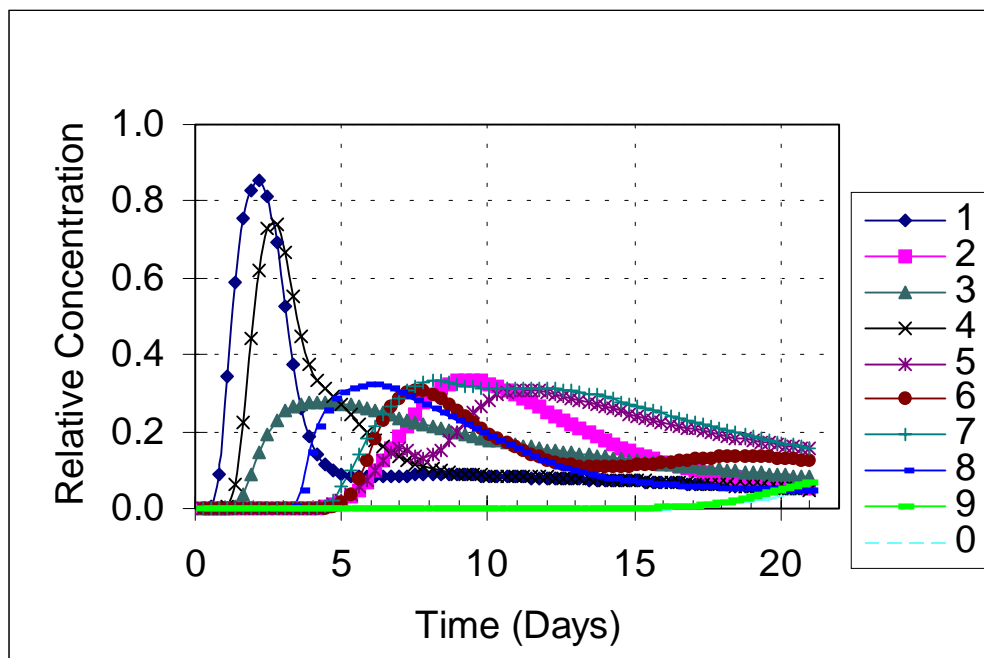


Figure 3. Breakthrough curves obtained for different locations shown in Figure 1.

FISSURES IN YUCCA FLAT DRY LAKE BED, NEVADA TEST SITE

Donald C. Helm, Morgan State University

Introduction

Fissures are observed on the dry lake bed (playa) of Yucca Flat which is located on the Nevada Test Site in the state of Nevada. They are surface expressions of long and deep cracks that extend from land surface to the water table at depth. During rainstorms, these cracks represent paths of preferential vertical flow of water through the vadose zone. Any pollutants on or near the land surface within the drainage area would tend to be washed towards these cracks with surface flow. They would also tend to be carried through the cracks to the underlying aquifer more swiftly than standard computer codes currently predict. Understanding the mechanisms that cause such cracks and predicting where and when fissuring events occur are important areas of research.

Description of the Fissures

Four major fissures are located on the south end of Yucca playa [Doty and Rush, 1985]. As shown on Figure 1, they are between one and two kilometers long; trend southwest to northeast; are roughly parallel to each other; are separated from a nearest neighbor by a few hundred meters; are roughly orthogonal to the trace of Yucca fault; and are roughly orthogonal to the direction of ground water flow (both before and after aquifer development). The fissure events time-step towards the south. The northernmost two occurred prior to 1950. The third occurred in 1960 and extended itself towards the northeast in 1966. The fourth occurred in 1969 with subsequent extension towards the northeast off the dry lake bed onto the surrounding desert. This observed extension of the fissure off the playa suggests that fissures originally mapped as faults on the desert to the west of the dry lake bed are likely to be extensions of earlier fissure events. Wells were drilled near the southern end of the playa in 1961 and 1962. The two northerly fissures predate not only the pumping, but also the use of Yucca Flat for nuclear weapons tests.

Characteristic Observed Processes

Fissures throughout the American southwest, including those on the Yucca playa, are observed first as a hairline crack with an aperture of a few millimeters [Bell, 1981]. Cracks migrate upwards from depth and intercept the land surface as a final step, before erosional processes take over. Subsequent rainstorms wash surface sand and other material into the crack. A linear string of tiny gullies (each about the size of a football) is an intermediate stage of erosional development. These tiny gullies are gradually joined. Additional cracking and the resulting erosional gullies may extend the lineaments with time. A long erosional gully (one to two kilometers long) is an eventual result and may become about a meter wide and a meter deep. Subsequent erosion tends to fill the gully.

As a case study, Doty and Rush [1985] used water inflow tests to determine the depth of the crack that underlies the southernmost fissure on Yucca dry lake bed. Their study concluded

that the crack extends at least to the limestone bedrock at a local depth of about 407 meters (1335 feet). This Paleozoic limestone serves as the local aquifer.

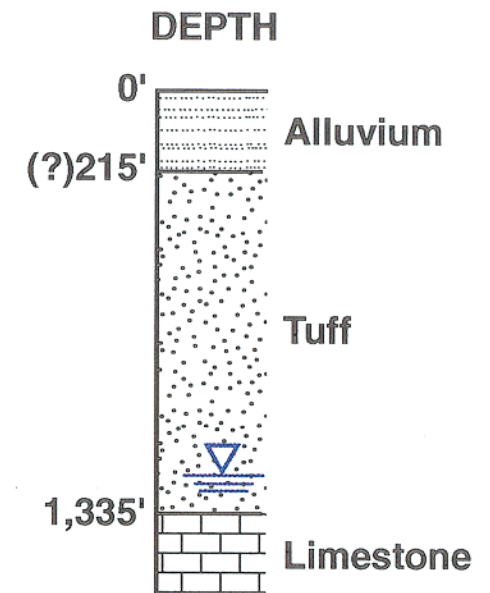
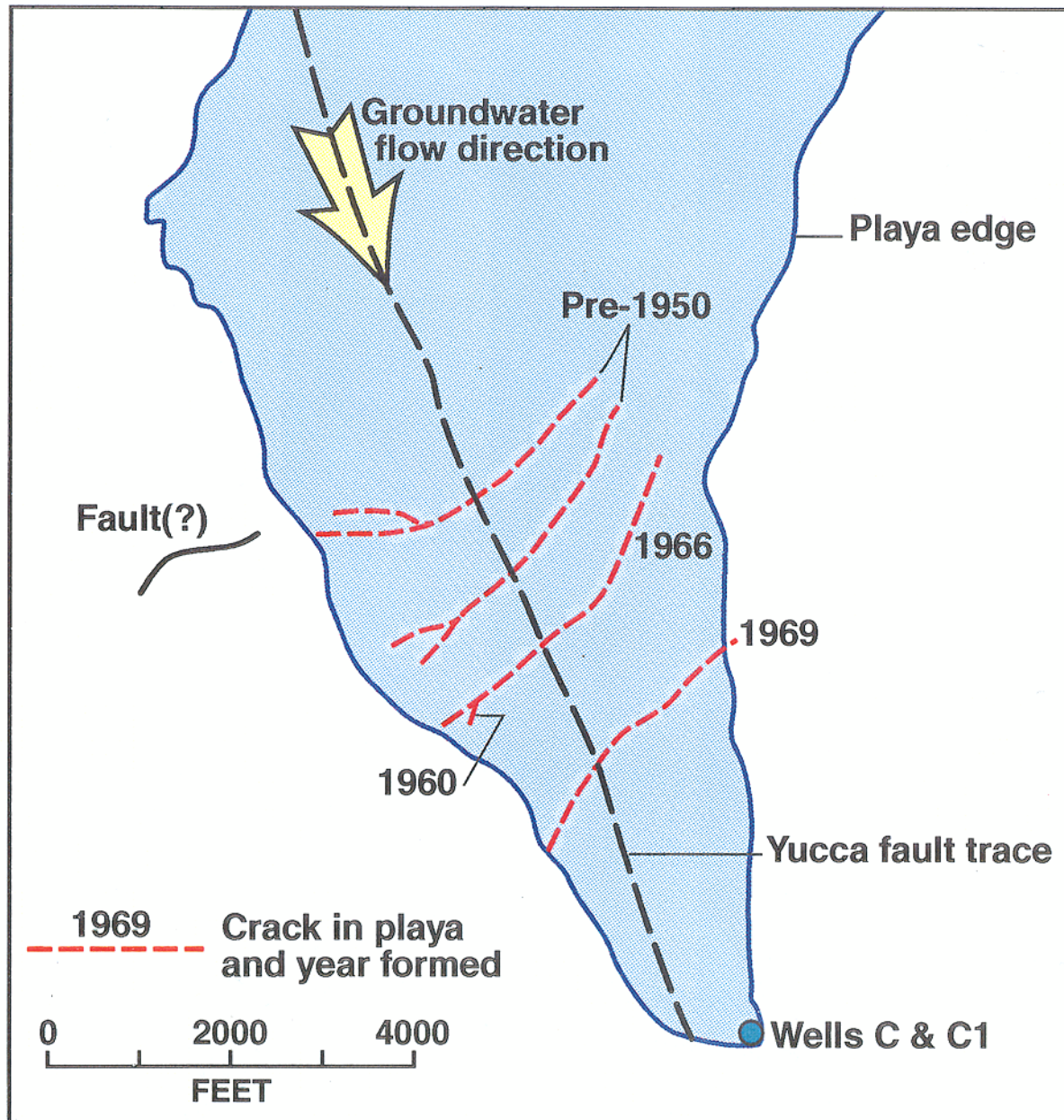
Mechanisms for the Initial Development of Cracks

Hydraulic forces are known to significantly deform aquifers that underlie the base of the vadose zone [Helm, 1994]. Laterally flowing ground water can move the skeletal frame of the aquifer horizontally by viscous drag on the grains. The resulting horizontal tensile zones, in the form of enhanced porosities, migrate upwards through the vadose zone from depth and intersect the land surface as a final step. In arid climates, such as that found at Yucca Flat, a tensile porosity heterogeneity might express itself as a vertical crack.

This hydraulic mechanism is distinct from a bending plate mechanism. The latter assumes the vadose zone is analogous to a plate that bends downward and inward towards the center of a real or supposed subsidence bowl. The bending plate mechanism requires the lateral tensile zone and the resulting enhanced porosity near land surface to occur along the shoulder of the bending bowl. Even more characteristically, it requires the tensile zone to migrate downward from the land surface. This type of downward migration is indeed observed to occur at land surface above the edges of abandoned mines and other underground excavations, but not at Yucca playa.

The straightness, length, parallel orientation, and depth of the cracks argue against their originating as desiccation cracks, as does the fact that they extend themselves well beyond the dry lake bed. Doty and Rush [1985] do not even consider this alternative.

More recent direct measurements by the USGS in Las Vegas valley (T.J. Burbey, unpublished data, 1997) using downhole inclinometers confirm the significant horizontal movement of the pumped aquifer at depth and the corresponding drag on the overlying vadose zone. Geologic structure and other heterogeneities at depth tend to control where related porosity heterogeneities occur within the vadose zone [Bell and Price, 1992]. Aquifer flow and possibly seismic events are likely triggers for these porosity heterogeneities when they initially develop at the base of the vadose zone.



Cracks of Yucca Lake Playa

Case Study: Inverse Modeling for Field-Scale Hydrologic and Transport Parameters of Fractured Basalt

Swen O. Magnuson, INEEL

1.0 BACKGROUND

The Subsurface Disposal Area (SDA) located in the southwestern portion of the Idaho National Engineering and Environmental Laboratory (INEEL) has been the subject of a series of environmental assessments dating back to 1970. The SDA is a radioactive disposal site that has received and buried transuranic and low-level waste in shallow pits, trenches, and soil vaults since 1952. Transuranic wastes have been stored above-grade since 1970. These wastes rest above an extensive vadose zone that is approximately 180 m thick and is comprised primarily of fractured basalt flows with thin sometimes continuous interbeds.

Early environmental assessments conducted for wastes disposed at the SDA used a greatly simplified conceptual model to represent water movement and contaminant transport in the vadose zone. The simplified model ignored the fractured basalt portion of the vadose zone and considered only the sedimentary interbeds. Water and contaminant movement through the fractured basalt was conservatively assumed to be instantaneous. The fractured basalts were ignored because there was a very limited basis by which to describe representative water movement within them. Although the basalt matrix had previously been hydrologically characterized at the core-scale (Bishop, 1991) and had a low saturated hydraulic conductivity, on the order of 10^0 to 10^1 m/yr, describing

representative water movement in the basalts was made difficult by having to include the effect of the fractures in a partially saturated flow regime.

A large-scale infiltration test was conducted in 1994 to provide a set of field-based observations to use in developing a description of the hydrological and transport properties for the fractured basalt portion of the vadose zone. Wood and Norrell (1996) present a complete detailed summary of the infiltration test. Dunnivant et al. (1998) present a shorter summary. In brief, water was ponded on the ground surface in a 180-m diameter circular basin. Monitoring equipment installed in 70 wells in a radial network provided information on the advance of water and tracers into the subsurface and the development of a perched water body on a thick sedimentary interbed at a depth of 55 m. These wells were both inside the infiltration basin and in two concentric rings (B ring and C ring) at distances of 15 and 90 m from the basin. Both conservative and non-conservative tracers were used and were introduced as a continuous pulse for 11 days. Ponded conditions were maintained for a total of 45 days.

2.0 SIMULATION STUDY OBJECTIVE

This case study summarizes results of an inverse modeling study of the large-scale infiltration test (Magnuson, 1995). The objective in the modeling study was to calibrate simulations of flow and transport to the vertical advance of the wetting front, the radial development of the perched water body, and the breakthrough curve of the conservative tracer in the perched water body. Two hydrologic conceptual models were considered. The first conceptual model treated the fractured basalt portion of the vadose zone as an equivalent porous media in which only fractures contributed to flow. The basalt matrix was considered to have a permeability low enough that it did not effect flow and was

therefore neglected. The second conceptual model treated the fractured basalt as a dual-porosity media in which both the matrix and the fractures influence the movement of water and contaminants.

It is important to realize that, in a modeling study of this type, the objective was not to exactly match each and every hydrologic or tracer concentration measurement. The data were too voluminous and small-scale spatial heterogeneity could not be described nor feasibly taken into account. Rather, the overall objective was to obtain field-scale hydrologic and transport descriptions that could be used in flow and transport simulations for risk assessments at the SDA. As such, the intent was to mimic the **general character** of flow and transport observed in the infiltration test. The TETRAD code (Vinsome and Shook, 1993) was used to simulate the infiltration basin for both the single-porosity and dual-porosity representations of the fractured basalt portion of the vadose zone. The code has complete multi-phase, multi-component capabilities.

3.0 LITHOLOGY AND SIMULATION GRID

The simulations were done using a two-dimensional vertical axi-symmetric representation of the vadose zone beneath the infiltration basin. The simulation model was built as if the lithologic contacts between the thin veneer of surficial sediments, the underlying fractured basalts, and the sedimentary interbed at a depth of 55-m were horizontal. No attempt was made to represent spatial variations in the elevation of these interfaces. The radial extent of the infiltration basin in the simulation was 91.5 m. A total of 1174 variably sized grid blocks were used. The simulations were run for 60 days following the onset of ponding. This covered the bulk of the period when sampling occurred.

4.0 CONSTITUTIVE RELATIONSHIPS

For the sediments and for the basalt matrix, van Genuchten (1980) equations from the soil physics literature were the basis for the constitutive relationships. The two-phase van Genuchten constitutive equations as adapted by Parker et al. (1987) with slight modifications to the normalized saturations terms were used.

Determining constitutive relationships for fractures continues to be an active research area. This study simply used a standard characteristic curve and applied it to the fractures. A Brooks-Corey (1966) analytical formulation was used to describe the constitutive relationships for the fractures. The general Brooks-Corey formulas implemented in TETRAD are

$$P_{c\ aw} = A_{aw}(1 - S_w)^{B_{aw}}$$
$$k_{rw} = A_w ((S_w - S_{wr}) / (1 - S_{wr}))^{B_i}$$

where

$P_{c\ aw}$ = capillary pressure between air and water (kPa),

k_{ri} = relative permeability of any phase i ,

S_i and S_{ir} = saturation and residual saturation of any phase i , and

A_{aw} , B_{aw} , A_i , B_i , are fitting parameters for the various curves.

5.0 BOUNDARY CONDITIONS

The rate of infiltration was varied to simulate the effect of ponding within the basin. Low background infiltration rates of 0.01 m/yr were assigned prior to and after ponding ponding. The infiltration rate during ponding was 0.12 m/day.

Evaluation of conservative tracer transport was included by keeping track of the types of water infiltrating in the simulation. A “clean” water infiltrated from day 0 through day 5. Then a different “tagged” water infiltrated from day 6 through 16, inclusive. Then “clean” water again infiltrated from day 17 through 35. In the simulation, the liquid phase mass or mole fractions of tagged water represented the tracer concentration normalized to the initial tracer concentration at any location. This simulated tracer concentration was compared to the normalized BTC results for the B ring monitoring locations.

6.0 METHODOLOGY AND PARAMETERIZATION

Calibration was performed in this simulation study by the direct trial-and-error method. It is important to keep in mind that inverse modeling in general does not yield unique solutions. This was the case in this simulation study. The method used in this study was to first calibrate model parameters in order to match the B and C ring hydrographs. It was found that there were multiple combinations of parameters that would yield reasonable matches to the observed perched water hydrographs. Then the evaluation of the tracer BTCs was included, and the number of possible combinations was reduced.

The overall guiding principle used in this modeling study was to obtain a simulation that matched the general character of the field test results while modifying a minimum number of parameters. For this reason not all parameters were treated as variable in order to improve the simulation agreement. Only the effective porosity, permeability, and anisotropy of the fracture domain and the permeability of the basalt matrix were varied. All other parameters were treated as constants and assigned values based on nearby hydrologic characterization data from elsewhere on the INEEL.

The relative permeability curve for the fractures was assumed to be linear. The fracture capillary pressure curve results in only slight capillary forces within the fracture. Gravity dominates by comparison. Other fracture properties necessary for the dual porosity model included the distance between fractures, the characteristic fracture aperture. These values were taken from Knutson et al. (1992).

7.0 VARIABLE PARAMETERS

The primary parameters adjusted as part of the calibration process were the permeability and the porosity of the basalt fractures. The fracture permeability was allowed to be anisotropic ($k_{v,b}$ and $k_{h,b}$) and were treated as if they were a continuum and not discrete fractures. The fracture porosity (ϕ) refers to the portion of the continuum that acts as fractures. This value was allowed to range from 0.01 to 0.05. This range was assigned in part based on an estimated “wetted volume fraction” or porosity for the fractured basalts of 0.02 (Porro and Bishop, 1995). The basalt matrix permeability (k_{bm}) was treated as a variable when dual porosity simulations were performed. The values assigned ranged from 0.1 to 10 mD. This is well within the range of reported basalt matrix permeabilities.

8.0 WETTING FRONT ADVANCE AND HYDROGRAPH COMPARISON

Initially, it was thought that the wetted porosity of 0.02 for the fractured basalt estimated by Porro and Bishop (1995) was too low. This number was considerably less than traditional estimates of basalt formation porosities which range from 0.05 to 0.15. So the low end from the traditional range (0.05) was used as the effective porosity for the fractured basalt portion of the domain in a single porosity simulation. A series of runs

were made in which first the fracture vertical permeability ($k_{v,b}$) was adjusted to match the observed advance of the wetting front. Using $k_{v,b}=250$ mD provided the best agreement to the first arrival of the wetting front. However, as part of the calibration to the hydrographs, it was found that using a higher fracture vertical permeability ($k_{v,b}=300$ mD) improved the agreement in perched water arrival at the B ring location.

The fracture horizontal permeability ($k_{h,b}$) was then adjusted in order to match the observed hydrographs at the selected B and C ring locations. It was necessary to increase the fracture horizontal permeability ($k_{h,b}$) to 90,000 mD in order to mimic the observed hydrograph at the C ring well location. Figure 1 shows the comparison between the observed and simulated perched water hydrographs for the single porosity conceptual models for an effective basalt fracture porosity of 0.05. The dashed line indicates the simulated interface between fractured basalt and the interbed. In the dual porosity model, the permeability of the basalt matrix was adjusted to improve the fit. The resulting basalt matrix permeability (k_{bm}) was 0.5 mD. The results for the dual porosity model were only slightly better in a qualitative sense and are not shown.

While the agreement between the simulated and observed hydrographs in Figure 1 appears quite good, it should be recognized that the set of model parameters that resulted in this fit is only one of several possible combinations. Non-uniqueness is a problem inherent to inverse modeling. To illustrate this nonuniqueness, a series of calibration runs was performed using effective fracture domain porosities of 0.03 and 0.01.

Although the agreement for each of these optimized fits is subjective, it can be said that in each case, the models mimic the general behavior. In each simulation, the arrival of perched water at the B ring location is very close (within ~1 day). The simulated arrival

at the C ring locations is always faster than the observed. This is undoubtedly in part due to variations in the elevation of the basalt/interbed interface and actual hydrologic properties, which the model does not capture. Also, in each case the simulated hydrograph at the B ring location drops off quicker than the observed hydrograph. Even so, it can be concluded that the general behavior is represented.

Given the demonstrated non-uniqueness of the inverse modeling results, it was difficult to determine at this point in the simulation study which set of parameters was best overall at describing the results of the infiltration test. In the next section, the observed conservative tracer BTCs were used to further refine the choice.

9.0 B RING BREAKTHROUGH CURVE COMPARISON

The simulated BTCs were obtained in a normalized sense using the mole fractions of tagged (tracer- containing) water. Single and dual porosity simulations were run with fracture effective porosities of 0.05, 0.03, and 0.01. Figure 2 shows normalized simulated BTCs for the single and dual porosity simulations with a fracture effective porosity of 0.03. Each of these simulations was performed with a longitudinal dispersivity set to 5.0 m and a transverse dispersivity set to 0.0 m. The 5 m value was selected by using the simulated set of properties that best matched the observed B ring hydrograph, varying the dispersivities, and selecting those that resulted in the best overall agreement to the shape of the observed BTCs. Shown for comparison as dotted lines are the three different B ring location BTCs after each was normalized to its own maximum value. There was some evidence that a portion of the “conservative” tracer precipitated out of solution as it passed through the surficial sediments during the infiltration test. This prevents comparisons to measured concentrations since the total tracer mass was not transported.

The simulation results indicate that the lower the effective basalt fracture porosity, the better the agreement with the general character of the B ring location BTCs. The difference resulted mainly from faster velocities both during vertical movement through the fractured basalt and within the perched water. This faster velocity resulted because, although the advance of the wetting front down to the interbed was kept the same, once near-equilibrium conditions were obtained during ponding, the same prescribed amount of water was moving through a smaller effective area. The faster velocity also resulted in water arriving at the C ring sooner than was observed. There is a trade-off in the simulations between matching the hydrograph at the C ring location and the concentration BTCs at the B ring location. Improving the match to the B ring BTCs makes the hydrograph match at the C ring worse.

There are several possible explanations for this trade-off. First, there are undoubtedly variations in the topography of the basalt/interbed interface and in the hydrologic properties of both the fractured basalt and the interbed that affect the spreading of perched water. None of these features are represented in the model. A second possibility is the effect of dead-end fractures as hypothesized in Dunnivant et al (1998). The simulation results of this study tend to support their hypothesis since the simulated breakthrough of water always occurs after the observed breakthrough, indicating that the actual breakthrough resulted from a faster velocity than that for the initial wetting front. While the question of why the C ring hydrograph and B ring BTCs need two different velocities cannot be answered, the solution for this simulation study was to recommend the median result ($\alpha=0.03$) with the fracture anisotropy of $k_{v,b} = 175$ mD and $k_{h,b} = 90,000$

mD as most appropriate and thereby split the difference between the two calibration targets.

10.0 SENSITIVITY TO SELECTED CALIBRATION PARAMETERS

Sensitivity of the simulation results to selected calibration parameters was analyzed.

Parameters tested (and listed in order of rank importance) were the fracture horizontal permeability (high), the longitudinal dispersivity (medium), and the basalt fracture relative permeability curve (small).

11.0 CONCLUSIONS

An inverse modeling study was conducted to obtain a representative description of flow and transport through vadose zone fractured basalts for use in field-scale modeling studies, in particular for risk assessments performed at the SDA. An equivalent porous media model using either single or dual porosity was used to obtain reasonable matches to calibration targets selected from observed hydrographs and conservative tracer breakthrough curves. Due to non-ideal behavior in the field results (which was to be expected), subjective judgement was used both in selecting the particular calibration targets and in determining the adequacy of the match between the simulated and observed results.

The fracture basalt effective porosity indicated by the calibration exercise is in contrast to the effective porosity generally accepted for the Snake River Plain aquifer, which is more on the order of 0.05 to 0.20. The latter porosity includes the effect of rubble zones, which primarily control flow within the aquifer but do not to any large extent, at least in the infiltration test, affect vertical movement within the vadose zone. Infiltrating water which

may have encountered rubble zones during the infiltration test apparently continued to migrate vertically. The results of this modeling study indicate that the large-scale infiltration test was successful in providing measurements upon which to base a description of flow and transport through the fractured basalt portion of the vadose zone. The description of field-scale hydrologic fracture properties obtained from this inverse modeling has since been used in environmental assessments at the SDA and elsewhere on the INEEL.

12.0 REFERENCES

- Bishop, C. W. (1991), Hydraulic Properties of Vesicular Basalt, Masters Thesis, University of Arizona, Tucson, AZ.
- Brooks, R. H. and A. T. Corey (1966), "Properties of Porous Media Affecting Fluid Flow," *J. Irrig. Drain. Div.*, Am Soc. Civil Eng., Vol. 92 (IR2), pp. 61-88.
- Knutson, C. F., K. A. McCormick, J. C. Crocker, M. A. Glenn, and M. L. Fishel (1992), *3D RWMC Vadose Zone Modeling (Including FY-89 to FY-90 Basalt Characterization Results)*, EGG-ERD-10246, EG&G Idaho, Inc., Idaho Falls, ID.
- Magnuson, S. O. (1995), *Inverse Modeling for Field-Scale Hydrologic and Transport Parameters of Fractured Basalt*, INEL-95/0637, Lockheed Martin Idaho Technologies, Idaho Falls, ID.
- Dunnivant, F. M., M. E. Newman, C. W. Bishop, D. Burgess, J. R. Giles, B. D. Higgs, J. M. Hubbell, E. Neher, G. T. Norrell, M. C. Pfeifer, I. Porro, R. C. Starr, A. H. Wylie (1998), "Water and Radioactive Tracer Flow in a Heterogeneous Field-Scale System," *Ground Water*, November-December, Vol. 36, Number 6, pp. 949-958..

Parker, J. C., R. J. Lenhard, and T. Kuppusamy (1987), "A Parametric Model for Constitutive Properties Governing Multiphase Flow in Porous Media," *Water Resources Research*, Vol. 23, No. 4, pp. 618- 624.

Porro, I. and C. W. Bishop (1995), *Large Scale Infiltration Test CPN Data Analysis*, EDF-WAG7-58, INEL- 94/040, Lockheed Martin Idaho Technologies, Idaho Falls, ID.

Van Genuchten, M. Th. (1980), "A closed-form equation for predicting the hydraulic conductivity of unsaturated soils," *Soil Science Society of America Journal*, 44, pp. 892-898.

Vinsome, P. K. W. and G. M. Shook (1993), "Multi-purpose Simulation," *Journal of Petroleum Science and Engineering*, Volume 9, pp. 29-38.

Wood, T. R., and G. T. Norrell (1996), *Integrated Large-Scale Aquifer Pumping and Infiltration Tests*, INEL-96/0256, Rev. 0, Lockheed Martin Idaho Technologies, Idaho Falls, ID.

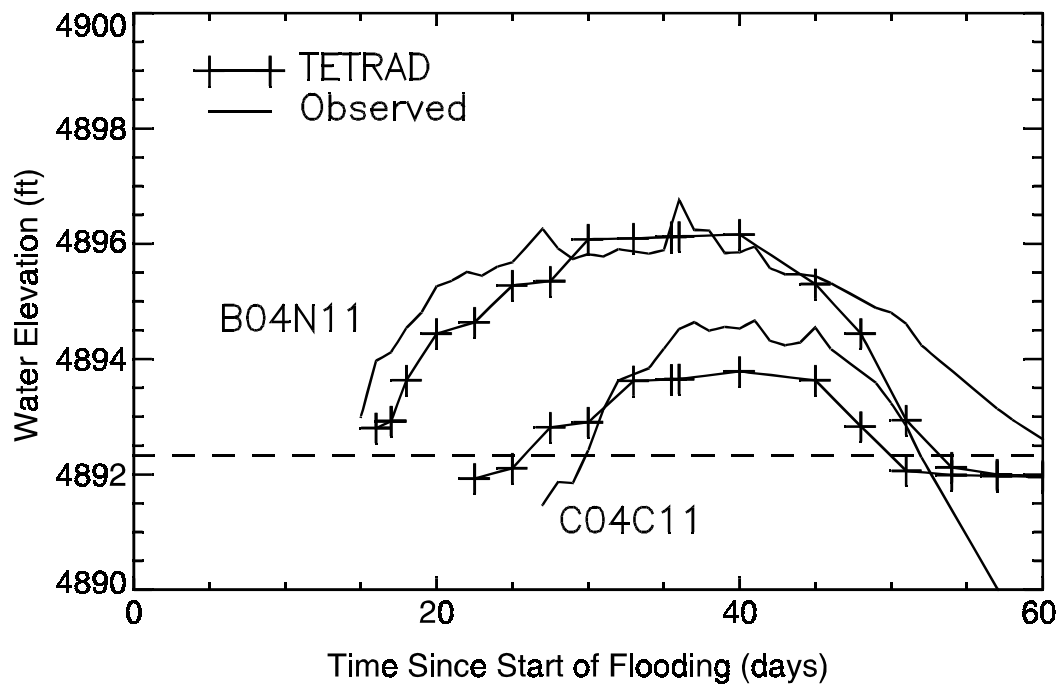


Figure 1. Comparison of single porosity simulated and observed B and C ring hydrographs for $\theta_b=0.05$.

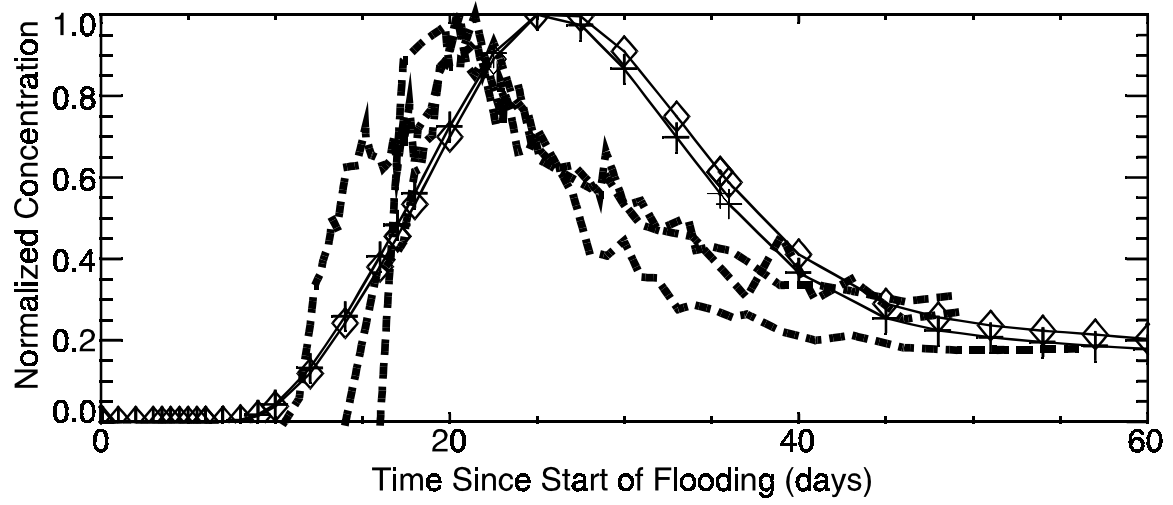


Figure 2. Comparison of simulated BTCs to B ring well BTCs (dashed lines) for single and dual porosity models for $\theta_b = 0.03$.

Modeling Preferential Flow in a Macroporous Field Soil - A Case Study

B. P. Mohanty and M. Th. van Genuchten
US Salinity Laboratory, USDA-ARS, Riverside, California

Introduction

Preferential flow under saturated as well as near-saturated conditions through macropores, cracks, and other nonmatrix domains that coexist with the soil matrix domain, has been found to be very common in structured field soils. Unfortunately, it is experimentally very difficult to measure the retention characteristics of a soil accurately and reproducibly at very low suctions close to saturation. It is further questionable whether retention curves can properly represent the pore-size distribution of a porous medium at high saturation where the nonwetting phase (air) is not continuous. This means that hydraulic conductivities predicted from retention data are inherently inaccurate when approaching saturation, even if one assumes the involved predictive conductivity model is error-free and applies to all pore sizes. As a consequence, hydraulic conductivity estimation from soil water retention functions that represent a certain pore space near saturation (e.g., suctions h less than 2 cm) are inherently unreliable.

Disc infiltrometry methods involving ponded and tension infiltrometers are now increasingly used for measuring the hydraulic conductivity *in situ* at low soil water tensions. Advantages of these methods is that negative soil water pressures at the soil-infiltrometer interface can be maintained very close to zero, and be decreased in small increments to get precise K-h functions near saturation. Using this macroscopic approach, one important assumption is that the soil water pressure head across the disc surface will remain uniform and thus in equilibrium with the soil medium for all conducting pore sizes and flow domains, including the larger macropores. Since the method assumes a uniform head (i.e., water maintained at a certain positive or negative soil water pressure) or uniform flux (i.e., water application rate) across the soil surface, flooding/ponded irrigation provides an attractive condition to test the performance of alternative functions to describe hydraulic conductivity data at and near saturation. The dual-porosity type approach followed in this study still assumes applicability of the Richard's equation, i.e., no bypass flow, as may occur under nonequilibrium conditions, will take place through macropores (all small pores at any given depth have to be partially or completely filled with water before flow occurs only or mainly through the larger pores).

Field Experiment

Our experimental field site was located on a 24-hectare commercial agricultural farm, situated on an alluvial flood plain of the Rio Grande, near Las Nutrias, New Mexico. In general, the field site consisted of silty clay loam sediments with moderate to poor drainage properties, underlain by fine sands, and with no impeding strata to a depth of about 7 m. Surface horizons, however, contained visible root channels, worm holes, and cracks, thereby composing a complex network of preferential flow paths. To sustain agricultural productivity, the field site was equipped with surface irrigation and subsurface (tile) drainage systems to reduce salinity in the crop-root zone. Two manholes allowed regular sampling of water quantity and quality entering and leaving the study section of the drain line.

Disc infiltrometers including ponded- and tension-infiltrometers were used to measure the K-h relationship in the near-saturation pressure head range (i.e., low soil water tension range).

Surface infiltration measurements at 0-, 30-, 60-, and 150-mm soil water tensions were made at more than 100 sites using experimental procedures described in Ankeny [1992]. In addition to measurements at these aforementioned soil water tensions, ten sites representing different soil types were selected for conducting infiltration measurements between 0- to 30-mm soil water tensions at 2~5 mm tension increments. Ankeny [1992] cautioned that infiltration for tensions below 10 mm should be interpreted carefully because of the possible inaccuracies in the applied tension due to bubbling. As such, we interpreted the infiltration rate in this narrow range of tensions only in a qualitative manner so as to reveal relative trends near saturation. Following the surface infiltration measurements, 5-cm diameter and 5-cm long undisturbed soil cores were collected directly below the disc from the same ten sites. The soil cores were subsequently used for measuring the water retention and hydraulic conductivity for a wider range (0 to 1700-mm) of soil water tensions. The laboratory method of Richards [1965] and the multi-step outflow approach of Gardner [1956] were used for measuring water retention and conductivity functions, respectively. We again were mostly interested in relative trends rather than absolute values of the retention data near saturation. The in situ and laboratory data were used to develop piecewise-continuous hydraulic conductivity functions whose fitting parameters could be further adjusted during flow-transport model calibration to better represent the scenario at the field site. Intermittent irrigation and rainfall volumes, profile soil water content, groundwater table depth along the field boundary, and tile flow volume were monitored regularly.

Soil Water Retention and Hydraulic Conductivity Functions

The hydraulic conductivity data obtained with the ponded infiltrometer, tension infiltrometer, and laboratory outflow experiments were superimposed across the tension range from 0 to 1700 mm for all measurement sites. Figure 1a shows log-log plots of the field-average K-h curve. Interestingly, the field-averaged hydraulic conductivity curve for the surface soil shows three turning (or two inflection) points within the measured tension range, i.e., at approximately 15, 30 and 300 mm. The sharp changes in K across the inflection point between 15 mm and 30 mm suggest the presence of relatively fast (preferential) flow phenomena near saturation. Figure 1b shows measured field-averaged soil water contents (θ -h) across the soil water tension range. A comparison of Figures 1a and 1b over the same (30- to 0-mm) tension range, indicate that while the hydraulic conductivity increased seven-fold (or 550%), water retention increased only very little. These findings seem to indicate that in this narrow soil water tension range, water is mostly gravity driven and partially mobile, and that this water can increase the flux many fold. At the same time, total water retained in the bulk soil appears to remain relatively constant in this range. The very small increase from $(\theta_h)^*$ to (θ_0) (in Figure 1b) may only be an experimental artifact, which, if true, suggests that water content at this tension range could be equated to $(\theta_h)^*$ for all practical purposes even for macroporous field soils.

Closed-form van Genuchten-Mualem type models [van Genuchten, 1980] for the soil water retention and hydraulic conductivity have been quite successful in describing variably-saturated flow as long as the soil has a relatively unimodal pore size distribution. When the soil has a multimodal pore-size distribution, these models become inaccurate close to saturation. One reason for this failure is a disruption in the otherwise smooth pore-size distribution of a macroporous soil at or near the larger pores. Also, gravity flow through the larger pores during near-saturated conditions will dominate capillary flow which was the basis of Mualem's model. More recently, several researchers [Zurmühl and Durner, 1996; Mallants et al., 1996; Durner, 1994; Othmer et al., 1991] have achieved

some success in modeling the hydraulic properties of bimodal or multimodal soils using sums of a number of van Genuchten-Mualem type functions. The same is true for flow in unsaturated fractured rock [e.g., Peters and Klavetter, 1988]. Most or all of these studies found that the multimodal hydraulic functions did perform better than unimodal hydraulic functions at intermediate soil water suctions (pF 1 to 5). Another group of researchers [Jarvis and Messing, 1995; Messing and Jarvis, 1993; Wilson et al., 1992] used a number of piecewise-continuous Russo-Gardner [Russo, 1988] type functions, joined at different junction points, for describing the retention and hydraulic conductivity of different pore groups. Although these exponential models (for the hydraulic conductivity) could somewhat better fit the actual data close to saturation [Messing and Jarvis, 1993], they become less accurate at mid-range soil water suctions. Thus, for field soils having multimodal pore size distributions, it may be more appropriate to invoke a hybrid sum-junction approach involving two or more piecewise-continuous functions based on the dominant physical (gravity, capillarity, or adsorption) forces associated with different conducting pore regions across the soil water tension range. For a multimodal pore-size distribution the hybrid sum-junction soil water retention and hydraulic conductivity functions can be written as [Mohanty et al., 1997, 1998]:

$$\theta(h) = \sum_c w_c \theta_c(h) = \sum_c w_c \left[\theta_{r,c} + \frac{\theta_{s,c} - \theta_{r,c}}{[1 + (\alpha_c |h|)^{n_c}]^{m_c}} \right] \quad h \leq h_\theta^* \quad (1)$$

$$\theta = \theta_{s(c=1)} \quad h > h_\theta^* \quad (2)$$

$$K(h) = \sum_c k_c K_c(h) = \sum_c k_c \frac{(1 - (\alpha_c |h|)^{n_c-1}) [1 + (\alpha_c |h|)^{n_c}]^{m_c}}{[1 + (\alpha_c |h|)^{n_c}]^{m_c/2}} \quad (m_c = 1 - 1/n_c) \quad h \leq h_K^* \quad (3)$$

$$K_{nc}(h) = K^* + K^* [\exp(h - h^*) \delta - 1] \quad h_K^* < h \leq 0 \quad (4)$$

$$K_{nc}(h) = K^* [\exp(-h^*) \delta - 1] \quad h > 0 \quad (5)$$

where, K_c is the hydraulic conductivity for capillary-dominated flow domain c [LT^{-1}],
 K_{nc} is the hydraulic conductivity for noncapillary-dominated flow domain nc [LT^{-1}],
 $\theta_{s,c}$ is the saturated water content for capillary-dominated flow domain c [L^3L^{-3}],
 $\theta_{r,c}$ is the residual water content for capillary-dominated flow domain c [L^3L^{-3}],
 h is the equilibrium soil water pressure head for bulk soil (across all flow domains) [L],

- $h_K^* . h_\theta^* = h^*$ is the critical or break-point soil water pressure head where flow changes from capillary-dominated to noncapillary-dominated flow or vice versa [L],
- K^* is the hydraulic conductivity corresponding to h^* [LT^{-1}],
- δ is a fitting parameter representing effective macroporosity or other structural features contributing to noncapillary dominated flow [L^{-1}],
- α_c, n_c are the van Genuchten fitting parameters [van Genuchten, 1980] for the capillary-dominated flow domain c [L^{-1} , -],
- c is the number of capillary-dominated flow domains. For $c = 1$, the sum type multimodal van Genuchten-Mualem hydraulic functions (equations 1 and 3) reduce to the original unimodal van Genuchten-Mualem type functions,
- nc is the noncapillary-dominated flow domain.
- w_c is the weighting factor for capillary-dominated flow domain c [-]; subjected to $3w_c = 1$, and $0 < w_c < 1$.
- k_c is the saturated hydraulic conductivity for capillary-dominated flow domain c [LT^{-1}]; subjected to $3k_c = K^*$.

The break-point soil water pressure head (h^*) of the bimodal hydraulic characteristics was determined by visual inspection, followed by separate nonlinear optimization of the hydraulic parameters for the capillary and noncapillary domains. Table 1 shows average values of the different hydraulic parameters optimized from field-averaged hydraulic functions (Figures 1a and 1b) at different depths for our field site.

Numerical Modeling

The hybrid sum-junction type hydraulic functions were incorporated into the CHAIN_2D computer model [Simunek and van Genuchten, 1994] to enable two-dimensional transient flow simulations at the field site. We assumed that water flow, overall, could be described with the Richards= equation (for Darcy-type flow under isothermal and variably-saturated conditions) in conjunction with our bimodal piecewise-continuous hydraulic functions. The soil was assumed to be rigid and nonhysteretic. For the two-dimensional numerical simulations, we implemented time-dependent boundary conditions, such as intermittent irrigation/precipitation rates at atmospheric boundary nodes, groundwater head values along hydrologic boundary nodes, tile-drain boundary, and no-flow conditions along impermeable bottom boundary nodes. Since this study focused on modeling preferential flow that would occur during or relatively soon after a large water input event (e.g., flood irrigation), we used hourly time steps and limited the simulations time to approximately 100 hrs from the start of individual irrigation events.

Simulation Results

One example of simulated tile flow using the field-averaged bimodal piecewise-continuous soil water retention and hydraulic conductivity functions is presented in Figure 2a and compared against the observed field values. We also compared the simulation results with results obtained using field-averaged unimodal van Genuchten-Mualem type soil water retention and hydraulic conductivity functions. To present a qualitative comparison, we used two unimodal functions in the surface horizon based on (1) K_{0-mm} through K_{30-mm} being included in the parameter optimization (unimodal_high), and (2) K_{0-mm} through K_{30-mm} being excluded from the parameter optimization

(unimodal_low). From the observed tile-drain flow it is clear that, following an irrigation event, water moves rapidly downward through the soil profile. After a few hours of irrigation, the tile flow rate suddenly increased and reached a peak almost instantly followed by a similar sharp drop (these results suggest preferential flow through the field macropore network). This situation was followed by a recession phase dominated by prolonged matrix flow and water redistribution in the profile. In general, predicted flow using the bimodal hydraulic functions matched the observed flow rates reasonably well, and far better than when the unimodal hydraulic functions were used. From the different simulation runs we conclude that using the piecewise-continuous hydraulic functions generally minimized the over- or under-predictions of flow in the different flow-domains as is typically obtained with the one-domain approach. Figure 2b shows corresponding nitrate transport (simulated vs. observed) at the field site. Further details of our study can be found in Mohanty et al. [1997 and 1998].

Concluding Remarks

Capillary-flow based unimodal soil water retention and hydraulic conductivity functions should be complemented with other functions to correctly simulate noncapillary dominated flow near saturation in field soils. In this study we measured the relative trend of soil water retention and hydraulic conductivity functions near saturation and established piecewise-continuous functions to predict flow across a wide range of soil water tensions. The hydraulic functions were reasonably successful in predicting the field-scale flow and transport under a flood-irrigated field in Las Nutrias, New Mexico. Even with the piecewise-continuous hydraulic properties, Figure 2a still shows deviations between predicted and measured tile flow rates. We believe that these deviations were caused primarily by a regional flow field which may not have been adequately captured with the two-dimensional model we used. A somewhat related study involving a much more flat water table and negligible regional flow effects was recently carried out by de Vos et al. (1999). These authors similarly accounted for the effects of macropores on tile drainage by using a more approximate linear extension of the hydraulic conductivity function near saturation (the retention function was not modified in their study). These and other ongoing studies at the U.S. Salinity Laboratory suggest that the piecewise-continuous functions, or similar bimodal type hydraulic properties, will lead to better predictions of preferential flow in the vadose zone. Further improvements in the predicted nitrate distributions of Figure 2b are possible when provisions for immobile water are included in the solute transport equation (e.g., Zurmühl et al., 1998; Simunek et al., 1999). The presence of immobile water will move the leading edge of the nitrate concentration in the tile drain further to the left toward the observed data.

References:

- Ankeny, M.D., Methods and theory for unsaturated infiltration measurements, In G. Topp et al. (editors), *Advances in Measurement of Soil Physical Properties: Bringing Theory into Practice*, *Soil Sci. Soc. Am. Spec. Publ.*, 30, 123-141, 1992.
- de Vos, J. A., J. Simunek, P.A.C. Raats, R.A. Feddes, Identification of the hydraulic characteristics of a layered silt loam soil. In: M. Th. van Genuchten, F.J. Leij, and L. Wu (eds.), *Proc. Int. Workshop on the Characterization and Measurement of the Hydraulic Properties of Unsaturated Porous Media*. University of California, Riverside, CA, in press, 1999.
- Durner, W., Hydraulic conductivity estimation for soils with heterogeneous pore structure, *Water Resour. Res.*, 30, 211-223, 1994.

- Gardner, W.R., Calculation of capillary conductivity from pressure plate outflow data, *Soil Sci. Soc. Am. Proc.*, 20, 317-320, 1956.
- Jarvis, N.J. and I. Messing, Near-saturated hydraulic conductivity in soils of contrasting texture measured by tension infiltrometers, *Soil Sci. Soc. Am. J.*, 59, 27-34, 1995.
- Mallants, D., P.-H. Tseng, N. Toride, A. Timmerman, and J. Feyen, Evaluation of multimodal hydraulic functions in characterizing a heterogeneous field soil, *J. of Hydrol.*, 195, 172-199.
- Messing, I., and N.J. Jarvis, Temporal variation in the hydraulic conductivity of a tilled clay soils as measured by tension infiltrometers, *J. Soil Sci.*, 44, 11-24, 1993.
- Mohanty, B.P., R.S. Bowman, J.M.H. Hendrickx, J. Simunek, and M.Th. van Genuchten, Preferential Transport of Nitrate to a Tile Drain in an Intermittent-Flood-Irrigated Field: Model Development and Experimental Evaluation. *Water Resour. Res.*, 34, 1061-1076, 1998.
- Mohanty, B.P., R.S. Bowman, J.M.H. Hendrickx, and M.Th. van Genuchten, New Piecewise-Continuous Hydraulic Functions for Modeling Preferential Flow in An Intermittent-Flood-Irrigated Field. *Water Resour. Res.*, 33, 2049-2063, 1997.
- Othmer, H., B. Diekkruger, and M. Kutilek, Bimodal porosity and unsaturated hydraulic conductivity, *Soil Sci.*, 152, 139-150, 1991.
- Peters, R.R., and E.A. Klavetter, A continuum model for water movement in an unsaturated fractured rock mass, *Water Resour. Res.*, 24, 416-430, 1988.
- Richards, L.A., Physical condition of water in soil. In C.A. Black et al., (editors), *Methods of Soil Analysis*. Part 1. Agronomy Monograph, 9, 128-152, 1965.
- Russo, D., Determining soil hydraulic properties by parameter estimation: On the selection of a model for the hydraulic properties, *Water Resour. Res.*, 24, 453-459, 1988.
- Simunek, J., M. Sejna and M. Th. van Genuchten. 1999. The HYDRUS-2D Software package for simulating the one-dimensional movement of water, heat and multiple solutes in variably-saturated media. IGWMC - TPS 53, Version 2.0. *Int. Ground Water Modeling Center*, Colorado School of Mines, Golden, CO.
- Simunek, J. and M.Th. van Genuchten, The CHAIN_2D code for simulating the two-dimensional movement of water, heat, and multiple solutes in variably-saturated porous media, *U.S. Salinity Laboratory*, Research report no. 136, 1994.
- van Genuchten, M.Th., A closed-form equation for predicting the hydraulic conductivity of unsaturated soils, *Soil Sci. Soc. Am. J.*, 44, 892-898, 1980
- Wilson, G.V., Modeling the hydraulic properties of a multiregion soil, *Soil Sci. Soc. Am. J.*, 56, 1731-1737, 1992.
- Zurmuhl, T. 1998. Capability of convection-dispersion transport models to predict transient water and solute movement in undisturbed columns. *J. Contaminant Hydrology*, 30:101-128.
- Zurmuhl, T. and W. Durner, Modeling transient water and solute transport in a biporous soil, *Water Resour. Res.*, 32, 819-829, 1996.

Table 1 <Field-Averaged> Parameters[¶] of Bimodal Piecewise-Continuous and Unimodal van Genuchten-Mualem Hydraulic Functions for Different Soil Horizons at the Field Site in Las Nutrias, New Mexico.

<u>Bimodal Piecewise-Continuous Hydraulic Functions</u>							
Depth (cm)	$\langle\theta_{s,i=1}\rangle$ (cm ³ cm ⁻³)	$\langle\theta_{r,i=1}\rangle$ (cm ³ cm ⁻³)	$\langle\alpha\rangle$ (cm ⁻¹)	$\langle n\rangle$ (-)	$\langle K^*\rangle$ (cm/sec)	$\langle h^*\rangle$ (cm)	$\langle\delta\rangle$ (cm ⁻¹)
0-40	.475	.110	.015	1.60	5.55E-04	3	.92
40-100 [§]	.459	.050	.021	1.40	4.16E-04	3	.70
100-700 ^{§§}	.430	.090	.083	2.12	2.73E-03	0	n/a

<u>Unimodal van Genuchten-Mualem Hydraulic Functions (high/low)</u>					
Depth (cm)	$\langle\theta_s\rangle$ (cm ³ cm ⁻³)	$\langle\theta_r\rangle$ (cm ³ cm ⁻³)	$\langle\alpha\rangle$ (cm ⁻¹)	$\langle n\rangle$ (-)	$\langle K_s\rangle$ (cm/sec)
0-40	.484/.475	.080/.120	.004/.015	1.44/1.55	4.08E-03/9.50E-04
40-100	.464/.459	.045/.050	.010/.021	1.25/1.38	3.50E-03/6.80E-04
100-700 ^{§§}	.430/.430	.090/.090	.083/.083	2.12/2.12	2.73E-03/2.73E-03

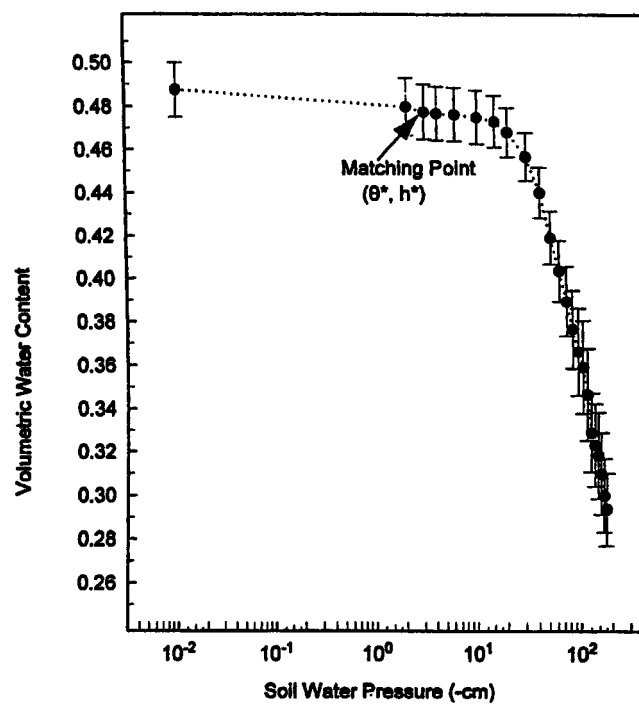
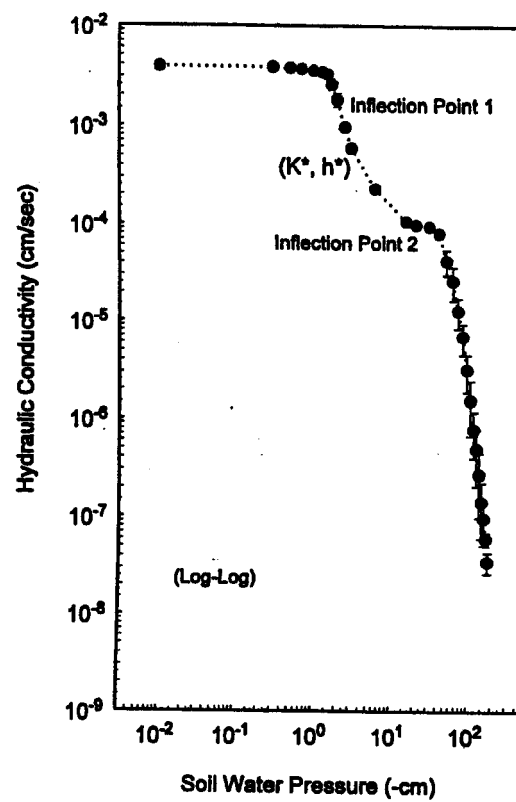
[¶] field-averaged parameters were obtained by fitting the van Genuchten-Mualem hydraulic functions (eqs. 1 and 3) or the inverted exponential function (eq. 4) to (geometric or arithmetic) mean hydraulic data (e.g., as shown in Figures 1 and 2)

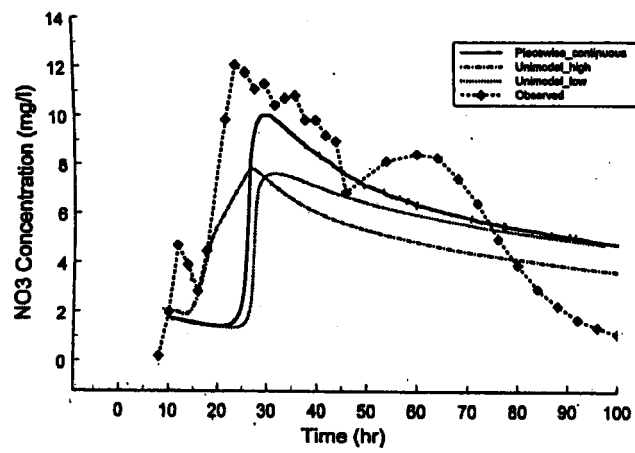
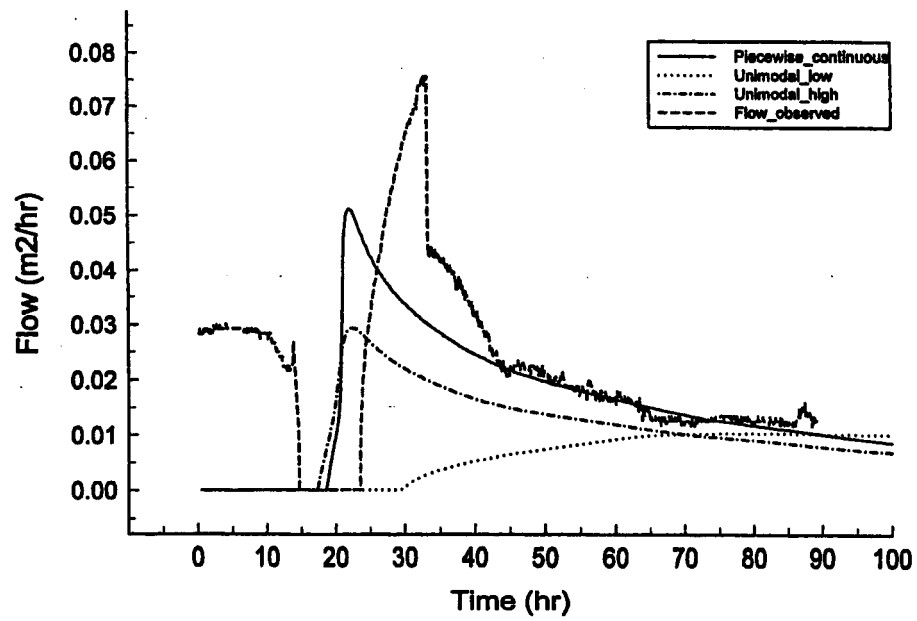
[§] as hydraulic parameters *near saturation* were not precise (using IP experiment) at deeper depths, thus, $\langle h^*\rangle$, $\langle\delta\rangle$ parameters were adopted and calibrated from the surface horizon

^{§§} as soil type varied from fine sand to sand in this depth range, flow was assumed to be well presented by unimodal van Genuchten-Mualem model

Figure 1 (a) Error bar (geometric mean and standard error) plots of the <field-averaged> soil hydraulic conductivity (K-h) function for the surface horizon by superimposing the *in situ* and laboratory measurements: (a) semi-log plot and (b) log-log plot. Inflection points were found between 1.5 cm and 3 cm (1), and between 3 cm and 30 cm (2). Inflection point (1) near-saturation indicates that the flow-governing process changes from noncapillary-dominated to capillary-dominated. (b) Error bar (arithmetic mean and standard error) plot of the <field-averaged> soil water retention (θ -h) function for the surface horizon measured in the laboratory. Turning point at 30 cm indicates the bubbling pressure. (after Mohanty et al., 1997).

Figure 2 (a) Comparison of simulated tile-drain flow (from the study section) using the piecewise-continuous hydraulic functions (bimodal soil porosity distribution) and the van Genuchten-Mualem (unimodal soil porosity distribution) hydraulic functions with observed data (net tile drain flow below the center bench) at the field site. Time 0 hr matches the midnight prior to the irrigation. (b) Comparison of predicted and observed tile flux NO_3^- concentrations following the irrigation event at the field site. Time 0 hr matches the midnight prior to the irrigation. (after Mohanty et al., 1997 and 1998).





Subsurface Remediation Optimization Using Artificial Neural Networks

L.L. Rogers and V.M. Johnson
Lawrence Livermore National Laboratory

ABSTRACT

One continuing difficulty in optimizing remediation management is reduction of computational burden which is particularly limiting in field-scale applications. Often evaluation of a single remediation strategy, i.e. one call to the subsurface flow and transport model (SFTM) may take several hours on a reasonably fast workstation. For computational flexibility and efficiency, optimal groundwater remediation design at Lawrence Livermore National Laboratory (LLNL) has relied on artificial neural networks (ANNs) trained to approximate the outcome of 2-D field-scale, finite difference/finite element SFTMs. The search itself has been directed primarily by the genetic algorithm (GA) or the simulated annealing (SA) algorithm. This approach has advantages of 1) up to a million fold increase in speed of remediation pattern assessment during the searches and sensitivity analyses for the 2-D LLNL work, 2) freedom from sequential runs of the SFTM (enables workstation farming), and 3) recycling of the knowledge base (i.e. runs of the SFTM necessary to train the ANNs). Reviewed here are the background and motivation for such work, recent applications, and continuing issues of research.

BACKGROUND AND MOTIVATION

Many researchers integrate optimization and subsurface transport modeling to search for efficient remediation strategies (Wagner, 1995). In this effort, much of the detailed character of the subsurface aquifer system is incorporated in a geologic model, then upscaled (i.e. coarsened or simplified) into a subsurface flow and transport model (SFTM) to predict the fate and transport of contaminants over time. Whatever their current limitations, SFTMs are the current state of the art for integration of field data with fluid transport theory aimed at prediction of future contaminant transport. Since we believe that such subsurface models will continue to be used to make subsurface remediation management decisions, how do we best exploit or leverage the considerable effort that goes into the construction and computationally-intensive calibration of these models during our search for an optimal remediation strategies?

Neural network based optimization is one path to exploit an existing SFTM. Optimization techniques are commonly used to find strategies for industrial efficiency, providing a formal, mathematical search which maximizes the objectives while considering the constraints on a system. In this area, example objectives could be minimizing costs or maximizing contaminant mass removed; constraints might be avoiding dewatering or a total pumping volume limit. In well-field design problems, optimization techniques need to evaluate the success of many, many individual remediation scenarios. The dilemma is that part of the evaluation of just one of these scenarios takes a call to the SFTM which may take several hours to run on a fast computer. How can one evaluate the thousands of remediation strategies necessary in the search for an optimal one? The use of artificial neural networks (ANNs) poses one possible solution to this difficult question.

ANNs can be trained to predict essential elements of the flow and transport simulation results from the SFTM for different combinations of wells. This paper uses the term wells as the methodology was originally developed for saturated conditions; however, it is not limited to saturated conditions and one may consider such installations as vapor phase extraction wells or lysimeter monitoring installations in place of wells for unsaturated analogs. Using this technique, one may rely on the ANN as an approximator rather than using a full numerical flow simulation during the search for an optimal remediation scenario. By using the ANN, different remediation strategies can be evaluated in fractions of a second rather than several hours. In order to provide training data for ANNs an initial computational investment is required. It is necessary to run a suite of actual flow and transport simulations that would cover the range of possible remediation well combinations. Once this database, or knowledge base, of SFTM runs is obtained, ANNs are trained on input-output relationships drawn from this knowledge base. Note these runs can be done in parallel and once the knowledge base is created, such a knowledge base may be recyclable (see discussion in the next section).

Once trained to acceptable levels of accuracy on the test patterns, the ANNs stand in for the original SFTM, predicting the effectiveness of new remediation patterns generated by the optimization driver, usually the GA or SA. It is the optimization driver which is responsible for generating increasingly successful patterns and which eventually determines the optimal set of patterns. A flowchart summarizing the elements of the methodology is shown in Figure 1.

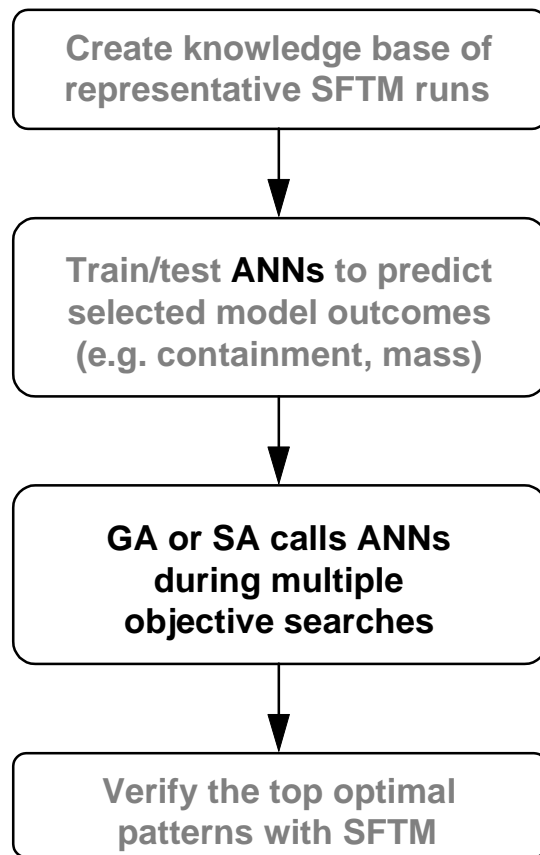


Figure 1: Flowchart of Methodology

RECENT APPLICATIONS

Previous nonlinear, large-scale, optimal, remediation design at LLNL has been based on 2-D numerical SFTMs of the LLNL site and vicinity. A finite-element/finite SFTM, SUTRA (Voss, 1984), was used to evaluate the outcome of remediation scenarios. The upper 200 feet of the saturated zone were modeled in a vertically averaged, steady-state, saturated approach. A 2385 element grid was superimposed on the square mile site of LLNL and approximately 15 surrounding square miles. The SUTRA model was calibrated to a larger regional model which had been extensively calibrated to water-table conditions, known source and sink phenomena, and other field observations (Tompson et al., 1991).

Rogers and Dowla (1994) first used the approach of combining the GA with ANNs which predicted the fitness measure of the generated pumping patterns. A 20 well problem was used to compare the GA-ANN optimization with the more conventional approach of combining the

SFTM with a nonlinear programming with a quasi-Newton search. Rogers et al. (1995) used a 28 well problem considering both injection and pumping as part of the possible remediation strategies. Both applications suggested the GA-ANN approach has the advantage of 10^6 increase in pumping pattern assessment speed during the searches for the 2-D LLNL work. For example, one evaluation of a single pumping strategy, i.e. one call to the SFTM, took approximately 2 hours on the SUN workstations available at the time. Yet a trained ANN could predict selected outcomes of the SFTM at the rate of 2000 evaluations per second. An additional advantage is freedom from sequential runs of the SFTM. Many traditional search algorithms need the results of one SFTM evaluation before deciding on the next perturbation of the pumping pattern. In the ANN approach, the knowledge base, which is the SFTM runs of various well combinations used to train the ANNs, can be created by separate workstations in parallel. This enables “workstation farming”, or sending the SFTM runs out to many different idle workstations. A third advantage is that the knowledge base can be recycled. If relevant results of the SFTM outcomes have been saved, new nets can be trained to predict different types of parameters appropriate to new remediation objectives. This is in contrast to traditional approaches where a change in the objective function would involve less opportunity to use the knowledge or computational investment from past searches in the new search. (see Website:<http://www-ep.es.llnl.gov/www-ep/esd/sstrans/pmp.html>).

The type of ANN used in the methodology learns by the backpropagation learning (Rumelhart and McClelland, 1986) named for its propagation of errors backwards through the network to update the weights. A conjugate gradient method algorithm (Johansson et al. , 1992) was employed to implement the backpropagation learning. The ANNs were formulated with the top or input layer using one node to represent each of the prospective well locations. Each input node, which can be thought of as an independent variable, was valued at 1 or 0, depending on its On or Off status in the remediation scenario or pumping pattern. This simple binary scheme was employed because, for the current problem, the pump rate at each location was fixed at the maximum appropriate level (anywhere from 10 to 50 gpm) for the location. Had pump rate been a design-variable being optimized, the input nodes could have taken on continuous values. In the 20 and 28 well problems an additional node was used to supply the network with what percentage of total possible wells were on for that particular pattern. The bottom or output layer represents the dependent variable which the network is learning to predict, in these applications the containment objective was expressed as a yes or no dichotomy. For mass and cost, the output node was a continuous variable.

With the speed of the ANN predictions, a monte-carlo approach sensitivity analyses was possible to rigorously examine the performance of wells individually and in combination with high performing wells. A demonstration of this method was applied to the 28 well problems at LLNL, using objectives of cost, mass-extraction and plume containment (Johnson et al., 1995). The top 250 optimal pumping patterns (out of over 4 million examined) first were used to classify popular vs. unpopular wells. Sensitivity analyses further distinguished: (1) locations which were strong performers more consistently from those which depended on other wells operating, and (2) locations which were not particularly helpful to remediation from those which were actually detrimental.

We have connected trained ANNs to two powerful heuristic combinatorial optimization techniques, the GA and the SA. The GA derived from the analogy between the vector of components representing the decision variables of an optimization problem and the genetic structure of a chromosome. GAs have been established as a reasonable and robust approach to problems requiring efficient search. The reliance of GAs on analogies to biology and genetics limited their appeal for some time, but this is being overcome and many new applications are being seen in business, engineering, and science [Goldberg, 1989]. Using a GA, the search begins from a population of parameter realizations, not a single realization as more conventional optimization procedures might. Other strengths are the GAs use probabilistic not deterministic rules for perturbation of the realizations and the objective function information is used directly rather than derivatives or other secondary descriptors. The three common basic operators of the GAs are selection, reproduction, and mutation. Selection determines which members of the current generation will go in some form into the next generation. Reproduction (connected with crossover) determines how the string creatures are paired up for mating and where the strings actually crossover. And mutation allows for some diversity in a population by random bit changes according to some rate.

The SA algorithm (Metropolis, 1953; Kirkpatrick, 1983; Reeves, 1993) evolved in analogy to the annealing of solids where the initial energy of the system is raised to allow molecules to be quite mobile; later the system is cooled into a lower energy crystalline form. The objective of the search such as cost is mapped onto the energy of the system and the feasible solutions onto the state of the system. At early times the perturbations to the feasible solutions are allowed to be large, as temperature decreases change is curtailed. Probabilistic rules are applied by the user to control the number of changes at given temperature steps. This method has

found success even in large-scale optimization applications and has been used in the groundwater field in recent years (Dougherty and Marryott, 1991; Rizzo and Dougherty, 1996).

We have conducted benchmarking studies finding very similar results from GA-ANN and SA-ANN searches and those connecting the GA and SA to full model runs to evaluate the objective function (Johnson and Rogers, 1998). For the objectives considered, the GA in general evaluated 30 -50% more potential pumping patterns to converge to a solution than the SA, but this was not a significant concern when using the time-saving ANN evaluation. In these heuristic approaches, both the objectives and constraints of an optimization are often included in the measure of success of the optimization, i.e. GA fitness measure, and SA energy function. Also a constraint can be handled by removing pumping patterns resulting in unacceptable conditions from the evolving population. Both continuous and dichotomous formulations of a plume containment and highest remaining contaminant level after 50 yr of remediation were explored. A dramatic improvement was obtained in the searches using continuous containment formulations. This benchmarking work also demonstrated more rigorously how the search results using ANNs as approximators were comparable to results from searches using full model runs to evaluate the objective function. Also, evaluations to measure computational effort expended suggested the ANN-based searches were three to five times more efficient than the model-based searches.

Concern for the expense and long time necessary to remediate a site with pump-and-treat technology has fueled development of innovative *in-situ* technologies. Nonisothermal and biofilter modeling has evolved to a significant level at LLNL (see Website: <http://www-ep.es.llnl.gov/www-ep/aet/ACI/aci-home.html>) focusing on rapid contaminant source destruction using a combination of new *in-situ* technology including hydrous pyrolysis by steam injection and microbial filters. A 3-D nonisothermal code has been employed for process simulations of hydrous pyrolysis to gauge the feasibility of field deployment on the LLNL site (Knapp, 1996). Ultimately some combinations of these technologies may be optimal for a particular site. There was interest in addressing the management issue of how resources might be balanced between pump-and-treat remediation of the plume and more aggressive *in-situ* source remediation. Unfortunately, there is not at this time a field-scale nonisothermal/microbial model to link to the optimization. As an approximation then three cases of increasing initial source remediation were considered with their associated economic estimates to implement hydrous pyrolysis (Rogers et al, 1998). The term tradeoffs is often used to indicate how emphasis of one objective compromises performance in

another conflicting objective. Tradeoff curves based on the SA searches were constructed to compare the economic feasibility of *in-situ* removal of the contaminated source area versus pump-and-treat remediation of the entire plume. Note that ANNs were not used in this particular study because of the availability of supercomputers and the current size of the SFTM, but this is discussed for background in the following section on continuing research.

CONTINUING AREAS OF RESEARCH

Our searches have most often involved multiple objectives. It is a strength of optimization techniques to find a non-biased solution to a complex, coupled problem. However, there is an art to unraveling how the weights of the individual components of the objective function affect the final recommended solutions. With this in mind and with the advantages of a rapid approach, we have explored the impact of interactive searches where the weights of the individual components of the objective function are varied to avoid stagnant areas of the search. This is a continuing area of our research viewed to be particularly useful where many combinations of objectives need to be explored. Some remediation situations where this might be particularly necessary would be those with large numbers of stakeholders (i.e. decision-makers or concerned parties) and negotiations of non-attainment of regulatory contaminant levels due to necessary prioritization of remediation resources.

Access to faster computers is a welcome constant in our work; however, we continue to expect ANNs to be a useful component in our toolbox with each new complexity in the subsurface remediation field. For example, interest in bounding uncertainty (e.g., involving numerous geologic realizations of hydraulic conductivity), considerations of health risk modeling, and accelerated *in-situ* remediation (e.g., steam stripping or bioremediation with their need for more complex field-scale models) continue to motivate computation efficiency in optimization (Figure 2). Our optimizations are currently building on a pump-and-treat model and scenarios assuming *a priori* removal of different portions of the source area have been run to address the evolving management issue of more aggressive source remediation with in-situ techniques. However, fuller incorporation of multi-phase, nonisothermal, and biological transport mechanisms into the SFTM as well as health risk components will further encourage our use of ANNs to streamline the search for optimal deployment of combined in-situ and pump-and-treat remediations.

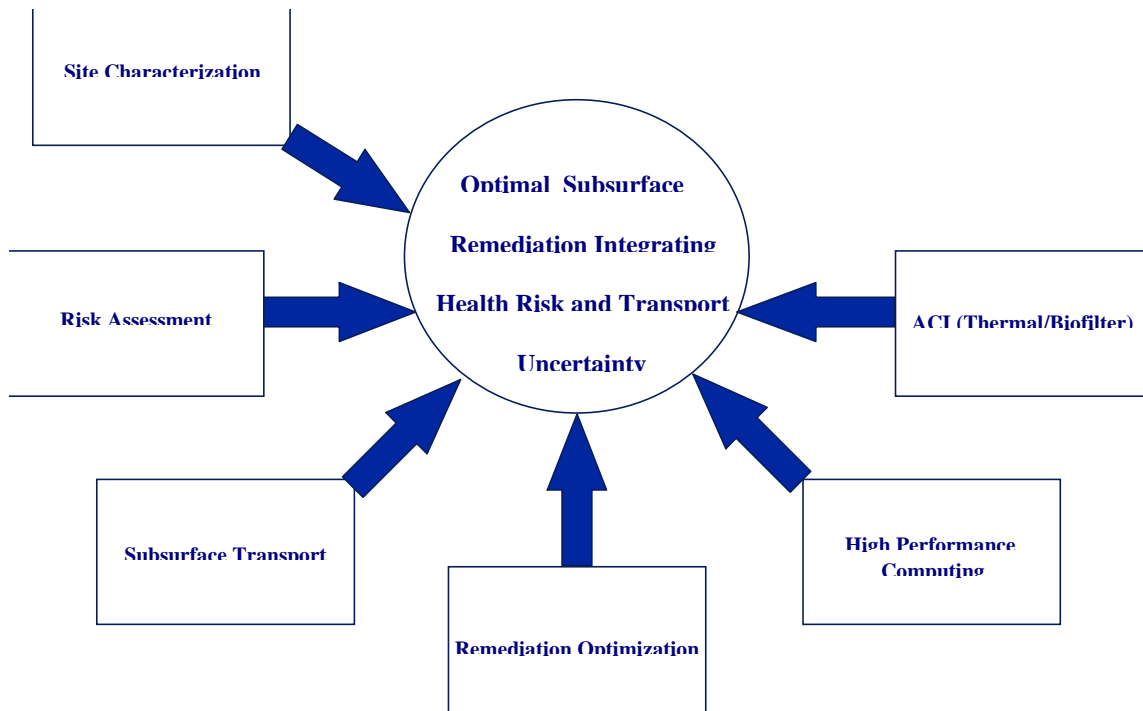


Figure 2: Future Integration of Optimal Subsurface Remediation with Transport Uncertainty, Health Risk, and In-Situ Remediation Components

REFERENCES

- Doughtery, D.E., and R.A. Marryott, Optimal groundwater management 1. Simulated Annealing, *Water Resources Research*, 27(10),2493-2508, 1991.
- Goldberg, D. E. *Genetic algorithms in search, optimization, and machine learning*. Addison-Wesley: Reading, MA, 1989.
- Johansson, E.M., F.U. Dowla, and D.M. Goodman, Backpropagation Learning for Multi-Layer Feed-Forward Neural Networks Using the Conjugate Gradient Method, *Int. J. of Neural Systems*, 2, 291, 1992
- Johnson, V.M. and L.L. Rogers, "Accuracy of neural network approximators in simulation-optimization", Lawrence Livermore National Laboratory UCRL-JC-Preprint #, Livermore, CA, also submitted to *Journal of Water Resources Planning and Management* (ASCE), 1998.
- Johnson, V.M., and L.L. Rogers, Location analysis in ground-water remediation using neural networks, *Ground Water*, 33(5),749-758, 1995.
- Kirpatrick, S., C.D. Gelatt, and M.P. Vecchi, Optimization by simulated annealing, *Science*, 220(4598), 671-680, 1983.

- Knapp, R.B., 1996. Feasibility Report for the Accelerated Cleanup Initiative (ACI). In progress.
- Metropolis, N., A.W. Rosenbluth, M.N. Rosenbluth, A.H. Teller, and E. Teller, Equations of state calculations by fast computing machines, J. Chem. Phys., 21(6), 1087-1091, 1953.
- Reeves, C.R. (ed.), Modern Heuristic Techniques for Combinatorial Problems, John Wiley and Sons, New York, NY, 1993.
- Rizzo, D.M., and D.E. Dougherty, Design optimization for multiple managment period groundwater remediation, Water Resources Research, 32(8), 2549-2561, 1996.
- Rogers, L.L. and F.U. Dowla, Optimal groundwater remediation using artificial neural networks with parallel solute transport. Water Resources Research, 30(2), 457-497, 1994.
- Rogers, L.L., V.M. Johnson, and F.U. Dowla, Optimal field-scale groundwater remediation using neural networks and the genetic algorithm, Environ. Sci. and Tech., 29(5), 1145-1155, 1994.
- Rumelhart, D. E.; McClelland, J. L. *Parallel Distributed Processing: Explorations in the Microstructure of Cognition*. MIT Press: Cambridge, MA, vol. 1, pp 318-362, 1986.
- Tompson, A. F. B.; Nichols, E. M.; McKereghan, P. R.; Small, M. C. Summary of preliminary ground water simulations in the Livermore Regional Modeling Study: CFEST finite element code. Lawrence Livermore National Laboratory, Livermore, CA, UCRL-AR-107049, 1991.
- Voss, C. I. A finite-element simulation model for saturated-unsaturated, fluid-density-dependent groundwater flow with energy transport or chemically-reactive single-species solute transport. U.S. Geological Survey, Water Resources Investigations Report #84-4369, 1984.
- Wagner, B.J., Recent advances in simulation-optimization groundwater management modeling, U.S. Natl. Rep. Int. Union Geod. Geophys. 1991-1994, Rev. Geophys., 33, 10-21-1028, 1995.

This work was made possible by support from the LLNL Environmental Restoration Division under the auspices of the U.S. Department of Energy under contract W-7405-Eng-48.

OXIDATIVE WEATHERING CHEMICAL MIGRATION THROUGH AN UNSATURATED-SATURATED MEDIUM

by Tianfu Xu, Karsten Pruess, and George Brimhall, Earth Sciences Division,
Lawrence Berkeley National Laboratory

Transport of oxygen gas from the land surface through an unsaturated zone has a strong influence on oxidative weathering processes. Oxidation of sulfide minerals such as pyrite (FeS_2), one of the most common naturally occurring minerals, is the primary source of acid drainage from mines and waste rock piles. Here we present a supergene copper enrichment problem that involves the oxidative weathering of pyrite (FeS_2) and chalcopyrite (CuFeS_2), and acidification that causes mobilization of metals in the unsaturated zone, with subsequent formation of enriched ore deposits in the reducing conditions below the water table. This problem serves as a prototype for oxidative weathering processes with broad significance for geoscientific, geological engineering, and environmental applications. Mathematical modeling of these processes is extremely challenging because (1) sulfide mineral oxidation occurs through a complex interplay of multiphase flow and transport processes; and (2) aqueous concentrations of key species vary over an enormous range, oxygen inventory and supply are typically small in comparison to mineral inventory; and (3) chemical reactions are complex, involving kinetic control and microbial catalysis.

Supergene copper enrichment: An example of oxidative weathering and chemical migration under variably saturated conditions

Tianfu Xu¹, Karsten Pruess¹, and George Brimhall²

¹Earth Sciences Division, Lawrence Berkeley National Laboratory, University of California, Berkeley, CA 94720.

²Department of Geology and Geophysics, University of California at Berkeley.

1. Introduction

Transport of oxygen gas from the land surface through an unsaturated zone has a strong influence on oxidative weathering processes. Oxidation of sulfide minerals such as pyrite (FeS_2), one of the most common naturally occurring minerals, is the primary source of acid drainage from mines and waste rock piles. Here we present a detailed numerical model of supergene copper enrichment that involves the oxidative weathering of pyrite (FeS_2) and chalcopyrite (CuFeS_2), and acidification that causes mobilization of metals in the unsaturated zone, with subsequent formation of enriched ore deposits of chalcocite (Cu_2S) and covellite (CuS) in the reducing conditions below the water table. This process serves as a prototype for oxidative weathering processes with broad significance for geoscientific, geological engineering, and environmental applications.

2. Hydrogeochemical system

Supergene enrichment involves hydrochemical differentiation by near-surface weathering processes in which water transports metals from a source region or leached zone to a locus of an enrichment blanket zone where these ions are reprecipitated as secondary ore compounds (Figure 1). The geochemistry for this work was based on field and laboratory studies of supergene copper systems as carried out by Brimhall and Alpers (1985), and Ague and Brimhall (1989). The model system as shown in Figure 1 captures, in simplified manner, conditions of desertification in Northern Chile that led to oxidation and chemical enrichment of copper deposits at certain times in the past when downward movements in the ground water table exposed sulfides to unsaturated conditions. Oxygen is supplied to a protore containing pyrite and chalcopyrite (Table 1) as a dissolved species in infiltrating rainwater (a rate of 0.07 m/yr), as well as by gaseous diffusion from the land surface boundary (an atmospheric O_2 partial pressure of 0.2 bar). A vertical column of 20 m thickness is used. The top 10 m represents the unsaturated zone, while the bottom 10 m represents the water saturated zone. A steady-state water flow regime is assumed throughout the simulation. A diffusion coefficient of $4.38 \times 10^{-5} \text{ m}^2 \text{ s}^{-1}$ and a tortuosity of 0.1 are used for gaseous oxygen.

The column is initially filled entirely with a protore mineral assemblage as listed in Table 1. The dissolution of the protore minerals is kinetically controlled. We used a first order kinetic rate expression given by Lasaga et al. (1994). The kinetic rate constants and specific surface areas used are also given in Table 1. A total of 52 aqueous species, 10 primary minerals and 6 secondary minerals are considered (Table 2). Oxygen is treated as ideal gas, its interaction with the aqueous solution is assumed at local equilibrium. The precipitation of secondary minerals during the simulation progress is modeled as instantaneous. A dilute oxidizing water in equilibrium with an oxygen partial pressure of 0.2 bar is initially placed in the unsaturated zone,

while a reducing water is assumed for the saturated zone. The infiltration water composition is the same as the initial unsaturated water.

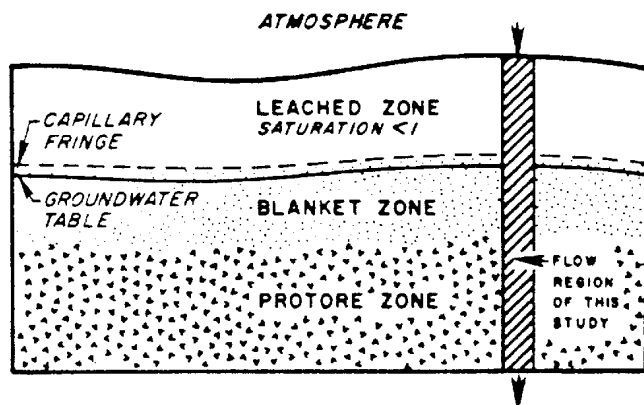


Figure 1. A schematic representation of a supergene copper enrichment system according to Ague and Brimhall (1989).

Table 1. Chemical properties of protore mineral reactants. Volume fraction, rate constant and specific surface area are based on Ague and Brimhall (1989).

Mineral	Volume fraction (%)	Abundance (mol/dm ³ medium)	Rate constant (mol/cm ² /s)	Surface area (cm ² /dm ³ medium)
Pyrite	9.0	3.76	4.0×10^{-15}	586.7
Chalcopyrite	4.5	1.05	4.0×10^{-15}	586.7
Magnetite	4.5	1.01	2.0×10^{-15}	586.7
K-feldspar	18.0	1.65	3.1×10^{-16}	2710.0
Albite	9.0	0.9	3.1×10^{-16}	1360.0
Anorthite	9.0	0.89	1.5×10^{-16}	1420.0
Annite	4.5	0.29	2.4×10^{-18}	586.7
Muscovite	9.0	0.64	2.4×10^{-18}	1230.0
Quartz	18.0	7.93	4.3×10^{-18}	850.0
Anhydrite	4.5	0.98	1.5×10^{-16}	510.0
Total=90				
Void=10				

Table 2. Aqueous species, gas and minerals considered in the simulation of supergene copper enrichment.

<i>Primary species:</i>	<i>Secondary species:</i>		<i>Primary minerals:</i>
H ⁺	OH ⁻	FeOH ⁺	Pyrite
H ₂ O	HSO ₄ ⁻	FeOH ²⁺	Chalcopyrite
O ₂ (aq)	H ₂ SO ₄ (aq)	Fe(OH) ₂ ⁺	Magnetite
SO ₄ ⁻	NaSO ₄ ⁻	Fe ₂ (OH) ₂ ⁴⁺	K-feldspar
Fe ²⁺	KSO ₄ ⁻	Fe(OH) ₂ (aq)	Albite
Cu ²⁺	CaSO ₄ (aq)	Fe(OH) ₃ (aq)	Anorthite
Na ⁺	FeSO ₄ (aq)	Fe ₃ (OH) ₄ ⁵⁺	Annite
K ⁺	Fe(SO ₄) ₂ ⁻	CaOH ⁺	Muscovite
Ca ²⁺	FeSO ₄ ⁺	Cu ⁺	Quartz
Al ³⁺	FeCl ⁺	CuOH ⁺	Anhydrite
SiO ₂ (aq)	AlSO ₄ ⁺	CuCl ₂ (aq)	
Cl ⁻	Al(SO ₄) ₂ ⁻	CuCl ₂ ⁻	<i>Secondary minerals:</i>
	AlOH ⁺⁺	CuCl ₄ ²⁻	Covellite
<i>Gas:</i>	Al(OH) ₂ ⁺	CaCl ⁺	Chalcocite
O ₂ (g)	Al ₂ (OH) ₂ ⁴⁺	KCl(aq)	Bornite
	Al ₃ (OH) ₄ ⁵⁺	Fe ³⁺	Goethite
	HAlO ₂ (aq)	HS ⁻	Hematite
	AlO ₂ ⁻	H ₂ S(aq)	Kaolinite
	FeCl ²⁺	HSiO ₃ ⁻	Alunite
	FeCl ₂ ⁺	NaHSiO ₃ (aq)	Amorphous silica

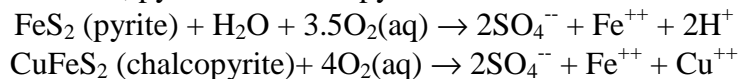
3. Modeling approach

In the present work, major assumptions are made as follows: (1) porosity and permeability change from mineral dissolution/precipitation is neglected, which is justified for shorter time scales of order 100 years; (2) aqueous chemical concentration changes do not influence fluid thermophysical properties such as density and viscosity; (3) changes in partial pressure of O₂ gas due to chemical reactions do not affect overall gas and liquid flow, and (4) heat generation due to chemical reactions is neglected.

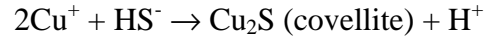
The oxidative weathering and supergene enrichment process is simulated with the multi-phase reactive transport model TOUGHREACT (Xu and Pruess, 1999b). The model is implemented by introducing reactive chemical transport into the framework of the existing non-isothermal multi-phase flow code TOUGH2 (Pruess, 1991). The model uses a sequential iteration approach, which solves the transport and the reaction equations separately. The flow and transport in geologic media is based on space discretization by means of integral finite differences (Narasimhan and Witherspoon, 1976). An implicit time-weighting scheme is used. The chemical transport equations are solved independently for each component, whereas the reaction equations are solved on a grid block basis using Newton-Raphson iteration. An improved equilibrium-kinetics speciation model for simulating water-rock-gas interaction is employed (Xu et al., 1999a). The code is operational on both PCs and massively parallel computers.

4. Results

In the unsaturated zone, pyrite and chalcopyrite are oxidized and dissolved (Figure 2a):



As aqueous phase oxygen is depleted through reaction with pyrite and chalcopyrite, it is replenished by dissolution from the gas phase, and by diffusive transport from the atmospheric boundary at the land surface. The pH (Figure 3a) decreases downward, and the total dissolved Cu concentration (Figure 3b) increase due to pyrite and chalcopyrite oxidation. When the aqueous solution reaches the reducing saturated zone, the secondary copper bearing minerals chalcocite and covellite are precipitated (Figure 2b),



forming the enrichment blanket immediately below the water table as shown in Figure 1. In addition, goethite precipitates in the unsaturated zone. At the same time magnetite, K-feldspar, albite, anorthite, annite and muscovite dissolve throughout the column due to decrease of pH. More detailed results are given in *Xu et al. [1999c]*. The alteration of primary minerals and development of secondary mineral assemblages predicted are consistent with observations in supergene copper deposits in the Atacama Desert, Northern Chile (Ague and Brimhall, 1989).

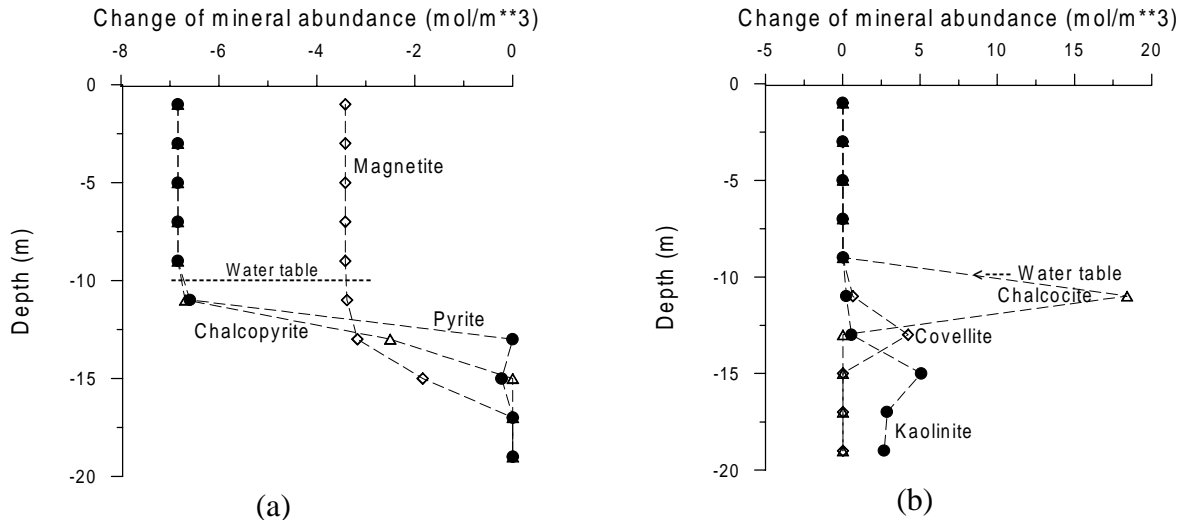


Figure 2. Change of mineral abundance (in moles per cubic meter medium) after 90 years. Negative values indicate dissolution, positive indicate precipitation.

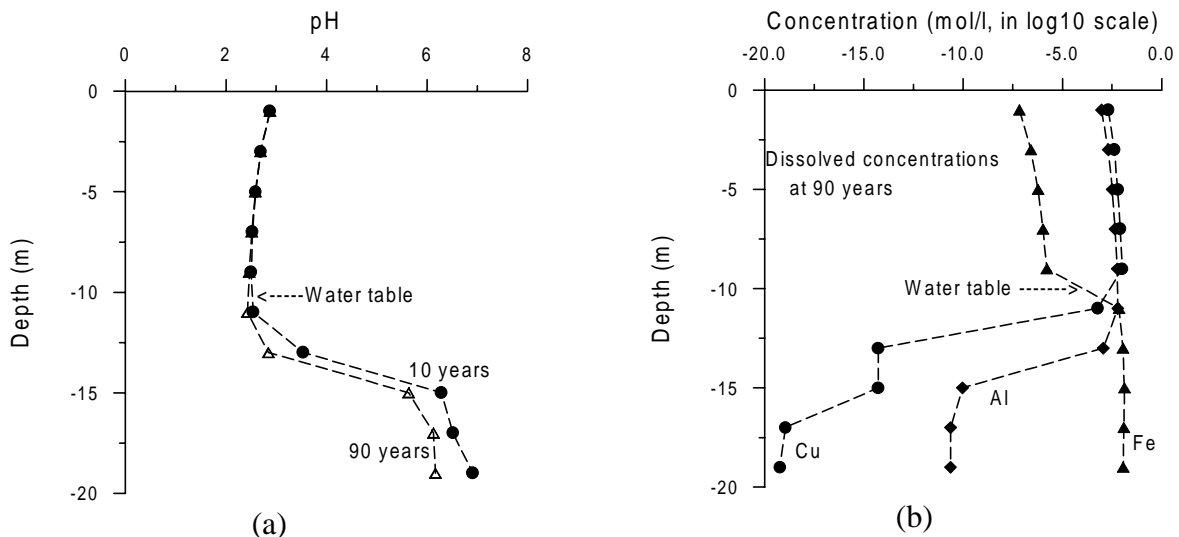


Figure 3. pH and total dissolved concentrations along the vertical column.

5. Discussion and conclusions

Mathematical modeling of rock-fluid interaction with redox processes is extremely challenging because (1) sulfide mineral oxidation occurs through a complex interplay of multiphase flow and transport processes; and (2) aqueous concentrations of key species (such as HS^- and SO_4^{2-}) vary over an enormous range, (3) oxygen inventory and supply are typically small in comparison to mineral inventory; and (4) chemical reactions are complex, involving kinetic control. Our model provides a comprehensive suite of process modeling capabilities. The application of TOUGHREACT to a supergene copper enrichment demonstrated stable convergence behavior and geochemically reasonable results. Although only a one-dimensional domain is used in the presented example, the model can be applied to two- or three-dimensional systems in hydrologically and geochemically heterogeneous media.

Acknowledgement

This work was supported by the Laboratory Directed Research and Development Program of the Ernest Orlando Lawrence Berkeley National Laboratory, under Contract No. DE-AC03-76SF00098 with the U.S. Department of Energy.

References

- Ague, J. J., and Brimhall, G. H., 1989, Geochemical modeling of steady state and chemical reaction during supergene enrichment of porphyry copper deposits, *Economic Geology*, v. 84, p. 506-528.
- Brimhall, G. H., Alpers, C. N., and Cunnigham, A. B., 1985, Analysis of supergene ore-forming processes and ground water solute transport using mass balance principles, *Economic Geology*, v. 80, p. 1227-1256.
- Lasaga, A. C., Soler, J. M., Ganor, J., Burch, T. E., and Nagy, K. L., 1994, Chemical weathering rate laws and global geochemical cycles, *Geochimica et Cosmochimica Acta*, v. 58, p. 2361-2386.
- Narasimhan, T. N., and Witherspoon, P. A., 1976, An integrated finite difference method for analyzing fluid flow in porous media, *Water Resource Research*, v. 12, p. 57-64.
- Pruess, K., 1991, TOUGH2: A general numerical simulator for multiphase fluid and heat flow, Lawrence Berkeley Laboratory Report LBL-29400, Berkeley, California.
- Xu, T., K. Pruess and G. Brimhall, An improved equilibrium-kinetics speciation algorithm for redox reactions in variably saturated flow systems, *Computers & Geosciences*, v. 25, p. 655-666, 1999a.
- Xu, T., and K. Pruess, Coupled modeling of non-isothermal multiphase flow, solute transport and reactive chemistry in porous and fractured media: 1. Model development and validation, submitted to *American Journal of Science*, 1999b.
- Xu, T., E. Sonnenthal, N. Spycher, K. Pruess, and G. Brimhall, Coupled modeling of non-isothermal multiphase flow, solute transport and reactive chemistry in porous and fractured media: 2. Applications, submitted to *American Journal of Science*, 1999c.

EXECUTIVE SUMMARIES FOR STUDIES AT MARICOPA ENVIRONMENTAL MONITORING SITE

Young, M.H., P.J. Wierenga, A.W. Warrick, L.L. Hofmann, S.A. Musil, M. Yao, C. Mai, B.R. Scanlon. 1999. Results of field studies at the Maricopa Environmental Monitoring Site, Arizona. NUREG/CR-5694, U.S. Nuclear Regulatory Commission, Washington, DC.

Executive Summary

U.S. Nuclear Regulatory staff identified a need for research to better assess unsaturated zone monitoring techniques and strategies applicable to LLW disposal facilities. The need was later expanded to include facilities designated under the Site Decommissioning Management Plan (SDMP). This research project originated from the need to evaluate a wide variety of issues related to alternative monitoring strategies, which could be used in long-term monitoring programs at disposal sites, and thus reviewed by NRC staff during the licensing process. Thus, field implementation and evaluation of alternative strategies were important and necessary components of this research project. The purpose of this NUREG is to report on the field activities and the results of the field experiments; NUREG/CR-5698 (Young et al., 1999) directly compares the strengths and weaknesses of the monitoring strategies.

Goals of the research were to: 1) assess capabilities, limitations, and usefulness of alternative techniques for monitoring water movement and contaminant transport in the unsaturated zone of humid and arid areas; 2) provide the technical bases for identifying and evaluating appropriate techniques for unsaturated zone monitoring at LLW and SDMP sites; 3) develop guidance on the design, installation, use, and decommissioning of unsaturated zone monitoring systems; 4) examine the issue of whether and how unsaturated zone monitoring systems may compromise the performance of natural and engineered barriers at LLW facilities and how to eliminate or mitigate such compromises; and 5) test monitoring strategies and instrumentation on a variety of field scales using actual water and solute tracer application rates and geometries.

To achieve these goals, a field site was designed for conducting controlled water flow and solute transport studies, and for testing the strengths and weaknesses of four monitoring strategies. The site is located at the Maricopa Agricultural Center, Maricopa, AZ, a research facility which is located about 42 km southwest of Phoenix and operated by the University of Arizona. The field was extensively instrumented using commercially-available monitoring systems. The monitoring systems overlap each other considerably, permitting them to support more than one monitoring strategies. Briefly described, the strategies are: 1) Monitoring Trench strategy - a 60 m trench excavated to 1.5-m depth, into which 13 instrumentation clusters were installed at 5 m lateral spacing; 2) Monitoring Island strategy - two vertical culverts (1.55 m diameter) drilled to 3-m depth with monitoring instruments installed radially around the islands into undisturbed soil; 3) Borehole Monitoring strategy - vertical and horizontal access tubes (120 total), into which permanently-installed (tensiometers and solution samplers) or portable sensors (neutron probe) were inserted for taking measurements; and 4) Geophysical Monitoring strategy - incorporated permanently-installed (ERT; 12 locations) and portable (EM-31, EM-38; 90 locations each)

sensors for monitoring changes in bulk electrical conductivity and resistivity.

Two experiments were conducted at the site covering the time frame from Spring 1997 through Summer 1998. During Experiment 1, an average flux of 1.85 cm d^{-1} was applied to the 50 m by 50 m field plot for 23 days for a total application of 44.4 cm. Bromide was added as a tracer for the first 15 days. Redistribution occurred for 69 days before the experiment ended. During Experiment 2, an average of 1.97 cm d^{-1} was applied to the soil for 33 days for a total application of 64.82 cm. Salt (NaCl) was added as a tracer for the first 7 days. Redistribution occurred for 177 days before field experiments at the site ended officially on July 1, 1998. Data were collected manually and through a series of data acquisition systems.

Water movement across the plot was spatially variable during Experiment 1, due mostly to variability in the initial water content, and thus, the hydraulic conductivity. The results of the intrusive and non-intrusive instruments, many of which provided redundant measurements of performance measures (e.g., water content, water tension, solute concentration), showed that 1) water movement in the western portion of the site was faster than the eastern portion, due most likely to soil texture and structure; 2) a zone of rapid water flow was observed near the northern and central areas of the plot; and 3) the variability of water movement, as measured using the neutron probe, decreased with increasing depth, when the effective thickness of the soil profile was increased. Spatial variability of water movement was significantly reduced in surface soils ($< 1.5 \text{ m}$), from a $\text{CV} = 41.8 \%$ to 4.7% between Experiments 1 and 2, respectively. The reduced variability was observed because the flux-controlled water application led to more uniform hydraulic property fields, and thus, more uniform water movement. A flood or sprinkler method of water application probably would have resulted in higher variability than we observed, because of the dependence of infiltration rates on the hydraulic conductivity of surface soils, an aspect of the field site that would be very difficult to characterize or monitor. Given that most infiltration in nature occurs in non-flood conditions (e.g., rainfall rate $<$ soil hydraulic conductivity), the boundary conditions used during the experiments are more realistic and easily monitored.

Most of the monitoring systems performed well during the field experiments, and the report presents and describes the data collected for each of the systems used. However, some data collected from the tensiometers were lost (or considered unreliable) due to corrosion of electrical connections where wire leads were spliced together with connectors. In fact, all pressure transducers installed in the trench tensiometers were replaced before Experiment 2 because of corrosion problems, and some units were still problematic. Tensiometers installed in the deep boreholes operated very well during Experiment 1, but many of them failed during Experiment 2. Over-designing these connections, to withstand the harsh ambient conditions, likely would have reduced some of this data loss. We noticed a significant amount of feedback through the A/C power system that led to larger variability in the TDR readings, especially during Experiment 1. We solved the problem by modifying the TDR cable testers so that all data would be collected using the backup battery. Data from most of the other monitoring systems exhibited some effects from the large changes in ambient temperature and humidity, requiring some secondary post-processing. For example, the neutron probe meter was effected by temperature fluctuations, requiring the collection of standard counts at least twice per day, and subsequent testing to ensure that the standard counts were within the 95% confidence interval established for each probe.

Young, M.H., A.W. Warrick, P.J. Wierenga, S.A. Musil, 1999. Comparing monitoring strategies at the Maricopa site, Arizona. NUREG/CR-5698, U.S. Nuclear Regulatory Commission, Washington, DC.

Executive Summary

U.S. Nuclear Regulatory staff identified a need for research to better assess unsaturated zone monitoring techniques and strategies applicable to LLW disposal facilities. A field work plan was developed and implemented at the Maricopa Environmental Monitoring site (Maricopa, AZ) where two field-scale infiltration experiments were conducted. A companion NUREG (i.e., NUREG/CR-5694) presents the results of the field experiments with respect to water movement and tracer migration.

This document discusses the need to emphasize redundancy in the monitoring of primary performance measures (e.g., water content, water tension and solute concentration). Each of these performance measures directly influences water movement and contaminant migration from disposal sites. Almost all monitoring instruments provide data on secondary measures, which are converted to primary measures using calibration curves. Using different instruments, whose data convert to the same primary performance measure, can account for limitations and sensitivities of each instrument.

This document also describes and compares four monitoring strategies that were implemented at the site. The strengths and weaknesses of each strategy were described with respect to installation, maintenance and replacement of monitoring systems and instruments. The comparisons stem directly from insights gained during the field experiments, and from the work of others. The comparisons are qualitative in nature, so that they are not influenced by the specific characteristics of the Maricopa site. The four strategies follow:

1. Monitoring Trenches consist of potentially long, wide or narrow trenches, into which instruments can be installed. Once opened, the trench provides direct access to the soil or engineered material. The material can be sampled and described easily. Instruments can be precisely placed and visually inspected for completion. Wiring and electrical connections can be placed in conduit and protected from environmental degradation. Maintenance and replacement of instruments in the trench are limited after the trench is closed.
2. Monitoring Islands consist of large diameter boreholes drilled vertically into the soil, allowing monitoring instruments to be installed into undisturbed material. This strategy permits excellent monitoring of vertical transects of soil water conditions, because the islands can be potentially installed to depths exceeding 10 m. However, the horizontal spatial resolution is limited because instruments must be installed close to the island wall. Instrument maintenance and replacement are easier than the other strategies that rely on fixed, subsurface instruments.
3. Borehole Monitoring consists of vertical and horizontal boreholes used for monitoring. Using portable probes (e.g., neutron probe), spatial and depth resolution of data can be

excellent. Fixed point devices can be installed in the borehole, enhancing the redundancy of monitoring for primary performance measures. Maintenance and replacement of portable probes is not an issue with this strategy, but is very difficult for permanently-installed instruments.

4. Geophysical monitoring consists of a combination of intrusive and non-intrusive techniques for measuring bulk electrical properties of subsurface material. The data cannot easily be converted to primary performance measures, and could require a significant amount of ground-truthing. However, portability of non-intrusive instruments (e.g., EM-31 and EM-38) permits rapid data collection. Intrusive techniques used at the Maricopa site (e.g., electroresistive tomography) can provide 2-D tomograms of electrical properties, which were shown to change with water content. Maintenance of ERT boreholes is not practical, requiring complete replacement.

We identified 12 subgoals for the monitoring program, all of which are compatible with the three major goals described in Section 2. The subgoals are intended to better define the important aspects of the monitoring program and how or whether use of the monitoring strategy can address the subgoal. We also included a section that deals with site conditions and processes and how they affect the choices of possible monitoring strategies. We further subdivided these into natural (e.g., precipitation, depth to water table) and anthropogenic (e.g., presence of buildings) conditions. A total of 12 site conditions were identified and opposing conditions were defined (e.g., shallow/deep water table). We then categorized each strategy as to whether the condition supported its use, weakened its use, or made no difference with respect to its use. When used in combination with the subgoals, the choice which strategy (or combination of strategies) to use becomes more clear.

The controlled flux experiments conducted at the Maricopa site provided a large set of data and information that can be used for directly comparing numerous monitoring systems, which were chosen to support four monitoring strategies, and for studying other aspects of monitoring systems that are not directly related to the field experiments. Three such studies were undertaken, ranging from analysis of monitoring programs to correction of individual monitoring instruments. Other future studies will be initiated using the existing database.

Moment Equation Approach to Unsaturated Fluid Flow

Dongxiao Zhang

Geoanalysis Group (EES-5), MS C306
Los Alamos National Laboratory
Los Alamos, NM 87545
Tel: 505 667 3541
dongzhang@lanl.gov

1 Introduction

Although geologic media exhibit a high degree of spatial variability, medium properties, including fundamental parameters such as permeability and porosity, are usually observed only at a few locations due to the high cost associated with subsurface measurements. This combination of significant spatial heterogeneity with a relatively small number of observations leads to uncertainty about the values of medium properties and thus, to uncertainty in predicting flow and solute transport in such media. The theory of stochastic processes provides a natural method for evaluating the prediction uncertainty. In the stochastic formalism, uncertainty is represented by probability or by related quantities like statistical moments. Medium properties, boundary conditions and/or initial conditions are treated as random fields (RFs) whose values are determined by probability distributions. In turn, dependent variables like pressure and flux are RFs, and the equations governing subsurface flow and transport become stochastic differential equations (SDEs) whose solutions are probability distributions of pressure and flux.

Generally we cannot solve an SDE exactly, but can only estimate the first few moments of the corresponding probability distribution, specifically its mean, variance and covariances. However, these moments usually suffice to approximate confidence intervals. In the last two decades, many stochastic theories have been developed to obtain statistical moments for subsurface flow and transport quantities [e.g., *Dagan*, 1989; *Gelhar*, 1993; *Dagan and Neuman*, 1997]. In this short note, we outline one such moment equation based theory, and in particular, the resultant moment equations, for unsaturated flow in heterogeneous media. The resultant moments provide a measure of prediction uncertainty caused by incomplete knowledge of medium heterogeneity.

2 Moment Equations

The moment equation approach is based on Richard's equation,

$$C[h, \cdot] \frac{\partial h(\mathbf{x}, t)}{\partial t} + \nabla \cdot \mathbf{q}(\mathbf{x}, t) = g(\mathbf{x}, t) \quad (1)$$

$$q_i(\mathbf{x}, t) = -K[h, \cdot] \frac{\partial}{\partial x_i} [h(\mathbf{x}, t) + x_1] \quad (2)$$

subject to initial and boundary conditions

$$h(\mathbf{x}, 0) = H_o(\mathbf{x}), \quad \mathbf{x} \in \Omega \quad (3)$$

$$h(\mathbf{x}, t) = H(\mathbf{x}, t), \quad \mathbf{x} \in \Gamma_D \quad (4)$$

$$\mathbf{q}(\mathbf{x}, t) \cdot \mathbf{n}(\mathbf{x}) = Q(\mathbf{x}, t), \quad \mathbf{x} \in \Gamma_N \quad (5)$$

$$\frac{\partial}{\partial x_1} [h(\mathbf{x}, t) + x_1] = 1, \quad \mathbf{x} \in \Gamma_G \quad (6)$$

where \mathbf{q} is the specific discharge (flux), $h(\mathbf{x}, t) + x_1$ is the total head, h is the pressure head, $i = 1, \dots, d$ (where d is the number of space dimensions), $g(\mathbf{x}, t)$ is the fluid source/sink term, $H_o(\mathbf{x})$ is the initial pressure head distribution in the domain Ω , $H(\mathbf{x}, t)$ is the prescribed head on Dirichlet boundary segments Γ_D at time t , $Q(\mathbf{x}, t)$ is the prescribed flux across Neumann boundary segments Γ_N at time t , $\mathbf{n}(\mathbf{x}) = (n_1, \dots, n_d)^T$ is a unit vector outward normal to the boundary, Γ_G is the boundary segment where flow is gravity-dominated so that the (total) pressure gradient is unit, $C[h, \cdot] \equiv d\theta_e/dh$ is the specific moisture capacity, and $K[h, \cdot]$ is the unsaturated hydraulic conductivity (assumed to be isotropic locally). Both C and K are functions of pressure head and soil properties at \mathbf{x} . For convenience, they will be written as $C(\mathbf{x}, t)$ and $K(\mathbf{x}, t)$ in the sequel. The elevation x_1 is directed vertically upward. In these coordinates, recharge has a negative sign.

To close the equations (1)-(6), some model is needed to describe the constitutive relationships of $K(h)$ and $C(h) = d\theta_e/dh$. In most stochastic unsaturated flow theories, the Gardner-Russo model [Gardner, 1958; Russo, 1988] is used due to its simplicity (see Zhang *et al.* [1998] and Zhang and Winter [1998] for the treatment of the Brooks-Corey [1964] model). The Gardner-Russo model reads as,

$$K(\mathbf{x}, t) = K_s(\mathbf{x}) \exp[\alpha(\mathbf{x})h(\mathbf{x}, t)] \quad (7)$$

$$\theta_e(\mathbf{x}, t) = (\theta_s - \theta_r) \{ \exp[0.5\alpha(\mathbf{x})h(\mathbf{x}, t)] [1 - 0.5\alpha(\mathbf{x})h(\mathbf{x}, t)] \}^{2/(m+2)} \quad (8)$$

where θ_e , θ_r and θ_s are the effective, residual and saturated water content, respectively, K_s is the saturated hydraulic conductivity, α is the soil parameter related to pore size distribution, and m is a parameter related to tortuosity. For simplicity, we let $m = 0$ in this study. In this simple case,

$$C(\mathbf{x}, t) = -\frac{\theta_s - \theta_r}{4} \alpha^2(\mathbf{x}) h(\mathbf{x}, t) \exp[0.5\alpha(\mathbf{x})h(\mathbf{x}, t)] \quad (9)$$

The extension to the case of $m \neq 0$ can be made by following the treatment of Zhang *et al.* [1998] for steady-state unsaturated flow. The variabilities of θ_s and θ_r are likely to be small compared to that of the effective water content θ_e . In this study, θ_s and θ_r are assumed to be deterministic constants. The soil property $\alpha(\mathbf{x})$, and the log transformed saturated hydraulic conductivity $f(\mathbf{x}) = \ln K_s(\mathbf{x})$ are treated as random variables. Hence, the dependent variables like pressure and flux are also random variables and Richard's equation becomes an SDE. As mentioned earlier, one may estimate the first few moments of the dependent variables based on the statistical moments of input parameters. In this study, both α and f are assumed to be second-order stationary such that their expected values are constant and their covariances depend on the relative distance of two points rather than their actual locations. Without loss of generality, $H_o(\mathbf{x})$, $H(\mathbf{x}, t)$, $Q(\mathbf{x}, t)$ and $g(\mathbf{x}, t)$ are assumed to be deterministic (i.e., known with certainty).

The moment equation approach starts with decomposing the input random variables as $f(\mathbf{x}) = \langle f \rangle + f'(\mathbf{x})$ and $\alpha(\mathbf{x}) = \langle \alpha \rangle + \alpha'(\mathbf{x})$, where $\langle \cdot \rangle$ stands for ensemble average (expectation) and the primed quantities are the zero-mean fluctuations. Since the variability of $h(\mathbf{x}, t)$ depends on those of the medium properties α and f and the variabilities of $Y =$

$\ln K(\mathbf{x}, t)$ and $C(\mathbf{x}, t)$ depend on those of h and the medium properties, one may express these quantities as an infinite series in the following form: $h(\mathbf{x}, t) = h^{(0)} + h^{(1)} + h^{(2)} + \dots$, $Y(\mathbf{x}, t) = Y^{(0)} + Y^{(1)} + Y^{(2)} + \dots$, and $C(\mathbf{x}, t) = C^{(0)} + C^{(1)} + C^{(2)} + \dots$ [Zhang, 1999]. In these series, the order of each term is with respect to the variability of the medium properties. After substituting these expressions into Richard's equation and collecting terms at separate order, and after some mathematical manipulations, one arrives equations governing $h^{(n)}$ ($n = 1, 2 \dots$) [Zhang, 1999]. It has been shown that $\langle h^{(0)} \rangle = h^{(0)}$ and $\langle h^{(1)} \rangle = 0$. Hence, the mean head $\langle h \rangle = h^{(0)}$ to zeroth- or first-order in terms of the variability of medium properties, and $\langle h \rangle = h^{(0)} + \langle h^{(2)} \rangle$ to second-order. For the head fluctuation, $h' = h^{(1)}$ to first-order. Therefore, to first-order the head covariance $C_h(\mathbf{x}, t; \boldsymbol{\chi}, \tau) = \langle h^{(1)}(\mathbf{x}, t) h^{(1)}(\boldsymbol{\chi}, \tau) \rangle$.

The equation for the first-order mean head reads as [Zhang, 1999],

$$\begin{aligned} \frac{\partial^2 \langle h(\mathbf{x}, t) \rangle}{\partial x_i^2} + a_i(\mathbf{x}, t) \frac{\partial \langle h(\mathbf{x}, t) \rangle}{\partial x_i} &= e(\mathbf{x}, t) \frac{\partial \langle h(\mathbf{x}, t) \rangle}{\partial t} - \frac{g(\mathbf{x}, t)}{K_m(\mathbf{x}, t)} \\ \langle h(\mathbf{x}, 0) \rangle &= H_o(\mathbf{x}), \quad \mathbf{x} \in \Omega \\ \langle h(\mathbf{x}, t) \rangle &= H(\mathbf{x}, t), \quad \mathbf{x} \in \Gamma_D \\ n_i(\mathbf{x}) \frac{\partial \langle h(\mathbf{x}, t) \rangle}{\partial x_i} &= -\frac{Q(\mathbf{x}, t)}{K_m(\mathbf{x}, t)} - \delta_{i1} n_i(\mathbf{x}), \quad \mathbf{x} \in \Gamma_N \\ \frac{\partial \langle h(\mathbf{x}, t) \rangle}{\partial x_1} &= 0, \quad \mathbf{x} \in \Gamma_G \end{aligned} \quad (10)$$

where $K_m(\mathbf{x}, t) = \exp[\langle f \rangle] \exp[\langle \alpha \rangle \langle h(\mathbf{x}, t) \rangle]$, $a_i(\mathbf{x}, t) = \langle \alpha \rangle J_i(\mathbf{x}, t)$ with $J_i(\mathbf{x}, t) = \partial \langle h(\mathbf{x}, t) \rangle / \partial x_i + \delta_{i1}$, and $e(\mathbf{x}, t) = C^{(0)}(\mathbf{x}, t) / K_m(\mathbf{x}, t)$ with $C^{(0)} = -0.25(\theta_s - \theta_r) \langle \alpha \rangle^2 \langle h(\mathbf{x}, t) \rangle \exp[0.5 \langle \alpha \rangle \langle h(\mathbf{x}, t) \rangle]$. This equation is nonlinear because the coefficients $K_m(\mathbf{x}, t)$, $a_i(\mathbf{x}, t)$ and $e(\mathbf{x}, t)$ all are functions of the dependent variable $\langle h \rangle$. The equation for the first-order head covariance is given as

$$\begin{aligned} \frac{\partial^2 C_h(\mathbf{x}, t; \boldsymbol{\chi}, \tau)}{\partial x_i^2} + b_i(\mathbf{x}, t) \frac{\partial C_h(\mathbf{x}, t; \boldsymbol{\chi}, \tau)}{\partial x_i} + c(\mathbf{x}, t) C_h(\mathbf{x}, t; \boldsymbol{\chi}, \tau) &= e(\mathbf{x}, t) \frac{\partial C_h(\mathbf{x}, t; \boldsymbol{\chi}, \tau)}{\partial t} \\ - J_i(\mathbf{x}, t) \frac{\partial C_{fh}(\mathbf{x}; \boldsymbol{\chi}, \tau)}{\partial x_i} - J_i(\mathbf{x}, t) \langle h(\mathbf{x}, t) \rangle \frac{\partial C_{\alpha h}(\mathbf{x}; \boldsymbol{\chi}, \tau)}{\partial x_i} \\ + d_1(\mathbf{x}, t) C_{fh}(\mathbf{x}; \boldsymbol{\chi}, \tau) + d_2(\mathbf{x}, t) C_{\alpha h}(\mathbf{x}; \boldsymbol{\chi}, \tau) \\ C_h(\mathbf{x}, 0; \boldsymbol{\chi}, \tau) &= 0, \quad \mathbf{x} \in \Omega \\ C_h(\mathbf{x}, t; \boldsymbol{\chi}, \tau) &= 0, \quad \mathbf{x} \in \Gamma_D \\ n_i(\mathbf{x}) \frac{\partial C_h(\mathbf{x}, t; \boldsymbol{\chi}, \tau)}{\partial x_i} + d_3(\mathbf{x}, t) C_h(\mathbf{x}, t; \boldsymbol{\chi}, \tau) \\ &= d_4(\mathbf{x}, t) C_{fh}(\mathbf{x}; \boldsymbol{\chi}, \tau) + d_5(\mathbf{x}, t) C_{\alpha h}(\mathbf{x}; \boldsymbol{\chi}, \tau), \quad \mathbf{x} \in \Gamma_N \\ \frac{\partial C_h(\mathbf{x}, t; \boldsymbol{\chi}, \tau)}{\partial x_1} &= 0, \quad \mathbf{x} \in \Gamma_G \end{aligned} \quad (11)$$

where $b_i(\mathbf{x}, t) = [2J_i(\mathbf{x}, t) - \delta_{i1}] \langle \alpha \rangle$, $c(\mathbf{x}, t) = -\langle \alpha \rangle d_1(\mathbf{x}, t) - J_t(\mathbf{x}, t) p_1(\mathbf{x}, t) / K_m(\mathbf{x}, t)$ with $J_t(\mathbf{x}, t) = \partial \langle h(\mathbf{x}, t) \rangle / \partial t$, $d_1(\mathbf{x}, t) = [g(\mathbf{x}, t) - J_t(\mathbf{x}, t) C^{(0)}(\mathbf{x}, t)] / K_m(\mathbf{x}, t)$, $d_2(\mathbf{x}, t) = d_1(\mathbf{x}, t) \langle h(\mathbf{x}, t) \rangle -$

$J_i(\mathbf{x}, t)[J_i(\mathbf{x}, t) - \delta_{i1}] + J_t(\mathbf{x}, t)p_2(\mathbf{x}, t)/K_m(\mathbf{x}, t), p_1(\mathbf{x}, t) = -0.25(\theta_s - \theta_r) \exp[0.5\langle\alpha\rangle\langle h(\mathbf{x}, t)\rangle][\langle\alpha\rangle^2 + 0.5\langle\alpha\rangle^3\langle h(\mathbf{x}, t)\rangle], p_2(\mathbf{x}, t) = -0.5(\theta_s - \theta_r) \exp[0.5\langle\alpha\rangle\langle h(\mathbf{x}, t)\rangle][\langle\alpha\rangle\langle h(\mathbf{x}, t)\rangle + 0.25\langle\alpha\rangle^2[\langle h(\mathbf{x}, t)\rangle]^2],$
 $d_3(\mathbf{x}, t) = \langle\alpha\rangle n_i(\mathbf{x})J_i(\mathbf{x}, t), d_4(\mathbf{x}, t) = -n_i(\mathbf{x})J_i(\mathbf{x}, t),$ and $d_5(\mathbf{x}, t) = -n_i(\mathbf{x})J_i(\mathbf{x}, t)\langle h(\mathbf{x}, t)\rangle.$

The cross covariances C_{fh} and $C_{\alpha h}$ are the solutions of the following equations,

$$\begin{aligned} & \frac{\partial^2 C_{fh}(\mathbf{x}; \boldsymbol{\chi}, \tau)}{\partial \chi_i^2} + b_i(\boldsymbol{\chi}, \tau) \frac{\partial C_{fh}(\mathbf{x}; \boldsymbol{\chi}, \tau)}{\partial \chi_i} + c(\boldsymbol{\chi}, \tau) C_{fh}(\mathbf{x}; \boldsymbol{\chi}, \tau) = e(\boldsymbol{\chi}, \tau) \frac{\partial C_{fh}(\mathbf{x}; \boldsymbol{\chi}, \tau)}{\partial \tau} \\ & - J_i(\boldsymbol{\chi}, \tau) \frac{\partial C_f(\mathbf{x}; \boldsymbol{\chi})}{\partial \chi_i} - J_i(\boldsymbol{\chi}, \tau) \langle h(\boldsymbol{\chi}, \tau) \rangle \frac{\partial C_{f\alpha}(\mathbf{x}; \boldsymbol{\chi})}{\partial \chi_i} + d_1(\boldsymbol{\chi}, \tau) C_f(\mathbf{x}; \boldsymbol{\chi}) + d_2(\boldsymbol{\chi}, \tau) C_{f\alpha}(\mathbf{x}; \boldsymbol{\chi}) \\ & C_{fh}(\mathbf{x}; \boldsymbol{\chi}, \tau) = 0, \quad \boldsymbol{\chi} \in \Omega \\ & C_{fh}(\mathbf{x}; \boldsymbol{\chi}, \tau) = 0, \quad \boldsymbol{\chi} \in \Gamma_D \\ & n_i(\boldsymbol{\chi}) \frac{\partial C_{fh}(\mathbf{x}; \boldsymbol{\chi}, \tau)}{\partial \chi_i} + d_3(\boldsymbol{\chi}, \tau) C_{fh}(\mathbf{x}; \boldsymbol{\chi}, \tau) \\ & \quad = d_4(\boldsymbol{\chi}, \tau) C_f(\mathbf{x}; \boldsymbol{\chi}) + d_5(\boldsymbol{\chi}, \tau) C_{f\alpha}(\mathbf{x}; \boldsymbol{\chi}), \quad \boldsymbol{\chi} \in \Gamma_N \\ & \frac{\partial C_{fh}(\mathbf{x}; \boldsymbol{\chi}, \tau)}{\partial \chi_1} = 0, \quad \boldsymbol{\chi} \in \Gamma_G \end{aligned} \tag{12}$$

$$\begin{aligned} & \frac{\partial^2 C_{\alpha h}(\mathbf{x}; \boldsymbol{\chi}, \tau)}{\partial \chi_i^2} + b_i(\boldsymbol{\chi}, \tau) \frac{\partial C_{\alpha h}(\mathbf{x}; \boldsymbol{\chi}, \tau)}{\partial \chi_i} + c(\boldsymbol{\chi}, \tau) C_{\alpha h}(\mathbf{x}; \boldsymbol{\chi}, \tau) = e(\boldsymbol{\chi}, \tau) \frac{\partial C_{\alpha h}(\mathbf{x}; \boldsymbol{\chi}, \tau)}{\partial \tau} \\ & - J_i(\boldsymbol{\chi}, \tau) \frac{\partial C_{\alpha f}(\mathbf{x}; \boldsymbol{\chi})}{\partial \chi_i} - J_i(\boldsymbol{\chi}, \tau) \langle h(\boldsymbol{\chi}, \tau) \rangle \frac{\partial C_{\alpha}(\mathbf{x}; \boldsymbol{\chi})}{\partial \chi_i} + d_1(\boldsymbol{\chi}, \tau) C_{\alpha f}(\mathbf{x}; \boldsymbol{\chi}) + d_2(\boldsymbol{\chi}, \tau) C_{\alpha}(\mathbf{x}; \boldsymbol{\chi}) \\ & C_{\alpha h}(\mathbf{x}; \boldsymbol{\chi}, \tau) = 0, \quad \boldsymbol{\chi} \in \Omega \\ & C_{\alpha h}(\mathbf{x}; \boldsymbol{\chi}, \tau) = 0, \quad \boldsymbol{\chi} \in \Gamma_D \\ & n_i(\boldsymbol{\chi}) \frac{\partial C_{\alpha h}(\mathbf{x}; \boldsymbol{\chi}, \tau)}{\partial \chi_i} + d_3(\boldsymbol{\chi}, \tau) C_{\alpha h}(\mathbf{x}; \boldsymbol{\chi}, \tau) \\ & \quad = d_4(\boldsymbol{\chi}, \tau) C_{\alpha f}(\mathbf{x}; \boldsymbol{\chi}) + d_5(\boldsymbol{\chi}, \tau) C_{\alpha}(\mathbf{x}; \boldsymbol{\chi}), \quad \boldsymbol{\chi} \in \Gamma_N \\ & \frac{\partial C_{\alpha h}(\mathbf{x}; \boldsymbol{\chi}, \tau)}{\partial \chi_1} = 0, \quad \boldsymbol{\chi} \in \Gamma_G \end{aligned} \tag{13}$$

In the above, C_f , $C_{f\alpha}$ and C_{α} are the input covariances of the medium properties. The moment equations (10)-(13) are in terms of the known input moments of the medium properties and thus are no longer stochastic partial differential equations but deterministic ones. Note that although the equation governing the first moment $\langle h \rangle$ is nonlinear, equations (12) and (13) are linear and solvable with the solution of $\langle h(\mathbf{x}, t) \rangle$. With C_{fh} and $C_{\alpha h}$, C_h can be solved from (11).

With these head moments, the statistical moments of water content, unsaturated conductivity, flux and velocity can be given readily [Zhang, 1999]. The mean can be used to estimate (or predict) the field of a flow quantity of interest, and the corresponding (co)variance to evaluate the uncertainty (error) associated with the estimation (prediction). These two moments can be used to construct confidence intervals for the flow quantities.

3 Implemetation

It is very difficult to obtain analytical or semi-analytical solutions for the statistical moments of head without further simplifying assumptions such as the (local) stationarity of flow quantities, unbounded domain, and slowly varying, uniform mean gradient. In the study of *Zhang* [1999], these moment equations are solved numerically. Hence, no additional assumption is needed except for the above mentioned one that the variability of medium properties is small. In solving these equations, it has been fully utilized that the moments C_h , C_{fh} and $C_{\alpha h}$ are governed by the same type of equations but with different forcing terms. The details in numerically implementing these equations and some illustrative examples are given by *Zhang and Winter* [1998] and *Zhang* [1999]; and a computer code is available through this author.

The moment equations have inherent parallel structures. For example, equation (12) for $C_{fh}(\mathbf{x}; \boldsymbol{\chi}, \tau)$ can be solved on different processes for different \mathbf{x} because they are independent; and this is also true for $C_h(\mathbf{x}, t; \boldsymbol{\chi}, \tau)$ with respect to each $(\boldsymbol{\chi}, \tau)$. Recognition and utilization of this parallelism may speed up the computation significantly. This research topic is of paramount importance for the application of moment equation approaches to real-world problems.

4 Discussion

This moment equation based stochastic model of transient flow is applicable to the entire domain of a bounded vadose zone in the presence of sink/source. The general equations governing the statistical moments of the flow quantities are derived by perturbation expansions. Due to the mathematical complexity of the equations, in general they need to be solved numerically. The numerical moment equation approach, however, has the flexibility in handling different boundary conditions, internal sink/source terms, input covariance structures, and soil constitutive relationships. The results from this stochastic model are the first two moments of flow quantities. The first two moments of a flow quantity may be used to approximate the confidence intervals for the quantity, which are a measure of uncertainty caused by incomplete knowledge of medium heterogeneity.

The conditional version of these equations can be given by the same theoretical procedure. The uncertainty in the moments of flow quantities may be reduced by conditioning on measurements of soil properties, as found by *Graham and McLaughlin* [1989] and *Zhang and Neuman* [1995] for solute transport. The conditional flow moment equations would remain the same except that the means and covariances of log saturated hydraulic conductivity f and soil pore size distribution parameter α become dependent on the locations relative to the measurement points; these equations can be solved by the same algorithm.

LIST OF REFERENCES

- Brooks, R.H., and A.T. Corey (1964), Hydraulic properties of porous media, *Hydrol. Pap.* 3, Colo. State Univ., Fort Collins.

- Dagan, G. (1989), *Flow and Transport in Porous Formations*, Springer-Verlag, New York.
- Dagan, G., and S.P. Neuman (1997), *Subsurface Flow and Transport: A Stochastic Approach*, Cambridge Univ. Press, New York.
- Gardner, W.R. (1958), Some steady state solutions of unsaturated moisture flow equations with application to evaporation from a water table, *Soil Sci.*, 85, 228-232.
- Gelhar, L.W. (1993), *Stochastic Subsurface Hydrology*, Prentice-Hall, Englewood Cliffs, N.J.
- Graham, W., and D. McLaughlin (1989), Stochastic analysis of nonstationary subsurface solute transport: 2. Conditional moments, *Water Resour. Res.*, 25(11), 2331-2355.
- Russo, D. (1988), Determining soil hydraulic properties by parameter estimation: On the selection of a model for the hydraulic properties, *Water Resour. Res.*, 24, 453-459.
- Zhang, D. (1999), Nonstationary stochastic analysis of transient unsaturated flow in randomly heterogeneous media, *Water Resour. Res.*, 35(4), 1127-1141.
- Zhang, D., and S.P. Neuman (1995), Eulerian-Lagrangian analysis of transport conditioned on hydraulic data: 1. Analytical-numerical approach, *Water Resour. Res.*, 31(1), 39-51.
- Zhang, D., and C.L. Winter (1998), Nonstationary stochastic analysis of steady-state flow through variably saturated, heterogeneous media, *Water Resour. Res.*, 34(5), 1091-1100.
- Zhang, D., T.C. Wallstrom, and C.L. Winter (1998), Stochastic analysis of steady-state unsaturated flow in heterogeneous media: Comparison of the Brooks-Corey and Gardner-Russo models, *Water Resour. Res.*, 34(6), 1437-1449.

A Case Study Involving Numerical Modeling of Transport and Removal of Volatile Organic Chemicals

By Wei Zhou

Introduction – This case study describes a modeling experience on how numerical modeling helps risk assessment of a landfill contaminated by volatile organic chemical (VOC) wastes. The Chemical Waste Landfill (CWL) that is contaminated by VOC is located in the southeast of Albuquerque, New Mexico State. Organic waste trichloroethylene (TCE) was dumped there since 1960's. Vapor concentrations of TCE were found in the vadose zone below the landfill by numerous monitoring wells. Traces of TCE were also found in groundwater approximately 490 feet below the ground surface. Department of Energy has conducted a study to assess and evaluate the risks of this contaminated site to the adjacent communities under a variety of remediation actions, including the no-action option [DOE 1997]. This work contains a demonstrative model of simulating VOC transport without any actions and under Soil Vapor Extraction (SVE) clean-up action. The obtained VOC concentrations at specified locations are then converted to risk factors for further evaluations.

The demonstrative model uses a three-dimensional model to represent heterogeneous soils in the vadose zone below and near the landfill and involves three phase fluids: gas, water, and organic phase (TCE liquid) and two gaseous species: VOC and air. The computer code used in the simulation is ECLIPSE developed by Schlumberger/GeoQuest (1996). ECLIPSE uses finite-difference method to simulate up to three-phase fluid flow and tracer transport in up to three-dimensional systems. The

code has been widely used by oil and gas industries and environmental modelers to study groundwater flow in fractured rocks and non-aqueous phase liquid (NAPL) transport.

Soil Profiles – The site’s hydrogeology has been characterized previously [Sandia 1995a; 1995b]. The soil under the landfill consists of sand, clay, and gravel layers. Annual precipitation is less than 10^{-6} ft/day. The information is reduced to a series of horizontal soil layers that have different hydraulic conductivities as shown in Figure 1 and Table 1. Characteristic curves for soils are also obtained from the previous work [Sandia 1995a]. The model horizontal extent is 977-ft x 764-ft to enclose all the investigation boreholes on the site. The total number of grids is 45144 with higher resolution assigned near those investigation boreholes where high VOC concentrations and TCE liquid are found.

Table 1. Soil Profiles and Properties used in the Model

Soils	Thickness [ft]	Depth of the Top [ft]	Porosity	Hydraulic Conductivity [cm/s]
Unconsolidated sand, silt, and gravel	107.5	0.0	0.3	7.6×10^{-3}
Sandy silt	65	107.5	0.3	10^{-4}
Silty sand	10	172.5	0.3	5×10^{-5}
Silty sand with gravel	82.5	182.5	0.3	7.6×10^{-3}
Sandy-clayey silt	40	265	0.3	5.3×10^{-6}
Silty sand	85	305	0.3	5×10^{-5}
Sandy-silt clay with gravel interbeds	75	390	0.3	5.3×10^{-6} for clay and 7.6×10^{-3} for gravel
Partly cemented sand and gravel	25	465	0.3	2×10^{-4}

Contaminant Characterization – Numerous investigation boreholes were installed to collect contamination data [Sandia 1995b]. TCE vapor concentrations at different locations and depths were obtained from soil gas analysis [Sandia 1995b]. TCE liquid is found to be at its residue saturation (0.17) at locations right below the CWL [Sandia

1995b]. This indicates that the free-phase TCE found at the site is immobile but can be a long-term source for TCE vapor. These field data serve as the initial and source conditions for TCE vapor transport in the demonstrative model.

Because of sparse distribution and fewer investigation boreholes compared with the total number of grids employed in the model, spatial interpolation of contaminant data is required. This is performed by INTERP, a program for two-dimensional interpolation of randomly spaced data to regular or irregular finite-difference grids using kriging or inverse distance algorithm [Zheng and Bennett, 1995]. The interpolation is performed in *x-y* planes at different simulation layers that are at depths where the concentration data were gathered. Interpolation parameters are chosen to confine the interpolated extent of VOC plume to the vicinity of investigation boreholes in order to avoid misrepresenting pollutant extent due to fewer data. One realization of the interpolated initial TCE vapor plume is shown in Figure 2.

Simulation of VOC Fate with No-Actions – It is assumed that in the vadose zone below the CWL, VOC migrates primarily by diffusion. Sorption is neglected. Zero concentration boundary conditions are assumed at the side and top planes of the model boundaries. No-flux boundary condition is assumed at the bottom boundary. Free-phase TCE is assumed to be in instant equilibrium with TCE vapor. A portion of VOC plume (transparent VOC concentration isosurface) after 10-year migration without actions obtained from the simulation is shown in Figure 3. It can be seen that the plume is nearly symmetric about the dumping location where TCE liquid resides. This indicates a diffusion-controlled transport process.

TCE tracer concentrations in groundwater below the CWL are obtained by converting the TCE vapor concentrations at the water table boundary and TCE Henry's law constant.

These tracer concentrations are in good agreement with those found in the monitoring wells below the CWL.

Simulation of SVE for Removing VOC – One of the purposes of the demonstrative model is to show the advantage of optimizing remediation plans using a robust numerical code and visualization tools. One can easily realize different remediation layouts and evaluate their effectiveness under complicated soil and contamination conditions [Zhou et al., 1994]. In this model, it is assumed that SVE starts after 10-year migration of VOC without actions. That is, VOC concentration distribution at 10 years shown in Figure 3 serves as initial conditions for the SVE simulation.

In this particular realization of SVE plans shown in the case study, five extraction wells are assumed to be installed across the plume by converting the investigation boreholes that have indicated the existence of TCE liquid, as shown in Figure 3. It is further assumed that in this realization, the passive SVE is employed. That is, no pumping wells are used. Air is drawn from surrounding reservoir. In this way, constant pressure boundary conditions are prescribed at side and top planes of the model boundaries. Initially, the wells are connected to soils throughout the penetration depths. Some connections are then turned off after contaminants near the connections are completely removed, as shown in Figure 4. Turning off unnecessary connections reduces the cost required for the operation and thus enhances well efficiencies. In this case, the well efficiency is defined as the amount of contaminant removal per unit volume of gas extracted.

Figure 5 shows that after 285 days of SVE operation, contaminants in soils with high permeabilities are removed. VOC trapped in soil layers with low permeabilities, however, is difficult to remove. Moreover, high VOC concentrations persist in locations where

TCE liquid exists. In order to enhance remediation efficiency, wells are shut off for a short period of time (see Figure 6). During this shut-off period, TCE vapor continues to diffuse from high concentration locations, such as low-permeability layers and soils containing TCE liquid, to the locations that are clean and have high-permeabilities. When the extraction wells are revived later, these contaminants can be quickly removed as shown in Figure 7.

Figure 8 shows the efficiencies of each extraction well, defined as the mass of TCE removal divided by the total volume of gas extracted by well. “E-C” and “E-C1” are wells located in the center of the plume where TCE liquid is found. These wells always have high removal efficiencies compared with surrounding wells, denoted as “E-E”, “E-W”, “E-S”, and “E-N”. It can be seen that every time the well is revived after shutting down, the efficiency is increased, especially for surrounding wells. It should be noted that this demonstrative model is not aimed at optimizing the SVE plan, but the same methodology can be used to optimize the SVE plan if the SVE is opted to be the remediation action of the site.

Conclusions – This case study demonstrates how to construct a conceptual model to assist risk assessment for this particular vadose zone contaminated by organic wastes by utilizing field data and advanced simulation and visualization tools. It also demonstrates how to evaluate and optimize remediation plans. The modeling results indicate that the remediation solely dependent on SVE may not be the most effective action for this site. SVE combined with other actions, such as digging up shallow soils contaminated by TCE liquid and shipping off-site, may be more effective. In addition, SVE is not the most effective action for cleaning VOC trapped in low-permeability layers below the CWL. SVE combined with heating or bio-remediation may be more effective.

References

- Department of Energy (1997), *Final Report: Risk Communication, Assessment, and Management at Hazardous Waste Sites*, DE-FC01-95EW55088.
- Sandia (1995a), *Chemical Waste Landfill Ground-Water Assessment Report*, Sandia National Laboratory, Albuquerque, New Mexico.
- Sandia (1995b), *Chemical Waste Landfill Final Closure Plan and Post Closure Permit Application*, Sandia National Laboratory, Albuquerque, New Mexico.
- Schlumberger/GeoQuest (1996), *ECLIPSE Technical References*, Schlumberger/GeoQuest, Abingdon, Oxfordshire, United Kingdom.
- Zheng, C.M., and G.D. Bennett, *Applied Contaminant Transport Modeling: Theory and Practice*, Van Nostrand Reinhold, New York, 1995.
- Zhou, W., C. Zheng, and M.A. Munoz, "Effectiveness of Soil Vapor Extraction for Removing Volatile Organic Compounds in Heterogeneous Soils: A Quantitative Evaluation," in *the Proceedings of 5th Annual West Coast Conference on Hydrocarbon Contaminated Soils*, Long Beach, California, March 29 - April 1, 1994.

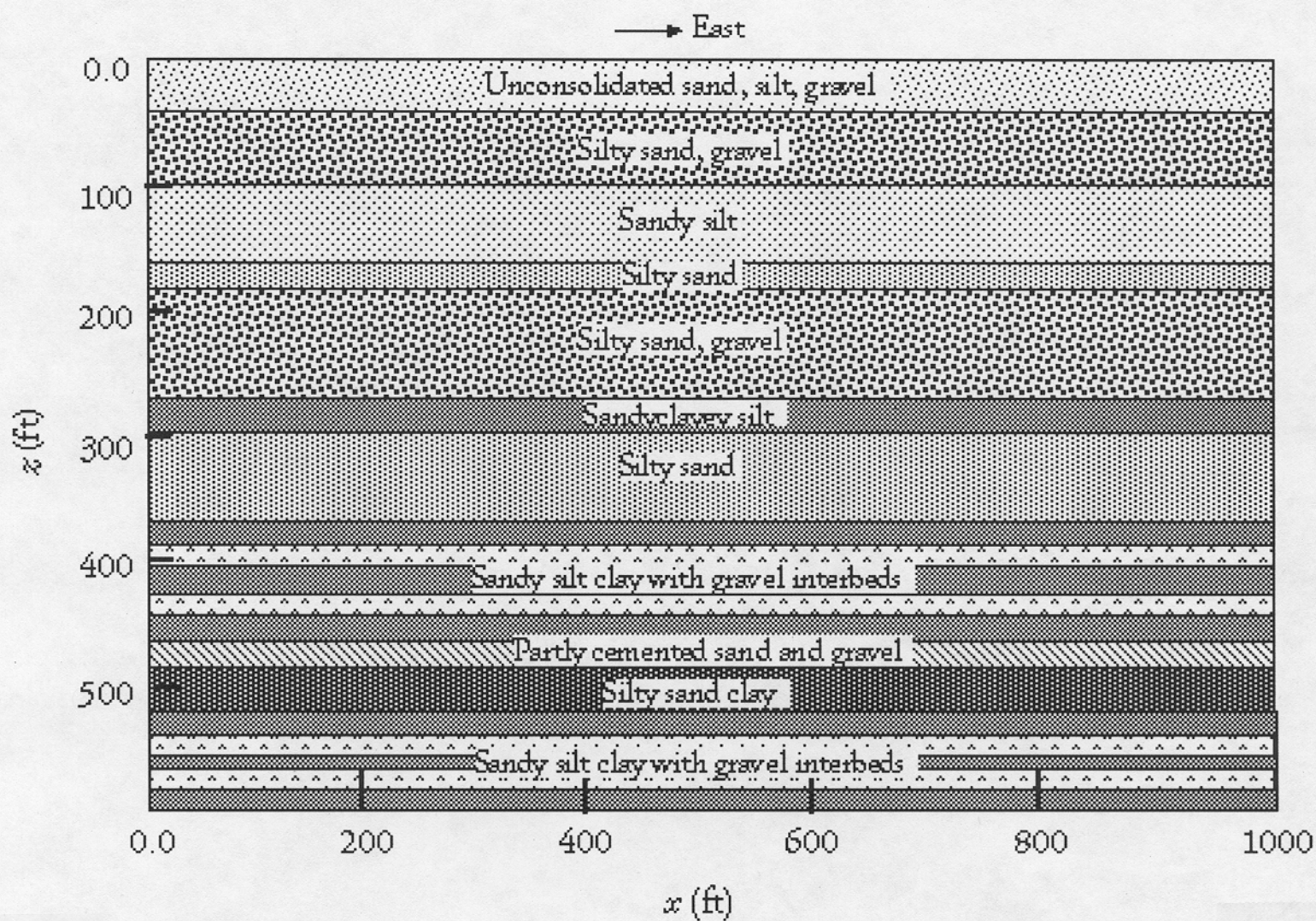


Figure 1. Soil profiles in the conceptual model for simulating transport and removal of TCE vapor in the CWL.

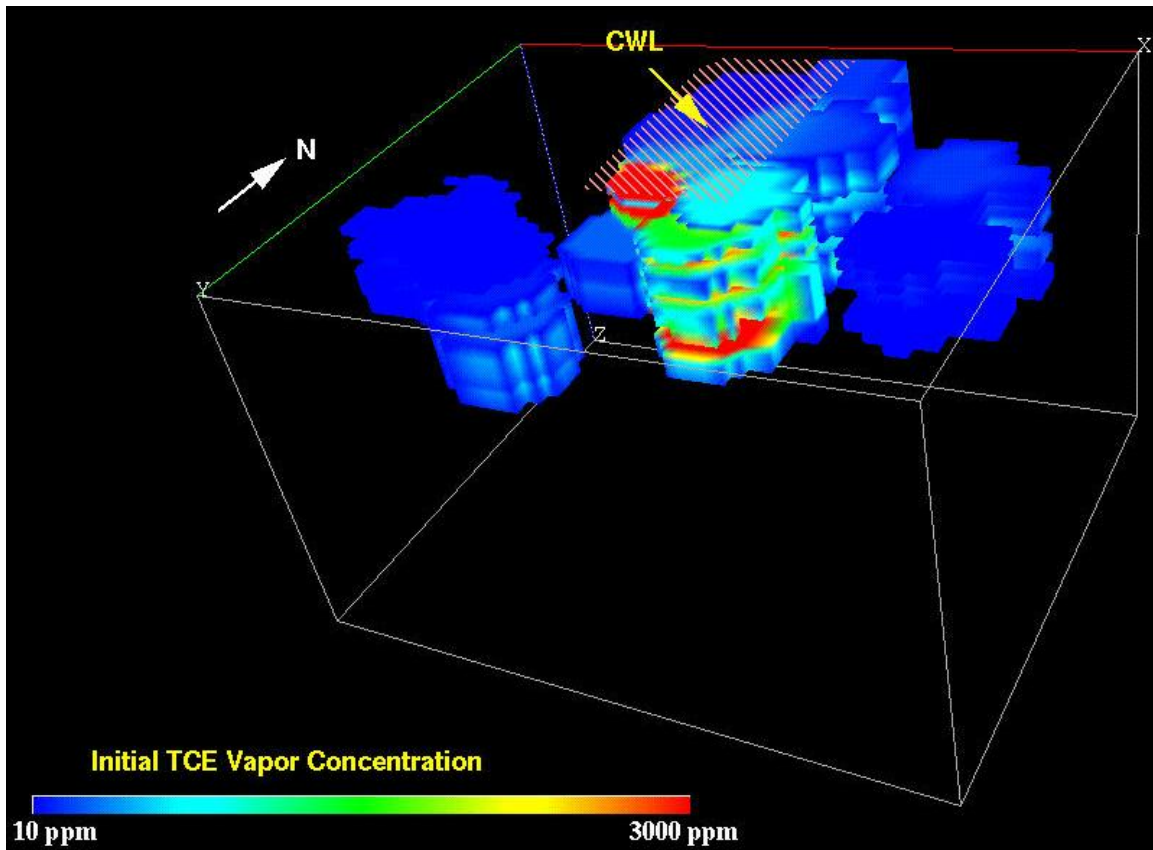


Figure 2. The three-dimensional view of interpolated initial TCE vapor concentration distribution. The shaded area is the Chemical Waste Landfill (CWL). Free-phase TCE exists near high (red color) vapor concentration locations.

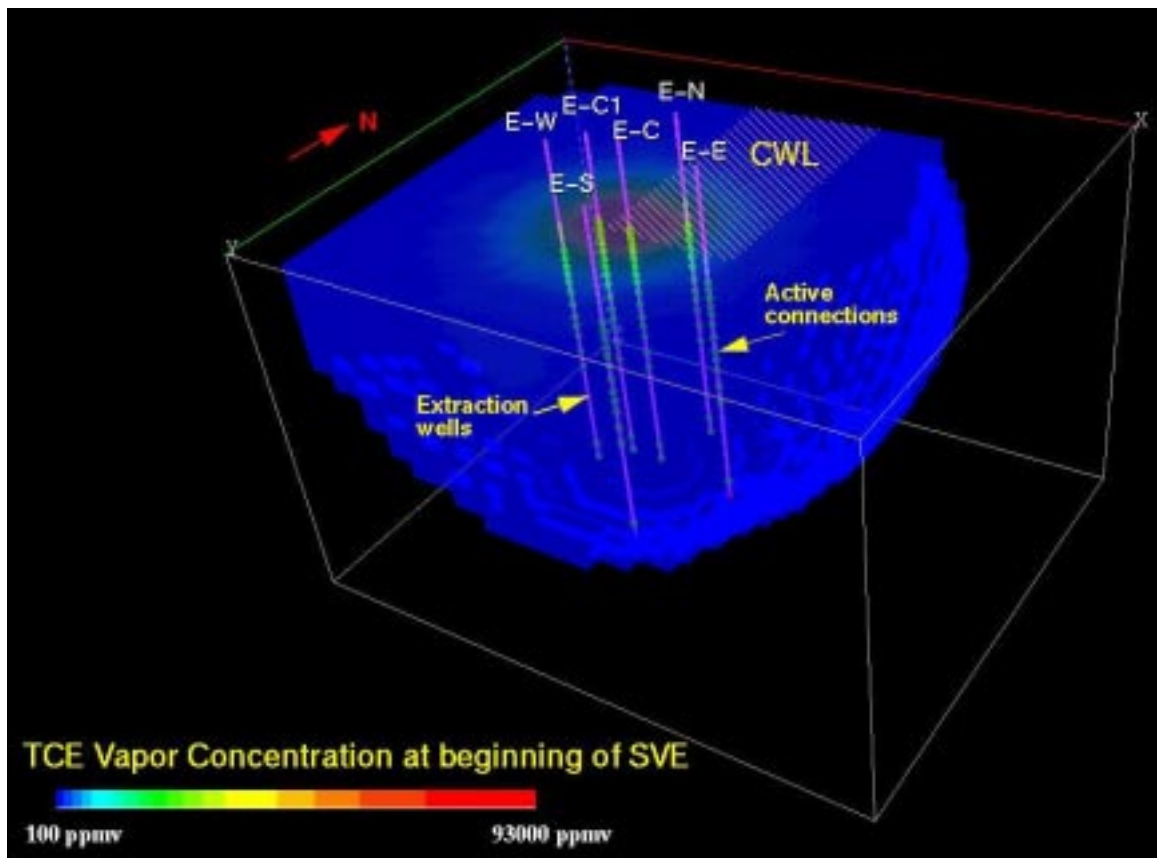


Figure 3. Three-dimensional view of TCE vapor plume after 10-year from initial conditions (shown in Figure 2) without any remediation actions. This VOC distribution serves as initial conditions for SVE simulation. Extraction wells are shown as magenta vertical lines. Active connections are shown as green points.

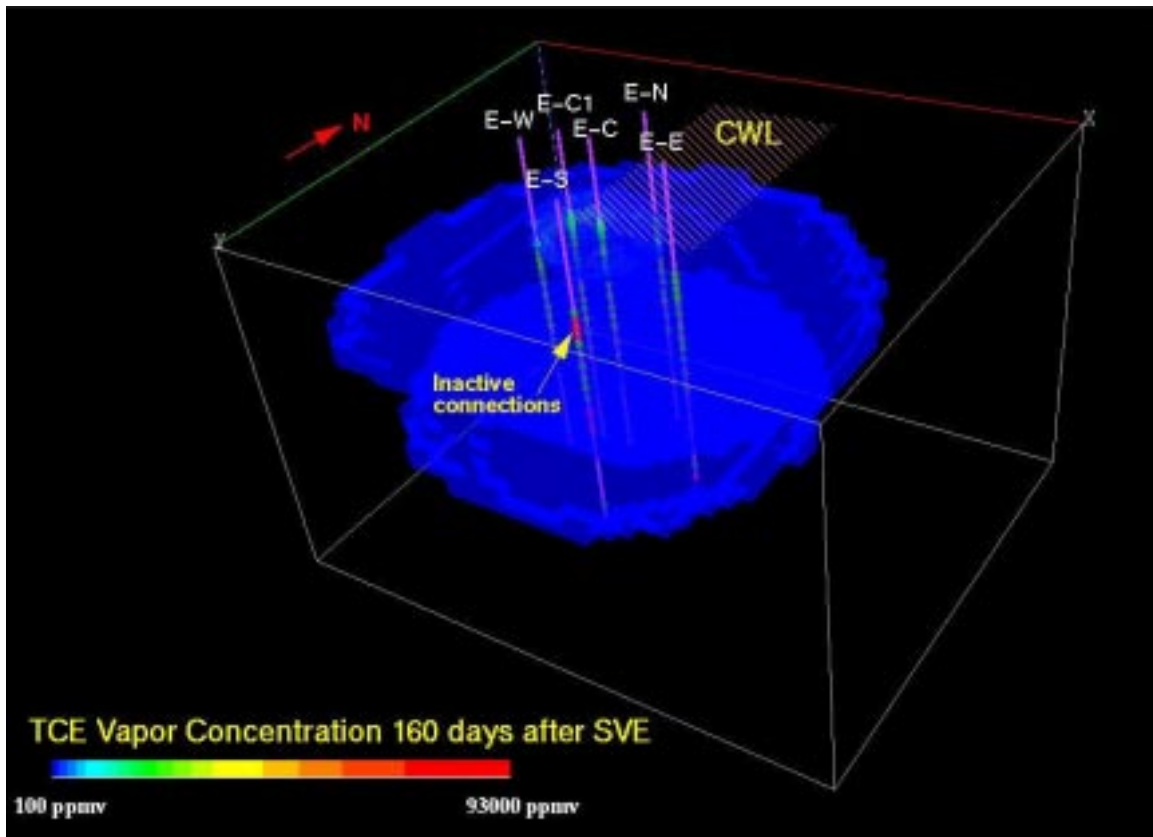


Figure 4. Three-dimensional view of VOC plume in the vadose zone under the CWL after 160-day operation of SVE. Inactive connections are shown as red points.

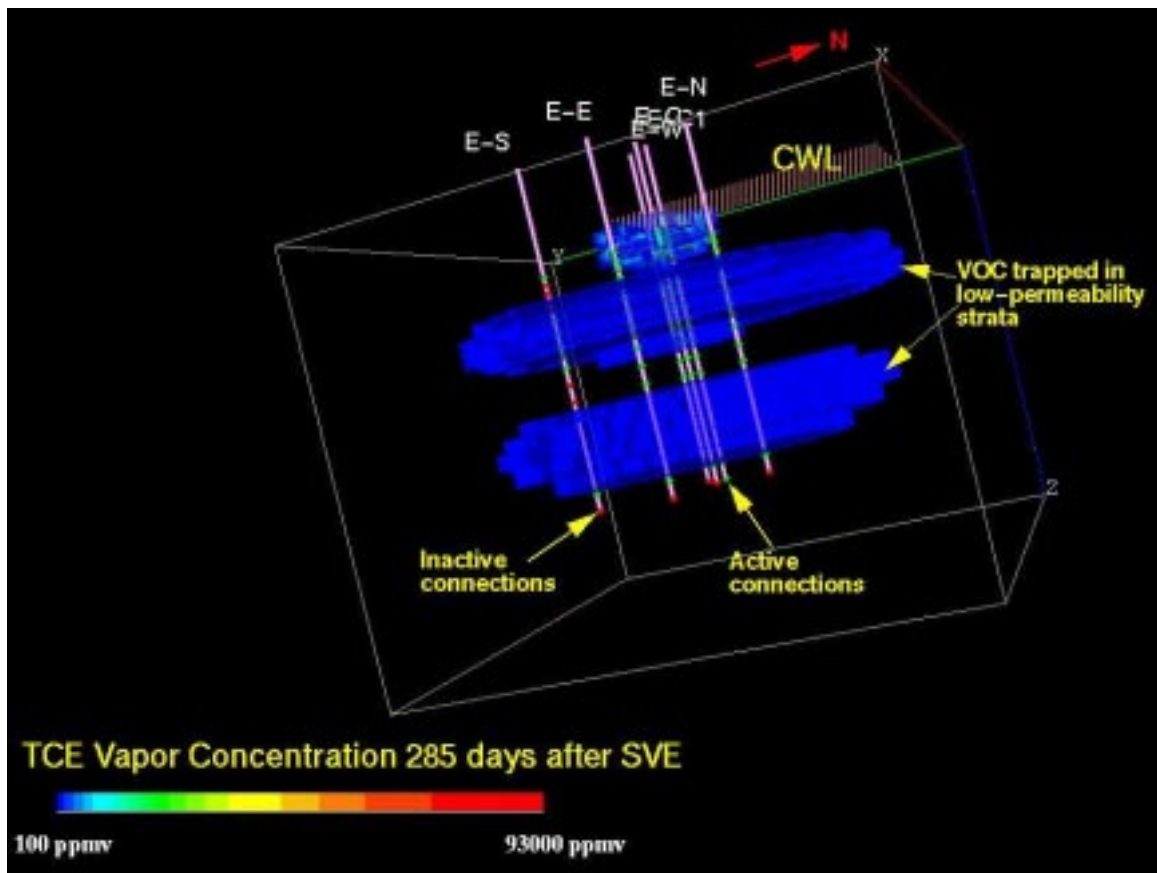


Figure 5. Three-dimensional view of VOC plume after 285-day operation of SVE.

Inactive connections are shown as red points in the figure.

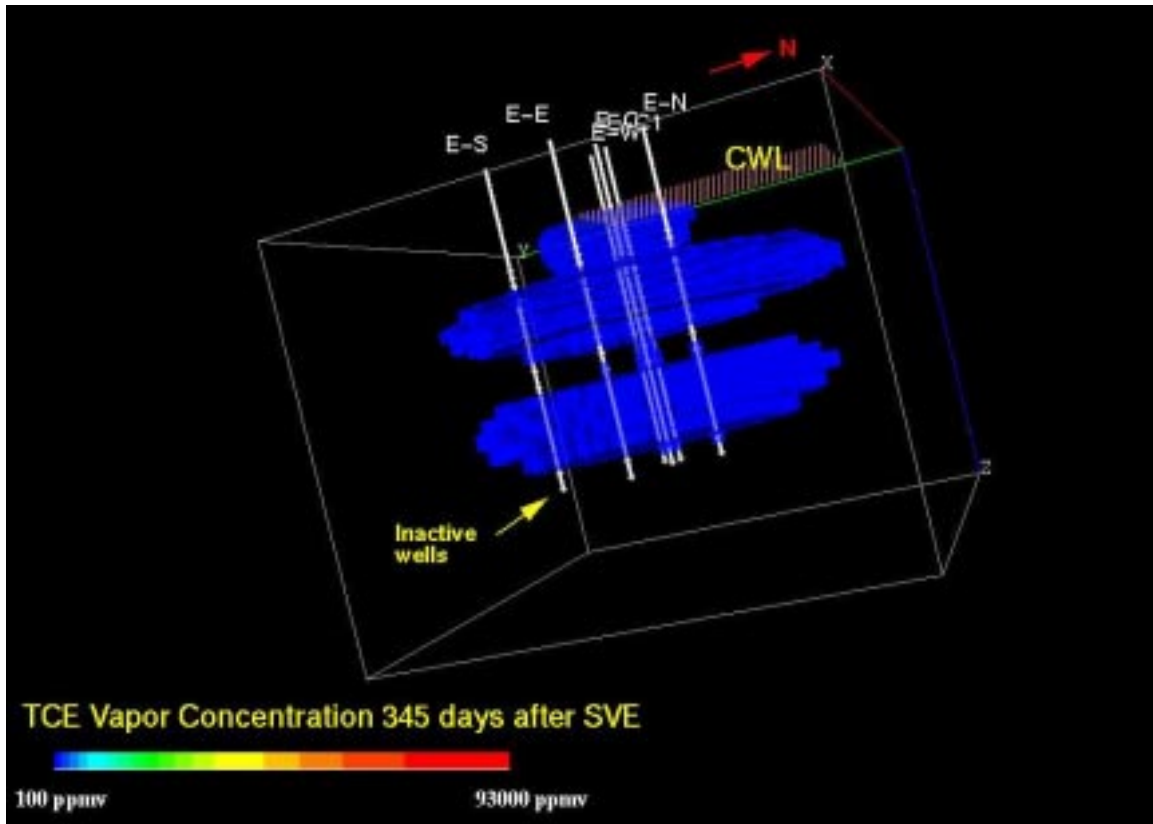


Figure 6. Three-dimensional view of VOC plume after 345-day operation of SVE. Wells are shown in gray color indicating they are turned off for a short period of time.

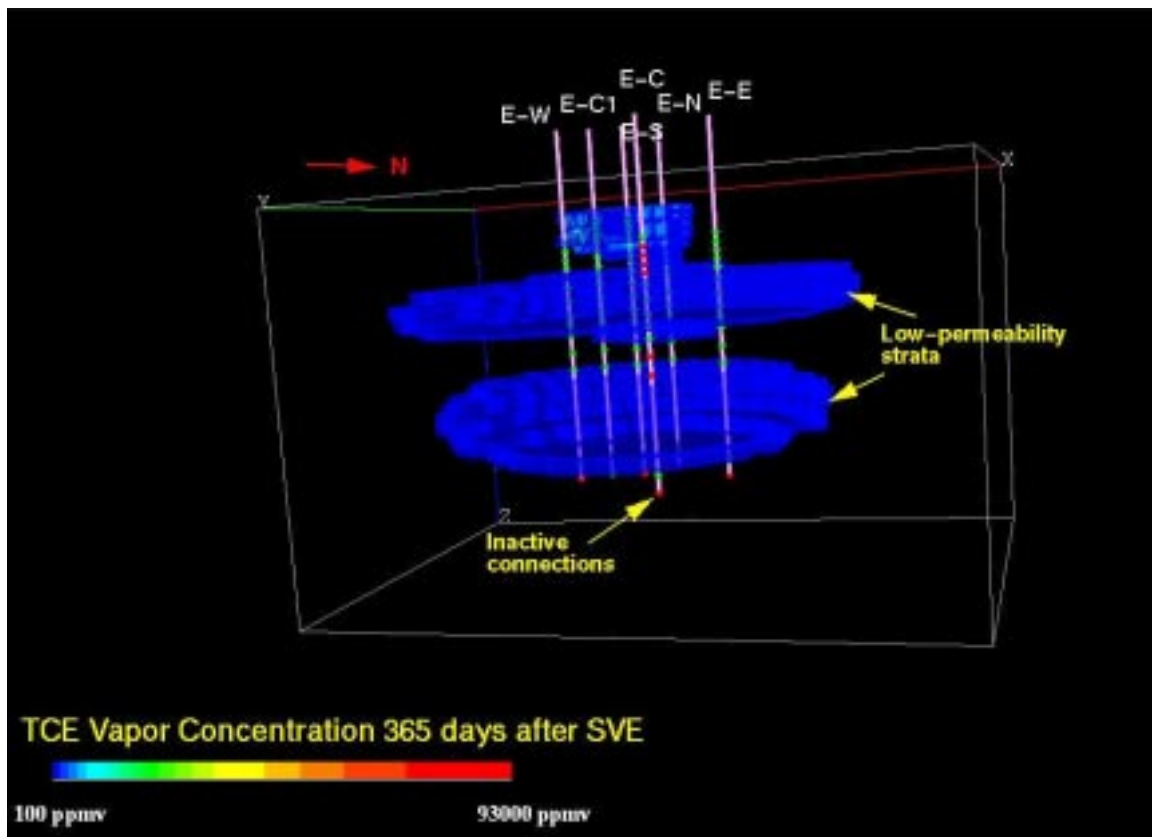


Figure 7. Three-dimensional view of VOC plume after 365-day operation of SVE below the CWL.

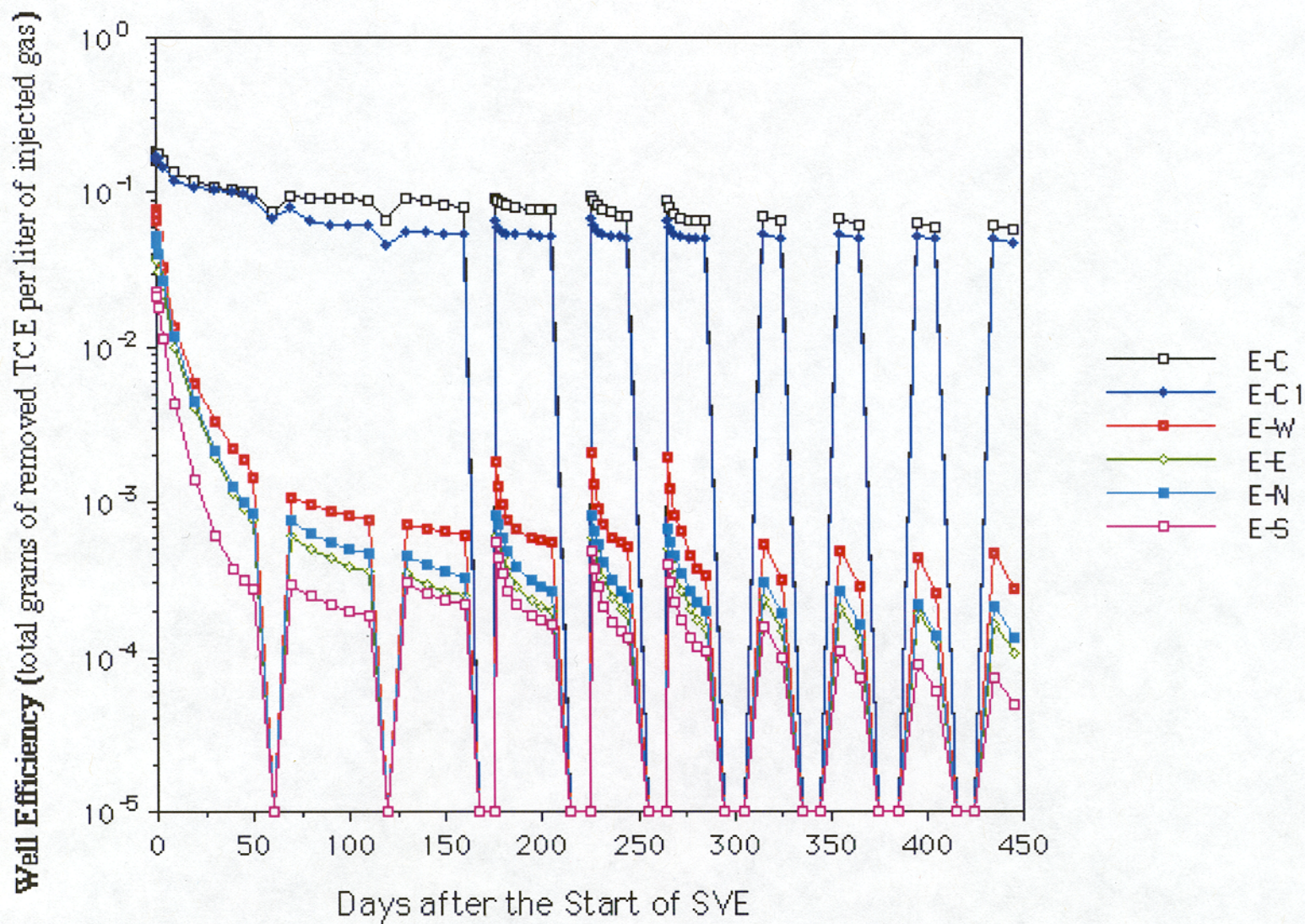


Figure 8. Extraction well efficiencies of removing VOC under the SVE plan shown in this case study. Legends are well names shown in Figures 3 through 7.

Gas Phase - Tritium

Ker-Chi Chang, Office Of Basic And Applied Research, EMSP/DOE

Detail: Show microbial conversion of sulfate to sulfite (fate of organic/inorganic).

Source of additional information:

This work is part of the research project that included the associated case study entitled “Simulated Landfill Leachate”, which is included in this book. The research project was conducted by the author in his doctoral research work entitled “Co-disposal of Low Level Radioactive Waste within Sanitary Landfills” at Georgia Institute of Technology, Atlanta, GA, September, 1982. All data can be requested from Georgia Tech and from the author.

Introduction:

Two laboratory scale simulated landfill units, each having a 208-liter in volume with 55 kg of municipal solid waste, were constructed and spiked with low-level radio-cobalt, -cesium, -strontium, and tritium to investigate containment of these radionuclides in landfills and associated attenuation mechanisms. These simulated low-level radioactive waste landfill units were operated under leachate recycle and non-recycle modes to assess the relative rates of stabilization of those landfill units, together with the fate of radionuclides within these systems.

Methods:

Two identical polyethylene containers were employed as experimental simulated landfills in this study. Equal amounts of solid wastes and radionuclides were placed in each container. The amount of distilled and deionized water added to each landfill unit as simulated precipitation was one liter per week. One unit was operated as the control unit with single-pass operation of the weekly added water. Since the weekly produced leachate from this unit was drained to the leachate reservoir without recycle, the organic materials within the solid wastes were washed out into the reservoir without further removal by biological activity within the landfill unit. The other simulated landfill unit was operated with leachate recycle. The produced leachate was drained to the leachate reservoir and then recycled to the landfill unit on a daily basis. Therefore, continuing biological removal of organics in the wastes and leachate was achieved.

Weekly samples of leachate were collected and analyzed for radioactivities, i.e., Co-58, Cs-134, Sr-85, and H-3. Other parameters that were used to define the degree of stabilization of the wastes which included gross parameters (five-day biochemical oxygen demand, total organic carbon, total inorganic carbon, pH, oxidation reduction potential, chemical oxygen demand, total suspended solids, volatile suspended solids, alkalinity, chloride, conductivity, etc.), volatile fatty acids, organic fractionation, sulfide, and metals (iron, magnesium, manganese, potassium, sodium, calcium, and nonradioactive strontium, cobalt, and cesium) were also analyzed. Gas samples were collected and analyzed for their composition (nitrogen, oxygen, carbon dioxide, methane, and hydrogen) and production rate on a weekly basis. Determinations of H-3 in the produced gas were also conducted during the study.

Results:

The gas production rate and gas composition reflect the relative biological activity within the landfill. They also provide information regarding the intrinsic roles of acid and methane formers during the course of anaerobic stabilization. The formation of methane (CH_4) and hydrogen (H_2) can be taken as indicators of the degree and stage of stabilization at a landfill site. The gas generated from the landfill units was collected and analyzed for the quantity, composition, and radionuclides (which might appear in the form as tritiated $^3\text{H}_2$, $^3\text{H}_2\text{O}$, and C^3H_4). The percentages of CH_4 , CO_2 , N_2 , and O_2 in the gas were analyzed to compare that with other parameters.

The amount of gas produced from the recycle unit increases slowly in the first three months, and then rapidly thereafter. The cumulative amount of gas produced from the control unit was 7.1 liter/kg dry weight as compare to 22.5 l/kg dry wt. of solid waste obtained with the recycle unit. Based on the amount of gas produced from the two units, it can be concluded that the recycle unit had more rapidly and completely stabilized organic constituents than the control unit.

The onset of methane generation from the control unit occurred one week later than from the recycle unit, whereas the hydrogen was two weeks later than the recycle unit. Since the formation of CH_4 and H_2 can be taken as indicators of the degree and stage of stabilization at a landfill site, it was expected that the recycle unit would provide complete leachate stabilization sooner than the control unit.

The carbon dioxide composition of the gas from both units increased to a maximum and then decreased. The maximum values for the control and the recycle units were 76.5% and 73.2%, respectively, whereas the ultimate values were 41.0% and 34.7%, respectively. The corresponding methane compositions increased from 0% to a maximum of 59.0% for the control and 59.5% for the recycle unit.

The oxygen content in the gas from both units was nearly depleted through aerobic decomposition within 30 days after initiation of operation. The nitrogen content of the control unit decreased from 38% to 1.5%, whereas that of the recycle unit decreased from 46% to 2% at the end of the study. Hydrogen in the gas was first detected from the control unit on Day 77, increased to 1.54%, and then disappeared in the next week; hydrogen appeared in the gas from the recycle unit on Day 63 and lasted for three weeks. The maximum hydrogen content of the recycle unit was 1.7%.

Tritium was found in the gas produced from both units in the form of methane gas, water vapor, and/or hydrogen. The activity of H-3 measured as methane and water vapor in the gas produced from the recycle unit was 9.1×10^{-5} uCi per liter of gas and 8.6×10^{-6} uCi/l, respectively. The activity of H-3 determined as methane from the control was 3.4×10^{-5} uCi/l, with little or no H-3 in the form of water vapor (the amount of water vapor collected from the produced gas of the control unit was negligible). Tritium in the form as hydrogen is possible but was too low to measure.

Conclusion:

Only approximately 0.1% and 0.01% of the added H-3 was found in the product gases from the recycle and the control units, respectively. The presence of low concentrations of H-3 in the gas was derived from microbially mediated conversion of $^3\text{H}_2\text{O}$ into C^3H_4 and/or $^3\text{H}_2$. The remainder of H-3 was present in the leachate. The produced gas should be burned prior to its final release to the atmosphere, and the condensed $^3\text{H}_2\text{O}$ should be collected and returned to the landfill or treated and disposed of as radioactive liquid waste

Simulated Landfill Leachate

Ker-Chi Chang, Office Of Basic And Applied Research, EMSP/DOE

Detail: Show microbial conversion of sulfate to sulfite (fate of organic/inorganic).

Source of additional information:

This study was conducted by the author in his doctoral research work entitled "Co-disposal of Low Level Radioactive Waste within Sanitary Landfills" at Georgia Institute of Technology, Atlanta, GA, September, 1982. All data can be requested from Georgia Tech and from the author.

Introduction:

Two laboratory scale simulated landfill units, each having a 208-liter in volume with 55 kg of municipal solid waste, were constructed and spiked with low-level radio-cobalt, -cesium, -strontium, and tritium to investigate containment of these radionuclides in landfills and associated attenuation mechanisms. These simulated low-level radioactive waste landfill units were operated under leachate recycle and non-recycle modes to assess the relative rates of stabilization of those landfill units, together with the fate of radionuclides within these systems.

Methods:

Two identical polyethylene containers were employed as experimental simulated landfills in this study. Equal amounts of solid wastes and radionuclides were placed in each container. The amount of distilled and deionized water added to each landfill unit as simulated precipitation was one liter per week. One unit was operated as the control unit with single-pass operation of the weekly added water. Since the weekly produced leachate from this unit was drained to the leachate reservoir without recycle, the organic materials within the solid wastes were washed out into the reservoir without further removal by biological activity within the landfill unit. The other simulated landfill unit was operated with leachate recycle. The produced leachate was drained to the leachate reservoir and then recycled to the landfill unit on a daily basis. Therefore, continuing biological removal of organics in the wastes and leachate was achieved.

Weekly samples of leachate were collected and analyzed for radioactivities, i.e., Co-58, Cs-134, Sr-85, and H-3. Other parameters that were used to define the degree of stabilization of the wastes which included gross parameters (five-day biochemical oxygen demand, total organic carbon, total inorganic carbon, pH, oxidation reduction potential, chemical oxygen demand, total suspended solids, volatile suspended solids, alkalinity, chloride, conductivity, etc.), volatile fatty acids, organic fractionation, sulfide, and metals (iron, magnesium, manganese, potassium, sodium, calcium, and nonradioactive strontium, cobalt, and cesium) were also analyzed. Gas samples were collected and analyzed for their composition (nitrogen, oxygen, carbon dioxide, methane, and hydrogen) and production rate on a weekly basis. Determinations of H-3 in the produced gas were also conducted during the study.

Results:

When dealing with an anaerobic system such as landfill, the concentrations of chemical oxygen demand (COD), five-day biochemical oxygen demand (BOD₅), and total organic carbon (TOC) may be used to reflect pollutional impact derived from the decomposition of the organic matter. Changes in levels of COD, BOD₅, and TOC are most important, concentrations tended to rise to a maximum and then decrease gradually as the anaerobic processes proceeded and the landfills became stabilized. For example, the initial values of COD in leachate from the control and the recycle units were 18,600 mg/l and 22,800 mg/l, respectively; the maximum values were observed at Day 45 at 28,800 mg/l and 29,500 mg/l, respectively; the ultimate values were 1,052 mg/l and 1,940 mg/l, respectively. Both BOD₅ and TOC concentrations were similar to that of COD.

Further interpretations of the observed changes in pollutional characteristics of the leachate can be based on the production of intermediates such as the volatile fatty acids. Analysis of volatile fatty acids included acetic acid, propionic acid, iso-butyric acid, butyric acid, and valeric acid. All acids increased from original concentrations to a maximum between Days 40 to 50 and then started decreasing. Acetic acid was the most predominant species in the leachate samples its concentration of the control unit increased from 2,700 mg/l to a maximum of 13,800 mg/l, and then decreased to zero (below the minimum detection limit (MDL)); those for the recycle unit increased from 3,700 mg/l to 10,800 mg/l, and then decreased to below MDL. This corresponds to a rapid rise in pH as well as an organism population shift from the acid formers to the methane formers. The methane former can convert acetic acid very rapidly to CH₄ and CO₂, which explains the sharp decrease of acetic acid concentrations and the increase in gas production. It also explains why the pH in the control unit increased from 5.3 to 7.0 in three weeks after the acetic acid peaked.

The pH of both the control and the recycle units increased from initial values of 5.35 to 7.08 and 5.25 to 7.07, respectively. The pH of the leachate samples collected from the control unit increased rapidly to neutral during a two-week period, whereas that from the recycle unit increased gradually to neutral in seven weeks. This implied that the predominant microorganisms in the simulated landfills shifts from acid formers to methane formers.

The appearance of sulfide and the mobility of metals in leachate are a function of environmental conditions such as oxidation-reduction potential (ORP). A more negative ORP value, less than -200 mV E_c, indicates the formation of sulfides by which the heavy metals will be immobilized, and their effect on microbial activity will then be removed. The ORP of leachate from the control unit reduced from 10 to -260 at Day 77; this reducing condition promoted an instant increase in sulfide concentrations in leachate from around 0.1 mg/l to 3.5 mg/l. A similar trend was observed for the recycle unit. The low ORP values indicated that both units were operating under highly reduced conditions, sulfates and that sulfites in leachate are transformed to sulfides under these conditions. The low ORP values also indicated that these landfill units were being operated under conditions conducive to anaerobiosis and methane production.

The conductivity of the leachate samples from the control unit increased from 7,600 umhos/cm to 15,500 umhos/cm and then decreased to 5,000 umhos/cm, whereas that of the recycle unit increased from 8,000 to 15,800 and then to 6,100 umhos/cm. The increase in conductivity was due to the formation of volatile acids and the release of inorganic and organic materials by the physical and biological activities during the early stages of landfill stabilization. When landfill stabilization was approached, less organic materials was present in the leachate, metal ions were precipitated and filtered out by sulfide under reduced chemical condition (ORP lower than -200 mV E_c), and a decrease in conductivity was observed.

The apparent mobility of most metal constituents in leachate strongly depends upon the sulfide-sulfate equilibrium. Whenever sulfides are formed they will precipitate most heavy metals almost instantly. The formation of sulfide in the landfill units was observed around three months after the operation. The higher maximum value of sulfide was double that of the control unit (6.5 mg/l v.s. 3.5 mg/l) and could be attributed to a more complete conversion of sulfates and sulfites to sulfides.

Nine metals, including sodium, potassium, cesium, magnesium, calcium, strontium, manganese, iron, and cobalt, were examined in this study. The discussion of the results with respect to these metals was divided into three groups as related to the periodic table, i.e., Group IA for the first three metals (Na, K, Cs), Group IIA for the next three metals (Mg, Ca, Sr), and heavy metals for the last three metals (Mn, Fe, Co). The concentrations of both sodium and potassium were decreased due to washout for the control unit and dilution for the recycle unit. The cesium concentrations were below the detection limit. In general, the alkaline metal cations could be considered as rather conservative substances and affected mostly by dilution, although the possibility of ion exchange, the formation of organometallic complexes for Ca and Mg, the effect of soil sorption for Cs, and formation of strontium carbonates should be considered.

The concentration of Mn in the control unit increased from 70 mg/l to 128 mg/l on Day 42, decreased sharply after Day 70, and reached an ultimate value of 4.0 mg/l. The recycle unit leachate exhibited a similar behavior for Mn. The increased leachate heavy metal concentration was enhanced by the acidic pH range prevailing in the landfill, whereas the following decrease was due to the formation as precipitated sulfides. The iron and cobalt behaved similarly as Mn in both the control unit and the recycle unit. Based on the results of these three alkalines, three alkaline earth metals, and three metals, it was clear that the fluctuation of these metal concentrations were to closely correspond to those of sulfide and other parameters, e.g., pH, ORP, conductivity. The removal mechanisms of these metals are mainly through physical-chemical processes, and the biological processes contributed to a lesser extent and probably mediated the reactions.

The results of analyses for total suspended solids (TSS) and volatile suspended solids (VSS) showed a slight initial decrease, and then increased dramatically to a maximum on Day 77 for the control unit and on Day 126 for the recycle unit. The sudden surge of TSS and VSS in the leachates can be interpreted by comparison with the respective ORP values, which show values lower than -200 mV E_c on Day 77 for the control and on Day 126 for the recycle unit. Under such a highly reduced condition, sulfide formation was likely. The subsequent precipitation of sulfide compounds would tend to cause a sudden surge in the TSS. These coincide with a significant drop in metal concentrations of the leachate samples as discussed earlier.

The variations of the radionuclides, i.e., Co-58, Sr-85, Cs-134, and H-3 did not show significant difference until the third month. The activity of Co-58 in the leachate from the control unit decreased abruptly from 1.0 to 0.05 uCi/l. During the same period, the corresponding ORP of the control unit decreased to below -200 mV E_c , at the same time, sulfide concentrations increased from zero to a peak of 3.6 mg/l. The same final low values of Co-58 activity were also observed in the leachate from the recycle unit. However, it took an additional six weeks to attain a peak sulfide concentration of 6.7 mg/l. Apparently, decreases in Co-58 activity were related to the presence of sulfides which promoted precipitation reactions. The decrease of Co-58 activity in the leachate of the recycle unit was smoother than that in the control unit. This appears to agree with the gradual changes of other parameters, such as pH and ORP, and the greater leachate homogeneity encouraged by the use of leachate recycle as opposed to single-pass operation. The activities of other radionuclides, however, only decreased slightly and were apparently not greatly influenced by the presence of sulfides. The activity of Sr-85 in the leachate of both units decreased from 6.0 to 0.6 uCi/l, which might be due to the formation of insoluble carbonates. The activity of Cs-134 also showed one order of magnitude decrease (from 1.2 to 0.06 uCi/l), which might be due to the adsorption/ion-exchange mechanism of the trace amount of soil present in solid waste. The activity of H-3 in the leachate of the control unit decreased slowly from 0.20 to 0.07 uCi/l, whereas the decrease for the recycle unit was from 0.20 to 0.11 uCi/l. The possible removal mechanisms included dilution effects, transformation into gaseous CH_4 and H_2 , and evaporation as water vapor.

Membrane ultra filtration and gel permeation chromatography were performed to separate and determine the classes of organic compounds presented in the leachate on a molecular weight (MW) basis. The results showed that in early stage the leachate consisted mainly of the low MW fraction, which confirmed the observation that the volatile fatty acids were major constituents of the leachate. After Day 70, the TOC value decreased, which indicated that the more readily available low MW biodegradable organics has been converted more completely by the microorganisms, and the organics remaining in the leachate has a high molecular weight. Results also showed that the recycle unit has a larger amount of high MW organics in the leachate than the control unit, thus, there was a higher potential to form metallic complexes in the leachate. The distribution of radioactivity after the ultra filtration process showed the activity of Co-58, Cs-134, and Sr-85 were higher in the retentate of all leachate samples from both units. This indicated that these metals were present in the leachate as organic complexes, and their solubility in the leachate was accordingly increased. The tendencies for the radionuclides to form soluble organic complexes were in the order of $Co > Sr > Cs$, especially for the recycle unit. For example, only 1.9% of the total activity of Co-58 was in the permeate of the leachate sample from the recycle unit on Day 238. The large amount of Co-58 existed in leachate as soluble organic complexes of the recycle unit explains why the Co-58 concentration was increased instead of precipitated out by sulfide and/or carbonate in the latter stages of this study.

Conclusions:

Based on the results of this study, the following conclusions can be drawn:

1. The radioactivity of Co-58, Cs-134, and Sr-85 has been effectively contained in the solid waste of the landfill unit. Of the amount added, about 1.6% of Co-58, 8% of Cs-134, 11% of Sr-85, and 66% of H-3 were present in the leachate of the recycle unit.
2. The major containment mechanism for Co-58 was the formation of insoluble cobalt sulfides and cobalt carbonates; that for Sr-85 was the formation of insoluble strontium carbonates; and that for Cs-134 was possibly sorption and ion exchange by the entrapped soil in the solid waste.
3. The results of the ultra filtration membrane suggested that both cobalt and strontium formed complexes with organics, especially with the organics having higher molecular weight (MW>500).
4. The more stable and predictable performance observed with leachate recycle reinforced the value of this operational techniques in landfill practice. Under the prevailing experimental conditions, the time required for the simulated landfill with leachate recycle to reach stabilization of the readily available organics was approximately six months; stabilization for the landfill without leachate recycle had yet to be established.
5. As a result of the single-pass operation of the control unit, the accumulated amount of organic pollutants and radionuclides were high, thus, the potential of leachate pollution was more prevalent and additional treatment of leachate would be required before ultimate disposal. For the recycle unit, the ultimate concentration of all the leachate parameters indicated that the potential of leachate pollution was considerably less. Hence, further leachate treatment prior to ultimate disposal would be minimized and final land disposal would be indicated as a cost effective option.

Batch K_d Tests versus Column R_f Tests

James L. Conca, UFA Ventures, Inc., 2000 Logston Blvd, Richland, Washington 99352

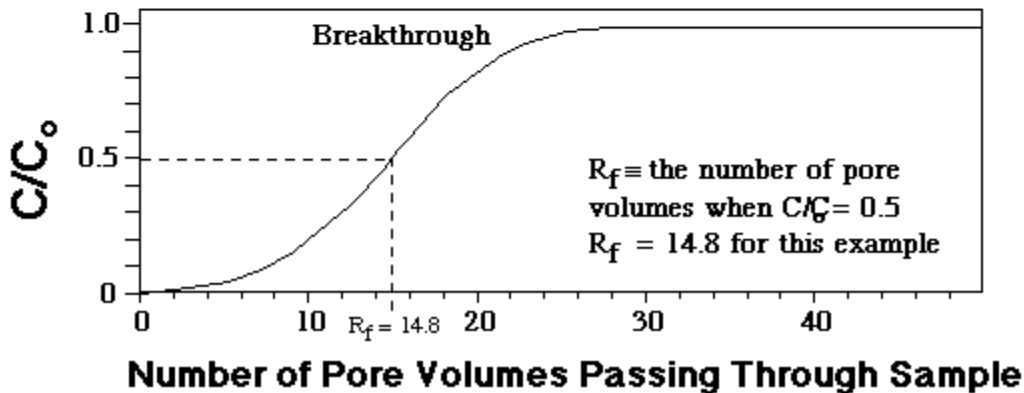
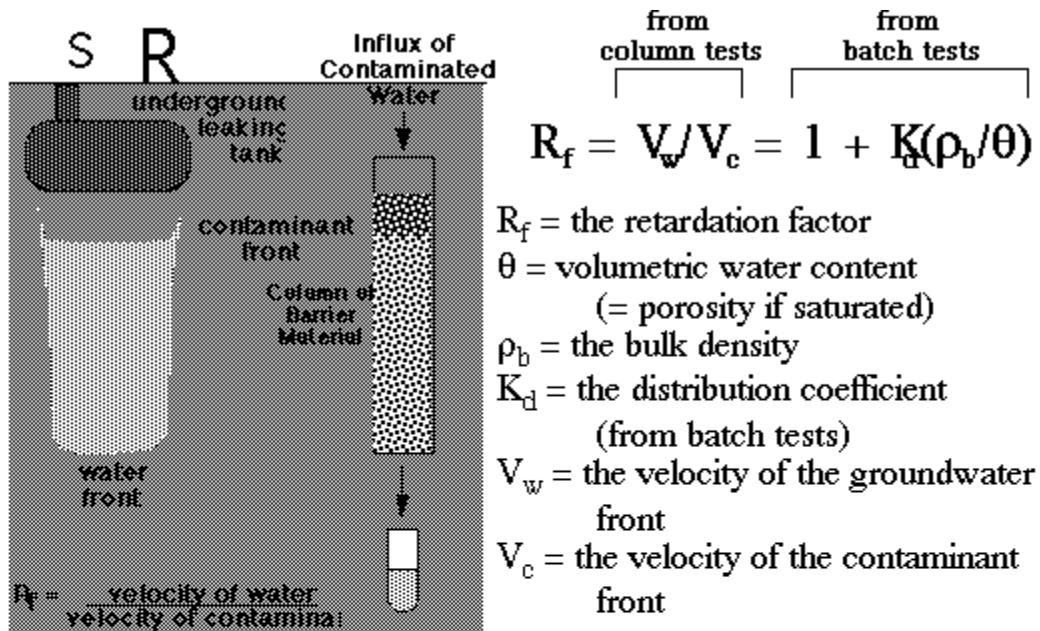
To model or predict contaminant transport at any site, or to model and plan remediation activities, both the hydrologic and chemical behavior need to be known, e.g., the hydraulic conductivity (or water permeability) and the chemical retardation factor. There are two types of experiments to determine the chemical transport behavior of contaminants through various media, especially potential reactive barrier materials or liners. These are K_d batch tests (quick and inexpensive) and R_f column tests (lengthy and expensive). The retardation factor, R_f , is the property that reflects all of the chemical transport behavior within a material as a bulk effect (Figure 1). Often the term R_d is used instead of R_f to denote the non-equilibrium conditions usually present in a column experiment and in the field. Retardation factors can be determined in column experiments where R_f for a particular species is the ratio of the solution velocity to the contaminant velocity. The R_f for that species is given by [Bouwer, 1991]:

$$R_f = V_{gw} / V_{sp} = 1 + \rho K_d / n$$

where V_{gw} is the velocity of the carrier fluid, V_{sp} is the velocity of the contaminant species, ρ is the dry bulk density and n is the porosity. The distribution coefficient, K_d , is defined as the moles of the particular species per gram of solid divided by the moles of that species per ml of solution. If none of a particular species is lost to the solid phase, then $K_d = 0$ and $R_f = 1$ for that species and the contaminant travels along with the water at the groundwater flow rate. When K_d is large, as for plutonium ($K_d > 10^4$ in most soil and sediments), the contaminant can take many years to migrate offsite. Most often, batch experiments are performed to measure the K_d where one part solid is placed into ten parts solution and shaken for 24 hours to observe the amount that is sorbed onto the solid. However, K_d is an equilibrium value developed to describe true adsorption phenomena and does not reflect other sorption/desorption processes such as precipitation and dissolution very well, and does not reflect the flow path geometries or microscopic accessibilities that can vary in the field. Therefore, for most subsurface conditions, batch experiments do not reproduce behavior in the field unless only adsorption is occurring, and usually underestimate the retardation of geologic materials. It is better to perform column experiments using the actual soil or sediment, groundwater, contaminants, and, in this case, barrier materials, under field conditions. Unfortunately, costs can limit the number of column studies that can be performed and batch tests should be used for obtaining true thermodynamic data, for studying relative behavior among many materials, and for rapid scoping studies.

In column experiments, contaminated groundwater is pumped into a column of material packed to field density. The effluent from the column is monitored for the contaminant of interest. R_f is defined as the number of pore volumes passed when the concentration, C , in the effluent is half that of the influent or the initial concentration, C_o , i.e., $C/C_o = 0.5$. Column breakthrough is sometimes defined as complete breakthrough, i.e., when $C/C_o = 1$, but in this report we will use it to mean the same as R_f , i.e., $C/C_o = 0.5$. Breakthrough is also loosely used to mean the point at which a barrier is no longer effectively retarding a specific contaminant. Figure 1 shows the definition of retardation and an example of a breakthrough curve.

Figure 1. Definition of retardation and an example of a breakthrough curve



An example of a breakthrough curve used to determine the retardation. The S-shape reflects hydrodynamic dispersion. The number of inflection points and the absolute position reflect the number and type of sorp. C/C_0 is the concentration of the specific chemical species in the solution divided by the concentration in the starting solution.

An example is illustrated in a study of permeable reactive barrier materials for the treatment of heavy-metal contaminated groundwater in the Bunker Hill Mining District in northern Idaho [Conca, 1997, 1998]. Acid mine drainage is seeping into the shallow groundwater contaminated with between 30 and 250 ppm of Zn, between 0.5 and 1 ppm of Cd, and between 1 and 10 ppm of Pb. Of the several materials investigated, apatite and zero valent iron were deemed the most promising for the retardation of these metals. Table 1 shows the measured values of K_d and R_f plus the R_f calculated from the K_d using the above relationship (the bulk densities and porosities were very different for each material). Batch studies suggested that zero valent iron would perform much better in a flow-through reactive barrier for Zn, Cd and Pb. However, actual column tests performed under field conditions demonstrated that the apatite was much better in a flow-through system. X-ray diffraction of the material after experiments showed that Pb-pyromorphite had precipitated in the apatite columns to an extent that accounted for all of the Pb sorption, and a combination of mostly adsorption with some precipitation in the apatite columns had occurred for the Zn and Cd sorption. No crystalline phases had precipitated in the iron columns, and it was assumed that adsorption dominated. However, large quantities of iron colloids were produced and other processes were acting to reduce the efficiency of the iron to immobilize these metals. These results illustrate the importance of performing both batch tests and column tests on systems where the sorption mechanisms may be in doubt or where non-equilibrium conditions may occur.

Table 1. K_d s and R_f s Determined from Batch Tests and Column Studies

Metal/Material	Measured Batch K_d	Calculated R_f from K_d	Measured Column R_f
Zn			
Apatite II	567	679	600
Iron Filings	27,323	116,125	60
Pb			
Apatite II	2,500	3,000	14,600
Iron Filings	2,500	11,000	1,700
Cd			
Apatite II	990	1,000	700
Iron Filings	990	4,200	20

References:

- Bouwer, H. (1991), Simple derivation of the retardation equation and application to preferential flow and macrodispersion, *Ground Water*, 29, 41-46.
- Conca, J. L. (1997), *Phosphate-Induced Metal Stabilization (PIMS)*, Final Report to the U.S. Environmental Protection Agency #68D60023, Washington, DC.
- Conca, J. L. (1998), *Success Mine Apatite Remediation Project Using Apatite*, Report to the Idaho State Department of Environmental Quality #QC038900, Boise, ID.

COST-EFFECTIVE SOLUTIONS TO SITE REMEDIATION: REDUCING RISK BY UNDERSTANDING ENVIRONMENTAL AND ENGINEERING PROCESSES

Micheline Devaurs (LANL)

1.1 INTRODUCTION

The overall goal of the site remediation is to reduce risks to human health and the environment that resulted from past Laboratory activities to an acceptable level and in a cost-effective manner. Understanding engineering and environmental processes is key to conducting in situ remediation in a cost-effective manner that minimizes risk and the maintenance associated with a site after it is remediated, referred to herein as post-closure maintenance. Engineering processes are those things that humans can do to aid remediation, such as design and use landfill covers of various textures and thicknesses and modify the slope and vegetation on and around a restoration site to effect erosion rates; meanwhile, environmental processes are the natural processes, such as plant succession and soil genesis, that would occur in an area without human intervention. Within the DOE complex, considerable radioactive wastes will be left in the environment because of the cost, lack of available technology, and increased risk of removing large volumes of contaminated soils; in order to do this, however, we must demonstrate that we clearly understand the environmental and engineering processes that affect risk and we must develop a high level of credibility with regulators.

Additional information on this case study is available from: Everett Springer, Environmental Science Group (EES-15), Los Alamos National Laboratory, PO Box 1663, MS J495, Los Alamos, New Mexico, 87545.

1.2 SETTING

The 43 square-mile Los Alamos National Laboratory (LANL) site is situated in northern New Mexico on the Pajarito Plateau. The Bandelier Tuff in this area was deposited as a result of major eruptions in the Jemez Mountains volcanic center about 1.2 to 1.6 million years ago. The ephemeral and intermittent streams that drain the plateau have created numerous narrow finger-like mesas, whose tops range in elevations from approximately 7800 ft on the flank of the Jemez Mountains to about 6200 ft at their eastern termination above the Rio Grande Valley. The eastern margin of the plateau stands 300 to 900 ft above the Rio Grande.

Groundwater occurs in three modes: water in shallow alluvium in canyons, perched water, and the main aquifer. Due to the hydrogeology of the area, the option of leaving contaminants in place for environmental remediation is a reasonable option for most sites.

1.2 INTEGRATED APPROACH

The EES-15 Surface Processes Pilot Studies integrate environmental and engineering factors to develop a remediation approach for a given site (see Figure 1). The benefits of this

integration are as follows:

First, and perhaps most important, within the Surface Processes Pilot Studies, process-level information related to water balance is translated into effects on risk. The real value of the pilot studies lies in the integration of information among these factors (Breshears et al., 1993). This is accomplished as follows. The data provide an engineering “tool box” of the design variables considered in landfill cover design such as cover layer textures and thickness, slope and vegetation, and how these variables relate to water balance design parameters (e.g., runoff, erosion, seepage, lateral subsurface flow, soil moisture, and precipitation).

Second, these engineering variables are integrated with our understanding of environmental processes. Conceptually, initial conditions considered in traditional engineering evaluations are most influential early in cover life, but become less important than environmental processes as time progresses (see Figure 2). Environmental processes are less important initially (e.g., plant succession and soil genesis), but eventually become most significant. The EES-15 integrated approach evaluates both engineering and environmental factors.

Third, the site’s location along the continuum of climate and ecological conditions present at the Laboratory is factored in (see Figure 3). Fourth, large temporal variation in parameters of interest, such as runoff and seepage, are evaluated over multiple years because short-term measurements are inadequate for long-term risk assessment. Fifth, spatial variation in parameters of interest, such as runoff and erosion, are included. Estimates of runoff are highly dependent on the scale of observation and must be extrapolated to other scales (e.g., one relevant to landfill cover design) on the basis of understanding processes.

1.4 DATA

The pilot studies data set includes both engineered test plots and natural analogs in the piñon-juniper, and ponderosa pine ecosystems. Table 1 briefly summarizes each study site. This network, from experimental to natural sites, enables us to address remediation of waste sites using an integrated approach. Various sites have instruments that provide detailed field measurements rather than anecdotal observations. The data from these sites provide a basis for improved conceptual models for environmental processes.

1.5 RESULTS: APPLICATION OF PILOT STUDIES TO LANDFILL COVER DESIGN

Surface covers are an alternative for remediation at many sites. The Surface Processes Pilot Studies provide an extensive data set from which to design an engineered cover for a given site and to assess future performance.

The pilot studies data provide an understanding of physical processes, such as interflow, soil moisture, and water balance parameters (e.g., erosion, runoff, seepage), that can affect both surface cover design, contaminant transport, and long-term monitoring. Pilot studies of both engineering aspects of covers and of environmental processes on undisturbed sites are providing

data to optimize cover design in terms of reduced risk and cost/benefit for the site and contaminants there.

1.5.1 Lateral Subsurface Flow (e.g., Interflow)

Areas in the ponderosa pine zone have a much higher propensity to generate lateral subsurface flow than previously thought (Wilcox and Breshears, 1997; Wilcox et al., 1997; Newman et al., 1998). Additional data suggest that lateral subsurface flow is not an important process in piñon-juniper woodlands because of less rainfall in those areas.

1.5.2 Erosion

Erosion rates are relatively low across much of the Pajarito Plateau, but significant areas within piñon-juniper woodlands (e.g., Bandelier Wilderness study site, which is representative of sites at the Laboratory) are eroding at rapid rates (Allen and Breshears, 1998). Such rapidly eroding areas, if contaminated at the surface, represent a large potential for redistribution of contaminants on the Pajarito Plateau. Rapid erosion rates can also result in surface cover loss and potential contaminant exposure. (Seyfried and Wilcox, 1995; Wilcox, 1994; Wilcox, et al., 1996; Davenport et al., 1998).

1.5.3 Surface Runoff

Runoff data from the pilot studies sites have shown that summer storms produce the highest peak flows and have the greatest potential for moving sediment (and any contaminants that may be present) to the stream channels, even though these storms generally last only a few hours (Wilcox et al., 1996; Wilcox et al., 1997; Reid et al., submitted for publication).

1.5.4 Soil Moisture/Seepage

The pilot studies data demonstrate temporal variability of soil moisture and seepage in natural systems; on engineered plots, the pilot studies data provide a data set to evaluate temporal soil moisture changes under different cover designs (Nyhan et al., 1997). The natural systems provide an analog for expected landfill conditions a century following cessation of maintenance (Breshears et al., 1997a; Breshears et al., 1997b; Newman et al., 1997; Breshears and Barnes, submitted for publication).

1.5.5 Biological Processes

Biological processes such as plant succession and animal intrusion will have direct and important effects on contaminant mobility and landfill stability, and these effects will increase through time (Gonzales et al., 1995). Soil pedogenesis is also such a factor (Davenport et al., 1996; Davenport et al., 1995).

1.5.5.1 Plant Succession

Plant succession occurs on landfill covers. At MDA B, 32 years after the site was closed, numerous native species had recolonized the waste site, including many ponderosa pine, the larger of which were 16 to 27 years old (Wenzel et al., 1987; Nyhan, et al., 1998). Ten years after the integrated test plots (Nyhan et.al., 1990) were installed, the plant covers on the integrated plots and conventional plots are substantially different and are progressing down distinct successional pathways. These data suggest that cover design has a significant impact on plant succession (Tierney and Foxx, 1982; Hakonson, 1986; Gladney et al., 1984).

1.5.5.2 Animal Intrusion

An animal intrusion barrier experiment conducted in 1981-1982 demonstrated that barriers made of cobble, cobble/gravel, and bentonite clay were equally effective in preventing pocket gopher intrusion with depth (Hakonson et al., 1982; Hakonson, 1986; Nyhan, 1989; Gonzales et al., 1995). A crushed tuff barrier offered little resistance to burrowing activity and is an ineffective barrier against tunneling. Pocket gophers move tremendous amounts of soil, which affects plant species diversity, soil bulk density, infiltration, and interflow.

1.5.6 Modeling

Predictions are needed to assess the performance of surface covers to select remediation options for sites. The Surface Processes Pilot Studies provide a high-quality, long-term dataset for parameterizing, validating, and refining the hydrologic models needed to predict the long-term fate of contaminants on the plateau. Pilot studies data are being used to test the HELP and HYDRUS codes, which can be used to evaluate landfill cover design performance.

1.5.7 Publication

As a result of this work, EES-15 has an extensive list of refereed journal articles . (An abbreviated list of these publications is included herein; a full list is available upon request.) These publications provide credibility in the scientific community and can help defend remedial action approaches with regulators.

1.6 CONCLUSIONS

The Surface Processes Pilot Studies data provide a process-based understanding of engineering and environmental processes occurring across the Laboratory's climate and ecological conditions. These data provide a technical basis for cost-effective remediation and risk reduction at ER Project sites across the Laboratory. This process understanding is key—nothing will be costlier than conducting site remediation more than once.

LIST OF REFERENCES

Submitted:

- Breshears, D. D., and F. J. Barnes. **Interrelationships between plant functional types and soil moisture heterogeneity for semiarid landscapes within the grassland/forest continuum: a unified conceptual model.** Submitted to *Landscape Ecology*.
- Reid, K. D., B. P. Wilcox, D. D. Breshears, and L. MacDonald. **Runoff and erosion for vegetation patch types in piñon-juniper woodland.** Submitted to *Soil Science Society of America Journal*.

Published:

- Allen, C. D., and D. D. Breshears, 1998. **Drought-induced shift of a forest/woodland ecotone: rapid landscape response to climate variation.** *Proceedings of the National Academy of Science* 95: 14839-14842.
- Breshears, D. D., P. M. Rich, F. J. Barnes, and K. Campbell. 1997a. **Overstory-imposed heterogeneity in solar radiation and soil moisture in a semiarid woodland.** *Ecological Applications* 7: 1201-1215.
- Breshears, D. D., O. B. Myers, S. R. Johnson, C. W. Meyer, and S. N. Martens. 1997b. **Differential use of spatially heterogeneous soil moisture by two semiarid woody species: *Pinus edulis* and *Juniperus monosperma*.** *Journal of Ecology* 85: 289-299.
- Breshears, D.D., F. W. Whicker, and T. E. Hakonson. 1993. **Orchestrating environmental research and assessment for remediation.** *Ecological Applications* 3: 590-594.
- Davenport, D. W., D. D. Breshears, B. P. Wilcox, and C. D. Allen. 1998. **Viewpoint: Sustainability of piñon-juniper woodlands: a unifying perspective of soil erosion thresholds.** *Journal of Range Management* 51: 231-240.
- Davenport, D. W., B. P. Wilcox, and D. D. Breshears. 1996. **Soil morphology as influenced by a piñon-juniper woodland.** *Soil Science Society of America Journal* 60: 1881-1887.
- Davenport, D. W., B. P. Wilcox, and B. L. Allen. 1995. **Micromorphology of pedogenically derived fracture fills in Bandelier Tuff, New Mexico.** *Soil Science Society of America Journal*, v. 59 (#6), pp. 1672-1683.
- Gladney, E. S.; Hakonson, T. E.; Muller, M. 1984. **Cesium as an activatable tracer for studying biological intrusion of plant roots into waste burial sites.** *Journal of Radioanalytical and Nuclear Chemistry*. 84(2): 423-429.
- Gonzales, G. J., M. T. Saladen, and T. E. Hakonson. 1995. **Effects of pocket gopher burrowing on cesium-133 distribution on engineered test plots.** *Journal of Environmental Quality* 24: 1056-1062.
- Hakonson, T.E.; Martinez, J.L.; White, G.C. 1982. **Disturbance of a low-level waste burial site cover by pocket gophers.** *Health Physics* 42 (6): 868-871.
- Hakonson, T.E. 1986. **Evaluation of geologic materials to limit biological intrusion into low-level radioactive waste disposal sites.** Los Alamos National Laboratory report; LA-10286-MS.
- Newman, B. D., A. R. Campbell, and B. P. Wilcox. 1997. **Tracer-based studies of soil water movement in semiarid forests of New Mexico.** *Journal of Hydrology* 196: 251-270.
- Newman, B. D., A. R. Campbell, and B. P. Wilcox, 1998. **Lateral subsurface flow pathways in a semiarid ponderosa pine hillslope.** *Water Resources Research* 34 (12): 3485-3496.
- Nyhan, J. W., J. A. Salazar, D. D. Breshears, and F. J. Barnes. 1998. **A water balance study of**

- four landfill cover designs at Material Disposal Area B in Los Alamos, New Mexico.** Los Alamos National Laboratory report LA-13457-MS.
- Nyhan, J. W., T. G. Schofield, and R. H. Starmer. 1997. **A water balance study of four landfill cover designs varying in slope for semiarid regions.** *Journal of Environmental Quality* 26: 1385-1392.
- Nyhan, J. W., T. E. Hakonson, and B. J. Drennon. 1990. **A water balance study of two landfill cover designs for semiarid regions.** *J. Environmental Quality* 19(2): 281-288.
- Seyfried, M. S., and B. P. Wilcox. 1995. **Scale and the nature of spatial variability: field examples having implications for hydrologic modeling.** *Water Resources Research* v. 31 (1), pp. 173-184.
- Tierney, G. D., and T. S. Foxx. 1982. **Floristic composition and plant succession on near-surface radioactive waste disposal facilities in the Los Alamos National Laboratory.** Los Alamos National Laboratory report LA-9219-MS.
- Wenzel, W. J., T. S. Foxx, A. F. Gallegos, G. Tierney, and J. C. Rogers. 1987. **Cesium-137, plutonium-239/240, total uranium, and scandium in trees and shrubs growing in transuranic waste at Area B.** Los Alamos National Laboratory report LA-11126-MS.
- Wilcox, B. P., and D. D. Breshears. 1997. **Interflow in semiarid environments: an overlooked process in risk assessment.** *Human and Ecological Risk Assessment* 3: 187-203.
- Wilcox, B. P., B. D. Newman, D. Brandes, D. W. Davenport, and K. Reid. 1997. **Runoff from a semiarid ponderosa pine hillslope in New Mexico.** *Water Resources Research* 33: 2301-2314.
- Wilcox, B. P., B. D. Newman, C. D. Allen, K. D. Reid, D. Brandes, J. Pitlick, and D. W. Davenport. 1996. **Runoff and erosion on the Pajarito Plateau: observations from the field.** 1996. *New Mexico Geological Society Guidebook, 47th Field Conference, Jemez Mountains Region*, pp. 433-440.
- Wilcox, B. P. 1994. **Runoff and erosion in intercanopy zones of a pinyon-juniper woodland, New Mexico.** *Journal of Range Management* 47:285-295.

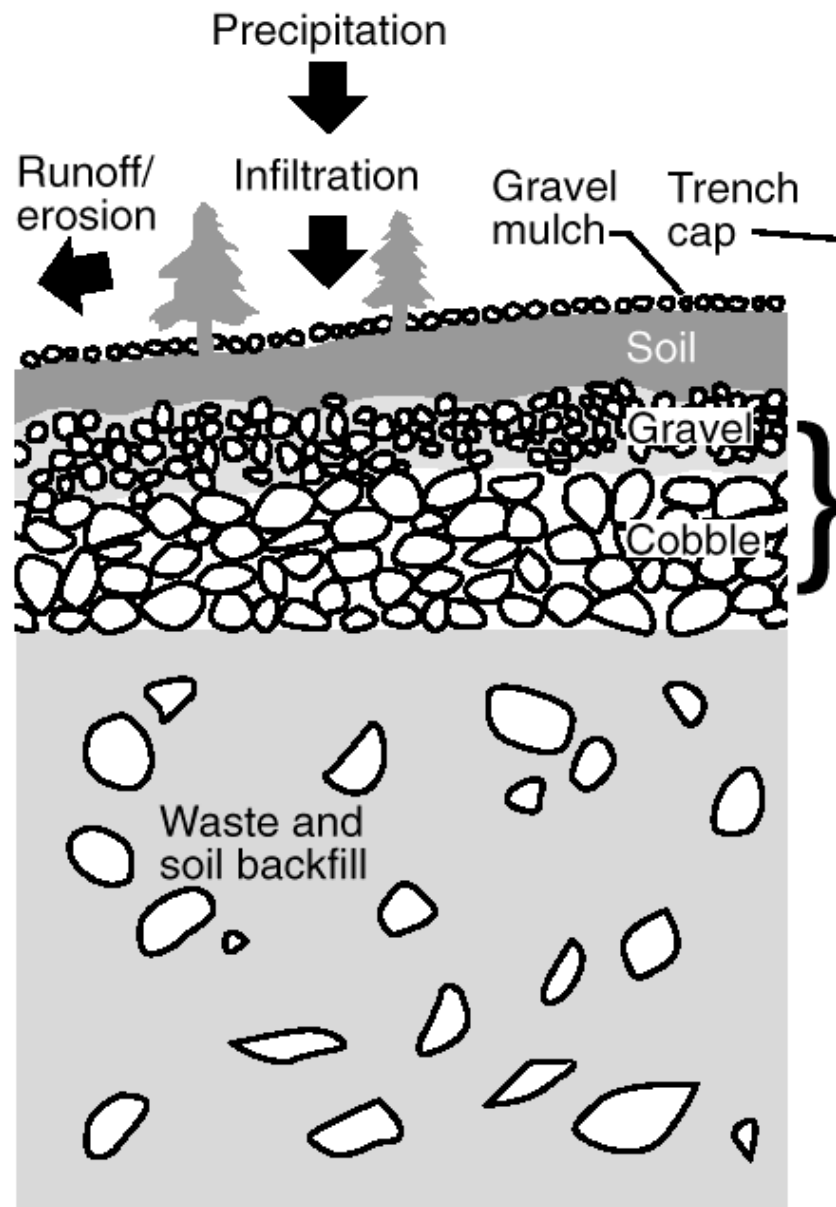


Figure 1

Conceptual graph illustrating likely trends in the relative influence of engineering and environmental processes in the long-term effectiveness of engineered landfill covers.

A: Three years or less after installation (Nyhan et al., 1990)

B: Ten years after installation (to be submitted to Journal of Environmental Quality)

C: Thirty years after closure (Wenzel et al., 1987)

D: One century or more after closure (no studies are available; therefore it is necessary to study natural systems, such as the Ponderosa and Piñon-Juniper Pilot Studies)

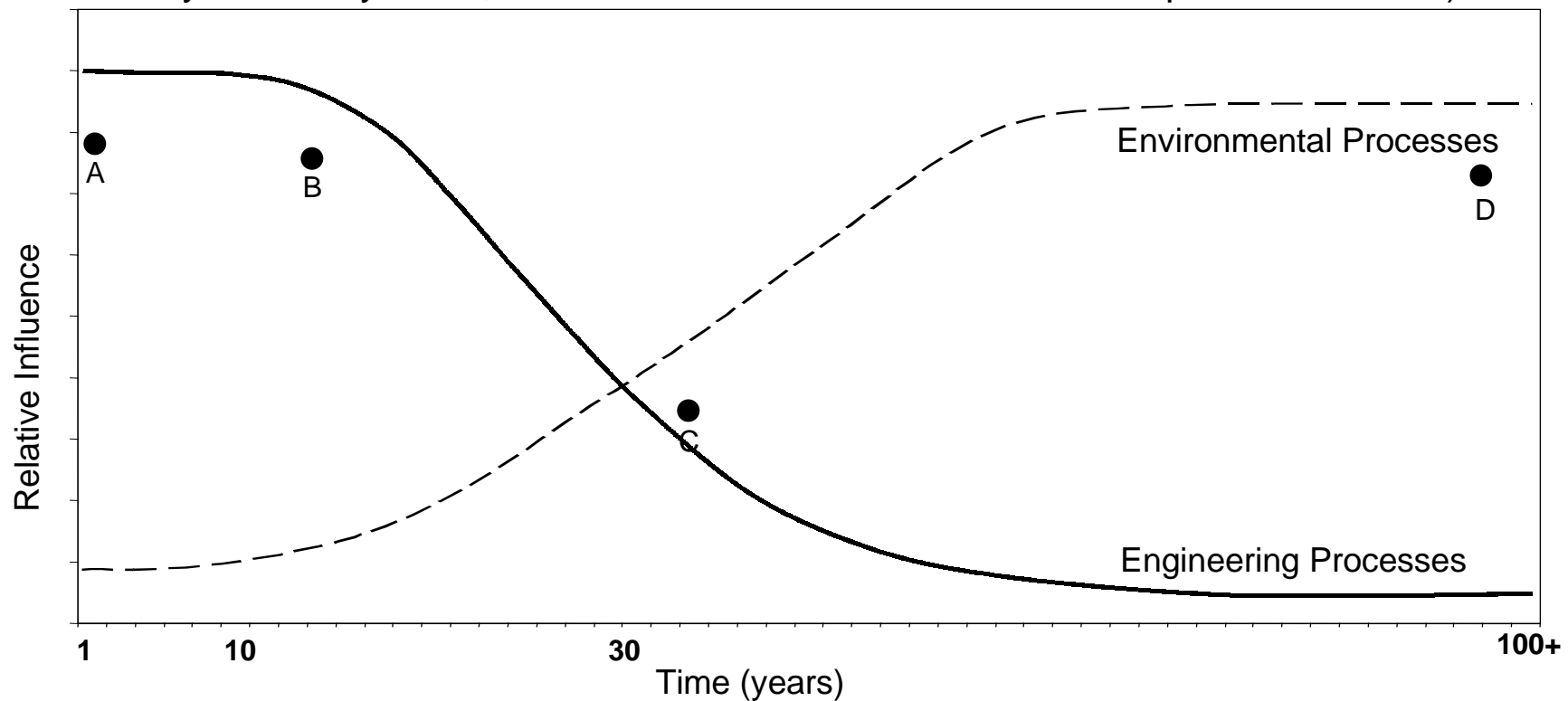


Figure 2

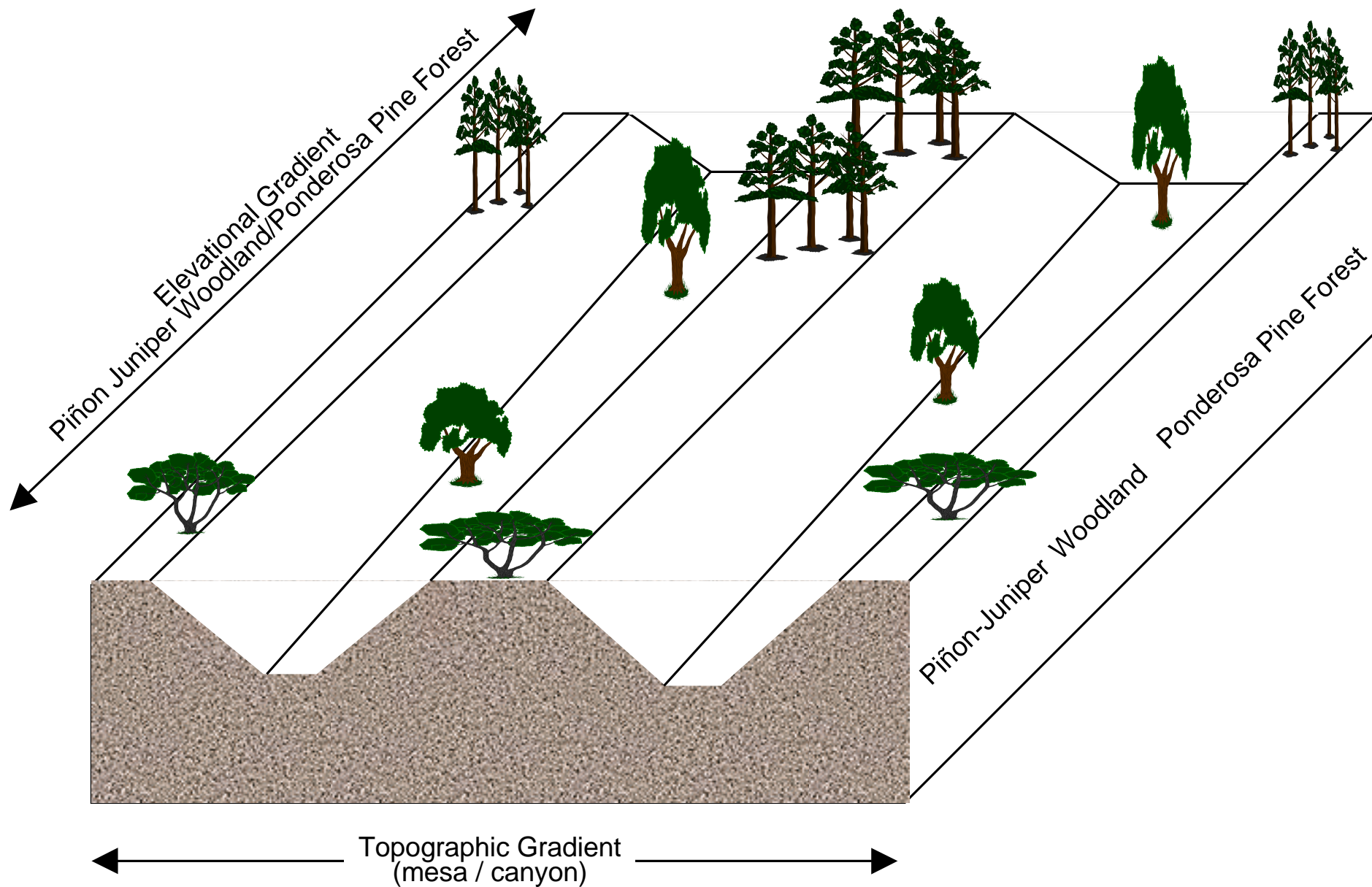


Figure 3

TABLE 1 SUMMARY OF SURFACE PROCESSES PILOT STUDIES DATABASE

<u>SITE</u>	<u>PURPOSE</u>	<u>DATA RECORD</u>	<u>EXPERIMENTAL DESIGN</u>	<u>PARAMETERS MEASURED</u>	<u>SIGNIFICANCE OF DATA</u>
TA-51 Protective Landfill Cover Demonstration	Provide data for alternative landfill cover designs	12/91 to 12/98	Four cover designs (conventional, EPA RCRA design, loam capillary barrier, and clay-loam capillary design) at four slopes (5, 10, 15, 25%); each on a 1.0 by 10.0m plot.	Precipitation, soil moisture, surface and subsurface runoff (i.e., interflow).	Provide data for alternative landfill cover designs; data set to validate hydrologic models; provide data to assist in selection of best landfill cover design for a specific site.
Ponderosa Pine hillslope study at TA-6	Provide data for sites located in Ponderosa Pine ecosystem.	2/93 to 10/98	Three experimental areas: a 485 m2 area on the north side of the hillslope; a 355 m2 area on the south side; a 10 X 3m plot at the northeast corner. Two lateral subsurface flow monitoring trenches.	Precipitation, soil moisture, surface runoff, lateral subsurface flow, subsurface flow chemistry, soil temperature, and stem diameter changes in Ponderosa pine.	Because of infrequent nature of runoff in semi-arid landscapes, observations need to be long-term and detailed. Runoff is variable, ephemeral, and occurs as a result of "extreme" precipitation events. Lateral subsurface flow (i.e., interflow) was identified as important episodic runoff pathway. Interflow could result in containment transport over much larger lateral extent than one might expect. In addition, it could also saturate buried waste if proper engineering controls are not put in place.

<u>SITE</u>	<u>PURPOSE</u>	<u>DATA RECORD</u>	<u>EXPERIMENTAL DESIGN</u>	<u>PARAMETERS MEASURED</u>	<u>SIGNIFICANCE OF DATA</u>
Pinon-Juniper woodland site at TA-51	Provide data for sites located in Pinon-juniper woodland with low erosion rates.	6 plots 1987-1998; P-J transect initially mapped in 1991. Soil moisture monitored since 1998. Lateral subsurface flow monitoring trench May 1994-1998.	Six 3 X 10m plots. 2 plots had all vegetation removed in 1987; 4 plots undisturbed. <u>P.J. transect:</u> 70m X 120m stand of PJ mapped. Tree height, crown diameter, stem diameter at base were measured for pinon and juniper <u>Monitoring trench:</u> Hillslope scale surface runoff & lateral subsurface flow.	Plots: Runoff and sediment collected on six plots since 7/91; precipitation. <u>PJ transect:</u> Near-ground solar radiation, soil temperature, soil moisture, runoff for canopy & intercanopy patches, plant water stress, ground cover. <u>Monitoring trench:</u> Timing and volumes of surface runoff and lateral subsurface flow.	Plots: Surface runoff was documented to be important mechanism for redistribution of water, sediments, nutrients and contaminants in P-J woodlands, especially on a local scale *. <u>P-J transect:</u> Large amounts of heterogeneity occur between canopy and intercanopy patches affecting infiltration, runoff and plant water use. An understanding of environmental processes in the natural system contributes to better design of engineered covers and an understanding of how to monitor cover performance over time. <u>Monitoring trench:</u> Only lateral subsurface flow monitoring in Pinon-Juniper and also only hillslope scale measurement of surface runoff in P-J.
Pinon-juniper woodland site in Bandelier National Monument.	Provide data for Pinon-Juniper system subject to high erosion rates cooperative study with NPS, USGS, Bandelier National Monument personnel.	7/93 to Present (Management transferred to Bandelier National Monument 1/99)	Several spatial scales within a watershed.	Ground cover, runoff, erosion, historical shifts in vegetation (1935 - present)	Documented rapid ecotone shift from Ponderosa pine forest to pinon-Juniper woodland in response to regional drought in 1950's. Has important implications for assessing impacts of climate change. Implement management strategies to reverse erosion by increasing herbaceous cover.

<u>SITE</u>	<u>PURPOSE</u>	<u>DATA RECORD</u>	<u>EXPERIMENTAL DESIGN</u>	<u>PARAMETERS MEASURED</u>	<u>SIGNIFICANCE OF DATA</u>
Decade-long study: Integrated test plots.	Provide data for alternative landfill cover designs after 10 year study.	1984-1994	<u>1984-1986:</u> Four 3 X 10m plots, two conventional cover designs (20 cm topsoil on top of 108 cm tuff) and two improved landfill cover designs (from surface: 71cm topsoil, geotextile with 5% slope, 46cm gravel, 91cm cobble, 38cm tuff). Plots have no slope to maximize potential for percolation.	Precipitation, runoff, soil water storage seepage.	Plots were excavated after 10 years to evaluate vegetation cover, biomass, species diversity, rooting pattern and soil profiles. Infiltration was found to occur primarily through macropores, diversity, including root channels and animal burrows. Vegetation was found to have increased on all plots, but rooting depth was limited to 70cm, and little change in soil profiles occurred over the length of this study.

<u>SITE</u>	<u>PURPOSE</u>	<u>DATA RECORD</u>	<u>EXPERIMENTAL DESIGN</u>	<u>PARAMETERS MEASURED</u>	<u>SIGNIFICANCE OF DATA</u>
Decade-long study: Area B	Provide data for alternative land-fill cover designs after 11 years on actual material disposal area.	1982 - 1995	<u>1982-1985:</u> Conventional cover (75 cm tuff, 15 cm top soil) and biobarrier test plots (75 cm cobble, 25 cm gravel) <u>1984 - 1986:</u> Twelve 3 X 10m plots, four each on eastern, central western areas of 6-acre MDA . Two plots had shrub cover, two mixed grasses and forbs. One of each vegetative type had surface gravel mulch.	<u>1982 - 1998:</u> Soil moisture, plant root penetration. <u>1987 - 1989:</u> Sediment transport. <u>1987 - 1995:</u> Precipitation, runoff, soil moisture, vegetative cover, periodic ground cover measurements.	MDA is an actual disposal site closed 32 years ago. The longest-term study of water balance on a remediated site occurred on 12 plots with varying covers, vegetation and gravel mulch, monitored from March 1987 through June 1995. The field results from this study document several improvements that can be made for conventional landfill surface covers (i.e., gravel mulch, ground cover and slope effects on runoff, vegetation effects on evapo- transpiration).

*Additional detail for PJ woodland site at TA-51 for significance of data:

- (1) Runoff amounts vary with scale: Runoff decreases as size of contributing area increases.
- (2) Infiltration capacity of soils is dynamic; it is tied to soil moisture content and/or soil frost conditions and is a major determinant of runoff amounts.
- (3) Soil erodibility follows annual cycle being highest in late winter at end of freeze-thaw period, and lowest at end of summer rainy season.

Vadose Zone Transport of VOCs in Landfill Gas

Jeffrey Forbes, Daniel B. Stephens & Associates, Inc.
6020 Academy NE
Albuquerque, NM 87109

Municipal landfills contain large quantities of organic refuse that slowly decompose, yielding biogenic landfill gas (EMCON, 1980). Landfill gas is generated by methanogenic bacteria through the anaerobic decomposition of organic matter and consists of roughly 50% methane and 50% carbon dioxide, with the proportions depending on the composition of the organic matter in the landfill. Landfill gas production usually declines in an exponential manner from the time of initial refuse emplacement, with a "half life" on the order of 10 years or so, though this can vary considerably depending on the site-specific moisture content and subsurface temperature (Barlaz et al., 1990). Many landfills that were closed 20 or more years ago are still generating large quantities of landfill gas.

The relative vapor density (RVD) of a gas is defined as the ratio of the density of the gas to that of pure air at the same temperature and total pressure. Thus, $RVD=1$ for pure air. Landfill gas composed of 50% methane and 50% carbon dioxide has a RVD of approximately 1.04. This means that the gas is 4% denser than air (or typical soil gas with a composition similar to air). On account of its density, this gas has a strong tendency to sink through the vadose zone, provided the geologic materials beneath the landfill have sufficient gas permeabilities. For reference, seawater is approximately 3% denser than fresh water, and it is well-known that density stratification of seawater beneath fresh water readily occurs. This illustrates that a few percent density contrast is sufficient to maintain stratification, or to cause density-driven advection (sinking or rising) of one fluid within another.

The large volume of landfill gas generated in the anoxic landfill core tends to move outward from its source, following zones of higher gas permeability. Some landfill gas escapes at the ground surface, but some may also move laterally outward or vertically downward into the surrounding materials. Small gas pressure gradients can develop that cause landfill gas to move in directions contrary to that predicted based on density alone. For example, dense gas can be driven upwards and out at the landfill surface because the total pressure inside the landfill is slightly greater than that at the surface.

Barometric pumping caused by atmospheric tides cause a twice daily rise and fall of surface atmospheric pressure of a few millibars (Chapman and Lindzen, 1970), and this oscillation of the surface pressure is sufficient to cause fluctuations in the rate of landfill gas emission from the ground, especially where the depth to groundwater is great. Our own observations at landfills in New Mexico and Arizona show that landfill gas emission rates are greatest during periods of falling barometric pressure, which generally occurs from 10:00AM to 4:00PM, and from 10:00PM to 4:00 AM. During periods of rising pressure, landfill gas emission slows or ceases entirely as fresh air enters the soil from above as a result of the greater atmospheric pressure (LANL, 1998). The patterns can, of course, be temporarily obscured by the passage of synoptic weather systems, which can cause even larger fluctuations in barometric pressure.

When anoxic landfill gas encounters oxygen, the methane is rapidly oxidized by methanotrophic bacteria. This occurs both at the ground surface and at the irregular outer perimeter of the landfill gas "halo" within the vadose zone. This results in consumption of the methane, and production of even more carbon dioxide, which in turn increases the RVD of the gas. Around the perimeter, it is not uncommon to find soil gas with up to 20% carbon dioxide, 80% nitrogen, and virtually no oxygen. This gas has $RVD=1.08$, which is much denser than air, and has a strong tendency to sink towards the water table. Two other factors that also contribute to sinking of landfill gas around the margins of a landfill gas halo are (1) cooling of the warm landfill gas and (2) condensation of water vapor, both of which result in an increase in gas density.

Landfill gas often contains appreciable concentrations of hazardous volatile organic compounds (VOCs) (CARB, 1990, Allen et al, 1997). VOCs in landfill gas that is denser than the surrounding soil gas will be transported downward along with the dense gas. Our observations are that landfill gas typically contains part per million levels of numerous VOCs that were disposed of in the landfill during operation. Many of these are or were formerly in common use as industrial solvents (e.g. toluene, PCE, TCE, TCA, Freons). In addition to the primary solvent VOCs, we also observe several of their anaerobic biodegradation products (e.g. DCE isomers, VC). The presence of these high molecular weight VOCs results in an even greater density in the resulting mixture, though their contribution is usually insignificant on account of their relatively low concentrations (ppm range) in landfill gas, as compared to major gases such as carbon dioxide.

There are a number of well-documented cases where contamination of groundwater has resulted from transport of vapor-phase VOCs from a landfill through the vadose zone to the water table (Murray et al., 1998, Ward and Smith, 1998). Sinking of dense landfill gas is most likely where gas permeabilities of the underlying unsaturated materials are high, such as in landfills underlain by coarse sandy or gravelly materials with high air-filled porosity, or along open fractures or solution conduits in bedrock. Vapor-phase VOC transport can even result in contamination of upgradient groundwater because the sinking gas plume tends to spread out upon encountering the water table (Ankeny and Hsu, 1998).

Multi-depth soil vapor monitoring techniques have been developed that permit sampling and analysis of soil gas from multiple depths within the vadose zone, as well as ground-water sampling in the saturated zone (Forbes et al., 1993). These methods allow delineation of the depth of penetration of VOCs and landfill gas and assessment of the potential for dense gases to sink to the water table. Impermeable caps placed on top of a landfill can exacerbate the problem, as all of the gas is then forced down and laterally away from the refuse (Ankeny and Hsu, 1998).

References:

- Allen, M.R., A. Braithwaite, and C.C. Hills, 1997, Trace Organic Compounds in Landfill Gas at Seven U.K. Waste Disposal Sites, *Env. Sci. Tech.* v. 31, p. 1054-1061.
- Ankeny, M. D. and K.-C. Hsu, 1998, The effects of gas flow on contaminant transport in landfills with synthetic or alternative covers, *Supplement to EOS*, December, 1998.
- Barlaz, M.A., R.K. Ham, and D.M. Schaefer, 1990, Methane Production from Municipal Refuse: A Review of Enhancement Techniques and Microbial Dynamics, *Critical Reviews in Environmental Control*, vol 19, no. 6, p. 557-584.
- California Air Resources Board (CARB), 1990, The Landfill Testing Program: Data Analysis and Evaluation Guidelines, Sept. 13, 1990.
- Chapman, Sydney, and R.S. Lindzen, 1970. *Atmospheric Tides*, Gordon and Breach Science Publishers,
- EMCON Associates, 1980, Methane Generation and Recovery from Landfills, Ann Arbor Science Publishers.
- Forbes, J., J. Havlena, M. Burkhard, and K. Myers. 1993. Monitoring of VOCs in the deep vadose zone using multi-port soil gas wells and multi-port soil gas/ground-water wells. *In* Proceedings of 7th National Outdoor Action Conference and Exposition, National Ground Water Association, May 25-27, 1993, Las Vegas, NV, p. 557-571.
- Los Alamos National Laboratory (LANL), 1998, RFI Report for Potential Release Sites, 73-001, Airport Landfill Areas, LA-UR-98-3824, Nov. 1998.
- Murray, Ray, D. Samorano, K. Masbruch, and N. Petersen, 1998, Vapor Transport as a Mechanism for Groundwater Contamination from Landfills, paper presented at 11th Annual Symposium of Arizona Hydrological Society, Tucson, Sept. 1998.
- Ward, John J., and S. J. Smith, 1998, Arid Zone Landfills: What do investigations and modeling of contaminant migration reveal about transport mechanisms?, paper presented at 11th Annual Symposium of Arizona Hydrological Society, Tucson, Sept. 1998.

EXPERIMENTS OF ^{90}Sr MIGRATION IN THE VADOSE ZONE

Kurochkin V.M., (VNIIPromtehnologii, Moscow, Russia)

Introduction

To evaluate the possibility of using the vadose zone for disposal of liquid Nuclear Power Plant (NPP) low - level waste, field investigations from 1966 to 1974 were conducted to evaluate ^{90}Sr migration from crib. These experiments took place near the Novovoronezhskiy NPP in Russia (see Fig. 1 of NPPs in western Russia¹). A published article, in Russian, describes the experimental methods used, the data processing methodology and the resulting ^{90}Sr distribution profile in the vadose zone [Kostin and Kurochkin, 1971]. The vadose zone in the experimental area has a very complex geological structure, primarily due to its fluvioglacial origin (Fig.2).

Methods

For the experiments, 0.799 Ci of ^{90}Sr was used. Cross sections and isolines that were typically used for evaluating the inventory of natural resources [Smirnov, 1960] helped identify the volume of each selected zone, and from the average concentration of ^{90}Sr we estimated the total amount in each zone.

We observed the ^{90}Sr migration in the contaminated area by drilling multiple wells in which we collected soil samples for radiometric and radiochemical analyses. In addition, we used these soil samples to identify the water content by laboratory methods. We used the neutron method [Kurochkin and Rybalchenko, 1970] for identifying the water content of the soils in the field. Over the entire period of observation 74 wells were drilled to a depth of 25 m with a total area of 855 m².

¹ Map courtesy of the International Nuclear Safety Center at Argonne National Laboratory

Results

Check sampling in the experimental area made it possible to identify ^{90}Sr distribution in the vadose zone under natural conditions. The local ^{90}Sr values were put into the cross sections selected in major directions, in accordance with the location of the observation wells. Then, specific areas (identified as 1 through 6 in Fig.3) were identified with the help of isolines of equal concentration. Fig.3 shows, as an example, distribution of ^{90}Sr concentrations in the vadose zone for one phase of the observations.

Discussion

For each phase of observation, we observed a decrease of the ^{90}Sr amount in the first zone, followed by its accumulation in the subsequent zones. This observation is explained by ^{90}Sr washing from the first zone and its major redistribution in the second zone, with less in the third zone. At the same time, no significant of ^{90}Sr migrated into zones 4 - 6, thereby causing its washing off the vadose zone, which decreased the average ^{90}Sr concentration in those zones. The ^{90}Sr distribution is affected by the presence of clays, mild clays and sands.

Conclusions

From these observations of the water content dynamics and ^{90}Sr migration in the vadose zone, we conclude that :

1. During the period of observations, the average water content of the soil decreased, restoring its equilibrium, which had been destroyed by filling the well with water, in accordance with climatic conditions of the region.
2. Mild clays in the sand significantly affect the contaminant transport, increasing their sorption and reducing the migration rate.
3. The results of the experimental field studies make it possible to recommend the application of vadose zone for disposal of radioactive NPP waste with restricted volumes and activity.
4. The results obtained can be used for testing numerical models of radioactive contaminant migration in the vadose zone.

5. The results obtained can be used for evaluation of contaminant plumes and prediction of their development at sites with conditions analogous to those in Novovoronezh.

References

- Kostin, P.P. and Kurochkin, V.M. (1971), Application of vadose zone for disposal of liquid radioactive waste, *Gorno - Metallurgicheskaya Promyshlennost* (Mining and Metallurgical Industry), N10, 162 -174.
- Kurochkin, V.M.and Rybalchenko, A.I. (1970) Application of neutron method for identification of water content in the vadose zone, *Deep - Well Injection of Liquid Radioactive Waste*, 16
- Smirnov, V.I. (1960) Evaluation of inventories of natural resources, M. *Gosgeotechizdat*.



Figure 1. Map of nuclear power plants in western Russia.

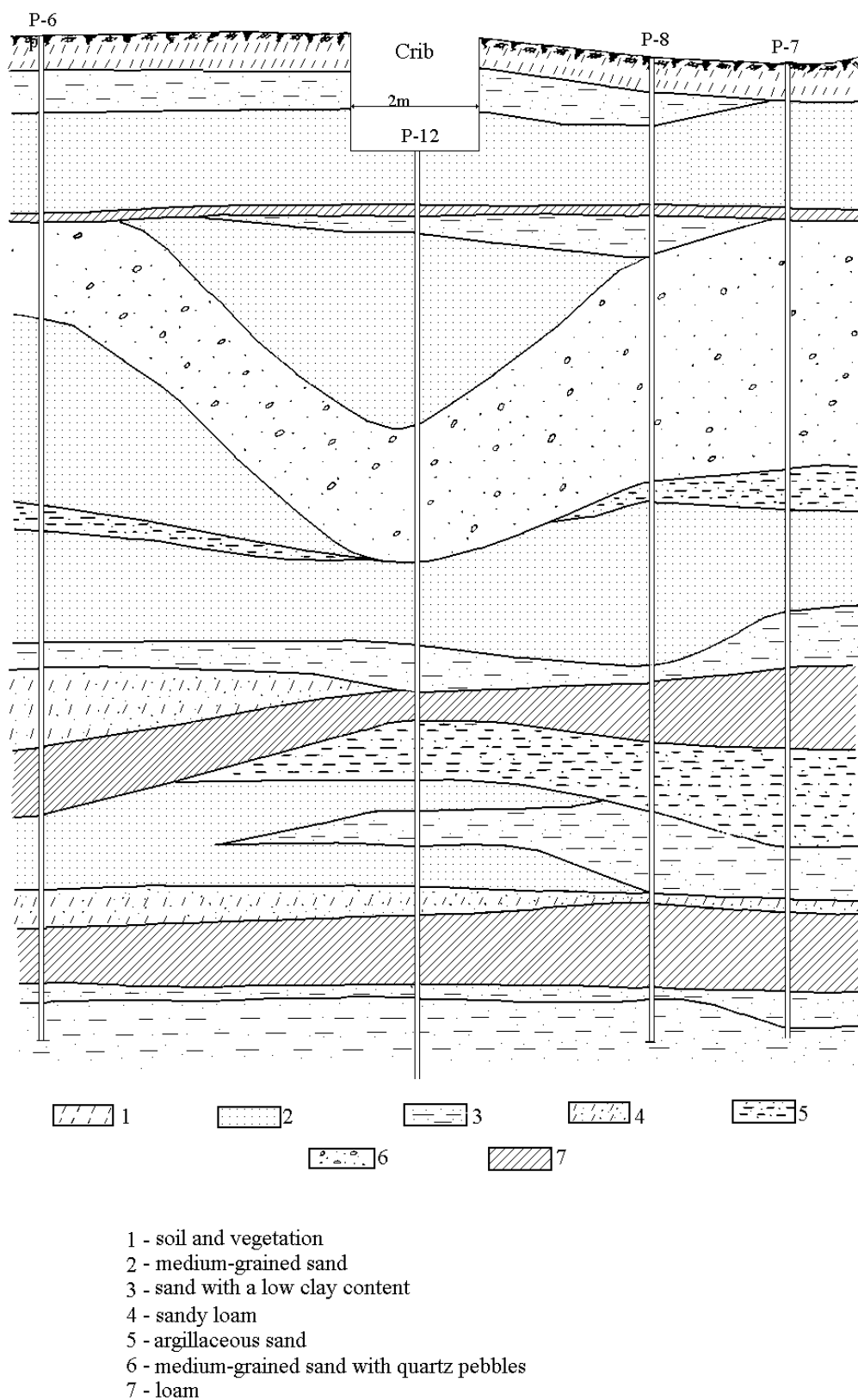


Figure 2. Distribution of ^{90}Sr concentration in the vadose zone during the third phase of study:
 1, 2, 3, 4, 5, and 6 – zones with the concentrations, respectively, $> 10^{-5}$, 10^{-5} to 10^{-6} , 10^{-6} to 10^{-7} , 10^{-7} to 10^{-8} , 10^{-8} to 10^{-9} , and 10^{-9} to 10^{-10} Ci Kg $^{-1}$.

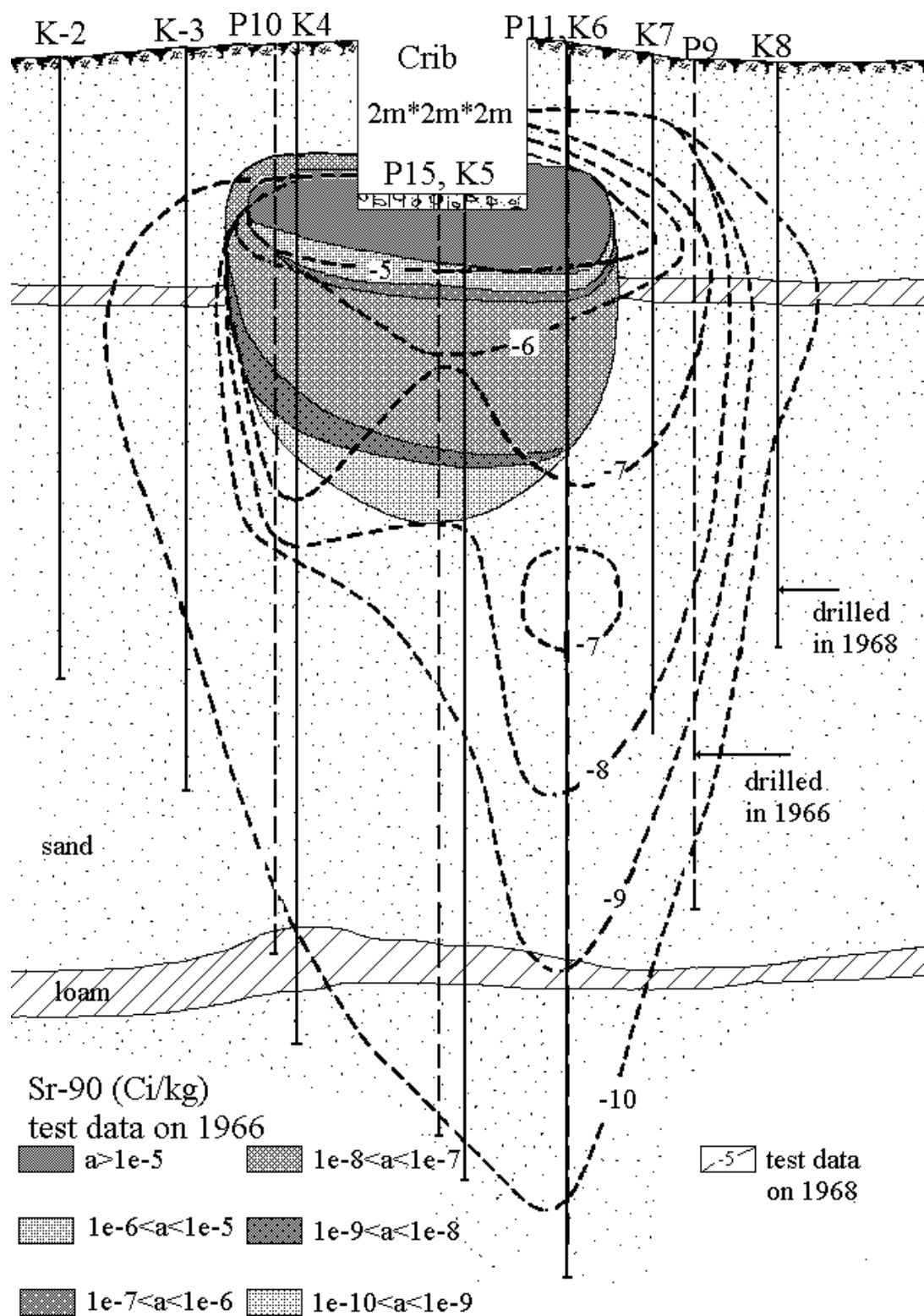


Figure 3. Distribution of Sr-90 concentration in the vadose zone during the first and the third phase of study.

Geostatistical Characterization and Numerical Modeling of the Vadose Zone Transport of Tritium Released from an Underground Storage Tank

Kenrick H. Lee and John J. Nitao

Lawrence Livermore National Laboratory, Livermore, CA

Introduction

The soil close to an underground tank storing tritiated water (HTO) at Lawrence Livermore National Laboratory was contaminated with tritium at levels up to 220×10^8 pCi/L of soil water. Tank leakage apparently resulted in a plume of tritium in the heterogeneous vadose zone, with lower concentrations reaching the water table 48 ft below the ground surface. Details of the tank history are unclear. However, records show that the tank contained HTO between 1977 and 1987. A site characterization and monitoring program was initiated in late 1989. The program included installation of a number of borings and wells, soil water and soil gas sampling, water content measurement using neutron probes, and laboratory measurement of saturated hydraulic conductivity, water retention functions, and particle size distribution.

The primary objective of our investigation was to use data generated from site characterization and monitoring to predict the impact of the release on future soil and groundwater quality at the site. Results of the study were intended to supply the basis for any appropriate remedial action, including the option to take no action. The tritium release also presented a rare opportunity for studying the applicability of numerical modeling and geostatistics to vadose zone transport through heterogeneous soils at a moderately well monitored field site in a semi-arid environment.

The methodology presented and demonstrated here will substantially increase the effectiveness of vadose zone contaminant transport analysis while reducing the high cost usually associated with site characterization in heterogeneous soils. The approach combines stochastic simulation and other geostatistical techniques, soil property correlation, and numerical modeling to maximize the utility of scarce data. Lee (1997) presents a more detailed description of the study.

Setting

The study site is the Building 292 Area at Lawrence Livermore National Laboratory (LLNL) in Southern Alameda County, approximately 3 miles east of the downtown area of Livermore, California. Livermore is located in the San Francisco Bay Area, about 40 miles east of San Francisco. LLNL is a research

facility owned by the U.S. Department of Energy (DOE) and operated by the University of California under contract with the DOE. Figure 1 is a plan view of the LLNL Livermore Site showing the location of the tritium release in the Building 292 Area. The LLNL Site, including an adjacent buffer zone, occupies approximately 800 acres, with the western boundary adjacent to the eastern Livermore city limits.

The climate is semiarid, characterized by warm, dry summers and mild, wet winters. The average precipitation is 14 in. per year. About 90% of the precipitation occur from November to April. Precipitation in the area is usually associated with winter storms. The average temperature is 62F (17C). Abundant sunshine occurs almost throughout the year.

LLNL is located near the southeastern margin of the Livermore depositional basin (Thorpe et al., 1990). Soil at the LLNL site consists of highly heterogeneous fluvial and lacustrine sediments, characterized by complexly interbedded clay, silt, sand, and gravel. The thickness of the vadose zone varies from 130 ft in the southeast corner of the LLNL site to less than 30 ft in the northwest.

The saturated zone beneath the LLNL site consists of multiple water bearing systems. The uppermost water bearing system is unconfined and is separated from the second system by a horizontally extensive confining layer consisting of low-permeability silt and clay. The upper system, also referred to as the upper aquifer, has a thickness of about 5 ft. in the vicinity of the tank. Groundwater flow is generally westward. The hydraulic gradient is steepest near the northeastern corner of LLNL, at about 0.15 ft/ft, and decreases to about 0.002 ft/ft west of LLNL.

Site Characterization and Monitoring

Site characterization and monitoring were initiated in late 1989, following the discovery of elevated concentrations of tritium in the soil around Tank R1U1. Twenty boreholes were drilled by the end of 1992. Figure 2 is a plan view of the release site showing locations of boreholes, the tank, and a blacktop that partially covers the soil. Three different types of boreholes were constructed: vadose zone monitoring boreholes, piezometers, and boreholes drilled exclusively for soil sampling. Boreholes drilled only for soil sampling were carefully grouted after the samples were recovered. Soil water tritium concentrations were measured from core samples recovered during drilling of all boreholes. Groundwater tritium concentration and water table elevation were monitored in piezometers.

Site characterization for numerical analysis was especially challenging because of the high degree of spatial variability observed in the soil hydraulic properties. Soil at the site consists of highly heterogeneous sediments, comprising clay, silt, sand, and gravel. Figure 3 shows the smoothing observed in a permeability field obtained by ordinary kriging, compared to the much higher degree of variability observed in a permeability field obtained by conditional simulation, using the same

data set. The soil had a mean permeability of 8.9 mdarcy, with a median of 2.9 mdarcy. The permeability ranged nearly 8 orders of magnitude, with the lowest class 1.2×10^{-5} darcy, in the clay range, and the highest class 98.0 darcy, in the sand to gravel range. The standard deviation of the natural log of permeability, σ_k , was 4.5 with permeability expressed in microdarcy.

Measurements of unsaturated hydraulic properties and other physical properties were made on sixteen soil samples taken from three boreholes. The properties measured were moisture retention, saturated hydraulic conductivity, initial water content, porosity, particle size distribution, bulk density, and skeletal density. Vertical profiles of water content were measured by neutron logging in boreholes.

Tritium concentration profiles measured in 5 boreholes close to the north face of the tank are shown in Figure 4. SEAMIST monitoring systems monitored concentrations in the vadose zone. SEAMIST (Science and Engineering Associates, Santa Fe, New Mexico) is a monitoring system in which an instrumented membrane is inserted into an open borehole (Keller and Lowry, 1990). The membrane is fitted with gas ports or absorbent pads placed against the borehole wall at different depths. The membrane can be held open by air pressure, sand, or grout. Martins (1990) describes the system in greater detail.

Analysis

Our approach relied heavily on statistical and geostatistical techniques to estimate soil hydraulic properties for input into the numerical model. We developed permeability sample variograms and soil property correlations from the data. Stochastic simulation and ordinary kriging techniques were applied to develop realizations of soil permeability fields. Other unsaturated flow properties and parameters were estimated from correlation with permeability. Ordinary kriging was applied to estimate the distribution of tritium concentration in the soil water and the total activity of tritium in the vadose zone.

We used routines from GSLIB, the Geostatistical Software Library (Deutsch and Journel, 1992), and the turning bands model by Tompson et al. (1989) to generate three-dimensional permeability fields by kriging and nonconditional simulation. We wrote a number of Fortran routines that prepared the field data for analysis by the geostatistical and stochastic simulation models, control execution of the models, and perform conditional simulation using the output from kriging and nonconditional simulation.

The conceptual transport model consists of two fluid phases and three chemical components. The fluid phases are liquid (or aqueous) and gas and the chemical components are air (treated as a pseudocomponent with averaged properties), water (H_2O), and tritiated water (HTO). The liquid phase is comprised mainly of water, with dilute concentrations of HTO and air. The gas phase is comprised of air, water vapor, and HTO vapor. Components may partition between the two phases.

Both phases are mobile. Radioactive decay of tritium occurs with a half-life of 12.4 yr. Both liquid and vapor diffusion are modeled using the Millington (1959) formulation for tortuosity. Mechanical dispersion is modeled only in the groundwater transport calculations. Mechanical dispersion in the vadose zone is effected through explicit incorporation of the high degree of heterogeneity in permeability shown in the data.

The flow and transport model is solved using the NUFT code, developed by Nitao (1998a, 1998b) at LLNL. NUFT (Nonisothermal Unsaturated-Saturated Flow and Transport) is an integrated suite of models for numerical solution of thermal and isothermal flow and transport in porous media, with application to subsurface contaminant transport problems. The code simulates the coupled transport of heat and multiple multicomponent fluid phases in both the vadose and saturated zones. Components may be volatile. Grid systems may be Cartesian or cylindrical, with one-, two-, or fully three-dimensional configurations possible.

We performed a Monte Carlo analysis to assess the effect of uncertainty in soil properties. The analysis included generating 100 realizations of the soil permeability field by conditional simulation and conducting two-dimensional numerical transport simulations using each of the realizations. Results of the Monte Carlo analysis were compared with the results of a numerical simulation run using a permeability field derived by ordinary kriging. We conducted a series of 2D runs as part of sensitivity analyses to investigate the effects of infiltration and vapor diffusion on the tritium transport.

We conducted a three-dimensional analysis that included details of site features that could not be included in two-dimensions. The features included partial surface cover by a blacktop, which allowed infiltration through only a fraction of the upper surface. Three-dimensional transport runs were done using ten different realizations of soil property fields generated by conditional simulation. To observe the effect of the blacktop on tritium transport, simulation runs for two of the realizations were repeated with the blacktop removed, allowing infiltration through the entire upper surface of the model. The results obtained using soil properties from conditional simulation were compared with results using soil properties obtained by kriging.

We compared the calculated tritium concentrations for each 3D realization at different times with concentrations measured in the field around 1990 to determine which realization best matches the conditions in the field. The quantitative measure of goodness-of-fit that was used as the basis for comparison is the root mean squared difference (RMSD) in concentration. The realization with the minimum RMSD between about 5 yr. to 20 yr. after leaking started was selected as the best realization to use for a forecast of future groundwater quality at the site.

Results

General Findings

- The artificial smoothing effect of kriging removes high-permeability flow paths and causes a reduction in calculated contaminant transport rates for heterogeneous vadose zone systems. Therefore, kriging used alone is not a recommended technique for estimating hydraulic soil properties for contaminant transport analyses at heterogeneous vadose zone sites.
- Traditional geostatistical analysis can be combined naturally with stochastic simulation to estimate the hydraulic properties of heterogeneous soils in vadose zone transport studies.
- Traditional geostatistical analysis using ordinary kriging is a viable technique for estimating the mass distribution of contaminants at vadose zone sites.

The techniques presented in this study represent a practical approach to the analysis of contaminated, heterogeneous vadose zone sites with limited data. The method, which we refer to as the Best Fitting Realization or simply the BFR method, is summarized as follows:

- Develop concentration sample variogram from field concentration data
- Estimate 3-D concentration field by kriging, using sample data and variogram
- Develop soil permeability sample variogram from laboratory and field data
- Develop or use any available soil property correlations to expand the permeability data set and to estimate additional unsaturated soil properties; permeability versus particle size distribution parameters is an example of a useful correlation
- Generate a number of realizations of soil permeability fields, with other soil properties estimated from correlations, and conduct a numerical simulation run using each realization.
- Compare the calculated concentration fields, at various times, with the measured concentration field, for which the time is usually not well known, and compute the RMSD for each realization at each time.
- Select the realization with the minimum RMSD, at some appropriate time, and use the results from this best-fitting realization, along with average results, to forecast future site conditions.

Findings Specific to the Building 292 Area

- The tritium release poses no serious long term threat to groundwater quality at the LLNL Livermore Site or any neighboring sites. For rl3d110, the 3D realization that showed the highest groundwater tritium concentrations, the maximum concentration 100 ft downstream of the leak was below the groundwater standard. For rl3d108, the best-fit 3D realization, the peak concentration 100 ft downstream of the leak was 7.59×10^3 pCi/L, only 38% of the groundwater standard.

- The impact of the release on groundwater quality is substantially reduced by the blacktop that partially covers the ground surface in the Building 292 Area. Results of the 3D analysis show that removing the blacktop results in large increases in groundwater tritium concentrations and in the cumulative flux of tritium entering the groundwater. The increases are due to higher downward liquid velocities in the vadose zone resulting from infiltration through the additional exposed soil surface.
- Numerical simulation runs using soil permeability fields derived by kriging yield significantly lower groundwater tritium concentrations than runs using fields derived by conditional simulation. The artificial smoothing effect of kriging removes high-permeability flow paths that are preserved by conditional simulation. Kriging under the present conditions yields unconservative and potentially misleading results.
- High soil-water tritium concentrations, over 1.0×10^7 pCi/L, are expected to persist in the vadose zone for the next 50 yr. or so. Because of low fluid velocities in the finer-grained soils, peak tritium concentrations in the vadose zone are controlled to a much greater extent by radioactive decay than by transport. The total activity of tritium in the vadose zone at any time is also controlled largely by radioactive decay because the percentage lost to the groundwater is very small.
- We estimate a total tritium activity of 5 Ci in the vadose zone around 1990--1991. This estimate was obtained by applying kriging and other geostatistical techniques to sample data collected between 1989 and 1992.
- Vapor diffusion is not important to tritium transport under current site conditions.
- The soil permeability variogram has a horizontal range of 14.0 ft and a vertical range of 4.5 ft.

Conclusions

This study highlights the danger in using kriging to estimate soil properties for vadose zone transport modeling. Geostatistical and numerical analyses show that the artificial smoothing effect of kriging tends to remove high-permeability flow paths from hydrogeologic data sets, reducing simulated contaminant transport rates in heterogeneous vadose zone systems. Therefore, kriging used alone is not recommended for estimating the spatial distribution of soil hydraulic properties for contaminant transport analysis at heterogeneous vadose zone sites. Vadose zone transport is modeled more effectively by applying conditional simulation to better represent the high degree of spatial variability usually found in the hydraulic properties of field soils.

References

- Deutsch, C.V, and A.G. Journel, (1992) *GSLIB Geostatistical Software Library and User's Guide*, Oxford University Press, New York.
- Keller, C., and B. Lowry, Eds. (1990), A New Vadose Zone Fluid Sampling System for uncased Holes. American Water Well Convention, Las Vegas, Nevada.
- Lee, K.H. (1997) *Analysis of vadose zone tritium transport from an underground storage tank release using numerical modeling and geostatistics*, Lawrence Livermore National Laboratory, Livermore, CA (UCRL-LR-128840).
- Martins, S.A. (1992), *A Method for Collecting Soil Vapor from the Vadose Zone with an Instrumented Membrane System*, Lawrence Livermore National Laboratory, Livermore, CA (UCAR-10299).
- Millington, R.J. (1959) "Gas diffusion in porous media," *Science*, 130, 100-102.
- Nitao, J.J. (1998a) *Reference Manual for the NUFT Flow and Transport Code*, Version 2.0, Lawrence Livermore National Laboratory, Livermore, CA (UCRL-MA-130651).
- Nitao, J.J. (1998b) *User's Manual for the USNT Module of the NUFT Code (NP-Phase, NC-Component, Thermal)*, Version 2.0, Lawrence Livermore National Laboratory, Livermore, CA (UCRL-MA-130653).
- Thorpe, R.K., W.F. Isherwood, M.D. Dresen, and C.P. Webster-Scholten (eds.) (1990), *CERCLA Remedial Investigations Report for the LLNL Livermore Site*, Lawrence Livermore National Laboratory, Livermore, CA (UCAR-10299).
- Tompson, A.F.B., R. Ababu, and L.W. Gelhar (1989), "Implementation of the Three-dimensional Turning Bands Random field Generator," *Water Resour. Res.*, 25(10), 2227-2243.

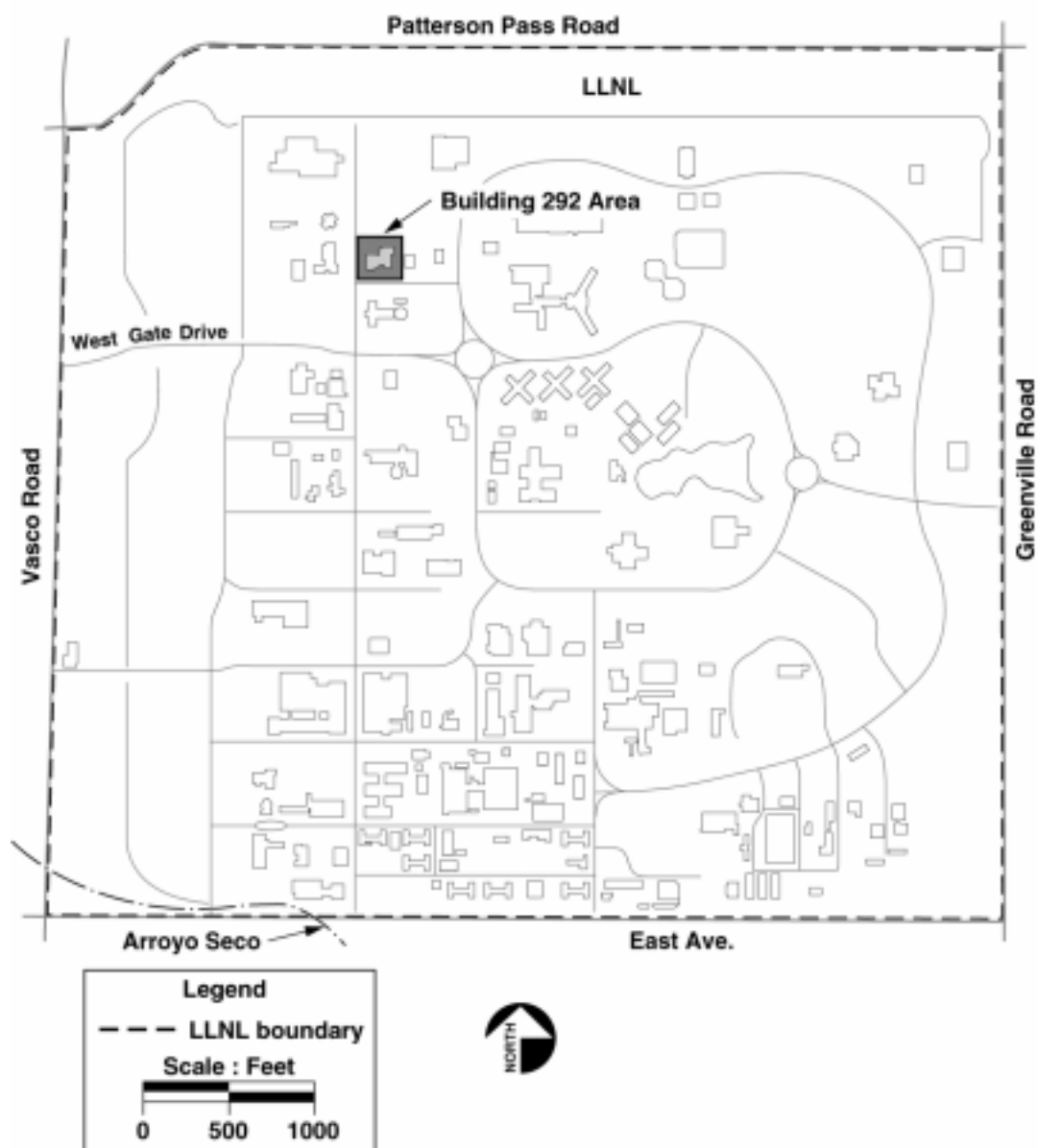


Figure 1: Layout of LLNL Livermore Site showing location of the ^3H release in the Building 292 Area.

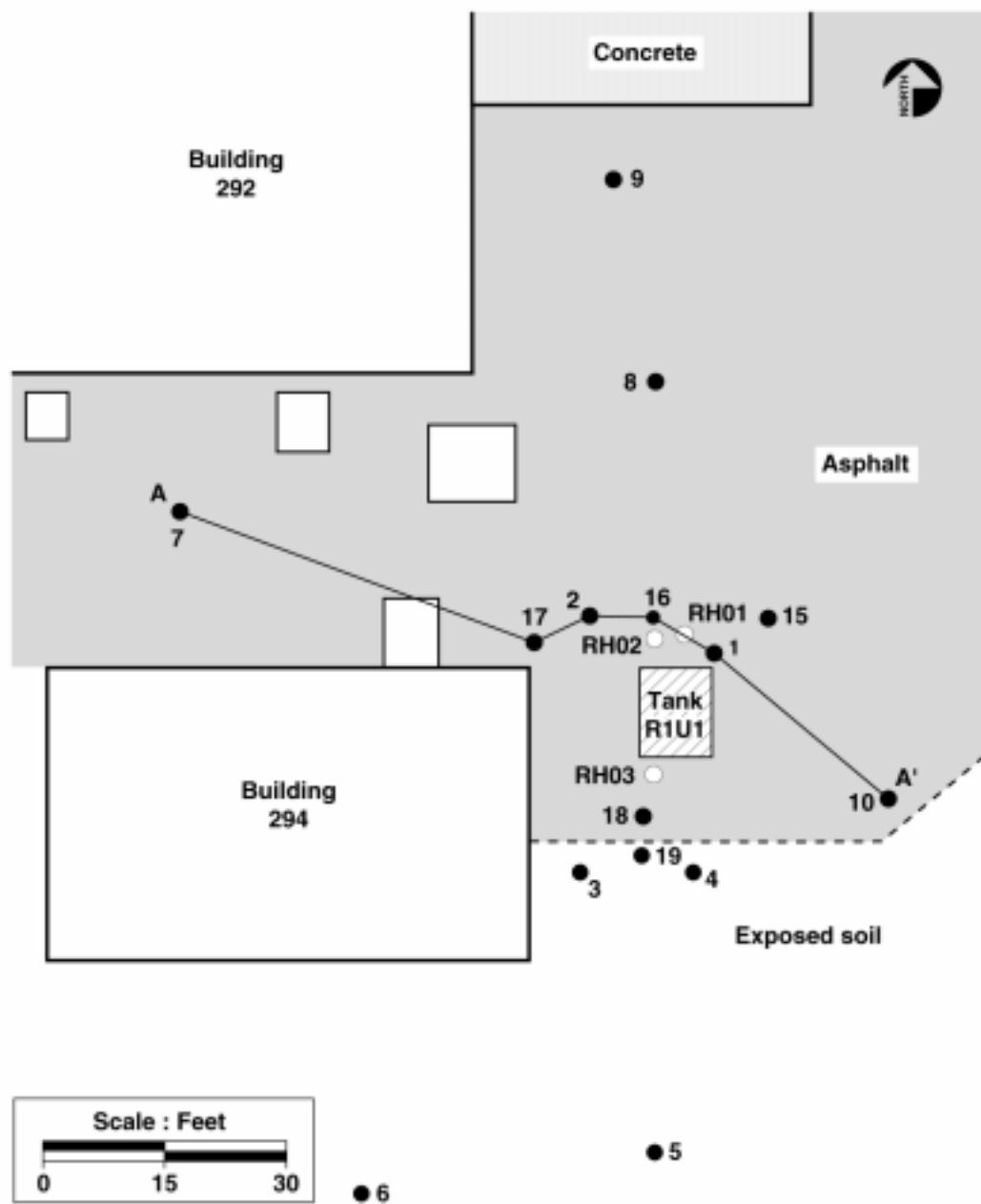


Figure 2: Plan view of the LLNL Building 292 Area showing locations of boreholes, Tank R1U1, and the blacktop.

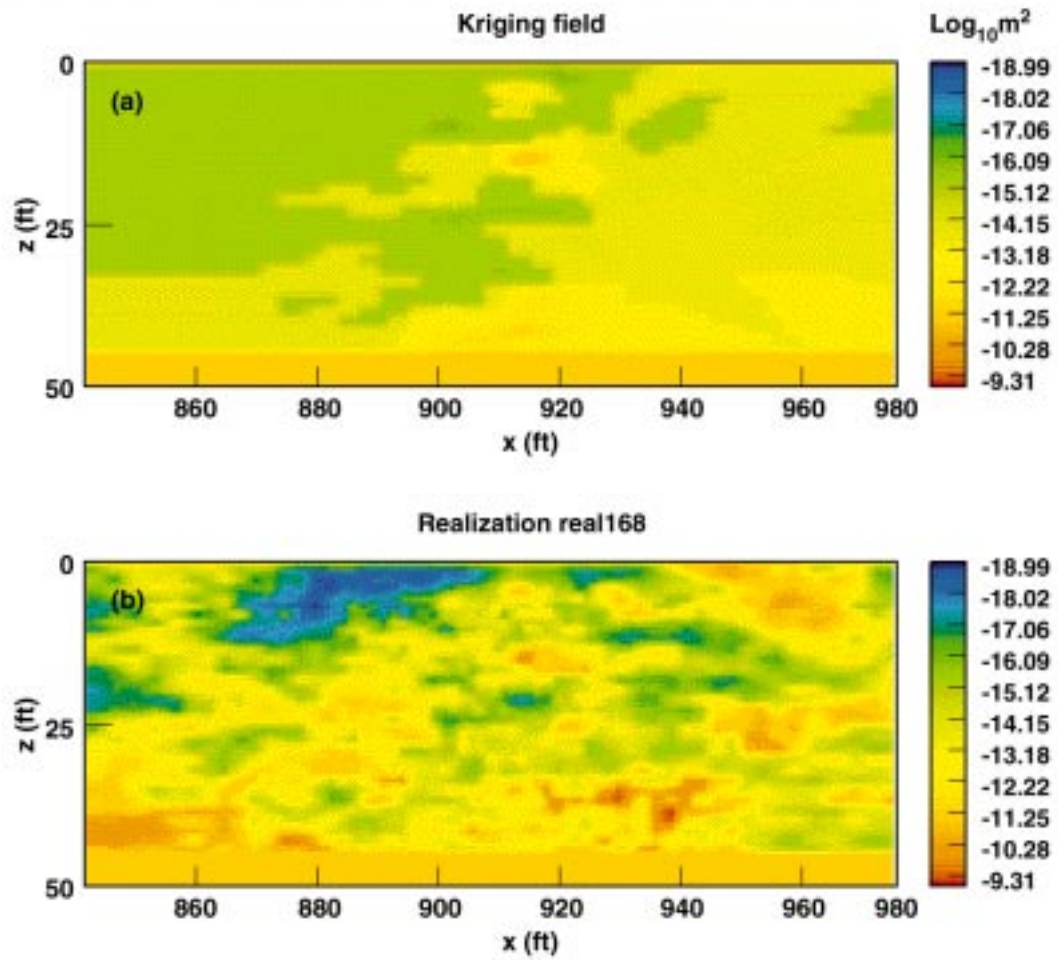


Figure 3: Comparison of permeability fields generated by kriging and conditional simulation, using the same sample data. The figure shows an east-west section through the leak point, with permeability generated by (a) kriging, and (b) conditional simulation.

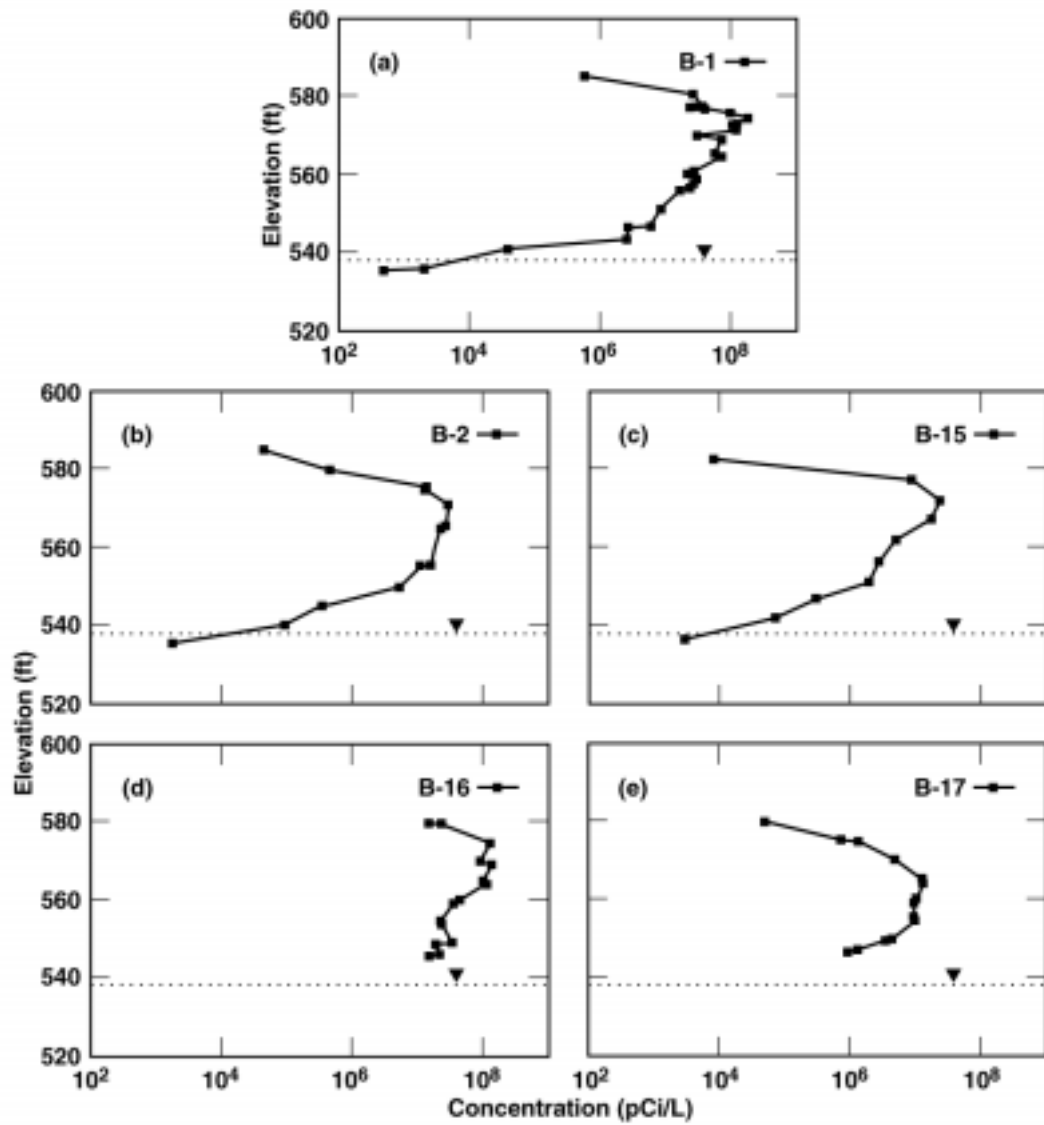


Figure 4: Soil water ^3H concentration profiles along boreholes (a) B-1, (b) B-2, (c) B-15, (d) B-16, and (e) B-17. Concentrations measured during initial site characterization in the period 1989-1992.

Facilitated Transport Fraction: A Provisional Improvement to Simple Kd Modeling for Scoping Calculations

Brian Looney, Savannah River Technology Center

National Environmental Policy Act documents and similar scoping activities require modeling of contaminant transport and subsequent estimation of exposure and risk. The need to evaluate and accumulate the impacts of multiple constituents at multiple sites requires the models used to be relatively simple – while at the same time being as accurate and defensible as possible. The desire for defensibility generally leads to the use of “standard” methods. In the case of transport geochemistry, this translates into use of simple linear Kd (i.e., retardation factor) estimates. If not implemented carefully, this approach can lead to undesirable consequences. For several contaminants, a standard Kd is a good approximation of the behavior of the bulk of the contaminant profile, with a small quantity of material moving ahead of the simplified prediction. This results in field data where “low but measured” concentrations are found deep in the vadose zone or in shallow groundwater wells when the predicted value is “zero.” Conversely, if the Kd and dispersion coefficient are adjusted to match the field data, the calibration process will allow all of the contaminant to migrate. In many cases this results in predicted arrival of high concentrations in the near future when most of the contaminant mass will actually be held up near the original release location. To support development of an Environmental Impact Statement (EIS) for forty-five waste site areas (each with multiple contaminants) at the Savannah River Site (SRS) in South Carolina, we implemented a simple modification to the linear Kd as a provisional improvement to account for various types of geochemical complications (Looney et al., 1987a and 1987b).

Several factors may enhance the mobility of chemicals in subsurface systems. Inorganic elements may associate with inorganic ligands, organic ligands, or colloids in these systems. This complexation and sorption of a small fraction of the mass will result in mobility in excess of that predicted using the single Kd value derived from simpler systems. Often a tabulated Kd is used for calculation or, in rare cases, a conditional Kd is estimated (e.g., based on pH and Eh and carbonates as the only ligands). We believe that the need for defensibility requires that facilitated transport (the enhanced mobility that results from varied and complex processes) be incorporated into assessment models in some fashion to allow reasonable estimations of risk to be made.

A simple approach in which a facilitated transport fraction (FTF) is used to estimate the portion of the total disposal mass that is subject to enhanced mobility was selected for assessing waste sites at SRS. This approach is carried out by:

- (1) determining FTF values for constituents based on field monitoring data from large well characterized sites,
- (2) applying the FTF values to the appropriate constituent(s) at each site to determine a mobile fraction and a fraction that is assumed to behave according to standard Kd formulations, and

- (3) using the resulting source information to carry out the environmental assessment assuming a K_d of 0.001 for the mobile fraction.

An implicit assumption in the FTF approach is that facilitated transport from waste disposal areas is dominated by the relatively abundant ligands and colloidal solids associated with the active disposal/operation. Continuous processes, such as mercury transformations or in situ colloid generation, that cause facilitated transport to continue are not predicted using the approach as it was applied.

FTF values were derived from data at the M-Area Settling Basin and the Radioactive Waste Burial Grounds. FTF values were generated if data for a constituent were available, and the resulting values were assumed to apply to all SRS waste sites. Note that the FTF values from the M-Area Settling Basin and the Radioactive Waste Burial Grounds would tend to be high relative to most other SRS sites because they are two of the most significant waste disposal operation at SRS. The large volume of wastes and high ligand concentrations at these sites would be expected to maximize facilitated transport relative to some of the other sites that were being analyzed (e.g., rubble piles). In the absence of additional data, the empirical FTF values are assumed to provide a rough approximation of enhanced transport from various complex processes. The approach does not differentiate or quantify the various processes and is not suited to final analysis of large and/or high risk sites.

The approximate FTF values generated are presented in Figure 1. In each case, the FTF for an element was derived based on the assumption that groundwater concentrations immediately downgradient of a waste site for a hydraulically conservative tracer (e.g., decay corrected tritium) was related to source strength (original disposal inventory to the soil from records) in a fashion similar to the element's mobile fraction.

Thus, for each constituent (i), we solved the following equation for FTF based on field measurements:

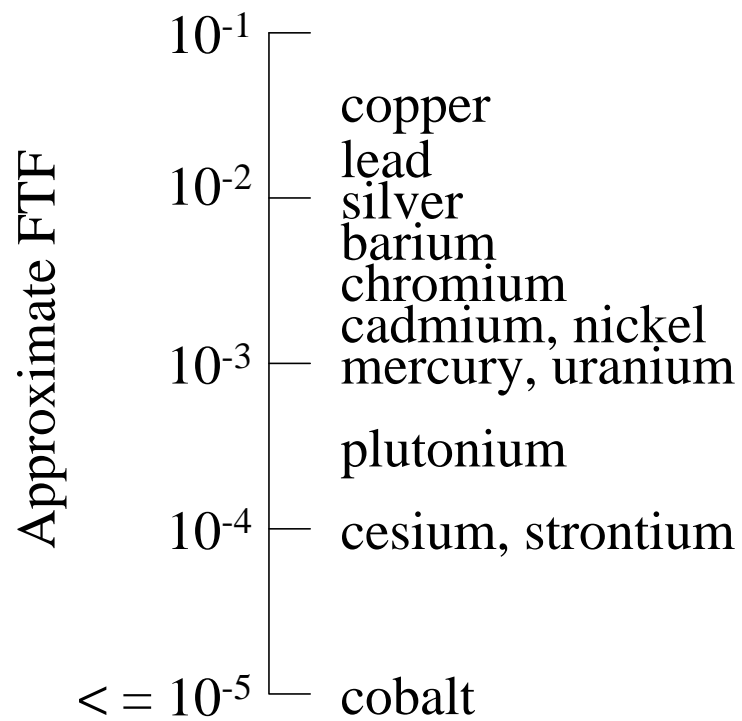
$$\frac{\text{disposal inventory of tracer}}{\text{groundwater concentration of tracer}} = \frac{(\text{FTF}_i)(\text{disposal inventory})_i}{(\text{groundwater concentration})_i}$$

The FTF values were simply and directly calculated based on the field measurements and operational history information and no attempt to discern which mechanism(s) were responsible for the transport or if the factors were related to any theoretical predictor.

In evaluating the performance of the overall EIS effort, we addressed the performance and limitations of the FTF approach (Looney et al., 1987b):

- “(T)he results suggest that chemical speciation must be addressed to adequately predict measured concentrations adequately; transient models that account for unsaturated zone transport predict higher peak concentrations than those predicted by the VHS model (VHS is a steady-state model that used the results of a leach test as the initial concentration); modeling objectives (e.g., determining relative risks as a function of closure scenario) should influence model selection due to differences of assumptions and results between simple analytical solutions and more robust numerical methods. Chemical speciation was approximated by assigning a fraction to the disposal mass which was subject to "facilitated transport" (transport of material associated with organic and inorganic ligands, and colloids). Although the quality assurance analysis suggests that simple analytical approximations are sufficiently accurate to make relative environment assessments, additional work (theoretical, field, and laboratory) in the areas of geochemistry and the applicability of advection-dispersion models in general is recommended.”
- “Recent publications (Higgo & Rees, 1986) support the concept of FTF for some elements.”
- “For sites with high potential risks or with ... unusual conditions, more robust calculations, including multiple equilibrium models and kinetic transformation rates, should be carried out as needed when developing detailed site specific closure plans.”

Figure 1. Estimated FTF for various contaminants based on field data at the M Area Settling Basin and the Radioactive Waste Burial Grounds at the Savannah River Site in South Carolina.



References:

- Higgo, J. J. and L.V.C. Rees, 1986. Adsorption of actinides by marine sediments, *Environmental Science and Technology*, 20:483-490.
- Looney, B. B., M. W. Grant and C. M. king, 1987a. *Estimation of geochemical parameters for assessing subsurface transport at SRP*, DPST-85-904, U. S. Department of Energy, Savannah River Site, Aiken SC 29808.
- Looney, B., B., C. M. King and D. E. Stephenson, 1987b. *Quality Assurance Program for Environmental Assessment of Savannah River Plant Waste Sites*, DPST-86-725, U. S. Department of Energy, Savannah River Site, Aiken SC 29808.

Cone Penetrometer-based Raman Spectroscopy for DNAPL Characterization in the Vadose Zone

J. Rossabi, B. D. Riha, J. Haas, C. A. Eddy-Dilek, A. Lustig, M. Carrabba, K. Hyde, and J. Belo

Abstract

Cone penetrometer based Raman spectroscopy was used to identify separate phase tetrachloroethylene (PCE) contamination in the vadose zone at two locations during field tests conducted at the Savannah River Site. Clear characteristic Raman spectral peaks for PCE were observed and, because of the uniqueness of Raman spectrum for a given compound, are compelling evidence that this method is a viable DNAPL characterization technique. In addition, the spectral data indications of DNAPL correlate with soil concentration data collected in the same zones. The Raman spectroscopic activities conducted in these tests represents the first in situ direct measurement of DNAPL in the subsurface.

Based on data from this field work, the Raman technique may require a threshold of DNAPL to provide an adequate optical cross-section for spectroscopic response. Similar to CPT-based laser induced fluorescence techniques, the detection limit of the technique is probably related to the probability of contaminant droplets coming in to contact with the optical window. It is also probable that the technique requires a separate phase liquid rather than an aqueous solution for adequate response.

Introduction

Raman Spectroscopy Sensors

The Raman effect occurs when light and matter interact resulting in the addition or subtraction of energy quanta in the scattered light (inelastic scattering). The energy shifts in the scattered light are correlated to the vibrational modes of the particular compound and constitute the Raman spectrum for the compound. The vibrational modes of the compound depend on the elemental constituents, energy state, and steric configuration of the molecule. The number of modes and associated energy of these modes is unique to the molecule and therefore produces a unique Raman spectrum for the compound (Colthup et al., 1990).

Raman spectra have been used to both identify unknown compounds and to probe their molecular state (Carrabba et al., 1990). Because of the number of vibrational modes possible for a given compound, Raman is most easily observed when probed with a monochromatic light source such as a laser.

Raman is similar to fluorescence spectroscopy in that both techniques result in light emanating from the compound in all directions that is wavelength-shifted from the original source light. Fluorescence spectra, however, are a result of an electronic transition caused by the quantum absorption and subsequent release of energy (in the

form of light) of the electron energy state of the compound. Raman spectroscopy does not involve an electronic energy transition and is inherently weaker in response than the fluorescent effect (Carrabba et al., 1992). Also, the fluorescence peaks are generally much broader with respect to wavelength than Raman peaks and can therefore obscure the Raman spectrum. As a result, it is important to try to minimize the fluorescence signal when performing Raman spectroscopy. Generally this involves changing the wavelength of the monochromatic probe light (usually to a longer, lower energy wavelength).

Method

A Raman spectroscopy system built by EIC Inc. for subsurface, cone penetrometer investigations was used for this work (Carrabba et al., 1998). The system consists of an infrared laser source and Echelle spectrometer located within the Department of Energy's Site Characterization and Analysis Penetrometer System (SCAPS) truck. The source and detector are connected by fiber optics through the cone rods to an optics assembly located in the cone near the tip and sensor end of the penetrometer. The optical assembly includes several lenses and filters designed to optimize light introduction to the formation and recovery of the Raman spectral signal. A sapphire window mounted to the cone rod is the interface between the formation and the sensor assembly. Raman spectral samples were generally taken every three feet as the cone penetrometer was pushed down. In sediments known from previous soil sampling and analysis to be likely to contain DNAPL, Raman spectral samples were taken every 0.5 feet to give detailed information about the depth and location of DNAPL. Generally these zones correlated to depths of fine grained sediment deposition in the vadose zone which can be detected using the standard cone penetrometer sensor suite (tip pressure, sleeve friction, pore pressure). The scans were integrated for 10 seconds as a rule and longer (60 seconds or 120 seconds) only if there was suspicion of DNAPL presence due to spectral or geologic evidence. All spectra presented in this report were collected with a 10-second integration time unless otherwise marked on the figures. Background intensity varied slightly between pushes as a result of differences in geology as well as examination of, and small adjustments made to, the optical window or train between pushes. The spectral data are printed as relative units with respect to the abscissa but correlate to the number of photons received by the detector (intensity) at a specific wavelength. Specific DNAPL compounds, such as tetrachloroethylene (PCE), are identified by their own unique spectral signature. Because of the probe wavelength (infrared laser diode at 785 nm), background fluorescence was expected to be low unless fluorescent compounds were present. Pure PCE essentially does not fluoresce at the wavelength of investigation, but some compounds (synthetic oils or natural organics) that are soluble in DNAPL may fluoresce. It is possible that high spectral fluorescence is indicative of DNAPL containing dissolved fluorescing compounds.

To assess the capability of the Raman technology to successfully identify compounds, sediment sampling for soil concentrations was conducted in the same location as the CPT/Raman pushes. The PCE and TCE soil concentration measurements were obtained by extracting sediment samples during drilling and performing laboratory analyses. In

clay layers known to contain DNAPL in the vadose zone, samples were taken every 0.5 feet to give the same detailed information about the depth and concentration of DNAPL as acquired by the Raman probe.

Results and Discussion

The first location used to evaluate the capability of Raman technology was adjacent to the A/M Area Seepage Basin. This was previously a waste disposal basin for caustic waste and spent machine oils and lubricants in addition to spent solvents; therefore, background fluorescence is expected to reflect some of these impurities. Dense contaminants from the 20-foot deep basin accumulated below the lighter aqueous phase in the basin and eventually made their way through the vadose zone and down below the water table. The subsurface geology in the area determined the vertical and lateral gravity-driven paths of the contaminants. The cone penetrometer test probe provided geophysical data based on tip pressure and sleeve resistance. The data from the standard CPT cone sensor suite are provided in Figure 1.

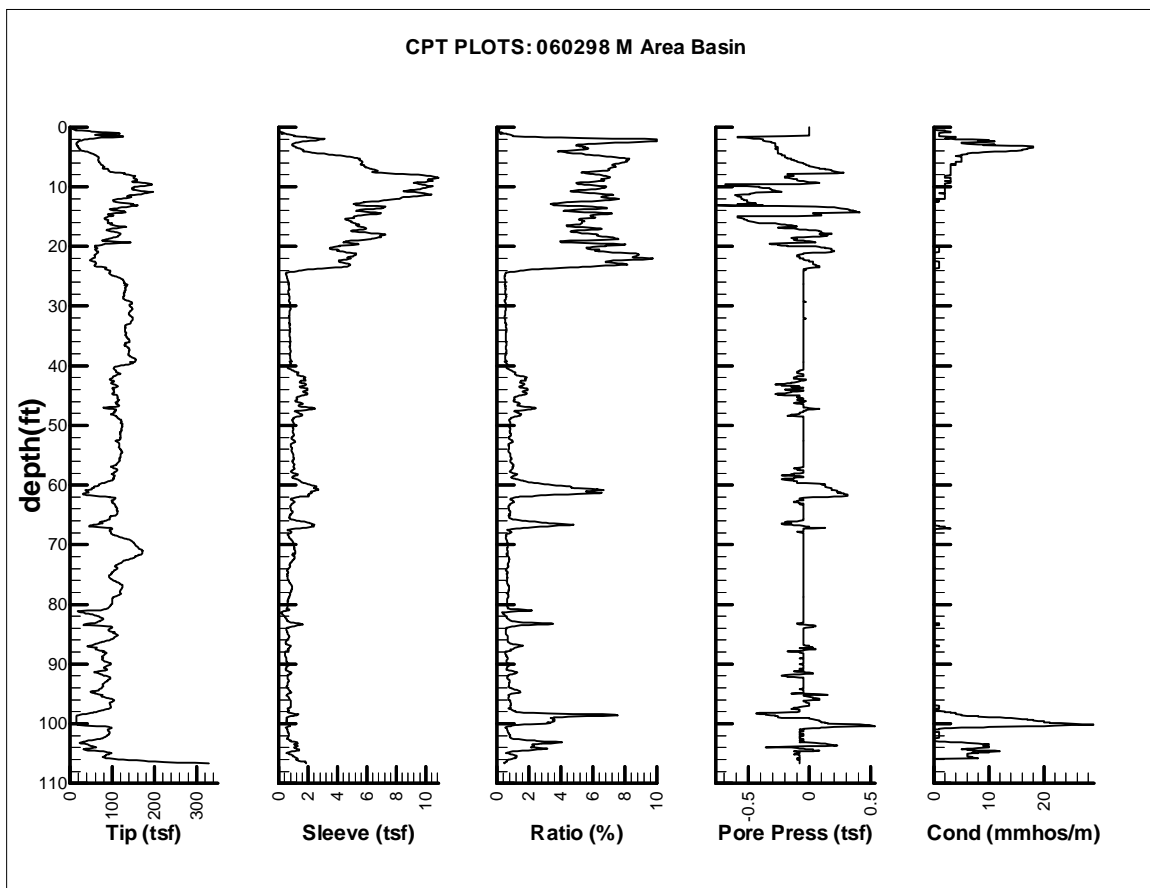


Figure 1. CPT Plot Adjacent to the M Area Basin

Using the plots of the sleeve friction/tip pressure ratio, pore pressure, and conductivity (Figure 2), the detailed lithology profile of the area can be clearly seen. This figure was constructed from CPT data collected during the Raman activities. From the surface to a depth of 24 feet, the sensors indicate a fine grain or clayey zone. A clean sand, (probably of medium to coarse grain size given the low conductivity and unchanging pore pressure response) follows from 24 feet to 40 feet. From 40 feet to 50 feet, some slightly finer grain material is evident, followed by another 10 feet of coarse grain material (50 to 60 feet). At 60 feet and 67 feet, two fine grain zones (probably clays) appear. From the conductivity plots, only the 67-foot clay is relatively moist. These clay zones have potential for retaining contaminant. After the fine grain zone at 67 feet, the profile indicates predominantly coarse-grained sand to a depth of 99 feet. There are a few thin zones of finer grain material, most notably at 84 and 87 feet. At 99 feet, a two foot thick wet clay zone is evident that is a likely DNAPL repository. Other interbedded clay and sand zones follow with a vertical period on the order of 6 inches to 3 feet until the water table is reached at a nominal depth of 130 feet. The lithology as inferred from this CPT plot is representative of all of the pushes adjacent to the M basin. Depths of the various zones shift slightly between CPT pushes, but the general patterns remain the same within the area around MSB-3D. These data inferring the geology of the area are critical in evaluating and focusing characterization efforts.

Knowing the behavior of contaminants when encountering these different types of material allows the optimization of characterization resources. For example, fine grain zones that are not completely water saturated tend to soak up and retain contaminants by capillary forces. The logical place to look for contaminants in the vadose zone, then, is within these layers. Raman spectra should be acquired with fine vertical depth resolution in the vicinity of these fine grain zones. Vertical data resolution in the coarse grain zones can be sparser without loss of important contaminant information.

Initial spectra of spectral grade PCE and DNAPL collected from well MSB-3D were acquired by holding samples against the optical window of the probe before any work below surface was performed. These spectra are provided in Figures 2 and 3, respectively, and were acquired using a laser excitation wavelength of 785 nm. The Raman spectral range shown is from 200 cm^{-1} to 600 cm^{-1} to capture several modes characteristic of PCE. Specifically, these peaks occur at 236 cm^{-1} and 448 cm^{-1} , with smaller peaks at 345 cm^{-1} and 513 cm^{-1} . There are also some characteristic peaks occurring further from the excitation line, but they are weaker than the two principal peaks. The spectrum acquired from the SRS DNAPL sample (well MSB-3D) shows the two strong peaks of PCE, but also a high broad background signal characteristic of fluorescence emission from the sample. This is probably due to the presence of co-constituents of PCE in the DNAPL sample.

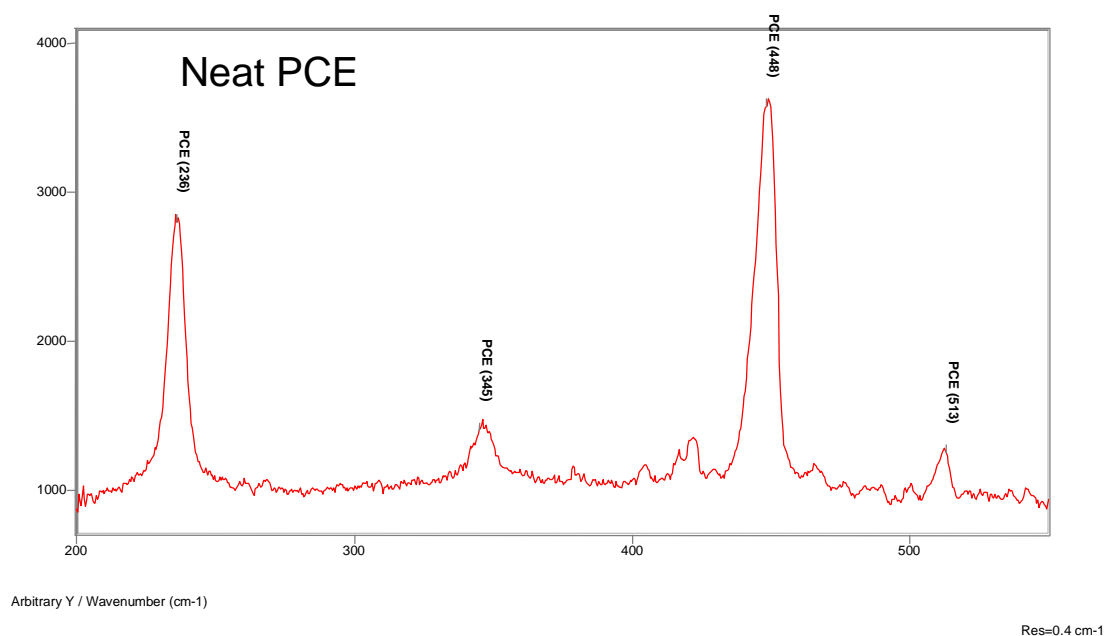


Figure 2. Characteristic Raman Spectrum for Tetrachloroethylene

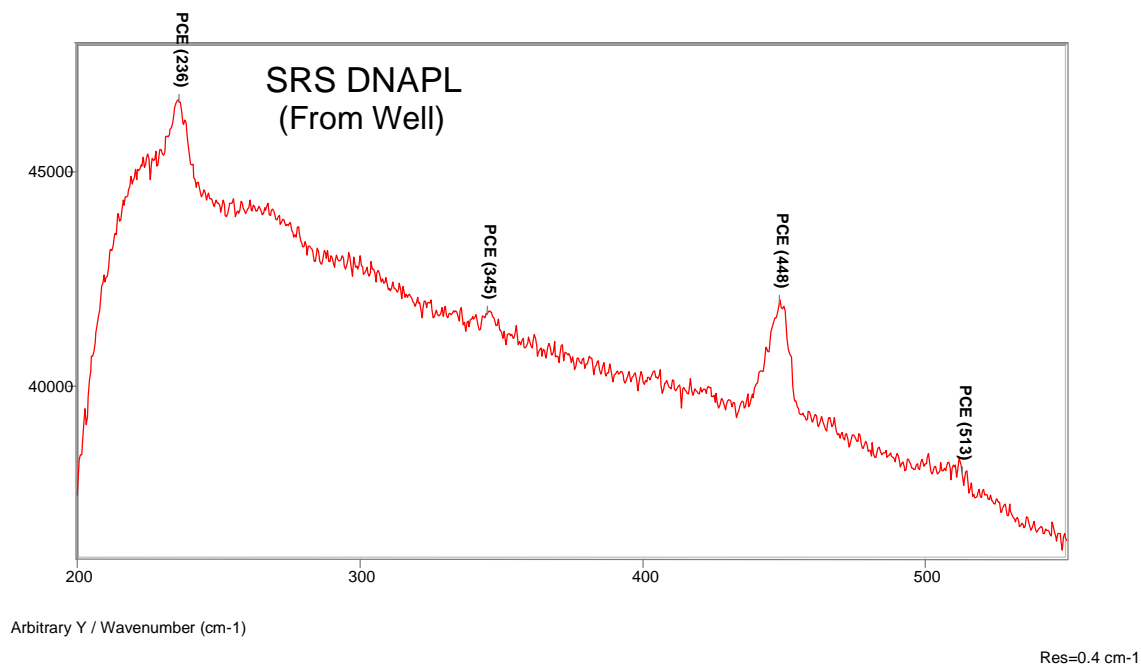


Figure 3. Characteristic Raman Spectrum for DNAPL collected from MSB-3D

For all pushes, spectra were taken every three feet through the coarse layers and every 0.5-foot through the clay layers. Raman spectral data collected from two consecutive pushes in February positively identified PCE located at depths of 101.5, 102.0, and 100.2' feet below ground surface, which corresponds to a clayey zone indicated by CPT geophysical data for that push. Fluorescent background levels were found to be much higher when DNAPL was present, as compared to average background fluorescence levels for uncontaminated soils. Figure 4 illustrates the large difference in fluorescence background over small vertical distances, as well as the presence or absence of characteristic Raman peaks from the data collected during the first push (RMA-01). It is clear that PCE is present at depths of 101.5' and 102' from the Raman spectra, but the fluorescence data strongly infer the presence of solvent at 100.9' as well. The fluorescence technique is inherently more sensitive than Raman as long as the contaminant fluoresces to a significant degree.

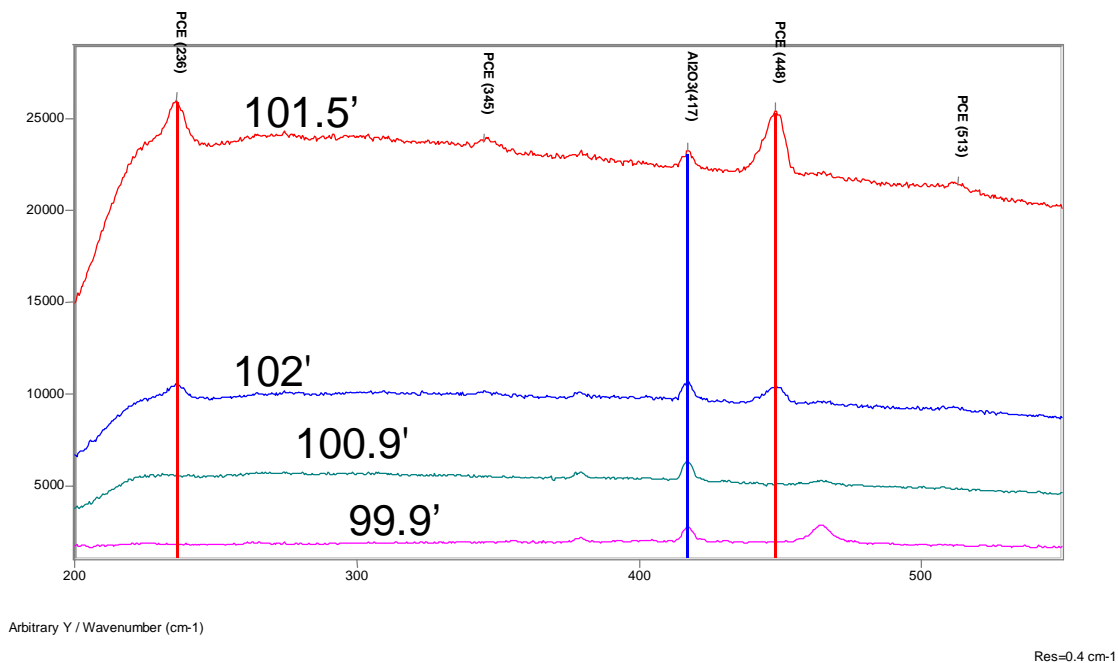


Figure 4. Raman and fluorescence spectra collected from RMA-01.

The effect of data collected during penetration or removal of the cone rods is shown in Figure 5. In this figure, the Raman spectra at the same depth indicate the presence of PCE on penetration, but not removal, of the rods. In figure 5, the background fluorescence of both spectra is comparable, implying that PCE is indeed present at the depth both during penetration and removal. These observations may be explained in several ways. Raman spectroscopy may require a threshold amount of DNAPL, either of a particular thickness or covering a certain percentage of the optical window, to produce the observable DNAPL characterize peaks. Fluorescence probably requires a much lower

threshold to respond. On penetration, it is conceivable that a relatively substantial drop (still less than 1 cm in diameter) of DNAPL was squeezed out of the pore throats as the cone passed through and compressed the formation. On retrieval of the rods, the borehole at that depth might have been wallowed by wander in the penetration path of the rods, or the drop may have moved or volatilized below the Raman threshold of response. In either case, this observed behavior supports the conceptual model of small, dispersed blobs of DNAPL, rather than the presence of pools at SRS.

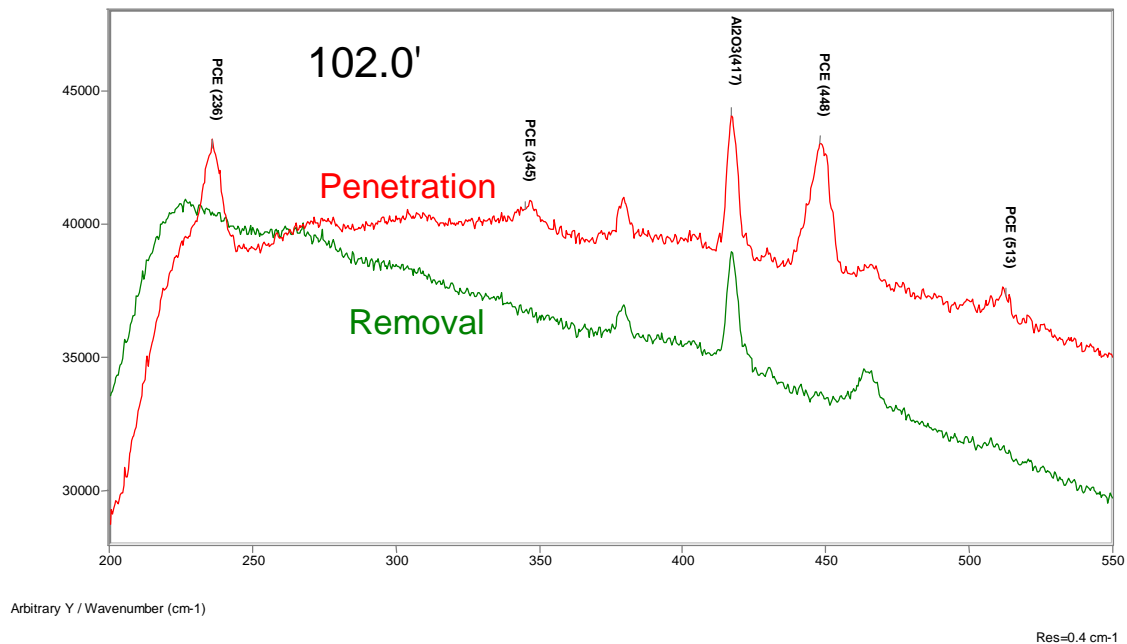


Figure 5. Comparison of spectra on penetration and removal collected from RMA-01.

Soil concentrations measured from sediment samples taken within a 5-foot radius of the CPT pushes showed high concentrations of both PCE and TCE from 97-104 feet. The sediment samples were collected by conventional hollow stem auger drilling with split spoon sampling. Figure 6 depicts the agreement between the two methods from the M Area Seepage Basin. PCE and TCE soil concentrations ($\mu\text{g/g}$) are plotted against depth using small, solid shapes. The Raman data are plotted with large open shapes at arbitrary values of 2000 for PCE and 3000 for TCE, which simply indicates presence or absence of PCE or TCE as indicated by spectral peaks. The cross symbols indicate depths that were characterized by high fluorescence in the background of the Raman spectrum.

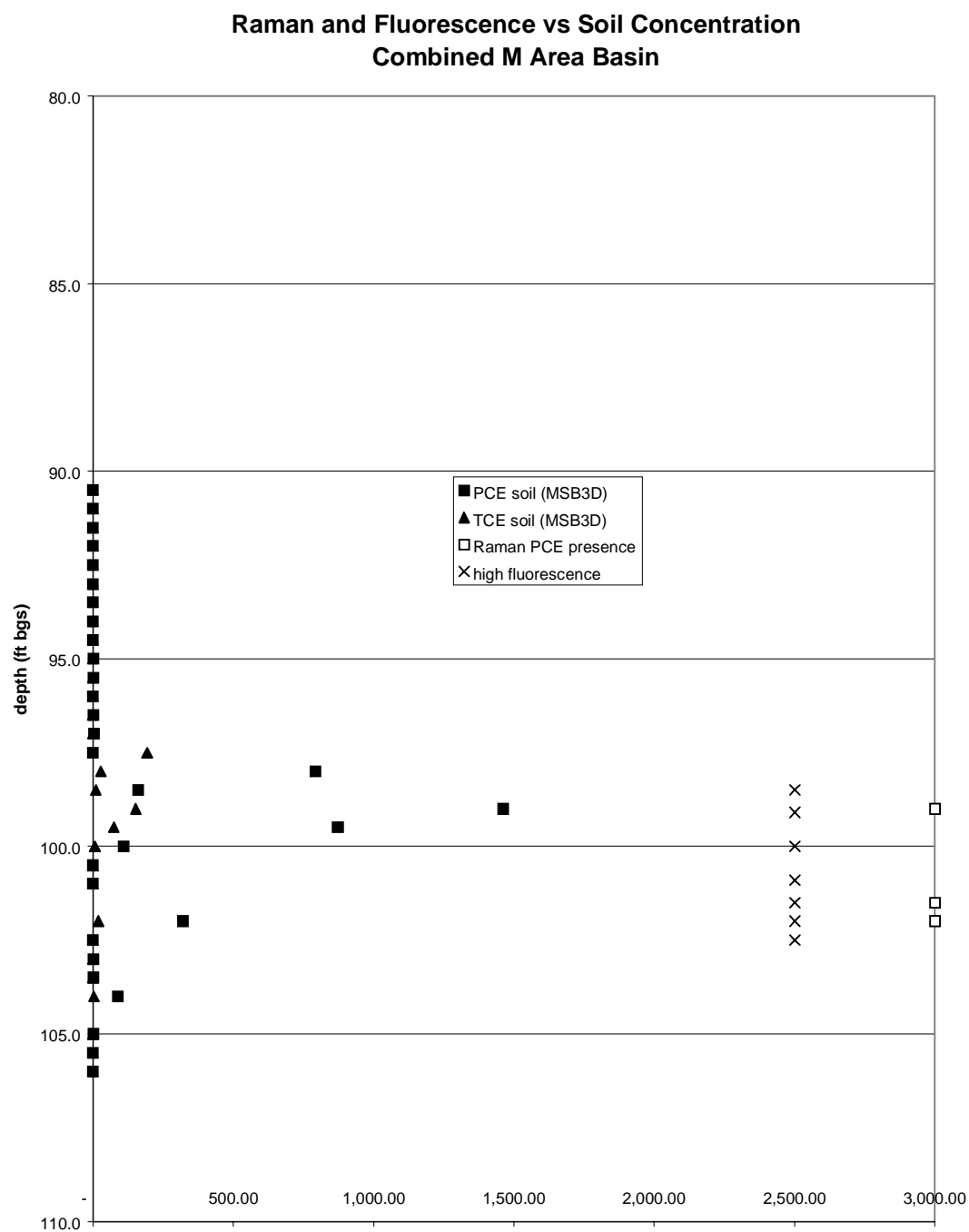


Figure 6. M Area Basin soil core and Raman data for both February and June Raman activities.

CPT-based optical spectroscopy was also performed at the 321 M Solvent Storage Tank. At this site, a 1200 gallon spill of unused solvent occurred in 1985. Because this was a clean solvent spill with no reported release of co-constituents, the fluorescence signal was expected to be weak at this site. Figure 7 shows some of the Raman spectra collected (RMA-5). In this figure, clear Raman peaks of PCE are evident at 25.6' and 26.6'. The background fluorescence is relatively low in these plots as expected. The spectra at 24.6' and 27.6' show no PCE Raman peaks and, in fact, exhibit slightly higher fluorescence than the spectra with Raman hits. Upon examination of all of the spectra from this push, this slightly higher fluorescence does not appear to be significant at this time.

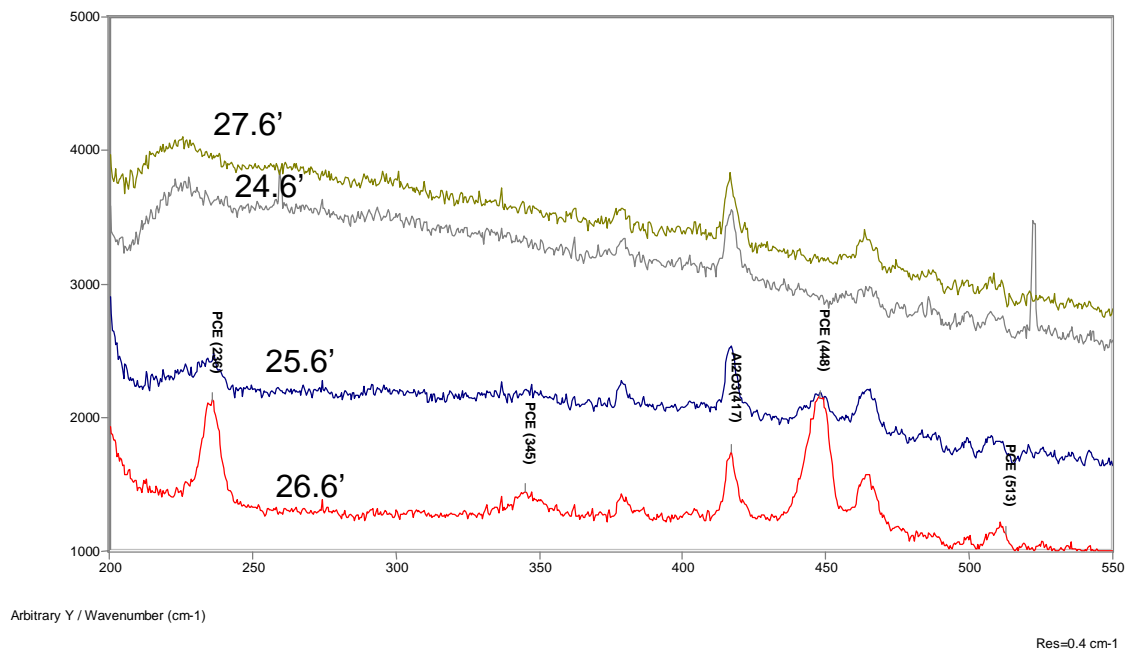


Figure 7. Raman spectra from RMA-5.

The 321 M CPT lithology plots are shown in Figure 8. All pushes conducted at the 321 M Solvent storage tank area required hand augering to a depth of 6 feet before pushing to avoid cutting cables, pipes or other underground interference. In general, the upper 30 feet at this site consist of clayey materials. Variations from this occur near man-made structures where backfilled and compacted sand was used, or occasional occurrences of heterogeneities. For example, a clayey sand layer is seen in this figure between 20 and 23 feet. From 30 feet to 43 feet there is mostly clayey sand with small clean sand intervals at 33', 35', and 38', and a one-foot clay interval at 34'. From 43' to 46' there is clean sand. Upon examination of the CPT lithology plots in Figure 8 and the Raman plots in Figure 7, it is clear that although good portions of the solvents are found in the clays, the sands below the clays contain solvents as well. From this observation we can theorize that the solvents are still descending.

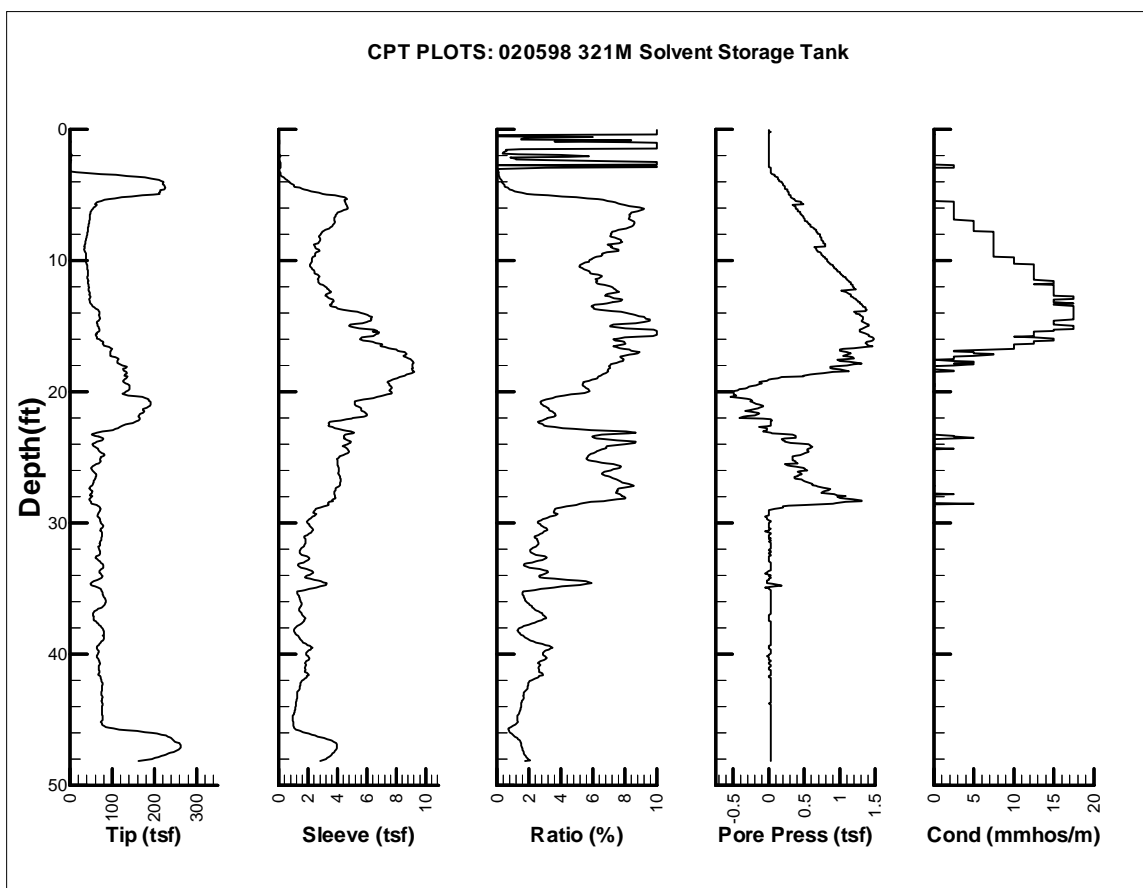


Figure 8. CPT Plot at 321 M Solvent Storage Tank Area

The results from the 321-M Solvent Storage area are shown in Figure 9. Two CPT/Raman pushes were done here within 20 feet of each other. The sediment samples were taken about 15 feet from the second Raman push. Spectra were taken at 3-foot intervals in coarse grain sediments and at 0.5-foot intervals in finer grained sediments until the probe was retrieved at a depth of 40 feet. The data collected in February indicated PCE at depths 25.6 and 26.6 feet, which correspond to the geophysical logging of a finer grained layer from 23-28 feet. The spectra with DNAPL peaks did not show higher background fluorescence, which can be explained by the lack of co-constituents in the DNAPL at this site.

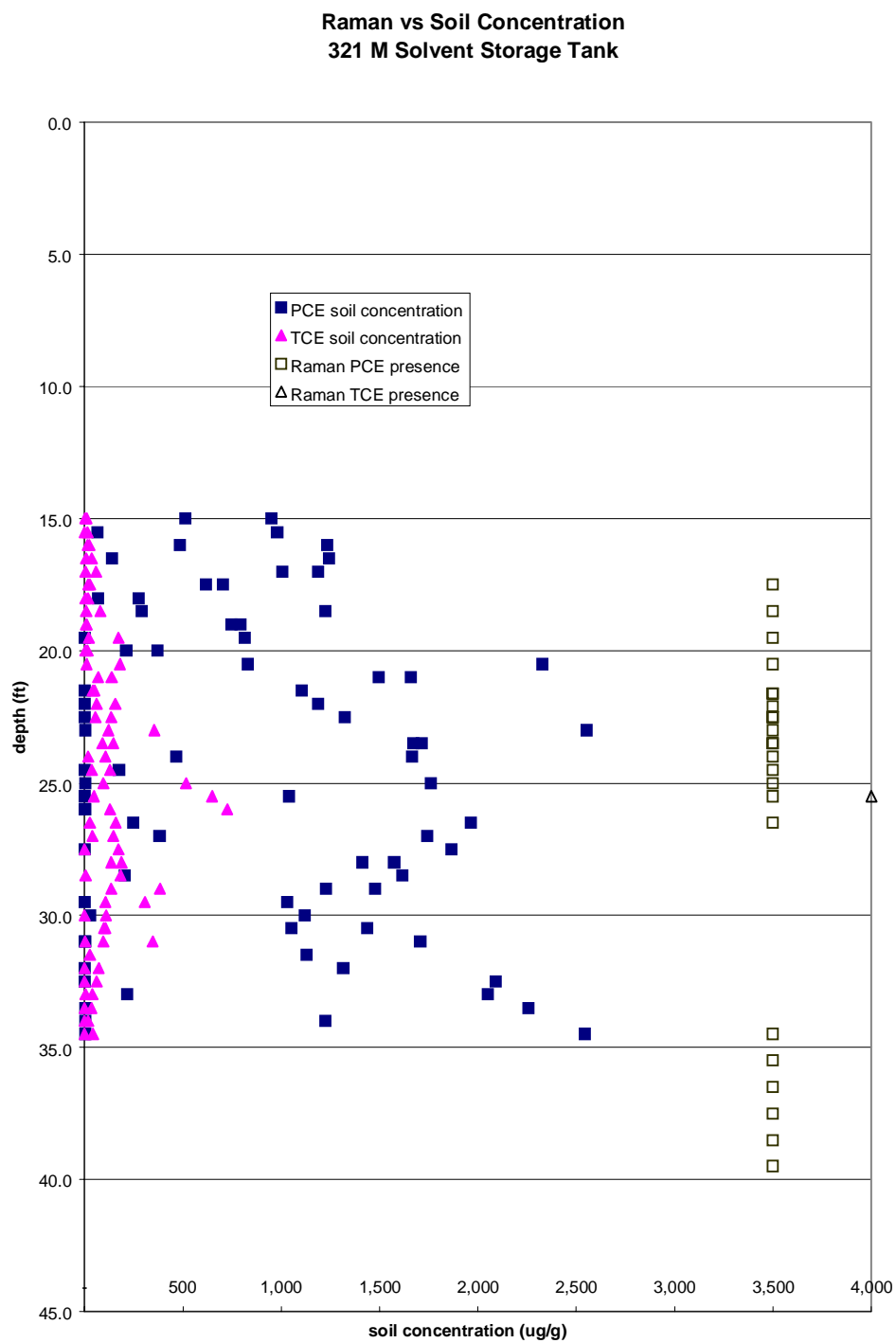


Figure 9. 321 M Solvent Storage Tank Area soil core and Raman data.

Depicted in data from the first June push at the 321-M Area, the Raman spectra indicated the presence of PCE at depths of approximately 21-28 feet, which corresponds to a fine grain layer, and 34-40 feet, which corresponds to a coarse grain layer. The presence of TCE was detected at 27.5 feet, which is just below a fine grain layer and is the depth with the highest soil concentration found in sampling. The second push showed spectral evidence of PCE from 17-23 feet, which corresponds to a fine grain layer from 17-20 feet and a coarse layer from 20-23 feet. Sediment sampling began at 15 feet and concluded at 35 feet, which explains why there is no soil concentration data to confirm the detection of DNAPL by the Raman probe from 35-40 feet.

Figure 10 depicts a vertical sequence of Raman plots with varying degrees of PCE peak intensities. The trace, taken with a ten second integration time at a depth of 17.5', does not indicate the presence of PCE. When integrated for 60 seconds, however, PCE is clearly evident in the spectrum as shown in Figure 11. Of course longer integration times produce longer and more expensive characterization pushes. Although for most characterizations a one or two minute pause for a measurement is acceptable, a balance must be struck between desired sensitivity and characterization cost. Many times the cost can be offset by intelligent selection of measurement intervals.

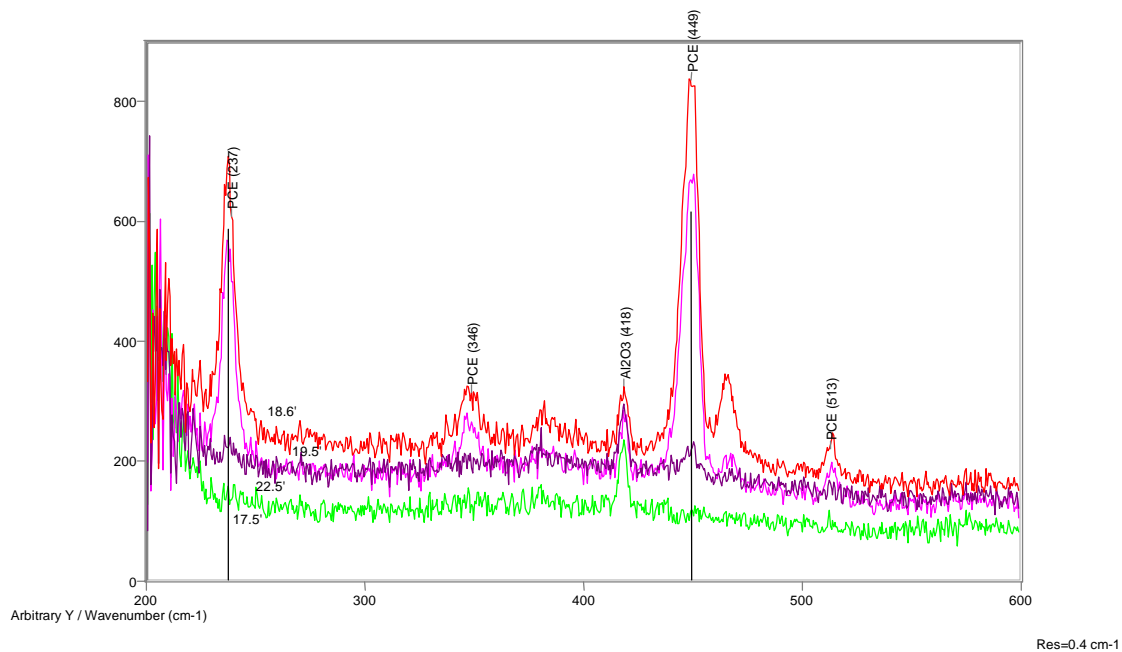


Figure 10. Raman spectra (RMA-5).

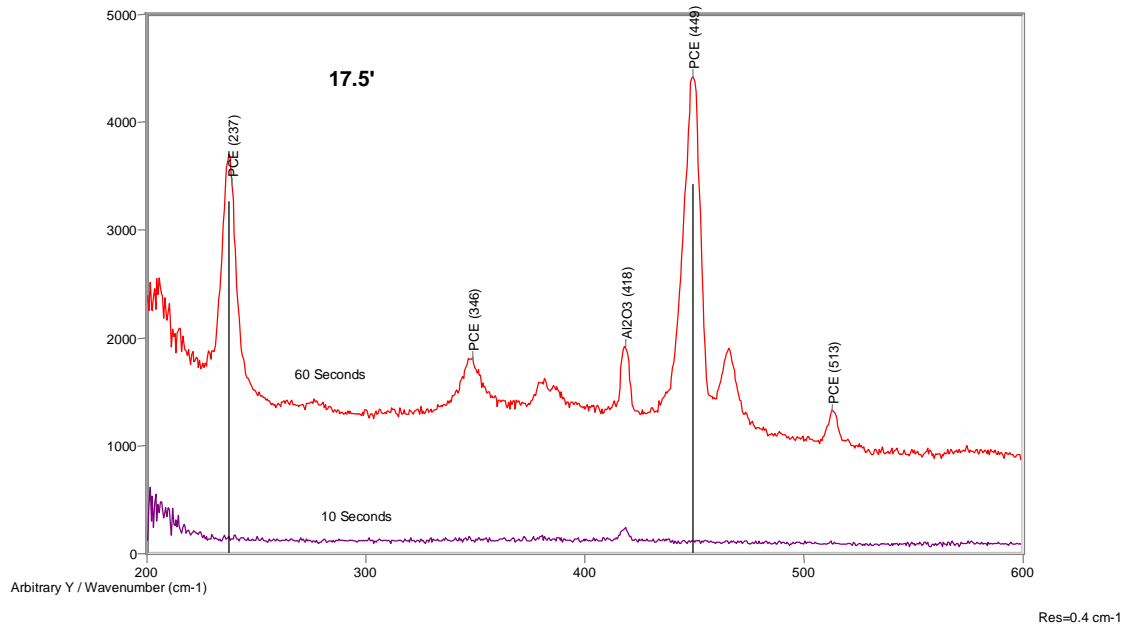


Figure 11. Raman spectra with 10 and 60 second integration times (RMA-5).

Conclusions

CPT-based Raman spectroscopy positively identified DNAPL at the M Area Seepage Basin and at the 321-M Area Solvent Storage Tanks. The very high signal to noise ratio of characteristic peaks for PCE are compelling evidence that the technique can see contaminants in the subsurface. The spectral data correspond well with the soil concentration data. Figure 6 from the M-Area Seepage Basin shows good agreement and successful detection of the thin layer of DNAPL contaminated clay. In both the M Area Basin and the 321 M Solvent Storage Tank areas, each DNAPL detection by the Raman probe was confirmed by presence of DNAPL through laboratory analysis of sediment samples.

Some concern arises over the areas of contamination that were not detected by the Raman technology. In Figure 9 from the 321-M Area, there is some disagreement between the soil and Raman data from 15-21 feet. Soil concentrations were high from 15-21 feet, but the spectral analyses did not show evidence of DNAPL peaks. One explanation for this could be the heterogeneities found in these sediments and very small droplets of DNAPL residing in clay lenses of varying depths and thicknesses. The Raman technique may require a threshold of DNAPL to provide an adequate optical cross-section for spectroscopic response. It is also probable that the technique requires a separate phase liquid rather than an aqueous solution for adequate response.

Similar to CPT-based laser induced fluorescence techniques, the detection limit of the technique is strongly correlated to the probability of contaminant droplets appearing on the optical window. This is related to the amount of contaminant in the sediments, the types of sediments, and other factors such as soil moisture content of the sediments and degree of heterogeneity. DNAPL droplets may be squeezed out of a formation and onto or away from the optical window, depending on all of these factors. It is very important to synthesize the spectroscopic characterization plan with an understanding of the subsurface geology obtained both prior to and concurrent with the spectroscopy.

Spectral integration times are important for determining the detection limits of the technique. Generally, spectra were taken for 10 seconds. If peaks were seen or there was suspicion of DNAPL, a longer spectrum was taken. There were instances when the only suspicion of DNAPL came from prior experience and testing, and knowledge of the geology, not from spectral evidence. In such cases, longer spectra were taken which often showed distinct DNAPL peaks. The danger of missing a DNAPL hit must be balanced with expense of pausing to acquire a spectrum with a longer integration time and better signal to noise ratio or lower detection limit. Some experience with, and refinement of, the technique may suggest the appropriate integration time for adequate detection capabilities.

The Raman spectroscopic activities conducted in these tests represents the first in situ direct measurement of DNAPL in the subsurface. The Raman technique offers one of the very few viable DNAPL characterization techniques to date.

References

- Carrabba, M. M., J. W. Haas, K. M. Spencer, R. W. Forney, T. M. Johnston, and J. M. Sylvia (1998), *Field Raman Spectrograph for Environmental Analysis, Final Report under Contract DE-AC21-92MC29108, Federal Energy Technology Center, Morgantown, WV.*
- Carrabba, M. M, K. M. Spencer, R. B. Edmonds, R. D. Rauh (1992), and J. W. Haas, Spectroelectrochemical technologies and instrumentation for environmental and process monitoring, *SPIE Proceedings vol 1637, Environmental and Process Monitoring Technologies.*
- Carrabba, M. M, L. S. Robblee, and R. D. Rauh (1990), *The prospect of utilizing surface enhanced Raman spectroscopy (SERS) for bio- and biomedical sensing*, SPIE Proceedings vol 1201, Optical Fibers in Medicine V, 14-19 January, Los Angeles, CA.
- Colthup, N. B., L. H. Daly, and S. E. Wiberley (1990), *Introduction to Infrared and Raman Spectroscopy*, 3rd ed., Academic Press, San Diego.

Case Study: In-Situ Bioremediation of TCE at Savannah River:

Numerical Modeling

Bryan J. Travis, Los Alamos National Laboratory, Los Alamos, NM

Nina D. Rosenberg, Lawrence Livermore National Laboratory, Livermore, CA

Introduction

Contamination of groundwater and vadose zone soils with chlorinated solvents such as trichloroethylene (TCE) is a major national problem. A very promising cleanup technology is in situ bioremediation, the use of microbes to convert hazardous chemicals to environmentally benign products such as water, carbon dioxide, biomass, and salts (Thomas and Ward, 1989). Because bioremediation relies on auto-catalytic processes that occur naturally in the environment, its use has great advantages in terms of cost, safety and effectiveness over other in situ destruction techniques which require conditions more difficult to achieve in situ. However, in situ bioremediation involves complex biochemical reactions by microbes, frequently in a heterogeneous geologic setting. Further, soil microbial species exist not as isolated groups, but as part of a microbial ecosystem, competing with some species for food, cooperating with other species, and suffering predation by still others. These factors must be considered when designing an efficient in situ bioremediation operation. Methanotrophs have been shown capable of co-metabolizing TCE, when stimulated with methane (Roberts et al, 1990). Soil heterogeneity has been recognized as a factor that can reduce the effectiveness of field implementation vis a vis laboratory results (e.g., Schafer & Kinzelbach, 1992), but little attention has been given to the impact of microbial species interactions. A subtask of the case study described below estimated the impact of one form of microbial interactions, predation, on in situ bioremediation efficiency.

A field demonstration of an in situ bioremediation technology was performed at the U.S. Department of Energy's Savannah River Site in 1992-1993 (Hazen, 1992a, 1992b). The technology employed a novel combination of injection of air, methane, N_2O and $TEPO_4$ (triethyl phosphate) below the water table and vacuum extraction in the vadose zone, using a pair of subparallel horizontal wells (Brockman et al., 1995). The object was to stimulate aerobic in situ bioremediation of TCE contamination in the vadose zone and the saturated zone by certain methanotrophs, i.e., methane-oxidizing bacteria which are capable of fortuitously co-metabolizing TCE under various conditions. TCE contamination occurred from the 1950s into the 1980s from a leaking process sewer line. Extensive geologic, hydrologic and microbiological sampling of the area provided a three-dimensional picture of the distribution of TCE and of various microbial species, including methanotrophs, before and during field operations.

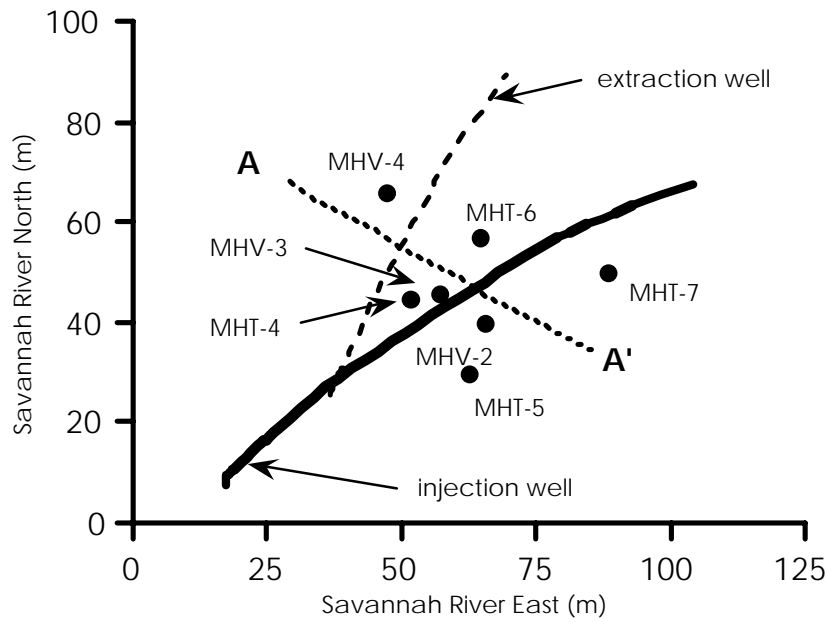
Numerical modeling supplemented engineering design and field operations. Modeling goals were (1) to demonstrate an ability to model changes in the methanotrophic populations and TCE concentration in partially saturated, heterogeneous media under the variety of stimulation strategies used in the Savannah River field demonstration and (2) to examine the sensitivities of TCE degradation to key model parameters, such as protozoan grazing. Mathematical models are valuable because they provide a mechanism for combining the various kinds of data we have on a site, from hydrologic and geologic data to microbiological information, into a dynamic system, subject to the constraints of physical laws such as conservation of mass and energy. Consistency

of data, interactions between processes, sensitivity analysis, interpretation of data, parameter estimation and field operation design are all common uses of models. A calibrated model can provide estimates of the temporal and spatial distribution of concentrations, pressures and saturations everywhere in the subsurface region, and can be used to determine other important quantities which are hard to measure, such as total biodegradation of TCE. The Savannah River modeling study (Travis & Rosenberg, 1997) differs from previous modeling studies (see Sturman et al., 1995, for a review) in that it includes both the vadose and groundwater zones, unsteady air and water flow, limited nutrients and airborne nutrients, in addition to toxicity, co-metabolic kinetics, predator grazing and kinetic sorption. Previous models have focused almost exclusively on steady saturated flow with water-borne delivery of nutrients or with nutrients in excess. None have considered predator grazing of microbes.

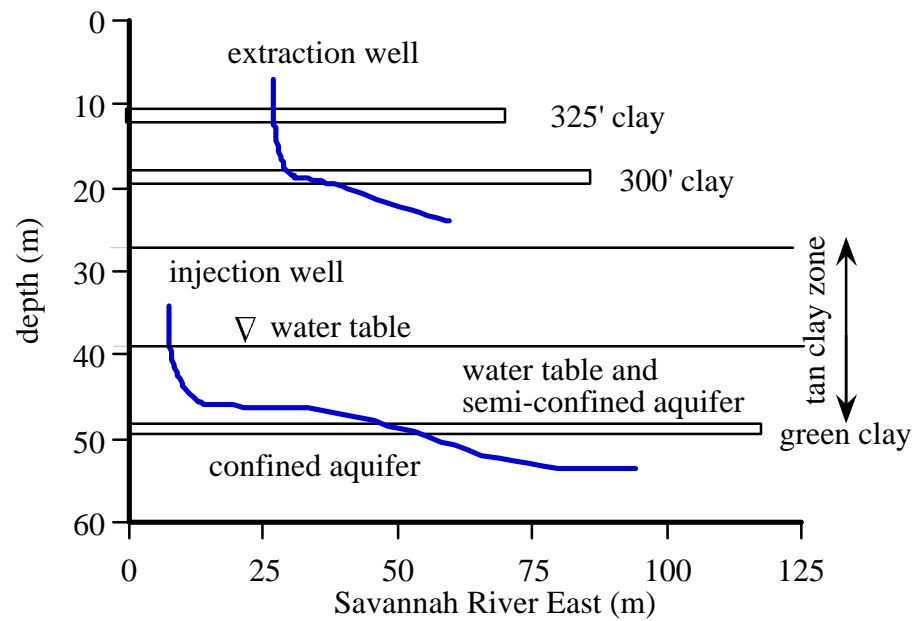
Setting

The Savannah River Site is underlain by sediments of the Atlantic Coastal Plain. The upper section of these sediments consist of interbedded sands and clays that were deposited in shallow marine, lagoonal and fluvial environments. These sediments are heterogeneous, varying greatly in thickness and continuity across the site. A generalized description includes a sand unit, four major clay units, and a water table which lies about 40 m below the surface (Eddy et al., 1991). Sediments samples taken before the field demonstration show the distribution of TCE at the site to have been very uneven, generally concentrated in clay zones. The in situ bioremediation demonstration began in late February 1992, lasted 428 days and consisted of seven injection/extraction phases. Details are given in Hazen (1992a, 1992b).

A plan view schematic of the target site is given in Figure 1-a, showing the paths followed by the horizontal wells, the location of several sampling wells, and the orientation of the cross-section A' - A used in the model study. A 2-D vertical cross-section domain approximately perpendicular to the direction of the horizontal wells and passing near well MHT-4 was used for the computational model domain. This region exhibited the greatest activity during the field demonstration, in terms of methanotroph population changes and TCE mineralization. The schematic of Figure 1-b presents a vertical section of the target area (in a direction perpendicular to A-A'), indicating the approximate depths, thicknesses and extent of the various soil layers, and the water table, and indicating the subhorizontal path of the injection and extraction wells.



(a)



(b)

Figure 1. Generalized hydrogeology and location of horizontal wells: (a) map view and (b) cross-section along the axis of wells. A-A' represents 2D cross-section used for model domain.

The model domain (Figure 2) includes the top 60 m of the subsurface and is 300 m in horizontal extent. The 300 m horizontal extent minimized the loss of methane from the model domain due to horizontal air flow. The simulation includes the seven injection/extraction phases given in Table 1. Travis and Rosenberg (1997) gives a more detailed account of the modeling analysis of the Savannah River bioremediation demonstration. Travis (1998) provides details of the numerical model used.

Table 1. Injection/Extraction Schedule

Phase	Begin (day)	Extraction (scfm)	Injection (scfm)
1	1	240	no injection
2	21	240	200 - air only
3	56	240	200 - air, 1% CH ₄ by volume
4	161	240	200 - air, 4% CH ₄ by volume
5	238	240	200 - air only, 2% & 4% pulse CH ₄ - 1 week each
6	302	240	200 - air only; 4% CH ₄ by volume 8 hrs per 48 hr cycle
7	336	240	200 - air only; 4% CH ₄ , 0.07% N ₂ O, 0.007% TEPO ₄ by volume 8 hrs per 48 hr cycle

scfm=standard cubic feet per minute

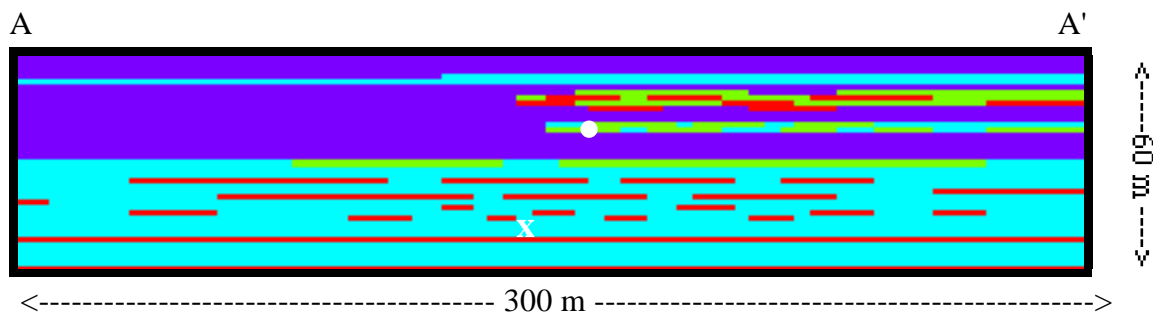


Figure 2. Model domain. The colors represent different hydrologic units: purple = sand, blue = tan clay, green = sandy clay and red = clay. X = injection well; * = extraction well.

A distinctive feature of the field demonstration at Savannah River was the use of airborne delivery of growth substrate and nutrients. An advantage in comparison to water-borne delivery is that nutrients will be distributed to greater distances through the air phase. Pulsing of nutrient injection was conducted in the latter stages of the field operation. Under water-saturated conditions, pulsing of methane can be very effective (e.g., Lang, 1995). Pulsing recognizes that competitive inhibition favors TCE degradation in the absence of growth substrate. The diffusivity of methane is very small in water, so pulses of methane will remain separated spatially in the formation, allowing the pulsing strategy to work well. Methane diffusivity in the air phase, however, is about 1,000-10,000 times larger than in the water-saturated case. In the vadose zone, this method is therefore less effective at the same pulsing rates, but nevertheless can have a beneficial effect.

Microbiological considerations

Microbiological assays at the site (Pfiffner et al., 1996) indicate that growth of the indigenous methanotroph population correlates with degradation of TCE. Methanotrophs can be divided into two types, based on the form of MMO (methane mono-oxygenase) they can express. Both types can express pMMO, the particulate, membrane bound form, which is relatively ineffective for TCE degradation. Only type II can express sMMO, the soluble form which is very effective at degrading TCE. Graham et al (1993) determined conditions favoring type II methanotrophs. Abundant evidence indicates that type II methanotrophs were the dominant methanotrophic strain at the site. PLFA assays from site groundwater isolates (Pfiffner et al, 1996) indicated that the PLFA marker 18:1w8c (a type II marker) was a major membrane PLFA and all the PLFA profiles resembled that of pure culture type II (Bowman et al, 1993). Tests specific for sMMO activity (PCR and DNA probes) indicated large increases during methane injection. Further, low Cu^{++} and high O_2 stimulate sMMO and inhibit pMMO expression; both conditions prevailed at the site. All the field data indicate that sMMO was expressed to varying degrees but pMMO was not. The model assumed that only type II methanotrophs expressing sMMO were responsible for TCE biodegradation.

An important feature of co-metabolic degradation is that one substrate can inhibit the uptake of the other (e.g., Semprini et al., 1991). MMO is not highly specific; it can also initiate the epoxidation of TCE. However, its affinity for methane is greater than for TCE. If methane is present, the rate of oxidation of TCE by MMO is reduced. Semprini and McCarty (1992) developed a formulation for competitive inhibition of TCE in the presence of methane. The capacity of MMO to degrade TCE is limited due to general protein damage from activity of TCE epoxides. Chang and Alvarez-Cohen (1995) determined the toxicity of TCE degradation products to methanotrophs. Nutrients (nitrate and phosphate) are needed to make protein and cell wall components. Field data at the site indicate that nitrate concentrations decreased approximately linearly throughout the demonstration, at some points by a factor of almost 10, with additional transient decreases occurring when methanotroph counts were rapidly rising, and rebounds when methanotroph counts diminished. It was assumed that nitrate was the limiting nutrient (Pfiffner et al, 1996).

Another process that can limit the effectiveness of bioremediation is protozoan grazing of bacteria. Protozoan predators include amoebae and various flagellates, and are observed in many

soils at significant numbers (10^3 to 10^5 /g dry soil weight). Predator-prey microbial processes have been studied for many years (e.g., van den Ende, 1973; Sinclair and Alexander, 1989; Recorbet, Steinberg, and Faurie, 1992). Several kinds of predation have been observed in soil systems (Casida, 1988). Factors that affect the extent and rate of predation include microbe concentrations and growth rates, availability of nutrients, water content (for unsaturated conditions), clay content and the manner in which bacteria are distributed on and in microscopic soil particle aggregates (see, e.g., England, Lee and Trevors, 1993). Protozoan increase in response to bacterial growth on hydrocarbon contamination has been documented recently (Sinclair et al, 1993). However, it appears there are no published measurements at sites contaminated with chlorinated hydrocarbons, although laboratory experiments on samples from Savannah River did show the presence of protozoa that would graze readily on methanotrophs. Menon et al (1996) have shown that protozoan predation of bacteria follows Monod kinetics.

Bioremediation Results

TCE Degradation

The total amounts of TCE vacuum-extracted and biodegraded in situ in the model simulation were 1867 kg and 730 kg, respectively, for a total TCE removed from the subsurface of 2597 kg. For the case with predators; 28 % of the TCE removed was removed via biodegradation. Without predation, the numbers were 1809 kg and 913 kg, for a total of 2722 kg. In this case, 33 % of the TCE removed was removed via biodegradation. Site data indicate that 2030 kg TCE were vacuum extracted and that anywhere from 230-900 kg of TCE may have been biodegraded in situ (Hazen, 1992b), for a total amount of 2260-2930 kg TCE removed. The model simulations agree well with the field data, especially the case with predation. The amount of TCE removed through in situ bioremediation in the model was 24% higher for the with-predators case, and 30% higher without predator grazing—a significant enhancement of the removal rate of TCE as compared to the non-biological methods alone. Figure 3 plots the domain-wide integrated mass of TCE vacuum-extracted and biodegraded as a function of time. This plot indicates that most of the TCE biodegradation occurred during the 4% methane phase, with additional degradation occurring during the nitrogen plus phosphate addition phase.

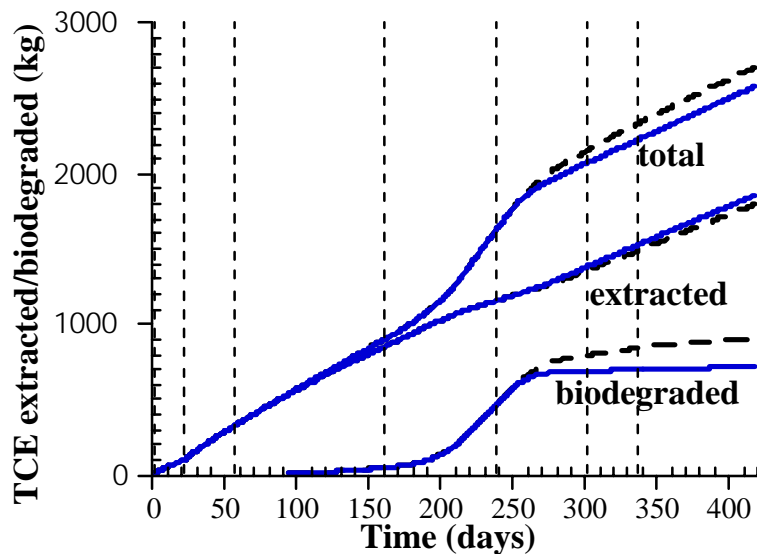


Figure 3 TCE extracted/biodegraded vs. time for in situ bioremediation simulation. Vertical dashed lines indicate the different injection phases. The dashed curves correspond to the no-predation case, the solid lines to the with-predation case.

Spatial Distributions

Numerical simulators can estimate the evolution of conditions throughout the subsurface domain, and these can be displayed graphically, providing a picture of the spatial distribution of conditions, as well as pointwise sampling typical of field data.

Throughout the demonstration, according to the model, there was a gradual reduction of TCE throughout the domain, except in the clays. The clays near the injection well, however, were desaturated by the injected air pressure (~ 1 atm overpressure) to a sufficient degree to allow removal of TCE. By the end of the field demonstration (428 days), the central region, between the injection and extraction wells, about 100 m wide and 20 m thick, was remediated to low levels. The injected air depressed the water table in the vicinity of the injection well, producing a considerably larger unsaturated zone than existed initially. The contaminated region at the bottom of the model domain was not remediated because injected air could not reach that area and diffusion of substrates through the water phase is too slow; a hard clay layer lies about 3 m below the injection well and blocks most downward air flow. The pervasive clay layers were effective at greatly reducing vertical flow while enhancing lateral flow of injected air, methane and nutrients. Microbial and protozoan populations varied spatially and temporally. Methanotroph populations reflected the distribution of methane and nutrients, while protozoan growth was episodic, growing rapidly where and when methanotroph populations became large, but decaying rapidly as well. For more details, the reader is directed to Travis and Rosenberg (1997).

Sensitivity Analysis

Sensitivity of the enhanced removal of TCE due to methanotroph catabolism was determined through a series of simulations in which biokinetic parameters of the system were varied one at a time. The parameters varied were: k_{CH4} , K_{CH4} , K_N , k_{TCE} , K_{TCE} , I_{CH4} , TC , and k_{MP} . Sensitivity was defined as:

$$\left(\frac{\Delta TCE - \Delta TCE_{base}}{\Delta TCE_{base}} \right) \left(\frac{X_{base}}{X - X_{base}} \right)$$

where X is a biokinetic parameter, ΔTCE is the total TCE removed by vacuum-extraction and biodegradation minus the total TCE extracted when biokinetics is not operating, and the subscript "base" refers to the simulation of the Savannah River site with protozoan grazing. Resulting sensitivities are listed in Table 2. The first row of numbers are the sensitivities as defined above. The second row of numbers are the sensitivities for biodegradation only (vapor extraction differences neglected). These results are site specific since the amount of TCE removed is a function of the injection/extraction strategy, the site hydrogeology, and the initial distribution of TCE. However, the relative rankings of the sensitivities are likely more site independent.

Table 2. Sensitivities of TCE removal to key parameters

Parameter	k_{CH4}	K_{CH4}	K_N	k_{TCE}	K_{TCE}	I_{CH4}	TC	k_{MP}
<u>Sensitivity</u>	1.86	-1.00	-0.42	-1.20	0.06	-0.004	-1.43	-0.24
	1.83	-0.94	-0.45	-1.08	0.07	-0.008	-1.30	-0.27

Conclusions that can be drawn from this sensitivity analysis are:

- (1) That TCE degradation is strongly sensitive to the factors controlling the rate at which microbes can grow (e.g., k_{CH4} , K_{CH4} , K_N)
- (2) Toxicity is also quite important. There is a strong sensitivity to k_{TCE} , the maximum utilization rate for TCE, but it is a negative correlation because TCE degradation products are toxic to methanotrophs. The faster TCE is degraded, the more toxic products are created and the more microbes are killed. These results imply that using bacteria that are not damaged by TCE, or that can even utilize TCE for energy, will be much more effective than simply using bacteria with higher growth rates.
- (3) Sensitivity to predators, k_{MP} , although significant, was not as strong as to toxicity. It is important to remember that our model is nonlinear, and so these sensitivities only apply to a limited part of the parameter space.

Discussion

The degree of agreement between model and field results at Savannah River indicates the utility of a model coupling transport and microbial processes. However, there are several factors that limit the general use of such models. First, knowledge of the microbial processes is incomplete, and the various rate coefficients used in the model are surely only approximately correct. Invariably some parameter fitting is required for field application as is the case here. Not everything has been measured in the lab, and even if it were, it wouldn't necessarily apply in the field. Differences in bacterial strains, and competition between bacterial populations, will prevent an exact analysis. For example, methane utilization rate can increase over time as bacteria apparently adapt (e.g., Semprini & McCarty, 1991). Another important factor is soil heterogeneity. The Savannah River model captured reasonably well the larger scale soil variations, but small scale heterogeneity can lead to additional channeling (see, e.g., Ji et al, 1993). Channeling could result in methane concentrations being lower at some points than expected.

Our model has included a novel feature in these kinds of models, i.e., protozoan grazing. This feature provided a distinctly better match to the variability in microbe counts vs. time seen in the field data, and brought the computed amount of TCE degraded to within the independently determined bounds. While it has been observed that protozoan grazing of bacteria occurs in many situations, both in aquatic systems and in hydrocarbon-contaminated soils, (and the present model can simulate the latter case reasonably well), there have been few if any attempts to measure predation of methanotrophs in soils contaminated with chlorinated hydrocarbons, and only very recently has attention begun to turn to protozoa at other contaminated sites.

The model results indicate that predator grazing could reduce the amount of TCE degraded by about 20-25%, a significant factor. This adverse affect on the rate of biodegradation will lead to underestimation of clean-up times if predator grazing is not considered at other sites.

The total amount of TCE biodegraded according to the model represents about a 25% enhancement over vacuum extraction only. This would doubtless have been much higher if the injected nutrients and growth substrate had spread farther. The model indicated that most of the enhanced microbial growth occurred in the region between the wells where much of the TCE had already been extracted or degraded before nutrients were added. The model also indicated that the nutrients were in fact widely distributed; it was the lack of methane that prevented a wider field of action for the methanotrophs. Microbes near the injection well consumed most of the methane.

A number of other bacterial species were measured in site soil samples. These included several nitrate/nitrite utilizers/transformers, whose population densities also responded to the air + methane + nutrient injection campaign. A more comprehensive model is needed, which includes other active, competing and cooperating microbe families. In addition, in order to provide the data needed for a more complete model, more attention must be given to monitoring the presence of other microbial species that will interact with the contaminant-degrading species.

References

- Bowman, J.P., L. Jimenez, I. Rosario, T.C. Hazen, and G.S. Sayler, 1993. Characterization of the methanotrophic bacterial community present in a trichloroethylene-contaminated subsurface groundwater site. *Appl. Environ. Microbiol.* 59: 2380-2387.
- Brockman, F. J., W. Payne, D. J. Workman, A. Soong, S. Manley and T. C. Hazen, 1995. Effect of gaseous nitrogen and phosphorus injection on in situ bioremediation of a trichloroethylene-contaminated site, *Journal of Hazardous Materials* 41: 287-298.
- Casida, L.E., 1988. Minireview: Nonobligate Bacterial Predation of Bacteria in Soil, *Microb.Ecol.* 15, 1-8.
- Chang, H. L. and L. Alvarez-Cohen (1995), Model for the cometabolic biodegradation of chlorinated organics, *Environmental Science and Technology* 29: 2357-2367.
- Eddy, C. A., B. B. Looney, J. M. Dougherty, T. C. Hazen and D. S. Kaback, 1991. Characterization of the Geology, Geochemistry, Hydrology and Microbiology of the In Situ Air Stripping Demonstration Site at the Savannah River Site, Westinghouse Savannah River Company report WSRC-RD-91-21.
- England, L. S., H. Lee, and J. T. Trevors, 1993. Bacterial Survival in Soil: Effect of Clays and Protozoa, *Soil Biol. Biochem.*, 25: 525-531.
- Graham, D.W., J.A. Chaudhary, R.S. Hanson, and R.G. Arnold, 1993. Factors Affecting Competition Between Type I and Type II Methanotrophs in Two-organism, Continuous-flow Reactors, *Microb. Ecol.*, 25: 1-17.
- Hazen, T. C., 1992a. Test Plan for In Situ Bioremediation Demonstration of the Savannah River Integrated Project DOE/OTD TTP No. SR 0566-01, Westinghouse Savannah River Company report WSRC-RD-91-23.
- Hazen, T. C., 1992b. Data for In Situ Bioremediation Demonstration of Savannah River Integrated Demonstration Project DOE/OTD, Westinghouse Savannah River Company report October 26, 1993.
- Ji, W., A. Dahmani, D.P. Ahlfeld, J.D. Lin, and E. Hill, III, 1993. Laboratory study of air sparging: air flow visualization, *Groundwater Monitoring & Review*, 13: 115-126.
- Lang, M. M. 1995. Design and optimization of in situ bioremediation systems relying on cometabolic degradation, Ph.D. dissertation, Stanford University, 183 pages.
- Menon, P., S. Becquevort, G. Billen and P. Servais, 1996. Kinetics of Flagellate Grazing in the Presence of Two Types of Bacterial Prey, *Microb. Ecol.*, 31: 89-101.
- Pfiffner, S. M., A. V. Palumbo, T. J. Phelps, D. B. Ringelberg, D. C. White and T. C. Hazen, Microbial monitoring as a measure of success for in situ TCE bioremediation, submitted to *Environmental Science and Technology*.
- Recorbet, G., C. Steinberg and G. Faurie, 1992. Survival in soil of genetically engineered *Escherichia coli* as related to inoculum density, predation and competition, *Microbiology Ecology* 101: 251-260.
- Roberts, P. V., G. D. Hopkins, D. M. Mackay, and L. Semprini, 1990. A Field Evaluation of In-Situ Biodegradation of Chlorinated Ethenes: Part 1, Methodology and Field Site Characterization, *Groundwater* 28: 591-604.
- Schafer, W., and Kinzelbach, W., 1992. Stochastic modeling of in situ bioremediation in heterogeneous aquifers, *J. Contam. Hydro.*, 10: 47-73.
- Semprini, L., and McCarty, P. L., 1992. Comparison Between Model Simulations and Field Results for In Situ Bioremediation of Chlorinated Aliphatics: Part 2. Cometabolic transformations, *Groundwater* 30: 37-44.

- Semprini, L., G. D. Hopkins, P. V. Roberts, D. Grbic-Galic, and P. L. McCarty, 1991. A Field Evaluation of In-Situ Biodegradation of Chlorinated Ethenes: Part 3. Studies of Competitive Inhibition, *Groundwater* 29: 239-250.
- Sinclair, J.L., and M. Alexander, 1989. Effect of protozoan predation on relative abundance of fast- and slow-growing bacteria. *Can. J. Microbiol.* 35: 578-582.
- Sinclair, J.L., D.H. Kampbell, M.L. Cook and J.T. Wilson, 1993. Protozoa in Subsurface Sediments from Sites Contaminated with Aviation Gasoline or Jet Fuel, *Applied & Environ. Microbiology*, 59: 467-472.
- Sturman, P. J., P. S. Stewart, A. B. Cunningham, E. J. Bouwer, and J. H. Wolfram, 1995. Engineering scale-up of in situ bioremediation processes: a review, *Journal of Contaminant Hydrology* 19: 171-203.
- Thomas, J. M. and C. H. Ward, 1989. In situ bioremediation of organic contaminants in the subsurface, *Environmental Science and Technology* 23: 760-766.
- Travis, B. J., and Rosenberg, N. D., 1997. Modeling In Situ Bioremediation of TCE at Savannah River: Effects of Product Toxicity and Microbial Interactions on TCE Degradation, *Environ. Sci. & Tech*, 31: 3093-3102.
- Travis, B.J., 1998. Numerical Simulation of In Situ Bioremediation. *Computational Methods in Water Resources* XII: 91-98.
- Van den Ende, P., 1973. Predator-prey interactions in continuous culture, *Science* 181: 562-564.

Acknowledgements - This research was funded by the Office of Technology Development, within the Department of Energy's Office of Environmental Management, under the Non-arid Soils Volatile Organic Compounds Integrated Demonstration.

Excerpt from:

**Dumping Pump and Treat:
Rapid Cleanups Using Thermal Technology**

Robin L. Newmark and Roger D. Aines
Lawrence Livermore National Laboratory

Why Use Heat?

The rationale behind using heat to speed groundwater cleanup is readily apparent; just as any of the more familiar cleaning tasks are accomplished more rapidly with hot water, the use of steam or electrical heating can dramatically increase the rate of soil and groundwater cleanup. Thermal remediation methods are effective due to a variety of factors; increased contaminant volatility, rapid mass transfer, diffusion and evaporation, lower viscosity of water and contaminants, decreased sorption, boiling of the formation, and overall increase in the speed of chemical reactions. Lawrence Livermore National Laboratory collaborated with the University of California at Berkeley (UCB) College of Engineering in the development and demonstration of thermal methods for the rapid cleanup of underground volatile contaminants. We developed a set of methods that can be used over a period of six months to one year to complete the cleanup of sites that routinely take decades to clean today. The Department of Energy's Office of Environmental Restoration and Waste Management sponsored a full-scale demonstration of this technique at the LLNL gasoline spill site. The most significant aspect of this work has been to demonstrate that these methods can be used safely, effectively, and that they can achieve the desired result (site closure and de-listing) in a short period of time. The focus of our effort has been in replacing pump-and-treat technology.

Dynamic Underground Stripping: A Worked Example

LLNL recently completed the cleanup and closure of a moderate-sized spill site in which thermal cleanup methods, and the associated control technologies, were used to remediate

over 10,000 gallons of gasoline trapped twenty feet below the standing water table (Newmark, 1992, 1994a). The spill originated from a group of four underground tanks, from which an estimated 17,000 gallons of gasoline leaked sometime between 1952 and 1979. The gasoline penetrated the soil, eventually reaching the water table, where it spread out. Subsequent rise in the water table due to changes in agricultural water use trapped considerable free product below the water table. Previous characterization results were combined with an extensive set of measurements taken during our installation of 22 process and monitoring boreholes to estimate that 6200 gallons of gasoline were present (both above and below the water table) within our target treatment area (Figure 1). Gasoline trapped up to 30 ft below the water table was there due to a rise in the water table after the spill occurred, with the gasoline held below water by capillary forces in the soil. Groundwater contamination extended about 200 m beyond the central spill area (Figure 2). The soils at the site are alluvial, ranging from very fine silt/clay layers to extremely coarse gravels, with unit permeabilities ranging over several orders of magnitude. There are two principal permeable zones, one above and one below the water table. The site was prepared for long-term groundwater pump-and-treat with vapor extraction; recovery rates prior to thermal treatment were about 2.5 gal/day (Figure 3).

The targeted volume was intended to include all of the free-phase gasoline at the site. Its shape is that of a distorted cylinder about 120 ft. in diameter and 80 ft high, extending from a depth of 60 ft to a depth of 140 ft. The water table is located at 100 ft. Later results indicated that two small areas of gasoline probably existed outside the treatment area, possibly from separate spills. Six steam injection/electric heating wells were placed to surround the free product in an irregular circle determined by the shape of the free product; and three additional electric heating wells were placed near the center of the spill. These were not part of the original design, but were required when the free-product zone was discovered to be larger than anticipated during the drilling of the injection wells. Each injection well was initially center-punched with a small-diameter hole for characterization. The discovery of unexpected free product in two of them had minimal impact; the holes were completed as monitoring locations and new injection wells drilled further from the spill center. Eleven monitoring/imaging wells were placed within and outside the target area to provide control of the heating processes. In an operational period of 1 year, followed by a monitoring period of

two years, a volume of soil of approximately 100,000 yd³ was cleaned and extraction/treatment operations were terminated. Following removal of more than 99% of the contaminant, and achievement of Maximum Contaminant Limit (MCL) levels in groundwater for five of the six contaminants, the site will now be passively monitored under an agreement with the California Regional Water Quality Control Board (RWQCB), California EPA's Department of Toxic Substances Control (DTSC), and the Federal EPA Region 9. This cleanup was achieved using a group of cleanup methods collectively called Dynamic Underground Stripping.

Results of first full-scale test

The first full-scale test at the LLNL gasoline site was extremely successful. Process results completed in June 1993 indicated that for the removal of contaminant, the process is 50 times as effective as the conventional pump and treat process now being used at 300 designated Superfund Sites, and is 10 times as effective as another enhanced new method (pump and treat with vacuum extraction). During 21 weeks of operation, the technique removed more than 7600 gallons of an estimated 6200 gallons of gasoline trapped in soil both above and below the water table, with separate phase contamination extending to >120 ft deep. The maximum removal rate was 250 gallons of gasoline a day. The process was limited only by the ability to treat the contaminated substance. Actual field experience indicates that the process costs \$65 a cubic yard. Approximately 100,000 yd³ were cleaned.

Dynamic Underground Stripping is based on three technologies

Dynamic Underground Stripping combines two methods to heat the soil, vaporizing trapped contaminants (Figure 4). Permeable layers (e.g., gravels) are amenable to heating by steam injection, and impermeable layers (e.g., clays) can be heated by electric current. These complementary heating techniques are extremely effective for heating heterogeneous soils; in more uniform conditions, only one or the other may be applied. Once vaporized, the contaminants are removed by vacuum extraction. All these processes - from the heating of the soil to the removal of the contaminated vapor - are monitored and guided by underground imaging, which assures effective treatment through *in situ* process control.

Steam Injection and Vacuum Extraction: Injection wells drilled around an area of concentrated contamination are used to supply both steam and electric current. Extraction wells placed near the center of the contamination are used to extract the contaminant. The steam is pumped in through the injection wells and advances in a wall, or front, toward the extraction wells. Concurrently, groundwater is pumped and vapor is extracted from the extraction wells. As the steam front advances, the permeable soils are heated to the boiling point of water (100°C), and volatile organic contaminants are vaporized from the hot soil. After the steam front reaches the extraction wells, steam injection is stopped; vacuum continues to be applied at the extraction wells. The lowered vapor pressure (resulting from the applied vacuum) forces the contaminants to boil and the concentrated contaminant-carrying vapor is then pumped to the surface and treated. When the steam zone collapses, groundwater reenters the treatment zone. The steam injection/vacuum extraction cycle is repeated, and additional contaminants are vaporized and removed.

Electrical Resistance Heating: Electric current is used to heat thick units of impermeable soils. It operates on the same principle that makes a heating coil work - heat builds up in a conductor that resists current flow. For this technique, the clay itself supplies the resistance. In the steam injection wells, electrodes are sunk into the ground. Each electrode supplies several hundred amperes of current at up to 600 V, heating the impermeable clays. Water and contaminants trapped in these (relatively) conductive regions are vaporized and forced into the steam zone for vacuum extraction.

These combined heating processes achieve a hot, dry zone surrounded by cool, damp, untreated areas. Electrical heating and steam injection are applied as long as underground imaging shows that cool (and therefore untreated) regions remain.

Underground Imaging and Process Control: Geophysical techniques are used to monitor the underground movement of steam and the progress of heating, including temperature measurements and electrical resistance tomography. Monitoring the progress of the heating fronts during operations allows the process engineer to ensure that all the soil is treated. If the monitoring indicates a region of cool, contaminated soil, the operational strategy can be altered to treat the offending area. Temperature measurements made in monitoring wells in the treatment area reveal details of the complex heating phenomena in the individual soil layers. Electrical resistance tomography provides near-real-time images of the underground

processes between wells. Because soil electrical properties vary with temperature, soil type and fluid saturation, electrical measurements can map the progress of the steam front and the heated zones. They are also useful for characterizing a given site and for predicting steam pathways.

Initial Operations

The first application of Dynamic Underground Stripping was conducted in three phases. Details of the operations can be found in Newmark et al., (1994). In November and December 1992, the electrical heating system operated at a maximum power of 800 kW, pre-heating the target volume clay layers in some areas to temperatures exceeding 70° C. Steam injection began in early February, 1993. The first steam pass lasted approximately 5 weeks, during which time steam penetrated permeable soils, and about 6500 liters of gasoline were recovered (Figures 5 and 6). The second steam pass, of about six weeks duration, was conducted in a huff and puff mode, alternating steam injection with vacuum extraction to remove about 19,000 liters. During this pass, the average extraction rate was more than 380 liters/day of gasoline (compared to 3 liters/day for pump-and-treat).

Drillback

The second steam pass completed the experimental phase of operations. After the second steam pass, six boreholes were drilled across the treated site as close to pre-treatment characterization wells as possible, to evaluate the extent of treatment. Recovered soil samples revealed that free-product gasoline had been removed from the edges of the spill and from the zone above the water table (Figure 5). They also revealed that contamination had not been spread: gasoline concentrations had not increased in the soil outside the treatment volume. Most of the soil within the treatment volume was heated to the boiling point of water; only a thick clay layer at 30 to 34 m was cooler, having reached only 80° C in places. This “cold spot” was where the largest concentration of free-product gasoline remained, an estimated 3000 liters.

Final Operations

In November 1993, electric heating was applied to the remaining cool clay-rich area. The overall temperature of the treated zone rose only slightly because the extraction systems were removing much of the deposited electrical energy. When groundwater pumping and vapor

extraction resumed in January, 1994, gasoline concentrations in the recovered groundwater had decreased and the gasoline vapor concentrations increased only slightly, suggesting that no significant amount of free-product gasoline remained to be volatilized. Benzene concentrations in the extraction wells were <200 ppb, down from their peak of 7000 ppb before the first steam pass. This last extraction phase removed about 3800 liters of gasoline, for a total of at least 29,000 liters removed during the three phases of the demonstration (Figure 5).

Subsequent Actions and Site Closure

In January 1994, groundwater pumping and extraction resumed at a reduced rate (nominally during working hours on weekdays), and effluent concentrations were monitored on a regular basis. Benzene concentrations in the extraction wells were less than 200 ppb from a peak of 7000 ppb before the start of steam injection. At a groundwater monitoring well within the pattern, benzene concentrations had decreased dramatically, from several thousand parts per billion before Dynamic Underground Stripping to less than 30 ppb in January of 1994. Other wells showed similar decreases. Of the six contaminants of regulatory concern at the beginning of the demonstration, five were below MCL in all wells. These factors indicate that there no significant free-phase gasoline remains in the treatment volume, although significant contamination might still lie outside the treatment volume.

In April, 1995, groundwater pumping and treating for fuel hydrocarbons ceased at the site. In July 1995, wells drilled through the treated area to a deeper, solvent-contaminated aquifer were sampled; only minor residual concentrations were detected (Figure 5). In August, 1995, regulatory approval for closure of the vadose zone vapor treatment system was received. In October, 1996 the San Francisco Bay Region, Regional Water Quality Control Board confirmed the completion of remedial action for petroleum hydrocarbon impacted groundwater underlying the area (RWQCB, 1996).

Discussion

The initial objective of this demonstration was to remove the separate phase gasoline from the treatment area. This objective was met and exceeded; Dynamic Underground Stripping

lowered the benzene concentrations inside the central region to levels below those observed outside the treated area (the so-called bathtub ring of untreated but slightly contaminated water). The regulated contaminants 1,2 dichloroethane (DCA), xylene, and toluene were at or near their allowed MCLs in the treated area groundwater at the conclusion of operations (Figure 7).

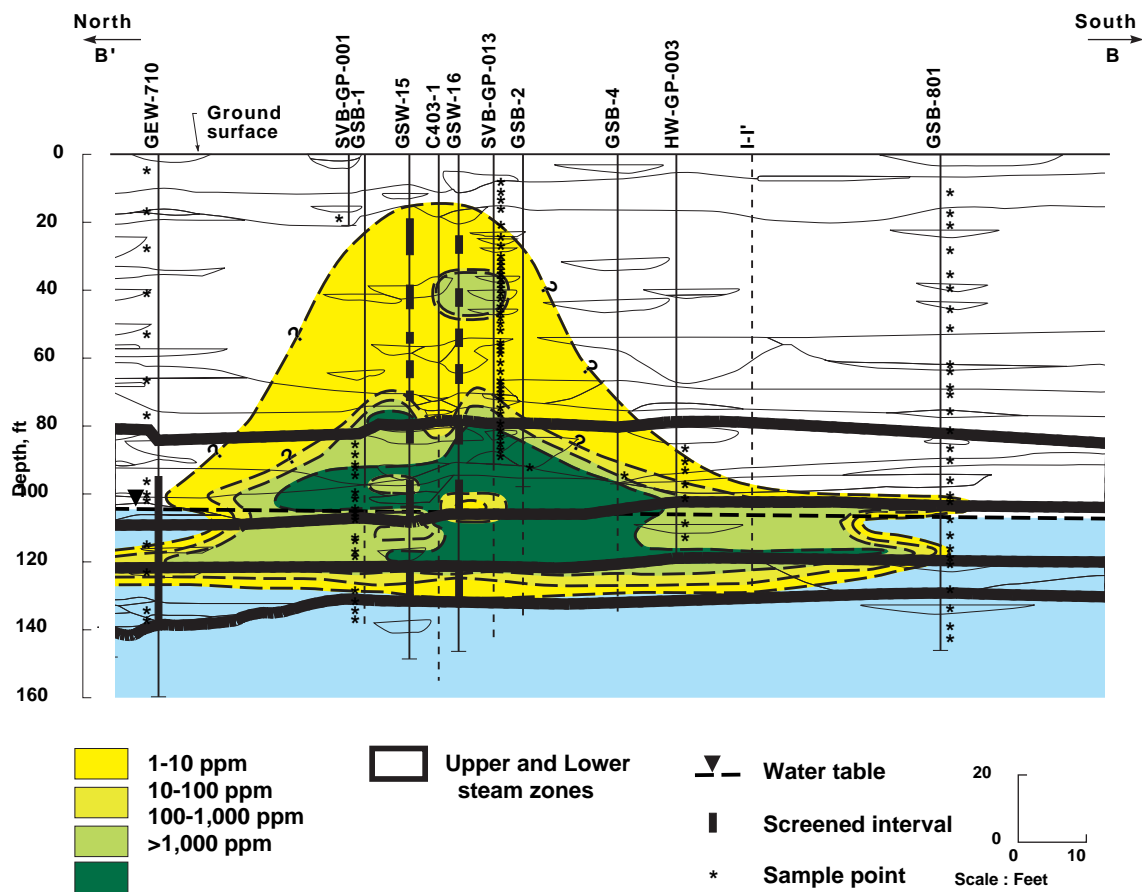
The ability of Dynamic Underground Stripping to remove contaminants to such low levels in groundwater is probably indicative of the boil-off distillation mechanism described by Udell (1994). Because volatile components are generally removed from boiling water at a mass-removal rate exceeding that of the water, boiling a small percentage of the pore water can dramatically reduce aqueous concentrations. Udell examines the effect as a function of boiling rate, solubility and Henry's law constants; unfortunately, solubility and Henry's law constants are not known at high temperatures for most groundwater contaminants. This mechanism may be responsible for the almost instantaneous removal of 1,2 DCA from the site groundwater and for the dramatic decrease seen in benzene relative to xylene.

Initial characterization revealed that a wide variety of microorganisms were actively degrading the BTEX components of the gasoline (Newmark, 1994a). The largest populations existed in areas where gasoline was present at low concentrations. In the capillary fringe zone, where gasoline concentrations were highest, there were low numbers of culturable organisms. Removing the separate phase gasoline should permit final reduction of contaminant levels to below MCLs. However, it was expected that thermal remediation might sterilize the soils or at least adversely affect the established microbial community. Post-test drill-back in August 1993 revealed extensive microbial communities flourishing in all samples, including those in which the soil was collected at temperatures greater than 90°C. The dominant species were no longer bacteria, but yeasts and related organisms which had been observed in small numbers before heating. Thermophiles previously identified from environments such as the hot springs at Yellowstone National Park were important members of the new community, as well as a number of other organisms apparently representing previously unidentified species. Despite the high temperature environment, McNab and others (1995, Happel et al., 1996) have shown that active intrinsic biodegradation of the hydrocarbons is occurring in the subsurface.

Conclusion

The gasoline spill demonstration clearly showed that innovative thermal methods can quickly and effectively clean a contaminated site. Not only was the separate phase gasoline removed, but the groundwater contamination was reduced to or near MCLs. Thermal treatment under these conditions did not sterilize the site, and instead led to the establishment of flourishing indigenous microbial ecosystems at soil temperatures up to 90 °C. The very positive response of California regulators, who provided quick closure authorization for the site, indicates that these methods will be accepted for use.

Acknowledgments - We gratefully acknowledge the support of the Department Of Energy, Office of Science and Technology (EM 50) and Environmental Restoration Program (EM 40) in the development and demonstration of these remediation methods. Dynamic Underground Stripping was jointly developed by LLNL and the UC Berkeley College of Engineering. Kent Udell of UCB developed the steam injection/vacuum extraction technology and the temperature logging system; he and his students were instrumental in this demonstration. Anne Happel, Paula Krauter and Walt McNab shared their bioremediation results with us, providing invaluable insights into the natural post-thermal processes. We greatly appreciate Anne's permission to reproduce Figures 2 and 5 from their work. Albert Lamarre and John Ziagos successfully negotiated the closure of the site with the regulators while providing us their technical insights and access to the remediation program at LLNL. This work was performed under the auspices of the US Department of Energy by Lawrence Livermore National Laboratory under contract No. W-7405-Eng-48.



ES9/1/95RA#13-04

Figure 1. Soil concentrations of total petroleum hydrocarbons measured in pre-operations core samples. Note position of the water table, at 105 ft.

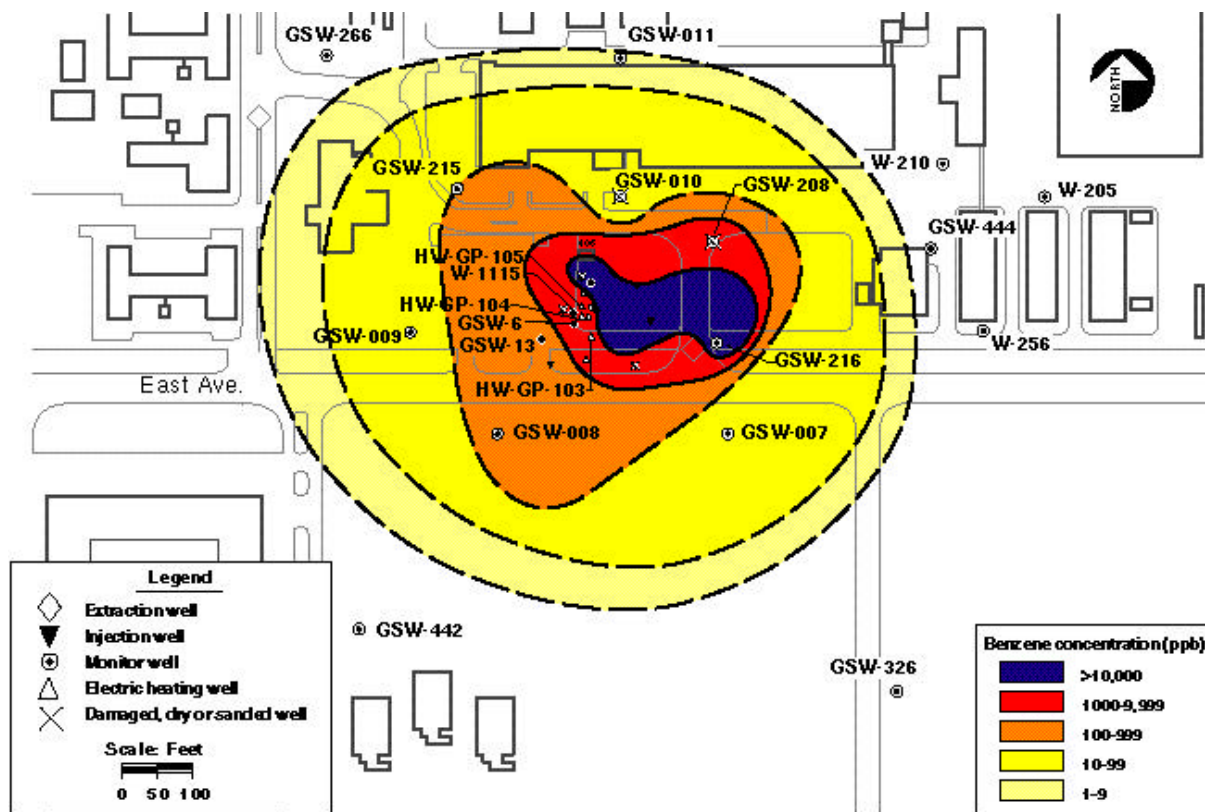


Figure 2. Maximum historical ground water benzene concentrations prior to remediation in HSU-3 (the target hydrostratigraphic zone)(from Happel et al., 1996).

Dynamic Underground Stripping vs Conventional Recovery Methods

LLNL Gasoline Spill Site

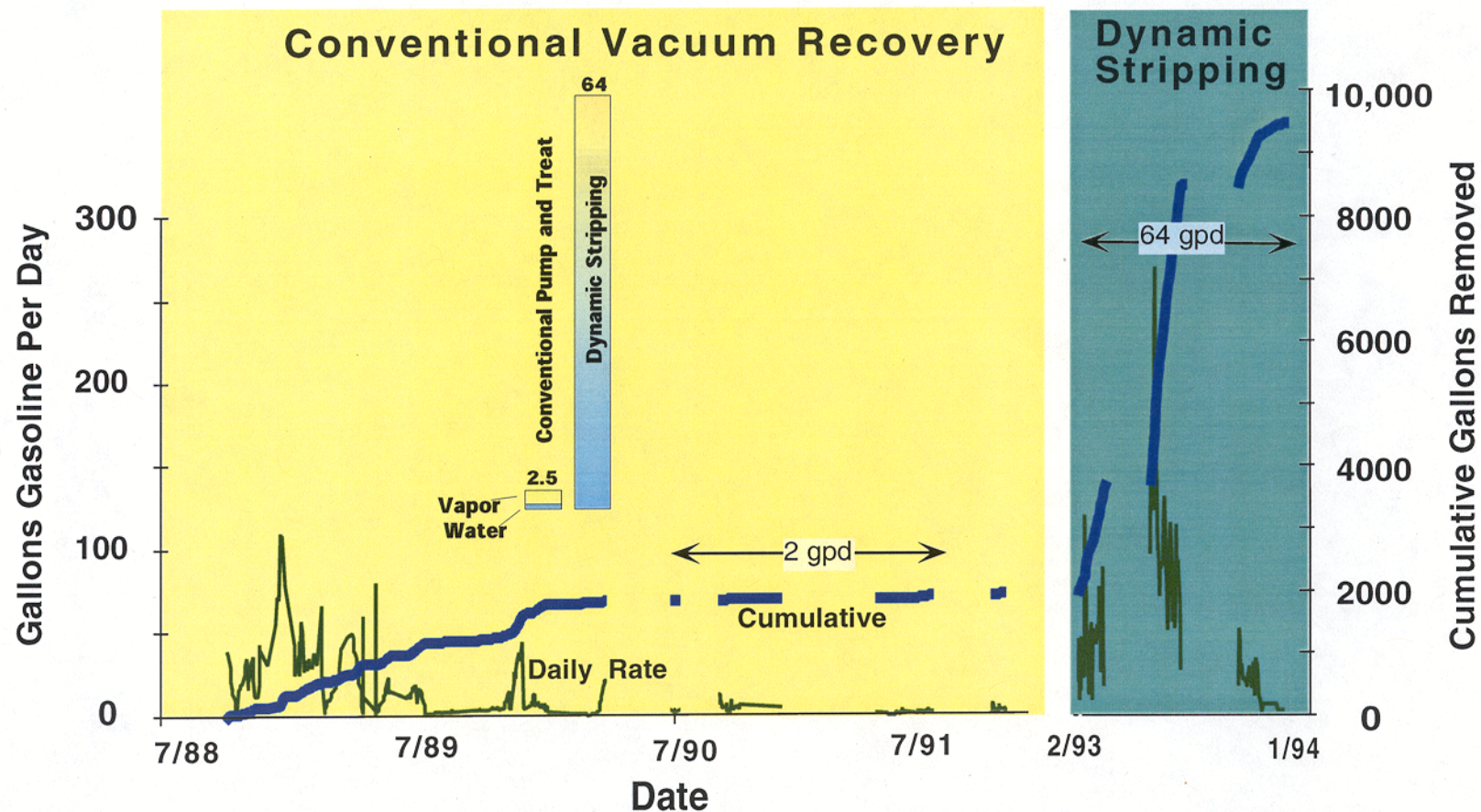


Figure 3. Recovery history of the gasoline spill site. Vacuum extraction began in 1988; after initial high rates, recovery leveled off at about 2 gpd. Groundwater extraction began early in 1993; recovery rates increased to 2.5 gpd. Dynamic Underground Stripping recovery operations began in February, 1993. Operating for 21 weeks over the period of a year, recovery averaged 64 gpd.

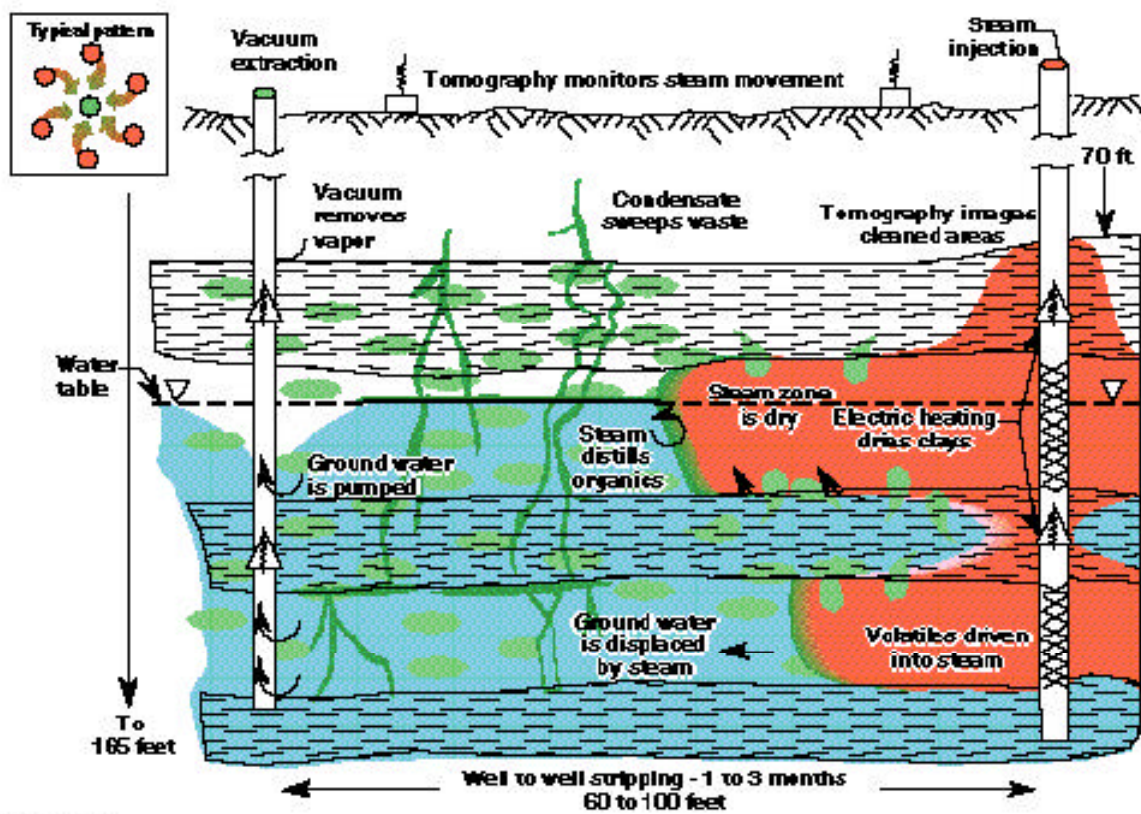


Figure 4. In Dynamic Underground Stripping, steam drives contaminated water toward extraction wells and then heats the soil to distill organic compounds. Electrical heating dries and distills contaminants from impermeable clays that the steam cannot readily penetrate. Geophysical techniques monitor the process. The method operates both above and below the water table and is particularly economically attractive for removing separate phase contaminants.

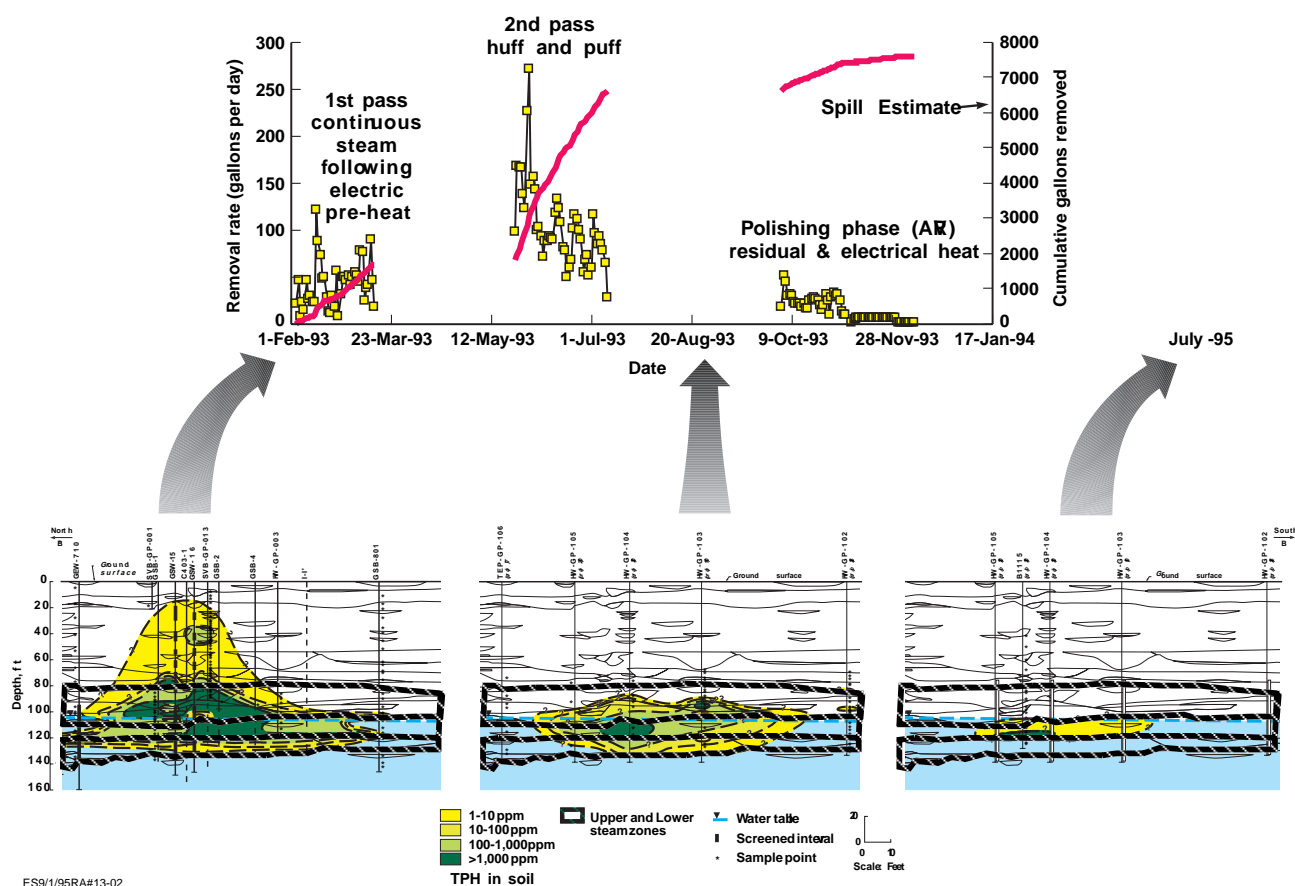


Figure 5. Daily extraction rates and cumulative gasoline recovery during the three extraction phases. Extraction rates were highest during the second phase, when extraction systems were optimized using a pulsed mode of operation. Cross sections show contaminant concentrations measured in soil samples before operations began, after the second steam pass and after groundwater extraction had ceased.

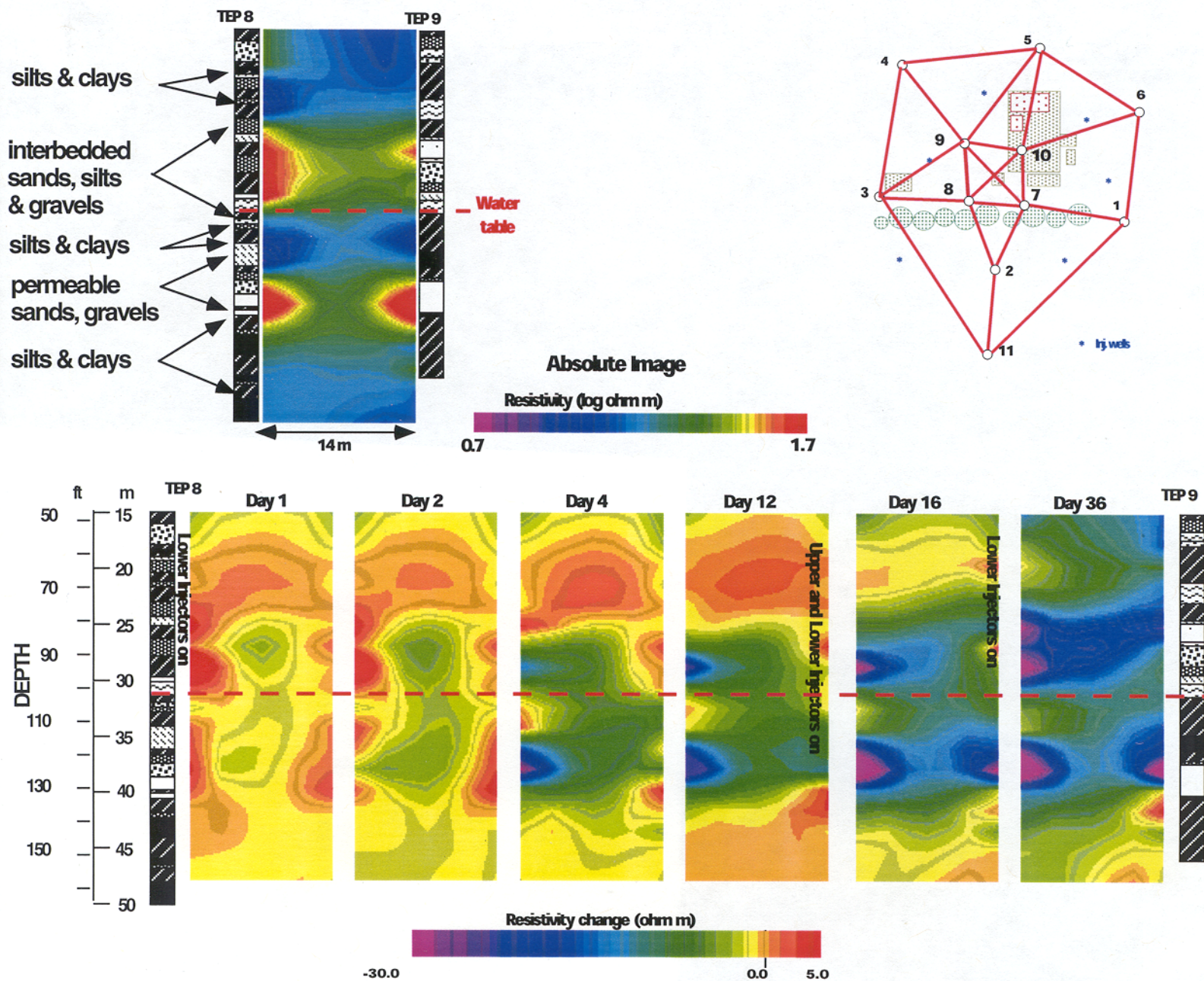


Figure 6. Electrical resistance tomography (ERT) images. Top: ERT absolute images reveal the continuity of soil units across image planes. The resistive units correspond to the more permeable sand and gravel zones; the conductive units correspond to the clay-rich intervals. (The apparent pinching-out of units in the center of the image is due to the increase in resolution radius toward the center of each image). Bottom: ERT difference images show the progress of the steam fronts across the image plane, starting from the first day of steam injection. This image plane (between wells TEP8 and TEP9) is located about 6 m from the nearest injection well, and is oriented nearly perpendicular to a line linking it and the extraction wells. Electrical resistivity decreases within hours of the start of steam injection. By the end of the first steam pass (Day 36), both the upper and lower steam zones are at or near steam temperature, with primarily conductive heating occurring in the neighboring clay-rich units. The preferential steam paths closely follow the more resistive units observed in the absolute images (from Newmark, 1994b)

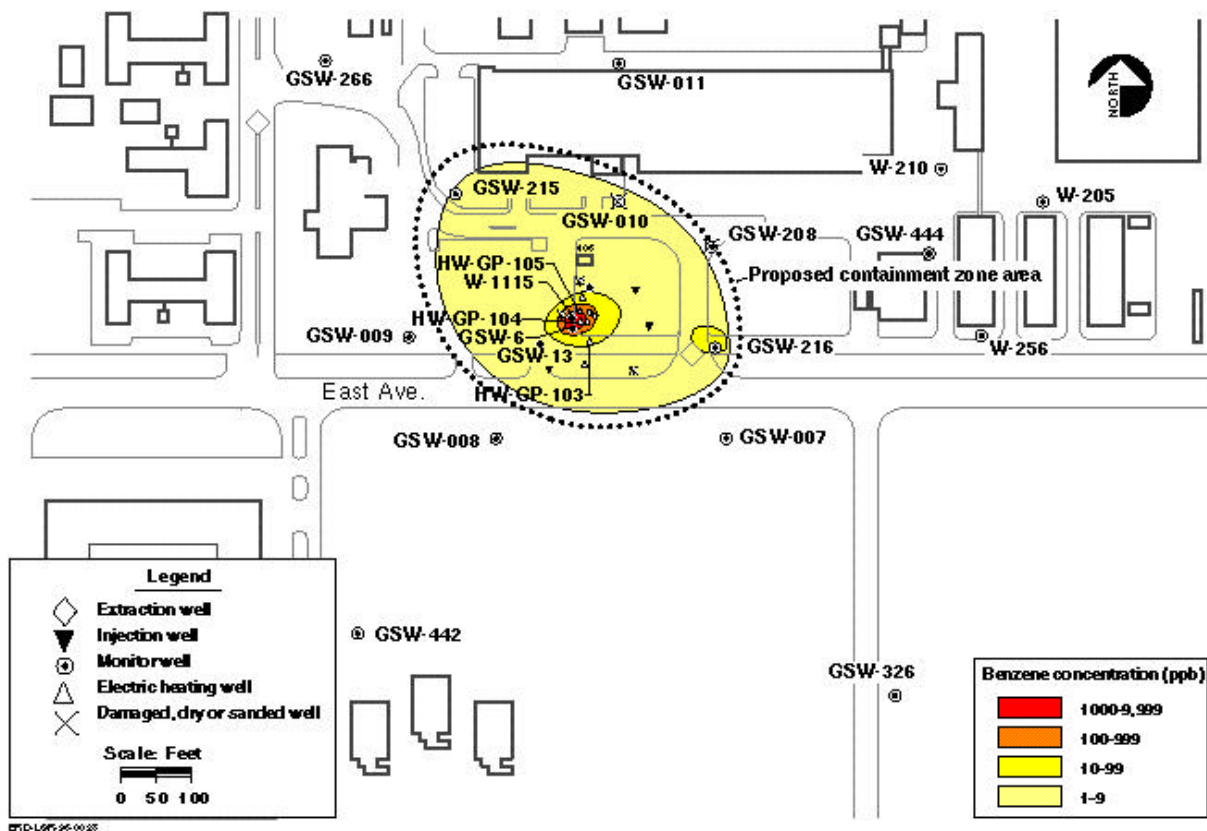


Figure 7. Maximum groundwater benzene concentration in HSU-3 (the target hydrostratigraphic zone) during the 1995 bioremediation study, following completion of vapor extraction, Dynamic Underground Stripping and pump-and-treat remediation, (from Happel et al., 1996).

References

- Happel, A.M., R.W. Bainer, L.L. Berg, M.D. Dresen and A.L. Lamarre, ed., 1996.
Application for Containment Zone for the Livermore Site hydrocarbon impacted zone at
Treatment Facility F., Lawrence Livermore National Laboratory *UCRL-AR-123385*.
- McNab, W. Jr., A. Happel, P.L. Krauter, M. Reinhard, A. Spormann and V. Warikoo, 1995.
Fuel hydrocarbon biodegradation in groundwater at elevated temperatures, abstract in
Eos Transactions, 76(46), p. F189.
- Newmark, R.L. 1992. Dynamic underground stripping demonstration project, interim
engineering report, Lawrence Livermore National Laboratory, *UCRL-ID-110064*.
- Newmark, R.L (ed.), 1994a. Dynamic underground stripping demonstration project, LLNL
gasoline spill demonstration report. Lawrence Livermore National Laboratory, *UCRL-
ID-116964*.
- Newmark, R.L., 1994b. Using geophysical techniques to control in situ thermal remediation,
Proc. Symp. on Application of Geophysics to Engineering and Environmental Problems,
Boston, MA., March 27-31, 195-211.
- Regional Water Quality Control Board (RWQCB), 1996. File 2199.9026 (MBR).
- Udell, K. S., 1994. Heat and mass transfer in cleanup of toxic waste, *Advances in Heat
Transfer Research*, C.L. Tien, ed., Environmental and Engineering Geophysical Society,
Englewood, CO., pp. 195-211.

DISCLAIMER

This document was prepared as an account of work sponsored by an agency of the United States Government. Neither the United States Government nor the University of California nor any of their employees, makes any warranty, express or implied, or assumes any legal liability or responsibility for the accuracy, completeness, or usefulness of any information, apparatus, product, or process disclosed, or represents that its use would not infringe privately owned rights. Reference herein to any specific commercial product, process, or service by trade name, trademark, manufacturer, or otherwise, does not necessarily constitute or imply its endorsement, recommendation, or favoring by the United States Government or the University of California. The views and opinions of authors expressed herein do not necessarily state or reflect those of the United States Government or the University of California, and shall not be used for advertising or product endorsement purposes.

Thin Diaphragm Wall Emplacement

Rich Landis

Introduction

Emplacement of physical hydraulic control barriers in unstable soils, near foundations, and around underground obstructions can be difficult, cost prohibitive, and/or technically impractical. Through the National Environmental Technology Test Sites (NETTS) program at Dover Air Force Base (AFB) and a program cosponsored by the U.S. Department of Energy and DuPont with participation from the U.S. Air Force and the U.S. Environmental Protection Agency, the use of high-pressure jetting was investigated as a means to emplace physical hydraulic control barriers.

Technology Overview

High-pressure jetting uses a high-energy fluid stream to erode a cavity in the soil. The two basic types of emplacements are thin diaphragm walls and columns. Both are created by jetting a slurry at approximately 90 gallons per minute (gpm) at a pressure of approximately 6,000 pounds per square inch. Columnar emplacements are created during the extraction of the drill string by rotating the drill string; a nonrotating drill string will create a thin diaphragm wall.

The key equipment components of a high-pressure jetting system are as follows:

- Small to medium-sized drill rig that can control rotation and drill string extraction rates
- Data acquisition system to monitor the jetting parameters
- Bulk materials handling and slurry mixing system
- High-pressure pumping system
- Jetting nozzle assembly
- Specialized drill string
- Spoils control equipment (vacuum trucks and a spoils control box)

Once the jetting equipment is set up, test emplacements are usually performed to determine the jetting parameters according to the site-specific soil conditions. After a batch of slurry is mixed, the process begins by drilling a borehole (roughly 8 inches in diameter) to the desired depth. During the drilling process, the high-pressure pumping system pumps slurry to the drill bit at a low flow rate and pressure to aid in cleaning the spoils from the borehole. Once at depth, the pump is shut down, the drill string is disconnected, and a ball bearing is placed into the central tubular to plug the fluid flow to the drill bit, thereby diverting all of the fluid flow to the jetting nozzles. The drill string is reconnected, the jetting nozzles are properly aligned (only for thin diaphragm walls), and the high-pressure pump is activated to the desired parameters. Once the desired jetting parameters are reached, the drill string is withdrawn at the desired extraction and rotation rates. Some spoils come to the surface during the jetting process with the volume of spoils being a function of the soil texture, the properties of the slurry, and the amount of slurry pumped during the emplacement efforts.

To help ensure that the jetting nozzles were within the zone of tolerance of the target, a directional drilling guidance tool was adapted to the jetting nozzle assembly. This device, manufactured by Tensor, measured the inclination and heading of the jetting nozzle assembly as well as the orientation of the jetting nozzles. Associated with the guidance tool is a “wet connect” that allowed an electrical connection to be made within the slurry. This connector (developed by Wireline) permitted power to be supplied to the guidance tool from the surface power supply and data to be transferred from the guidance tool to the surface instrumentation.

Objective and Scope of Work Summary

The objective of the study at Dover AFB was to investigate barrier emplacement performance and cost effectiveness of high-pressure jetting by emplacing a 12-sided circular thin diaphragm wall cofferdam keyed into a confining unit (see Figure 1). The cofferdam was constructed by jetting a cement/bentonite slurry with an in-situ target hydraulic conductivity of 1.0×10^{-7} centimeters per second (cm/sec). Once constructed, piezometers were installed to monitor the water levels inside and outside of the cofferdam in order to determine gradient across the cofferdam's walls and the cofferdam was covered by a geomembrane to minimize infiltration of precipitation, (see Figure 2). Relatively basic hydraulic tests were then performed and combined with the use of Darcy's Law to determine the bulk hydraulic conductivity performance of the cofferdam.

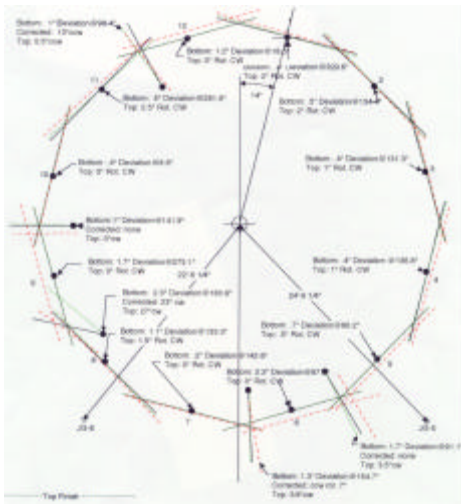


Figure 1: Illustration of the cofferdam design showing emplacement locations.



Figure 2: A picture of the geomembrane cover and piezometers.

Physical and Geologic Setting

The site at Dover AFB is a well characterized clean site, thereby facilitating technology development efforts. Dover AFB is generally level with little spatial variation and ranges in surface elevation from 10 to 35 feet above mean sea level. The AFB is underlain by sediments of the Cretaceous to Recent age, forming a wedge of sediments thickening to the southeast. The Pleistocene Columbia and Lynch Heights Formations form a water table aquifer in the area. Generally, these formations are composed of medium to fine

sands with gravelly sand, silt, and clay lenses. The Columbia Formation is characterized by a fining upward sequence of silty poorly sorted sands. The Lynch Heights Formation overlies the Columbia Formation and is composed of a coarsening upward sequence of silty sands. Discontinuous clay lenses are common in the Lynch Formation and occasional gravelly sand lenses are also present. Pumping tests in the Columbia Formation indicate an average hydraulic conductivity ranging from 2.8×10^{-3} to 1.2×10^{-2} cm/sec.

Underlying the Columbia Formation is the upper unit of the Calvert Formation (Miocene). This unit generally consists of gray, firm, dense marine clays with thin laminations of silt and fine sand. The underlying Calvert Formation is composed of marine, estuarine, and delta plain silty clays and forms an aquitard. The thickness of this aquitard ranges between 20 and 28 feet, averaging 22 feet. The vertical hydraulic conductivity of this unit is estimated between 2.7×10^{-8} to 1×10^{-7} cm/sec (Leahy 1982).

Results

Based on the Phase II test emplacements at Dover AFB, thin diaphragm panels with maximum tip-to-tip lengths in excess of 14 feet were emplaced with length depending on the extraction rate (see figure 3).



Figure 3: A picture showing an excavated thin diaphragm panel emplaced using high pressure jetting.

Based on the criteria of 8-foot minimum intersections for the coffer dam and a safety factor of greater than 20 percent, an extraction rate of 162 centimeters per minute (cm/min) or 64 inches/min was selected. The result was a thin diaphragm panel in excess of 13 feet long and an effective length of approximately 10.4 feet. Based on this result, a circular cofferdam with a radius of 17.39 feet containing 12 thin diaphragm panels with an effective tip to tip panel length of approximately 9.3 feet was designed. This design

resulted in a panel length safety factor of approximately 28 percent; therefore, 14 percent (1.8 feet) of the panel overlapped per side, (see Figure 1).

Upon completion of the emplacement efforts, piezometers were installed, and the cofferdam ground surface was covered with a geomembrane. Data were collected over a 12-day period to detect any abnormalities to the groundwater flow patterns. Background water levels of the piezometers were monitored using a Hermit 3000 data logger and Troll 4000 pressure transducers. Manual logging was conducted on five background wells, and confirmatory readings were obtained from the piezometers. Based on these data and the consistency of water level trends between piezometers, a zone of higher hydraulic conductivity located below the saturated zone was concluded to be present.

Once background data were collected and trends were understood, several flood tests were conducted to measure the bulk hydraulic conductivity of the coffer dam. Flood tests were conducted at 4, 8.5, 10, 12, and 15.2 gpm. Each flood test was run sufficiently long so that steady state conditions were met (see Figure 4).

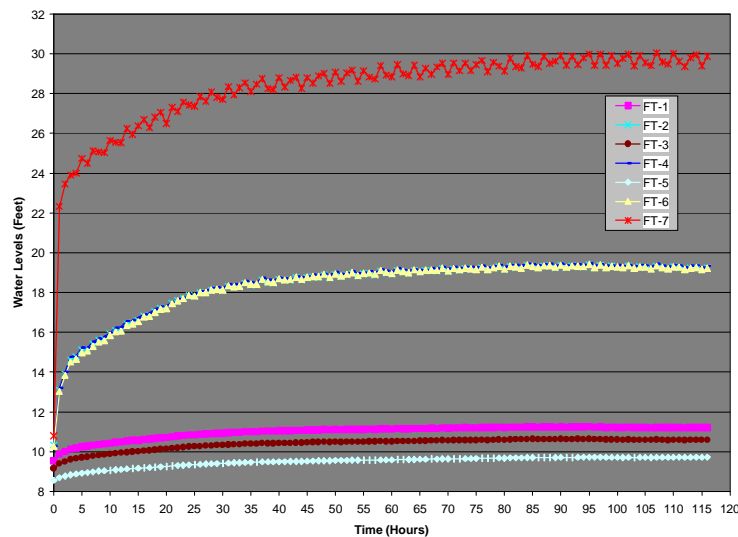


Figure 4: A graph of the water levels in the monitoring wells during a 8.5 gpm flood test. The bottom 3 curves (FT-1, FT-3, FT-5) are outside monitoring wells. The top curve (FT-7) is the injection well. The middle curves (FT-2, FT-4, FT-6) overlie each other and are inside monitoring wells.

Based on the flood test data, the bulk hydraulic conductivity of the coffer dam was calculated using Darcy's Law ($Q=KAI$, where "Q" is volumetric flow rate into and out of the cofferdam, "K" is bulk hydraulic conductivity of the cofferdam, "A" is the submerged cofferdam area through which flow occurs, and "I" is the hydraulic gradient across the cofferdam panel). The estimated range of K was from 1.88×10^{-5} to 2.88×10^{-5} cm/sec. Below is an example of the calculation using the data from a 10 gpm flood test. The data from the flood test for a 12-panel cofferdam are as follows:

- Steady state flow rate into the cofferdam = 10 gpm (2310 ft³/day)
- Hydraulic conductivity of the aquitard = 6.25×10^{-3} ft/day
- Area of the aquitard forming the bottom of the cofferdam = 962 ft²
- Thickness of the aquitard = 25 feet
- Length of each panel in the cofferdam = 9.32 feet
- Thickness of each panel in the cofferdam = 0.5 feet

$$Q_{\text{total}} = (K_{\text{wall}})(A_{\text{wall}})(I_{\text{wall}}) + (K_{\text{aquitard}})(A_{\text{aquitard}})(I_{\text{aquitard}})$$

$$2310 \text{ ft}^3/\text{day} = (K_{\text{wall}})[(9.32 \text{ ft/panel})(12 \text{ panels})(21.7 \text{ ft})][(21.7 \text{ ft} - 11.1 \text{ ft})/0.5 \text{ ft}] + (6.25 \times 10^{-3} \text{ ft/day})(962 \text{ ft}^2)(21.7 \text{ ft} / 25 \text{ ft})$$

$$K_{\text{wall}} = 0.0448 \text{ ft/day} = 1.58 \times 10^{-5} \text{ cm/sec}$$

If an average is obtained for the five flood tests, the average bulk hydraulic conductivity for the cofferdam is 2.29×10^{-5} cm/sec. Using Darcy's Law and the average bulk hydraulic conductivity, a percentage can be estimated for the overall completeness of the cofferdam's wall area. Below is an example of the calculation. Necessary data for a 12-panel cofferdam are as follows, assuming that (1) the depth of the cofferdam is 36 feet, (2) the hydraulic conductivity of the defect equals that of the aquifer, and (3) the flow through the aquitard is inconsequential:

- Length of each panel in the coffer dam = 9.3 feet
- Thickness of each panel in the coffer dam = 0.5 feet
- Hydraulic conductivity of the aquifer = 1×10^{-3} cm/sec (2.83 ft/day from NETTS reports)
- Hydraulic conductivity of the wall = 2.4×10^{-7} cm/sec (0.0007 ft/day as measured in the laboratory)

$$(K_{\text{bulk}})(A_{\text{bulk}})(I_{\text{bulk}}) = (K_{\text{wall}})(A_{\text{wall}})(I_{\text{wall}}) + (K_{\text{defect}})(A_{\text{defect}})(I_{\text{defect}}) + (K_{\text{aquitard}})(A_{\text{aquitard}})(I_{\text{aquitard}})$$

Assuming $I_{\text{total}} = I_{\text{wall}} = I_{\text{defect}}$ and rearranging yields:

$$(K_{\text{bulk}})(A_{\text{bulk}}) = (K_{\text{wall}})(A_{\text{wall}}) + (K_{\text{defect}})(A_{\text{defect}})$$

But $A_{\text{wall}} = A_{\text{total}} - A_{\text{defect}}$ and rearranging yields:

$$(K_{\text{bulk}})(A_{\text{bulk}}) = (K_{\text{wall}})(A_{\text{bulk}}) + (A_{\text{defect}})(K_{\text{defect}} - K_{\text{wall}}) \text{ and rearranging to solve for } A_{\text{defect}} \text{ yields:}$$

$$A_{\text{defect}} = [(A_{\text{bulk}})(K_{\text{bulk}} - K_{\text{wall}})] / (K_{\text{defect}} - K_{\text{wall}})$$

$$A_{\text{defect}} = [(9.30 \text{ ft})(36)(12)(2.29 \times 10^{-5} \text{ cm/sec} - 2.4 \times 10^{-7} \text{ cm/sec})] / (1 \times 10^{-3} \text{ cm/sec} - 2.4 \times 10^{-7} \text{ cm/sec})$$

Yielding an estimated area of the defect of approximately 91 ft².

The surface area of the panels is approximately 4017 ft², resulting in a completeness of roughly 98 percent, $[(4017\text{ft}^2 - 91\text{ft}^2)/4017\text{ft}^2](100) = 98\%$

The other hydraulic test that was performed was a pulse test to attempt to delineate the type and location of defects, whether localized or distributed in nature. The intent of the pulse test was to create a pressure pulse within the cofferdam and to measure whether or not the pressure pulse was attenuated by the cofferdam's walls. The pressure pulse was generated in the central 4 inch well casing by using a timing circuit to open and close a solenoid valve connected to a water source. From the solenoid valve, hard piping was run and attached to a packer and foot valve assembly located slightly below the water table. High frequency differential pressure transducers were then installed in all wells to capture the pressure pulse. All the transducers were then connected to a recording device and the system was activated, (see Figures 5, 6, 7, and 8).

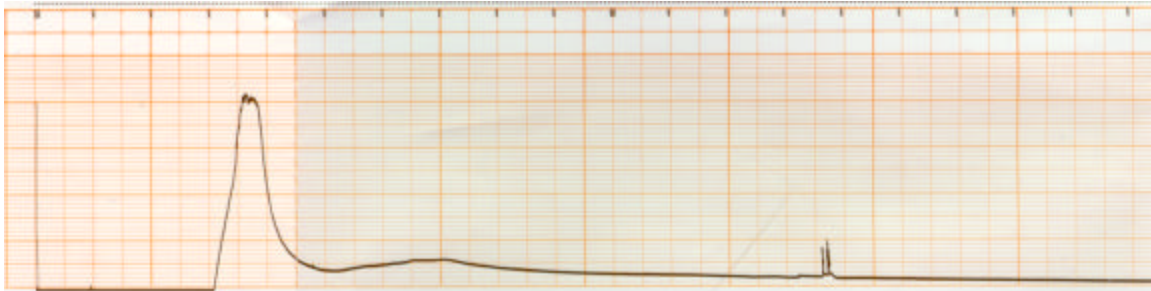


Figure 5: Graph of FT-7 showing the initial pressure pulse below the packer in the central injection well, (1.0 psig full scale, 1mm/sec).

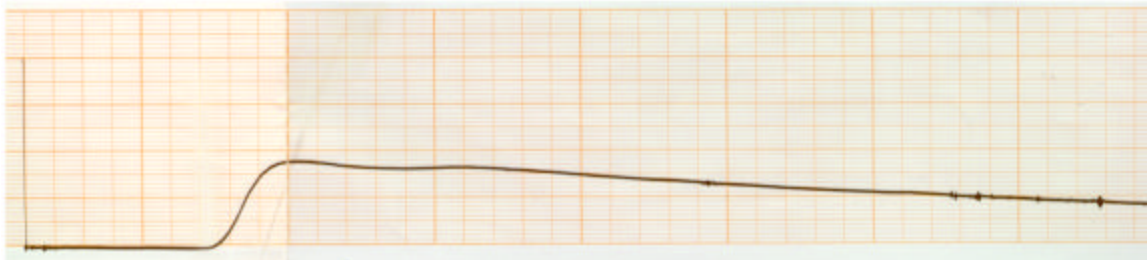


Figure 6: Graph showing the typical pressure pulse for one of the internal monitoring wells (FT-2, FT-4, Ft-6 and 0.10 psig full scale, 1mm/sec)).

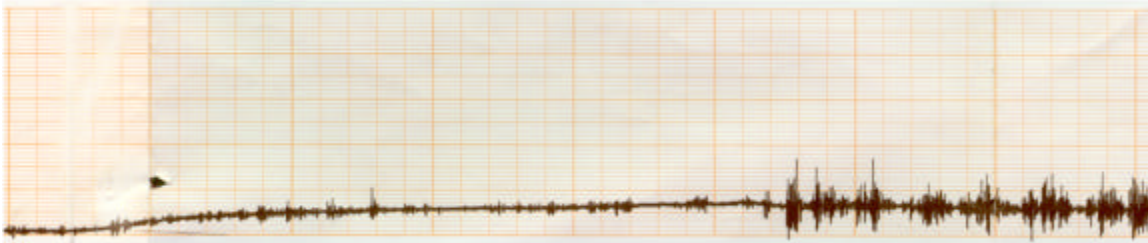


Figure 7: Graph of FT-1 showing the only pressure pulse in an external well that was not totally attenuated by the walls of the cofferdam, (0.025 psig full scale, 1mm/sec).

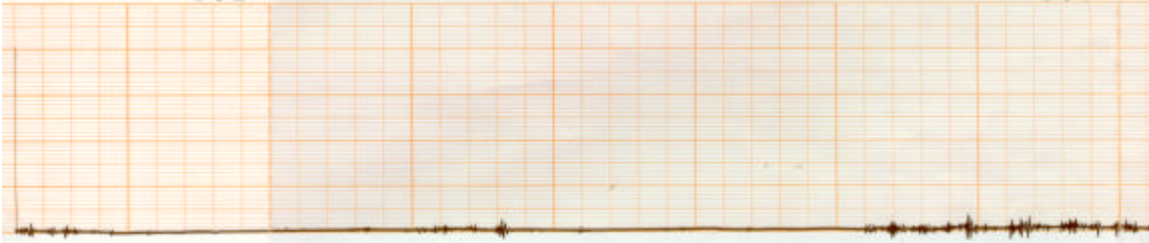


Figure 8: Graph showing the typical pressure pulse for two of the external monitoring wells (FT-3 and FT-5) where the initial pressure pulse was totally attenuated, , (0.50 psig full scale, 1mm/sec).

Based upon these results, it appears that the defect is located near the FT-1 external monitoring well since a pressure rise correlating with the pulse was measured at FT-1. Further, the pressure transducers were so sensitive that the noise that is recorded on the above graphs show the acoustic impact of C-5A aircraft taking off from the base.

Discussion

Based upon the test panel emplacements, the properties of the wall met the goal hydraulic conductivity goal of 1.0×10^{-7} cm/sec. However, a defect within the saturated zone exists near the FT-1 monitoring well thereby increasing the bulk hydraulic conductivity to 2.29×10^{-5} cm/sec. The vertical location of the defect was not identified, but appears to be associated with a particular coarse grained zone (cobble zone) encountered during the drilling and jetting operations.

The cobble zone was located in the saturated zone and since grout was lost to the formation over time, it is believed that the groundwater in this transmissive zone diluted the grout before the grout had time to set. This zone was unanticipated since two geotechnical borings (JG-5 and JG-6) nearby did not indicate the presence of cobbles, (see Figure 1). Modifying the grout formula to a higher solids grout or quicker setting grout would have helped to plug the zone.

Due to encountering this cobble zone the drillstring and jetting assembly was frequently pushed outside of the target's zone of tolerance (+/- 0.5 degree of vertical). Further, due to subsurface magnetic anomalies (steel cofferdams) near the test site, the nozzle orientation capability of the guidance tool was compromised since it uses a magnetometer for this function. This resulted in some of the panels being jetting slightly out of the targeted angular orientation (+/- 1 degree of the target). However, based upon the guidance tool's ability to measure inclination and heading, an "as built" cofferdam diagram could be determined. The "as built" cofferdam indicated that potential discontinuities at the interfaces between some of the panels could be present. Based upon this determination, several extra panels were emplaced at the interfaces to remedy the potential discontinuities, (see Figure 1).

Emplacement of the thin diaphragm panels was accomplished at a production rate of roughly 4 panels per day with a drilled depth of 43 feet and a jetted length of 40 feet. Assuming

that the effective width of panel is 9.3 feet, roughly 1490 ft² was jetted per day. Assuming a unit rate of roughly \$10,000 per day for equipment and crew, an estimated unit price per square foot is roughly \$6.71/ft². This cost does not include the cement or bentonite materials, mobilization/demobilization, spoils disposal, or costs associated with the guidance tool. The total cement-bentonite slurry material cost was roughly \$2,200. Mobilization and demobilization cost was \$13,000; however, the equipment was relatively local. A more typical mob/demob cost would be \$25,000. The spoils volume generated during the emplacement operation was at a ratio of 60 percent that of the jetted volume resulting in roughly 40 yd³ of spoils generated. The spoils generated as part of this project were clean and were disposed of as on site fill. The typical rental fee for the guidance tool is roughly \$1,500 per day. Based upon these cost data, an overall estimated cost to emplace the cofferdam at the Dover AFB test site is \$8.21/ft², not including mobilization and demobilization.

Conclusions

Based upon the results of this program at the National Environmental Technology Test Sites (NETTS) program at Dover Air Force Base (AFB) and a program cosponsored by the U.S. Department of Energy and DuPont with participation from the U.S. Air Force and the U.S. Environmental Protection Agency, high-pressure jetting appears to be a cost effective means to emplace physical hydraulic control barriers. This is especially true for emplacement of physical hydraulic control barriers in unstable soils, near foundations, and around underground obstructions that can be difficult, cost prohibitive, and/or technically impractical.

References

Leahy, P 1982. *Groundwater Resources of the Piney Point and Cheswold Aquifers in Central Delaware as Determined by a Flow Model*. Delaware Geological Survey, Bulletin No. 16

THIN DIAPHRAGM WALL DEMONSTRATION AT THE DOVER AIR FORCE BASE

David Reichhardt, Andrea Hart

Through the Department of Defense Strategic Environmental Research and Development Program (SERDP), the National Environmental Technology Test Sites (NETTS) Program and a program co-sponsored by the Department of Energy (DOE) Office of Science and Technology, U.S. Air Force/Armstrong Labs, and DuPont, the use of high-pressure jet grouting to emplace thin diaphragm walls was investigated at the Groundwater Remediation Field Laboratory (GRFL) National Test Site located at DAFB in Dover, Delaware (MSE, 1998). The objectives of the field study were to further understand and document the use of high-pressure jet grouting for emplacing thin diaphragm walls as hydraulic control for environmental applications and to develop a verification and monitoring methodology to describe the quality of the emplaced subsurface barrier.

The thin diaphragm wall application is planned for use as part of a containment strategy to control contaminated groundwater from migrating from a hot spot; divert groundwater flow; emplace materials for innovative remediation techniques; or provide short- and perhaps long-term containment for pits, trenches, and landfills.

The thin diaphragm walls were created by simultaneously injecting, in this case, a cement bentonite grout, at approximately 6,600 psi in two opposing directions without rotating the drill string during the extraction process (conventional columnar-type pillars are created by rotating the drill string during extraction of the drill string). The resultant thin diaphragm walls were emplaced to act as a barrier of lower hydraulic conductivity than the surrounding soil.

There are few field experiences or documented case studies that exist today for the emplacement of thin diaphragm walls using a dual-phase grouting system. One thin diaphragm wall hydraulic control barrier was emplaced in Italy along the Po River. The data from the Po River activity presented some interesting questions, not all of which are addressed specifically by this demonstration. The barrier wall emplacement on the banks of the Po was several miles long and it had a reported core sample hydraulic conductivity of 1×10^{-9} to 1×10^{-10} cm/sec. No Verification and monitoring of the barrier was performed; the purpose of the walls was for river bank erosion control rather than environmental containment. In addition, it was not clear what methods were used to test and calculate the hydraulic conductivity of the barrier.

Based on the data from the Po River emplacement and the need to have an inexpensive and easy method to emplace subsurface barriers, a team was established to investigate: (1) the constructability of a high pressure jet-grouted containment barrier; (2) the continuity of the barrier as built; and (3) the development of an appropriate methodology to verify and monitor the integrity of a grouted barrier.

The demonstration was planned in stages to increase project control, specifically to control cost. Phase I included the installation of test panels and small barrier boxes. The primary purpose of the test panels was to refine the grouting parameters for site-specific conditions. Then, small

barrier boxes were emplaced using the refined grouting parameters. Based on the results of the Phase I testing, a large double-walled coffer dam, approximately 30 feet in diameter, was planned as Phase II of the demonstration.

Concurrent with the barrier emplacement, Verification and monitoring work was performed. The first objective of the verification testing performed on the thin diaphragm wall emplacements was to determine if the barrier met the emplacement criteria included in the work plan. These criteria included specified wall thickness, wall permeability, wall verticality, and continuity. The second objective was to test the proposed Verification and monitoring technologies to determine which provided the best methods for verifying whether the barrier met design specifications. It was likely that a combination of the proposed methods would be necessary to verify barrier emplacement.

Excavation of one of the barriers was accomplished to help validate the results from some of the innovative Verification and monitoring technologies. A photograph of an excavated wall of the barrier is shown in Figure 1.



Figure 1 Photograph of an exposed wall of the barrier during the excavation process.

The objective of Phase II was to build, verify, and monitor a double-walled coffer dam. Specifically, the objective was to determine if the Phase II cell was constructed as planned and met the emplacement criteria documented in the emplacement work plan, which resulted from the data quality objective process.

All work performed in Phase I and II was completed with the understanding that the primary goal of the overall thin diaphragm wall barrier project was to create an in situ continuous barrier with a hydraulic conductivity of 1×10^{-7} cm/sec or less.

Results of the Emplacement Phase I

Based on the Constructive Quality Assurance (CQA) inspections performed during Phase I emplacement of the test panels and small barrier boxes, all of the quality criteria specified were

satisfactorily met with the following exceptions:

- jet orientation at the completion of grouting for nine panels was out of alignment beyond the specified criteria; and
- grout rod verticality (at full panel depth) exceeded the specified criteria in 50% of the small barrier box panels.

Based on the performance of the Verification and monitoring technologies in Phase I it was decided to go forward with deployment of all the tested Verification and monitoring systems in Phase II.

The Go/No-Go decision to proceed with Phase II was based primarily on a flood test of one of the shallow barrier boxes. The result from the one-week flood test of the box was a calculated bulk hydraulic conductivity of approximately 3.3×10^{-6} to 3.8×10^{-6} cm/sec. Because the box held water, the recommendation was made and approved by the executive committee to move on to Phase II.

Results of the Emplacement Phase II

The Phase II barrier containment was built, although not as originally planned. Because of unanticipated subsurface characteristics, the emplacement organization elected to build two separate coffer dams that were not concentric, which did not produce the planned double-walled coffer dam.

Some of the verification technologies used in Phase I were used to test the Phase II coffer dam located at the site selected for Phase II. Flood testing was planned for the second Phase II coffer dam.

Costs

Data was collected to provide cost information for the emplacement effort. That data correlation remains in progress.

Conclusions and Recommendations

The Phase I and II emplacement efforts were completed, although not entirely as planned. Their success was significant; it was demonstrated that an environmental containment barrier could be built using the thin diaphragm wall technology, although emplacement technology gaps remain to be addressed.

Substantial advancements were also made in the area of verification technologies for subsurface barriers. These technological advancements support progress for all subsurface barriers, not only the thin diaphragm wall technology.

A demonstration at a contaminated site is the next recommended step. Jet alignment is an

important area for future work, especially if the application for the technology at greater depths is desirable. A more comprehensive engineering design approach should be included.

Technology gaps identified during the project should be addressed. These include emplacement/design gaps such as operation parameters and nozzle alignment. Material selection, not only as a process to address site specific contaminants but also to address cold joint issues and saturated zone applications, also remains to be addressed.

The Phase II barrier used for geophysical testing should be tested by other verification technologies. This barrier should also be considered for development into a verification testing site.

Acknowledgments

The thin diaphragm wall field demonstration was funded and overseen by the Department of Energy (DOE)/Office of Science and Technology and DuPont. The U.S. Air Force, Dover Air Force Base was the host for the demonstration site, and the Environmental Protection Agency (EPA) provided support. Project team members are listed below with a brief explanation of their roles and responsibilities:

- DOE—funding entity;
- DuPont—co funder responsible for emplacement team lead and provider of in-kind support;
- EPA—collaborator for independent data validation;
- Florida State University (FSU)—contracting agency;
- Hayward Baker—subcontractor to FSU for grout emplacement and in-kind support as a team member;
- SERDP/NETTS/GRFL—host for a demonstration site and provider of in-kind services;
- MSE Technology Applications, Inc. (MSE)—DOE funded for the integrated project management and geophysical verification;
- Westinghouse Savannah River Co. (WSRC)—DOE funded for the Verification and monitoring team lead and geotechnical testing;
- Lawrence Berkeley National Laboratory (LBNL)—DOE funded for geophysical support;
- Sandia National Laboratory (SNL)—DOE funded for hydraulic and tracer support; and
- Lawrence Livermore National Laboratory (LLNL)—DOE funded for geophysical support.

References

MSE Technology Applications, Inc., *Final Report-Cement Bentonite Thin Diaphragm Wall Jet-Grouting Demonstraion Project, Dover, Delaware, HMP-52*, September, 1998 (Prepared for the U.S. Department of Energy).

Viscous Liquid Barrier Cold Site Demonstration at the Brookhaven National Laboratory

David Reichhardt, Mary North-Abbott

Within the DOE facilities, many waste contaminated areas exist that require interim or long-term containment. In some cases, this requirement buys time to allow technologies to be developed that can treat the isolated waste or allows the waste to degrade to a level to which the risk to human health and the environment is minimal. The waste requiring containment is mainly mixed waste containing hazardous and radioactive constituents or highly radioactive waste. The viscous liquid barrier (VLB) technology has the ability to provide long-term or interim containment of waste in unsaturated and saturated areas. Since the emplacement of this containment system uses a low-energy (permeation) implementation method, few contaminants are brought to the surface during grouting, and destruction to fragile infrastructure does not occur. Technology advantages include reduced worker exposure at hazardous/radioactive sites, long-term isolation of waste, reduced costs, limited site subsurface disruption, and increased ability to isolate contamination that is in an infrastructural setting.

The basic approach of this technology is to ultimately construct and verify the integrity of a subsurface hydraulic barrier of a viscous liquid chemical grout material [i.e., colloidal alumina silica (CS)] using the permeation grouting method. The chemical grout is chemically and biologically benign and permeates the soil matrix, displaces the pore water, and seals the pore voids. The barrier fluid containment performance is controlled by the gel time, which depends on identified parameters such as the pH, temperature, chemistry of the grout mixture, and the geochemistry of the interstitial pore water and the soil matrix.

A small-scale field demonstration was conducted at the Los Banos Site in California by Lawrence Berkeley National Laboratory (Ref. 1), using single row injections of CS, resulting in hydraulic conductivities on the order of 1×10^{-4} cm/sec from excavated field samples. The challenge of this project was to determine if multiple injections of CS would reduce the hydraulic conductivity of the grouted sand to the project objective of 1×10^{-7} cm/sec.

The objectives for the VLB Cold Demonstration Site project were to: emplace VLB using the permeation grouting method; lance injection equipment; CS grout material; and to emplace a continuous barrier with minimum wall thickness of 3 feet and a maximum hydraulic conductivity of 1×10^{-7} cm/sec. (Ref. 2) The geology of the BNL site is fluvial outwash sediments at the depth of the barrier emplacement. The groundwater level is at approximately 43 feet below ground level (bgl), but may fluctuate as much as 10 feet.

Before emplacing the VLB, a preliminary site characterization was performed at the BNL Cold Demonstration Site including a ground-penetrating radar (GPR) survey and percolation and soil boring tests. This work was completed to address the immediate baseline informational requirements at the Cold Demonstration Site. Because the site characterization information indicated the near-surface stratigraphy was fairly uniform across the site, the project advanced with the Lance Water Injection Testing (LWIT). The LWIT provided information pertaining to site hydrogeological parameters (such as the water/CS injection rates) and site injection parameters (such as the size of grout bulbs,) and an estimate of in situ gel rates. These tests also provided information to help define the optimal grout injection equipment configuration and design for the VLB.

The VLB was designed to be emplaced in the vadose zone and constructed with a viscous liquid consisting of CS and an electrolyte solution that would get to form a containment barrier. The conceptual VLB design configuration was a wedge, with three vertical walls and one 45-degree slanted wall, as shown in Figure 1. The VLB was emplaced using downstage permeation grouting techniques at a Brookhaven National

Laboratory (BNL) site during the summer of 1997. After emplacement, the site was cleaned and returned to approximately the original topographical surface.

As part of the verification and monitoring (V&M) of the emplaced barrier, in situ Guelph permeameter tests, geophysical studies, and gaseous tracer tests were performed. Because some of the methods used for these data collections were not yet validated, this data could not be the primary method of determining achievement of project objectives. Excavation and sampling of the VLB was therefore used to attempt to provide a means of validating the V&M technology results as well as addressing the attainment of project objectives. The partial destructive examination of the barrier was performed in 1998.

Two gaseous tracer studies were performed on the emplaced VLB in 1997. Results of the perfluorocarbon (PFT) tracer study are presented in Reference 3. The results of the sulfur hexafluoride (SF₆) tracer study are presented in Reference 4. In situ Guelph permeameter tests were also conducted on the VLB in 1997.

In 1998, the VLB was excavated, examined, and the actual shape and size of the exposed portions of the subsurface structure were documented. During the excavation (Figure 2), wall thickness measurements were taken on the exposed barrier wall surfaces for each of the excavation lifts. Samples were collected at each of the specified barrier sample locations and shipped for ex situ laboratory testing including hydraulic conductivity, triaxial compression, consolidation, and moisture content tests. After the excavation of the VLB, 3-D as-built models of the VLB were created using the construction data, surveyed excavation data, and wall thickness measurements. A 3-D as-built model of the VLB is shown in Figure 3.

Once the excavation and sampling efforts were completed, seismic and electrical resistivity geophysical studies were performed on the remaining portion of the barrier. This data confirmed vertical barrier wall total depth within a few feet of the injection data.

While most of the vertical walls of the barrier were destroyed during the excavation, the slant wall and the bottom section of the vertical walls remained intact. The slant wall will be used as a test area for V&M technologies to allow technology developers an opportunity to attempt to locate the existence of the subsurface structure and define the wall integrity.

Costs

Since the total costs for a VLB cold demonstration are not applicable for end-user field applications, a cost model comparing the VLB technology with baseline technologies was created. (Ref. 5) The model does not include costs associated with project management, permitting, engineering support, engineering design, and site characterization since these items depend on site specific considerations as well as experience level. For the BNL site, the applicable VLB costs were tabulated, and the model costs were compared to the demonstration costs. The core cost for the VLB was \$593,00 and the cost model predicted a cost of \$550,000. The model shows concurrence with actual demonstration costs within about 10%. For the same size site and conditions, the excavation/disposal option would cost \$2,122,000, and slurry wall containment would cost \$91,000. (Note: The slurry wall alternative would only be a partial containment or hanging wall because there is no confining layer to key the slurry walls into at the BNL site.) Comparing the VLB technology to the excavation/disposal and slurry wall options resulted in a net savings of \$1,572,000 and \$459,000, respectively.

Conclusions

During the emplacement phase of this project, it was demonstrated that downstage permeation grouting using

lance injection equipment was feasible. While there was limited grout injection success at depths between 3 and 9 ft bgl, a more robust lance rod system combined with the use of hydraulic hammers would likely promote better injection at shallower depths and less deviation of the rods during emplacement. The majority of the wall thickness measurements met the project objective of ≥ 3 ft thickness. To determine the overall hydraulic performance of the VLB, all hydraulic conductivity data from in situ and ex situ analysis were compared. Table 1 summarizes the in situ and ex situ results.

Table 1. In situ and ex situ hydraulic conductivity (HC) results.

Analysis	Geometric Mean HC (cm/sec)	Minimum HC (cm/sec)	Maximum HC (cm/sec)
Ex situ MSE Lab	5.0×10^{-4}	6.9×10^{-6}	3.4×10^{-3}
Ex Situ GeoTesting	2.5×10^{-4}	4.2×10^{-7}	5.1×10^{-3}
In Situ Guelph Permeameter	1.78×10^{-5}	8.93×10^{-7}	1.35×10^{-4}

These results indicate that ex situ values were consistently greater than in situ values for hydraulic conductivity. Sample disturbance during sampling, shipping, and laboratory preparation may account for these differences.

Although the hydraulic conductivity values did not meet the project objectives, the ex situ hydraulic conductivity values indicate a 1 to 4 order of magnitude decrease in hydraulic conductivity while the in situ testing suggests a 2 to 4 order of magnitude decrease. The reduction of hydraulic conductivity of the BNL sands is significant, considering this was the first emplacement of a VLB. The results show this technology has the potential to address contaminant transport issues at DOE sites by hydraulic conductivity reduction.

Acknowledgments

The Viscous Liquid Barrier (VLB) Cold Site Demonstration was funded by the U.S. Department of Energy (DOE)/Office of Science and Technology. Brookhaven National Laboratory (BNL) was the host for the demonstration site. Project team member are listed below with a brief explanation of their roles and responsibilities.

- DOE Subsurface Contaminant Focus Area (SCFA)—funding entity
- MSE Technology Applications, Inc. (MSE)—DOE funded for the engineering design, emplacement, excavation, sampling, analyses, and reporting efforts
- BNL—host for the demonstration site, tracer support, and provider of in-kind services
- EKA Nobel—subcontractor to MSE for grout materials
- Hayward Baker—industrial partner with MSE for grout emplacement and in-kind support
- Westinghouse Savannah River Co. (WSRC)—DOE funded for the Integrated Project team lead during fiscal years 1996 and 1997
- Lawrence Berkeley National Laboratory (LBNL)—DOE funded for geophysical and modeling support
- Sandia National Laboratory (SNL)—DOE funded for tracer support
- Science and Engineering Associates, Inc.—tracer subcontractor to SNL
- Lawrence Livermore National Laboratory (LLNL)—DOE funded for geophysical support

References

1. Moridis, Dr. G. J. et al., *First-Level Field Demonstration of Subsurface Barrier Technology using Viscous Liquids*, July 1995.
2. MSE Technology Applications, Inc., *Final Report–Viscous Liquid Barrier Cold Site Demonstration*, HMP-55, February, 1999 (prepared for the U.S. Department of Energy).
3. Brookhaven National Laboratory, *Verification of Subsurface Barrier Integrity Using Perfluorocarbon Gas Tracers*, March, 1998.
4. Sandia National Laboratories, *Subsurface Barrier Validation of a Colloidal Silica and Jet Grouted Barrier with the SEAttrace™ System*, June, 1998.
5. MSE technology Applications, Inc., *Viscous Liquid Barrier Costing Model*, HMP-43, June, 1998 (prepared for the U.S. Department of Energy).

Conceptual Viscous Liquid Barrier Wedge Trough Design

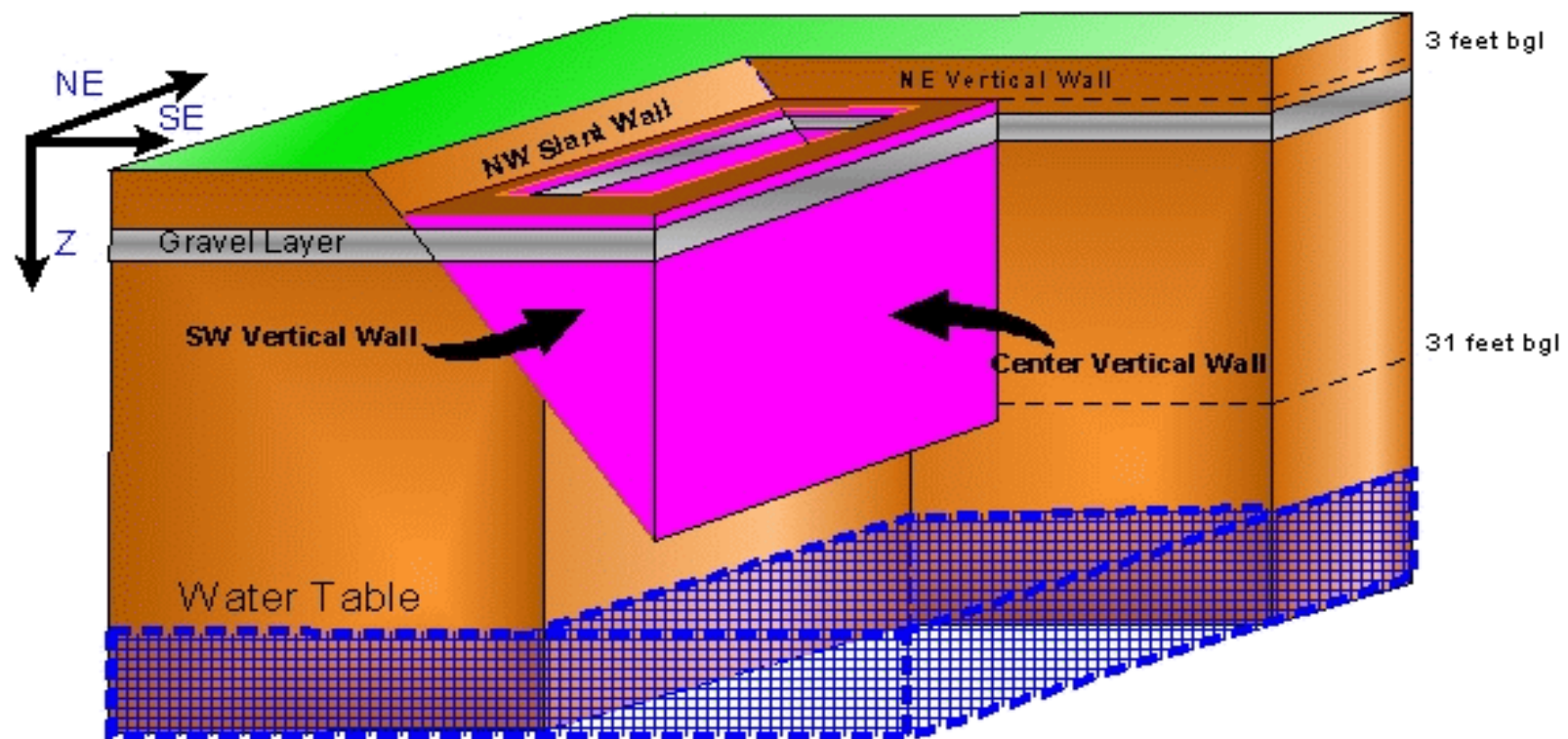


Figure 1. Conceptual Barrier



Figure 2. VLB during the excavation of lift 4 before sample collection.

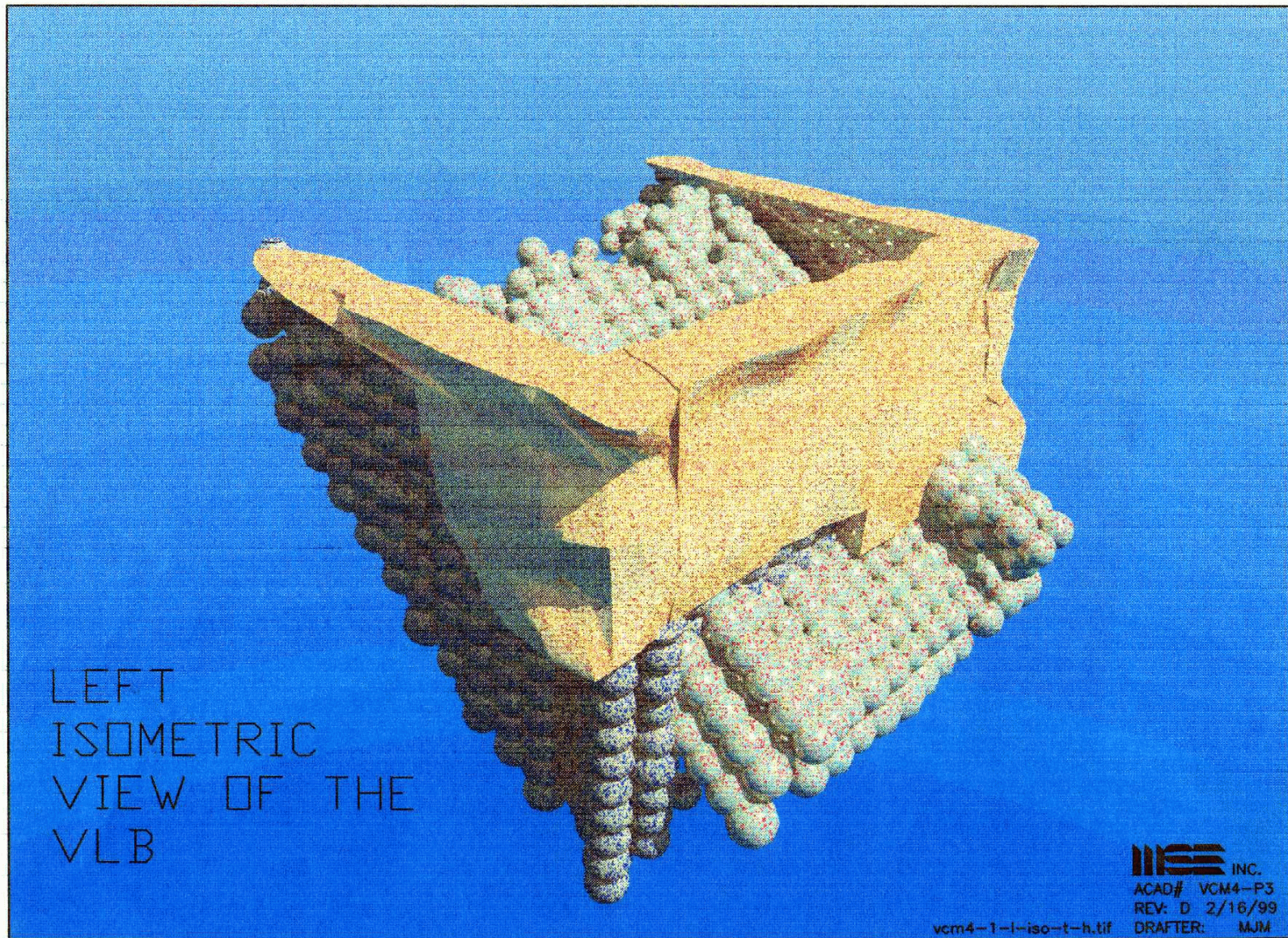


Figure 3. Left isometric view of the 3-D as-built model of the VLB.

Application of the Naturally-Occurring Deuterium Isotope to Tracing the Capillary Fringe

William C. Sidle

INTRODUCTION

Within the vadose zone, heterogeneity of sediments and temperate rainfall areas may combine to create a complex array of saturated lenses above the local water table. Discontinuous saturated units may exist with unsaturated conditions occurring below and above saturated lenses. Freeze and Cherry (1979) noted both perched water tables (ABC) and inverted water tables (ADC) (Figure 1) could occur particularly in mixed sand and clay geologic environments.

The capillary fringe or tension-saturated zone associated with these localized and possibly storm-flow induced water tables (Sidle, 1998) can vary in extent. Entrapped air during infiltration (Guymon, 1994) and grain-size distribution (Gillham, 1984) may result in a capillary fringe several meters from the saturated zone at atmospheric pressure. This is particularly the case for clay-rich sediments where air entry pressure has large negative matric potentials ($\phi_{\text{AIR}} < 0$) since

$$j = \frac{\mathbf{r}_{\text{ATM}} - \mathbf{r}_{\text{FLUID}}}{\mathbf{r}_{\text{WATER}} \cdot g} \quad (1)$$

Measurement and forecasting fluctuations of the capillary fringe may guide appropriate isolation of hydrophilic substances in the vadose zone. In many glaciofluvial sediment environments of temperate regions of the United States, multiple and discontinuous water tables occur above the local water table. Barriers installed into and through such hydrologic environments may be penetrated by rising water tables, albeit very localized. Gerla (1992) has noted that even small values of air-filled porosity are likely to be maintained and lead to a rise of a water table.

Early research (e.g. Zimmerman, et al., 1965) indicated deuterium was a useful tracer of soil moisture. Ongoing research into the application of naturally-occurring tracers for storm-water investigations may be transferable to vadose monitoring of barrier systems installed in the unsaturated zone. Work by Sidle and Lee (1999) has documented

the measurement of an isotope tracer for the purpose of detecting leakage of storm pipes and other barriers. Subtle isotopic differences can now be discerned at close intervals to trace origins, flow components, and even residence times of waters (Sidle, 1998). This preliminary research note provides a comparison of matric potential (ϕ), specific moisture content or saturation (θ), and deuterium ($\delta^2\text{H}$) isotope value for wet-weather flow study site. The focus is on outlining the capillary fringe at a pre-storm interval and during a storm event.

METHODS

The research site includes a known storm sewer paralleling an unnamed first-order stream (Longitude N 84° 35', Latitude E 39° 15') in the urban Mill Creek watershed, Hamilton County, Ohio. Clayey-sand glaciofluvial outwash deposits overlay carbonate bedrock, and the stream channel consists of erosional valley-fill deposits of sand and gravel. Twenty-two boring nests across a 110 m transect normal to the stream identified several sand lenses within a silty-clay matrix (Sidle and Lee, 1999). The unsaturated zone is approximately 2.5 m thick where the capillary fringe experiments were conducted.

These borings into the vadose zone encountered perched water tables above the local water table. Three nested borings with one pair each encountered three perched water tables. Of these borings, three holes were instrumented with modified USEPA vacuum-type tensiometers (Sidle, 1997) that included multiple ceramic cups at approximately 0.1 m intervals in the same boring. Each tensiometer array was capable of a 2 m extension. Matric potential was recorded electronically prior to a storm event. Soil moisture content characteristic curves generated for the alluvial sediments and transported soils were calibrated with matric potential readings and further checked with selected gravimetric analyses. Lysimeters were fitted into the other nested three borings. Water sampling was collected by vacuum pump from 0.1 m intervals prior to a storm event. Both tensiometer and lysimeter data were collected prior to a storm event on March 1, 1997. Deuterium samples were filtered through in-line 0.45 μm polycarbonate filters and were collected in 500 ml amber glass bottles.

Deuterium (^2H) is a naturally-occurring heavy isotope of hydrogen with a mass of 2. When phase changes (e.g. evaporation) occur in the hydrologic cycle, heavier (^2H) and lighter (^1H) isotopes fractionate, thus imparting a unique isotopic signature to that process (e.g. rainfall event). Very small fractionations may be possible and can be discriminated with preparations techniques for isotope ratio mass spectrometry (IRMS). These subtle $\delta^2\text{H}$ fractionations may occur where vadose air pressures are significant during infiltration (de Marsily, 1986). Generally though, a water molecule isotope, maintains its source signature through the subsurface into the receiving water or water table, unless significant mixing occurs with another water source. At least this has been conventional thought partly predicated on available instrument sensitivity.

Natural abundance of deuterium is 0.015 % and is measured as the ratio $^2\text{H}/^1\text{H}$ in an IRMS. Hydrogen isotope δ -values, are expressed in parts per thousand (per mil or ‰) difference from the international reference VSMOW (Vienna Standard Mean Ocean Water) as

$$\delta^2\text{H}_{\text{sample}} \text{‰} = \left[\frac{(^2\text{H}/^1\text{H})_{\text{sample}}}{(^2\text{H}/^1\text{H})_{\text{reference}}} - 1 \right] \bullet 1000 \text{‰ VSMOW} \quad (1)$$

Further, VSMOW corrected values are normalized to VSMOW-SLAP (Standard Light Antarctic Precipitation) scale (Coplen (1988)). For example, a δ -value of -20‰ indicates that the sample contains 20 per mil less ^2H than the reference or is depleted by 20‰ . Preparation of hydrogen from water samples was completed with the Cr catalyst in the reaction:

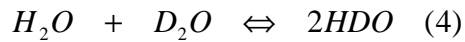


after Gehre et al (1996) and Sidle (1998). The on-line HD preparation system is connected directly to a Finnigan MAT Delta+ IRMS. Precision for $\delta^2\text{H}$ was 0.2‰ .

RESULTS AND DISCUSSION

Matric potential data (Table 1) does indicate variable unsaturated conditions. Boring 1 represents a relatively smooth progression toward saturation below the near surface 0.1 m interval. Matric potential versus soil moisture (Figure 2) is complex in Boring 3. It is difficult to infer the number of possible capillary fringes present associated with multiple perched zones (Hillel, 1988). There may be significant hysteresis (Lehmann et al., 1998) superimposed on these zones.

From prior test borings it is known that at least three perched zones exist beneath this experimental site. Figure 3 shows schematically these zones and inferred capillary fringes that may exist. A total of four capillary fringes should be present, including that above the local water table, in this glaciofluvial unit. Deuterium values (Table 1) generally become progressively more depleted with depth. The exchange reactions



are sensitive to atmospheric vapor/liquid processes (Ingraham and Criss, 1998) but reach equilibrium conditions at very shallow depths. Generally the δ^2H values of shallow ground waters represent a surrogate for local precipitation δ^2H values. Recharge then is smoothed out as a result of the infiltration through the unsaturated zone. Percolates from lysimeters generally smooth out the local precipitation recharge in temperate climates and is a common observation long recognized (e.g. Eichler, 1965). Seasonal composition fluctuations smooth out as a result of the transition of water through the unsaturated zone. Yet the δ^2H data (Table 1) indicate variable enrichments and depletions. It is possible that there are variable interstitial waters present although erratic δ^2H values are expected to be a temporary nonequilibrium condition of equations (3) and (4).

Instead the shifts in δ^2H at depth (Figure 4) are interpreted as indicative of increasing water content. Each of the perched units would be saturated with possibly an earlier recharged source of water providing a different δ^2H signature. If these perched

waters remained isolated, their capillary fringes would also reflect the $\delta^2\text{H}$ differences. It is also possible that there is simply variable interstitial waters present. Several possible capillary fringe boundaries are suggested. A capillary fringe (CF1) in Boring 1 may be approached near 0.4 m where $\delta^2\text{H}$ jumps to -58.2 ‰ VSMOW. A second capillary fringe (CF2) is inferred in Borings 2 and 3 at approximately 0.5 m with $\delta^2\text{H}$ values shifting to -60.2 ‰ VSMOW and -60.1 ‰ VSMOW respectively. Another capillary fringe may be present at 0.7 m in Boring 3 where $\delta^2\text{H}$ jumps to -61.3 ‰ VSMOW. Boring 3 was sampled at 1.4 m depth and it appears that the capillary fringe (CF4) is encountered. From earlier work (Sidle and Lee, 1999), it is known that the local water table is approximately 1.65 m depth.

CONCLUSION

Naturally-occurring deuterium is a useful tracer of subsurface hydrologic processes. A possible application includes the identification of capillary fringes in the vadose zone. Multiple and discontinuous water tables persist in many temperate regions, under various hydrogeologic conditions. It would appear that careful measurements of deuterium can augment more traditional indicators of soil moisture in the unsaturated zone. Possibly then leak detection of barrier systems can be improved.

ACKNOWLEDGEMENTS

This research is part of wet-weather flow and water quality program initiatives being focused on urban watersheds. The Groundwater Research Company conducted the drilling and sampling operations. Analyses were completed at the Isotope Hydrology Laboratory at the U. S. Environmental Protection Agency (USEPA). Dr. P.Y. Lee supplied the instruments and assisted in their calibration.

REFERENCES

- Coplen, T.B. 1988. Normalization of oxygen and hydrogen isotope data. Chem. Geol. 72, 293-294 pp.
- de Marsily, G. 1986. Quantitative Hydrogeology. Academic Press. 440 pp.

- Eichler, R. 1965. Deuterium isotopengeochemie des Grund- und Oberflächenwassers. Geol. Rundsch. 55. 144-150 pp.
- Freeze, R.A. and Cherry, J.A. 1979. Groundwater. Prentice Hall. 604 pp.
- Gehre, M. Hoefling, Kowski, P., and Strauch, G. 1996. Sample preparation device for quantitative hydrogen isotope analyses using chromium metal. Anal. Chem. 68. 4414-4417 pp.
- Gerla, P. J. 1992. The relationship of water-table changes to the capillary fringe, evapotranspiration, and precipitation in intermittent wetlands. Wetlands. 12. 91-98 pp.
- Gillham, R.W. 1984. The capillary fringe and its effect on water-table response. J. Hydrol. 67. 307-324 pp.
- Guymon, G.L. 1994. Unsaturated Zone Hydrology. Prentice Hall. 210 pp.
- Hillel, D. and Baker, R.S. 1988. A descriptive theory of fingering during infiltration into layered soils. Soil Sci. 146. 51-56 pp.
- Ingraham, N.L. and Criss, R.E. 1998. The effect of vapor pressure on the rate of isotopic exchange between water and vapor. Chem. Geol. 150. 287-292 pp.
- Lehmann, P., Stauffer, F., Hinz, C., Dury, O., and Flöhler, H. 1998. Effect of hysteresis on water flow in a sand column with a fluctuating capillary fringe. J. Contam. Hydrol. 33. 81-100 pp.
- Sidle, W.C. 1997. Comparison of on-line H₂ –water equilibration method and off-line Zn-catalyst method for determination of deuterium. U.S. Environmental Protection Agency Technical Memorandum: NRMRL\WSWRD\WQMB 97-2. 24 pp.
- _____. 1998. Basis and application of environmental isotopes for resolution of hydrological problems: a review. Environmental Monitoring and Assessment. 52. 389-410 pp.
- _____ and Lee, P.Y. 1999. Urban storm water tracing with the naturally-occurring deuterium isotope. Water Env. Res. (in press).
- Zimmerman, U., Munnich, K.O., and Roether, W. 1965. Tracers determine movement of soil moisture and evaporation. Science. 152. 346-347 pp.

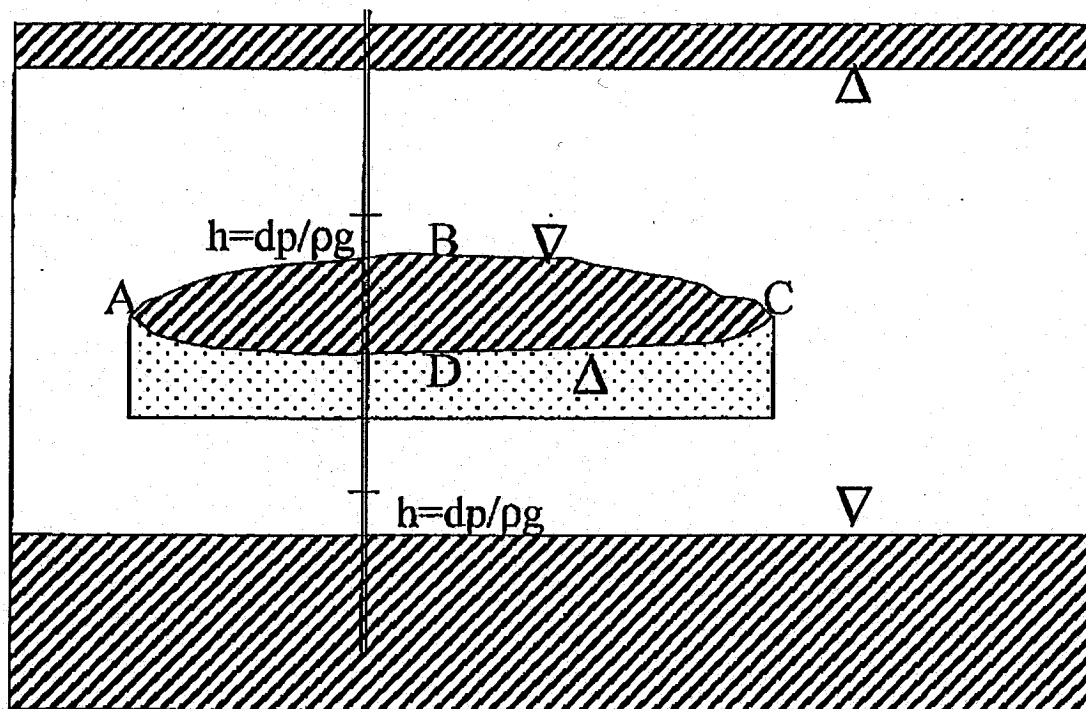


Figure 1 Schematic representation of a perched water table (ABC) and an inverted water table (ADC) above a local water table

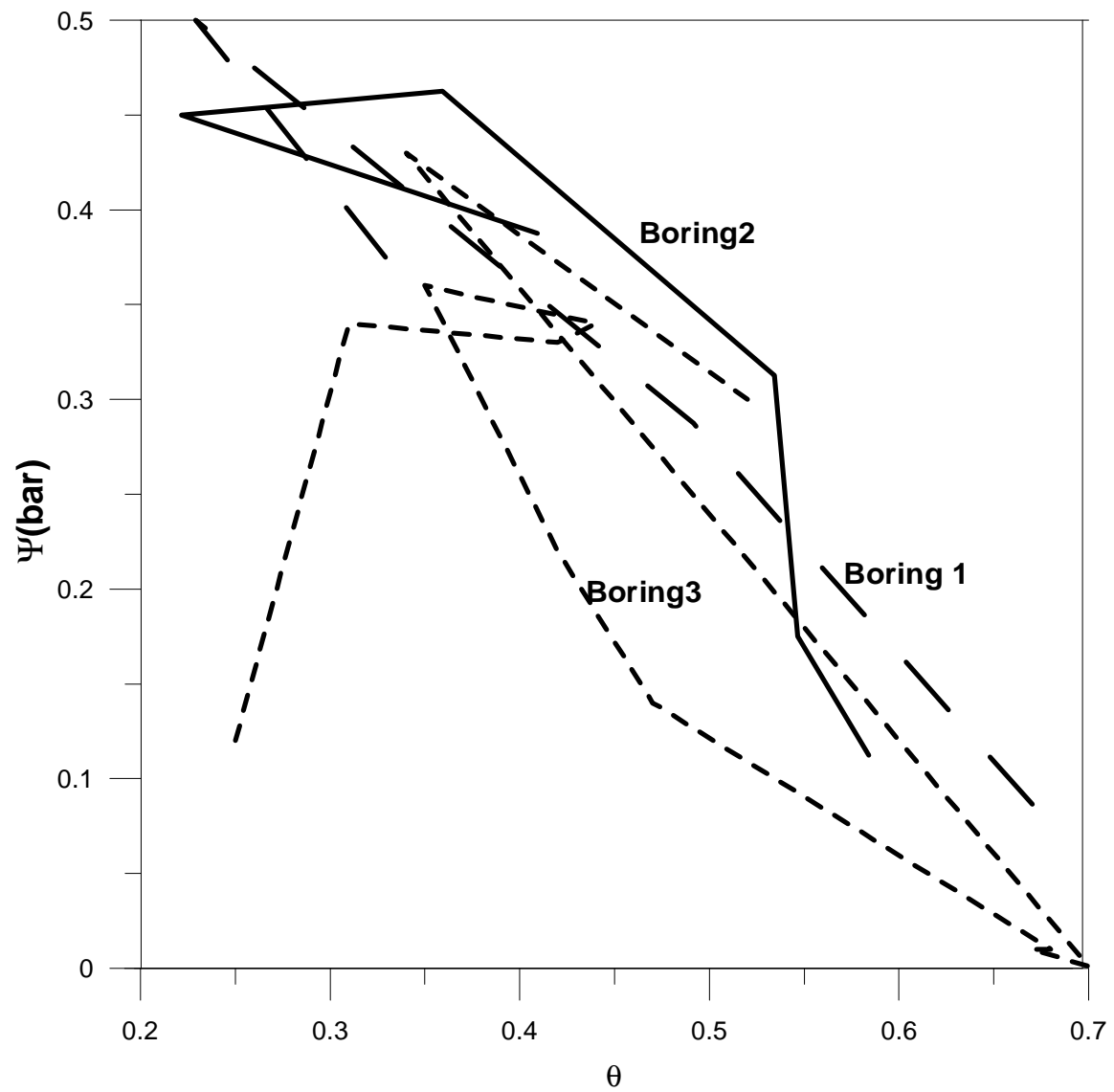


Figure 2 Specific Moisture (θ %), versus matric potential (ψ cm) in Boring 1 and Boring 3 into the vadose zone at the experimental storm water research site (Mt. Healthy, OH).

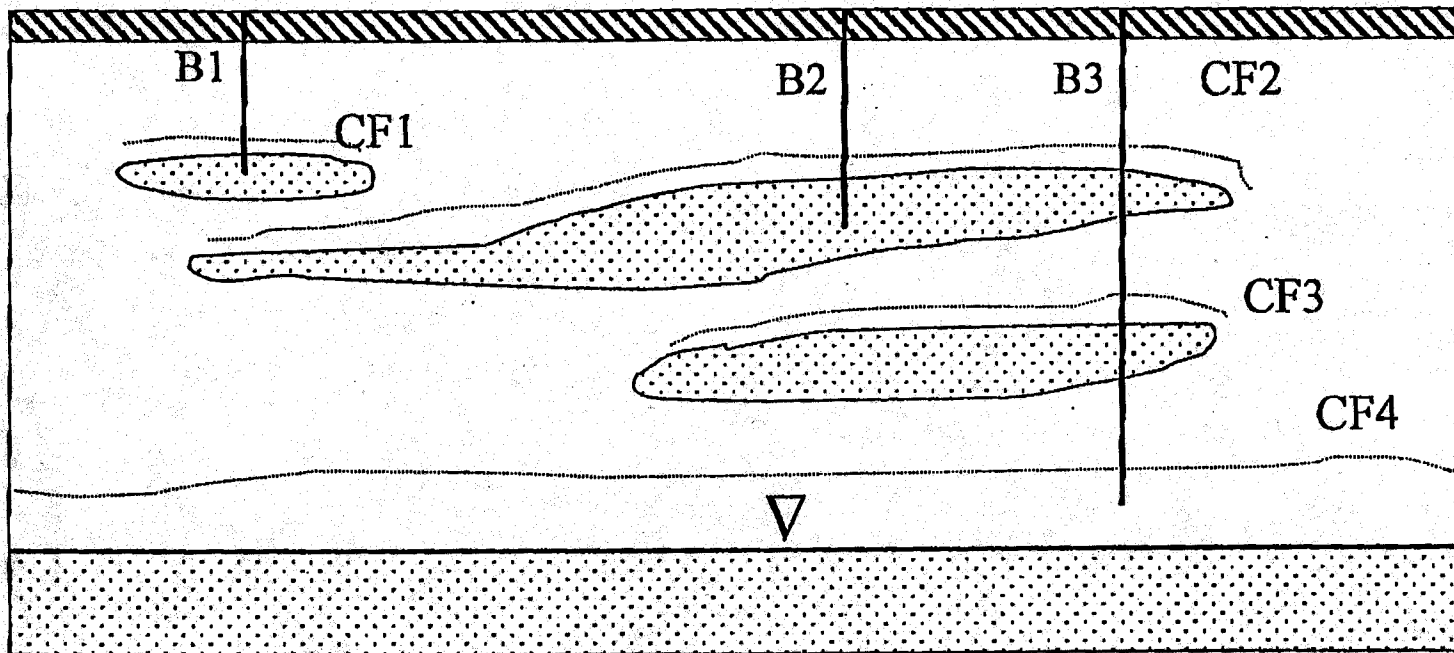


Figure 3 Schematic representation of capillary fringes (CF1-CF4) associated with three perched water tables above a local water table, inferred from three borings into the vadose zone at the experimental storm water research site (Mt. Healthy, OH).

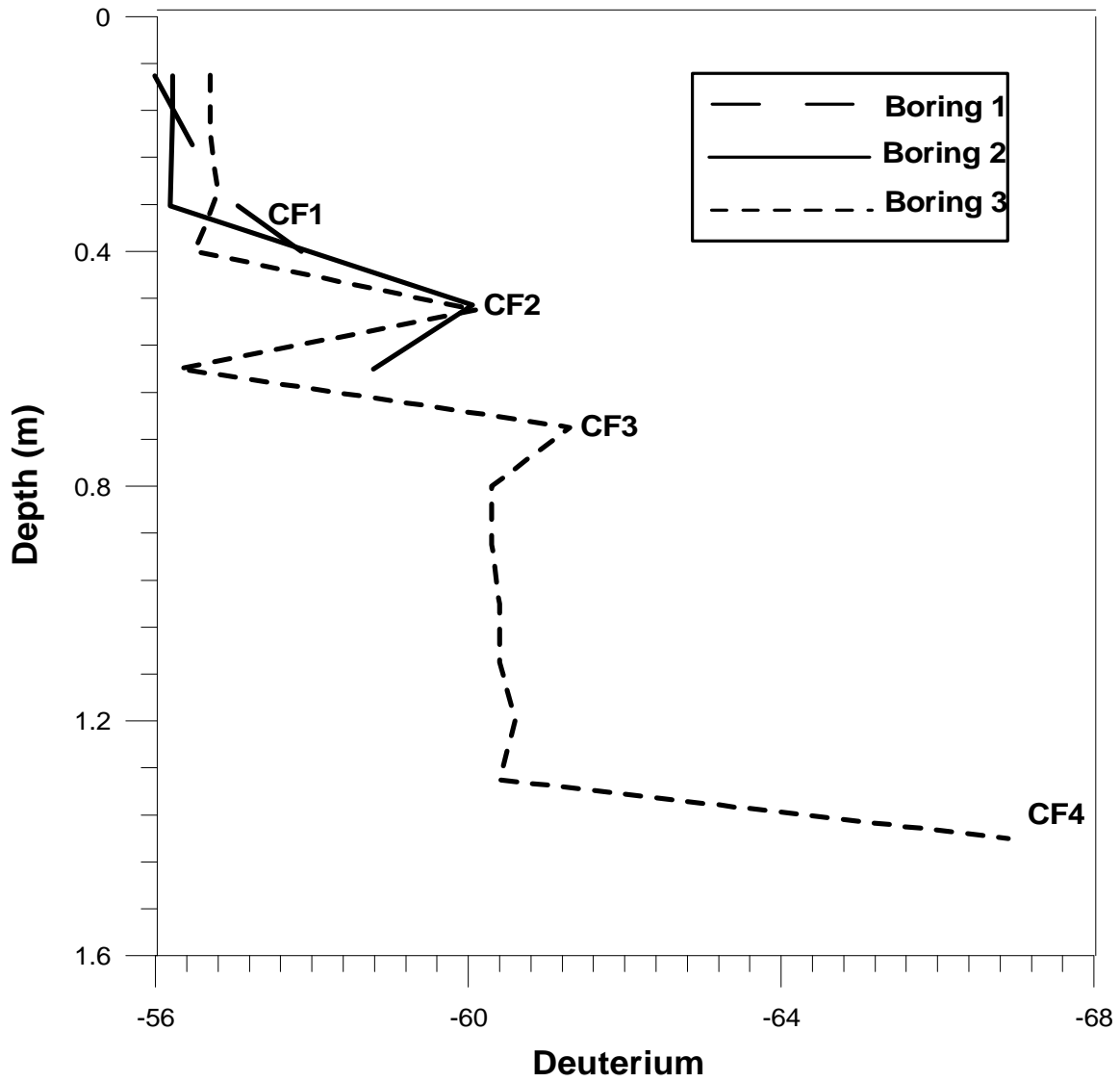


Figure 4 Deuterium ($\delta^2\text{H}$) versus depth (m) with suggested capillary fringes (CF1-CF4) in three borings into the vadose zone at the experimental storm water research site (Mt. Healthy, OH).

Boring 1				Boring 2				Boring 3			
(m)	ψ	θ	δ^2D	(m)	ψ	θ	δ^2D	(m)	ψ	θ	δ^2D
0.1	0.30	0.31	-56.0	0.1	0.31	0.47	-56.3	0.1	0.12	0.25	-56.7
0.2	0.40	0.23	-56.3	0.2	0.36	0.32	-56.3	0.2	0.34	0.31	-56.7
0.3	0.23	0.44	-56.8	0.3	0.37	0.43	-56.2	0.3	0.33	0.42	-56.8
0.4	0.05	0.60	-58.2	0.4	0.25	0.57	-58.4	0.4	0.34	0.44	-56.5
				0.5	0.14	0.58	-60.2	0.5	0.36	0.35	-60.1
				0.6	0.09	0.61	-58.9	0.6	0.22	0.42	-56.3
								0.7	0.14	0.47	-61.3
								0.8	0.01	0.68	-60.3
								0.9	0.01	0.67	-60.3
								1.0	0.001	0.70	-60.4
								1.1	0.001	0.70	-60.4
								1.2	0.001	0.70	-60.6
								1.3	0.43	0.34	-60.4
								1.4	0.30	0.52	-66.9

Table 1

Experimental storm water research site (Mt. Healthy, OH) data for matric potential (ψ cm), moisture (θ %), and deuterium (δ^2H) in three borings into the vadose zone.